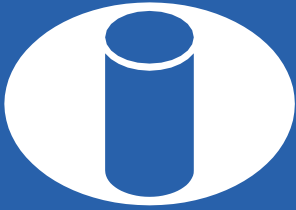


ISSN 1983-4195



**IBRACON**

**IBRACON Structures and Materials Journal**  
Revista IBRACON de Estruturas e Materiais

---

**Volume 13, Number 5**  
October 2020



# IBRACON Structures and Materials Journal

## Revista IBRACON de Estruturas e Materiais

### Contents

*Analysis of constructive parameters of vertical reinforced concrete structure with self-compacting concrete*..... 13501  
J. H. F. SERRA and A. E. B. CABRAL

*The cover thickness design of concrete structures subjected to chloride ingress from RBDO solution technique*..... 13502  
G. P. PELLIZER and E. D. LEONEL

*Study of the influence of jiggling of recycled coarse aggregate on the compressive strength of concrete*..... 13503  
G. N. MALYSZ, D. C. C. DAL MOLIN and A. B. MASUERO

*Proposition of a simplified analytical design procedure for lattice girder slabs with shuttering in cold-formed steel lipped channel section* ..... 13504  
L. F. FAVARATO, A. V. S. GOMES, D. C. M. CANDIDO, A. F. G. CALEZANI, J. C. V. PIRES and J. A. FERRARETO

*A simplified numerical approach to the evaluation of residual shaft friction induced by concrete curing in drilled shafts on granular soils*..... 13505  
A. B. BORGES, R. V. LINN, F. SCHNAID and S. MAGHOUS

*A multi-physics modelling based on coupled diffusion equations to simulate the carbonation process* ..... 13506  
M. OLIVEIRA, M. AZENHA and P. LOURENÇO

*Strength optimization of reactive powder concrete* ..... 13507  
A. B. ROHDEN, A. P. KIRCHHEIM and D. DAL MOLIN

*Ultrasonic investigation on the effectiveness of crack repair in concrete* ..... 13508  
F. C. SOUZA and R. C. A. PINTO

*Structure and nanomechanical characterization of synthetic calcium-silicate-hydrate with poly-methacrylic acid*..... 13509  
F. PELLISSER, P. J. P. GLEIZE and A. MIKOWSKI

*Numerical simulation of steel-concrete composite beams: updated strategies of finite element modeling*..... 13510  
M. E. BENINCÁ, R. J. SCHMITZ and I. B. MORSCH

*Parametric analysis of analytical solutions of the rollover of precast beams on bearing pads* ..... 13511  
M. F. A. OLIVEIRA, P. A. KRAHL and M. C. V. LIMA

*Parametric study of the strength of reinforced concrete polygonal sections submitted to oblique composite flexion*..... 13512  
L. P. SOUZA and M. A. ARGENTA

*Numerical analysis of composite steel and concrete beams subjected to fire under different support conditions*..... 13513  
L. C. ROMAGNOLI and V. P. SILVA

*Study of the physical and mechanical properties of permeable concrete with the addition of TiO<sub>2</sub> for the treatment of sewage* ..... 13514  
W. M. P. ARAÚJO, F. P. AVELINO, M. S. PICANÇO and A. N. MACÊDO

*Nonlinear analysis of monolithic beam-column connections for reinforced concrete frames* ..... 13515  
G. ALVA and A. TSUTAKE



Cover: Parametric Tower

Courtesy: Marcela Noronha P. de O. e Sousa



**IBRACON Structures and Materials Journal** is published bimonthly (February, April, June, August, October, and December) by IBRACON.

**IBRACON**  
Instituto Brasileiro do Concreto  
Founded in 1972

Av. Queiroz Filho, nº 1700 — sala 407/408  
Torre D — Villa Lobos Office Park  
CEP 05319-000 — São Paulo, SP — Brazil  
Phone: +55 11 3735-0202  
Fax: +55 11 3733-2190  
E-mail: [riem@ibracon.org.br](mailto:riem@ibracon.org.br)  
Website: <http://www.ibracon.org.br>

Cover design & Layout:  
Editora Cubo  
[www.editoracubo.com.br](http://www.editoracubo.com.br)

---

## Aims and Scope

### Aims and Scope

The IBRACON Structures and Materials Journal (in Portuguese: Revista IBRACON de Estruturas e Materiais) is a technical and scientific divulgation vehicle of IBRACON (Brazilian Concrete Institute), published every two months. Each issue has 12 to 15 articles and, possibly, a technical note and/or a technical discussion regarding a previously published paper. All contributions are reviewed and approved by professionals with recognized scientific competence in the area. The IBRACON Structures and Materials Journal is an open access Journal, free of charges for authors and readers.

### Objectives

The IBRACON Structures and Materials Journal's main objectives are:

- Present current developments and advances in concrete structures and materials.
- Make possible the better understanding of structural concrete behavior, supplying subsidies for a continuous interaction among researchers, producers, and users.
- Stimulate the development of scientific and technological research in the areas of concrete structures and materials, through papers peer-reviewed by a qualified Editorial Board.
- Promote the interaction among researchers, constructors and users of concrete structures and materials and the development of Civil Construction.
- Provide a vehicle of communication of high technical level for researchers and designers in the areas of concrete structures and materials.

### Submission Procedure

The procedure to submit and revise the contributions, as well as the formats, are detailed in the Journal Website ([ismj.org](http://ismj.org)).

The papers and the technical notes are revised by at least two reviewers indicated by the editors. Discussions and replies are accepted for publication after a review by the editors and at least one member of the Editorial Board. In case of disagreement between the reviewer and the authors, the contribution will be sent to a specialist in the area, not necessarily linked to the Editorial Board. Conflict of interests is carefully handled by the Editors.

### Contribution Types

The Journal will publish original papers, short technical notes, and paper discussions. Original papers will be accepted if they are in accordance with the objectives of the Journal and present quality of information and presentation. A technical note is a brief manuscript. It may present a new feature of research, development, or technological application in the areas of Concrete Structures and Materials, and Civil Construction. This is an opportunity to be used by industries, companies, universities, institutions of research, researchers, and professionals willing to promote their works and products under development.

A discussion is received no later than 3 months after the publication of the paper or technical note. The discussion must be limited to the topic addressed in the published paper and must not be offensive. The right of reply is granted to the Authors. The discussions and the replies are published in the subsequent issues of the Journal.

The submission file should be in accordance with the paper template available at the Journal Website. It is recommended that the length of the papers does not exceed 25 pages. Where available, URLs for the references should be provided.

The IBRACON Structures and Materials Journal will conduct the review process for manuscripts submitted in English. Titles, abstracts, and keywords are presented in English, and in Portuguese or Spanish. Articles and technical notes are peer-reviewed and only published after approval of the reviewers and the Editorial Board.

Once accepted, an article is typeset according to the journal layout. The author will be required to review and approve the galleys before publishing. At this stage only typesetting errors will be considered.

### Internet Access

The IBRACON Structures and Materials Journal Webpage is available at <http://ismj.org>.

### Sponsors

The funds for the maintenance of the Journal are currently obtained from the IBRACON. The Journal is not supposed to be maintained with funds from private sponsorship, which could diminish the credit of the publications.

### Photocopying

Photocopying in Brazil. Brazilian Copyright Law is applicable to users in Brazil. IBRACON holds the copyright of contributions in the journal unless stated otherwise at the bottom of the first page of any contribution. Where IBRACON holds the copyright, authorization to photocopy items for internal or personal use, or the internal or personal use of specific clients, is granted for libraries and other users registered at IBRACON.

### Copyright

All rights, including translation, reserved. Under the Brazilian Copyright Law No. 9610 of 19th February, 1998, apart from any fair dealing for the purpose of research or private study, or criticism or review, no part of this publication may be reproduced, stored in a retrieval system, or transmitted in any form or by any means, electronic, mechanical, photocopying, recording or otherwise, without the prior written permission of IBRACON. Requests should be directed to IBRACON:

### IBRACON

Av. Queiroz Filho, 1700 – sala 407/408 – Torre D  
Villa Lobos Office Park  
05319-000 – Vila Hamburguesa  
São Paulo – SP  
Phone: +55 (11) 3735-0202  
E-mail: [riem@ibracon.org.br](mailto:riem@ibracon.org.br)

### Disclaimer

Papers and other contributions and the statements made or opinions expressed therein are published on the understanding that the authors of the contribution are the only responsible for the opinions expressed in them and that their publication does not necessarily reflect the views of IBRACON or of the Journal Editorial Board.

---

## Editorial Board

### Editor-in-chief emeritus

José Luiz Antunes de Oliveira e Sousa, Universidade Estadual de Campinas - UNICAMP, Campinas, SP, Brazil, jls@fec.unicamp.br

### Editor-in-chief

Guilherme Aris Parsekian, Universidade Federal de São Carlos – UFSCAR, São Carlos, SP, Brazil, parsekian@ufscar.br

### Associate Editors

Antônio Carlos dos Santos, Universidade Federal de Uberlândia – UFU, Uberlândia, MG, Brazil  
Bernardo Horowitz, Universidade Federal de Pernambuco - UFPE, Recife, PE, Brazil  
Bernardo Tutikian, Universidade do Vale do Rio dos Sinos – UNISINOS, São Leopoldo, RS, Brazil  
Bruno Briseghella, Fuzhou University, Fujian, China  
David Oliveira, Jacobs Engineering, Sydney, Australia  
Edgar Bacarji, Universidade Federal de Goiás - UFG, Goiânia, GO, Brazil  
Edna Possan, Universidade Federal da Integração Latino Americana – UNILA, Foz do Iguaçu, PR, Brazil  
Fernando Pelisser, Universidade Federal de Santa Catarina – UFSC, Florianópolis, SC, Brazil  
Fernando Soares Fonseca, Brigham Young University – BYU, Provo, UT, USA  
José Marcio Fonseca Calixto, Universidade Federal de Minas Gerais – UFMG, Belo Horizonte, MG, Brazil  
José Tadeu Balbo Universidade de São -Paulo, São Paulo, SP, Brazil  
Leandro Mouta Trautwein, Universidade Estadual de Campinas - UNICAMP, Campinas, SP, Brazil  
Leandro F. M. Sanchez, University of Ottawa, Ottawa, Canada  
Lia Lorena Pimentel, Pontifícia Universidade Católica de Campinas – PUCCAMP, Campinas, SP, Brazil  
Luís Oliveira Santos, Laboratório Nacional de Engenharia Civil, Lisboa, Portugal  
Mark G Alexander, University of Cape Town, Cape Town, South Africa  
Marco Di Prisco, Politecnico di Milano, Milan, Italy  
Mário Jorge de Seixas Pimentel, Universidade do Porto - FEUP, Porto, Portugal  
Maurício de Pina Ferreira, Universidade Federal do Pará - UFPA, Belém, PA, Brazil  
Mauro de Vasconcellos Real, Universidade Federal do Rio Grande – FURG, Rio Grande, RS, Brazil  
Nigel G. Shrive, University of Calgary, Calgary, Canada  
Osvaldo Luís Manzoli, Universidade Estadual Paulista “Júlio de Mesquita Filho” - UNESP, Bauru, SP, Brazil  
Rebecca Gravina, RMIT University, Melbourne, Australia  
Ricardo Carrazedo, Universidade de São Paulo - USP, São Carlos, SP, Brazil  
Samir Maghous, Universidade Federal do Rio Grande do Sul - UFRGS, Porto Alegre, RS, Brazil  
Sérgio Hampshire de Carvalho Santos, Universidade Federal do Rio de Janeiro - UFRJ, Rio de Janeiro, RJ, Brazil  
Túlio Nogueira Bittencourt, Universidade de São -Paulo, São Paulo, SP, Brazil  
Vladimir Guilherme Haach, Universidade de São Paulo - USP, São Carlos, SP, Brazil  
Yury Villagrán Zaccardi, Universidad Tecnológica Nacional Facultad Regional La Plata, Buenos Aires, Argentina

### Editorial Comission

Antônio Carlos R. Laranjeiras, ACR Laranjeiras, Salvador, BA, Brazil  
Emil de Souza Sánchez Filho, Universidade Federal Fluminense, UFF, Rio de Janeiro, RJ, Brazil  
Geraldo Cechella Isaia, Universidade Federal de Santa Maria, UFSM, Santa Maria, RS, Brazil  
Gonzalo Ruiz, Universidad de Castilla-La Mancha - UCLM, Ciudad Real, Spain  
Ivo José Padaratz, Universidade Federal de Santa Catarina - UFSC, Florianópolis, SC, Brazil  
Joaquim de Azevedo Figueiras, Faculdade de Engenharia da Universidade do Porto - FEUP, Porto, Portugal  
Paulo Monteiro, University of California Berkeley, Berkeley, CA, USA  
Pedro Castro Borges, CINVESTAV, Mérida, Yuc., México  
Vladimir Antônio Paulon, Universidade Estadual de Campinas - UNICAMP, Campinas, SP, Brazil

### Former Editors

Américo Campos Filho, Universidade Federal do Rio Grande do Sul - UFRGS, Porto Alegre, RS, Brazil  
Denise C. C. Dal Molin Universidade Federal do Rio Grande do Sul - UFRGS, Porto Alegre, RS, Brazil  
Eduardo Nuno Brito Santos Júlio, Instituto Superior Técnico - IST, Lisboa, Portugal  
Guilherme Sales Melo, Universidade de Brasília, UnB, Brasília, DF, Brazil  
Luiz Carlos Pinto da Silva Filho, Universidade Federal do Rio Grande do Sul - UFRGS, Porto Alegre, RS, Brazil  
Mounir Khalil El Debs, Universidade de São Paulo - USP, São Carlos, SP, Brazil  
Nicole Pagan Hasparyk, Eletrobras Furnas, Aparecida de Goiânia, GO, Brazil  
Paulo Helene, Universidade de São Paulo - USP, São Paulo, SP, Brazil  
Roberto Caldas de Andrade Pinto, Universidade Federal de Santa Catarina - UFSC, Florianópolis, SC, Brazil  
Ronaldo Barros Gomes, Universidade Federal de Goiás - UFG, Goiânia, GO, Brazil  
Romilde Almeida de Oliveira, Universidade Católica de Pernambuco - UNICAP, Recife, PE, Brazil  
Romildo Dias Toledo Filho, Universidade Federal do Rio de Janeiro - UFRJ, Rio de Janeiro, RJ, Brazil  
Rubens Machado Bittencourt, Eletrobras Furnas, Aparecida de Goiânia, GO, Brazil



## **Board of Direction 2019/2021 Biennium**

### **President**

Paulo Helene

### **1<sup>st</sup> Vice-President Director**

Júlio Timerman

### **2<sup>nd</sup> Vice-President Director**

Enio José Pazini Figueiredo

### **Presidency Advisors**

Antônio Domingues de Figueiredo

Iria Lícia Oliva Doniak

Jairo Abud

Jorge Batlouni Neto

Luís Aurélio Fortes da Silva

Mario William Esper

Maurice Antoine Traboulsi

Paula Baillot

Simão Priskulnik

### **1<sup>st</sup> Director-Secretary**

Cláudio Sbrighi Neto

### **2<sup>nd</sup> Director-Secretary**

Carlos José Massucato

### **1<sup>st</sup> Treasurer Director**

Júlio Timerman

### **2<sup>nd</sup> Treasurer Director**

Hugo S. Armelin

### **Marketing Director**

Jéssika Pacheco

### **Marketing Director Advisor**

Guilherme Covas

### **Publications Director**

Guilherme Parsekian

### **Publications Director Advisor**

Túlio Nogueira Bittencourt

### **Event Director**

Rafael Timerman

### **Event Director Advisor**

Luis César De Luca

### **Technical Director**

José Tadeu Balbo

### **Technical Director Advisor**

Selmo Chapira Kuperman

### **Institutional Relations Director**

César Henrique Daher

### **Institutional Relations Director Advisor**

José Vanderley de Abreu

### **Course Director**

Leandro Moura Trautwein

### **Course Director Advisor**

Antônio Carlos dos Santos

### **Student Activities Director**

Jéssica Andrade Dantas

### **Student Activities Director Advisor**

Sandra Regina Bertocini

### **Personnel Certification Director**

Adriano Damásio Soterio

### **Personnel Certification Director Advisor**

Gilberto Antonio Giuzio

### **Research and Development Director**

Bernardo Tutikian

### **Research and Development Director Advisor**

Roberto Christ

## **Council 2019/2021 Biennium**

### **Individual Members**

Antônio Carlos dos Santos

Antônio Domingues de Figueiredo

Arnaldo Forti Battagin.

Bernardo Fonseca Tutikian

Carlos José Massucato

César Henrique Sato Daher

Cláudio Sbrighi Neto

Enio José Pazini Figueiredo

Hugo da Costa Rodrigues Filho

Inês Laranjeira da Silva Battagin

Iria Lícia Oliva Doniak

Jéssika Mariana Pacheco

José Tadeu Balbo

Leandro Moura Trautwein

Luiz Carlos de Almeida

Luiz Prado Vieira Júnior

Mário William Esper

Maurice Antoine Traboulsi

Rafael Timerman

Vladimir Antônio Paulon

### **Past President Members**

Eduardo Antônio Serrano

José Marques Filho

Júlio Timerman

Paulo Helene

Ronaldo Tartuce

Rubens Machado Bittencourt

Selmo Chapira Kuperman

Simão Priskulnik

Túlio Nogueira Bittencourt

### **Corporate Members**

ABCIC - Associação Brasileira da  
Construção Industrializada de Concreto –  
Iria Lícia Oliva Doniak

ABCP - Associação Brasileira de Cimento  
Portland – Paulo Camilo Penna

ABECE - Associação Brasileira de  
Engenharia e Consultoria Estrutural –  
João Alberto de Abreu Vendramini

ABESC - Associação Brasileira das  
Empresas de Serviços de Concretagem –  
Jairo Abud

EPUSP - Escola Politécnica da  
Universidade de São Paulo – Túlio  
Nogueira Bittencourt

FURNAS Centrais Elétricas S/A – Flávio  
de Lima Vieira

IPT - Instituto de Pesquisas Tecnológicas  
do Estado de São Paulo – José Maria de  
Camargo Barros

L. A. FALCÃO BAUER Centro  
Tecnológico – Patrícia Bauer

PhD Engenharia Ltda – Douglas de  
Andreza Couto

TQS Informática Ltda – Nelson Covas

VOTORANTIM Cimentos S/A –  
Maurício Bianchini



ORIGINAL ARTICLE

# Analysis of constructive parameters of vertical reinforced concrete structure with self-compacting concrete

*Análise de parâmetros construtivos de estrutura de concreto armado vertical com concreto autoadensável*

Jordana Herbster Ferraz Serra<sup>a</sup> Antonio Eduardo Bezerra Cabral<sup>a</sup>

<sup>a</sup>Federal University of Ceará – UFC, Post-Graduate Program in Civil Engineering (Structures and Civil Construction), Fortaleza, CE, Brasil

Received 15 November 2018

Accepted 07 April 2019

**Abstract:** The objective of this paper is to quantify the improvements due to the use of self-compacting concrete (SCC) as a replacement to a conventional Portland Cement Concrete (PCC) in the production of a reinforced concrete structure of a typical residential building in Brazil. To achieve the proposed objectives, a SCC mix was developed in the laboratory and tests were performed in the fresh and hardened states. Two floors, consisting of columns, beams and slabs, were built with SCC and a third with PCC. Pouring time and its generated noise, appearance of pathological manifestations after pouring, amount of labor required for pouring, costs and the risk of work-related accidents were evaluated. The results indicate that the floors produced with the SCC obtained 60.5% less pouring time, a reduction of 50% and 62.8% in the quantity and costs of labor, respectively; 260.8% reduction in the accident risk factor and, finally, a reduction of 56.4% in the total cost.

**Keywords:** self-compacting concrete, productivity, unit production ratio, costs.

**Resumo:** O objetivo deste artigo é quantificar as possíveis melhorias do uso do concreto autoadensável (CAA) em substituição ao concreto convencional plástico (CCV) na produção de uma estrutura de concreto armado de edificação vertical típica do Brasil. Para se atingir os objetivos propostos, um traço de CAA foi desenvolvido em laboratório, tendo sido executados ensaios no estado fresco e no estado endurecido. Dois pavimentos, constituídos de pilares, vigas e lajes, foram executadas em CAA e um terceiro foi executado em CCV. O tempo de concretagem e seu ruído gerado, o aparecimento de manifestações patológicas posteriormente à concretagem, a quantidade de mão de obra necessária para a concretagem, os custos e o risco de acidentes de trabalho foram avaliados. Os resultados obtidos indicam que os pavimentos produzidos com o CAA obtiveram tempo de concretagem 60,5% menor, redução de 50% e 62,8% na quantidade e custos de mão de obra, respectivamente, redução de 260,8% no fator de risco de acidentes e, por fim, uma redução no custo total de 56,4%.

**Palavras-chave:** concreto autoadensável, produtividade, RUP, custos.

**How to cite:** J. H. F. Serra, A. E. B. Cabral, “Analysis of constructive parameters of vertical reinforced concrete structure with self-compacting concrete,” *IBRACON Struct. Mater. J.*, vol. 13, no. 5, e13501, 2020, <https://doi.org/10.1590/S1983-41952020000500001>

## 1 INTRODUCTION

Self-compacting concrete (SCC) is already used in several countries, representing one of the greatest advances in concrete technology in recent decades. The SCC has the capacity to fill in all the spaces destined to it in the mold on its own. It does not require any external intervention or vibration, and it does not segregate or trap an excessive amount of air. Thus, its application is easier, faster, avoids pathological manifestations such as concreting nests, as well as eliminates the noise caused by vibrators. Additionally, it is possible to build more durable and economical structures by using SCC [1], [2].

**Corresponding author:** Antonio Eduardo Bezerra Cabral. E-mail: [eduardo.cabral@ufc.br](mailto:eduardo.cabral@ufc.br)

**Financial support:** JVS Engenharia and Research Group on Construction Materials and Structures (GPMATE) at the Federal University of Ceará (UFC).

**Conflict of interest:** Nothing to declare.



This is an Open Access article distributed under the terms of the Creative Commons Attribution License, which permits unrestricted use, distribution, and reproduction in any medium, provided the original work is properly cited.

Moreover, the use of SCC can also reduce the number of employees needed to carry out the concrete pouring, as it does not require any vibration nor spreading. In addition to shortening the pouring time, the use of SCC in construction buildings can potentially reduce the risk of the workers falling during the pouring spreading and vibrating phases [2].

To be classified as a SCC, the concrete must fulfill three requirements simultaneously: fluidity, passing ability and resistance to segregation [3]. In order to assure the proper behavior of the SCC in the fresh state, it is necessary to carry out the tests prescribed in ABNT NBR 15823, so that, once these requirements are met, it is also possible to meet the requirements for the concrete's hardened state. The structure of SCC is denser than one of conventional Portland cement concrete (PCC), in other words, there is less void volume, which provides a better adhesion between concrete and steel [4]. This can also contribute to a better mechanical behavior of the structural elements produced with SCC when compared to those produced with PCC.

SCC is vastly used in the precast concrete industry due to its better adjustment to variations in shape relatively to the PCC. In addition, the production in a precast concrete plant is more controlled than at construction sites. However, the employment of SCC is restricted to complex projects and special structures, since it can be dosed in construction sites or in concrete plants, with the same ease in manufacturing. [5].

In addition to SCC applications in the production of precast parts, there are examples of applications in tunnels, overpasses and roads in several countries, such as Sweden and France, where this concrete technology is widely used in the repair and structural strengthening of old structures, where the use of vibration is not advised, due to the risk of worsening the state of the structure. An example of this application is The Katelbridge bridge, in the Netherlands, which was repaired after 45 years of service, in 2002 [6].

Along with the advantages of the finished material, the use of SCC may turn out to be a way to enhance the productivity during the concreting of vertical projects, in view of the reduction of the manpower and waiting periods between concrete trucks, which results in a reduction on the overall construction cost. Brazilian civil construction has its own characteristics, with a focus on high employment of labor force [7]. However, there is no Brazilian standard to measure the productivity indexes for concrete pouring, making each company search for its own indexes, often with different criteria, so that comparison between companies is oftentimes difficult or even impossible.

Even with various advantages, there are still not many records of SCC use in Brazil, especially in vertical constructions. Although there is an increase, its use is still small, but the potential for expanding grows every day through research and practical applications. Therefore, the lack of studies, the need to adapt the technology to the construction reality in Brazil and, customarily, the higher cost of this type of concrete, are the main reasons why there are still few works that have used this constructive technology [8].

Hence, the objective of this article is to evaluate the use of self-compacting concrete to replace conventional concrete in a vertical building project in Brazil. The study was divided into the following stages: design of a self-compacting concrete mix with local materials, so that it meets the criteria in NBR 15823; applying the self-compacting concrete in a vertical construction, evaluating concreting time, amount of labor force needed, possible pathological manifestations in the structure and the related costs; comparing these data to those of regular Portland Cement Concrete.

## 2 METHODOLOGY

The methodology was divided into three stages. The first refers to the SCC laboratory mix design; the second, regards the application of the SCC in a vertical construction building; and the third, encompasses the comparative analysis between SCC and PCC, through the determination of indices.

### 2.1 SCC mix design at the laboratory

In the SCC mix design, it was used a Brazilian Portland cement type CP II F 32 with the physical and chemical characteristics shown in Table 1.

**Table 1.** Chemical and physical characteristics of used cement.

<b>Chemical composition (%)</b>		
		<b>Standards limits (NBR 11578)</b>
Loss of ignition	4.90%	< 6.5%
MgO content	3.41%	< 6.5%
SO <sub>3</sub> content	3.15%	< 4.0%
Fe <sub>2</sub> O <sub>3</sub> content	3.25%	-
Al <sub>2</sub> O <sub>3</sub> content	4.45%	-
CaO content	60.67%	-
SiO <sub>2</sub> content	19.48%	-
Insoluble waste	1.94%	< 2.5%
<b>Physical properties</b>		
<b>Compressive strength</b>		<b>Standards limits</b>
3 days	31.5 MPa	> 10 MPa
7 days	35.3 MPa	> 20 MPa
28 days	39.4 MPa	> 32 MPa
<b>Fineness</b>		
#200	1.83%	< 12%
#325	9.33%	Not applicable
<b>Blaine</b>	4568 cm <sup>2</sup> /g	> 2600 cm <sup>2</sup> /g
<b>Consistency water</b>	27.49%	Not applicable
<b>Setting time</b>		
Begin	2h:05min	> 1h
End	3h:04min	< 10h
<b>Hot expansibility</b>	0.38mm	< 5mm

The fine aggregate used was a quartz sand from a riverbed and the coarse aggregate was of granitic origin. The characteristics of the aggregates are shown in Table 2.

**Table 2.** Characterization of aggregates.

<b>Granulometry</b>				
<b>Sieve #</b>	<b>Fine (sand)</b>		<b>Coarse (gravel)</b>	
	<b>% Average Retained</b>	<b>% Retained Accumulated</b>	<b>% Average Retained</b>	<b>% Retained Accumulated</b>
12.7	-	-	0.3	0
9.5	-	-	11.8	12
6.3	-	-	46.1	58
4.8	8	8	20.5	78.6
2.36	5	13	16.6	95.2
1.18	13.7	26.7	2.6	97.8
0.6	33.7	60.4	0.5	98.3
0.3	30.9	91.3	0.5	98.8
0.15	5.4	96.7	1.2	100
Bottom	3	100	0	-
Maximum Dimension	6.3mm		12.7	
F.M.	2.96		5.8	
<b>Physical Indexes</b>				
	<b>Sand</b>	<b>Standard method</b>	<b>Gravel</b>	<b>Standard method</b>
Specific gravity	2.60 g/cm <sup>3</sup>	NBR NM 52 e 53	2.69 g/cm <sup>3</sup>	NBR NM 52 e 53
Bulk density	1.52 g/cm <sup>3</sup>	NBR NM 45	1.45 g/cm <sup>3</sup>	NBR NM 45

The mineral addition used was cretaceous natural calcium carbonate, of marine sedimentary origin, with high purity, which is applied as filler in many products. It presents a crystalline structure and its specific density is  $2.70 \text{ g/cm}^3$ , according to the supplier. Its physical and chemical characteristics are described in Table 3.

**Table 3.** Characterization of limestone filler used in the production of SCC.

Physical characteristics	
Humidity (%)	0.3
Bulk density ( $\text{g/cm}^3$ )	1.2
pH	9
Chemical Characteristics	
CaCO <sub>3</sub> (%)	92.5
CaO (%)	52.5
Fe <sub>2</sub> O <sub>3</sub> (%)	0.05
Al <sub>2</sub> O <sub>3</sub> (%)	0.03
SiO <sub>2</sub> (%)	0.35
MgO (%)	1.5
Pb (mg/g)	0.06
Cd (mg/g)	0.009
Loss of ignition (900°C) (%)	42.5

The chemical admixtures used in this research were: a third generation superplasticizer based on polycarboxylate, free of chlorides, with 40% of solids, density of  $1.1 \text{ g/cm}^3$ , pH equal to 6 and soluble in water; and a setting time retardant multifunction plasticizer as a dispersing agent for cement particles, with a density of  $1.2 \text{ g/cm}^3$ , pH equal to 9 and soluble in water. The information regarding the admixtures was provided by the manufacturer. The water used in the tests came from the public supply system in the city of Fortaleza, Brazil.

The concrete mix design was based on the method proposed by Gomes [9]. This method is divided into three phases: obtaining the composition of the paste, determining the proportion of the mixture, and selecting paste content. The mix was designed for a 30 MPa characteristic strength ( $f_{ck}$ ) at 28 days.

Table 4 shows the PCC mix, from the concrete plant hired by the construction, and the SCC mix, which was obtained in the laboratory and later adapted for the concrete plant to suit the needs of the construction and the concrete supplier.

**Table 4.** Concrete mixtures.

Material	PCC	SCC
Cement (kg)	349	406
Limestone filler (kg)	-	125
Sand (kg)	787	779
Gravel type 1 (kg)	749	-
Gravel type 0 (kg)	249	-
Gravel 9,5 (kg)	-	819
Gravel 12,7 (kg)	-	-
Superplasticizer (L)	2.16	2.7
Plasticizer (L)	-	2
Water (L)	188	200

## 2.2 Case study of SCC application in a vertical construction building

The case study was carried out in a vertical construction building, in Fortaleza, Brazil. SCC was poured in two floors, and PCC pouring was performed once, for comparison, as follows:

- First SCC pouring: slab and beams from the 4th floor, columns and stairs from the 3<sup>rd</sup> to the 4<sup>th</sup> floor;

- Second SCC pouring: slab and beams from the 5th floor, columns and stairs from the 4<sup>th</sup> to the 5<sup>th</sup> floor;
- PCC pouring: slab and beams from the 6th floor, columns and stairs from the 5<sup>th</sup> to the 6<sup>th</sup> floor.

The concrete supplier was the same for both types of concrete.

Concrete volume per floor is 105.6 m<sup>3</sup>, divided into 61 m<sup>3</sup> for slabs, 27.5 m<sup>3</sup> for beams, 16 m<sup>3</sup> for columns and 1.1 m<sup>3</sup> for stairs. Figure 1 shows the floor plant on which the concreting took place. The characteristic strength of both concretes (SCC and PCC) was 30 MPa.

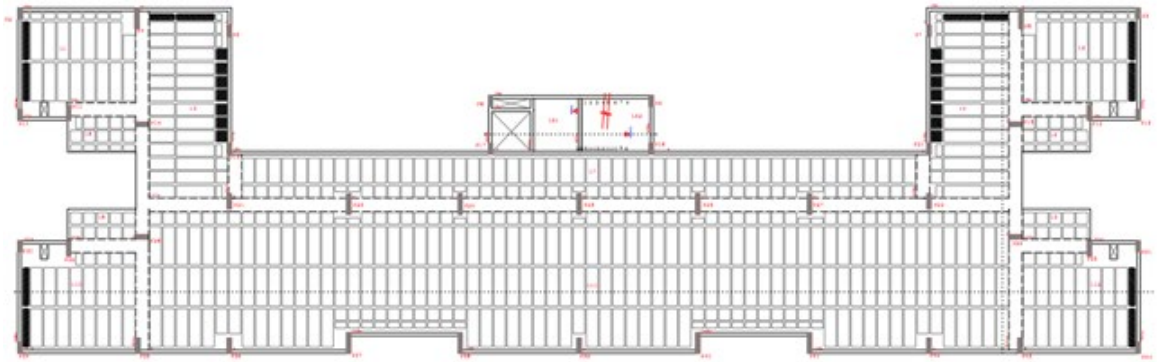


Figure 1. Floor plant.

After the superficial hardening of the concrete, a 5 mm layer of water was kept on the slab for 3 days to prevent the loss of water from the concrete (wet curing). After this period, for another 4 days the concrete was watered at least twice a day.

Slump test for the PCC and slump flow, L-Box and Funnel V tests for the SCC were carried out, according to respective Brazilian standards. For each concrete mixer truck, 6 cylindrical specimens (10x20) cm (diameter x height) were molded to test the compressive strength at 3, 7 and 28 days. However, the specimens that were supposed to be tested on the 3<sup>rd</sup> day were tested only on the 4<sup>th</sup> and 5<sup>th</sup> days due to some holidays.

### 2.3 Comparative analysis of SCC and PCC indexes

In order to analyze productivity, the advantages and disadvantages of using the SCC in comparison to PCC in the execution of the concrete parts of the vertical building, the following items were analyzed and considered: amount of labor force and the its related costs; work safety; amount of tools and equipment used during the pouring; total time and costs to complete the concrete parts. Descriptions of each indicator are as follows:

#### - Labor force

Labor productivity was measured by a partial index called Unit Production Ratio (UPR), which corresponds to the ratio of the number of worker-hours (Wh) spent to perform a given service, in this case the volume of concrete poured and finished, over the amount of service performed (Equation 1). It is important to note that the higher the value of the UPR, the worse the productivity [10].

$$UPR = Wh / Q \quad (1)$$

Where UPR = unit production ratio; Wh = number of workers times the number of hours of service; Q = quantity of service, which, in this case, is the volume of concrete used.

The UPR considered for the concreting service was the cyclic UPR, in which the service execution cycle is analyzed [11]. It was necessary to homogenize the means of UPR evaluation, and four aspects were standardized: definitions of which collaborators (workers) and their role in the construction are included in the evaluation; the quantification of the hours of work to be considered (hours); the quantification of the service (volume of concrete); and the definition of the time period to which the input and output measurements refer. Three UPRs were calculated: the first one contemplates only

the time to cast the concrete; the second one added the waiting time between the concrete mixer trucks; and the third one covers, in addition to the two periods mentioned, the waiting time for the arrival of the 1<sup>st</sup> truck.

The number of hours spent from the beginning to the end of the concrete casting was considered, linked to the value worker/hour. The time and cost of labor for analysis was considered up to the moment when the concreting reached 88 m<sup>3</sup> in all concretes, as it would make possible to compare SCC more accurately to PCC. This volume of concrete was defined due to the impossibility of completing the 1<sup>st</sup> and 2<sup>nd</sup> concreting with SCC in the whole floor, due to the lack of concrete inputs (lack of mineral addition).

The administration staff of the construction was the same for the three concreting, which was formed by an engineer, a building technician, a work safety technician, a supervisor, a construction foreman and a civil engineering undergraduate student. Despite being the same work force for all pourings, the cost increases according to the pouring time. The worker-hour value of each employee mentioned was taken as their respective salaries and charges provided by the construction company.

However, the number of employees directly involved in the process varied. In the first pouring, the number of workers was higher as a precaution, as it was the first time that the construction company would use SCC and there was a fear that something unforeseen would arise in relation to the compacting of the concrete and that it would be necessary to use the PCC again. Although there were no problems in that regard, it was necessary to use PCC to complete the concreting, as the amount of mineral addition was not enough to produce all the SCC needed. In the second concreting, now more confident, the number of employees directly involved in the concreting was reduced. In concrete pouring with SCC, the number of workers was the standard for the work - already used for the other slabs of the same project. The distribution of employees by function is shown in Table 5.

**Table 5.** Distribution of non-administrative collaborators of the work in the 3 concreting.

Office	Number of workers			Occupation
	1 <sup>a</sup> SCC	2 <sup>a</sup> SCC	CPC	
Blacksmith	1	1	1	Hardware monitoring
Carpenter	1	1	2	Review of forms
Masons	2	2	3	Scraping
Servant	1	1	1	Pump hose boom
Servant	4	2	4	Pulling / lathing the concrete
Servant	-	-	4	Vibrator
Aux. Electrician	-	-	1	Maintenance of vibrators / possible temporary installation
TOTAL	9	7	16	

**– Accidents at work**

An index was determined to measure the possibility of accidents at work due to falls at the time of pouring, the number of employees working at height versus the time needed to complete their activities. That is, the risk of accidents at work due to falls from height is the amount of time worked at height times the number of employees.

**– Tools and equipment**

To measure and evaluate the use of tools and equipment, the following data was recorded: delays in the concrete mixer truck due to equipment breakage or due to the return of a concrete truck; time to unload each truck; waiting time for each truck; total pouring time, from the beginning of the unloading of the first truck to the end of the last; rental value of vibrators, where the amount of R\$ 66.00 per work-day for each equipment was considered; value of the unit volume of the concrete charged by the concrete company (R\$ 280.0 for the PCC and R\$ 332.50 for the SCC).

**3 RESULTS**

**3.1 SCC mix design**

The results of the tests carried out in the fresh state for the acceptance of the mix designed in the laboratory and adjusted in the concrete plant are shown in Table 6. The results of the tests carried out in the hardened state are shown

in Table 7. A small dimension column was molded (20cm x 20cm x 1.5m) in the laboratory, for which was observed a smooth finish, free of bubbles or concrete failures, indicating the good self-compacting ability of the concrete.

Figure 2 shows the L-Box test in the laboratory. It is observed that the concrete passed through the obstacles without blocking the passage. Figure 3 shows the SCC's edge after the slump flow test, in which it is observed that the concrete is cohesive and without segregation. Figure 4 shows the appearance of the SCC at the time of pouring on the slab.



**Figure 2.** L-Box test in laboratory.



**Figure 3.** Focus on the end of the SCC in the slump flow trial.

**Table 6.** Result of SCC tests in the fresh state.

Test	Laboratory SCC	SCC in the site		Classification	Test Method
		1 <sup>a</sup> pouring	2 <sup>a</sup> pouring		
Slump Flow	690 mm	677 mm	675 mm	SF 2	ABNT, 2010 a
T <sub>500</sub>	1.8 s	1.6 s	1.7 s	VS 1	ABNT, 2010 a
V funnel	5 s	2.8 s	3.0 s	VF 1	ABNT, 2010 b
L box	0.8	0.8	0.8	PL 2	ABNT, 2010 c
J ring	685 mm	685 mm	-	PJ 2	ABNT, 2010 f



**Figure 4.** SCC pouring in the site.

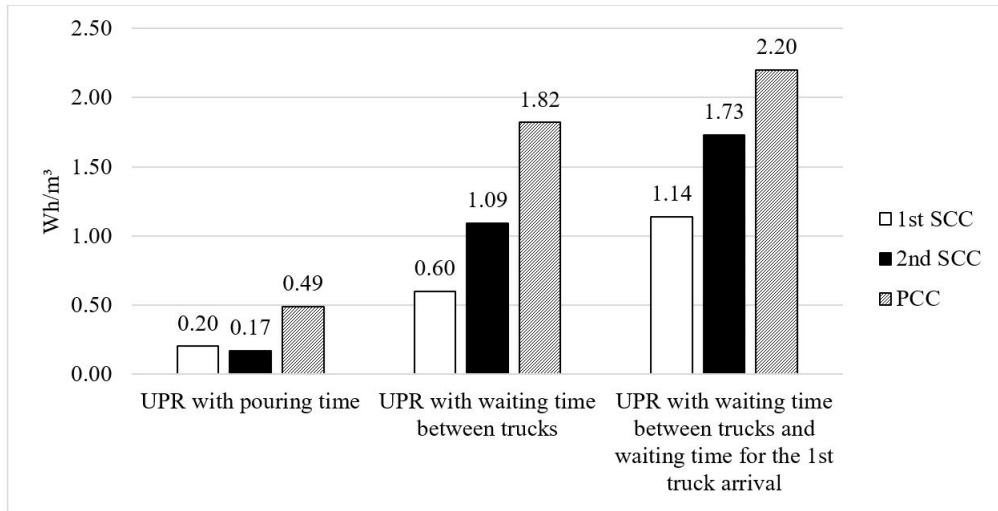
According to data in Table 7, the compressive strength of SCC at 3 days already represents, on average, 90% of the  $f_{ck}$  value, which is 30 MPa. Thus, the construction process was improved in terms of time, considering that it was only possible to perform prestressing when the concrete reached 70% of the characteristic strength required in the project. Therefore, according to the results of compressive strength of the SCC, it would be possible to advance the prestressing work by 3 days per slab, taking into account that conventional concrete reaches 75% of the required strength only at 7 days. The strength of the SCC is greater than that of the CPC in these early ages due to the greater amount of cement and limestone filler required for the concrete to be self-compacting.

**Table 7.** Result of SCC tests in the hardened state.

Test	SCC at the laboratory	SCC at site – 1 <sup>st</sup> pouring	SCC at site – 2 <sup>nd</sup> pouring	PCC at site	Test method
Absorption	4.65%	-	-	-	NBR 9778 (ABNT, 2009)
Voids index	10.4%	-	-	-	
Specific gravity	2.21 g/cm <sup>3</sup>	-	-	-	
Compressive strength at 3 days	33.4 MPa	27 MPa	24 MPa	21.5 MPa	NBR 5739 (ABNT, 2007)
Compressive strength at 7 days	-	30 MPa	28 MPa	27.6 MPa	
Compressive strength at 28 days	41.7 MPa	37 MPa	37 MPa	35 MPa	

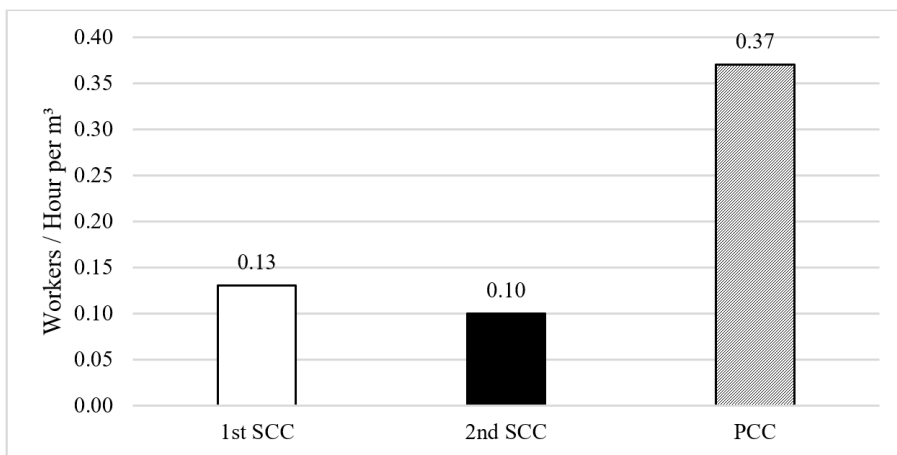
### 3.2 COMPARATIVE ANALYSIS BETWEEN PCC AND SCC POURING

Graph 1 shows the UPR of SCC and PCC pouring, considering pouring times versus the total number of employees needed. Considering only the launch time for calculating the UPR, it appears that the UPR of PCC pouring ( $0.49 \text{ Wh/m}^3$ ) is 165% higher than the average UPR of SCC pouring ( $0.19 \text{ Wh/m}^3$ ). If the waiting time between trucks is included in the UPR calculation, the increase is 115%, and if the waiting time for the first truck to arrive since ordering is considered, as well as the waiting time between trucks, the increase is 53%. So it turns out that whatever the scenario, productivity with SCC is always higher than with PCC, enabling the transfer of workers from the pouring to other services, helping to reduce the work schedule.



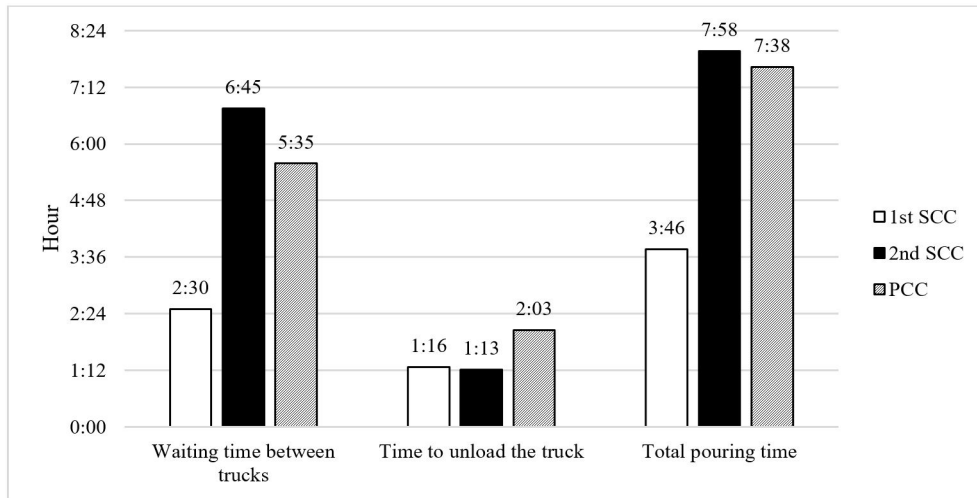
**Graph 1.** UPR pouring ( $\text{Wh/m}^3$ ).

Graph 2 shows the number of workers needed in pouring per hour and volume of concrete ( $\text{Wh/m}^3$ ). It is observed that PCC pouring used 221.7% more workers per hour and per concrete volume, than the average of SCC pouring. The explanation for the better performance of SCC is that, through this technology, fewer workers are needed in the pouring operation (see Table 5), since it is not necessary to vibrate the concrete, besides taking less time to pour the same volume of material.



**Graph 2.** Number of worker per hour per  $\text{m}^3$  of concrete.

Graph 3 shows the waiting time between trucks, the casting time of the concretes and the total time spent on each concreting.



Graph 3. Total concreting time.

According to data in Graph 3, the time to unload the concrete mixer truck with the SCC is, on average, 39.4% less than the time to unload a mixer truck of the same volume with PCC. This reduction in the discharge time for the SCC is a function of the uninterrupted pumping operation for this type of concrete, since in concretes with the PCC there are pauses for the spreading of the concrete, whereas in concretes with SCC this activity is not required.

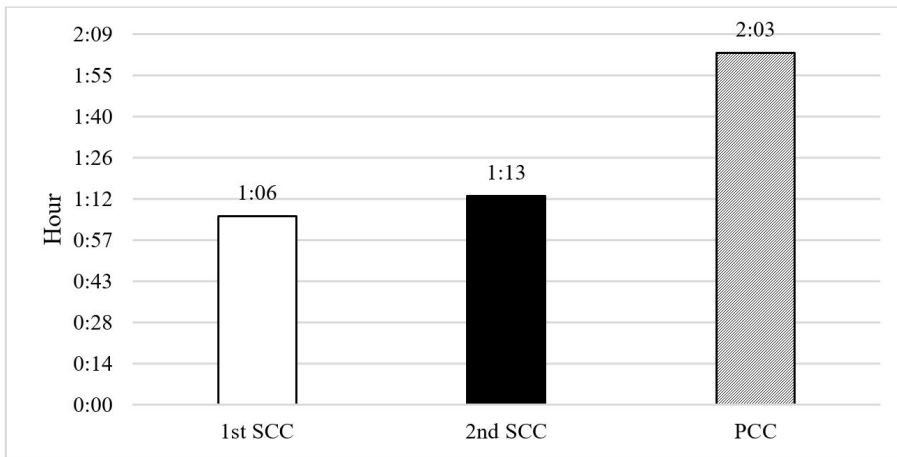
However, there is a variable that interferes with the total concreting time that does not depend on the type of concrete, which is the waiting time between trucks. This time is related to the operational activities of the concrete company and depends on the management of its processes. In the case under study, in the first concreting with the SCC this waiting time was 55.2% less than the time spent for concreting with the PCC. However, in the second concreting with the SCC this time was 20.9% longer than that of the concreting with the PCC. The explanation for the increase of this time in the second concreting were technical difficulties of the concrete plant in simultaneously making a SCC concreting in a construction and a PCC one in another.

It is also necessary to consider the waiting time to start pouring, which is the interval between the time when the first truck was scheduled to arrive and the time when it actually arrived. These data are presented in Table 8, in which the average waiting time is 3.5 hours for the SCC, 121% higher than waiting for concreting with the PCC. This longer time exposes the lack of mastery of the concrete plant with the initial actions to start the SCC. However, this time was not accounted for in costs since the focus of the work is the comparison between the types of concrete from the start of pouring onwards.

Table 8. Waiting time to initiate pouring.

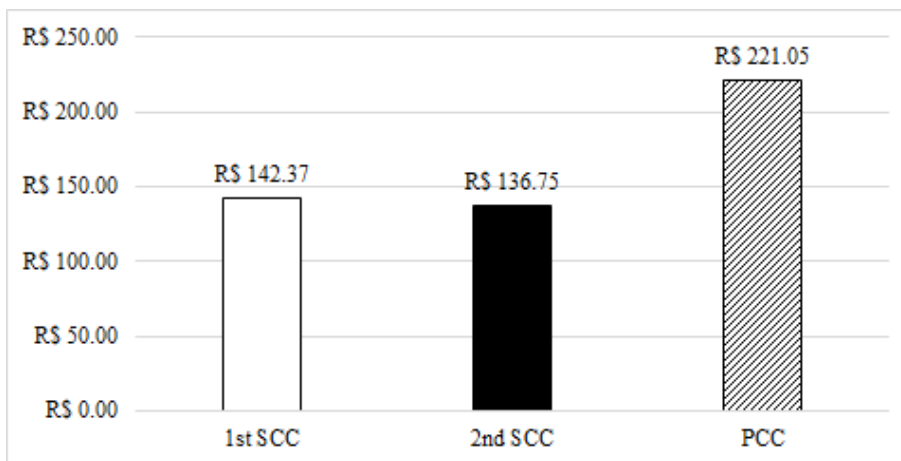
Type of concrete	Waiting time for the beginning of pouring (hours)
1 <sup>st</sup> SCC	03:15
2 <sup>nd</sup> SCC	04:10
PCC	01:35

Graph 4 shows the time of pouring, vibrating and spreading (in the case of slabs) of the concrete, in other words, the time between the start of the concrete pumping and the delivery of the finished piece. It is observed that this time is on average 39.4% shorter for concreting with SCC than for concreting with PCC, due to the absence of the vibrating step and the ease in the spreading step. However, given that it was the first time that a concreting with SCC was carried out with the construction team and, therefore, the collaborators still did not have the experience to launch, spread and finish it, it was realized that there is a possibility of reduction of the measured time, when the workforce is properly trained to handle this type of concrete.



**Graph 4.** Time of pouring, vibrating and spreading of the concrete.

Graph 5 presents the costs with the administration staff of the construction for each concreting, considering that this cost is proportional to the time. The administration staff was described in the methodology section.



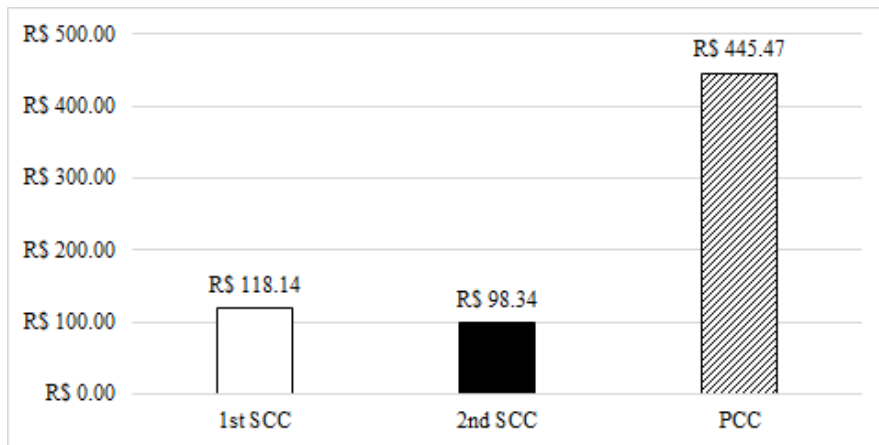
**Graph 5.** Total cost with administration staff.

It is possible to see in Graph 5 that the cost reduces when SCC is used due to the significant reduction in pouring time and the labor force employed. The cost with administrative staff in the 1<sup>st</sup> and 2<sup>nd</sup> concreting with SCC is 35.6% and 38.1% lower comparatively to that of concreting with the PCC, respectively. These values are representative, considering that the company can save an average of 36.9% with management employees by concreting. When this value is multiplied by each concreting performed by the company, the financial amount becomes significant.

Table 5, previously presented in the methodology, shows the number of employees that were required in each concreting, by function. The use of SCC reduced manpower by 43.8% in the 1<sup>st</sup> concreting and 56.3% in the 2<sup>nd</sup> concreting. This can be explained in part by the fact that there is no need for the use of vibrators in the SCC, thus allowing the suppression of the workers who handled this equipment and of the electrician's assistant who was on standby to fix for any damage to it. Another reason for reducing manpower is the ease of spreading the SCC. Thus, the number of workers who pulled and littered the concrete was reduced by almost half; and the number of carpenters by half, as the SCC did not accumulate on the moulds, reducing the risk of their rupture. Also, according to Table 5, it appears that the number of workers in the 1<sup>st</sup> concreting with the SCC is greater than that of the 2<sup>nd</sup> concreting. The reason for this is that the construction company, apprehensive about the new method, placed spare employees in the 1<sup>st</sup>

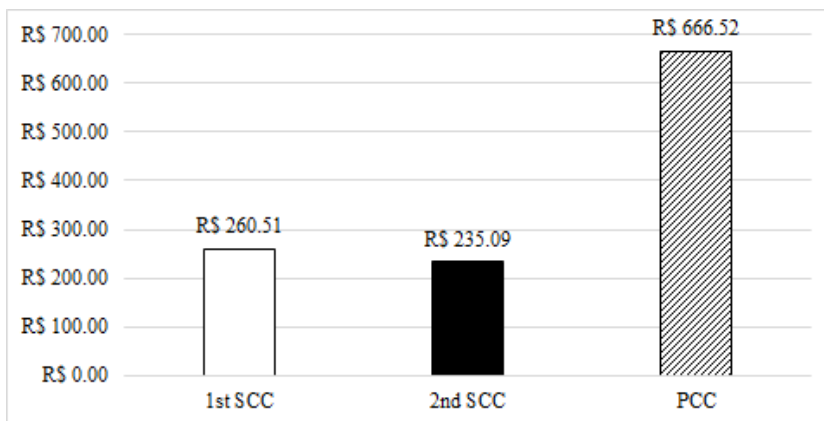
concreting so that there were no unforeseen events that would prevent the execution of the concreting of the planned pieces.

As already stated in the methodology, the costs were elaborated considering a concrete volume of 88 m<sup>3</sup> in each execution, as this way the comparison is in accordance to the 2<sup>nd</sup> day of the SCC, considering that the concreting with SCC of the 1<sup>st</sup> day was greater than that of the 2<sup>nd</sup> day. Graph 6 shows the cost of field labor for each concreting. The reduction in the number of employees involved with concreting provided by the use of SCC resulted in an average reduction of 75.7% in labor costs.



Graph 6. Comparison between labor cost for each pouring work.

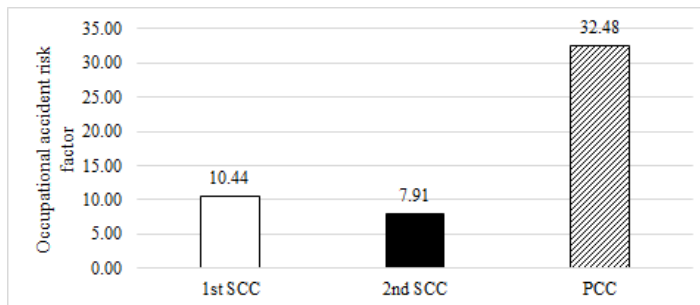
Graph 7 shows the total labor costs spent on each concreting, considering the administration staff and the field team directly involved in the concreting. It can be seen that the cost of labor force decreased by 61% in the 1<sup>st</sup> concreting with SCC and 64.7% in the 2<sup>nd</sup> concreting with SCC, when compared to the labor cost of concreting with the PCC. Once again, these reductions in labor costs are the result of the faster pouring speed with the SCC and its easier spreading, leveling and finishing, thus reducing the pouring time, as already shown.



Graph 7. Total labor cost.

Graph 8 shows the result of the occupational accident risk index, in which it can be observed that the risk of accidents at work due to falls from a height when using the PCC is 211.11% higher than in the 1<sup>st</sup> use of the SCC and 310, 6% than in the 2<sup>nd</sup> use of the SCC. This makes the use of SCC advantageous, as the reduction of accidents at work due to falls from a height is an incentive for employees and the company, positively impacting the market. The reduction in the risk factor for occupational accidents caused by the use of SCC is the result of the higher speed of concreting,

leaving employees less exposed to the risk of accidents, and of the reduction in the number of employees involved in concreting.



**Graph 8.** Occupational accident risk index.

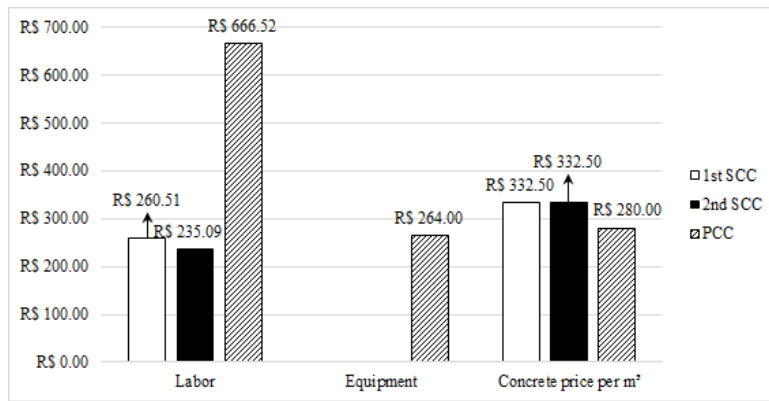
If the construction uses the PCC, it is necessary to use vibrators to densify the concrete. In the present case study, the construction company used four vibrators in the concreting of the PCC, while in the concreting with the SCC, no vibrators were needed. Out of the four vibrators, two are for direct use and two are in standby, in case of any mishap, such as breakage or electrical failures. Table 9 shows the rental value of this equipment per day, an expense that is unnecessary when using the SCC.

**Table 9.** Spending with vibrator.

Quantity	Occupation	Rental price (daily)	Total
02	Use	R\$ 66.00	R\$ 132.00
02	Reservation	R\$ 66.00	R\$ 132.00
<b>TOTAL</b>			<b>R\$ 264.00</b>

The construction in study used two sets of moulds for the production of two slabs per month. To achieve this, it was necessary to wait 7 days to prestress the cables and start to deform the boxes and cover the ribs. With the use of SCC, the time for the prestressing can be reduced from 7 to 3 days, since at 3 days the concrete already has adequate strength to perform this procedure. This saves work time and possibly saves a mould set while maintaining the goal of achieving two slabs a month. According to the construction company, the amount spent only with the necessary materials, such as wood, boxes and ribbing, to execute a mould set is R\$ 107,734.50, that is, it was seen that there is a possibility to save this value when using SCC.

Finally, Graph 9 shows the total cost of the cubic meter of the concrete used, already accounting the pouring, vibration (only for the PCC) and the finishing. The data considered for comparing the total cost was: the cost of the cubic meter of concrete, the volume of concrete, the cost of equipment and labor to achieve the accounted volume. It was also considered the amount spent with the rental of the mould set in the following proportion: one set of mould for the SCC and two sets of moulds for the PCC.



**Graph 9.** Cost per m<sup>3</sup> of finished concrete.

As can be seen in Graph 9, the labor cost for concreting with SCC is, on average, 62.1% cheaper than the cost of labor to build with PCC. This lower value is due to the smaller number of employees in concreting with SCC and the shorter concreting time. The cost of equipment is only accounted for concreting with PCC, since it uses vibrators. As concreting with SCC does not use vibrators, it has no equipment cost. Finally, it is possible to notice that the cubic meter of the SCC (only material, not poured) is 18.75% more expensive than that of the PCC. This overprice is justified by the higher consumption of cement and mineral addition to achieve self-compacting properties.

Table 10 shows a simulation for obtaining the total cost of the concreting work, considering that the building has 22 floors and 88 m<sup>3</sup> of concrete is consumed on each floor.

**Table 10.** Comparison between the total cost of SCC and PCC.

1 <sup>st</sup> SCC pouring				
Costs	Quant.	Nº Floors	Unit Cost (R\$)	Total Cost (R\$)
Labor	1 day	22	260.51	5,731.22
Equipment	0	22	0.00	0.00
Concrete	88 m <sup>3</sup>	22	332.50	643,720.00
Forms	1	-	107,734.50	107,734.50
Total				757,185.72
2 <sup>nd</sup> SCC pouring				
Costs	Quant.	Nº Floors	Unit Cost (R\$)	Total Cost (R\$)
Labor	1 day	22	235.09	5,171.98
Equipment	0	22	0.00	0.00
Concrete	88 m <sup>3</sup>	22	332.50	643,720.00
Forms	1	-	107,734.50	107,734.50
Total				756,626.48
PCC pouring				
Costs	Quant.	Nº Floors	Unit Cost (R\$)	Total Cost (R\$)
Labor	1 day	22	666.52	14,663.44
Equipment	1 day	22	264.00	5,808.00
Concrete	88 m <sup>3</sup>	22	280.00	542,080.00
Forms	2	-	107,734.50	215,469.00
Total				778,020.44

According to data on Table 10, the labor and equipment costs of concreting with SCC are much lower than those of concreting with PCC, while the cost of PCC itself is much lower than the cost of SCC. Since it is consumed in large quantities, the cost of concrete is much more representative than the costs of labor and equipment. On the other hand,

due to the fact that the SCC achieves high resistance in young ages and allows the use of only one set of moulds instead of two, as in concreting with PCC, there is a considerable cost reduction in this item for concreting with SCC. Thus, it appears that in the cost simulation to build the entire work with the SCC, it was only 2.7% cheaper than building the entire work with the PCC. Tutikian, Dal Molin and Cremonini (2005) evaluated the SCC cost they developed, verifying that it was 41% more expensive than the reference concrete. These authors did not consider the costs of labor, equipment and moulds in their work.

The cost of SCC can be further reduced by looking for cheaper fines to replace cement, as well as cheaper superplasticizer admixtures than the once used in this research.

## 4 CONCLUSIONS

According to the results obtained in the experimental part of this article, it can be concluded that:

- SCC already presents, at 3 days of age, on average, 90% of the  $f_{ck}$  value of the concrete used in the study, allowing the prestressing to be advanced from 7 to 3 days of age. This allows the construction that uses this SCC to use only one set of moulds for concrete instead of two sets, as is the case with the use of PCC, reducing some of in the costs;
- The productivity of concreting with SCC, calculated by UPR, in worker-hours per cubic meter of concrete, is greater than the productivity of concreting with PCC, considering any of the three concreting times: only the time of casting the concrete, the launch time plus the waiting time between trucks, and the launch time plus the waiting time between trucks and the time for the concrete truck to arrive at the construction site.
- The number of workers employed in concreting per hour of work and per volume of concrete ( $Wh/m^3$ ) is about 3 times lower for concreting with SCC than for concreting with PCC. The explanation for the better performance of SCC is that, through this technology, fewer workers are needed in the concreting operation, aside from taking less time to pour the same volume of concrete;
- In the best scenario between the two concreting with SCC, the total pouring time with this type of concrete came to be in the order of half the total pouring time with the PCC. However, the waiting time of the concrete mixer truck with the SCC was 134% longer, on average, than the waiting time of the concrete mixer truck with the PCC;
- The SCC's launch, vibrating and sealing time was 39.4% less, on average, than the time taken to carry out these activities with the PCC. This reduction in time meant that the cost of administration personnel was reduced by 36.9%, on average;
- The cost of labor involved in concreting was reduced by 50%, on average, when using the SCC due to the lack of need of employees who handled the vibrators, the electrician's assistant who was on standby for any damage and due to the ease of spreading the SCC, the number of workers who pulled and lathed the concrete was reduced by almost half, along with the number of carpenters, given that the SCC did not accumulate on the moulds, reducing the risk of their rupture;
- The index called occupational accident risk factor was reduced by 71.8% when concreting with the SCC as a result of the higher speed of concreting, leaving employees less exposed to the risk of accidents, and reduction in the number of employees involved in concreting with this type of concrete;
- The cost of concreting with SCC, considering that the building has 22 floors and 88  $m^3$  of concrete is used on each floor, was 2.7% lower than the cost of concreting with the PCC.

## ACKNOWLEDGEMENTS

The authors would like to thank JVS Engenharia for the support in providing a construction site for the application of the SCC and the Research Group on Construction Materials and Structures (GPMATE) at the Federal University of Ceará (UFC) for their support in carrying out the tests on site and in the laboratory.

## REFERENCES

- [1] W. L. Repette, "Concreto autoadensável," in *Concreto: Ciência e Tecnologia*, G. C. Isaia, Ed., São Paulo: Ibracon, 2011, ch. 48, pp. 1169-1806.
- [2] P. C. Gomes and A. R. Barros, *Métodos de Dosagem de Concreto Autoadensável*, São Paulo: Pini, 2009.
- [3] EFNARC, *Specification and Guidelines for Self-Compacting Concrete*. Surrey, UK, Concrete, Association House, 2002.
- [4] F. M. Almeida Fo., "Contribuição ao estudo da aderência entre barras de aço e concretos autoadensáveis," Ph.D. dissertation, Escola de Engenharia de São Carlos, USP, São Paulo, 2006.
- [5] B. F. Tutikian, "Métodos para dosagem de concretos autoadensáveis," M.S. thesis, UFRGS, Porto Alegre, 2004.

- [6] B. F. Tutikian and D. C. Dal Molin, *Concreto Autoadensável*, São Paulo: Pini, 2008.
- [7] H. R. Thomas and I. Ylakoumis, "Factor model of construction productivity," *J. Constr. Eng. Manage.*, 1987.
- [8] B. F. Tutikian, D. Dal Molin, and R. Cremonini, "Viabilização econômica do concreto autensável," in *12º Concurso Falcão Bauer. Câmara Brasileira da Indústria da Construção Civil*, 2005.
- [9] P. C. C. Gomes, "Optimization and characterization of high-strength self-compacting concrete," Ph.D. dissertation, Escola Técnica Superior D'Enginyers de Camins, UPC, Espanha, 2002, p. 139.
- [10] U. E. L. Souza, *Como Aumentar a Eficiência da Mão de Obra*, São Paulo: Pini, 2006.
- [11] M. M. Dantas and U. S. Souza "Produtividade e consumo na concretagem: comparação quanto a execução do serviço sob condições diversas," in *III SIBRAGEC*, São Carlos, 2003.

---

**Author contributions:** J. H. F. Serra: conceptualization, methodology, experimental procedures, data acquisition and curation, analysis, writing. A. E. B. Cabral: conceptualization, methodology, funding acquisition, supervision, writing.

**Editors:** José Tadeu Balbo, José Luiz Antunes de Oliveira e Sousa, Guilherme Aris Parsekian.



## ORIGINAL ARTICLE

# The cover thickness design of concrete structures subjected to chloride ingress from RBDO solution technique

## *Determinação da espessura do cobrimento de estruturas em concreto sujeitas ao ingresso de cloretos pela técnica RBDO*

Giovanni Pais Pellizzer<sup>a</sup> Edson Denner Leonel<sup>b</sup> <sup>a</sup>Universidade Federal de Mato Grosso do Sul – UFMS, Faculdade de Engenharia, Arquitetura e Geografia, Campo Grande, MS, Brasil<sup>b</sup>Universidade de São Paulo – USP, Escola de Engenharia de São Carlos, Departamento de Engenharia de Estruturas, São Carlos, SP, Brasil

Received 22 October 2019

Accepted 05 June 2020

**Abstract:** Diffusion is the principal transport mechanism of chloride ions into concrete pores. The chlorides trigger the reinforcements' depassivation when its concentration at the concrete/reinforcement interface reaches the threshold level. Thus, the depassivation defines the initiation stage end and the propagation stage start. The structural safety reduces widely during the propagation stage because of the various deleterious mechanisms triggered by reinforcement's corrosion. Therefore, the engineers should accurately predict and prevent the propagation stage start. The literature describes several models for evaluating the end of the initiation stage. However, few of them applies the Boundary Element Method (BEM) for this purpose, despite its known accuracy. Besides, enormous randomness affect the phenomenon. Thus, it is adequately handled solely in the probabilistic context. Optimisation techniques may be coupled in the problem modelling to propose adequate cover thickness values accounting for probabilities of failure. This study presents a Reliability-Based Design Optimisation (RBDO) approach for designing accurately the cover thickness of concrete structures subjected to chloride ingress. The BEM handles the diffusion modelling whereas the Monte Carlo simulation assesses the probabilities of failure. The RBDO is formulated in the context of Weighted Average Simulation Method (WASM), which requires only one assessment of the reliability analysis. It leads to a reliable and computationally efficient solution technique. The problem formulation and the implemented solution scheme are described herein. Moreover, one application is presented, in which the design results are interpreted properly.

**Keywords:** chloride diffusion, boundary element method, probabilistic modelling, RBDO, optimisation.

**Resumo:** Difusão é o principal mecanismo de transporte de íons cloreto nos poros do concreto. Os cloretos conduzem a depassivação quando sua concentração na interface concreto/armadura atinge o nível limite. Nesse momento, o período de iniciação termina e o período de propagação começa. A segurança estrutural é largamente reduzida durante o período de propagação por conta dos diversos mecanismos deletérios desencadeados pela corrosão de armaduras. Então, este fenômeno deve ser prevenido. Diversos modelos têm sido propostos na literatura para a determinação do final do período de iniciação. Contudo, poucos deles utilizam o Método dos Elementos de Contorno (MEC) para este propósito, apesar da sua conhecida precisão no domínio. Além disso, o fenômeno é sujeito a enormes aleatoriedades. Assim, este é somente adequadamente modelado no contexto probabilístico. Técnicas de otimização podem ser acopladas à modelagem do problema, com o objetivo de propor valores adequados para a espessura do cobrimento levando-se em consideração probabilidades de falha. Este estudo apresenta uma abordagem *Reliability Based Design Optimisation* (RBDO) para o projeto adequado da espessura do cobrimento de estruturas em concreto sujeitas ao ingresso de cloretos levando-se em consideração índices de confiabilidade alvo. O MEC efetua a modelagem da difusão enquanto a simulação de Monte Carlo avalia as probabilidades de falha. O RBDO é formulado no contexto do *Weighted Average Simulation Method* (WASM), no qual análises de confiabilidade através do MEC são necessárias apenas uma única vez. Isso conduz a um modelo adequado e eficiente do ponto de vista de técnica computacional. A formulação do problema e a implementação da técnica de solução são descritos. Além disso, um exemplo é apresentado, no qual os resultados do projeto são adequadamente interpretados.

**Palavras-chave:** difusão de cloretos, método dos elementos de contorno, modelagem probabilística, RBDO, otimização.

**How to cite:** G. P. Pellizzer and E. D. Leonel, "The cover thickness design of concrete structures subjected to chloride ingress from RBDO solution technique," *Rev. IBRACON Estrut. Mater.*, vol. 13, no. 5, e13502, 2020, <https://doi.org/10.1590/S1983-41952020000500002>

**Corresponding author:** Edson Denner Leonel. E-mail: [edleonel@sc.usp.br](mailto:edleonel@sc.usp.br)

**Financial support:** This study was financed in part by the Coordenação de Aperfeiçoamento de Pessoal de Nível Superior – Brasil (CAPES) – Finance Code 001.

**Conflict of interest:** Nothing to declare.



This is an Open Access article distributed under the terms of the Creative Commons Attribution License, which permits unrestricted use, distribution, and reproduction in any medium, provided the original work is properly cited.

## INTRODUCTION

Structural durability is a concern in the context of engineering design, particularly in reinforced concrete (RC) structures. In recent decades, various RC structures suffered from durability-related problems, which reduce its lifetime. Alkali-aggregate reaction, cracking caused by reinforcements corrosion and sulphate expansion [1], [2], for instance, reduce the lifetime of RC structures. Nevertheless, the chloride penetration and its consequences stand out in the literature as the principal causes of durability reduction of RC structures [3]–[5].

Tuutti [6] proposed the classic scheme for RC durability assessment, in which two macro periods divide the structural lifetime, i.e., initiation and propagation. The initiation part involves the time-span from construction until depassivation. Complementarily, the propagation part starts at the reinforcements' depassivation and finishes at the structural collapse. Diffusion-like mechanisms majorly govern the initiation part whereas enormous mechanical degradations processes are triggered during the propagation part. It is well-known in the literature that the propagation is considerably shorter than the initiation [7]. Therefore, the accurate description and representation of the initiation part have principal importance for RC design because it avoids and prevents unexpected and sudden collapses associated to the degradation phenomena from propagation part.

The chloride penetration process into concrete is nonlinear and time-dependent. Besides, it is associated to various transport mechanisms such as capillarity, advection, permeation and ionic diffusion, for instance [8]. Despite the above-mentioned complexities, this phenomenon has been often modelled in the literature accounting exclusively for diffusion mechanism [9]–[11]. Analytical solutions for the diffusion problem handle the modelling in various studies in the literature. In this context, it is worth mentioning the Fick's solutions [12], [13], which incorporate strong simplification assumptions. The Fick's approach accounts for semi-infinite domains and constant boundary conditions along time. These assumptions restrict the accurate representation of chloride ingress in real-world problems, which make it non-robust and inaccurate for a large number of applications.

Numerical methods provide alternative solution schemes for chloride diffusion modelling. Among them, it is worth citing the Boundary Element Method (BEM). The BEM represents accurately the diffusion problem by writing the governing differential equations into an integral form along the body's boundary. Therefore, the BEM reduces the order of mesh dimensionality by one, i.e., plane problems contain unidimensional BEM elements. Besides, BEM does not require a domain mesh. Because domain meshes (domain approximations) are avoided, the BEM enables the accurate evaluation of internal fields. This aspect has high importance for chloride diffusion modelling, in which chloride concentration at the reinforcements interface must be accurately evaluated along time. Moreover, the mesh is positioned only at the boundary. Thus, the problem can be solved through a small system of algebraic equations leading to computational efficiency [14], [15]. In addition, the BEM enables the representation of time dependent boundary conditions and complex geometries. These aspects make it superior to the classical analytical solutions.

It is worth remarking that randomness affect widely the chloride ingress modelling into concrete pores. Experimental studies demonstrate such observation [16], [17], which make the deterministic approach inefficient. The random behaviour governs, for instance, the chloride concentration values at the structural surface [18], [19] and the threshold chloride concentration for the reinforcements' depassivation [20]. Besides, the concrete mixture components are essentially random in space [21], [22], which introduces important randomness on the coefficient of diffusion. Therefore, the chloride ingress modelling into concrete pores by diffusion-like approaches requires probabilistic schemes for the accurate phenomena representation.

Such coupling procedure, i.e., the coupling of robust and accurate diffusion models to reliability algorithms, provides important constraints for the proposition of optimisation formulations. In this case, the probability of failure values along time can be utilised as constraints for determining optimised design for cover thickness, maintenance intervals and concrete mixtures, for instance. It is worth mentioning that optimisation formulations have been required widely in structural engineering once it enables economy and rational design.

In this context, Mori and Ellingwood [23], [24] demonstrated the relevance of inspection, repair and maintenance into the reliability of RC structures. The Bayesian scheme has been applied for updating the damage function along time after inspection and repair procedures. Therefore, the trade-off analysis between inspection/repair costs and reliability is addressed adequately.

The probabilistic evolution of mechanical damage in RC bridge decks subjected to reinforcements' corrosion triggered by chloride ingress is presented by Enright and Frangopol [25], [26]. In their study, the Monte Carlo simulation (MCS) assesses the probability of failure. Besides, the Bayesian updating technique enables the optimisation modelling of inspection intervals, which provides optimised conditions for bridge operation. Similar developments have been proposed by Biondini et al. [27], in which the researches applied the cellular automata scheme during the diffusion modelling.

The pioneer study of Val and Stewart [28] addresses the life-cycle cost analysis of RC structures in marine environments. The durability requirements and different repair strategies have been accounted into the limit states of the optimisation modelling. The influence of climate-changes in the durability of RC structures has been studied by El Hassan et al. [29]. The proposed model handles the randomness over moisture and temperature caused by climate-changes. Moreover, uncertainty quantification associated to the diffusion of chlorides into the concrete pores has been performed. Climate-change effects have been also studied by Stewart et al. [30]. The authors analysed the growth on the probability of depassivation caused by the climate-changes. Moreover, their study reports that 1 of 6 RC structures will present loss of performance caused by environmental conditions. Finally, they conclude that small increase on the cover, such as 5 or 10 mm, will improve substantially the structural performance against the climate-change. Optimisation strategies have been utilized by Bastidas-Arteaga and Stewart [31]. These authors propose mitigatory actions against the impacts of climate-change in RC structures.

Finally, Andrade [32] suggests the proposition of an additional limit state in RC structures design codes. Such limit state refers to the corrosion initiation. The author puts in check the reliability indexes of FIB Model Code 2010 and claims for improvements on the design procedures.

The present study contributes in this complex and ebullient scientific domain by proposing an optimisation model. The model determines the cover thickness of RC structures accounting for a target reliability value and the randomness associated to the chloride diffusion phenomenon. The transient BEM approach solves the chloride diffusion modelling along time. The potential (chloride concentration) is accurately evaluated because BEM does not require a domain mesh. The Monte Carlo simulation (MCS) assesses the probabilities of failure. The coupling of transient BEM and MCS is reliable due to the computational efficiency of BEM in the problem. Finally, the optimisation problem is formulated in the context of Reliability Based Design Optimisation (RBDO) approach. The Weighted Average Simulation Method (WASM) scheme solves the optimisation problem, which requires only one reliability analysis per optimisation iteration. The problem formulation and its implementation solution scheme are detailed described herein. Finally, the performance of the proposed model is illustrated through one application. The design results are interpreted and it could be utilised for further calibration of RC design codes.

### The transient BEM approach

The differential equation for transient potential problems represents the transient chloride ingress process into concrete pores along time. This equation is as follows:

$$\nabla^2 u - \frac{1}{\kappa} \frac{\partial u}{\partial t} = 0 \quad (1)$$

in which  $u$  represents the potential or chloride concentration,  $\kappa$  indicates the domain-related parameter such as thermal diffusivity or coefficient of diffusion, for instance, and  $t$  is the time.

The solution of the last differential equation requires the enforcement of boundary conditions, which are as follows:

- Dirichlet:  $u = \bar{u}$  at  $\Gamma_1$
- Neumann:  $q = \bar{q} = \frac{du}{d\eta}$  at  $\Gamma_2$

where  $\bar{u}$  is the prescribed potential values,  $\bar{q}$  refers to the prescribed flux values,  $\tilde{\Gamma}_1$  and  $\tilde{\Gamma}_2$  represent the boundaries in which potential or flux are prescribed, respectively. It is worth mentioning that the body's boundaries are:  $\Gamma = \Gamma_1 \cup \Gamma_2$ . In

addition, the flux is associated to the potential as follows:  $= \frac{du}{d\eta}$ . Thus, the flux represents the directional derivative of  $u$

in relation to the outward normal vector  $\eta$ . The present study handles the chloride diffusion modelling into concrete pores. In this complex transient problem, potential values indicate the chloride concentration along time and the flux refers to the chloride flux along the time.

Equation 1 leads to a boundary integral representation by applying either the finite differences technique, the Laplace transform or the time dependent fundamental solutions [14], [33]–[35]. In this study, the latter approach has been applied. Then, the time dependent fundamental solutions, the weighted residuum technique and the classical limit analysis carried out by BEM lead to the following boundary integral equation:

$$c(\underline{\xi})u(\underline{\xi}, t_F) = \kappa \int_{t_0}^{t_F} \int_{\Gamma} q(\underline{x}, t) u^*(\underline{\xi}, \underline{x}, t_F, t) d\Gamma(\underline{x}) dt - \kappa \int_{t_0}^{t_F} \int_{\Gamma} u(\underline{x}, t) q^*(\underline{\xi}, \underline{x}, t_F, t) d\Gamma(\underline{x}) dt \tag{2}$$

in which  $u^*$  and  $q^*$  represent the time-dependent fundamental solutions for potential and flux, respectively,  $\underline{\xi}$  represents the source points,  $t_0$  is the initial time,  $\underline{x}$  indicates the field points,  $t_F$  represents the observation time and  $c$  is the classical BEM free term. The free-term is unity for source points positioned at the domain. Besides,  $c$  equals 0.5 for source points at smooth boundary geometries. The time-dependent fundamental solutions are as follows [14], for the plane case:

$$u^*(\underline{\xi}, \underline{x}, t_F, t) = \frac{I}{4\pi\kappa\tau} \exp\left(-\frac{r^2}{4\kappa\tau}\right) \tag{3}$$

$$q^*(\underline{\xi}, \underline{x}, t_F, t) = \frac{r}{8\pi\kappa^2\tau^2} \frac{\partial r}{\partial \eta} \exp\left(-\frac{r^2}{4\kappa\tau}\right) \tag{4}$$

where  $\tau = t_F - t$ ,  $r$  is the distance between the source  $\underline{\xi}$  and the field  $\underline{x}$  points whereas  $\frac{\partial r}{\partial \eta} = r_{,k} \eta_k$ .

The solution of Equation 2 requires temporal and spatial integrations [14]. The BEM solves the spatial integrations by discretising the entire boundary geometry by boundary elements, over which polynomial functions approximate the diffusion fields and geometry. High-order BEM elements can be utilised for this purpose. The temporal integrations have been solved by the constant integration scheme, which enables the analytical integration of kernels Equation 3 and Equation 4 [44]. Besides, the analytical integration along time and the Lagrangian approximations on Equation 2 lead to the classical BEM algebraic system of equations  $HU = GQ$ , in which  $H$  and  $G$  are the influence matrices associated to the spatial integration of  $q^*$  and  $u^*$ , respectively.  $U$  and  $Q$  contain the potential and flux at the collocations [44].

In addition to the algebraic representation previously-mentioned, the solution of the transient problem requires a time-marching process. Because the constant time integration scheme solve this time-dependent problem, the time-marching process is as follows [44]:

$$\sum_{k=1}^{NT} H^k U^{NT-k+1} = \sum_{k=1}^{NT} G^k Q^{NT-k+1} \tag{5}$$

The Gauss-Legendre integral scheme handles the spatial integrations in the problem. Besides, the singular kernels have been regularized by the Subtraction Singularity Method (SSM). For sake of clarity [44], describes in detail the implementation of this approach and presents the SSM expressions for the kernels regularization.

### Probabilistic modelling by Monte Carlo simulation

The Monte Carlo simulation (MCS) technique is a well-established numerical simulation approach for uncertainty quantification purposes. In a very brief overview, the MCS assesses the probability of failure from a sampling of random variables, which describes the physical-mechanical random space. This sampling accounts for the statistical distribution assigned for each random variable (the CDF curves, for instance). Thus, the probability of failure,  $P_f$ , is assessed by MCS through the simulation of the limit state function for each random variable ensemble. Consequently, the structural failure occurs for sampling points at the failure domain. Otherwise, the safe condition occurs. The ratio between the sampling points at the failure domain and the total number of simulations leads to the probability of failure [36]. Then:

$$p_f = \int_{\Omega} I[x] f_X(x) dx = \frac{1}{n_t} \sum_{j=1}^{n_t} I[x_j] = \frac{n_f}{n_t} \tag{6}$$

in which  $n_t$  indicates the sampling range and  $n_f$  refers to the number of failures. The indicator function  $I[x]$  is unity for failure condition and nil for safe condition.  $f_X(x)$  represents the joint density function of the random variables  $x_j$ .

It is worth mentioning that MCS requires wide range of sampling for the accurate description of failure and safe domains. Therefore, computational time consuming models make prohibitive such type of analysis. Nevertheless, the MCS is applied herein because the BEM model has demonstrated computational efficiency. Besides, one applies the MCS because the limit state function and consequently the safe and failure spaces remain implicit during the time evolution. Therefore, gradient-based schemes such as First Order Reliability Method (FORM) or Second Order Reliability Method (SORM) could be not robust in this problem. Such approaches require derivatives of the limit state functions for assessing the probability of failure. Because the limit state functions are implicit, such derivatives must be evaluated numerically. As a result, errors during this phase may lead to inaccurate values of probability of failure. Besides, these approaches may stuck in local minima solutions, which also lead to the inaccurate values of probability of failure.

The limit state function  $\gamma$  defines the interface between safe and failure domains. The limit state function described in Equation 7 governs the probabilistic modelling herein:

$$Y(x_i) = \Xi(x_i) - \Psi(x_i, t) \tag{7}$$

where  $\Xi$  represents the resistance part, which in this problem is the chloride threshold content. This parameter is usually a function of concrete mixture and water/cement ratio.  $\Psi$  indicates the solicitation part and accounts for the chloride concentration at the observation point for the structural life-time. The transient BEM model provides this variable values, which in this problem are the potential values at the observation points.

**Optimisation problem formulation. Problem statement**

The structural modelling and design require the application of mathematical functions, which describe the evolution of the system behaviour along time. In this regard, optimisation techniques may be valuable tools because they enable the determination of proper design parameters for leading to the extreme (maximum and minima) values of such functions. The optimisation approaches have been largely desired in probabilistic modelling. Then, the optimum design parameters may be utilised accounting for the inherent uncertainties over it.

Among the coupled optimisation/probabilistic schemes available in the literature it is worth citing the reliability based design optimisation (RBDO). The RBDO approach defines functions of probabilistic parameters as constraints into the optimisation problem. The usual RBDO problem is formulated as follows [37]:

Find:  $d^*$   
Which minimizes:  $f(d)$

$$\text{Subject to: } \begin{cases} P_{f_i}(d) \leq P_{f_{t_i}}, i = 1, \dots, n_{LS} \\ d \in S \subset \mathbb{R}^{n_d} \end{cases} \tag{8}$$

in which  $d^*$  represents the objective variables vector,  $f(d)$  indicates the objective function,  $P_{f_i}(d)$  is the probability of failure function for failure mode  $i$ ,  $P_{f_{t_i}}$  represents the target (threshold) probability of failure for the failure mode  $i$ ,  $n_{LS}$  indicates the number of limit states,  $S$  is the allowable design domain and  $n_d$  is the number of design variables.

Such problem may be alternatively formulated as follows:

Find:  $d^*$   
Which minimizes:  $f(d)$

$$\text{Subject to: } \begin{cases} \beta_i(\mathbf{d}) \geq \beta_{T_i}, i = 1, \dots, n_{LS} \\ \mathbf{d} \in S \subset \mathbb{R}^{n_d} \end{cases} \quad (9)$$

where  $\beta_i(\mathbf{d})$  indicates the reliability index for the failure mode  $i$  and  $\beta_{T_i}$  represents the target (threshold) reliability index for the failure mode  $i$ .

It is worth citing that Equation 8 and Equation 9 may contain equalities and inequalities constraints. Besides, such equations also handle system reliability problems, in which the system probabilities of failure and system reliability index are accounted. Finally, the probabilistic constraints for the individual failure modes can coexist with the probabilistic system failure constraints. Analytical solutions for RBDO problems are available for a narrow number of problems, in which objective and constraints functions are simpler. Thus, complex and real-world problems require simulation-based approaches. These methods handle adequately nonlinear response problems and non-Gaussian random variables. Alternatively, approximation methods may be adopted, which demonstrate adequate performance in linear response problems and Gaussian random variables.

The performance of RBDO solution schemes has been analysed by Rashki et al. [38]. In their study, the authors proposed an interesting strategy for incorporating the reliability analysis into the optimisation step. Such strategy utilises the concepts of sampling weight and weighting flexibility for assessing the probability of failure. This approach consists of generating samples uniformly distributed into the design space, which enable the optimised configurations. Therefore, only one probabilistic simulation procedure is required for each individual sample. This characteristic has major importance within complex systems behaviour, where usually complex and computational costly models have been required.

The weighted average simulation method (WASM), presented by Rashki et al. [39], is composed of simple procedures, in which MCS has been applied. The first step consists of generating  $n_{sim}$  samples uniformly distributed into the design space for each random variable. Such sample accounts for predetermined bounds, which accelerate the responses. Then, the weight  $w_i$  for each sample  $i$  is assessed through the probability density functions  $f_j(\cdot)$ . for each random variable as follows:

$$w_i = \prod_{j=1}^{n_{RV}} f_j(i) \quad (10)$$

The probability of failure  $P_f$  is assessed through the indicator function  $I$  in each sample  $i$ , as usual in MCS. Such indicator is weighed by  $w_i$  as follows:

$$P_f = \frac{\sum_{i=1}^{n_{sim}} I_i w_i}{\sum_{i=1}^{n_{sim}} w_i} \quad (11)$$

The main advantage of this solution technique involves the assessment of updated probability of failure values,  $P_f'$ , without the requirement of additional evaluations of the indicator function. If statistical parameters and/or the type of a random variable  $j$  are modified, the weights are recalculated as follows:

$$w'_i = \prod_{j=1}^{n_{RV}} f'_j(i) \quad (12)$$

Therefore, the updated values for the probability of failure are straightforward assessed as follows:

$$P'_f = \frac{\sum_{i=1}^{n_{sim}} I_i w'_i}{\sum_{i=1}^{n_{sim}} w'_i} \quad (13)$$

It is worth stressing that the indicator function is kept constant during the assessment of updated probability of failure values,  $P_f'$ , because the sample values must not be updated. Therefore, for each iteration, only the weights must be updated. Consequently, the updated values for the probability of failure are assessed through the updated weights and the same indicator function. Such feature is named as “weighting flexibility” and is widely helpful in complex real-world problems, in which computational costly approaches have been usually required for system behaviour modelling. Besides, such advantage has major importance within RBDO techniques, in which constraints related to the probability of failure of different limit states must be updated at each optimisation iteration. Then, this technique makes reliable the analysis and solution of complex problems accounting for robust system behaviour models.

The methodology proposed by Rashki et al. [38], through the coupling the WASM into RBDO problems, is utilised herein. Such methodology consists of five steps as follows:

### Step 1: Uniform sample generation into the design space

Regardless the random variables type, samples uniformly distributed along the design space are generated for each random variable handled in the problem. The upper and lower bounds for each of them have been determined from the estimated reliability index for the problem. Rashki et al. [39] provide details for choosing properly this sampling interval. Thus, a sample vector  $\mathbf{x}_j$  of the random variable  $j$  have sample values  $x_{j,i}$ , as follows:

$$\mathbf{x}_j = \{x_{j,1}, x_{j,2}, \dots, x_{j,i}, \dots, x_{j,n_{im}}\} \quad (14)$$

### Step 2: Indicator function assessment

The sample values generated in step 1 simulate the limit state functions. Then, the indicator function is the unit when the limit state function is negative. In this case, the sample belongs to the failure domain,  $\tilde{U}_f$ . Otherwise, the indicator function is nil and the safe domain,  $\tilde{U}_s$ , is assessed.

### Step 3: Probability of failure assessment using the weighting flexibility scheme

It is worth mentioning that the samples at the safe domain are potential solutions for the RBDO problem. For each of these candidate solutions, the probability of failure is assessed through Equation 13. In this procedure, the sample value at the design space is assumed as the mean value of their respective probability distribution. Then, sample weights are recalculated from Equation 12, which lead to the updated values of the probability of failure. Therefore, the probabilities of failure associated to the candidate samples can be assessed from only one indicator function evaluation process.

### Step 4: The candidate samples choice procedure

The probability of failure,  $P_f$ , for each sample at the safe domain has been assessed. Then, the samples are eliminated if  $P_f$  is higher than  $P_{f_t}$ . The  $P_{f_t}$  represents the threshold probability of failure and indicates a constraint in the optimisation problem. The remaining samples belong to the reliable domain. Consequently, the optimal solution may be achieved among them.

### Step 5: Objective function evaluation accounting for the samples in the reliable domain

The last step concerns the objective function evaluation. Then, such function is evaluated for each of the samples at the reliable domain, as described in step 4. The optimal solution leads to the lowest value of the objective function.

The BEM model interacts with the optimisation methodology in the indicator function procedure (step 2). Thus, the indicator function is evaluated only once for each sample throughout the entire optimisation process. This is the main advantage of this methodology, as previously mentioned. The summary of the optimisation process steps is illustrated in Figure 1.

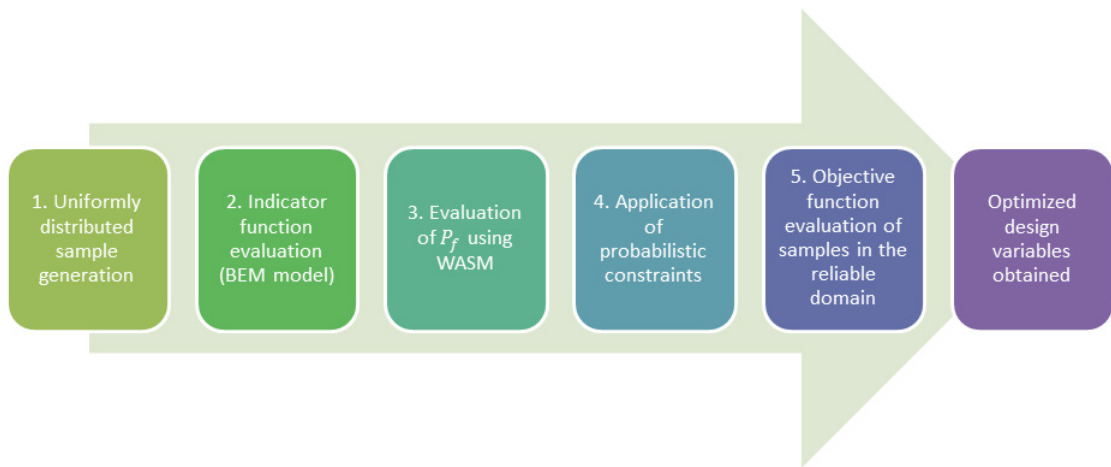


**Figure 1.** Flowchart of the proposed numerical approach.

**Solution problem**

The framework previously presented has been utilised for optimising the cover thickness of concrete structures subjected to chloride ingress. Because this problem is subjected to huge randomness, its solution is properly handled solely in the context of probabilistic modelling. The chloride diffusion phenomenon into concrete pores is handled through the robust transient potential BEM approach. Moreover, the WASM scheme handles the optimisation problem accounting for randomness, which leads to the optimum cover thickness value.

For sake of simplicity, the cross-section illustrated in Figure 2 has been accounted in the following analyses. This cross-section contains a reinforcement of 10 mm diameter, in which an initial cover of 40 mm has been assumed. It is worth mentioning that this reinforcement has been utilized solely to illustrate the cover limit. The reinforcement itself has not been accounted in the modelling.

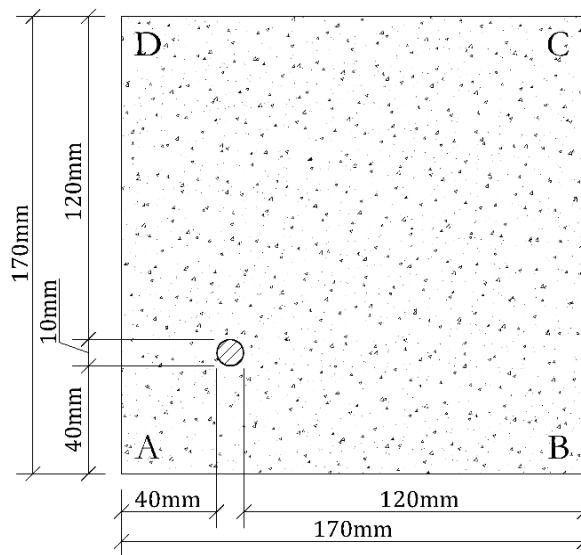


**Figure 2.** Cross-section geometry.

This analysis handles the two different boundary conditions illustrated in Figure 3. The case 1 involves the one-directional flow condition whereas case 2 represents the fully two-dimensional flow condition.

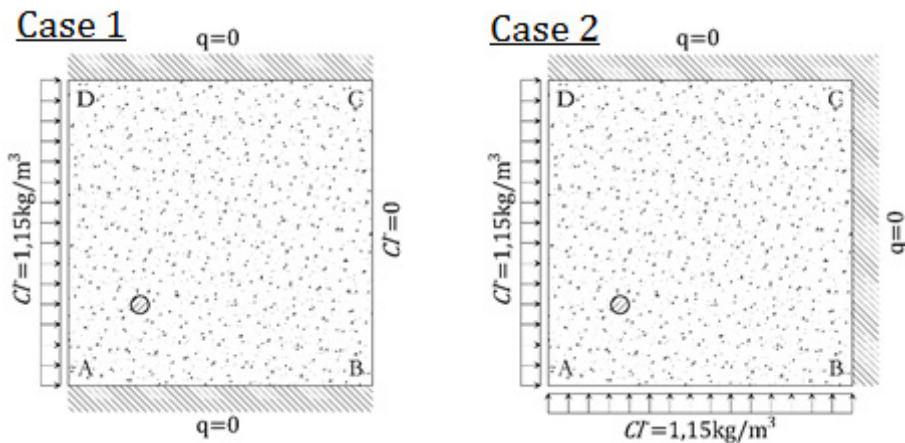


Figure 3. Boundary conditions. Case 1 and Case 2.

The limit state function for the probabilistic modelling has been defined as a function of the depassivation time as follows:

$$G = t_{dep} - t_{s.d.l.} \tag{15}$$

where  $t_{dep}$  indicates the time predicted as a function of random variables for depassivation phenomenon start. Such variable has been evaluated by the transient BEM approach.  $t_{s.d.l.}$  represents the structural lifetime, which is usually defined during the design phase.

The random variables parameters are illustrated in Table 1.

Table 1. Random variables parameters.

Parameter	Distribution type	Mean	C.V.	Reference
$C_{lim}$	Uniform	0.90 kg/m <sup>3</sup>	0.15	Mehta and Monteiro [42]
$\kappa_0$	Lognormal	23.0572 mm <sup>2</sup> /year (w/c=0.4)	0.30	Bentz et al. [17]
$C_0$	Lognormal	1.15 kg/m <sup>3</sup>	0.30	McGee [43]/ Val and Stewart [28]
$COV$	Normal	40.00 mm	0.30	-

where  $C_{lim}$  indicates the chloride threshold content for depassivation,  $\kappa_0$  represents the chloride diffusion coefficient,  $C_0$  is the chloride concentration at the structural surface and  $COV$  is the concrete cover thickness. The latter parameter refers to the objective parameter, i.e., the parameter to be optimised.

Besides, the chloride concentration (potential value) has been calculated at the random  $cov_i$  position, which corresponds to the sample value  $i$  of cover thickness. The transient BEM model determines such values along time. For case 1, the chloride concentration has been evaluated along a parallel line to the boundary AB. For case 2, the chloride concentration has been determined along the diagonal AC. Figure 4 illustrates such positions. It is worth mentioning that the parameter  $cov_\mu$  represents the mean concrete cover thickness, which has been assumed as 40 mm.

The diffusion modelling is handled by the BEM. The BEM mesh is composed of 68 discontinuous isoparametric linear elements with 10 mm length each. It lead to 136 source points and 272 degrees of freedom. The fundamental kernels are integrated with only 10 Gauss points per element. Moreover, the time discretisation is performed through 25 time steps, from year 0 to year 50. It is worth mentioning that space and time discretisations have been determined accounting for standard convergence procedure. Then, further refined discretisations do not introduce significant changes into the diffusion fields modelling. The probabilistic MCS simulations have been handled through 10,000 samples for each random variable.

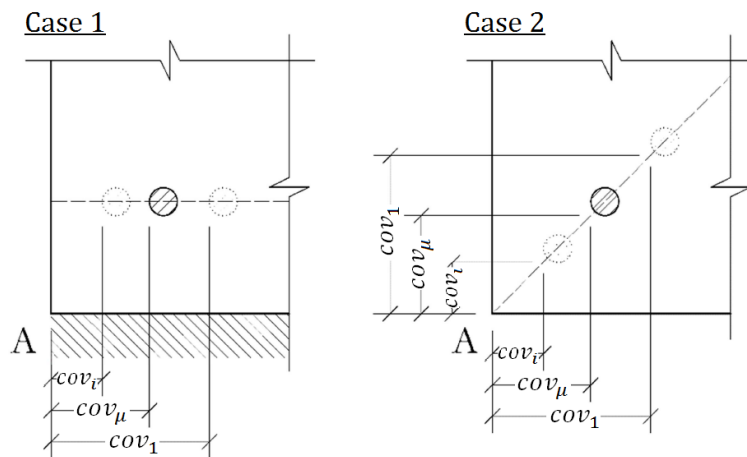


Figure 4. Cover values for chloride concentration assessment. Case 1 and Case 2.

The framework previously presented has been applied accounting for deterministic structural lifetimes of 30, 40 and 50 years. Moreover, the target reliability indexes  $\beta_T$  are assumed into the interval -1.0 to 3.0. From such data, the WASM approach provides the optimised concrete cover thickness. The evolution of concrete cover thickness for boundary conditions defined from case 1 and case 2 is illustrated in Figure 5.

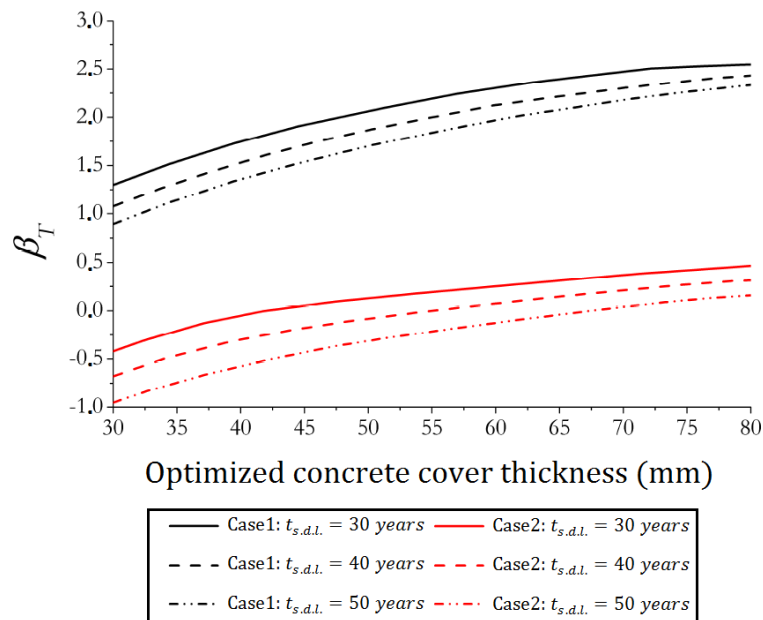


Figure 5. Optimised concrete cover thickness.  $\beta_T$  condition. Case 1 and Case 2.

Figure 6 presents an equivalent illustration, in which the evolution of cover thickness is presented as a function of the target probability of failure.

It is worth emphasizing the large difference behaviour for cases 1 and 2 when the same cover thickness value is accounted. Similar observation can be performed in Figure 5, in terms of target probability of failure values. Besides, one observes the cover thickness values in the range from 30 mm to 80 mm. For case 1, the associated target reliability index range is 0.8 to 2.6. For case 2, the correspondent range is -1.0 to 0.5. Such behaviour corroborates with responses presented in literature [40], in which two-dimensional flux conditions lead to severe conditions for depassivation in

comparison with one-dimensional case. These results put in check models based exclusively in one-dimensional conditions, such as those based on Fick’s law.

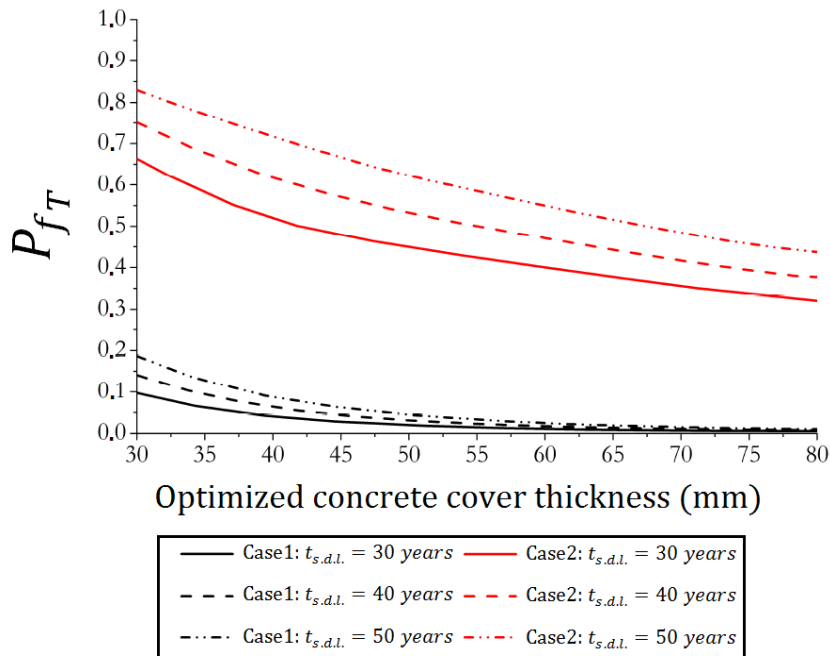


Figure 6. Optimised concrete cover thickness.  $P_{fT}$  condition. Case 1 and Case 2.

Besides, the triplets of curves illustrated in Figure 6 demonstrate convergence behaviour, i.e., such curves tend to the horizontal position for increasing values of cover thickness, as expected. Because of such behaviour, the increase on the cover thickness values does not lead to similar increase on the durability safety level. Thus, from certain values of thickness, the safety level is not effectively increased, which may indicate threshold values of cover.

It is worth stressing the nonlinear behaviour between  $\beta_T$  and  $P_{fT}$ , in which  $P_{fT} = \Phi(-\beta_T)$ . Such nonlinear dependency lead to different growth rates for curves, as observed in Figure 5 and Figure 6. Then, linear increments into cover thickness values do not lead to the similar growth rates in  $\beta_T$ . In the context of design, it means that the increase in the cover thickness in case 2 (two-dimensional flow) leads to the higher safety improvement than the same increase in cover thickness on case 1 (one-dimensional flow). This result emphasizes the importance of controlling and designing the adequate cover thickness for the proper protection of reinforcements.

The JCSS [41] recommends target reliability indices for irreversible service limit states in the range from 1.3 to 2.3. Figure 5 demonstrates that the three curves for case 1 (one-dimensional flow) respect almost entirely the minimum value of 1.3. The same behaviour has not been observed for case 2 (two-dimensional flow). Because the increase on the cover thickness values does not seem to be effective in the latter case, it is suggestable to reduce the water/cement ratio of the concrete mixture. It reduces the velocity of the chloride diffusion process and, consequently, enables accomplishing with JCSS [41] requirements.

## CONCLUSIONS

This study demonstrates the performance of the coupling between transient BEM model and a RBDO formulation through the WASM scheme. The objective is the assessment of optimum cover thickness values accounting for randomness. The diffusion phenomenon has been accurately modelled by the BEM, which handles transient potential and flux conditions. Besides, the diffusion model enables the representation of one and two dimensional flux conditions. The WASM approach is widely adequate into an RBDO design. This optimisation scheme requires the probability of failure assessment only once for each point into the reliable space. Thus, the coupled scheme is efficient in terms of computational time consuming.

The performance and analyses results have been handled for one and two dimensional flux conditions. In addition, the differences among the results are discussed once the cover values for cases 1 and 2 are considerable different.

The proposed framework may be utilised for suggesting proper cover thickness values as a function of target reliability. Thus, in the absence of design code recommendations, this model is largely helpful. Moreover, parametric analyses may be helpful for improving the current durability recommendations of the Brazilian design code. Thus, the information of reliability is properly accounted into the cover prescription.

Such model may be improved in the future by incorporating complex diffusion effects such as chloride binding capacity and concrete cracking, for instance. In this case, the proposed framework is still valid. It requires only the update of the diffusion modelling. Such developments are due in course by the research group of the senior author of this study.

## REFERENCES

- [1] D. Bru, A. González, F. J. Baeza, and S. Ivorra, "Seismic behavior of 1960's RC buildings exposed to marine environment," *Eng. Fail. Anal.*, vol. 90, pp. 324–340, 2018, <http://dx.doi.org/10.1016/j.engfailanal.2018.02.011>.
- [2] J. R. A. Goncalves, Y. Boluk, and V. Bindiganavile, "Crack growth resistance in fibre reinforced alkali-activated fly ash concrete exposed to extreme temperatures," *Mater. Struct.*, vol. 51, no. 2, pp. 3, 2018, <http://dx.doi.org/10.1617/s11527-018-1163-6>.
- [3] F. Shaikh, "Effect of cracking on corrosion of steel in concrete," *Int. J. Concr. Struct. Mater.*, vol. 12, no. 1, pp. 1–12, 2018, <http://dx.doi.org/10.1186/s40069-018-0234-y>.
- [4] A. Silva, R. Neves, and J. Brito, "Statistical modelling of carbonation in reinforced concrete," *Cement Concr. Compos.*, vol. 50, pp. 73–81, 2014, <http://dx.doi.org/10.1016/j.cemconcomp.2013.12.001>.
- [5] T.-B. Tran, E. Bastidas-Arteaga, F. Schoefs, and S. Bonnet, "A Bayesian network framework for statistical characterisation of model parameters from accelerated tests: application to chloride ingress into concrete," *Struct. Infrastruct. Eng.*, vol. 14, no. 5, pp. 580–593, 2018, <http://dx.doi.org/10.1080/15732479.2017.1377737>.
- [6] K. Tuutti, *Corrosion of Steel in Concrete Swedish*. Stockholm: Cem. Concr. Res. Inst., 1982, 460 p.
- [7] E. A. P. Liberati, C. G. Nogueira, E. D. Leonel, and A. Chateauneuf, "Nonlinear formulation based on FEM, Mazars damage criterion and Fick's law applied to failure assessment of reinforced concrete structures subjected to chloride ingress and reinforcements corrosion," *Eng. Fail. Anal.*, vol. 46, pp. 247–268, 2014, <http://dx.doi.org/10.1016/j.engfailanal.2014.09.006>.
- [8] L. Saad, A. Aissani, A. Chateauneuf, and W. Raphael, "Reliability-based optimization of direct and indirect LCC of RC bridge elements under coupled fatigue-corrosion deterioration processes," *Eng. Fail. Anal.*, vol. 59, pp. 570–587, 2016, <http://dx.doi.org/10.1016/j.engfailanal.2015.11.006>.
- [9] E. Bastidas-Arteaga and F. Schoefs, "Stochastic improvement of inspection and maintenance of corroding reinforced concrete structures placed in unsaturated environments," *Eng. Struct.*, vol. 41, pp. 50–62, 2012, <http://dx.doi.org/10.1016/j.engstruct.2012.03.011>.
- [10] A. Ben-Fraj, S. Bonnet, and A. Khelidj, "New approach for coupled chloride/moisture transport in non-saturated concrete with and without slag," *Constr. Build. Mater.*, vol. 35, pp. 761–771, 2012, <http://dx.doi.org/10.1016/j.conbuildmat.2012.04.106>.
- [11] P.-T. Nguyen, E. Bastidas-Arteaga, O. Amiri, and C.-P. El Soueidy, "An efficient chloride ingress model for long-term lifetime assessment of reinforced concrete structures under realistic climate and exposure conditions," *Int. J. Concr. Struct. Mater.*, vol. 11, no. 2, pp. 199–213, 2017, <http://dx.doi.org/10.1007/s40069-017-0185-8>.
- [12] M. G. Stewart, "Spatial variability of pitting corrosion and its influence on structural fragility and reliability of RC beams in flexure," *Struct. Saf.*, vol. 26, no. 4, pp. 453–470, 2004, <http://dx.doi.org/10.1016/j.strusafe.2004.03.002>.
- [13] K. A. T. Vu and M. G. Stewart, "Structural reliability of concrete bridges including improved chloride-induced corrosion models," *Struct. Saf.*, vol. 22, no. 4, pp. 313–333, 2000, [http://dx.doi.org/10.1016/S0167-4730\(00\)00018-7](http://dx.doi.org/10.1016/S0167-4730(00)00018-7).
- [14] L. C. Wrobel, *The Boundary Element Method: Applications in Thermos-fluids and Acoustics, vol. 1*. New York: John Wiley & Sons; 2002.
- [15] E. D. Leonel and W. S. Venturini, "Non-linear boundary element formulation applied to contact analysis using tangent operator," *Eng. Anal. Bound. Elem.*, vol. 35, no. 12, pp. 1237–1247, 2011, <http://dx.doi.org/10.1016/j.enganabound.2011.06.005>.
- [16] H. E.-D. H. Seleem, A. M. Rashad, and B. A. El-Sabbagh, "Durability and strength evaluation of high-performance concrete in marine structures," *Constr. Build. Mater.*, vol. 24, no. 6, pp. 878–884, 2010, <http://dx.doi.org/10.1016/j.conbuildmat.2010.01.013>.
- [17] D. P. Bentz, E. J. Garboczi, Y. Lu, N. Martys, A. R. Sakulich, and W. J. Weiss, "Modeling of the influence of transverse cracking on chloride penetration into concrete," *Cement Concr. Compos.*, vol. 38, pp. 65–74, 2013, <http://dx.doi.org/10.1016/j.cemconcomp.2013.03.003>.
- [18] K. Y. Ann, J. H. Ahn, and J. S. Ryou, "The importance of chloride content at the concrete surface in assessing the time to corrosion of steel in concrete structures," *Constr. Build. Mater.*, vol. 23, no. 1, pp. 239–245, 2009, <http://dx.doi.org/10.1016/j.conbuildmat.2007.12.014>.

- [19] S. Zhou, "Analytical model for square root increase of surface chloride concentration and decrease of chloride diffusivity," *J. Mater. Civ. Eng.*, vol. 28, 04015181, 2016, [http://dx.doi.org/10.1061/\(ASCE\)MT.1943-5533.0001483](http://dx.doi.org/10.1061/(ASCE)MT.1943-5533.0001483).
- [20] M. Shakouri, D. Trejo, and P. Gardoni, "A probabilistic framework to justify allowable admixed chloride limits in concrete," *Constr. Build. Mater.*, vol. 139, pp. 490–500, 2017, <http://dx.doi.org/10.1016/j.conbuildmat.2017.02.053>.
- [21] M. Shekarchi, A. Bonakdar, M. Bakhshi, A. Mirdamadi, and B. Mobasher, "Transport properties in metakaolin blended concrete," *Constr. Build. Mater.*, vol. 24, no. 11, pp. 2217–2223, 2010, <http://dx.doi.org/10.1016/j.conbuildmat.2010.04.035>.
- [22] F. Farmani, B. Bonakdarpour, and A. A. Ramezani-pour, "pH reduction through amendment of cement mortar with silica fume enhances its biological treatment using bacterial carbonate precipitation," *Mater. Struct.*, vol. 48, no. 10, pp. 3205–3215, 2015, <http://dx.doi.org/10.1617/s11527-014-0391-7>.
- [23] Y. Mori and B. R. Ellingwood, "Maintaining reliability of concrete structures. I: role of inspection/repair," *J. Struct. Eng.*, vol. 120, no. 3, pp. 824–845, 1994, [http://dx.doi.org/10.1061/\(ASCE\)0733-9445\(1994\)120:3\(824\)](http://dx.doi.org/10.1061/(ASCE)0733-9445(1994)120:3(824)).
- [24] Y. Mori and B. R. Ellingwood, "Maintaining reliability of concrete structures. II: optimum inspection/repair," *J. Struct. Eng.*, vol. 120, no. 3, pp. 846–862, 1994, [http://dx.doi.org/10.1061/\(ASCE\)0733-9445\(1994\)120:3\(846\)](http://dx.doi.org/10.1061/(ASCE)0733-9445(1994)120:3(846)).
- [25] M. P. Enright and D. M. Frangopol, "Service-life prediction of deteriorating concrete bridges," *J. Struct. Eng.*, vol. 124, no. 3, pp. 309–317, 1998, [http://dx.doi.org/10.1061/\(ASCE\)0733-9445\(1998\)124:3\(309\)](http://dx.doi.org/10.1061/(ASCE)0733-9445(1998)124:3(309)).
- [26] M. P. Enright and D. M. Frangopol, "Condition prediction of deteriorating concrete bridges using Bayesian updating," *J. Struct. Eng.*, vol. 125, no. 10, pp. 1118–1125, 1999, [http://dx.doi.org/10.1061/\(ASCE\)0733-9445\(1999\)125:10\(1118\)](http://dx.doi.org/10.1061/(ASCE)0733-9445(1999)125:10(1118)).
- [27] F. Biondini, F. Bontempi, D. M. Frangopol, and P. G. Malerba, "Probabilistic Service Life Assessment and Maintenance Planning of Concrete Structures," *J. Struct. Eng.*, vol. 132, no. 5, pp. 810–825, 2006, [http://dx.doi.org/10.1061/\(ASCE\)0733-9445\(2006\)132:5\(810\)](http://dx.doi.org/10.1061/(ASCE)0733-9445(2006)132:5(810)).
- [28] D. V. Val and M. G. Stewart, "Life-cycle cost analysis of reinforced concrete structures in marine environments," *Struct. Saf.*, vol. 25, no. 4, pp. 343–362, 2003, [http://dx.doi.org/10.1016/S0167-4730\(03\)00014-6](http://dx.doi.org/10.1016/S0167-4730(03)00014-6).
- [29] J. El Hassan, P. Bressolette, A. Chateaufneuf, and K. El Tawil, "Reliability based assessment of the effect of climatic conditions on the corrosion of RC structures subject to chloride ingress," *Eng. Struct.*, vol. 32, no. 10, pp. 3279–3287, 2010, <http://dx.doi.org/10.1016/j.engstruct.2010.07.001>.
- [30] M. G. Stewart, X. Wang, and M. N. Nguyen, "Climate change impact and risks of concrete infrastructure deterioration," *Eng. Struct.*, vol. 33, no. 4, pp. 1326–1337, 2011, <http://dx.doi.org/10.1016/j.engstruct.2011.01.010>.
- [31] E. Bastidas-Arteaga and M. G. Stewart, "Damage risks and economic assessment of climate adaptation strategies for design of new concrete structures subject to chloride-induced corrosion," *Struct. Saf.*, vol. 52, pp. 40–53, 2015, <http://dx.doi.org/10.1016/j.strusafe.2014.10.005>.
- [32] C. Andrade, "Reliability analysis of corrosion onset: initiation limit state," *J. Struct. Integr. Maint.*, vol. 2, no. 4, pp. 200–208, 2017, <http://dx.doi.org/10.1080/24705314.2017.1388693>.
- [33] D. Curran, M. Cross, and B. A. Lewis, "A preliminary analysis of boundary element methods applied to parabolic partial differential equations," in *New Developments in Boundary Element Methods*, C. A. Brebbia, Ed., Southampton: Comput. Mech. Publ., 1980.
- [34] L. C. Wrobel and C. A. Brebbia, "A formulation of the boundary element method for axisymmetric transient heat conduction," *Int. J. Heat Mass Transfer*, vol. 24, no. 5, pp. 843–850, 1981, [http://dx.doi.org/10.1016/S0017-9310\(81\)80007-5](http://dx.doi.org/10.1016/S0017-9310(81)80007-5).
- [35] L. C. Wrobel and C. A. Brebbia, "The dual reciprocity boundary element formulation for nonlinear diffusion problems," *Comput. Methods Appl. Mech. Eng.*, vol. 65, no. 2, pp. 147–164, 1987, [http://dx.doi.org/10.1016/0045-7825\(87\)90010-7](http://dx.doi.org/10.1016/0045-7825(87)90010-7).
- [36] A. H.-S. Ang and W. H. Tang, *Probability Concepts in Engineering, Emphasis on Applications to Civil and Environmental Engineering*, vol. 1, 2nd ed. Hoboken: John Wiley & Sons, 2007.
- [37] R. E. Melchers and A. T. Beck, *Structural Reliability Analysis and Prediction*, 3rd ed. West Sussex, UK: Wiley, 2017, 527 p. <http://dx.doi.org/10.1002/9781119266105>.
- [38] M. Rashki, M. Miri, and M. A. Moghaddam, "A simulation-based method for reliability based design optimization problems with highly nonlinear constraints," *Autom. Construct.*, vol. 47, pp. 24–36, 2014, <http://dx.doi.org/10.1016/j.autcon.2014.07.004>.
- [39] M. Rashki, M. Miri, and M. A. Moghaddam, "A new efficient simulation method to approximate the probability of failure and most probable point," *Struct. Saf.*, vol. 39, pp. 22–29, 2012, <http://dx.doi.org/10.1016/j.strusafe.2012.06.003>.
- [40] D. V. Val and P. A. Trapper, "Probabilistic evaluation of initiation time of chloride-induced corrosion," *Reliab. Eng. Syst. Saf.*, vol. 93, no. 3, pp. 364–372, 2008, <http://dx.doi.org/10.1016/j.res.2006.12.010>.
- [41] Joint Committee on Structural Safety. "JCSS Probabilistic model code." Denmark, 2001, 179 p. [Online]. Available: <http://www.jcss.ethz.ch/>
- [42] P. K. Mehta and P. J. M. Monteiro, *Concrete: Microstructure, Properties, and Materials*. New York: McGraw-Hill, 2005.
- [43] R. McGee, "Modelling of durability performance of tasmanian bridges," in *ICASP8 Applications of Statistics and Probability in Civil Engineering*, vol. 1, R. E. Melchers and M. G. Stewart, Eds. Rotterdam: Balkema, 1999, pp. 297–306.

- [44] G. P. Pellizzer and E. D. Leonel, "Probabilistic corrosion time initiation modelling in reinforced concrete structures using the BEM," *Ibracon Struct. Mater. J.*, vol. 4, 10, 2012.

---

**Author contributions:** GPP implemented the numerical formulations and tested it in several problems. Besides, GPP performed the literature review and wrote this article. EDL proposed the research and supervised the PhD student GPP. EDL wrote this article and handled its review.

**Editors:** Bernardo FonsecaTutikian, José Luiz Antunes de Oliveira e Sousa, Guilherme Aris Parsekian.



## ORIGINAL ARTICLE

# Study of the influence of jiggling of recycled coarse aggregate on the compressive strength of concrete

## *Estudo da influência da jigagem do agregado graúdo reciclado na resistência à compressão do concreto*

Gabriela Nunes Malysz<sup>a</sup> Denise Carpena Coitinho Dal Molin<sup>a</sup> Angela Borges Masuero<sup>a</sup>

<sup>a</sup>Universidade Federal do Rio Grande do Sul – UFRGS, Programa de Pós-Graduação em Engenharia Civil: Construção e Infraestrutura, Porto Alegre, RS, Brasil

Received 14 May 2019  
 Accepted 26 January 2020

**Abstract:** The composition heterogeneity of this type of aggregate is indicated as one of the main restrictions to its potential utilization since it generates great variability in the performance of the types of concrete produced with recycled aggregate. To reduce the use limitations of recycled coarse aggregate (RCA), this study aimed to analyze the use of a jig, a type of equipment used in mining, which performs density separation through air sprinkling in the selection of large aggregates of CDW crushing. To evaluate the equipment performance in the selection of RCA materials, specimens of concrete with recycled aggregate of three different sources were molded before and after selection in the jig, as well as reference concrete with natural aggregate. To measure the performance of the types of concrete produced, axial compressive strength tests were performed. Additionally, a statistical and comparative analysis of the results was performed to seek a better basis for possible conclusions. Analysis of the results of the axial compression strength tests showed that the variability of the recycled aggregates reflected in the inconstancy of the behavior of the concrete produced with them; it was not possible to perceive a common or uniform performance between the three sources of recycled aggregate for the mix design produced. Although some studies point to good separation results with jiggling, it was found that with the use of recycled aggregates available in the local market, for the three studied sources, the selection was not able to minimize the variability of the properties of the recycled types of concrete produced with the selected aggregates.

**Keywords:** construction and demolition waste (CDW), recycled coarse aggregate (RCA), jig, compressive strength, variability.

**Resumo:** A heterogeneidade da composição dos agregados de RCD é apontada como uma das principais restrições ao seu potencial aproveitamento, por gerar grande variabilidade no desempenho dos concretos produzidos com estes. Visando à redução das limitações do uso de agregado graúdo reciclado (AGR), esse estudo buscou analisar a utilização do jig, um equipamento amplamente empregado na área da mineração, o qual realiza separação densitária por meio de aspersão de ar, na seleção de agregados graúdos oriundos da britagem de RCD. Para avaliar o desempenho do equipamento na seleção dos materiais constituintes do AGR, foram moldados corpos de prova de concretos com agregado graúdo reciclado de três fontes distintas, antes e após passagem por processo de jigagem, além de concreto de referência com agregado graúdo natural. Com o propósito de mensurar o comportamento dos concretos produzidos, foram realizados ensaios de resistência à compressão axial e buscando um melhor embasamento das conclusões, foi realizada uma análise estatística e comparativa dos resultados. Os resultados mostraram que a variabilidade dos agregados reciclados refletiu na inconstância do comportamento dos concretos produzidos com eles, onde, não se pôde perceber um desempenho comum ou uniforme entre as três fontes de agregado reciclado, para os traços produzidos. Contudo, embora alguns estudos apontem bons resultados de separação com jigagem, foi verificado que com a utilização de agregados graúdos reciclados disponíveis no mercado local, para as três fontes estudadas, a seleção

Corresponding author: Gabriela Nunes Malysz. E-mail: gabi14nunes@hotmail.com

Financial support: None.

Conflict of interest: Nothing to declare.



This is an Open Access article distributed under the terms of the Creative Commons Attribution License, which permits unrestricted use, distribution, and reproduction in any medium, provided the original work is properly cited.

não conseguiu minimizar a variabilidade da propriedade mecânica estudada nos concretos reciclados produzidos com os agregados selecionados.

**Palavras-chave:** resíduo de construção e demolição (RCD), agregado graúdo reciclado (AGR), jigge, resistência à compressão, variabilidade.

---

**How to cite:** G. N. Malysz, D. C. C. Dal Molin, and A. B. Masuero, “Study of the influence of jiggling of recycled coarse aggregate on the compressive strength of concrete”, *Rev. IBRACON Estrut. Mater.*, vol. 13, no. 5, e13503, 2020, <https://doi.org/10.1590/S1983-41952020000500003>

## 1 INTRODUCTION

The high consumption of construction materials, coupled with the search for sustainable development, has driven studies on the use of Construction and Demolition Waste (CDW). Recycling within the production chain itself presents itself as an alternative for the preservation of natural resources that comprise the raw material of the construction industry. Moreover, the incorporation of recycled materials as aggregates in the composition of concrete in civil construction can bring important advantages from the standpoint of sustainability, such as the reduction of landfill areas for the disposal of these materials, reduction of extraction, and use of natural aggregates from non-renewable sources. In addition to meeting a growing demand for material consumption, recycling construction and demolition waste could also minimize problems with municipal or local solid waste management [1]–[4].

According to Angulo [5], construction and demolition waste (CDW) is responsible for approximately 50% of the mass of municipal solid waste (MSW), which can be considered a significant amount of material available, with an increasing source, which makes feasible the study of its reuse. In contrast with the large generation of waste, there is a concern regarding finding good natural aggregates close to urban areas, particularly when considering transportation costs between sources and construction sites, which are becoming increasingly significant in the composition of work budgets.

Construction and demolition waste have been used for some time in paving, serving as a base and sub-base, as well as in types of concrete and blocks with or without structural function. Nevertheless, as it consists of different materials, aggregates obtained from CDW processing become extremely variable, which directly interferes with the behavior of the concrete produced with them. This circumstance can hinder, prevent, or limit its reuse or recycling [6]–[9].

Research with the use of recycled aggregates has been developed for a few years, and the variability of the materials that compose them and their properties have proved to be obstacles to their use on a large scale. Consequently, studies and proposals for methods or processes that promote the separation or selection of recycled aggregates are becoming evident [10]–[12].

In this context, this study aims to analyze the use of pneumatic jigs to promote a quick separation of the nobler materials, which can be used to replace the natural coarse aggregate in structural concrete. Thus, through laboratory experiments, it aims to research the influence of this selection on the compressive strength of the resulting types of concrete.

This study involved the analysis of the mechanical property of compressive strength in the hardened state of concrete, as it is one of the most widely evaluated concrete properties, which can be considered a parameter capable of indicating quality variations between different types of concrete.

Therefore, the study sought to contribute to the evolution of research with recycled aggregates and collaborate with the possibilities of more noble and economically more advantageous uses for these materials.

## 2 MATERIALS

The following is a description of the materials used in this research, defining the outline of this study.

### 2.1 Cement

For this research, Portland cement CP IV 32 RS, comparable to Type IP by C595/C595M [13], which has pozzolanic additions, was used, as it is a material produced in the region where the tests are carried out and thanks to its widespread use.

The cement used has physical, chemical and mechanical characteristics according to NBR 5736 [14] and NBR 5737 [15], having a unit mass of  $0.876\text{g/cm}^3$ , a specific mass of  $2.65\text{g/cm}^3$  and other characteristics according to tests performed, and provided by the manufacturer [16], which are presented in Table 1.

**Table 1.** Chemical, physical, and mechanical properties of the cement used

Property	CP IV 32	Unit	Requirements
Fineness (waste in 75 $\mu$ sieve)	0.32	%	$\leq 8.0$
Blaine fineness	4920	cm <sup>2</sup> /g	$\geq 3000$
Start of setting	405	min	$\geq 60$
Setting end time	520	min	$\leq 720$
Compressive strength at 3 days	22.3	MPa	$\geq 10$
Compressive strength at 7 days	26.2	MPa	$\geq 20$
Compressive strength at 28 days	41.2	MPa	$\geq 32$
Fire loss (% in mass)	3.78	%	$\leq 4.5$
SO <sub>3</sub> (% in loss)	2.16	%	$\leq 4.0$
MgO (% in loss)	4.21	%	$\leq 6.5$

Source: data supplied by the manufacturer (Interceмент) [16]

## 2.2 Natural fine aggregate

The fine aggregate used was quartz sand, of natural origin, obtained and available in the region of the development of the study, with particle size determined by passing the material through a #4.75 mm mesh sieve.

The sand was characterized according to its physical properties, based on the tests to determine the granulometric composition and fineness modulus according to NBR NM 248 [17], unit mass according to NBR NM 45 [18] and specific mass according to the procedure described in NBR NM 52 [19]. Before conducting the characterization tests, the samples were subjected to the quartering process as prescribed by NBR NM 27 [20], aiming to ensure that the samples represent the material as closely as possible.

The characterization tests were performed at the Construction Environment Materials and Technology Laboratory (LAMTAC/NORIE) at the Federal University of Rio Grande do Sul (UFRGS). Figure 1 shows the granulometric curve of the natural fine quartz aggregate obtained through the results of the granulometry test. As can be seen, the granulometric curve, which characterizes the fine aggregate used, is within the zone considered usable.

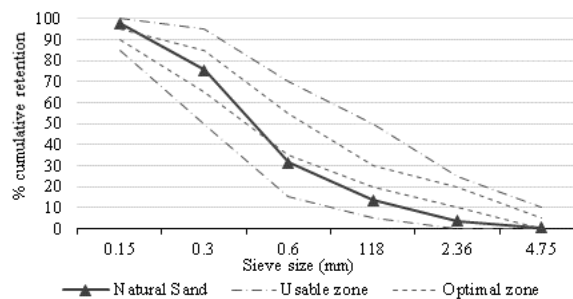


**Figure 1.** Granulometric curve of the natural fine quartz aggregate.

The results for the fineness modulus, maximum aggregate size, specific gravity, and unit mass are shown in Table 2. The characteristics found meet the requirements established by the NBR 7211 standard [21].

**Table 2.** Physical properties of the fine aggregate

Property	Values	Unit	Standard
Fineness Module	2.22	-	NBR NM 248 [17]
Maximum Dimension	2.40	mm	NBR NM 248 [17]
Specific Mass	2.507	g/cm <sup>3</sup>	NBR NM 52 [19]
Unit mass	1.54	g/cm <sup>3</sup>	NBR NM 45 [18]

## 2.3 Natural coarse aggregate

The natural coarse aggregate used was of basaltic origin, with dimensions between 25 mm and 4.8 mm, obtained in the city of Montenegro, in the Brazilian state of Rio Grande do Sul (RS), and sold in the region where the study was developed.

Prior to conducting the characterization tests, the samples were subjected to the quartering process as prescribed by NBR NM 27 [20], aiming to ensure that the samples represent as closely as possible the material. All characterization tests were performed at the Construction Environment Materials and Technology Laboratory (LAMTAC/NORIE) at UFRGS.

The coarse natural aggregate was characterized as to its physical properties according to the determination tests of the granulometric composition of NBR NM 248 [17]. The granulometric curve characteristic of the natural coarse aggregate can be seen in Figure 2, alongside the delineation of the granulometric zone 9.5/25, as specified by the standard to which the results most fit, although it presented a point outside the boundary.

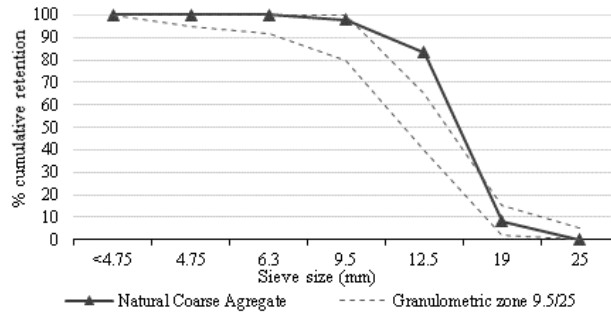


Figure 2. Granulometric curve of the natural coarse basaltic aggregate.

Unit mass tests were carried out according to NBR NM 45 [18], index as prescribed in NBR 7809 [22], specific mass and absorption described in NBR NM 53 [23], the results of which are presented in Table 3 and through which it is possible to observe the fulfillment of the requirements established in the NBR 7211 standard [21].

Table 3. Physical properties of the fine aggregate

Property	Values	Unit	Standard
Fineness Module	7.06	-	NBR NM 248 [17]
Shape Index	2.20	-	NBR 7809 [22]
Water Absorption	0.023	%	NBR NM 53 [23]
Maximum Dimension	25	mm	NBR NM 248 [17]
Specific Mass	2.964	g/cm <sup>3</sup>	NBR NM 53 [23]
Unit Mass	1.694	g/cm <sup>3</sup>	NBR NM 45 [18]

## 2.4 Recycled coarse aggregate

### 2.4.1 Constitution

Construction and demolition waste generally have a high degree of heterogeneity in their composition. For this reason, constitution or composition tests were carried out, with the aim of characterizing the samples of recycled coarse aggregate as to the parcels coming from the different materials that compose them.

The constitution or composition test was performed manually by visually separating the constituent materials from three representative samples of each batch of recycled coarse aggregate, before and after the jiggling process. The samples were previously oven-dried until achieving mass consistency, and aggregates with particle size between 25 and 4.75 millimeters were analyzed, with the passing of material in this last sieve being disregarded.

The samples were weighed, and each piece of material was then separated and weighed separately. The mass percentages of each constituent material in relation to the total mass of the sample were obtained. The final result was achieved through the mean value of the percentages obtained in the analyses carried out by three different persons, seeking a result that could be deemed more assertive and closer to the reality of the materials that compose the batch of recycled coarse aggregate.

The following is the classification of the CDW following separation. In this research, the most representative materials, which were used for separation and classification, were:

- a) Mortar: considering all cementitious material consisting of sand and cement and/or lime, which visually did not contain coarse aggregates or gravel;
- b) Concrete: any material composed by the union of sand, cement and coarse aggregate, whose identification was possible;
- c) Rock: any fragment of natural rock, which may have the presence of some adhered agglomerating material in a small amount, constituting in its largest portion of rocks of different types, except sandstone;
- d) Rock – sandstone: fragments of natural rock that have been identified as sandstone;
- e) Ceramics: all unpolished ceramic material, consisting essentially of bricks and ceramic tiles;
- f) Ceramics – enameled or polished: a portion composed of ceramic materials with at least one of its surfaces being polished and enameled, such as tiles, enameled ceramic tiling, sinks, and sanitary ware;
- g) Mixed: aggregates that were visually formed by two materials, with no predominance of either.
- h) Tailings: other materials that have not been previously classified, considered as contaminants, such as wood, metals, plastics, asbestos, clods of earth or lime, organic materials, glass, plaster, and coal, among others.

Table 4 shows the fractions, in percentage values, of each classified material, for the three sources studied and for the jigged and non-jigged plots. As shown in Table 4, the three sources studied have highly different compositions. Source 1 has significant amounts of sandstone and presents the highest fraction of concrete aggregates. The analysis of source 2 indicates the presence of a larger portion of mortar and ceramic material, including enamel. In turn, source 3, despite being processed and collected at the same location as source 2, but from different batches of CDW, does not present similar characteristics, having the highest amounts of rocks and mixed material among the studied sources.

**Table 4.** Composition of the different materials obtained from the studied sources, before and after jigging, in percentage (%)

MATERIAL	RCA1	RCA1J	RCA2	RCA2J	RCA3	RCA3J
Mortar	28.3	27.2	37.5	33.7	29.1	35.3
Concrete	11.8	11.8	4.2	4.8	6.5	6.0
Rock	32.8	36.6	18.4	21.3	38.7	32.0
Sandstone	22.6	20.9	0.8	0.8	14.7	9.8
Others	10.2	15.7	17.6	20.5	24.0	22.2
Ceramics	25.6	22.0	37.3	37.7	21.5	21.2
non-enameled	21.9	17.2	25.6	22.2	10.7	13.9
Enameled	3.7	4.8	11.7	15.5	10.8	7.3
Mixed	0.3	1.3	1.8	1.8	4.0	5.2
Tailings	1.2	1.1	0.8	0.7	0.2	0.4

Legend: RCA1= Recycled Coarse Aggregate from Source 1, RCA1J= Recycled Coarse Aggregate from Source 1 selected by jigging, RCA2= Recycled Coarse Aggregate from Source 2, RCA2J= Recycled Coarse Aggregate from Source 2 selected by jigging, RCA3= Recycled Coarse Aggregate from Source 3, RCA3J= Recycled Coarse Aggregate from Source 3 selected by jigging.

### 2.4.2 Granulometric composition and fineness module

The granulometric composition tests were performed according to the prescription of NBR NM 248 [17], through which the maximum characteristic dimension of 25 mm was obtained for sources 1 and 3, while 19 mm was obtained for source 2, and a fineness module ranging from 6.66 and 7.06 for the recycled aggregates used in this research. Figure 3 shows the granulometric curves for each recycled aggregate configuration, coupled with the results obtained for the natural coarse aggregate and the limits established by the NBR 7211 standard [21].

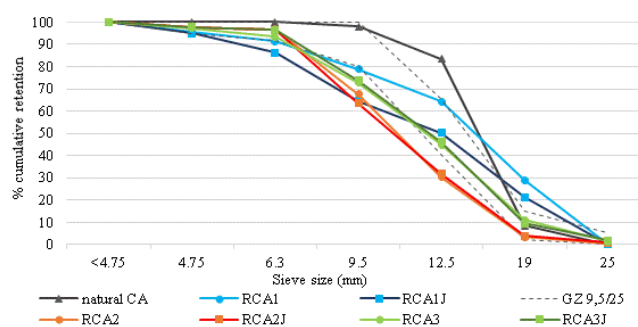


**Figure 3.** Granulometric curves of recycled coarse aggregates from sources 1, 2 and 3.

It can be observed that the granulometric composition of the natural aggregate and some recycled aggregates used in the research did not fully fit the limits of the granulometric zone 9.5/25 (established by NBR 7211 [21]) and used in this study for comparative purposes. Irrespective of comprising coarse, natural, or recycled aggregates, in some cases, not being fully included in the granulometric composition ranges determined by the standard, they were used without alterations or framing in terms of particle size. This choice aimed to employ recycled aggregates in the way they are arranged in the sources and how they are produced, avoiding imposing an additional processing step to their application and use.

### 2.4.3 Shape index

To determine the shape index, the direct method based on measurements of 200 particles with the use of a caliper was adopted, as prescribed by NBR 7809 [22]. The shape index is obtained by the ratio between the maximum length and the minimum thickness of all the measured grains, weighted by the number of grains retained in each granulometric fraction.

The results for this test are shown in Figure 4, for all coarse aggregates involved in the experimental phase of this study, alongside the limit indicated by the standard as the ideal quantity for use in concrete. Considering that the aggregates with cubic grains, considered as the optimal form for crushed aggregates, have an index close to 1, the grains considered lamellar have higher values, i.e. above 2. The higher these values are, the more lamellar is the shape of the grain. Thus, the values obtained indicate that the recycled aggregates can be considered more lamellar.

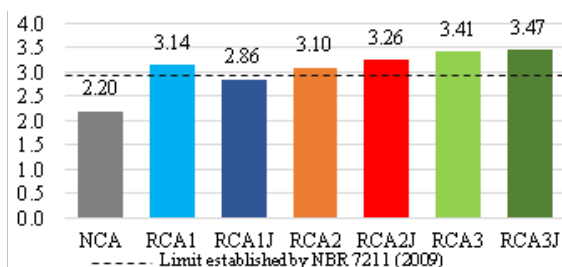


Figure 4. Shape index of the natural and recycled coarse aggregates from sources 1, 2 and 3, before and after jiggling.

### 2.4.4 Unit mass and specific mass

The specific mass is the relation between the dry aggregate mass and its volume, without considering water-permeable pores. The specific mass test adopted was the methodology developed by Leite [1], as it is believed to be the most suitable for recycled coarse aggregates.

Figure 5 shows the specific masses of recycled coarse aggregates, obtained through Leite’s method [1]. Additionally, the value obtained for the natural coarse aggregate is presented, seeking a reference and comparison of the magnitude of the result.

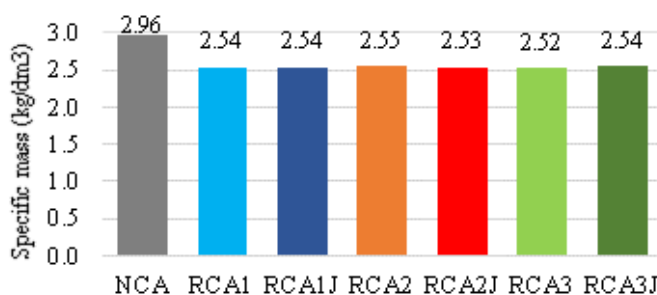


Figure 5. Specific mass of the recycled coarse aggregates from sources 1, 2 and 3.

As shown in Figure 5, the recycled aggregates had a specific mass lower than that of natural aggregates. When comparing the specific mass values between the recycled coarse aggregates analyzed, they did not present significant differences among themselves as to the processing performed for each source or among the different sources.

The values obtained for the unit mass of the aggregates used in this study are shown in Figure 6, in which the results ranged between 1.10 g/cm<sup>3</sup> and 1.20 g/cm<sup>3</sup> for recycled aggregates. Compared to the unit mass value of the natural coarse aggregate, the results found for all recycled aggregates studied were lower; however, when comparing the values of sources 1 and 2 before and after jigging, there is a slight increase in values.

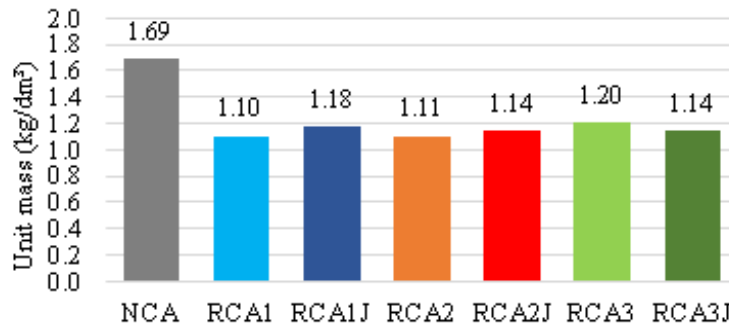


Figure 6. Unit mass of the recycled coarse aggregates from sources 1, 2 and 3

### 2.4.5 Water absorption

The determination of the absorption rate of the recycled aggregates is important for the study of the dosage of types of concrete that will use this material, as the recycled aggregate is a material with higher porosity than the natural aggregate [24]. In this study, the method chosen to assess the absorption rate was the one presented by Leite et al. [25], which was adapted from the method proposed by Leite [1]. This test methodology has better applicability and shows more realistic results for recycled coarse aggregates, thanks to the high porosity and the possibility of material loss due to disintegration.

Figure 7 illustrates the results obtained for the tests performed, in which it can be seen that the natural coarse aggregate used as a reference – of basaltic origin and with very low porosity – presents extremely low absorption rates when compared with the rates achieved by recycled aggregates. Nevertheless, when comparing the results obtained for each source of recycled coarse aggregate, before and after jigging, it can be seen that there was a reduction in the absorption rates, which can be attributed to the density selection carried out on these materials.

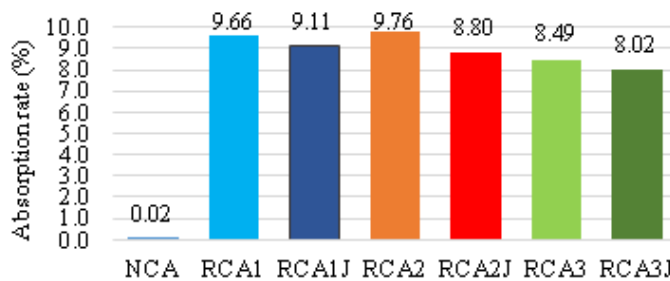


Figure 7. Absorption rate of the natural and recycled coarse aggregates

### 2.5 Water

The water used for the production of concrete, as well as for saturation of recycled aggregates and the performance of certain tests, was obtained at the public supply network of the city of Porto Alegre, in the state of Rio Grande do Sul, Brazil.

## 3 EXPERIMENTAL PROGRAM

The experimental program of this research was designed with the aim of analyzing the properties of the concrete produced with recycled coarse aggregate before and after the processing of these aggregates via jigging. To this end, three different sources of aggregates obtained by the construction and demolition waste crushing process were studied. Suppliers market or dispose of recycled aggregates with a particle size between 4.75 mm and 25 mm, with all the material necessary to carry out this research obtained through donation.

Characterization tests were carried out, with representative samples of the aggregates, before and after jiggling. The characterization tests selected included those most performed in studies with coarse aggregate, which were presented in item 2. The relevance of these tests is justified by the fact that the results obtained may have an influence on their method of disposal into cementitious matrices, workability, and cement consumption, thereby reflecting the consistency and compactness of the resulting concrete and affecting the performance and costs of types of concrete made with these materials [26].

Three concrete mixes were molded for each sample of recycled aggregate (jigged and non-jigged). The three features chosen for this research were compositions with more resistant matrices, intending to verify the resistance of the recycled aggregate in the recycled concrete, as opposed to the matrix. Reference concrete was also produced with natural coarse aggregates, for comparative analysis.

### 3.1 Sampling

The acquisition of recycled aggregates was carried out in landfills, demolition companies, and non-governmental organizations, which receive or collect construction and demolition waste. These institutions perform the visual and manual removal of impurities and process this material in crushers for later sale or donation.

In this research, Source 1 comprises the coarse aggregates recycled from the company that collects CDW through dumpsters, performs the material crushing, and markets the recycled aggregates in three granulometric ranges. The company is in the city of Montenegro, RS, and the collection was carried out in May 2017. The recycled bulk CDW aggregates from Source 2 were obtained from a non-governmental organization in the south of the city of Porto Alegre in November 2017, with the NGO receiving construction and demolition waste from the community in which it is inserted, performing the crushing and donating this material to the local population. For the Source 3 of recycled coarse aggregates, the materials were obtained at the same location as Source 2. These, however, came from the processing of a different batch of construction and demolition waste, crushed, and collected in February 2018.

The collections were carried out with the aid of a shovel and the material was collected along the entire height of the pile. The recycled aggregates were packed in 30 bags for the storage and transportation of construction materials. Upon arrival at the laboratory, the bags were weighed, their masses being between the values of 30 kg and 36 kg, with the total material collected close to 1 metric ton.

The recycled coarse aggregates were homogenized and quartered using the procedure described in NBR NM 27 [20], from which the necessary quantities of the material were separated, in terms of mass, for each of the tests carried out and for subsequent preparation of the types of concrete. Through this technique, samples of material from each source were separated (around 70% of the total), which were transported to the Mineral Processing Laboratory (LAPROM) of the Federal University of Rio Grande do Sul to be processed in the pneumatic jig.

### 3.2 Separation tests

The particle separation method selected for the development of this research was air jiggling, which was carried out using a pneumatic jig. This choice was made as it is a type of equipment capable of processing large amounts of material, with studies that show its good performance in the selection of particles with particle size close to those of the coarse aggregate, as well as thanks to its low cost of acquisition and maintenance, which increases the possibilities of applying the process on a large scale.

As described by Sampaio and Tavares [27], the first step in the sequence of the jiggling operation concerns the selection of the equipment's operating settings. For this choice, a search was made for works that carried out the process of jiggling with construction and demolition waste, such as those published by Cazacliu et al. [28], Silva et al. [29], Ambrós [30], Sampaio et al. [31], and Cunha [32], among others. In parallel, pilot tests were carried out with the recycled aggregates from Source 1. Based on the parameters already used by the aforementioned researchers, tests were carried out to adapt the processed material to the operating parameters of the jig. The visual analysis of the stratification of the layers of the material, coupled with the experience of the equipment operator and the values previously adopted in other studies pointed to the choice of the criteria that were used. These operating parameters of the equipment were introduced in the control panel and kept constant for the three evaluated sources. They are:

- a) Frequency of 180 rpm, which is the rate of air pulsation in the stratification chamber;
- b) Expansion Bed rate of 70%, due to the power of the airflow;
- c) Processing time of 120 seconds.

The amount of material used in each jiggling process was approximately 60 kg, and the expectation after jiggling was that the denser coarse aggregates would be deposited in the lower tray from which they were collected. At the end of

each test, the material was collected from the lower layer of the separation chamber. After the processing of the coarse aggregates, the total amount collected, from each specific source, was again homogenized and quartered in the portions necessary to carry out the characterization and preparation of types of concrete tests, aiming to ensure that all portions of samples were representative of the material.

### 3.3 Production of the concretes

The recycled coarse aggregates underwent the wetting or pre-saturation stage before making the mixtures for concrete, aiming to compensate for the difference in absorption between natural and recycled aggregates [33], [34].

The research sought to stipulate a standard procedure for all recycled aggregates that were studied, the immersion time being chosen based on the absorption rate obtained in the first test performed for Source 1. The aggregates were submerged for 2 hours, seeking a minimum saturation of 80%. Afterwards, they were placed in a sieve, with a mesh opening of 0.15 mm, for drying in open air, for a period of 4 hours, until the condition of saturation with a dry surface was obtained.

### 3.4 Experimental dosage and definition of the reference line and recycled concrete

The dosage method adopted for this study was the IPT/EPUSP developed by Helene and Terzian [35], which consists of adjusting the ideal mortar content by setting the Slump cone test value (as prescribed in NBR NM 67 [36]), taking it as a control parameter. Aiming at a better analysis of the concrete behavior, three mass mixes were made for each aggregate to be studied, with lower, intermediate, and higher consumption of cement, which can be called, in a simplified way, poor, intermediate and rich mixes. The workability adjustment was performed exclusively by correcting the amount of water necessary to achieve the reduction defined for this research, set at 100 +/- 20mm, i.e., plasticizers or superplasticizers were not used to obtain the predetermined consistency.

The materials were mixed using a concrete mixer with a vertical axis previously imprinted with the application of a mixture of cement, natural fine aggregate, and water, both in its drum and in its shovels. The idea of priming aims to prevent the mortar from the first concrete mixture from being lost because of the concrete mixer walls or from adhering to the paddles. Soon after, the priming mortar was removed and discarded, so that the mixtures could then be made.

The order of placing the materials in the mixer was as follows: cement, sand, and an initial amount of water, to provide a kind of bed to protect the recycled aggregates and avoid breaking the grains and altering their particle size by the movement of the concrete mixer, as recommended by Cordeiro's research [24].

Unit mixes were made in relation to the 1:m cement mass, where m is the sum of the mass quantities of coarse and fine aggregates. The experimental dosage was carried out with the recycled coarse aggregates from source 1 (RCA1), with mixtures being produced for the unitary mix in relation to the cement mass quantities of 1:2.5; 1:4, and 1:5.5. Concreting started with the intermediate line with m equal to 4, followed by the rich and poor lines, with values of m equal to 2.5 and 5.5, respectively. The ideal mortar content, defined experimentally, was 55%.

The consistency determination was performed through the Slump Clone Test, as prescribed in NBR NM 67 [36], and the amount of water used in the mixture was quantified to reach the defined values of 100 +/- 20mm.

The experimental program included the implementation of types of concrete for the unit mixes in relation to the cement mass quantities of 1:2.5; 1:4.0 and 1:5.5 with natural coarse aggregate (reference) and for the three batches of recycled coarse aggregate before and after jiggling.

### 3.5 Production of specimens

For each of the twenty-one mixes defined, six cylindrical specimens were molded, with dimensions of 10 x 20 cm, for the performance of the axial compressive strength tests, and the manufacture of the specimens followed the parameters established by NBR 5738 [37] for molding and curing. All the test specimens (TSs) relating to a specific concrete mix were molded simultaneously. After pouring and filling the metal molds, they were compacted on a vibrating table. The preparation of the metal molds was carried out through the cleaning and application of release agent (mineral oil) to facilitate their dismantle or removal.

After molding, the specimens were covered with a plastic bag to avoid water loss, being kept in the test site during the first 24 hours. Subsequently, they were dismantled and stored in a wet chamber with a controlled temperature of 23 +/- 2°C and relative humidity of 90-100% to ensure curing during the period stipulated for carrying out the tests in a hardened state.

### 3.6 Axial compressive strength test

For the evaluation of the influence of the density separation process of the recycled coarse aggregate on the behavior of the hardened concrete, axial compression resistance tests were carried out, according to procedures prescribed in NBR 5739 [38].

The standard time adopted for the analysis of the mechanical property of types of concrete was 28 days, and all specimens had their bases previously rectified as recommended in NBR NM 77 [39].

All tests of this research were carried out at the Construction Environment Materials and Technology Laboratory (LAMTAC /NORIE), located at central campus of the Federal University of Rio Grande do Sul, using the computerized press of the EMIC MCT30 PC 200i model, with repetitions performed for three specimens per family of concrete produced.

## 4 RESULTS AND DISCUSSIONS

The results achieved for the axial compressive strength of the produced concrete are shown in Table 5. Each value represents the average of three experimental observations, the standard deviation of these results, and the coefficient of variation also being described. To facilitate the visual analysis, the values were plotted in Figure 8.

**Table 5.** Mean, standard deviation and coefficient of variation of axial compressive strength (MPa).

Aggregate type	Unit mix	Mean (MPa)	Standard deviation (MPa)	CV (%)
NCA	2.5	35.18	0.96	2.7
	4.0	31.51	1.45	4.6
	5.5	24.88	0.04	0.1
RCA1	2.5	22.16	1.04	4.7
	4.0	18.80	0.57	3.0
	5.5	14.52	1.03	7.1
RCA1J	2.5	24.73	1.63	6.6
	4.0	22.54	0.70	3.1
	5.5	17.30	0.75	4.3
RCA2	2.5	26.35	2.22	8.4
	4.0	20.68	0.41	2.0
	5.5	14.86	1.19	8.0
RCA2J	2.5	24.96	1.44	5.8
	4.0	19.84	0.76	3.8
	5.5	16.86	0.91	5.4
RCA3	2.5	23.08	1.05	4.5
	4.0	17.83	1.55	8.7
	5.5	18.13	1.24	6.8
RCA3J	2.5	22.34	1.80	8.1
	4.0	21.14	1.55	7.3
	5.5	15.54	0.90	5.8

Legend: NCA= Natural Coarse Aggregate, RCA1= Recycled Coarse Aggregate from Source 1, RCA1J= Recycled Coarse Aggregate from Source 1 selected by jiggling, RCA2= Recycled Coarse Aggregate from Source 2, RCA2J= Recycled Coarse Aggregate from Source 2 selected by jiggling, RCA3= Recycled Coarse Aggregate from Source 3, RCA3J= Recycled Coarse Aggregate from Source 3 selected by jiggling.

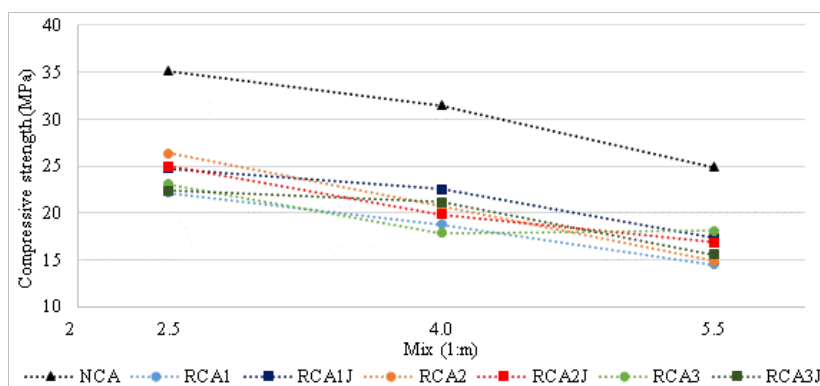


**Figure 8.** Influence of the mix on the axial compressive strength at 28 days (MPa)

Due to the variability of recycled aggregates, the types of concrete produced with them also showed inconsistent behavior. As shown in Figure 8, there was no common or uniform performance among the three sources of recycled aggregate for the three mixes produced.

Still, in Figure 8, the analysis of the values for the types of concrete produced with aggregates from source 1 revealed an increase in compressive strength of the recycled aggregates compared to those that were not selected by jigging, for all mixes investigated. For source 2, the results obtained were different from those expected, and the aggregates that did not undergo density selection showed better performance for the rich and intermediate mixes, while the selected aggregates showed better results only for the poorest cement mix. For source 3, it can be concluded that jigging did not promote improvements for the rich and poor cement mixes, presenting gains for the axial compressive strength parameter only for the intermediate mix.

Thus, Figure 8 shows that the only aggregates that showed gains in the axial compressive strength values, for all mixes that underwent the density separation process were the aggregates from source 1. The same could not be stated for sources 2 and 3, which show a reduction in the compressive strength value for some mixes. A hypothesis for this behavior can be because source 1 has a smaller amount of enameled and polished ceramic lamellar material. Such peculiarity may have generated interferences in the density separation process, as it was possible to observe in the information on the characterization of composition, particle size, shape index and unit mass of the recycled aggregates analyzed, while for source 1, gains and improvements could be identified, as opposed to what was observed for the other sources.

Aiming at a more consistent evaluation of the axial compression resistance data, a statistical treatment was performed using the analysis of variance (ANOVA). The results obtained can be seen in Table 6.

**Table 6.** Analysis of Variance (ANOVA) for compressive strength.

Variation source	SQ	GDL	MQ	Test F	Probability	Significance
A: RCA Source	5.58	2	2.79	1.82	17.70%	NO
B: Selection by Jigging	9.07	1	9.07	5.90	2.02%	YES
C: Mix	533.99	2	266.99	173.82	0.00%	YES
AB	22.83	2	11.41	7.43	0.20%	YES
AC	28.51	4	7.13	4.64	0.40%	YES
BC	5.84	2	2.92	1.90	16.43%	NO
ABC	16.26	4	4.07	2.65	4.91%	YES
Error	55.30	36	1.54			
TOTAL	677.37	53				

To assess this study, a significance level of 5% was considered, in which only factors or combinations with a probability of less than 5% are considered significant, i.e., they cause changes in the response variable. Therefore, through the analysis of variance, the source effect of the recycled aggregates did not have a significant impact on the axial compressive strength results. The controllable factors evaluated represented by the letters B and C (processing and mix, respectively) were significant, concomitantly with the interactions AB and AC. Thus, these factors and interactions will be shown separately below.

Figure 9 shows the isolated effects for the selection by jigging (a) and the mix (b) on the compressive strength, through the mean and standard deviation bars, of all observations referring to recycled aggregates that have not undergone treatment, as well as the recycled aggregates that were selected by jigging and through the mean axial compressive strength values obtained for each line.

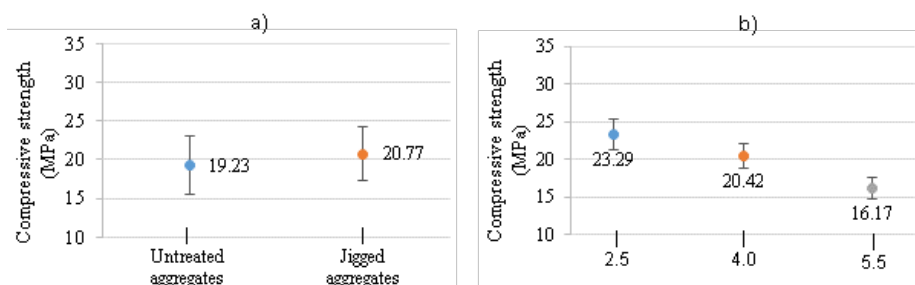


**Figure 9.** Isolated effects in axial compressive strength.

As shown in Figure 9a, for all sources and all mixes produced, the mean results of the axial compression test for the aggregates that were selected by jiggling show slightly higher values than those that did not undergo this process. The analysis of variance shows significant improvement and considers that the processing has an impact on the values for the analyzed parameter. In mining, the jiggling process provides the selection of the densest materials, so it was expected that there would be a separation of the most resistant aggregates. This may explain the fact that the compressive strength values of types of concrete produced with the aggregates selected in the jig are higher than those that were not been processed.

The knowledge that the mix, particularly water/cement ratios used in concrete mixtures, is impactful for the strength values achieved by concrete in the hardened state is already a consensus in the scientific community. Complementing the results and justifications presented in Figure 9b, for the axial compressive strength results of types of concrete per line used, its isolated effect shows that the richer the line is (the lower water/cement ratio), the higher the values reached for the compressive strength of concrete.

Figure 10 shows the interaction of the effects of the source and the selection by the density of the recycled aggregates studied, in relation to the response variable. For sources 1 and 3, the separation process by jiggling generated strength gains in the types of concrete produced with the processed aggregates, whereas for source 1, this increase was more noticeable. Nevertheless, there was an inversion in source 2, in which the density selection generated discrete losses in the strength values.

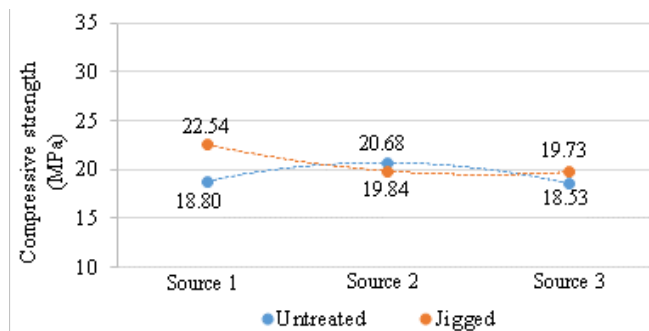


Figure 10. Effect of the source-treatment interaction in axial compressive strength.

The variability of the materials that make up the recycled aggregates, as evidenced in their characterization tests, coupled with the difficulty in promoting an effective separation of their components using jiggling, may have influenced the results, which did not show significant gains as expected, particularly for sources 2 and 3.

The effectiveness of jiggling is linked to the source of origin of the recycled aggregate, through the composition of the CDW and form of crushing. Contrary to what was expected, the density selection was not able to reduce the variability of the axial compressive strength of types of concrete produced with aggregates, since by comparing the values obtained between the sources, it is not possible to notice a constant behavior or close results, among them, for this mechanical property.

Figure 11 shows the effect of the interaction between the studied traits, and the sources from which the recycled aggregates were obtained.

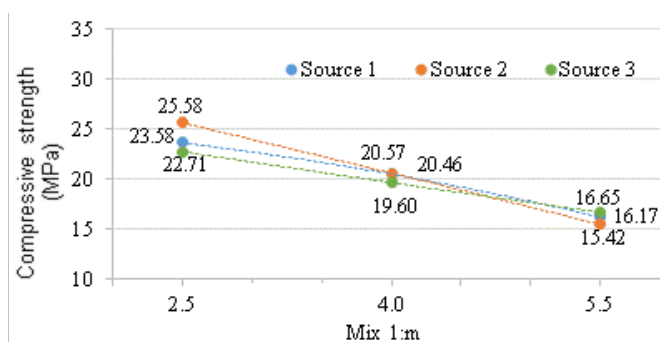


Figure 11. Effect of the mix-source interaction in axial compressive strength.

In Figure 11, it can be seen that the recycled aggregates present different behaviors, as they come from the transformation of different materials, in which the variability of their characteristics, already presented, generate different behaviors and results for the compressive strength of concrete produced with these aggregates. Only in the richest mixes is it possible to prove the influence of the quality of the recycled CDW aggregate. Therefore, it is noticeable that the limiting factor for the improvement of the strength of the produced concrete was the aggregates, as the improvement of the matrix, with the enrichment of the mix and subsequent reduction of the water/cement ratio, generated slight increases or increases below expectations.

## 5 CONCLUSIONS

Considering the axial compressive strength, all results obtained with the types of concrete produced with recycled aggregates were lower than for those obtained with the reference aggregate, as predicted. The density selection reflected gains in compressive strength of the concrete produced with aggregates from source 1, for all mixes, ranging from 12% to 20%. Nevertheless, for the other sources, no uniform behavior was observed, with strength losses even for the concrete produced with recycled aggregates that had undergone jiggling.

Although the analysis of variance showed significant gains and considered the jiggling process as having an impact on the values for compressive strength, complementary studies must be carried out to evaluate the feasibility of the implementation of the process, coupled with the gain it can provide.

The variability of the materials that make up the recycled coarse aggregates, which was noticed in the characterization tests, as well as the difficulty in promoting an effective separation of the materials, may have influenced the variability of the results of axial compression strength. One hypothesis was raised for the reason why the jiggling process was not effective, which is the presence of enameled or polished ceramic lamellar material, which may have generated interferences in the density separation process.

Therefore, the use of jig for the selection of large aggregates of construction and demolition waste from commercial sources should be better studied and evaluated, to understand the phenomena and particularities of processing this type of material.

## ACKNOWLEDGEMENTS

The Federal University of Rio Grande do Sul (UFRGS), the Graduate Program in Civil Engineering: Construction and Infrastructure (PPGCI), the Center for Innovation in Construction (NORIE), the Construction Environment Materials and Technology Laboratory (LAMTAC,) and the Mineral Processing Laboratory (LAPROM).

## CITATIONS

- [1] M. B. Leite, "Avaliação de propriedades mecânicas de concretos produzidos com agregados reciclados de resíduos de construção e demolição," M.S. thesis, Prog. Pós-grad. Eng. Civ., Univ. Fed. Rio Grande do Sul, Porto Alegre, 2001.
- [2] J. Santos, F. Branco, and J. Brito, *Mechanical Properties of Concrete with Coarse Recycled Concrete Aggregates* (paper 047). Oslo, Norway: Sustainable Building, 2002.
- [3] E. Mulder, T. P. R. Jong, and L. Feenstra, "Closed Cycle Construction: an integrated process for the separation and reuse of C&D waste," *Waste Manag.*, vol. 27, no. 10, pp. 1408–1415, 2007.
- [4] S. Luo, S. Ye, J. Xiao, J. Zheng, and Y. Zhu, "Carbonated recycled coarse aggregate and uniaxial compressive stress-strain relation of recycled aggregate concrete," *Constr. Build. Mater.*, vol. 188, pp. 956–965, 2018.
- [5] S. C. Angulo, "Caracterização de agregados de resíduos de construção e demolição reciclados e a influência de suas características no comportamento de concretos," M.S. thesis, Prog. Pós-grad. Eng. Civ., Univ. São Paulo, São Paulo, 2005.
- [6] A. Rao, K. N. Jha, and S. Misra, "Use of aggregates from recycled construction and demolition waste in concrete," *Resour. Conserv. Recycling*, vol. 50, no. 1, pp. 71–81, 2007.
- [7] R. V. Silva, R. Dhir, and J. Brito, "The influence of the use of recycled aggregates on the compressive strength of concrete: a review," *Eur. J. Environ. Civ. Eng.*, vol. 19, no. 7, pp. 825–849, 2015.
- [8] C. Medina, W. Zhu, T. Howind, M. Frías, and M. I. Sánchez de Rojas, "Effect of the constituents (asphalt, clay materials, floating particles and fines) of construction and demolition waste on the properties of recycled concretes," *Constr. Build. Mater.*, vol. 79, pp. 22–33, 2015.
- [9] J. Pacheco, J. Brito, C. Chastre, and L. Evangelista, "Experimental investigation on the variability of the main mechanical properties of concrete produced with coarse recycled concrete aggregates," *Constr. Build. Mater.*, vol. 201, pp. 110–120, 2019.
- [10] P. Kamrath, "Demolition techniques and production of construction and demolition waste (CDW) for recycling," in *Handbook of recycled concrete and demolition waste*, F. Pacheco-Torgal et al., Eds., Germany: Woodhead Publishing, ch. 8, pp. 186–209, 2013.

- [11] K. Pandurangan, A. Dayanithy, and S. Om Prakash, "Influence of treatment methods on the bond strength of recycled aggregate concrete," *Constr. Build. Mater.*, vol. 120, pp. 212–221, 2016.
- [12] R. S. Paranhos, B. G. Cazacliu, C. H. Sampaio, C. O. Petter, R. Oliveira No., and F. Huchet, "A sorting method to value recycled concrete," *J. Clean. Prod.*, vol. 112, pp. 2249–2258, 2016.
- [13] American Society for Testing and Materials, *Standard Specification for Portland Cement*, ASTM C 150, 2018.
- [14] Associação Brasileira de Normas Técnicas, *Cimento Portland Pozolânico – Especificação*, NBR 5736, 1991.
- [15] Associação Brasileira de Normas Técnicas, *Cimento Portland Resistentes à Sulfatos – Especificação*, NBR 5737, 1992.
- [16] A. Lemos. "RES: caracterização de cimento". Apr. 24, 2018.
- [17] Associação Brasileira de Normas Técnicas, *Agregados – Determinação da Composição Granulométrica*, NBR NM 248, 2003.
- [18] Associação Brasileira de Normas Técnicas, *Agregado – Determinação da Massa Unitária e dos Espaços Vazios*, NBR NM 45, 2006.
- [19] Associação Brasileira de Normas Técnicas, *Agregado Miúdo – Determinação da Massa Específica e Massa Específica Aparente*, NBR NM 52, 2009.
- [20] Associação Brasileira de Normas Técnicas, *Agregados – Redução da Amostra de Campo para Ensaio de Laboratório*, NBR NM 27, 2001.
- [21] Associação Brasileira de Normas Técnicas, *Agregados para Concreto – Especificação*, NBR 7211, 2009.
- [22] Associação Brasileira de Normas Técnicas, *Agregado Graúdo – Determinação do Índice de Forma pelo Método do Paquímetro – Método de Ensaio*, NBR 7809, 2006.
- [23] Associação Brasileira de Normas Técnicas, *Agregado Graúdo – Determinação da Massa Específica, Massa Específica Aparente e Absorção de Água*, NBR NM 53, 2009.
- [24] L. N. P. Cordeiro, "Análise dos parâmetros principais que regem a variabilidade dos concretos produzidos com agregados graúdos reciclados de concreto," M.S. thesis, Prog. Pós-grad. Eng. Civ., Univ. Fed. Rio Grande do Sul, Porto Alegre, 2013.
- [25] M. B. Leite, L. N. P. Cordeiro, A. B. Masuero, and D. C. C. Dal Molin, "Proposta de adaptação do procedimento proposto por Leite (2001) para determinação da absorção de agregados reciclados de resíduo de construção demolição," in *An. Cong. Int. Patol. Reabil. Estrut.*, 2011.
- [26] A. Coutinho, *Fabrico e Propriedades do Betão*. Lisboa: LNEC, 2000, v. I, II, III.
- [27] C. H. Sampaio and L. M. M. Tavares, *Beneficiamento Gravimétrico: uma Introdução aos Processos de Concentração Mineral e Reciclagem de Materiais por Densidade*. Porto Alegre: Book, 2005.
- [28] B. Cazacliu et al., "The potential of using air jigging to sort recycled aggregates," *J. Clean. Prod.*, vol. 66, pp. 46–53, 2014.
- [29] R. B. Silva, S. C. Angulo, R. G. Pileggi, and C. O. Silva, "Concretos secos produzidos com agregados reciclado de RCD separados por densidade," *Ambient. Constr.*, vol. 15, no. 4, pp. 335–349, 2015.
- [30] W. M. Ambrós, C. H. Sampaio, B. G. Cazacliu, G. L. Miltzarek, and L. R. Miranda, "Usage of air jigging for multi-component separation of construction and demolition waste," *Waste Manag.*, vol. 60, pp. 75–83, 2017.
- [31] C. H. Sampaio et al., "Stratification in air jigs of concrete/brick/gypsum particles," *Constr. Build. Mater.*, vol. 109, pp. 63–72, 2016.
- [32] M. G. C. Cunha "Viabilidade do uso de RCD proveniente da geração dos concretos convencional e Alta Resistência através da utilização do jigge como agente do beneficiamento," M.S. thesis, Prog. Pós-grad. Eng. Min., Metal. Mater., Univ. Fed. Rio Grande do Sul, Porto Alegre, 2017.
- [33] Cement and Concrete Association of New Zealand, *Best Practice Guide for the Use of Recycled Aggregates in New Concrete*. New Zealand: CCANZ, 2011, pp. 49.
- [34] A. Coelho, and J. Brito, "Preparation of concrete aggregates from construction and demolition waste (CDW)," in *Handbook of recycled concrete and demolition waste, civil and structural engineering*, F. Pacheco-Torgal, V. W. Y. Tam, and J. Brito, Ed., Cambridge: Woodhead Publishing, ch. 9, pp. 210–245, 2013.
- [35] P. R. L. Helene, and P. Terzian, *Manual de Dosagem e Controle do Concreto*. São Paulo: Book São Paulo, 1992.
- [36] Associação Brasileira de Normas Técnicas, *Concreto – Determinação da Consistência pelo Abatimento do Tronco de Cone*, NBR NM 67, 1998.
- [37] Associação Brasileira de Normas Técnicas, *Concreto – Procedimento para Moldagem e Cura de Corpos de Prova*, NBR 5738, 2015.
- [38] Associação Brasileira de Normas Técnicas, *Concreto – Ensaio de Compressão de Corpos-de-Prova Cilíndricos*, NBR 5739, 2007.
- [39] Associação Brasileira de Normas Técnicas, *Concreto – Preparação das Bases dos Corpos-de-Prova e Testemunhos Cilíndricos para Ensaio de Compressão*, NBR NM 77, 1996.

---

**Author contributions:** DCDM and ABM: conceptualization, methodology, funding acquisition and supervision.

**Editors:** Jose Tadeu Balbo, José Luiz Antunes de Oliveira e Sousa, Guilherme Aris Parsekian.



ORIGINAL ARTICLE

# Proposition of a simplified analytical design procedure for lattice girder slabs with shuttering in cold-formed steel lipped channel section

*Proposição de procedimento analítico simplificado para dimensionamento de lajes treliçadas com forma em perfil de aço formado a frio do tipo U enrijecido*

Lucas Fadini Favarato<sup>a,b</sup>

André Vasconcelos Soares Gomes<sup>a</sup>

Daniel Carvalho de Moura Candido<sup>a</sup>

Adenilcia Fernanda Grobério Calenzani<sup>a</sup>

Juliana da Cruz Vianna Pires<sup>a</sup>

Johann Andrade Ferrareto<sup>b</sup>

<sup>a</sup>Universidade Federal do Espírito Santo – UFES, Programa de Pós-graduação em Engenharia Civil, Vitória, ES, Brasil

<sup>b</sup>ArcelorMittal Tubarão, Serra, ES, Brasil

Received 01 September 2019  
Accepted 13 February 2020

**Abstract:** This paper presents an analytical procedure to determine the resistance of a new composite ribbed lattice slab system, composed by a lipped channel cold-formed steel (CFS) profile in minor bending fastened to a lattice girder by plastic connectors, as well as light filling elements and additional rebar. Motivated by the lack of standardized procedures for such system, this paper combines slab design prescriptions to create a computational tool that estimates load capacity and required propping during construction, serving as a basis for a design catalogue. Finally, a strong limitation of unpropped construction due to the low performance of the cold-formed profile under minor axis bending was observed, being the system able to reach spans up to 1.5 m between props in general.

**Keywords:** lattice girder slab, cold-formed steel shuttering, design procedure, composite slab, span and live-load.

**Resumo:** Este artigo apresenta um procedimento analítico para determinação da resistência de um novo sistema de lajes mistas nervuradas treliçadas, composto por um perfil de aço formado a frio (PFF) do tipo U enrijecido fletido em torno do eixo de menor inércia acoplado a uma treliça eletrossoldada através de conectores plásticos, além de blocos de enchimento e armaduras adicionais. Em decorrência da falta de procedimentos normatizados para esse tipo de sistema, este trabalho combina métodos de dimensionamento de lajes em uma ferramenta computacional capaz de estimar as sobrecargas máximas e escoramento requerido na etapa de construção, base para a tabela de vãos e cargas. Por fim, observou-se forte limitação à construção não escorada pela baixa rigidez do perfil de aço, sendo o sistema capaz de atingir vãos entre escoras de até 1.5 m, em média.

**Palavras-chave:** laje treliçada, forma de aço formado a frio, procedimento para dimensionamento, laje mista, tabela de vãos e cargas.

**How to cite:** L. F. Favarato, A. V. S. Gomes, D. C. M. Candido, A. F. G. Calenzani, J. C. V. Pires, and J. A. Ferrareto, "Proposition of a simplified analytical design procedure for lattice girder slabs with shuttering in cold-formed steel lipped channel section," *Rev. IBRACON Estrut. Mater.*, vol. 13, no. 5, e13504, 2020, <https://doi.org/10.1590/S1983-41952020000500004>

**Corresponding author:** Lucas Fadini Favarato. E-mail: [lucasffavarato@gmail.com](mailto:lucasffavarato@gmail.com), [lucas.favarato@arcelormittal.com.br](mailto:lucas.favarato@arcelormittal.com.br)

**Financial support:** ArcelorMittal Tubarão, Federal University of Espírito Santo, CAPES, CNPq and FAPES.

**Conflict of interest:** Nothing to declare.



This is an Open Access article distributed under the terms of the Creative Commons Attribution License, which permits unrestricted use, distribution, and reproduction in any medium, provided the original work is properly cited.

## 1 INTRODUCTION

Since the beginning of the XIX century, structural engineering has undergone considerable changes in the development of structural materials and design methodologies. Initially presented as a combination of concrete or steel elements working independently, the first composite slab systems combining these materials were developed in the United States of America in 1930. Further studies resulted in the development of the steel deck slabs used in modern buildings [1], [2].

Steel-concrete composite systems present several benefits such as architectural flexibility, simplified construction procedures and diminished material waste. When compared to structures built exclusively of steel, composite structures may reduce the use of such material, as well as increase global structural stiffness. Alternatively, in comparison with reinforced concrete (RC) structures, implementation of steel-concrete composite elements can result in improvements in constructional precision, reduction of weight and estimated time of construction, as well as considerable reduction of propping and shuttering [2]–[4]. As such, a steady increase in the use of structures of this nature, such as composite slabs, is observed. Although steel-concrete composite behavior may increase mechanical efficiency, there are specific design cases in which the composite behavior is not accounted for [1], [2].

In this context, a new composite slab system, called Trelifácil®, was developed as an alternative for the traditional lattice girder precast concrete slabs. The system is composed by a CFS lipped channel section subjected to minor axis bending, fastened to a lattice girder by uniformly distributed plastic spacers, as shown in Figure 1. The system also uses filling material, such as Expanded Polystyrene, additional rebar if needed, and concrete. Some of the advantages of using Trelifácil®, as stated by the manufacturer are; ease of assembly, 80% weight reduction of each rib, increased dimensional precision during construction and improvements on safety and ergonomic conditions during assembly. Furthermore, since concrete casting occurs in a single stage, as opposed to the interaction of concrete with distinct curing ages observed in the traditional lattice girder slabs, less deformation and increased material homogeneity are expected during serviceability of Trelifácil® slabs [5].

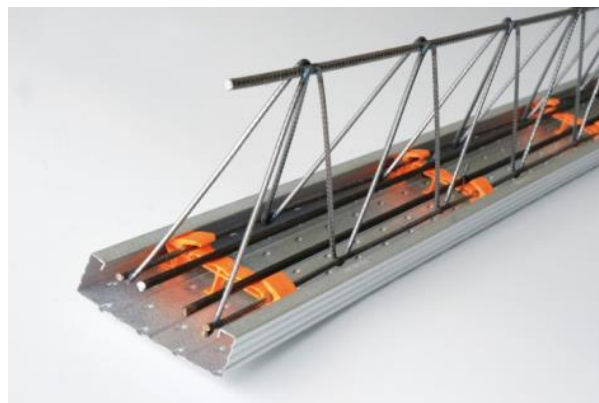


**Figure 1.** Single rib system - Trelifácil® [5].

In the structural arrangement, each rib behaves as a simply supported beam, subjected to bending about the minor axis of inertia of the CFS profile, with no negative rebar needed at the edges. The distance between ribs, occupied by filling material, depends on the size and type of said material, e.g., ceramic or polystyrene blocks, in accordance to the Brazilian national standard ABNT NBR 14859-2 [6]. Parameters that influence final resistance are: compressive strength of the concrete, additional rebar, thickness of concrete layer and lattice girder geometry. Due to the similarity between the aforementioned system and unidirectional ribbed slabs, Trelifácil® may be considered as a set of juxtaposed concrete “T” beams. Thus, for design considerations, a portion of the concrete, adjacent to each rib, contributes significantly to the resistance of compressive forces acting on a given rib cross section.

As a consequence of insufficient research aimed at the mechanical behavior of Trelifácil®, the present study provides a simplified analytical design procedure for this system, based on a computational tool created as a combination of the Brazilian design standards ABNT NBR 14762 [7], ABNT NBR 8800 [8], ABNT NBR 6118 [9] and ABNT NBR 14859-2 [6].

## 2 RECENT ADVANCES IN COMPOSITE SLAB RESEARCH

A rational design of flooring systems produces high impact to the overall weight of steel or composite steel-concrete buildings and it becomes more significant with the increased demand for higher column spacing. Moreover, the reduction in floor depth due to composite construction may offer many benefits regarding to costs reduction and structural performance enhancement [10]. Despite the previously mentioned demand for studies on the mechanical behavior of the Trelifácil® system, there is a considerable amount of academic studies concerning similar types of steel-concrete composite structures.

Experimentally, Andrade et al. [11] assessed the shear resistance and ultimate material slip strength of a composite wide-rib steel deck system as a function of web corrugations and indentations with different slopes, as well as additional shear transfer devices implemented on a new proposal of composite slab system. Vianna et al. [12] performed a numerical optimization of a cold-formed steel profile, subsequently used for the proposal of a steel deck composite slab configuration. The authors then determined flexural and material slip strengths of the new system by means of 4-point flexure tests and push-out tests, respectively. Performance comparisons were drawn in relation to similar slab systems, and noticeable financial and workability advantages are observed.

Jeong [13] conducted several non-linear partial steel-concrete interaction experimental analyses on slab prototypes with different degrees of steel-concrete interaction and shear-span ratios. The results were compared with data extracted from push-out tests and statistical analyses to investigate the reliability of the model to predict partial composite behavior. The same experimental tests were carried out by Vianna et al. [14], [15] to assess the resistance of T-Perfobond shear connectors used in composite beams or columns, focusing on shear transfer capacity, ductility and collapse modes. Design guidelines for this connector were proposed and the devices proved to be an efficient and economical solution for shear transfer in steel concrete composite elements.

Holomek and Bajer [16] investigated the shear behavior of CFS corrugated sheets with embossments, by means of full-scale four-point bending and vacuum tests, as well as shear tests on a reduced scale. The numerical models were calibrated with test results in order to assess the load bearing capacity of the slab. Hsu et al. [17] performed 12 full-scale tests on a beam-floor system consisting of a concrete slab supported by a corrugated CFS deck, CFS joists and continuous cold-formed shear connectors. The moment carrying capacity, end slip strength and vertical displacement are compared with a non-composite section. Results indicate an increase in mechanical resistance of 14-38% and no shear or compression buckling of the composite section was observed.

Still within the field of experimental research, many authors have explored the structural efficiency of steel-concrete composite beams and slabs related to the material properties of concrete, with variation in material composition and/or inclusion of chemical additives. Such studies include the investigations performed by Alenezi et al. [18], Hossain et al. [19], Lasheen et al. [20] and Waldmann et al. [21].

A number of numerically oriented studies concerning the topic at hand are also observed in academic literature. Majdi et al. [22] proposed a non-linear tridimensional finite element analysis (FEA) via ANSYS to simulate a four-point bending test of a composite floor. The models considered multi-linear material behavior and large-displacement theory, and numerical results present acceptable agreement with experimental tests. Despite the finite element (FE) model yielding conservative results, these were suitable for posterior parametric analyses.

Florides and Cashell [23] developed and validated a FE model via ABAQUS and VULCAN, to investigate failure behavior of composite one-directional and two-directional reinforced floors at ambient and elevated temperatures. The model included time-dependent material properties attributed to temperature change, as well as geometric nonlinearities. Experimental tests served as a basis to validate the model. Suizi et al. [24] performed cyclic load tests on frame-supported ribbed-grid composite slabs (FSRGCS). The authors used the IDARC program to elaborate a mathematical model using the hysteretic law of Park's degradation. ANSYS was then used to simulate load capacity and seismic performance of the slab system considering elastoplastic material. The results were consistent with the experiments.

Hossain et al. [25] elaborated a non-linear Finite Element model to study the behavior of steel deck composite slabs using Engineered Cementitious Composite (ECC). The numerical model was validated with experimental tests and a parametric study was conducted to assess the influence of various parameters. Numerical and experimental results were in agreement and suggest a superior ductile behavior of ECC slabs in relation to self-consolidating concrete (SCC) counterparts. Zhou et al. [26] studied the flexural capacity of a composite floor with lightweight cold-formed channel joists and oriented strand boards. A FE model was developed and validated by experimental test results, followed by a parametric study to determine how screw and joist spacing, as well as plate thickness, affect flexural strength. Local buckling was observed to be the critical failure mode of the joists and a tendency of lateral-torsional buckling was also observed. The study culminated in a simplified model to predict the bending capacity of these slabs.

## 2.1 Recent advances in design procedures for composite slabs

The scope of this topic is to present recent researches that proposed optimizations of standardized design procedures. Kyvelou et al. [27] provided practical design rules for composite CFS beams and wood-based floorboards, suitable for future incorporation in European standards. They demonstrated the proposed method by comparing results from twelve experimental tests with numerical analyses available in the literature, focusing on moment capacity and flexural stiffness.

Chien and Ritchie [28] summarized the main recommendations for the design of composite structures based on *in-situ* experience. The authors presented the main characteristics that contributed to the successful implementation of the systems. The study focused on conventional beam-girder, composite steel trusses and stud-girders as systems used for composite floors. These items were discussed and additional comments regarding deck-slab interaction and slab reinforcing requirements were made. Johnson and Shepherd [29] analyzed composite slabs with trapezoidal steel sheeting and longitudinal reinforcements, found to significantly contribute to shear resistance. The research proposed a design procedure that accounts for these elements, based on experimental data. Furthermore, the authors analyzed the contribution of reinforcements to the strength of partial interaction between materials. It is concluded that shear strength at material interface is not affected by additional reinforcements.

Limazie and Chen [30] analyzed elastic and plastic moment capacity of composite slim floor beams, and suggested a design procedure for these elements, validated by comparisons with existing research data. A predictive model was elaborated, considering material nonlinearity and composite behavior at material interface. The relations between moment and curvature, as well as moment and displacement, were also provided. Ranzi and Ostinelli [31] conducted an experimental study on post-tensioned composite slabs to assess ultimate resistance with relation to slab thickness, number of prestressing strands, span length and continuity of profile sheeting. A mathematical model was supplied for calculation of bending capacity, and the theoretical approach was compared with experimental data, demonstrating acceptable agreement.

In closure, Li et al. [32] presented an energy-based method to assess the structural response of steel beam-concrete slabs subjected to side column removal scenarios. A resistance-displacement curve was proposed and parametric studies were carried out to investigate the effect of various parameters. The proposed method was compared to numerical results and a difference of less than 15% is noted.

## 3 PROPOSITION OF ANALYTICAL DESIGN PROCEDURE

The simplified analytical design procedure proposed for Trelifácil® slabs is detailed in this topic. Whereas no previous researches are found in the literature for this exact floor system, Favarato et al. [33] suggested an alternative to assess the resistance of Trelifácil® for unpropped construction. Based on numerical buckling analyses, the author evaluates the maximum allowed unpropped span as well as maximum live load capacity. Nevertheless, on account of the high slenderness and low stiffness of the steel cross section, the unpropped spans can reach up to 1.40 m depending on section geometry [33]. Here, a computational tool is developed to estimate the number of props and maximum force applied on propping devices.

The general cross-section disposition of Trelifácil® slabs is shown in Figure 2a, and the cold-formed lipped channel section is detailed in Figure 2b. Different configurations are possible depending on concrete compressive strength, additional reinforcement, concrete layer thickness, lattice girder specification, density and dimensions of filling materials and yield strength of steel. This last parameter is taken as 280 MPa in this research.

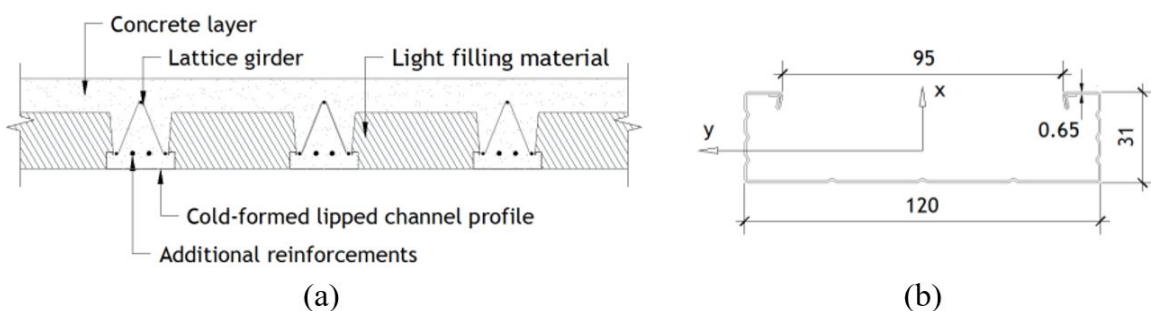


**Figure 2.** (a) General cross section of Trelifácil® slabs (extracted from Favarato et al. [33]); (b) cold-formed lipped channel cross section in mm (adapted from Favarato et al. [33]).

Initially, the bending moment and shear resistance of concrete elements are determined considering ultimate limit state design recommendations. Additionally, the serviceability limit state of excessive deflection is also verified, accounting for the influence of creep and crack width of the concrete. Based on the span length  $L$  and using the appropriate load combination, one can define the live load bearing capacity, in  $\text{kg/m}^2$ , that causes the predominant limit state [33].

Sequentially, the CFS shuttering is analyzed considering the ultimate limit states for combined bending, shear and web crippling. The serviceability limit state of excessive deflection is verified as well. The latter allows the calculation of the number of props and maximum force in each propping device. As a conservative approach, steel-concrete interaction during serviceability is not accounted for, hence, each steel and concrete system is designed separately. This arises from the absence of experimental data concerning the behavior of the system.

### 3.1 Main assumptions

The assumptions about the mechanical behavior of Trelifácil®, that serve as basis for the proposition of a simplified design procedure are listed as follows.

- The bending moment acts in a single direction, and the slab is simply supported by beams on opposite edges.
- Before concrete curing, the cold-formed lipped channel steel section resists to all the dead loads (steel shuttering, concrete, lattice girder and filling material), in addition to a construction live load of  $1 \text{ kN/m}^2$ .
- Any possible additional resistance provided by the coupling of the lattice girder to the CFS profile is neglected. Thus, stiffness and resistance to combined bending and shear during construction, are estimated considering minor axis bending of the lipped channel profile exclusively.
- Each concrete rib is assumed to behave as a simply supported T-shaped beam, and dimensions depend on filling element and steel profile geometry [33], in accordance with Figure 3. Equation 1 presents the dimensions shown in Figure 3, in mm, in which  $b_b$  is the width and  $h_b$  the height of inert elements.

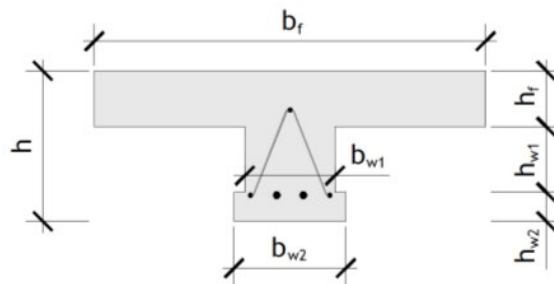


Figure 3. T-shaped concrete beam cross section (extracted from Favarato et al. [33]).

$$\begin{aligned}
 b_f &= b_b + 95 \\
 h &= h_b + h_f \\
 h_f &= h_c \\
 b_{w1} &= 95 \\
 b_{w2} &= 120 \\
 h_{w1} &= h_b - 31 \\
 h_{w2} &= 31
 \end{aligned} \tag{1}$$

- Conservatively, any lateral bracing provided to the CFS profile by the inert elements is neglected. Hence, the limit states related to lateral-torsional buckling must be verified. Nevertheless, linear elastic numerical analyses have shown that filling material may reduce the incidence of lateral-torsional buckling [34].
- The contribution of the cold-formed steel profile to the resistance of the final slab is neglected. As such, after concrete curing, only concrete contributes to the final resistance. The design is also performed in the third domain of deformations of reinforced concrete sections [9], in order to guarantee ductile structural behavior.

- g) The filling elements are standardized by ABNT NBR 14859-2 [6]. Furthermore, block width ( $b_b$ ) should be no longer than 555 mm so that each T-shaped element can be designed using beam theory, without accounting for flange bending [9].
- h) As a result of assumption g, the serviceability limit-state of crack width must be verified.
- i) For medium spans, additional positive reinforcements may be provided to increase the resistance of the T-shaped beams. For longer spans, this inclusion may be done to reduce vertical displacement.
- j) The lattice girders provide the shear resistance of the T-shaped concrete beams after curing. Whereas ABNT NBR 6118 [9] suggests a simplified criterion for slabs to assess the shear capacity, the full criterion for lattice girder beams is used.
- k) Increases in yield strength of steel as result of cold forming are neglected.
- l) The concrete must be produced with class 0 gravel to guarantee acceptable material homogeneity.
- m) Since this slab system is intended for construction in residential areas, class II of environmental aggressiveness was chosen. As such, in accordance with ABNT NBR 6118 [9], minimum rebar cover is taken as 25 mm and maximum crack width as 0.30 mm.
- n) When the maximum span of the cold-formed steel element is inferior to that of the concrete beam, the maximum length of the former, governs prop spacing.
- o) The uniformly distributed propping must be placed under the steel shuttering in such a way that vertical and lateral displacements are constrained.
- p) The propping elements are assumed to be rigid, behaving as hinge or roller supports for vertical loads.
- q) The shuttering is designed as a continuous beam during construction stage and bending moment redistribution due to support displacements is not accounted for.
- r) CFS profile limit-states govern structural safety during construction phase.
- s) Before concrete curing, ponding is considered for steel shuttering design.

### 3.2 Design before concrete curing

Before concrete curing, the cold-formed steel shuttering must be verified as a continuous beam (Figure 4) and four limit-states are considered. Initially, the resistance to combined positive bending moment and shear force must be determined in the critical span. If propping is necessary, the limit state associated with combined negative bending moment and shear force must be considered as well, adjacent to intermediate supports. Subsequently, support reactions must be small enough to avoid web crippling. Maximum deflection must also be verified.

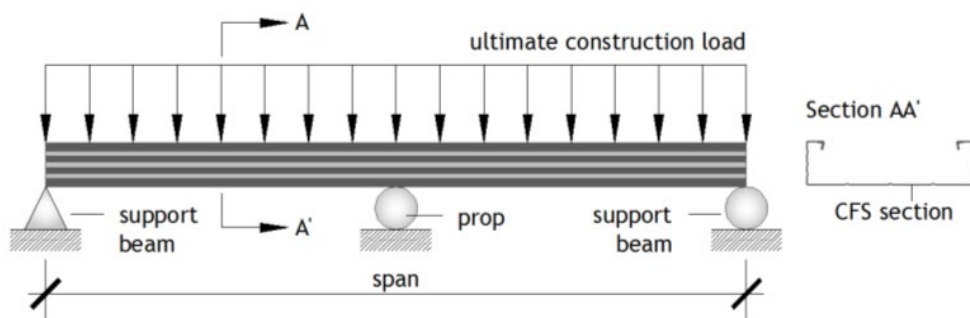


Figure 4. Structural arrangement of the steel shuttering (source: authors).

#### 3.2.1 Resistance to combined bending and shear

The Direct Strength Method (DSM), prescribed in ABNT NBR 14762 [7], was chosen to assess the design resistance of cold-formed members, due to its simplicity since it considers the analysis of the gross cross section [7], [35]–[37]. The final resistance of elements under flexure depends on the occurrence of three limit-states related to global, distortional and local buckling. Global buckling parameters are determined with Equations 2 and 3:

$$\lambda_0 = \sqrt{\frac{Wf_y}{M_e}} \tag{2}$$

$$M_{k,Re} = \begin{cases} Wf_y & \lambda_0 \leq 0.6 \\ 1.11(1 - 0.278\lambda_0^2)Wf_y & 0.6 < \lambda_0 \leq 1.336 \\ \frac{Wf_y}{\lambda_0^2} & \lambda_0 > 1.336 \end{cases} \tag{3}$$

where  $\lambda_0$  is the reduced slenderness attributed to global buckling;  $f_y$  is the steel yield strength;  $W$  is the elastic modulus about the minor axis of inertia;  $M_e$  is the elastic critical moment of lateral-torsional buckling; and  $M_{k,Re}$  is the characteristic value of resistant global bending moment. Local buckling parameters can be obtained by Equations 4 and 5:

$$\lambda_l = \sqrt{\frac{M_{k,Re}}{M_l}} \tag{4}$$

$$M_{k,RI} = \begin{cases} M_{k,Re} & \lambda_l \leq 0.776 \\ \frac{M_{k,Re}}{\lambda_l^{0.8}} \left( 1 - \frac{0.15}{\lambda_l^{0.8}} \right) & \lambda_l > 0.776 \end{cases} \tag{5}$$

where  $\lambda_l$  is the reduced slenderness associated to local buckling;  $M_l$  is the elastic critical moment of local buckling; and  $M_{k,RI}$  is the characteristic value of resistant bending moment related to local buckling. Distortional buckling verification is performed according to Equation 6 and 7:

$$\lambda_{dist} = \sqrt{\frac{Wf_y}{M_{dist}}} \tag{6}$$

$$M_{k,Rdist} = \begin{cases} Wf_y & \lambda_{dist} \leq 0.673 \\ \frac{Wf_y}{\lambda_{dist}} \left( 1 - \frac{0.22}{\lambda_{dist}} \right) & \lambda_{dist} > 0.673 \end{cases} \tag{7}$$

where  $\lambda_{dist}$  is the reduced slenderness related to distortional buckling;  $M_{dist}$  is the elastic critical moment of distortional buckling; and  $M_{k,Rdist}$  is the characteristic value of resistant bending moment of distortional buckling. Finally, the design resistance for bending moment ( $M_{Rd}$ ) is calculated using the smallest value obtained from Equations 3, 5 and 7, as shown by Equation 8.

$$M_{Rd} \leq \frac{I}{1.10} \begin{cases} M_{k,Re} \\ M_{k,RI} \\ M_{k,Rdist} \end{cases} \tag{8}$$

The design resistance to shear force ( $V_{Rd}$ ) is calculated considering the limit-state of web buckling due to shear stress [7]. The procedure outlined in Equations 9 and 10 must be applied to all flat portions of the web ( $h_w$ ). It's important to state that, since the CFS profile is in minor bending, the flanges behave as webs and the web behaves as a single bottom flange.

$$\lambda_w = \frac{h_w}{t_w} \tag{9}$$

$$V_{Rd} \leq \begin{cases} \frac{0.6h_w t_w f_y}{1.10} & \lambda_w \leq 1.08 \sqrt{\frac{E_s k_v}{f_y}} \\ \frac{0.65 t_w^2 \sqrt{k_v f_y E_s}}{1.10} & 1.08 \sqrt{\frac{E_s k_v}{f_y}} < \lambda_w \leq 1.40 \sqrt{\frac{E_s k_v}{f_y}} \\ \frac{0.905 E_s k_v t_w^3}{1.10 h_w} & \lambda_w > 1.40 \sqrt{\frac{E_s k_v}{f_y}} \end{cases} \tag{10}$$

where  $t_s$  is web thickness;  $E_s$  is Young’s modulus (200GPa); and  $k_v$  is the shear buckling coefficient, taken as 5 since no web stiffener has been considered. Following calculation of resistant bending moment and shear force, the combined resistance is verified according to Equation 11, where  $M_{sd}$  and  $V_{sd}$  are the design values for bending moment and shear force, respectively.

$$\left(\frac{M_{sd}}{M_{Rd}}\right)^2 + \left(\frac{V_{sd}}{V_{Rd}}\right)^2 \leq 1 \tag{11}$$

### 3.2.2 Evaluation of critical buckling bending moments

The assessment of flexural resistance via DSM depends on the critical load related to global buckling, in a first moment, according to Equation 2. For lipped channel sections bent about the centroidal y-axis (perpendicular to the axis of symmetry, Figure 2b),  $M_e$  is calculated according to Equation 12 [7], [36], [37].

$$M_e = \frac{C_s N_{ex}}{C_m} \left[ j + C_s \sqrt{j^2 + r_0^2 \left(\frac{N_{ex}}{N_{ex}}\right)} \right] \tag{12}$$

It is important to state that  $C_s$  accounts for the bending moment orientation, taken as -1 for lips under compression and 1 for web under tension. The  $C_m$  parameter accounts for the bending moment distribution in the element and is calculated in consonance with Equation 13.

$$C_m = 0,6 - 0,4 \frac{M_1}{M_2} \tag{13}$$

where  $M_2$  is the largest bending moment on the edges of the analyzed element; Alternatively,  $M_1$  is the smallest one; in addition,  $M_1/M_2 > 0$  for reverse curvature and  $M_1/M_2 < 0$  for simple curvature. The coefficient  $j$ , shown in Equation 12, is obtained with Equations 14 to 17.

$$j = \frac{I}{2I_y} (\beta_w + \beta_f + \beta_l) + x_0 \tag{14}$$

$$\beta_w = - \left( \frac{t x_m a_m^3}{12} + t x_m^3 a_m \right) \tag{15}$$

$$\beta_f = \frac{t}{2} [(b_m - x_m)^4 - x_m^4] + \frac{ta_m^2}{4} [(b_m - x_m)^2 - x_m^2] \tag{16}$$

$$\beta_l = 2c_m t (b_m - x_m)^3 + \frac{2}{3} t (b_m - x_m) \left[ \left( \frac{a_m}{2} \right)^3 - \left( \frac{a_m}{2} - c_m \right)^3 \right] \tag{17}$$

where  $a_m$  is web width;  $b_m$  is the flange width;  $c_m$  is the lip width;  $t$  is profile thickness;  $x_m$  is the distance from shear center to web mid-thickness; and  $x_0$  is the distance from the shear center to the centroid.

The compression buckling loads needed in Equation 12 are evaluated in agreement with Equations 18 and 19, where  $I_x$  is the major axis moment of inertia (Figure 2b);  $L$  is member length;  $G_s$  is the transverse modulus of elasticity (77 GPa);  $J$  is the constant of torsion;  $C_w$  is the warping constant; and  $r_0$  is the polar radius of gyration of the gross cross section.

$$N_{ex} = \frac{\pi^2 E_s I_x}{L^2} \tag{18}$$

$$N_{ez} = \frac{I}{r_0^2} \left( \frac{\pi^2 E_s C_w}{L^2} + G_s J \right) \tag{19}$$

Finally, to calculate the elastic critical moments associated with distortional and local buckling of the steel profile cross section, the authors performed a Finite Strip Analysis via CUFSM [38]. When the lips are under compression due to the action of sagging bending moment, the elastic critical moments are  $M_{l1} = 118.55 \text{ kN}\cdot\text{cm}$  and  $M_{dist} = 60.45 \text{ kN}\cdot\text{cm}$ , for local and distortional buckling, respectively (Figure 5); and when the web is under compression due to the action of hogging bending moment, the elastic critical moment of local buckling is  $M_{l2} = 9.18 \text{ kN}\cdot\text{cm}$  (Figure 6).

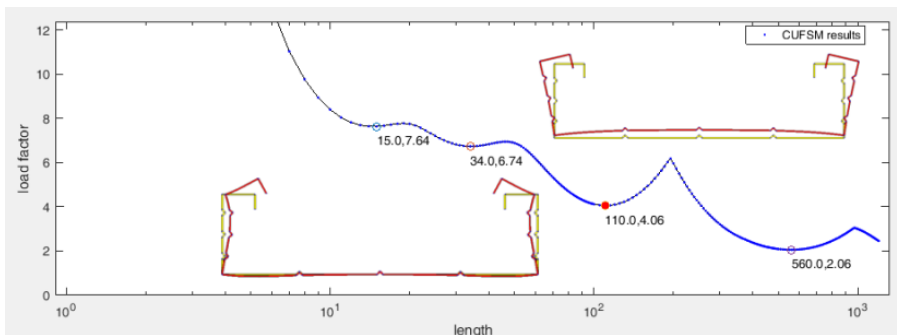


Figure 5. Finite-strip analysis result for sagging bending moment [38].

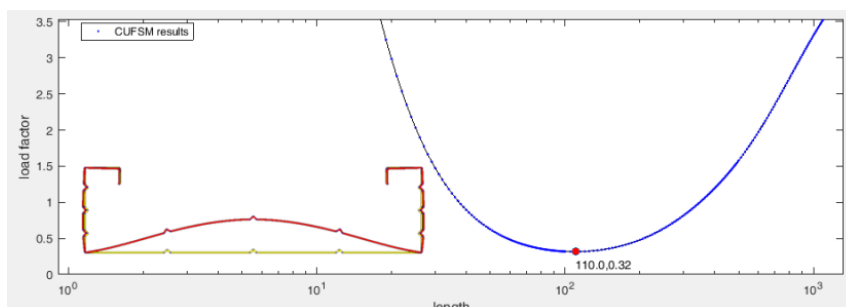


Figure 6. Finite-strip analysis result for hogging bending moment [38].

### 3.2.3 Web crippling

Under the action of concentrated loads such as external forces or reactions, cold-formed steel elements can fail due to compression of non-stiffened webs. The maximum design force for each flat portion of the web ( $F_{wc,Rd}$ ) must be compared to the largest applied force in the ultimate limit state, according to Equation 20 [7].

$$F_{wc,Rd} = \frac{\alpha t_w^2 f_y \sin \varphi}{1,35} \left( 1 - \alpha_r \sqrt{\frac{r_i}{t_w}} \right) \left( 1 + \alpha_c \sqrt{\frac{c}{t_w}} \right) \left( 1 - \alpha_h \sqrt{\frac{h_w}{t_w}} \right) \quad (20)$$

where  $\alpha$  is a parameter that depends on flange condition and load case;  $t_w$  is the web thickness;  $f_y$  is the design yield strength;  $\varphi$  is the angle between the plane of the web and bearing surface, taken as  $90^\circ$ ;  $\alpha_r$ ,  $\alpha_c$  and  $\alpha_h$  are coefficients that depend on the internal bending radius, bearing length and web slenderness, respectively;  $r_i$  is the internal bending radius;  $c$  is the bearing length; and  $h_w$  is the flat dimension of web measured in its plane.

### 3.2.4 Displacement control

During construction, the CFS shuttering must have enough stiffness to grant structural safety and ensure shape and dimension of the molded concrete element [39]. Hence, it's important to control the deflections in the serviceability limit-state under the action of a uniformly distributed service load accounting for ponding. Since the shuttering is designed as a continuous beam, the Direct Stiffness Method was used to carry out the structural analysis and to calculate the displacements. The maximum deflection ( $f_{max}$ ) of the beam must respect the limits of ABNT NBR 8800 [8], according to Equation 21, where  $L$  is the span measured between props.

$$f_{max} \leq \begin{cases} 2cm \\ L/180 \end{cases} \quad (21)$$

Nevertheless, if  $f_{max}$  exceeds  $L/250$ , regardless of the limits stipulated in Equation 21, the service load must be incremented by 70% of the weight of a fictitious concrete layer with thickness  $f_{max}$ . Then, a new displacement must be calculated and it must respect Equation 21.

## 3.3 Design after concrete curing

The design procedure for T-shaped concrete beams was previously detailed by Favarato et al. [33]. Here, only the key equations will be presented.

### 3.3.1 Bending moment

According to Figure 7a, the equilibrium of horizontal forces is given by  $R + C + T = 0$ , where  $R$  is net compression on concrete,  $C$  is the force on the upper bar of the lattice girder (tension or compression, depending on neutral axis depth) and  $T$  is net tension on the lattice girder's lower bars and additional rebar, taking compression as negative and tension as positive.

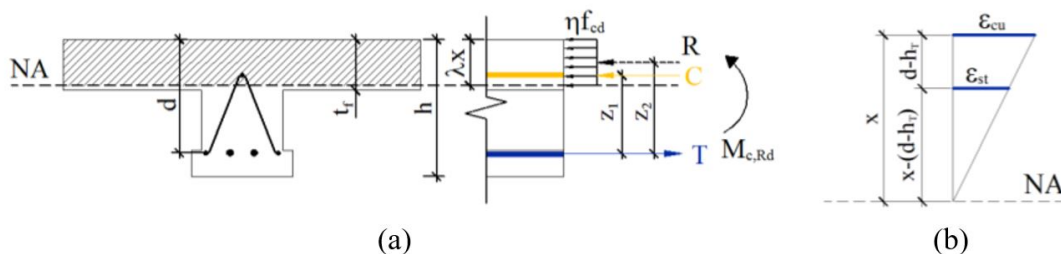


Figure 7. T-shaped beam under bending (extracted from Favarato et al. [33]).

The depth of the Neutral axis (NA) is defined according to Equation 22:

$$-\eta f_{cd} b_f \lambda x + E_{sa} \varepsilon_{st} A_{s,ct} + f_{yd} (A_{s,lt} + A_{s,ta}) = 0 \quad (22)$$

$$\lambda x \leq t_f \quad (23)$$

If Equation 23 is not satisfied, then Equation 24 shall be used, being Equation 25 now satisfied.

$$-\eta f_{cd} (b_f - b_{wl}) h_f - \eta f_{cd} b_{wl} \lambda x + E_{sa} \varepsilon_{st} A_{s,ct} + f_{yd} (A_{s,lt} + A_{s,ta}) = 0 \quad (24)$$

$$\lambda x > t_f \quad (25)$$

where  $b_f$  is the flange width;  $b_{wl}$  is the web thickness;  $h_f$  is the flange thickness;  $E_{sa}$  is the Young's Modulus of the steel lattice bars and rebar (210 GPa);  $A_{s,ct}$  is the cross-sectional area of the upper lattice girder bar;  $f_{cd}$  is the design compressive strength of concrete;  $f_{yd}$  is the design yield strength of reinforcement steel;  $A_{s,lt}$  is the total cross-sectional area of lower bars of the truss; and  $A_{s,ta}$  is the total area of additional rebar. The parameter  $\varepsilon_{st}$  is the strain of the upper bar of the lattice girder, calculated according to Equation 26, derived from Figure 7b.

$$\varepsilon_{st} = \varepsilon_{cu} - \frac{\varepsilon_{cu} (d - h_f)}{x} \quad (26)$$

where  $\varepsilon_{cu}$  is the strain of the concrete T-shaped section (0.35‰);  $d$  is defined in Figure 7a;  $h_f$  is the lattice girder height; and  $x$  is the neutral axis depth. Finally, the design bending moment shall be calculated as  $M_{c,Rd} = Cz_1 + Rz_2$  [33], where the distances  $z_1$  and  $z_2$  can be determined with trigonometry.

### 3.3.2 Shear force

The design shear force on concrete beams with lattice girder reinforcements are determined by Equation 27, considering the ultimate limit-states of concrete crushing and diagonal tension [9].

$$V_{c,Rd} \leq \begin{cases} 0.54 \left( 1 - \frac{f_{ck}}{250} \right) f_{ctd} b_{wl} d \sin^2 \theta (\cotg \alpha + \cotg \theta) \\ 0.6 f_{ctd} b_{wl} d + 1.8 \frac{A_{sw}}{s} d (\cotg \alpha + \cotg \theta) \sin \alpha \sin \beta f_{yd} \end{cases} \quad (27)$$

where  $\theta$  is the inclination of concrete rods;  $\alpha$  is inclination of transversal reinforcements (Figure 8);  $\beta$  is inclination of transversal reinforcements in its plane (Figure 8);  $d$  is the distance from the center of gravity of tensioned reinforcements to the top of the concrete surface;  $f_{ctd}$  is the design tensile strength of concrete;  $f_{ck}$  is the nominal compressive strength of concrete;  $A_{sw}$  is the total area of transversal reinforcements;  $s$  is the distance between successive transversal reinforcements; and  $f_{yd}$  is the design yield strength of steel, as stated by Favarato et al. [33]. It's important to state that Equation 27 was adapted from ABNT NBR 6118 [9] – section 17.4.2, where the factor  $\sin \alpha \sin \beta$  in the second line includes the effects of shear reinforcements slope in its plane.

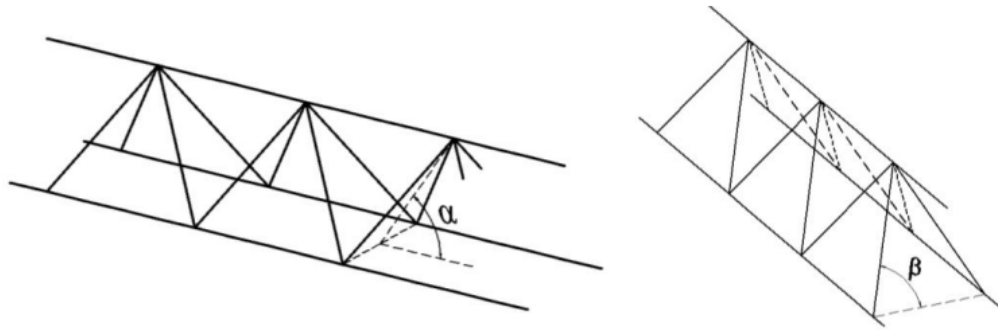


Figure 8. Slope of shear reinforcements (source: authors).

### 3.3.3 Deflection

In accordance with ABNT NBR 6118 [9], the maximum displacement are evaluated considering the effects of creep, limited to  $L/350$ , where  $L$  is the unpropped span. Furthermore, the reduction in the moment of inertia of the T-shaped concrete section due to cracking must be accounted for in the final deflection ( $f_t$ ), calculated with Equation 28.

$$f_t = \frac{5q_{qp}L^4}{384E_{cs}I_e}(1 + \alpha_f) \leq \frac{L}{350} \quad (28)$$

where  $q_{qp}$  is the uniformly distributed load for quasi-permanent combination;  $E_{cs}$  is the secant Modulus of Elasticity of the concrete;  $I_e$  is the reduced moment of inertia of the T-shaped concrete beam, considering the effects of cracking in the concrete's tensioned zone [9]; and  $\alpha_f$  accounts for the effects of creep.

### 3.3.4 Crack width

This verification must use frequent load combinations [9] to assess the tensile stress in the steel bars in stage II. As stated before, the maximum crack width ( $w_k$ ) shall be restricted to  $w_{k,max} = 0.30 \text{ mm}$  in the serviceability limit-state. Crack width size is evaluated according to Equation 29.

$$w_k \leq \begin{cases} \frac{\phi}{12.5\eta_l} \frac{\sigma_s}{E_s} \frac{3\sigma_s}{f_{ctm}} \\ \frac{\phi}{12.5\eta_l} \frac{\sigma_s}{E_{sa}} \left( \frac{4}{\rho_r} + 45 \right) \end{cases} \quad (29)$$

where  $\phi$  is the largest diameter of rebar;  $\eta_l$  is the adhesion coefficient;  $E_{sa}$  is the Young's Modulus of the steel reinforcement;  $f_{ctm}$  is the average concrete tensile strength;  $\rho_r$  is the passive adherent reinforcement ratio; and  $\sigma_s$  is stress on tensioned reinforcements on stage II, as detailed by Favarato et al. [33].

### 3.4 Flow chart

The proposed design procedure is summarized in Figure 9. The coefficients of utilization defined in the sequence are the relation between the parameter value, calculated with the program, and its maximum value regarding a limit-state, such as maximum bending moment and design bending moment, maximum deflection and limit deflection.

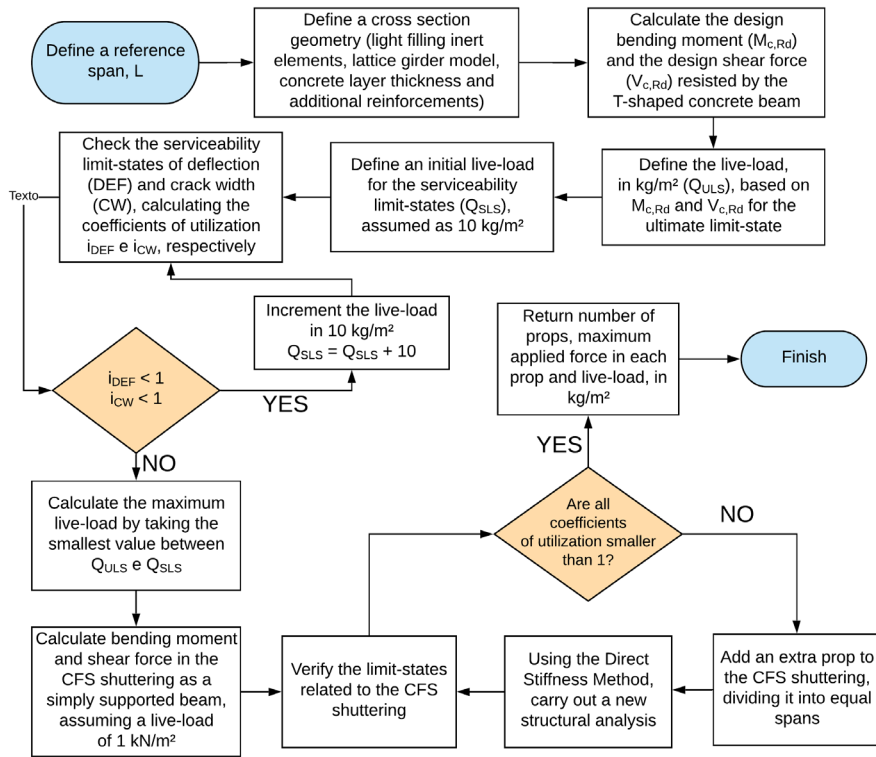


Figure 9. Design flow char (adapted from Favarato et al. [33]).

#### 4. RESULTS AND DISCUSSIONS

To exemplify the design procedure for lattice girder slabs with CFS lipped channel section shuttering, the same geometries tested by Favarato et al. [33] were chosen for analysis, with the inclusion of propping (Table 1). The following material and cross-section geometric properties are considered: concrete compressive strength of  $25\text{ MPa}$ ; lattice girder model 8645 ( $f_{yk} = 600\text{ MPa}$ ), according to Figure 10; two additional reinforcement bars,  $\varnothing 6.30\text{ mm}$  and  $f_{yk} = 500\text{ MPa}$ ; specific weight of light filling material taken as  $0.37\text{ kN/m}^3$ ; and a yield strength of cold-formed steel profile of  $280\text{ MPa}$ . Two geometries were tested:

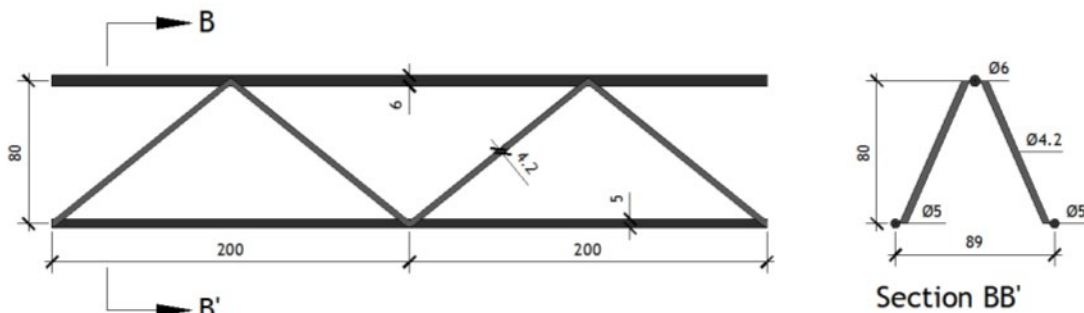


Figure 10. Lattice girder chosen for example, with dimensions in millimeters (source: authors).

- a) Scenario 1: 5 cm concrete layer thickness and 27x8 cm light filling inert blocks.
- b) Scenario 2: 6 cm concrete layer thickness and 37x8 cm light filling inert blocks.

The following convention has been used to indicate the limit-states in the graphs: BMac – bending moment after concrete curing; SFac – shear force after concrete curing; DEFac – deflection after concrete curing; CWac – crack width after concrete curing; BS+bc – combined sagging bending moment and shear force before concrete curing; BS-bc – combined hogging bending moment and shear force before concrete curing; WCbc – web crippling before concrete curing; and DEFbc – deformation before concrete curing.

**Table 1.** Input data for analysis.

Data type	Parameter	Value	Unit
GENERAL DATA	Shuttering yield strength	280	MPa
	Concrete compressive strength	25	MPa
	Lattice girder model	TR8645	--
	Lattice girder yield strength	600	MPa
	Additional rebar	2Ø6.30	mm
	Additional rebar yield strength	500	MPa
	Light filling material density	0.37	kN/m <sup>3</sup>
SCENARIO 1	Concrete layer thickness	5	cm
	Blocks dimensions	27 x 8	cm
SCENARIO 2	Concrete layer thickness	6	cm
	Blocks dimensions	37 x 8	cm

For scenario 1, according to Figure 11, the limit-state related to shear governs design for spans of up-to 1.60 m, while bending moment is the critical limit-state for spans ranging from 1.60 m to 3.40 m. For spans outside of these ranges, excessive deflection is the governing parameter. If the coefficient of utilization related to the governing limit-state for a given propped span exceeds 1.0, maximum prop spacing is equal to the length of that span. As such, the saw tooth graph presented in Figure 12 reports the number of props needed for each span: each time it reaches a peak, an extra prop must be included within the next span. Furthermore, local buckling of CFS profile elements in the region where props are introduced governed the design for all spans above 1.40 m, which is attributed to the low buckling resistance to hogging bending moment. The coefficient of utilization related to the governing limit-state in Figure 12 does not need to reach 1.0 to stop the iterative process of analysis, since before concrete curing the steel element is only verified with regards to the aforementioned limit-states, considering a pre-defined live-load of 1 kN/m<sup>2</sup>.

For scenario 2, similar conclusions are drawn from Figure 13 and Figure 14. The shear resistance in the concrete section also governs the design for short spans, followed by bending moment and, finally, total deflection. However, it is important to state that the maximum unpropped span in this scenario is reduced from 1.2 m to 1.0 m when compared to the previous analysis. This arises from the low buckling resistance of the CFS profile and the heavier concrete dead-load due to wider concrete section flanges.

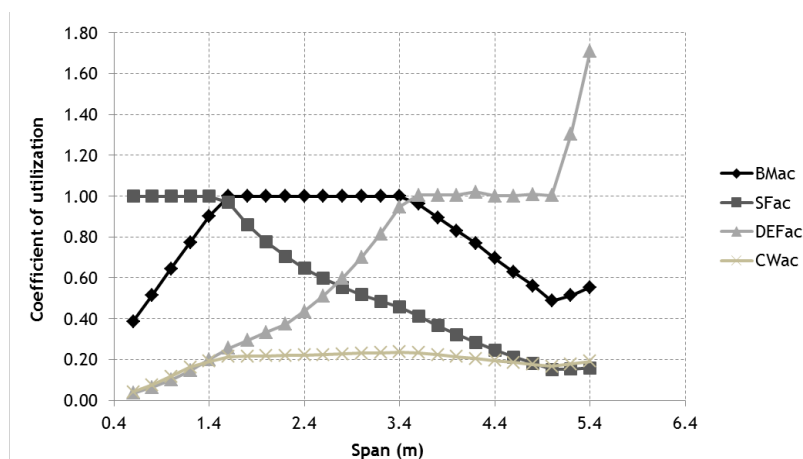


**Figure 11.** Scenario 1 analysis result – limit-states after concrete curing (source: authors).

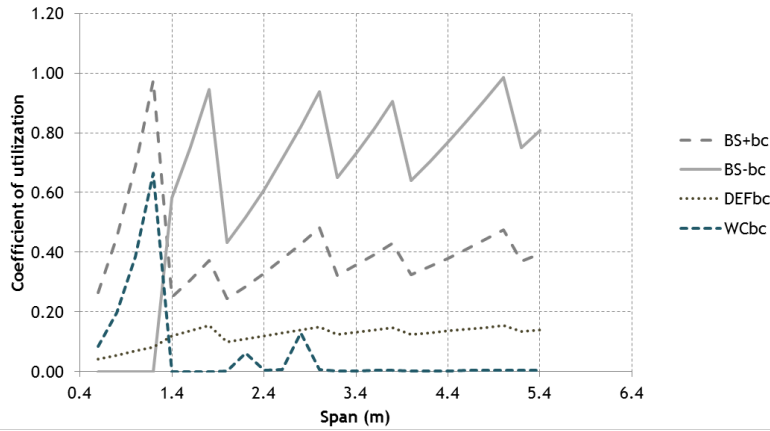


Figure 12. Scenario 1 analysis result – limit-states before concrete curing (source: authors).

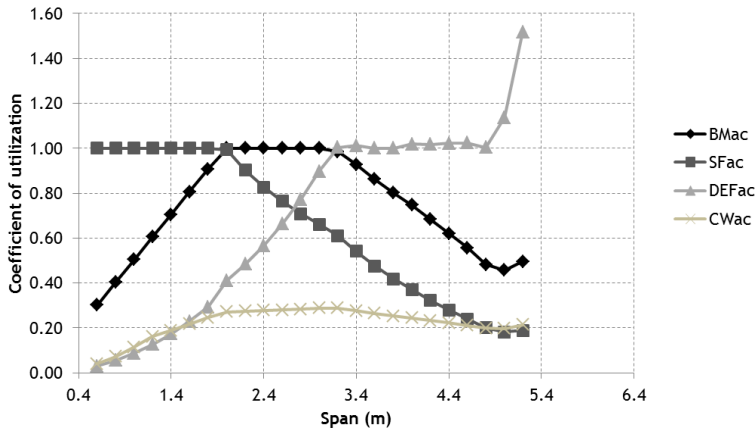


Figure 13. Scenario 2 analysis result – limit-states after concrete curing (source: authors).

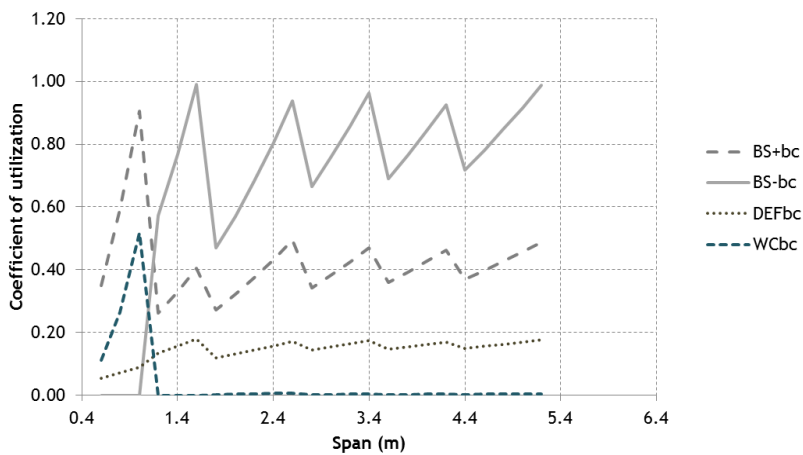


Figure 14. Scenario 2 analysis result – limit-states before concrete curing (source: authors).

The graph in Figure 15, compares the load capacity of scenarios 1 and 2 as a function of span. In scenario 1, heavier service loads can be applied to spans of up-to 1.80 m due to shear failure being the predominant limit-state. From 1.80 m to 3.40 m, the maximum service load of scenario 2 becomes larger since bending moment governs the design.

This is a result of the T-shaped concrete beams having larger flanges. After 3.40 m, the deflection governs the design and any marginal increase of section height in scenario 2 does not compensate for the increase in weight. In general, scenario 1 shows a better performance when compared to its alternative.

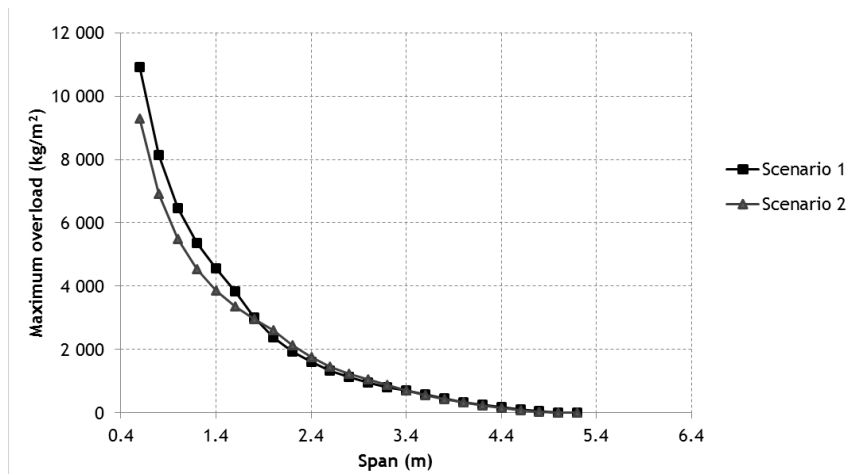


Figure 15. Service loads for both scenarios 1 and 2 (source: authors).

Lastly, the maximum allowable force on propping devices is assessed. This parameter is plotted against unpropped span (Figure 16) – the slab’s span in service, highlighting the linear relationship between them. The saw tooth behavior is attributed to the gradual increase in the number of props added during construction, and each peak indicates the occurrence of a limit state of the steel shuttering. The graph shows that the average applied force is 1.50 kN in each rib, for spans from 2.0 m up-to 5.2 m.

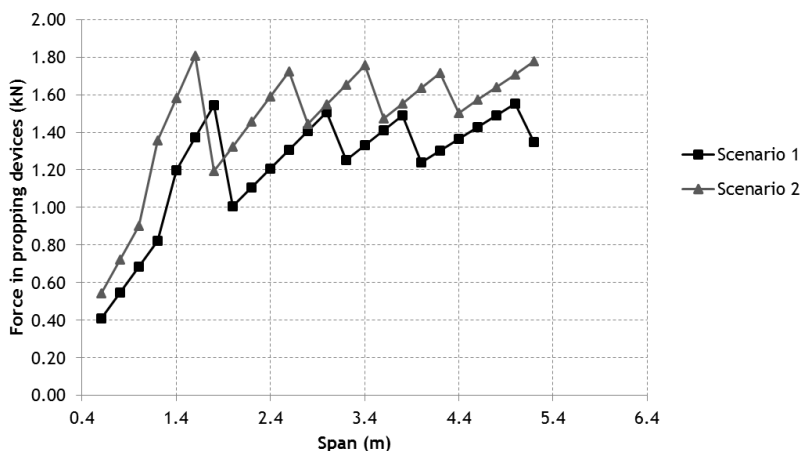


Figure 16. Maximum force applied in the propping devices during construction phase (source: authors).

In summary, the computational tool presented can be used to propose design guidelines for this new slab system, regardless of changes in configuration (lattice girder model, concrete strength, light filling material specification, steel yield strength, additional reinforcements, unpropped span). Since there are no specifications and no previous research for this exact slab system, the results obtained herein are conservative and can be taken as an estimation of design parameters that ensure minimum structural safety. On another note, the large number of props needed before concrete curing is a result of the low stiffness of each cold-formed steel rib, which is a critical factor for unpropped construction.

## 5. SUMMARY AND CONCLUSIONS

This research is inspired by a recently released solution in the civil construction market for composite slabs. In this paper, a practical design procedure is proposed to evaluate the load capacity of lattice girder slabs with CFS lipped channel sections, bent about the minor axis of inertia. In general, the following conclusions can be drawn:

- The combination of different design standards gave rise to a simplified procedure to determine the maximum service load of Trelifácil® slabs. The amount of propping needed in the construction phase and the maximum forces applied in propping devices are also determined. Since no data is available from experimental tests to assess shear transfer due to the action of embossments, the composite action was neglected. Thus, the service load is conservatively estimated.
- Different limit-states control the system's behavior. The resistance of short spans ( $L \leq 1.40\text{ m}$ ) is governed by shear force, while medium ( $1.40 < L \leq 3.40\text{ m}$ ) and long ( $L > 3.40\text{ m}$ ) spans are governed by bending moment and maximum displacements, respectively, in the serviceability phase.
- The reduced spacing between props in the construction phase and the maximum length of unpropped spans are a consequence of the CFS profile presenting low stiffness, in turn due to its thickness and cross-sectional dimensions. However, the coupling between the CFS profile and the lattice girder – neglected here on the absence of experimental results – can potentially allow for longer unpropped spans. This combined action could reduce compression on the lower flange. As such, resistance to local buckling of flanges, the ultimate limit-state that governs almost all propped design, would increase.
- The results suggest a strong limitation of unpropped construction due to the low performance of the cold-formed profile under minor axis bending. On the other hand, the coupled behavior and the actual composite action would certainly lead to less conservative results.

## ACKNOWLEDGEMENTS

The authors acknowledge ArcelorMittal Tubarão, Federal University of Espírito Santo, CAPES, CNPq and FAPES for the financial support during this research.

## REFERENCES

- [1] A. P. A. Sieg, "Estudo de um sistema de laje com forma de aço incorporada," M.S. thesis, Esc. Eng., Univ. São Paulo, São Carlos, 2015.
- [2] M. Crisinel and D. O'Leary, "Recent developments in steel/concrete composite slabs," *Struct. Eng. Int.*, vol. 6, pp. 41–46, 1996, <http://dx.doi.org/10.2749/101686696780495923>.
- [3] C. E. Javaroni, "Perfis de aço formados a frio: análise teórico-experimental", Ph.D. dissertation, Esc. Eng., Univ. São Paulo, São Carlos, 1999.
- [4] G. Queiroz, R. J. Pimenta, and A. G. Martins, *Estruturas Mistas – vol. 1*, 2nd ed. Rio de Janeiro: Instituto Aço Brasil, Centro Brasileiro da Construção em Aço, 2012.
- [5] ArcelorMittal, *Trelifácil® – Informative folder*, 2017.
- [6] Associação Brasileira de Normas Técnicas, *Lajes Pré-fabricadas de Concreto – Parte 2 – Elementos Inertes para Enchimento e Forma – Requisitos*, NBR 14859-2, 2016.
- [7] Associação Brasileira de Normas Técnicas, *Dimensionamento de Estruturas de Aço Constituídas por Perfis Formados a Frio*, NBR 14762, 2010.
- [8] Associação Brasileira de Normas Técnicas, *Projeto de Estruturas de Aço e de Estruturas Mistas de Aço e Concreto de Edifícios*, NBR 8800, 2008.
- [9] Associação Brasileira de Normas Técnicas, *Projeto de Estruturas de Concreto – Procedimento*, NBR 6118, 2014.
- [10] I. M. Ahmed and K. D. Tsavdaridis, "The evolution of composite flooring systems: applications, testing, modelling and Eurocode design approaches," *J. Construct. Steel Res.*, vol. 155, pp. 286–300, Apr 2019, <http://dx.doi.org/10.1016/j.jcsr.2019.01.007>.
- [11] S. A. L. Andrade, P. C. G. S. Vellasco, J. G. S. Silva, and T. H. Takey, "Standardized composite slab systems for building constructions," *J. Construct. Steel Res.*, vol. 60, no. 3-5, pp. 493–524, Mar-May 2004, [http://dx.doi.org/10.1016/S0143-974X\(03\)00126-3](http://dx.doi.org/10.1016/S0143-974X(03)00126-3).
- [12] J. C. Vianna, S. A. L. Andrade, P. C. G. S. Vellasco, L. R. O. Lima, and J. G. S. Silva, "Um sistema de laje mista para edificações residenciais usando perfis de chapa dobrada com corrugações," *REM Rev. Escola Minas*, vol. 60, no. 2, pp. 325–331, Apr-Jun 2007, <http://dx.doi.org/10.1590/S0370-44672007000200015>.

- [13] Y. J. Jeong, "Simplified model to predict partial-interactive structural performance of steel-concrete composite slabs," *J. Construct. Steel Res.*, vol. 64, no. 2, pp. 238–246, Feb 2008, <http://dx.doi.org/10.1016/j.jcsr.2007.05.003>.
- [14] J. C. Vianna, L. F. Costa-Neves, P. C. G. S. Vellasco, and S. A. L. Andrade, "Structural behaviour of T-Perfobond shear connectors in composite girders: An experimental approach," *Eng. Struct.*, vol. 30, no. 9, pp. 2381–2391, Sep 2008, <http://dx.doi.org/10.1016/j.engstruct.2008.01.015>.
- [15] J. C. Vianna, L. F. Costa-Neves, P. C. G. S. Vellasco, and S. A. L. Andrade, "Experimental assessment of Perfobond and T-Perfobond shear connectors' structural response," *J. Construct. Steel Res.*, vol. 65, no. 2, pp. 408–421, Feb 2009, <http://dx.doi.org/10.1016/j.jcsr.2008.02.011>.
- [16] J. Holomek and M. Bajer, "Experimental and numerical investigation of composite action of steel concrete slab," *Eng. Procedia*, vol. 40, pp. 143–147, 2012, <http://dx.doi.org/10.1016/j.proeng.2012.07.070>.
- [17] C. T. T. Hsu, S. Punurai, W. Punurai, and Y. Majdi, "New composite beams having cold-formed steel joists and concrete slab," *Eng. Struct.*, vol. 71, pp. 187–200, Jul 2014, <http://dx.doi.org/10.1016/j.engstruct.2014.04.011>.
- [18] K. K. Alenezi et al., "Behavior of pre-cast U-shaped composite beam integrating cold-formed steel with ferro-cement slab," *Thin-walled Struct.*, vol. 102, pp. 18–29, May 2016, <http://dx.doi.org/10.1016/j.tws.2016.01.014>.
- [19] K. M. A. Hossain, S. Alam, M. S. Anwar, and K. M. Y. Julkarnine, "High performance composite slabs with profiled steel deck and engineered cementitious composite – strength and shear bond characteristics," *Constr. Build. Mater.*, vol. 125, pp. 227–240, Oct 2016., <http://dx.doi.org/10.1016/j.conbuildmat.2016.08.021>.
- [20] M. Lasheen, A. Shaat, and A. Khalil, "Behaviour of lightweight concrete slabs acting compositely with steel I-sections," *Constr. Build. Mater.*, vol. 124, pp. 967–981, Oct 2016, <http://dx.doi.org/10.1016/j.conbuildmat.2016.08.007>.
- [21] D. Waldmann, A. May, and V. B. Thapa, "Influence of the sheet profile design on the composite action of slabs made of lightweight woodchip concrete," *Constr. Build. Mater.*, vol. 148, pp. 887–899, Sep 2017, <http://dx.doi.org/10.1016/j.conbuildmat.2017.04.193>.
- [22] Y. Majdi, C. T. T. Hsu, and M. Zarei, "Finite element analysis of new composite floors having cold-formed steel and concrete slab," *Eng. Struct.*, vol. 77, pp. 65–83, Oct 2014, <http://dx.doi.org/10.1016/j.engstruct.2014.07.030>.
- [23] M. M. Florides and K. A. Cashell, "Numerical modelling of composite floor slabs subject to large deflections," *Structures*, vol. 9, pp. 112–122, Feb 2017, <http://dx.doi.org/10.1016/j.istruc.2016.10.003>.
- [24] J. Suizi, C. Wanlin, Z. Yuchen, and Y. Quan, "Simplified calculation model and finite-element analysis of frame-supported ribbed-grid composite slab structure," *KSCSE J. Civ. Eng.*, vol. 22, no. 9, pp. 3383–3394, Jan 2018, <http://dx.doi.org/10.1007/s12205-017-0457-5>.
- [25] K. M. A. Hossain, S. Attarde, and M. S. Anwar, "Finite element modelling of profiled steel deck composite slab system with engineered cementitious composite under monotonic loading," *Eng. Struct.*, vol. 186, pp. 13–25, May 2019, <http://dx.doi.org/10.1016/j.engstruct.2019.02.008>.
- [26] X. Zhou, Y. Shi, L. Xu, X. Yao, and W. Wang, "A simplified method to evaluate the flexural capacity of lightweight cold-formed steel floor system with oriented strand board subfloor," *Thin-walled Struct.*, vol. 134, pp. 40–51, Jan 2019, <http://dx.doi.org/10.1016/j.tws.2018.09.006>.
- [27] P. Kyvelou, L. Gardner, and D. A. Nethercot, "Design of composite cold-formed steel flooring systems," *Structures*, vol. 12, pp. 242–252, Nov 2017, <http://dx.doi.org/10.1016/j.istruc.2017.09.006>.
- [28] E. Y. L. Chien and J. K. Ritchie, "Composite floor systems – a mature design option," *J. Construct. Steel Res.*, vol. 25, no. 1-2, pp. 107–139, 1993, [http://dx.doi.org/10.1016/0143-974X\(93\)90055-W](http://dx.doi.org/10.1016/0143-974X(93)90055-W).
- [29] R. P. Johnson and A. J. Shepherd, "Resistance to longitudinal shear of composite slabs with longitudinal reinforcement," *J. Construct. Steel Res.*, vol. 82, pp. 190–194, Mar 2013, <http://dx.doi.org/10.1016/j.jcsr.2012.12.005>.
- [30] T. Limazie and S. Chen, "Numerical procedure for nonlinear behavior analysis of composite slim floor beams," *J. Construct. Steel Res.*, vol. 106, pp. 209–219, Mar 2015, <http://dx.doi.org/10.1016/j.jcsr.2014.12.015>.
- [31] G. Ranzi and A. Ostinelli, "Ultimate behaviour and design of post-tensioned composite slabs," *Eng. Struct.*, vol. 150, pp. 711–718, Nov 2017, <http://dx.doi.org/10.1016/j.engstruct.2017.07.075>.
- [32] G. Q. Li, J. Z. Zhang, and J. Jiang, "Analytical modeling on collapse resistance of steel beam-concrete slab composite substructures subjected to side column loss," *Eng. Struct.*, vol. 169, pp. 238–255, Aug 2018, <http://dx.doi.org/10.1016/j.engstruct.2018.05.038>.
- [33] L. F. Favarato, A. F. G. Calenzani, J. C. V. Pires, E. Junges, and J. A. Ferrareto, "Evaluation of the resistance of trussed slabs with steel formwork in cold formed U profile," *Lat. Am. J. Solids Struct.*, vol. 16, no. 7, pp. 1–18, Aug 2019, <http://dx.doi.org/10.1590/1679-78255304>.
- [34] D. C. M. Candido, A. P. Storch, A. V. S. Gomes, L. F. Favarato, and A. F. G. Calenzani, "Análise numérica de flambagem de perfis de aço formados a frio empregados em lajes nervuradas mistas," in *An. XIII Simp. Mec. Comp.*, Vitória, ES, Brasil, Oct. 2018.
- [35] W. W. Yu and R. A. Laboube, *Cold-formed Steel Design*, 4th ed. Hoboken: John Wiley e Sons, 2010.
- [36] American Iron And Steel Institute, *North American Specification for the Design of Cold-Formed Steel Structural Members*, S100-16, 2016.

- [37] Standards Association of Australia. Standards New Zealand, *Cold-formed Steel Structures*, AS/NZS 4600, 2005.
- [38] B. Schafer, *WCUFMS 5.01 – Finite Strip Elastic Buckling Analysis Application*. Baltimore, USA: Johns Hopkins University, 2018. [Online]. Available: <https://www.ce.jhu.edu/cufsm/downloads/>
- [39] Associação Brasileira de Normas Técnicas, *Fôrmas e Escoramentos para Estruturas de Concreto – Projeto, Dimensionamento e Procedimentos Executivos*, NBR 15696, 2009.

---

**Author contributions:** Conceptualization: L. F. Favarato, A. V. S. Gomes, D. C. M. Candido, A. F. G. Calenzani, J. C. Vianna, J. A. Ferrareto / Methods: L. F. Favarato / Analysis: L. F. Favarato / Writing – original draft: L. F. Favarato / Writing – review and editing: L. F. Favarato, A. V. S. Gomes, D. C. M. Candido, A. F. G. Calenzani, J. C. Vianna, J. A. Ferrareto / Resources: J. A. Ferrareto / Supervision: J. C. Vianna, J. A. Ferrareto, A. F. G. Calenzani.

**Editors:** Vladimir Guilherme Haach, José Luiz Antunes de Oliveira e Sousa, Guilherme Aris Parsekian.



## ORIGINAL ARTICLE

# A simplified numerical approach to the evaluation of residual shaft friction induced by concrete curing in drilled shafts on granular soils

*Uma abordagem numérica simplificada para a avaliação do atrito lateral induzido pela cura do concreto em estacas escavadas em solos granulares*

Augusto Bopsin Borges<sup>a</sup>

Renato Vaz Linn<sup>a</sup>

Fernando Schnaid<sup>b</sup>

Samir Maghous<sup>a</sup>

<sup>a</sup>Universidade Federal do Rio Grande do Sul – UFRGS, Centro de Mecânica Aplicada e Computacional – CEMACOM, Departamento de Engenharia Civil, Porto Alegre, RS, Brasil

<sup>b</sup>Universidade Federal do Rio Grande do Sul – UFRGS, Departamento de Engenharia Civil, Laboratório de Ensaios Geotécnicos e Geoambientais – LEGG, Porto Alegre, RS, Brasil

Received 26 August 2019  
Accepted 13 February 2020

**Abstract:** Conventional interpretation procedures of load tests on instrumented piles rely upon measurements of strains that assume as zero for strains measured at the instant immediately before starting the test as reference configuration. However, some experimental evidence shows that concrete in drilled shafts undergoes strains induced by the curing process comparable in magnitude to the strains measured during the load tests. It is therefore expected that mobilization of shaft friction takes place before the load test. Several authors have performed experimental and numerical analyses aiming to quantify the influence of those pre-load test concrete volumetric strains on the measured bearing capacity using different approaches. The present work aimed to establish a reference framework for the existing and future works on this topic. In order to assess the influence of concrete strains induced by curing process on the shaft friction before the start of the load tests in drilled shafts, several finite element numerical simulations are performed, considering the thermal, autogenous and drying strains. The analyses consider concrete as an isotropic linear-elastic material and the soil as an elastic-plastic material using the Mohr-Coulomb constitutive model natively implemented in the software ABAQUS. The results are interpreted focusing on the relevancy on the bearing capacity and load distribution along drilled shafts considering or not the strains induced by concrete curing.

**Keywords:** residual stresses, numerical modeling, shaft friction, design parameters, drilled shafts.

**Resumo:** Procedimentos convencionais de interpretação de provas de carga em estacas escavadas instrumentadas baseiam-se em medidas de deformações para as quais assume-se como configuração de referência e deformação nula o instante imediatamente anterior ao início da prova de carga. No entanto, algumas evidências experimentais mostram que o concreto, em estacas escavadas, apresenta deformações devidas ao processo de cura do concreto de magnitude comparável às medidas durante as provas de carga. Portanto, pode-se esperar que a mobilização de atrito lateral comece a se desenvolver antes mesmo do início das provas de carga. Alguns autores através de procedimentos experimentais e análises numéricas buscaram quantificar a influência de tais deformações volumétricas do concreto em etapa anterior à prova de carga na capacidade de carga das estacas através de diferentes abordagens. O presente trabalho busca estabelecer um quadro de referência sobre o tema para trabalhos existentes e futuros. Buscando avaliar a influência das deformações do concreto induzidas pelo o processo de cura no atrito lateral desenvolvido antes de provas de carga em estacas escavadas, foram realizadas simulações numéricas por elementos finitos considerando deformações térmicas, autógenas e por secagem do concreto. As análises foram realizadas considerando o concreto como material elástico linear e isotrópico e o solo como elastoplástico seguindo o modelo constitutivo de Mohr-Coulomb, nativamente implementado no *software* ABAQUS. Os resultados são interpretados

**Corresponding author:** Augusto Bopsin Borges. E-mail: [augusto.borges@ufrgs.br](mailto:augusto.borges@ufrgs.br)

**Financial support:** CAPES; CNPq (process number 130119/2018-0).

**Conflict of interest:** Nothing to declare.



This is an Open Access article distributed under the terms of the Creative Commons Attribution License, which permits unrestricted use, distribution, and reproduction in any medium, provided the original work is properly cited.

focando na relevância das deformações de cura para a capacidade de carga e distribuição de carga ao longo de estacas escavadas em solo granular, considerando ou não as deformações no concreto devidas ao seu processo de cura.

**Palavras-chave:** tensões residuais, modelagem numérica, atrito lateral, parâmetros de projeto, estacas escavadas.

**How to cite:** A. B. Borges, R. V. Linn, F. Schnaid, and S. Maghous, "A simplified numerical approach to the evaluation of residual shaft friction induced by concrete curing in drilled shafts on granular soils," *Rev. IBRACON Estrut. Mater.*, vol. 13, no. 5, e13505, 2020, <https://doi.org/10.1590/S1983-41952020000500005>

## INTRODUCTION

The consideration of shaft friction mobilized during the installation of driven piles, prior to load test procedures, is a fundamental issue in foundation engineering [1]. In the context of drilled shafts, variations of normal stresses as well as associated mobilized shaft friction at the pile-soil interface, prior to external load application, should be also properly evaluated [2]. These distributions are expected to be notably governed by concrete volumetric shrinkage or expansion strains during pre-load test phase.

Measurements during pre-load stage of instrumented pile load tests revealed significant variations in the strain profile, which would alter the reference configuration for the instrumentation zero readings [3]–[5]. In particular, Viggiani and Vinale [4] and Pennington [5] reported strain measurements along the shaft of instrumented piles, illustrated in Figure 1 and Figure 2, where negative strains refer to swelling, while positive strains reflect shrinkage.

The results emphasized that the concrete undergoes significant volumetric shrinkage strains in a pre-load test phase.

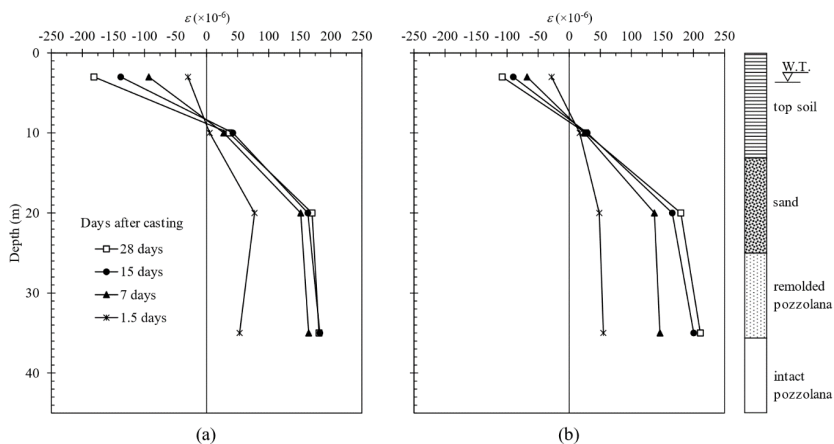


**Figure 1.** Strain measurements along the depth for two different drilled shafts; (a) pile A and (b) pile C [4].

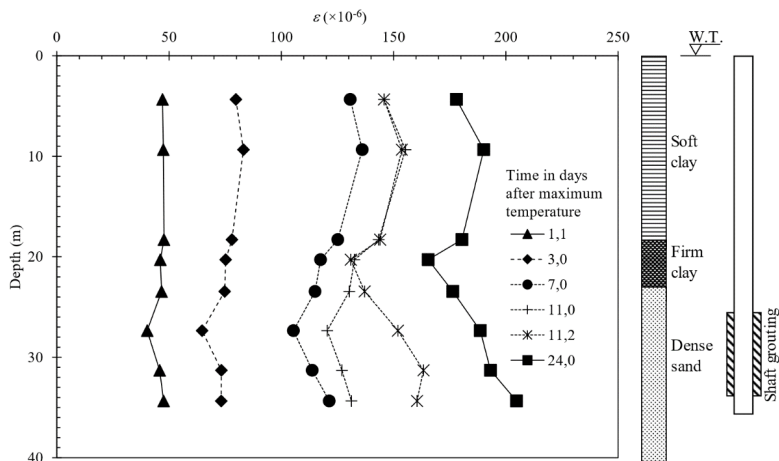


**Figure 2.** Strain measurements during the curing period for a drilled pile with 1.5 m diameter [5].

Based on strain measurements together with temperature rising profiles induced by the concrete curing process recorded immediately after concrete casting in large diameter drilled shafts, Pennington [5] estimated the mobilized shaft friction. Calculated values for the unit shaft friction for both residual stresses prior to test and during pile load tests are shown in Figure 3. For residual shaft friction, the volumetric strains in the pile due to the curing induced contraction in the upper portion of the pile, generating downward relative movements and consequently positive shaft friction. On the contrary, the residual shaft friction is negative along the lower part. Although it may appear that the average of the residual stresses tends to a vanishing value, it is however expected to modify the equilibrium stress distribution along the pile during loading.

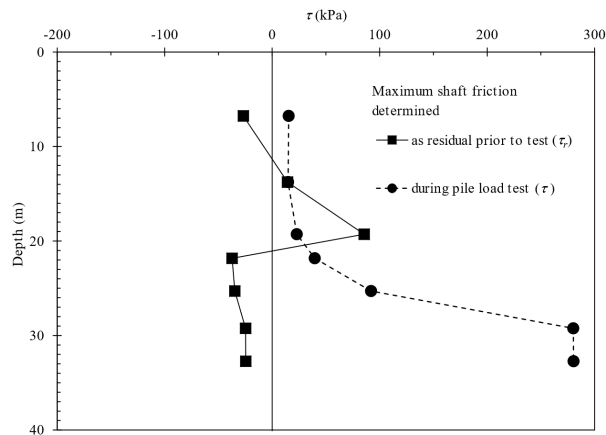


Figure 3. Comparison of residual shaft friction with shaft friction established from load test for a 1.5 m diameter pile [5].

It comes from the above experimentally based analyses that the concrete curing phenomena can be viewed as an important component of pile-soil interaction, thus affecting the mechanical state in the soil around the pile.

Concerning the available shaft resistance in drilled shafts, rational procedures for its evaluation in granular soils are classically based on the assumption that the shaft friction mobilized at the pile-soil interface follows the linear Coulomb friction model. In the simplified framework in which the residual stresses are disregarded and the geostatic state of stresses is preserved, the shaft friction at any depth  $z$  along the pile-soil interface may be expressed as:

$$\tau(z) = \sigma'_h(z) \tan \delta(z) = K_s(z) \sigma'_{v0}(z) \tan \delta(z) = \beta(z) \sigma'_{v0}(z) \tag{1}$$

It comes from the above experimentally based analyses that the concrete curing phenomena can be viewed as an important component of pile-soil interaction, thus affecting the mechanical state in the soil around the pile.

Concerning the available shaft resistance in drilled shafts, rational procedures for its where  $\tau$  is the unit shaft friction,  $\sigma'_h$  is the acting effective horizontal stress,  $\delta$  is the interface friction angle,  $\sigma'_{v0}$  is the effective initial vertical stress,  $K_s = \tau/(\sigma'_{v0} \tan \delta) = \sigma'_h/\sigma'_{v0}$  is a measure of the acting lateral earth pressure, and  $\beta = \tau/\sigma'_{v0} = K_s \tan \delta$  is a shaft friction design parameter.

Although this assumption might appear at first glance questionable from the mechanical viewpoint, Burland [6] highlighted that this expression represents a simple and logical starting point evaluating the pile shaft friction from well-established soil mechanics properties.

Parameters  $K_s(z)$  and  $\beta(z)$  seek to encompass in a global manner the essential soil characteristics and associated uncertainties in pile analysis and design. This formulation takes implicitly into account the stress history of the soil, mobilized friction angle and pile-soil interface properties, grain-size distribution, as well as changes in lateral stresses induced by pile installation procedures and straining at the pile-soil interface caused by concrete curing process. To illustrate the importance given to stress history and related  $K_0$  profile Mayne and Kulhawy [7] and Kulhawy [8], using  $K_s = K_0$  for  $\beta$ , considers that if overconsolidation is disregarded at shallow depths (constant value of  $K_0$  – Normally Consolidated soil), the respective  $\beta$  profiles would also be constant with depth (dashed lines in Figure 4). Considering  $\delta$  constant with depth, one can note that the main influent factor on the increase of  $\beta$  at shallow depth should precisely be the preexisting  $K_0$  profile.

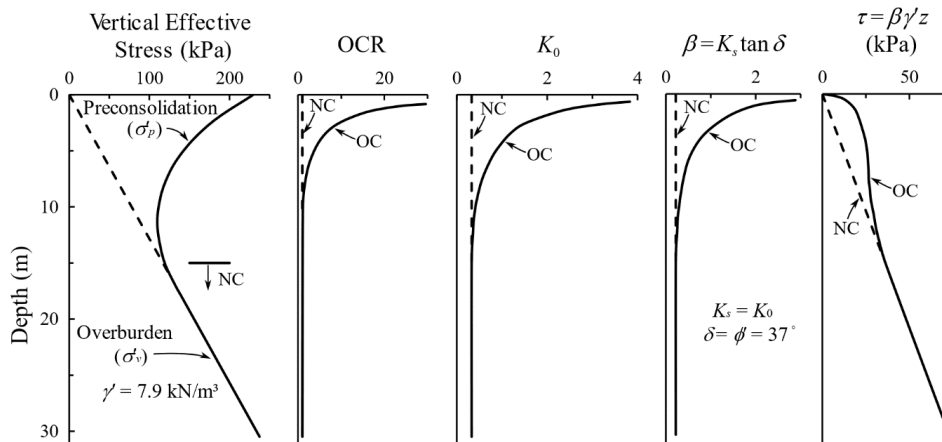


Figure 4. Example illustrating the principles of shaft resistance [8].

The mobilized interface friction angle  $\delta(z)$  has been the subject of several studies pointing out its dependence on the pile-soil interface roughness. Typical  $\delta(z)$  values range from the critical state friction angle  $\phi'_{crit}$ , for smoothed interfaces, to the peak friction angle  $\phi'_{peak}$ , for rough interfaces. Drilled shafts always exhibit high roughness at the pile-soil interface and failure yielding is likely to occur in the soil mass, following a simple shear mode governed by  $\phi'_{crit}$  angle.

According to Kulhawy [8] and [9], the typical profiles for  $\beta$  and  $K_s$  decreasing with depth (Figure 4) can be explained as reflecting the reduction in  $K_0$  with depth together with the decrease in soil friction angle as confining stresses increase.

Focusing the analyses on the effects induced on the shaft friction of floating drilled shafts embedded in granular soils, in the pre-load test stage, Mascarucci [10] and Mascarucci et al. [11] performed axisymmetric numerical simulations in axially load piles considering curing strains coupled with evolving stiffness during the curing process. Both approaches used the standard finite-difference FLAC 2D software with a strain softening behavior for the interface constitutive model and a *Strain Softening Model* for the soil [12]. These studies emphasized that restarting the strain measurements in instrumented piles immediately before the load test would introduce significant errors in the distribution of shaft friction along the pile-soil interface.

Based on a simplified but consistent formulation, the present work aims at presenting a reference framework for existing and future numerical analyses. Restricting the subsequent analysis to concrete drilled shaft embedded in granular soils, this work focuses on the effects induced on the shaft friction by concrete curing strains during pre-load test stage. In that respect, the analysis is undertaken in the context of fully drained conditions, indicating that pore pressure effects are not relevant for the proposed approach.

### Numerical Model

As the problem of cylindrical piles axially loaded in homogeneous soil (usual configuration for drilled shafts) complies with the revolution symmetry with respect to the pile axis, axisymmetric modeling is adopted for bearing capacity analyses. The overall dimensions of the model in terms of the pile length  $L$  and pile diameter  $D$ , together with model boundary conditions are shown in Figure 5. The different zones in Figure 5 were established for mesh control and refinement. The typical finite element model discretization used is shown in Figure 6. Four-node axisymmetric quadrilateral elements with bilinear displacement CAX4, available in the ABAQUS finite element library, were used for both pile and soil. Due to the roughness classically observed along drilled pile shaft [13], resulting from drilling and casting concrete processes, a perfect bonding condition is assumed at the pile-soil interface.

The width and height of the geometric model are respectively fixed as  $B = 25D$  and  $H = 2.5L$ , according to standard discretization used in foundation analyses [14]. As regards material constitutive characteristics, concrete was modeled as an isotropic linear-elastic material, with Young's modulus  $E_c = 30$  GPa (corresponding approximately to  $f_{ck} = 30$  MPa [15]) and Poisson's ratio  $\nu_c = 0.2$ , whereas the behavior of the homogeneous soil is described by means of an non associated elasto-plastic Mohr-Coulomb model, with Young's modulus  $E_s = 50$  MPa, Poisson's ratio  $\nu_s = 0.2$ , friction angle  $\phi = 29^\circ$  and dilatancy angle  $\psi = 1^\circ$ . Physical material parameters of Ottawa sand defined in Han et al. [16] as specific gravity  $G_s = 2.65$ , minimum void ratio  $e_{min} = 0.48$  and maximum void ratio  $e_{max} = 0.78$  were used. The value of the coefficient of earth pressure at rest is fixed to  $K_0 = 0.4$ .



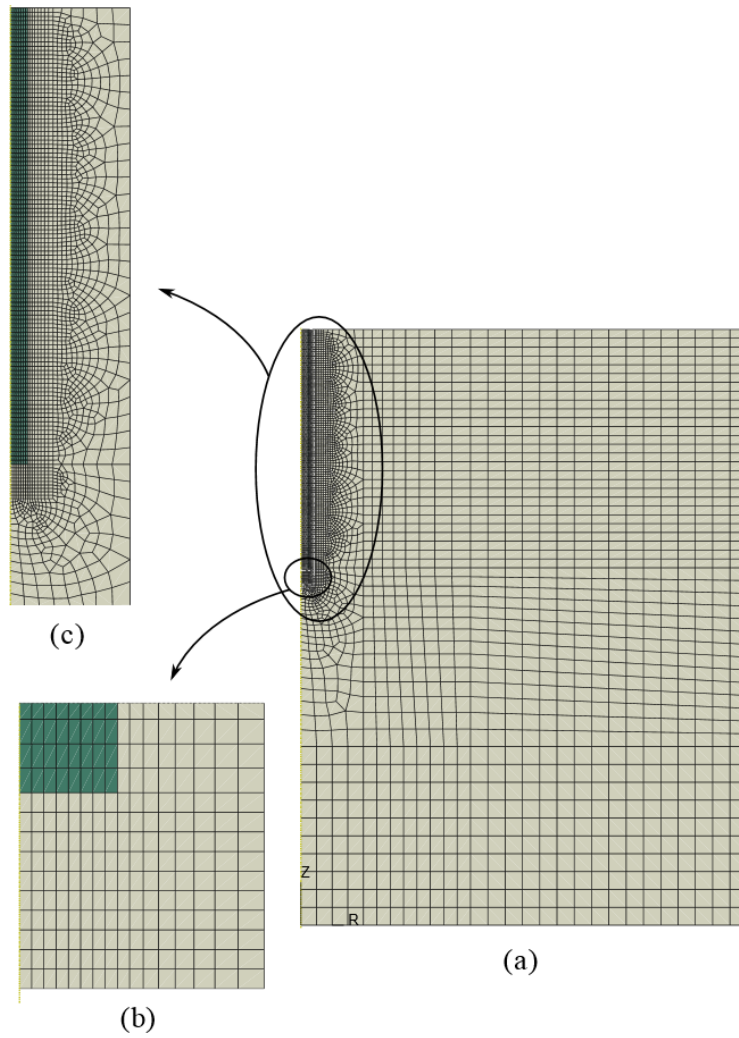


**Figure 6.** Finite element mesh used for model geometry (a), detailed mesh at pile tip (b) and detailed mesh at pile shaft (c).

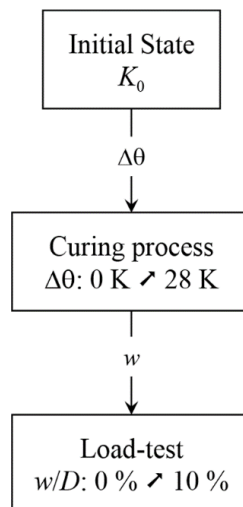


**Figure 7.** General scheme of the analyses.

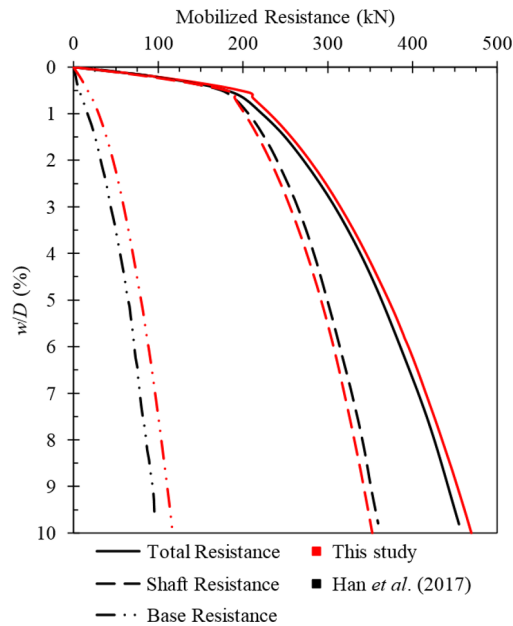


**Figure 8.** Results for the mobilized resistance as a function of the relative settlement of the pile head.

**Table 1.** Ultimate total, lateral and base resistances ( $w/D = 10\%$ ).

Resistance component	Present study	Han et al. [16]
$Q_{ult}$ (kN)	463.85	454.93
$Q_{l,ult}$ (kN)	352.57	359.49
$Q_{b,ult}$ (kN)	114.80	96.19

### Numerical assessment of residual shaft friction

A The purpose of this section is to perform a series of finite element simulations to investigate the effects of concrete curing on the mobilized shaft friction of drilled shafts. Keeping the pile length fixed to  $L = 20$  m, assessment of pile slenderness  $L/D$  effects were investigated varying the pile diameters in the range of 0.5 m to 1.5 m ( $L/D$  ranging from 40 to 13.33) for both dry ( $S = 0$ ) and saturated ( $S = 1$ ) sand. Appropriate effective specific unit weight of  $\gamma' = 15.95$  kN/m<sup>3</sup> ( $d = 1,625.77$  kg/m<sup>3</sup>) and  $\gamma' = 9.93$  kN/m<sup>3</sup> ( $d = 1,012.27$  kg/m<sup>3</sup>) were respectively adopted for the dry and saturated conditions. General characteristics of the numerical finite element discretization used in each configuration are summarized in Table 2.

**Table 2.** Numerical finite element discretization used in the analyses.

Analysis	$S$	Pile Diameter	$L/D$	Number of elements – soil	Number of elements – pile
SIM-01	0%	0.50 m	40	9,676	2,560
SIM-02	100%				
SIM-03	0%	1.00 m	20	4,880	1,280
SIM-04	100%				
SIM-05	0%	1.50 m	13.33	3,359	856
SIM-06	100%				

### Simulation of concrete curing process

Due to microstructural mechanisms, concrete shrinkage is classically separated into autogenous and drying shrinkage [17], [18]. Hydration of the cement compounds involves mainly exothermic reactions that raise the temperature of the concrete mass (Figure 9), inducing thermal volumetric strains ( $\epsilon_{th}$ ). The total volumetric strains ( $\epsilon_{cs}$ )

resulting from the concrete curing process  $\epsilon_{cs}$  is a sum of those three strain components (Equation 2): autogenous shrinkage  $\epsilon_{cas}$ , drying shrinkage  $\epsilon_{cds}$ , and thermal shrinkage  $\epsilon_{th}$ .

$$\epsilon_{cs} = \epsilon_{cas} + \epsilon_{cds} + \epsilon_{th} \tag{2}$$

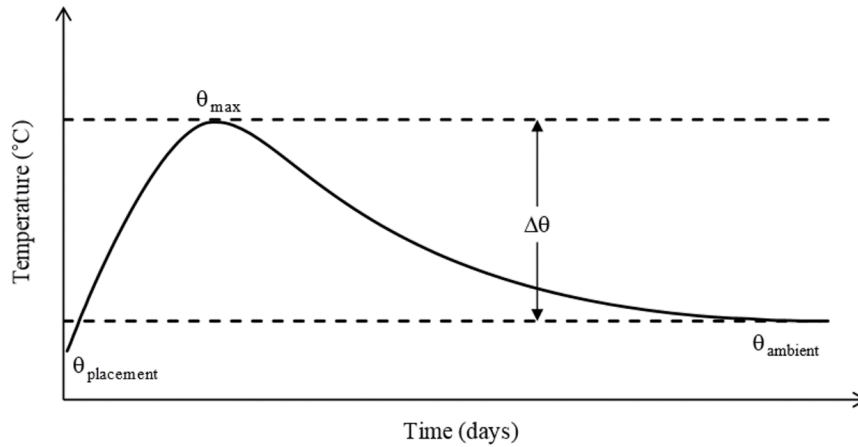


Figure 9. Temperature change with time. Adapted from Mehta and Monteiro [19].

The development of the autogenous and drying shrinkage during the curing period of 28 days was calculated following *fib* Model Code recommendations [17]. Physically, these shrinkage components are a function of factors such as water-cement ratio, cement type and content, strength class, environmental conditions, type of aggregate, among others. In the model, these components are computed using the concrete compressive strength as a design parameter accounting at macroscopic scale for concrete strength class, aggregate type, cross-section geometry, relative humidity and duration of drying. The thermal shrinkage resulting from the temperature change  $\Delta\theta$  induced by curing process is calculated from concrete thermal expansion, with a thermal expansion coefficient  $\alpha_c = 1 \times 10^{-5} \text{ K}^{-1}$  as: [19]

$$\epsilon_{th} = \alpha_c \Delta\theta \tag{3}$$

where  $\Delta\theta \in [0 \text{ K}, 28 \text{ K}]$  is considered in the analysis.

The distribution of temperature variation raising in concrete during the curing varies with depth and is heteronomous within the cross-section of the pile. For simplicity, however, a spatially uniform temperature profile was assumed, using the temperature profile measured in a large diameter drilled shaft by Pennington [5] (Figure 10), for the entire pile. The temperature is assumed to remain constant after 20 days, with further curing strains calculated by *fib* Model Code recommendations [17].

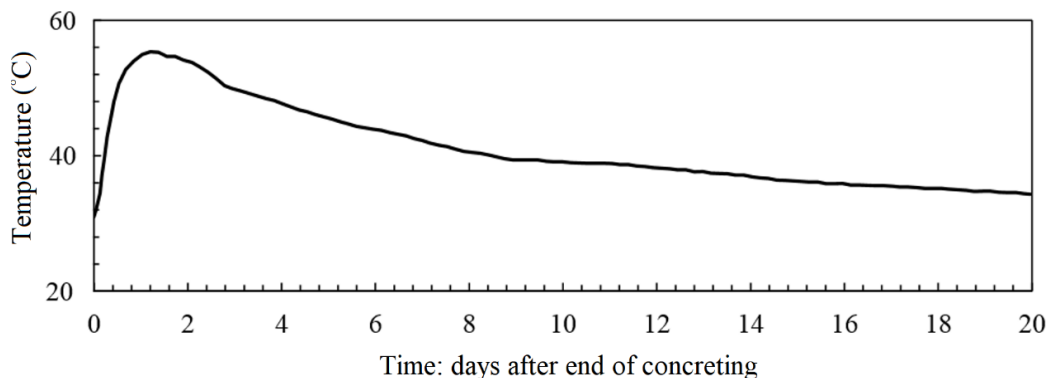


Figure 10. Experimental profile of temperature change with time [5].

In the thermal analysis it is assumed that concrete sets at maximum temperature, so that the development of differential strains between the contracting pile and the soil can be estimated from this reference time. Strains due to the thermal expansion of the pile before the maximum temperature is reached are therefore disregarded, as well as associated loading that is transferred to the soil.

Note that, in the numerical simulation of the curing process, the evolution of the strains in the concrete is imposed in the *curing\_process* step. The temperature change  $\Delta\theta$  was used as a kinematic time for assessing the mechanical state of the system, since material properties can be expressed as a function of temperature through a thermo-mechanical coupling. To meet the model of thermal strains proposed in *fib* recommendations, as displayed in Figure 11, the curing strains that are actually imposed to the pile have been evaluated considering an appropriate fictitious non-linear coefficient of expansion  $\alpha_{c,fic}$  for each  $\Delta\theta \in [0 \text{ K}, 28 \text{ K}]$  by means of Equation 3.

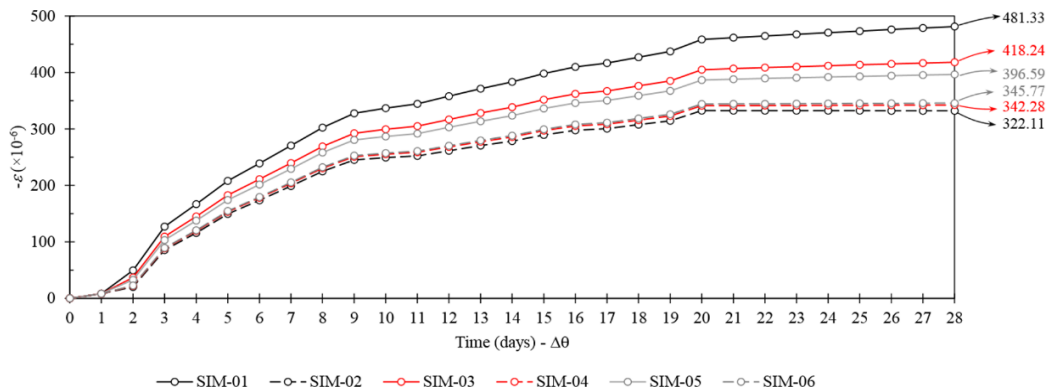


Figure 11. Imposed curing strains in the *curing\_process* step.

## RESULTS AND DISCUSSION

In the *load\_test* step, a total displacement of  $10\%D$  was prescribed at the pile head, linearly applied during the time step. Although this maximum value of displacement has been adopted to ensure the validity of small strain framework, it is often assumed a representative of ultimate state in foundation design. For comparison purposes, numerical simulations were performed with and without accounting for the curing process for each selected slenderness  $L/D$  and saturation condition. The numerical load test simulation consisted in applying incrementally a total displacement of  $10\%D$  to the pile head after completion of the curing process.

The mobilized shaft friction  $\tau$  along depth obtained from the simulations of the six different configurations defined in Table 2 are presented in Figure 12. Results correspond to the ultimate pile load obtained for  $10\%D$  total displacement. Solid lines represent simulations carried out with account for concrete curing and dashed lines stands for simulation disregarding this process (suppressing the *curing\_process* step).

In Figure 12,  $\tau_{real}$  refers to shaft friction computed from the initial reference configuration when concrete curing starts, whereas  $\tau_{virtual}$  is computed considering the configuration reached after completion of the curing process (immediately before the start of the load test) as the reference configuration. Deviation between  $\tau_{real}$  and  $\tau_{virtual}$  can be quantified by means of:

$$\tau_r = \tau_{real} - \tau_{virtual} \tag{4}$$

which represents the error  $\tau_r$  introduced when volumetric concrete curing strains are disregarded in the analysis.

The most important feature of numerical predictions lies in the fact that the actual distribution in shaft friction  $\tau_{real}$  at ultimate state coincides with the values calculated when the curing process is disregarded. This fact is consistent with general theorems of plasticity stating that the stress field at ultimate state is insensitive to initial stress distribution state [20], [21].

In addition, Figure 12 emphasize that significant errors can be induced when the unit shaft friction is evaluated based on the so-called *virtual* reference configuration. This is mainly explained as follows. The volumetric strains in the pile due to the curing induce contraction in the whole pile, generating downward relative movements in the upper part of the pile and upward relative movements in its lower part. These relative movements between the contracting

pile and the adherent soil elements mobilize shaft friction in the soil elements (considered positive upwards and negative downwards). It is therefore demonstrated that “zeroing” the instruments immediately before starting a load test may reveal mechanically inconsistent for stress pile analysis.

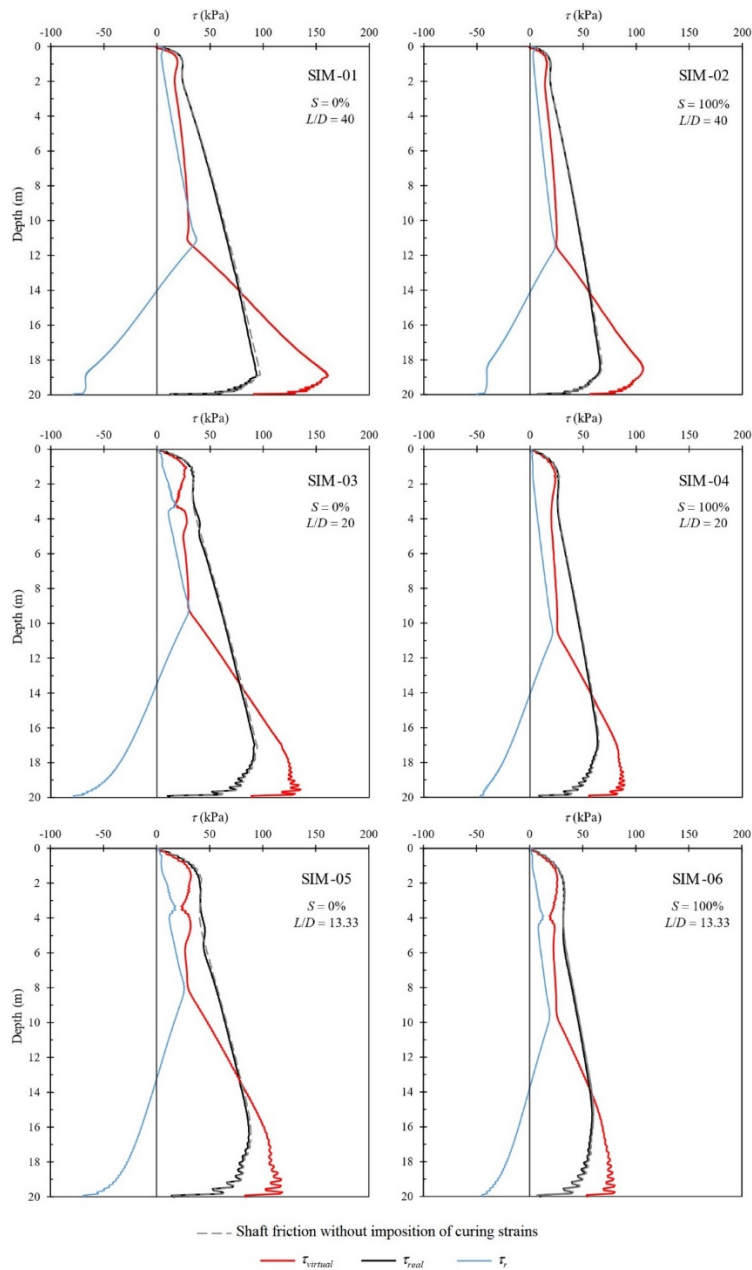


**Figure 12.** Distribution of unit shaft friction on soil elements adjacent to the pile for 10%D total displacement:  $L/D = 40$  (SIM-01 and SIM-02),  $L/D = 20$  (SIM-03 and SIM-04), and  $L/D = 13.33$  (SIM-05 and SIM-06).

In order to observe the impact of the concrete curing strains on the total load distribution along the pile at ultimate state, normalized load distribution curves are shown in Figure 13 for the cases described in Table 2.

It is observed from curves in Figure 13 that although the normalized load distribution computed from both *real* and *virtual* conditions differ along the shaft, the corresponding values of base resistance are close to each other. It implies that the predicted ultimate shaft and base load components are not affected by the procedure adopted regarding the reference configuration in instrumented load tests.

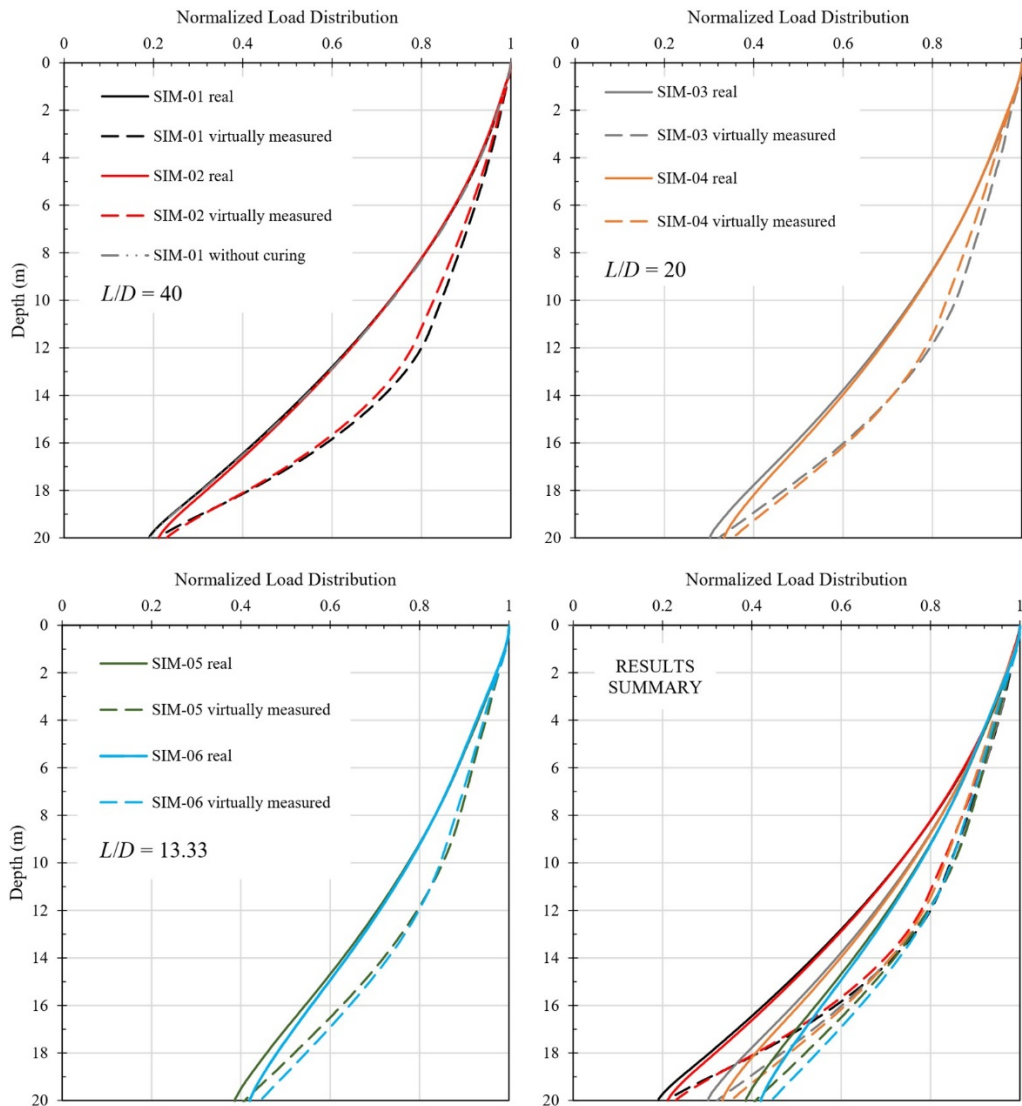


**Figure 13.** Normalized load distribution curves for 20 m long non-displacement drilled shafts for analyses with  $L/D = 40$  (SIM-01 and SIM-02),  $L/D = 20$  (SIM-03 and SIM-04), and  $L/D = 13.33$  (SIM-05 and SIM-06).

Going back to unit shaft friction analysis, the pile equilibrium expressed under *real* and *virtual* conditions respectively read:

$$\int_0^L \tau_{\text{real}}(z) dz + Q_b^{\text{real}} = \gamma_c L \tag{5}$$

$$\int_0^L \tau_{\text{virtual}}(z) dz + Q_b^{\text{virtual}} = \gamma_c L \tag{6}$$

where  $Q_b^{\text{real}}$  and  $Q_b^{\text{virtual}}$  are the base resistance computed for real and virtual conditions, respectively. Combining the above Equations 5 and 6, and observing that  $\Delta Q_b = Q_b^{\text{real}} - Q_b^{\text{virtual}} \approx 0$ , yield

$$\int_0^L \tau_r(z) dz = -\Delta Q_b \approx 0 . \tag{7}$$

Equation 7 indicate that the distribution of  $\tau_r$  shall always exhibit a neutral point where a change in signal occurs. The location of this neutral point depends on soil and pile parameters. In homogenous soils, as considered in the present analysis, the neutral point approximately lies at a depth of  $z = 2/3L$ , which is in accordance with previous numerical works performed by Mascarucci [10] and Mascarucci et al. [11].

Numerical predictions for distributions of  $\tau_r$  and  $\tau_{virtual}$  are in agreement with experimental data measured from instrumented piles, such as the results previously displayed in Figure 3. It is emphasized that experimental works [22]– [24] give evidence that  $\tau_{virtual}$  distribution along depth can significantly differ from the actual  $\tau$  distribution, although both yield the same bearing capacity.

The calculated load-displacement curves for each case are presented in Figure 14 with and without consideration of the curing process and associated pre load-step strains.

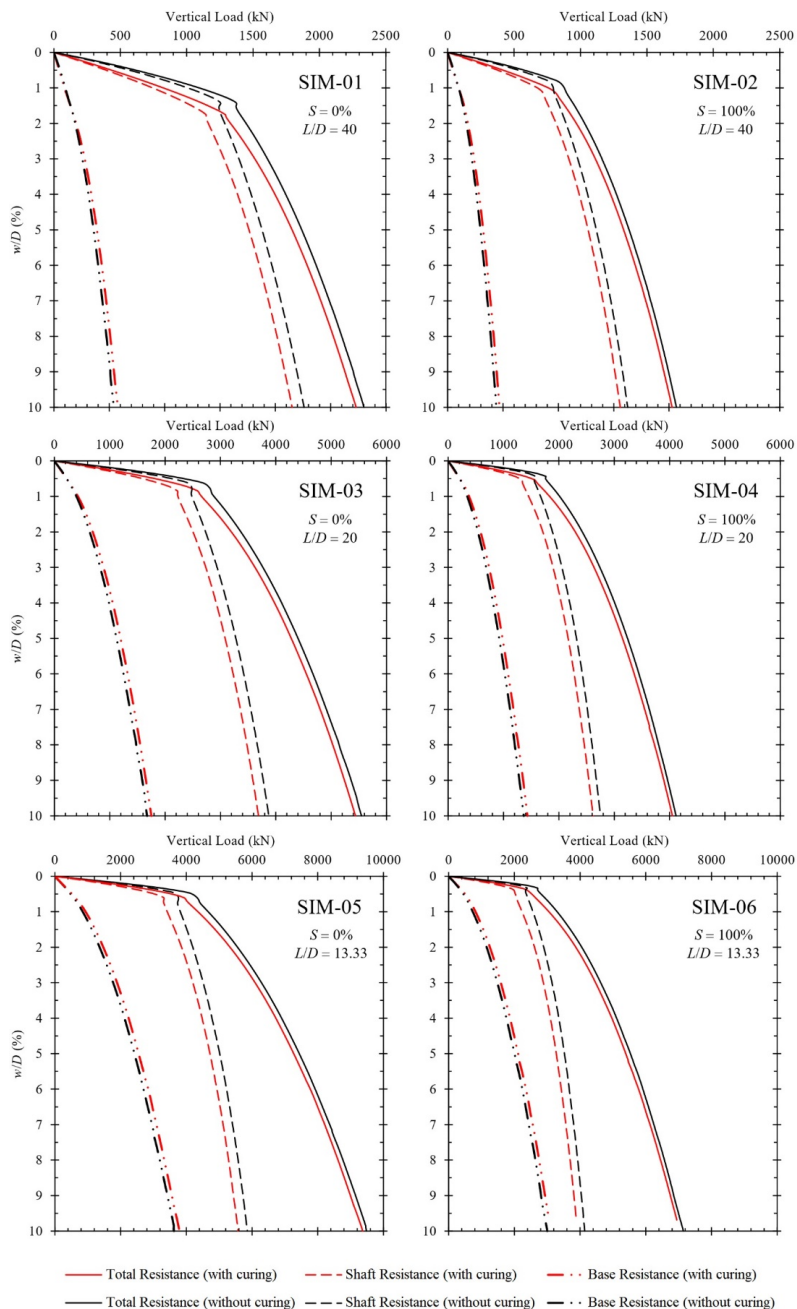


**Figure 14.** Load-settlement curves for 20 m long drilled shafts for analyses with  $L/D = 40$  (SIM-01 and SIM-02),  $L/D = 20$  (SIM-03 and SIM-04), and  $L/D = 13.33$  (SIM-05 and SIM-06).

It can be noted from Figure 14 that consideration of curing strains has little effect on the ultimate load ( $Q_{ult}$ ) distribution. The results summarized in Table 3 are in accordance with limit analysis theory [21], as already mentioned when discussing unit shaft friction distribution.

**Table 3.** Results for the analyses at  $w/D = 10\%$ .

Analysis	$Q_{l,w/c}$ (kN)	$Q_{l,w/c}/Q_l$	$Q_{b,w/c}$ (kN)	$Q_b/Q_{b,w/c}$	$Q_{ult,w/c}$ (kN)	$Q_{ult,w/c}/Q_{ult}$
SIM-01	1,794.37	95.24%	481.47	93.74%	2,275.85	97.45%
SIM-02	1,299.62	95.88%	389.57	94.14%	1,689.18	98.08%
SIM-03	3,687.05	95.18%	1,752.05	95.59%	5,439.10	98.03%
SIM-04	2,617.98	95.13%	1,433.29	95.30%	4,051.28	98.38%
SIM-05	5,576.58	95.19%	3,791.08	95.63%	9,367.66	98.77%
SIM-06	3,885.15	93.83%	3,058.89	98.13%	6,944.05	97.22%

\*  $w/c$  means 'with curing'.

This set of results demonstrates that curing strains slightly affect the ultimate state design of drilled shafts. However, this phenomenon is expected to influence the shaft friction distribution and bearing load–strain behavior at earlier stages, such as loads controlling serviceability limit state.

### Influence of concrete curing on design parameters

The influence of concrete curing on the  $K_s$  and  $\beta$  parameters (related by Equation 1), which control the distribution of shaft friction in conventional pile design, has been evaluated by mean of a series of numerical simulations with consideration for the virtual and real cases. The obtained  $K_s$  profiles are shown in Figure 15 and computed for an interface friction angle  $\delta = 29^\circ$ . It should be recalled that perfect bonding condition at the pile-soil interfaced has been assumed throughout the paper and the interface friction angle is used only to calculated  $K_s$ . The distribution of coefficient  $\beta$  can be directly deduced from  $K_s$  since the soil profile is considered homogeneous with constant interface friction angle ( $\beta = K_s \tan\delta$ ).

Referring to Figure 15, the following comments may be made to guide engineering design of drilled shafts:

- The singularity associated with the high values of  $K_s$  computed in the upper soil layers is reflecting vanishing vertical stresses in this region.
- Disregarding this upper crust, the values of  $K_s$  exhibit a slight reduction with depth and rapidly tends to a constant value.
- Referring to the so-called virtual case, it appears that  $K_{s,virtual} = \tau/(\sigma'_{v0}\tan\delta)$  with  $\delta = \phi$  constant along the depth and  $K_{s,virtual} = \sigma'_h/\sigma'_{v0}$  exhibit close profiles along the region laying above the neutral point, whereas they progressively deviate from each other as depth increases. Except in a narrow zone located beneath the upper surface, the ratio  $K_{s,virtual} = \sigma'_h/\sigma'_{v0}$  reveals close to  $K_0$  value. The latter can therefore be conveniently used in drilled pile design to characterize the initial stress state.
- The estimates of  $K_{s,real}$  and  $K_{s,virtual}$  for the earth pressure coefficient could significantly differ, indicating that disregarding the concrete curing effect amounts, the initial horizontal stress distribution at shallow depths tends to be underestimated.
- $K_s$  is a valuable design parameter for shaft resistance, but it has no physical meaning limiting  $K_s$  value by active ( $K_a$ ) and passive ( $K_p$ ) earth pressure coefficient values, given that  $K_s$  always refers to the initial condition and not the current condition in the soil.
- The pile slenderness  $L/D$  has only some effect on  $K_s$  distribution close to the upper surface, without affecting its asymptotic value.
- For the two limiting saturation conditions ( $S = 0\%$  and  $S = 100\%$ ) evaluated in this paper, it is found from the numerical simulations that saturation has qualitatively similar effects on  $K_s$  than  $L/D$ .

### CONCLUSIONS

It is widely accepted that load test performed at relatively large prescribed displacements to reach the ultimate limit state is the most reliable procedure to analyze the behavior of piles, although technological factors, such the method of construction, are expected to affect the measured response.

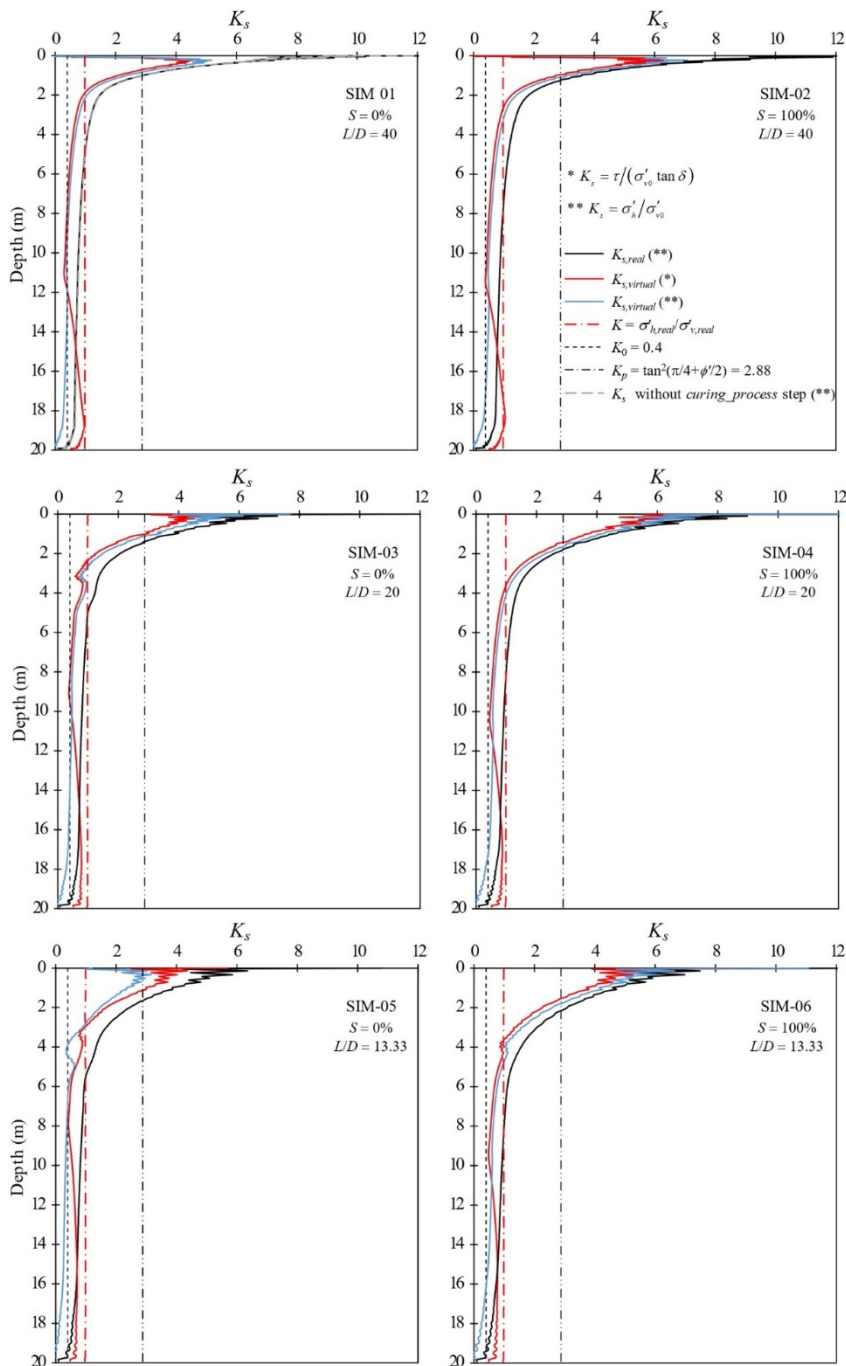


Figure 15.  $K_s$  distribution along pile shaft.

Based on these premises, numerical analyses were performed to assess the effect of curing process on the shaft friction regarded as a major parameter in pile design. The numerical analyses indicate that ultimate resistance is in fact not significantly affected by the curing process-imposed strains. The same trend is observed for base and lateral mobilized resistances.

The volumetric strains in the pile due to concrete curing induce contraction in the whole pile, generating downward relative movements in the upper part of the pile and upward relative movements in its lower part. This phenomenon explains the errors that can be introduced by “zeroing” the instruments immediately before starting a load test.

In regard to pile analysis and design, the distribution of the stress parameter  $K_s$  along the pile shaft, classically used to evaluate ultimate shaft friction profile, could be significantly affected by concrete curing while pile slenderness ratio or saturation conditions in homogeneous soils are not.

## ACKNOWLEDGEMENTS

The authors wish to explicit their appreciation to CAPES and CNPq for the support provided to the research group.

## REFERENCES

- [1] R. D. Rieke and J. C. Crowser, "Interpretation of pile load test considering residual stresses," *J. Geotech. Eng.*, vol. 113, no. 4, pp. 320–334, Apr 1987, [http://dx.doi.org/10.1061/\(ASCE\)0733-9410\(1987\)113:4\(320\)](http://dx.doi.org/10.1061/(ASCE)0733-9410(1987)113:4(320)).
- [2] B. H. Fellenius, *Basics of Foundation Design*. Vero Beach: Pile Buck Int., 2017.
- [3] C. F. Leung, R. Radhakrishnan, and Y. K. Wong, "Observations of an instrumented pile-raft foundation in weak rock," *Proc.-Inst. Civ. Eng.*, vol. 84, no. 4, pp. 693–711, Aug 1988.
- [4] C. Viggiani and F. Vinale, "Comportamento di pali trivellati di grande diametro in terreni piroclastici," *Riv. Ital. Geotec.*, vol. 2, pp. 59–84, 1983.
- [5] D. S. Pennington, "Cracked? Exploring post construction evidence in the interpretation of trial pile data," *Proc. Inst. Civ. Eng. Geotech. Eng.*, vol. 113, no. 3, pp. 132–143, Jul 1995, <http://dx.doi.org/10.1680/igeng.1995.27809>.
- [6] J. B. Burland, "Shaft friction of piles in clay," *Gr. Eng.*, vol. 6, no. 3, pp. 30–42, 1973.
- [7] P. W. Mayne and F. H. Kulhawy, " $K_0$  - OCR relationships in soil," *J. Geotech. Eng. Div.*, vol. 108, no. 6, pp. 851–872, 1982.
- [8] F. H. Kulhawy, "Drilled shaft foundations," in *Foundation Engineering Handbook*, H.-Y. Fang, Ed., Boston, MA: Springer US, 1991, pp. 537–552. [http://dx.doi.org/10.1007/978-1-4615-3928-5\\_14](http://dx.doi.org/10.1007/978-1-4615-3928-5_14).
- [9] F. H. Kulhawy, "Limiting tip and side resistance – fact or fallacy," in *Analysis and Design of Pile Foundations*, J. R. Meyer, Ed., New York: American Society of Civil Engineers, 1984, pp. 80–98.
- [10] Y. Mascarucci, *Un Nuovo Approccio per la Valutazione della Resistenza Laterale dei Pali Trivellati in Terreni Sabbiosi*. Roma: La Sapienza, 2012.
- [11] Y. Mascarucci, A. Mandolini, and S. Miliziano, "Effects of residual stresses on shaft friction of bored cast in situ piles in sand," *J. Geo-Engineering Sci.*, vol. 1, no. 1, pp. 37–51, 2013, <http://dx.doi.org/10.3233/JGS-13009>.
- [12] Itasca Consulting Group. US Minneapolis. "FLAC constitutive models". 2020. [Online]. Available: <https://www.itascacg.com/software/flac-constitutive-models>
- [13] D. Loukidis and R. Salgado, "Analysis of the shaft resistance of non-displacement piles in sand," *Geotechnique*, vol. 58, no. 4, pp. 283–296, 2008, <http://dx.doi.org/10.1680/geot.2008.58.4.283>.
- [14] M. F. Randolph and C. P. Wroth, "Analysis of deformation of vertically loaded piles," *J. Geotech. Eng. Div.*, vol. 104, no. 12, pp. 1465–1488, 1978.
- [15] Associação Brasileira de Normas Técnicas, *Design of Structural Concrete – Procedure*, NBR 6118:2014, 2014.
- [16] F. Han, R. Salgado, M. Prezzi, and J. Lim, "Shaft and base resistance of non-displacement piles in sand," *Comput. Geotech.*, vol. 83, pp. 184–197, Mar 2017, <http://dx.doi.org/10.1016/j.compgeo.2016.11.006>.
- [17] International Federation for Structural Concrete, *(fib) Model Code for Concrete Structures 2010*, 2013.
- [18] E. E. Holt, "Early age autogenous shrinkage of concrete," Ph.D. dissertation, Tech. Res. Cent. Finland, Espoo, 2001.
- [19] P. K. Mehta and P. J. M. Monteiro, *Concrete – Microstructure, Properties, and Materials*, 3rd ed. New York: McGraw-Hill, 2006.
- [20] B. Halphen and J. Salençon, *Élastoplasticité*. Paris: Press. Ec. Natl. Ponts et Chaussées, 1987.
- [21] J. Salençon, *Calcul à la Rupture et Analyse Limite*. Paris: Press. Ec. Natl. Ponts et Chaussées, 1983.
- [22] A. Altaee, B. H. Fellenius, and E. Evgin, "Load transfer for piles in sand and the critical depth," *Can. Geotech. J.*, vol. 30, no. 3, pp. 455–463, 1993, <http://dx.doi.org/10.1139/t93-039>.
- [23] T. A. B. P. Pereira, "Análise e dimensionamento de estacas sujeitas a compressão axial: aplicações na região administrativa especial de Macau," M.S. thesis, Univ. Porto, Porto, 2012.
- [24] A. S. Vesic, "Tests on instrumented piles - Ogeechee River site," *J. Soil Mech. Found. Eng. Div.*, vol. 96, no. SM2, pp. 561–584, 1970.

---

**Author's contributions:** Contribution description of each co-author for the study; Conceptualization: Fernando Schnaid and Augusto Bopsin Borges; Supervision: Renato Vaz Linn, Fernando Schnaid and Samir Maghous; Writing: Augusto Bopsin Borges, Fernando Schnaid and Samir Maghous; Data curation, formal analysis and methodology: Augusto Bopsin Borges, Renato Vaz Linn and Samir Maghous.

**Editors:** José Marcio Calixto, José Luiz Antunes de Oliveira e Sousa, Guilherme Aris Parsekian.



ORIGINAL ARTICLE

# A multi-physics modelling based on coupled diffusion equations to simulate the carbonation process

*Modelagem multi-física baseada em equações acopladas para a simulação da carbonatação*

Mateus Oliveira<sup>a</sup> Miguel Azenha<sup>b</sup> Paulo Lourenço<sup>b</sup> <sup>a</sup>Universidade Federal de Minas Gerais – UFMG, Departamento de Engenharia de Estruturas – DEES, Belo Horizonte, MG, Brasil<sup>b</sup>Universidade do Minho – UM, Instituto para a Sustentabilidade e Inovação em Estruturas de Engenharia – ISISE, Guimarães, Portugal

Received 25 June 2018

Accepted 12 February 2020

**Abstract:** Carbonation is widely recognized as a cause of significant pathologies in reinforced concrete structures and different modelling strategies are presented in literature to simulate the phenomenon evolution. In opposition to the deleterious effect in reinforced concrete, for historical mortar made with aerial lime, the carbonation is essential for the hardening process. For both materials, carbonation process presents similarities. This work presents the background/implementation of an algorithm for a multi-physics simulation of the main fields associated with the carbonation process. This modelling was previously validated in literature. A 1D algorithm is implemented, using the Finite Difference Method. Its feasibility is demonstrated through the simulation of results presented in the literature. A parametric study is also shown considering the main parameters involved, important observation regarding the influence of the parameters on the carbonation depth are detailed.

**Keywords:** multi-physics modelling, carbonation, concrete, aerial lime, finite difference method.

**Resumo:** A carbonatação é amplamente reconhecida como causa de patologias significativas em estruturas de concreto armado e diferentes estratégias de modelagem são apresentadas na literatura para simular a evolução do fenômeno. Ao contrário do efeito deletério do concreto armado, para argamassas históricas feitas com cal aérea, a carbonatação é essencial para o processo de endurecimento. Para ambos os materiais, o processo de carbonatação apresenta semelhanças. Este trabalho apresenta a implementação de um algoritmo para uma simulação multi-física dos principais campos associados ao processo de carbonatação. Essa modelagem foi validada anteriormente na literatura. Um algoritmo 1D é implementado, usando o Método das Diferenças Finitas. A viabilidade é demonstrada através da simulação dos resultados apresentados na literatura. Também é mostrado um estudo paramétrico, considerando os principais parâmetros envolvidos. São detalhadas observações importantes sobre a influência dos parâmetros na profundidade da carbonatação.

**Palavras-chave:** modelagem multi-física, carbonatação, concreto, cal aérea, método das diferenças finitas.

**How to cite:** M. Oliveira, M. Azenha, and P. Lourenço, “A multi-physics modelling based on coupled diffusion equations to simulate the carbonation process,” *Rev. IBRACON Estrut. Mater.*, vol. 13, no. 5, e13506, 2020, <https://doi.org/10.1590/S1983-41952020000500006>

## INTRODUCTION

In reinforced concrete structures, over their service life, external deleterious substances may penetrate (e.g. carbon dioxide, chloride, sulfate) into concrete and find the rebars, altering the pore solution composition into aggressive conditions [1], [2]. Specifically considering the penetration of CO<sub>2</sub>, the main consequence is the occurrence of carbonation process. Carbonation is a major cause of concrete structures deterioration, therefore its evaluation should be carefully considered in the durability design of reinforced concrete structures [2]–[8].

**Corresponding author:** Mateus Oliveira. E-mail: [mateusengcivil@gmail.com](mailto:mateusengcivil@gmail.com)

**Financial support:** None.

**Conflict of interest:** Nothing to declare.



This is an Open Access article distributed under the terms of the Creative Commons Attribution License, which permits unrestricted use, distribution, and reproduction in any medium, provided the original work is properly cited.

In concrete or cement mortar, carbonation leads to a progressive decalcification of the hydrated cement paste. The pore interstitial solution constitutes a very alkaline environment (pH close to 13.5), in which for reinforced concrete the rebars are passive [3]. When carbon dioxide (CO<sub>2</sub>) from the atmosphere penetrates into the concrete pores, it dissolves in the interstitial solution and thereby modifies the chemical balances between the solution and the hydrates. This leads to the precipitation of calcium carbonates (CaCO<sub>3</sub>) in ordinary Portland cementitious materials [9]–[11], as well as the densification of the microstructure and the decrease of the pH of interstitial solution [3]. Therefore, the reinforcement is not protected anymore, in this sense, carbonation leads to the degradation of the reinforced concrete structures. The reactions of cement-based materials occur in natural environment at a quite slow rate due to the reduced CO<sub>2</sub> concentration in the atmosphere [1], [2]. In opposition to the deleterious effects, recently, research interests focusing on the beneficial aspects of carbonation of cement-based materials have been observed [12]. In literature, there are two major beneficial of carbonation [12], [13]: (i) rapid strength gain of the cementitious matrix when subjected to curing in the presence of CO<sub>2</sub> [12], [13], and (ii) sequestration of CO<sub>2</sub> in concrete [14], [15].

Concrete is the second largest commodity (in terms of volume) consumed annually (after water) [12], [13]. Therefore, concrete and other cement-based materials may present the potential to be one of the largest global CO<sub>2</sub> sequestration [14]. As mentioned, the carbonation phenomenon in cementitious materials is a very relevant subject, and it has been studied by different authors [2]–[8].

However, the development of Portland cement is relatively recent, in the 19th century [6], consequently several other materials were previously used. One example of these materials is the aerial lime (non-hydraulic lime). The application of aerial lime in construction was recurrent until the 19<sup>th</sup> century [16], [17]. Aerial lime is frequently found in historical structures in several parts around the world. This material is basically composed of CaO and, in some cases, it may present a considerable amount of MgO as well.

In recent times, the interest in lime-based materials is increasing due to study, restoration and preservation of historic buildings [10], [11], as they are compatible with traditional building materials [6], [18], since Portland cement shows low chemical and physical affinity [6], [19], [20]. There are few studies about carbonation in aerial lime-based materials, when comparing with concrete, especially regarding the numerical aspect [10], [21], [22]. In terms of experiments, some references are present in literature [10], [23]–[25].

After this introduction, it should be highlighted that for both material (concrete and aerial lime-based mortars), several factor affect the process [26], such as: ambient relative humidity, concentration of carbon dioxide, surface protection, concrete permeability, water-binder ratio, time of exposure, and other [27], [28].

In summary, carbonation is a major cause of concrete structures deterioration, therefore its evaluation should be carefully considered in the durability design of reinforced concrete structures and for aerial lime based-materials, it is essential for the development of mechanical properties. Due to the complexity involved on the phenomenon, the use of multi-physics formulations are suggested by different authors [10], [21], [22].

The present paper presents a critical literature review about multi-physics models, considering scientific aspects. A recognized formulation is chosen and implemented using Finite Difference Method. In sequence, adopting this software, several studies are presented analyzing the evolution of carbonation process. The influence of different parameters on the carbonation depth is evaluated, in association with the study of the effect of the size/dimensions of the specimen, see Figure 1.

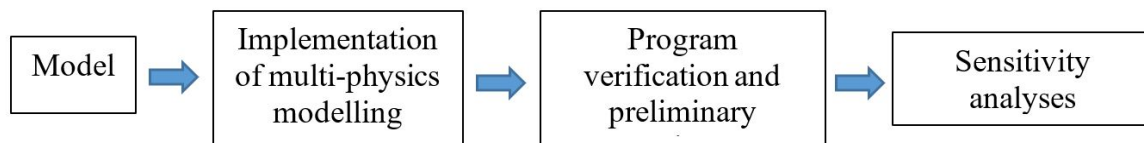


Figure 1. Work organization

### Multi-physics models for simulation of carbonation process

In this section, some general information about different multi-physics models are presented. Different strategies were chosen with a large number of parameters involved. A model based on thermo-hygro physics is presented by Ishida and Li [29], Ishida and Maekawa [30] and Ishida et al. [31]. The model coupled with moisture equilibrium/transport, temperature dependent parameters were also assumed [29].

The modelling recommended by Bary and Sellier [2] is based on macroscopic mass balance equations for water, the carbon dioxide contained in gaseous phase and the calcium present in the pore solution [2]. These equations rule the diffusion and permeation processes of the three variables: saturation degree, carbon dioxide partial pressure and calcium concentration in pore solution [2].

Coupling between carbonation and chloride diffusion is explored in the context of both homogeneous and heterogeneous concrete models [32], this model considers the coupling of heat, relative pore humidity, chloride, and carbonation fields [32].

### Models based on simple diffusion equations

The multi-physics models from literature summarized in this section are based on the CO<sub>2</sub> modeling using a simple diffusion equation.

The study done by Burkan Isgor and Razaqpur [4] presents a general diffusion model implemented in Finite Element Method) for thermo-carbo-hygro simulations, the modelling strategy is decoupled with mechanical aspects. In another research, Steffens et al. [33] adopted a diffusion model to study the carbonation. The model proposed by the authors [33] combines results of extensive studies by Bunte and Rostasy [34] on diffusion of CO<sub>2</sub> in different types of concrete and the modeling of the reaction kinetics of carbonation by Sietta et al. [35] with a coupled temperature and moisture modelling strategy, it considers that the CO<sub>2</sub> penetrates into the concrete mainly gaseous by diffusion through air-filled pores [10], [33]. Additionally, Meier et al. [36] presents a similar mathematical, in continuity, Peter et al. [37] include the hydration reactions in strategy presented by Meier et al. [36].

The mathematical modelling of carbonation process for concrete and mortars is complex [10]. The first model adopted to simulate the aerial lime mortar carbonation was shown by Ferretti and Bažant [21], for that reason, and considering the complexity involved and the requirements of information about the material, the strategy presented by Ferretti and Bažant [21] has been chosen for this work (description may be see next section). This modelling strategy has been chosen because it is the only modelling presented in literature to simulate the carbonation process in aerial lime mortar.

#### • Model of Ferretti and Bažant [21]

This section presents the mail information about the modelling strategy presented by Ferretti and Bažant [21] This model is a multi-physics coupled model involving four fields, humidity, heat, pollutant flow (CO<sub>2</sub>) and reaction [10]. The numerical model for deterioration was developed, considering the characterization of the concrete and the environmental conditions [10]. The present mathematical model is based on studies conducted by Sietta [38], Sietta et al. [35] and Sietta et al. [39], Sietta and Vitaliani [9]. The modelling presented herein was also experimentally validate in previous studies conducted by Sietta and Vitaliani [9]. The equations used to model the phenomena are presented below.

The humidity field [21], [28], [39], [40] is governed by:

$$\frac{\partial h}{\partial t} = \nabla(C_w \nabla h) + \alpha_2 \frac{\partial R}{\partial t} \quad (1)$$

where: h reads as the humidity (%),  $\alpha_2$  means the parameter related to the water generation during the carbonation process (more details are presented in sequence),  $C_w$  is the diffusion of water (mm<sup>2</sup>/day) and R is the degree of chemical reaction (%) [9].

The coefficient  $\alpha_2$  is related to the maximum content of calcium carbonate  $[CaCO_3]_{\max} = P_{\max}$  (the term  $P$  represents the formation of CaCO<sub>3</sub>), which depends mostly on the material composition. The angular coefficient of the sorption-desorption isotherm  $k$ , dependent fundamentally on temperature [9]:

$$\alpha_2 = \frac{PM(H_2O)}{PM(CaCO_3)} k P_{\max} = 0.18 k P_{\max} \quad (2)$$

where:  $PM$  represents the molecular weight of the molecule.

This equation derives from the kinetic of the carbonation reaction [9], [10]. For each CaCO<sub>3</sub> molecule produced by the reaction, a molecule of water is also created, consequently, considering the molecular mass [9], [10]:

$$M_{H_2O} = M_{CaCO_3} \frac{PM(H_2O)}{PM(CaCO_3)} \tag{3}$$

where: *M* denotes the molecular mass of the molecule specified.

Accordingly, in terms of mass per unit volume, Equation 3 may be redefined as:

$$\frac{M_{H_2O}}{V_{cls}} = \frac{M_{CaCO_3}}{V_{cls}} \frac{PM(H_2O)}{PM(CaCO_3)} \tag{4}$$

where: *V<sub>cls</sub>* is the considered volume of element, consequently [9]:

$$dw = dP^* \frac{PM(H_2O)}{PM(CaCO_3)} \tag{5}$$

where: *dw* represents the water content variation per unit volume and unit time, while *dP\** is the variation of the calcium carbonate concentration (such variables are both expressed in kg/m<sup>3</sup>) [9].

By using the well-known expression of the sorption-desorption isotherms, i.e., *khdw = dh* [10], [41], and expressing the calcium carbonate content as *dR = dP\*/P<sub>max</sub>*, it is possible to write [9]:

$$\frac{\partial h}{\partial t} = \frac{PM(H_2O)}{PM(CaCO_3)} kP_{max} \frac{\partial R}{\partial t} \tag{6}$$

which compared with Equation 6, with PM(H<sub>2</sub>O) = 18.015 and PM(CaCO<sub>3</sub>) = 100.088 [10], [42], gives Equation 2. Assuming, for illustration, that *P<sub>max</sub>* = 0.0096 kg/m<sup>3</sup> and *kh* = 1 m<sup>3</sup>/kg, then *α<sub>2</sub>* = 0.0017. The analytical determination of the coefficient *α<sub>2</sub>* proves somewhat uncertain because it is difficult to unequivocally assign the coefficients *k<sub>h</sub>* and *P<sub>max</sub>*. The carbon dioxide diffusion field is governed by:

$$\frac{\partial c}{\partial t} = \nabla(D_c \nabla c) - \alpha_3 \frac{\partial R}{\partial t} \tag{7}$$

where: *α<sub>3</sub>* is the parameter related to gas consumption during the carbonation process, *D<sub>c</sub>* represents the diffusion of the gas (CO<sub>2</sub> for instance) and *c* is the gas concentration (%).

Equation 7 is based on the second Fick's law. Parameter *α<sub>3</sub>* is influenced by the carbonation, and based on a considerations on the chemistry of this reaction. The reaction field is governed by:

$$\frac{\partial R}{\partial t} = \alpha_4 \times F_1^R(h) \times F_2^R(c) \times F_3^R(R) \times F_4^R(T) \tag{8}$$

where: *T* means the temperature (K).

The carbonation (the degree of reaction) is defined as:

$$R = \frac{[CaCO_3]}{[CaCO_3]_{max}} \tag{9}$$

where:  $[CaCO_3]_{max}$  is the maximum mass concentration of calcium carbonate ( $kg/m^3$ ), and  $[CaCO_3]$  is the actual mass concentration of  $CaCO_3$  ( $kg/m^3$ ) [10], [28], [40].

The functions  $F_1$  to  $F_4$ , are defined in sequence, further information may be seen in literature [10], [21], [28], [39], [40].

$$C_w = C_{w,ref} \times f_1^*(h) \times f_2(T) \times f_3(t_e) \times f_4(R) \tag{13}$$

$$Dc = D_{c,ref} \times f_1(h) \times f_2(T) \times f_3(t_e) \times f_4(R) \tag{14}$$

where:  $C_{w,ref}$  and  $D_{c,ref}$  are the diffusivities in standard conditions for water and  $CO_2$  respectively ( $mm^2/day$ ).

The function  $f_1^*(h)$  is defined as:

$$f_1^*(h) = \alpha + \frac{1-\alpha}{1 + \left(\frac{1-h}{1-h_c}\right)^n} \tag{15}$$

where:  $\alpha$ ,  $h_c$  and  $n$  were already defined in Equation ( $\alpha = 0.05$ ,  $h_c = 0.75$  and  $n = 6$ ).

For gas diffusion phenomena (for instance  $CO_2$ ), the following expressions are given:

$$f_1(h) = (1-h)^{2.5} \tag{16}$$

$$f_2(T) = \exp\left[\frac{E_a}{R}\left(\frac{1}{T_0} - \frac{1}{T}\right)\right] \tag{17}$$

where:  $T_0$  means the reference temperature (296 K),  $E_a$  is defined as the activation energy (kJ/mol),  $R$  reads the universal gas constant ( $J/mol \times K$ ), and  $T$  is temperature.

Function  $f_3(t_e)$  is related to the concept of equivalent age, and it is defined as:

$$f_3(t_e) = \chi + (1-\chi)\left(\frac{28}{t_e}\right)^{0.5} \tag{18}$$

where:  $t_e$  is the equivalent age (days).

The diffusion process is reduced with the decreasing of the porosity, to simulate this phenomenon a function  $f_4(R)$  may be defined as [43]:

$$f_4(R) = 1 - \zeta R \tag{19}$$

where: parameter  $\zeta$  varies between 0 and 1, and measures the slowing of diffusion phenomenon due to reduction of the porosity [38]–[40]. Ferretti and Bažant [21] adopted  $\zeta = 0.3$ , meaning that a reduction of 30% for the diffusivity value occurs with the total reaction, further information and other values for this value can be seen in literature [10], [28], [40].

Function  $F_4^R$  describes the influence of temperature on the progress of the chemical reaction, it may be expressed as [21], [33]:

$$F_4^R(T) = A \times e^{-\frac{E_a}{RT}} \tag{20}$$

where:  $A$  is the impact number [33] and  $E_a$  means the activation energy (kJ/mol).

After the description of the modelling approach, some considerations should be addressed. Considering these facts, in literature the number of works that use the multi-physics modelling strategies are raising, however more development are necessary [10]. In general terms, the multi-physics modelling strategy may be still considered a complex simulation, since it required advanced computational tools and a deep understand of the material behavior and phenomena coupling and the process of obtaining parameters is still a challenge.

Specifically considering the modelling strategy implemented in the present work [21], it may be considered a powerful tool, however some limitations are implicates: e.g. it does not consider others couplings with aggressive agents (e.g. chlorides, sulfates) and the movement of fluids are based are based on simple processes. A general review about the modelling strategies and the complexities involved may be seen in literature [10].

## RESULTS AND DISCUSSIONS

### Implementation of multi-physics modelling: A brief discussion

This section describes the strategy of implementation used to simulate the carbonation process. The coupled model is based on the work of Ferretti and Bažant [21], and it is implemented using the Finite Difference Method (FDM) [44].

The decoupled humidity field for 1D using FDM is previously presented in Oliveira et al. [45]. For carbon dioxide field, the mathematical implementation is similar, thus for the sack of brevity, the implementation of both fields are herein omitted, further details may be seen in literature [45].

All simulations of present work assume constant temperature, for the sake of brevity, no further details will be herein. The model has been implemented in 1D, axisymmetric and 2D conditions, further information may be found in and Oliveira [10]. For brevity and due to the similarity with the 1D implementation, the 2D and axisymmetric implementations are not presented herein, more details can be seen in Oliveira [10]. The chosen notation for reaction field  $R$  is the same adopted in Oliveira et al. [45], where “ $i$ ” represents the node, and “ $n$ ” reads as the time step [10]. Adopting small values of time step and of length between the nodes in FDM grid, it may be assumed  $dx = \Delta x$  and  $dt = \Delta t$ .

Equation 21 represents the equation used to simulate the reaction field. Replacing in Equation 21 the definition of  $F_2(c)$ , provides:

$$\frac{\partial R}{\partial t} = \alpha_1 \times F_1^R(h) \times \frac{c}{c_{\max}} \times F_3(R) \times F_4(T) \tag{21}$$

The evolution of reaction field over time in Finite Difference Method may be expressed as:

$$\frac{\partial R}{\partial t} = \frac{R_{n+1}^i - R_n^i}{\Delta t} \tag{22}$$

Substituting Equation 22 in Equation 21, it may be obtained:

$$R_{n+1}^i = R_n^i + \Delta t \times (\alpha_1 \times F_4^R(T) \times F_1^R(h) \times \frac{c_{n+1}^i}{c_{\max}} \times (1 - R_{n+1}^i)) \tag{23}$$

This equation may be reorganized as:

$$\left( 1 + \Delta t \times \left( \alpha_1 \times F_4(T) \times F_1(h) \times \frac{c_{n+1}^i}{c_{\max}} \right) \right) \times R_{n+1}^i = R_n^i + \Delta t \times \left( \alpha_1 F_4(T) \times F_1(h) \times \frac{c_{n+1}^i}{c_{\max}} \right) \tag{24}$$

Rearranging the equation, the expression for inner nodes, it reads:

$$\left( I + \Delta t \times \left( \alpha_1 \times F_4^R(T) \times F_1^R(h) \times \frac{c_{n+1}^i}{c_{\max}^i} \right) \right) \times R_{n+1}^i - \Delta t \left( \alpha_1 F_4^R(T) \times F_1^R(h) \times \frac{c_{n+1}^i}{c_{\max}^i} \right) = R_n^i \tag{25}$$

The definition of  $F_4^R(T)$  will not be used herein, because the temperature is assumed constant.

For coupled humidity field, considering the development done in Oliveira [10] (decoupled humidity field) and the humidity coupled equation with reaction field ( $\alpha_2(\partial R/\partial t)$ ), the final equation for humidity field for inner nodes (except in the boundary and symmetry) is given by:

$$h_{n+1}^i \times \left( \left( I + 2 \times \Delta t \times \frac{C_{w,n+1}^i}{(\Delta x)^2} \right) - \Delta t \times \left( C_{w,n+1}^i \times \frac{h_{n+1}^{i+1} + h_{n+1}^{i-1}}{(\Delta x)^2} \right) \right) - \alpha_2 \times R_{n+1}^i = h_n^i - \alpha_2 \times R_n^i \tag{26}$$

As already cited, the effective humidity and CO<sub>2</sub> diffusivity depends on the other fields ( $R$ ,  $h$  and  $c$ ) and  $C_w$ , from Equation 26 is needed to solve numerically the problem. Herein, details about this development is omitted, for the sake of brevity. More details may be seen in literature [10].

Considering the equation for carbon dioxide, with the coupling term related to reaction field (term  $\alpha_3(\partial R/\partial t)$ ), the following expression is obtained in case of the inner nodes (except in the boundary and symmetry):

$$c_{n+1}^i \times \left( \left( I + 2 \times \Delta t \times \frac{Dc_{n+1}^i}{(\Delta x)^2} \right) - \Delta t \times \left( Dc_{n+1}^i \times \left( \frac{c_{n+1}^{i-1} + c_{n+1}^{i+1}}{(\Delta x)^2} \right) \right) \right) + \alpha_3 R_{n+1}^i = c_n^i + \alpha_3 R_n^i \tag{27}$$

For the boundary and symmetric nodes, Equations 26 and 27 may be adapted as also done for the decoupled humidity field in applying Neumann boundary condition, or an imposed/fixed value adopting the Dirichlet formulation [44].

The terms of equation expressed in time “ $n+1$ ” are in the left side, while terms in time “ $n$ ” are shown in right side. In sequence, general considerations regarding the numerical simulation of humidity field for 2D condition in FDM are following discussed. The current implementation considers the field equation, which may be revised adopting the application of the chain rule [46]:

$$\frac{\Delta h}{\Delta t} = \nabla D_h \nabla h + D_h \nabla^2 h + \alpha_2 \frac{\partial R}{\partial t} \tag{28}$$

After this discussion, Figure 2 schematic represents the solution of the coupled system of equations. The symbol ( $\wedge$ ) denotes a matrix or a vector, while the superscript/subscript denotes the iteration/step.  $\hat{H}_n$ ,  $\hat{R}_n$  and  $\hat{c}_n$  represent respectively the humidity, reaction and carbon dioxide vectors for each field in time “ $n$ ”.  $\hat{RHc}$  is a vector with all the fields (reaction, humidity and carbon dioxide). Generically the matrix in right side matrix is denominated  $\hat{F}_n^i$ , the vector presenting all the fields expressed in time “ $n+1$ ” as  $\hat{RHc}_{n+1}^i$  and the residual vector of iterations is expressed as  $\hat{\psi}$ .

It should be highlighted that, for tolerance, three different values ( $toler_{humidity}$ ,  $toler_{reaction}$  and  $toler_{carbon\ dioxide}$ ) were chosen, since the order of magnitude of each field was dissimilar, further information may be seen in literature [10]. With the purpose of validate the implemented modelling, the 1D results presented in the work of Ferretti and Bažant [21] were numerically simulated. The authors [21] studied the failure of Pavia Tower in Italy [10], [47]–[49]. In order to validate the independence of the analysis from time and spacing discretization, diverse values of time steps and nodal distance were tested. The results presented small discrepancies further details may be seen in Oliveira [10].

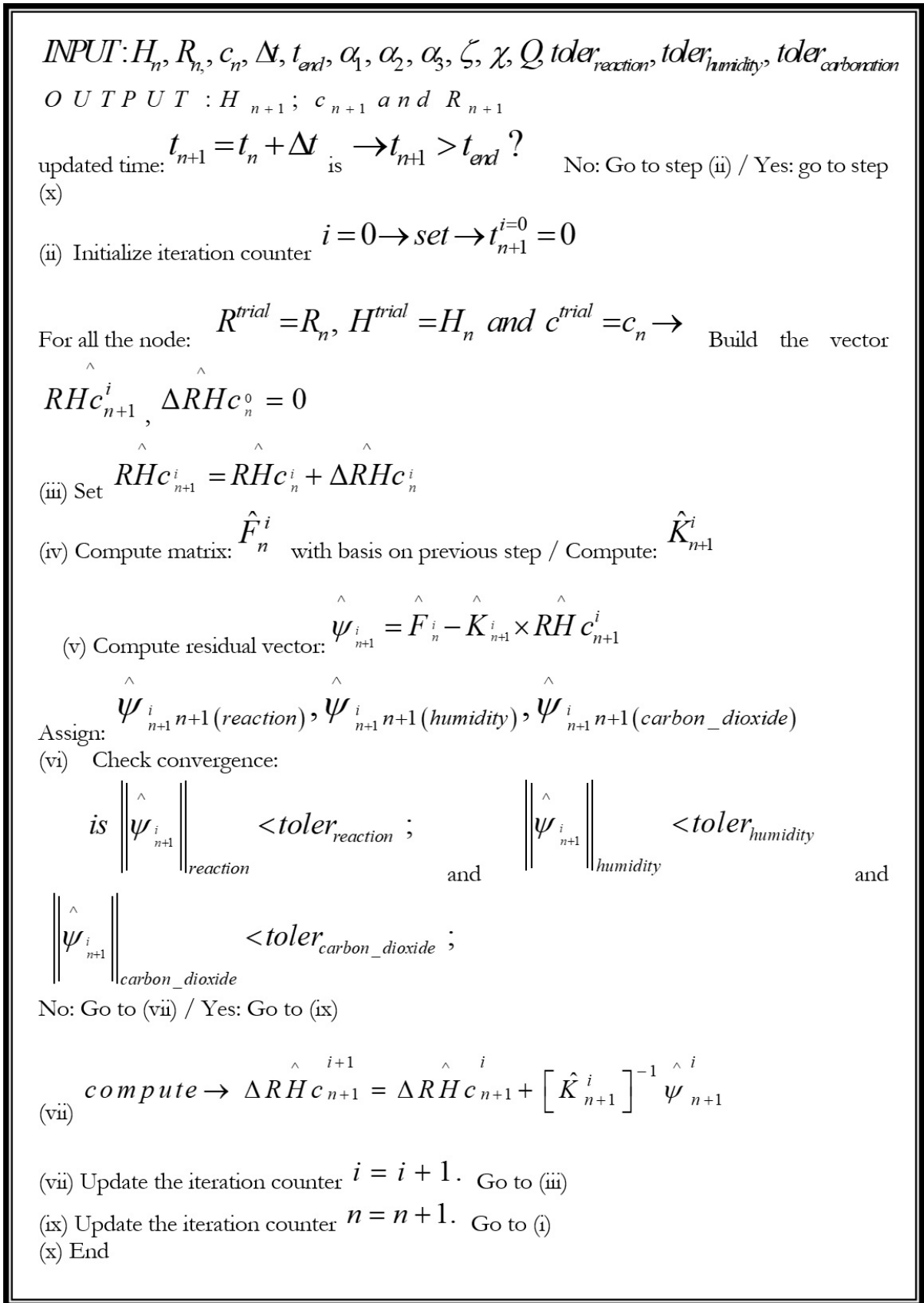


Figure 2. Coupled problem - System of nonlinear equations

### RESULTS: SENSITIVITY ANALYSES

Several sensitivity analyses were done during the study, changing the input model parameters, more information can be seen in Oliveira [10]. For these, a 1D wall with two meters (2 m) length, in contact with the environment in the two boundaries was simulated. The obtained results are presents for one meter, because of the symmetry condition (at 1 meter). For the numerical simulations, the distance “zero” (the first node) represented the node in contact with the environment, and the node located at distance one meter (1 m) was the symmetric one, more information can be seen in Oliveira [10]. In order to illustrate the obtained results, the analyses for 50 years are shown. The parametric analyses regarding the CO<sub>2</sub> initial diffusivity ( $D_{c,rif}$ ) was studied and wholly parameters were based on the Ferretti and Bažant [21].

The parametric results for CO<sub>2</sub> initial diffusivity are shown, since the large influence of this parameter on the final carbonation results. A range from one hundred times higher and smaller the value adopted by Ferretti and Bažant [21] was considered ( $D_{c,rif} = 2400 \text{ mm}^2/\text{day}$ , this is cited as the next figures as “typical value”). Time and nodal discretization were adopted with constant values ( $\Delta t = 1 \text{ day}$  and  $\Delta x = 1.25 \text{ cm}$ ). For the initial conditions, the considerations adopted above were maintained. Figure 3 shows the results for CO<sub>2</sub> concentration and Figure 4 shows the results for the reaction field.

The carbonation profile was expressively affected by the initial diffusivity of CO<sub>2</sub>. This effect was expected. After 50 years, the wall presented distinct reaction profiles, according to the used parameter. For instance, the carbonation front was located on the first 5 cm of the wall, if the diffusivity  $D_{c,rif} = 24 \text{ mm}^2/\text{day}$  (the smallest value); while the wall presented around 80 cm with  $R = 1$ , for  $D_{c,rif} = 240000 \text{ mm}^2/\text{day}$ . These cases with extreme values illustrated, the importance of the parameters’ selection for the numerical model, further information can be seen in Oliveira [10].

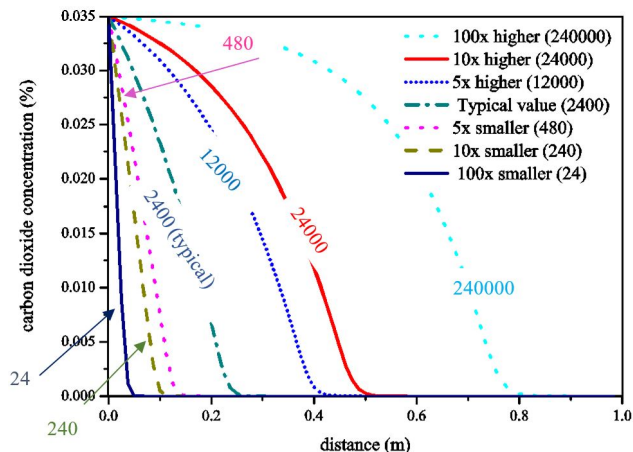


**Figure 3.** Parametric analyses, results for carbon dioxide field - Initial CO<sub>2</sub> diffusivity (values in mm<sup>2</sup>/day) - 50 years - Given the symmetry, in this figure only half of the profile is presented

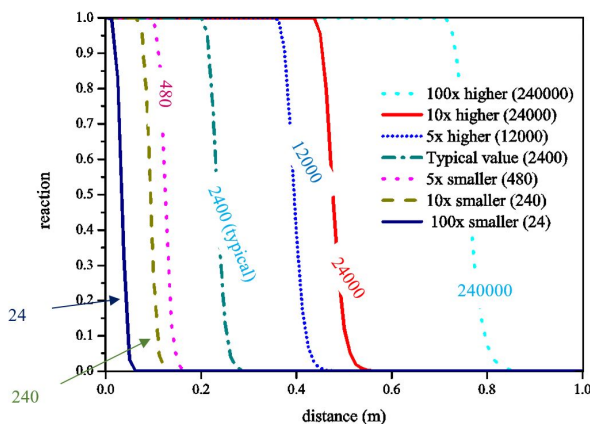


**Figure 4.** Parametric analyses, results for reaction field - Initial CO<sub>2</sub> diffusivity (values in mm<sup>2</sup>/day) - 50 years - Given the symmetry, in this figure only half of the profile is presented

Results for the humidity field are shown in Figure 5. The influence of  $D_{c,rif}$  was on the carbon dioxide and reaction fields. On the contrary, the parameter did not affect significantly the results in terms of humidity field. The tendency for 50 years was also observed for different ages, further information can be seen in Oliveira [10].

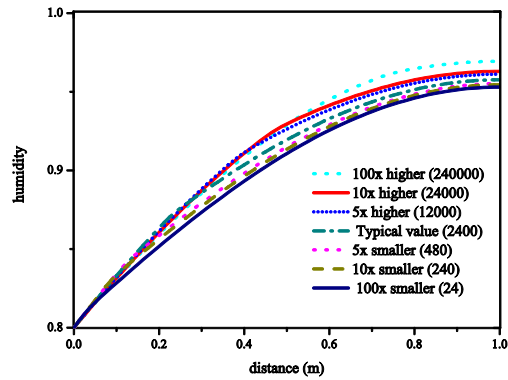


**Figure 5.** Parametric analyses, results for humidity field - Initial CO<sub>2</sub> diffusivity (values in mm<sup>2</sup>/day) - 50 years - Given the symmetry, in this figure only half of the profile is presented

The same range of values for the initial carbon dioxide diffusivity ( $D_{c,rif}$ ) was adopted, and in order to illustrate the behavior for longer ages, further information can be seen in Oliveira [10]. A node located at 40 cm from the boundary in contact with the environment was selected. The results for reaction field, for this node, in analyses over 500 years (~182500 days) are shown in Figure 6. For horizontal axis, the upper scale in Figure 6 indicated in “years” and the bottom is indicated in “days” to facilitate the understanding, further information can be seen in Oliveira [10].

The results presented in Figure 6, indicated the significant dependence of the reaction profile for this depth, according with the value for the initial the CO<sub>2</sub> diffusivity. The same dependence happened for the others depths, further information can be seen in Oliveira [10].

Unambiguously for the results presented in Figure 6, when the highest value for the carbon dioxide diffusivity was adopted,  $D_{c,rif} = 240000$  mm<sup>2</sup>/day, or equivalently one hundred time higher than the value cited by Ferretti and Bažant [21], after around 30 years (~1095 days), the reaction was completely ( $R = 1$ ). On the other hand, for the  $D_{c,rif} = 2400$  mm<sup>2</sup>/day or equivalently the value cited by Ferretti and Bažant [21], the reaction reached values close to one ( $R \approx 1$ ) after around 400 years (~146000 days), further discussion about this issue can be seen in Oliveira [10].

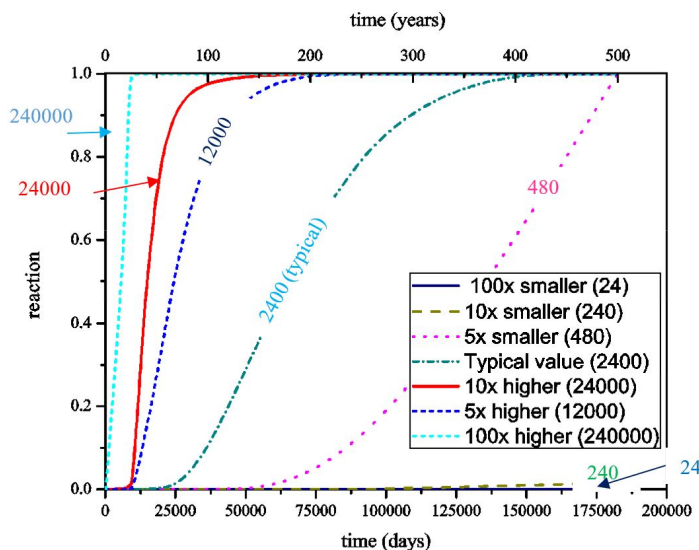


**Figure 6.** Parametric analyses, results for reaction field over time – Initial CO<sub>2</sub> diffusivity (values in mm<sup>2</sup>/day) (time of study: 0 to 500 years)

For the two lower values  $D_{c,rif}=24\text{ mm}^2/\text{day}$  and  $D_{c,rif}=240\text{ mm}^2/\text{day}$  (respectively one hundred times and ten times smaller than the value cited by Ferretti and Bažant [21], after 500 years, almost no reaction was observed for this node. All over again, these results illustrated the significant relevance of the parameters values, for the final results.

Considering the dimension/thickness of the wall, several parametric analysis were also performed, however for the sack of brevity there results are not presented herein, further details may be seen in Oliveira [10]. For large structures, according with the adopted numerical modeling [21], the inner part of the material supplies humidity for the external one, therefore the structure maintains elevated values of humidity for longer ages. For structures with smaller dimension, the humidity diffusion happens faster, because of the smaller contribution of those parts. In coherence with the results obtained in the parametric analyses herein, experimentally, the work presented by Oliveira et al. [11] and Oliveira [10] considered a geometry simulating axisymmetric conditions in aerial lime mortar, the results indicated that there is an effect of the specimen's size on the carbonation depth. The smaller specimens presented higher carbonation depth. Further information about the multi-physics process in aerial lime can be seen in literature [50], [51].

## CONCLUSIONS

This work presented a simple algorithm to simulate the carbonation evolution using a multi-physics modelling. The modelling was able to reproduce the results of Ferretti and Bažant [21], Since this work was the only publication about multi-physical simulation of aerial lime mortars, it was adopted as reference.

The sensitivity analyses were done with the presented 1D model, principally focused on the effect of carbon dioxide diffusivity and the consequence of the thickness on the studied wall. After the initial study, the results achieved demonstrated that the initial  $\text{CO}_2$  diffusivity is one of the parameters that mostly influences the carbonation profile. This conclusion indicated the relevance of an appropriate estimation of the mentioned parameter. Herein, a range from one hundred times higher and smaller the value adopted by Ferretti and Bažant [21] was considered, consequently different results for carbonation were obtained. After 50 years, the carbonation front was  $\sim 5\text{ cm}$ , for the smallest value adopted ( $D_{c,rif}=24\text{ mm}^2/\text{day}$ ); while for the highest diffusivity value,  $D_{c,rif}=240000\text{ mm}^2/\text{day}$ , the wall presented  $\sim 80\text{ cm}$  carbonated. Similar conclusions were obtained for other ages. This work is part of a larger project undergoing at Federal University of Minas Gerais and University of Minho.

## ACKNOWLEDGEMENTS

This research was Funding provided by the "Science without Frontiers" program supported by Brazilian National Council of Technological and Scientific Development (CNPq). University of Minho and Federal University of Minas Gerais are also gratefully acknowledged.

## CITATIONS

- [1] B. Lagerblad, "Carbon Dioxide Uptake During Concrete Life, State of the Art. Sweden, Denmark: Nordic Innovation Centre, 2006.
- [2] B. Bary and A. Sellier, "Coupled moisture-carbon dioxide-calcium transfer model for carbonation of concrete," *Cement Concr. Res.*, vol. 34, no. 10, pp. 1859–1872, 2004, <http://dx.doi.org/10.1016/j.cemconres.2004.01.025>.
- [3] G. Villain, M. Thiery, and G. Platret, "Measurement methods of carbonation profiles in concrete: thermogravimetry, chemical analysis and gammadensimetry," *Cement Concr. Res.*, vol. 37, no. 8, pp. 1182–1192, 2007, <http://dx.doi.org/10.1016/j.cemconres.2007.04.015>.
- [4] O. Burkan Isgor and A. G. Razaqpur, "Finite element modeling of coupled heat transfer, moisture transport and carbonation processes in concrete structures," *Cement Concr. Compos.*, vol. 26, no. 1, pp. 57–73, 2004, [http://dx.doi.org/10.1016/S0958-9465\(02\)00125-7](http://dx.doi.org/10.1016/S0958-9465(02)00125-7).
- [5] C.-F. Chang and J.-W. Chen, "The experimental investigation of concrete carbonation depth," *Cement Concr. Res.*, vol. 36, no. 9, pp. 1760–1767, 2006, <http://dx.doi.org/10.1016/j.cemconres.2004.07.025>.
- [6] G. Cultrone, E. Sebastián, and M. O. Huertas, "Forced and natural carbonation of lime-based mortars with and without additives: mineralogical and textural changes," *Cement Concr. Res.*, vol. 35, no. 12, pp. 2278–2289, 2005, <http://dx.doi.org/10.1016/j.cemconres.2004.12.012>.
- [7] C. Ewertson and P. E. Petersson, "The influence of curing conditions on the permeability and durability of concrete: results from a field exposure test," *Cement Concr. Res.*, vol. 23, no. 3, pp. 683–692, 1993, [http://dx.doi.org/10.1016/0008-8846\(93\)90019-6](http://dx.doi.org/10.1016/0008-8846(93)90019-6).
- [8] F. P. Glasser, J. Marchand, and E. Samson, "Durability of concrete - Degradation phenomena involving detrimental chemical reactions," *Cement Concr. Res.*, vol. 38, no. 2, pp. 226–246, 2008, <http://dx.doi.org/10.1016/j.cemconres.2007.09.015>.
- [9] A. V. Saetta and R. V. Vitaliani, "Experimental investigation and numerical modeling of carbonation process in reinforced concrete structures: Part I: theoretical formulation," *Cement Concr. Res.*, vol. 34, no. 4, pp. 571–579, 2004, <http://dx.doi.org/10.1016/j.cemconres.2003.09.009>.

- [10] M. A. Oliveira, "A multi-physics approach applied to masonry structures with non-hydraulic lime mortars," Ph.D. dissertation, Dep. Eng. Civ. Univ. Minho, Guimarães, Portugal, 2016.
- [11] M. A. Oliveira et al., "Experimental analysis of the carbonation and humidity diffusion processes in aerial lime mortar," *Constr. Build. Mater.*, vol. 148, pp. 38–48, 2017, <http://dx.doi.org/10.1016/j.conbuildmat.2017.04.120>.
- [12] W. Ashraf, "Carbonation of cement-based materials: challenges and opportunities," *Constr. Build. Mater.*, vol. 120, pp. 558–570, 2016, <http://dx.doi.org/10.1016/j.conbuildmat.2016.05.080>.
- [13] R. L. Berger, J. F. Young, and K. Leung, "Acceleration of hydration of calcium silicates by carbon dioxide treatment," *Nat. Phys. Sci.*, vol. 240, no. 97, pp. 16–18, 1972, <http://dx.doi.org/10.1038/physci240016a0>.
- [14] L. Shen et al., "Factory-level measurements on CO<sub>2</sub> emission factors of cement production in China," *Renew. Sustain. Energy Rev.*, vol. 34, pp. 337–349, 2014, <http://dx.doi.org/10.1016/j.rser.2014.03.025>.
- [15] E. Possan et al., "CO<sub>2</sub> uptake potential due to concrete carbonation: a case study," *Case Stud. Constr. Mater.*, vol. 6, pp. 147–161, 2017, <https://doi.org/10.1016/j.cscm.2017.01.007>.
- [16] R. M. H. Lawrence, "A study of carbonation in non-hydraulic lime mortars," Ph.D. dissertation, Dep. Architec. Civ. Eng., Univ. Bath, Bath, 2006.
- [17] R. Langenbach, "Rescuing the baby from the bathwater: traditional masonry as earthquake-resistant construction," in *Proc. 8th Int. Masonry Conf. 2010*, Dresden, Germany, 2010.
- [18] A. Moropoulou, A. Bakolas, P. Moundoulas, E. Aggelakopoulou, and S. Anagnostopoulou, "Strength development and lime reaction in mortars for repairing historic masonries," *Cement Concr. Compos.*, vol. 27, no. 2, pp. 289–294, 2005, <http://dx.doi.org/10.1016/j.cemconcomp.2004.02.017>.
- [19] L. Binda, A. Saisi, and C. Tiraboschi, "Investigation procedures for the diagnosis of historic masonries," *Constr. Build. Mater.*, vol. 14, no. 4, pp. 199–233, 2000, [http://dx.doi.org/10.1016/S0950-0618\(00\)00018-0](http://dx.doi.org/10.1016/S0950-0618(00)00018-0).
- [20] J. Lanás and J. I. Alvarez, "Masonry repair lime-based mortars: factors affecting the mechanical behavior," *Cement Concr. Res.*, vol. 33, no. 11, pp. 1867–1876, 2003, [http://dx.doi.org/10.1016/S0008-8846\(03\)00210-2](http://dx.doi.org/10.1016/S0008-8846(03)00210-2).
- [21] D. Ferretti and Z. P. Bažant, "Stability of ancient masonry towers: moisture diffusion, carbonation and size effect," *Cement Concr. Res.*, vol. 36, no. 7, pp. 1379–1388, 2006, <http://dx.doi.org/10.1016/j.cemconres.2006.03.013>.
- [22] D. Ferretti and Z. P. Bažant, "Stability of ancient masonry towers: Stress redistribution due to drying, carbonation, and creep," *Cement Concr. Res.*, vol. 36, no. 7, pp. 1389–1398, 2006, <http://dx.doi.org/10.1016/j.cemconres.2006.03.014>.
- [23] A. Arizzi and G. Cultrone, "The influence of aggregate texture, morphology and grading on the carbonation of non-hydraulic (aerial) lime-based mortars," *Q. J. Eng. Geol. Hydrogeol.*, vol. 46, no. 4, pp. 507–520, 2013, <http://dx.doi.org/10.1144/qjgegh2012-017>.
- [24] P. Faria, F. Henriques, and V. Rato, "Comparative evaluation of aerial lime mortars for architectural conservation," *J. Cult. Herit.*, vol. 9, no. 3, pp. 338–346, 2008, <http://dx.doi.org/10.1016/j.culher.2008.03.003>.
- [25] J. Lanás et al., "Mechanical behavior of masonry repair mortars: aerial and hydraulic lime-based mixtures," in *Proc. 10th Int. Congr. Deterior. Conserv. Stone*, Stockholm, 2004.
- [26] Y. Lo and H. M. Lee, "Curing effects on carbonation of concrete using a phenolphthalein indicator and Fourier-transform infrared spectroscopy," *Build. Environ.*, vol. 37, no. 5, pp. 507–514, 2002, [http://dx.doi.org/10.1016/S0360-1323\(01\)00052-X](http://dx.doi.org/10.1016/S0360-1323(01)00052-X).
- [27] V. G. Papadakis et al., "Fundamental modeling and experimental investigation of concrete carbonation," *Mater. J.*, vol. 88, pp. 363–373, 1991.
- [28] A. V. Saetta, B. A. Schrefler, and R. V. Vitaliani, "The carbonation of concrete and the mechanism of moisture, heat and carbon dioxide flow through porous materials," *Cement Concr. Res.*, vol. 23, no. 4, pp. 761–772, 1993, [http://dx.doi.org/10.1016/0008-8846\(93\)90030-D](http://dx.doi.org/10.1016/0008-8846(93)90030-D).
- [29] T. Ishida and C. Li, "Coupling of mass transport and equilibrium in micro-pore structure of concrete," *J. Adv. Concr. Technol.*, vol. 6, no. 2, pp. 303–316, 2008, <http://dx.doi.org/10.3151/jact.6.303>.
- [30] T. Ishida and K. Maekawa, "Modeling of pH profile in pore water based on mass transport and chemical equilibrium theory," *Concr. Libr. JSCE*, vol. 37, pp. 151–166, 2001.
- [31] T. Ishida, K. Maekawa, and M. Soltani, "Theoretically identified strong coupling of carbonation rate and thermodynamic moisture states in micropores of concrete," *J. Adv. Concr. Technol.*, vol. 2, no. 2, pp. 213–222, 2004, <http://dx.doi.org/10.3151/jact.2.213>.
- [32] W. Puatatsananon and V. Saouma, "Nonlinear coupling of carbonation and chloride diffusion in concrete," *J. Mater. Civ. Eng.*, vol. 17, no. 3, pp. 264–275, 2005, [http://dx.doi.org/10.1061/\(ASCE\)0899-1561\(2005\)17:3\(264\)](http://dx.doi.org/10.1061/(ASCE)0899-1561(2005)17:3(264)).
- [33] A. Steffens, D. Dinkler, and H. Ahrens, "Modeling carbonation for corrosion risk prediction of concrete structures," *Cement Concr. Res.*, vol. 32, no. 6, pp. 935–941, 2002, [http://dx.doi.org/10.1016/S0008-8846\(02\)00728-7](http://dx.doi.org/10.1016/S0008-8846(02)00728-7).
- [34] D. Bunte and F. Rostasy, "Ingenieurmodell zur Vorhersage der Dauerhaftigkeit gegen karbonatisierungsinduzierte Korrosion der Bewehrung," in *Proc. 12th Int. Conf. Build. Mater.*, Weimar, Germany, 1994.
- [35] A. V. Saetta et al., "Analysis of chloride diffusion into partially saturated concrete," *Mater. J.*, vol. 90, pp. 441–451, 1993.

- [36] S. A. Meier, M. A. Peter, A. Muntean, and M. Böhm, "Dynamics of the internal reaction layer arising during carbonation of concrete," *Chem. Eng. Sci.*, vol. 62, no. 4, pp. 1125–1137, 2007, <http://dx.doi.org/10.1016/j.ces.2006.11.014>.
- [37] M. A. Peter, A. Muntean, S. A. Meier, and M. Böhm, "Competition of several carbonation reactions in concrete: A parametric study," *Cement Concr. Res.*, vol. 38, no. 12, pp. 1385–1393, 2008, <http://dx.doi.org/10.1016/j.cemconres.2008.09.003>.
- [38] A. V. Saetta, "Durabilità delle strutture di calcestruzzo armato e analisi dei fenomeni di diffusione dei materiali multifase," Ph.D. dissertation, Univ. Padova, Padova, 1992.
- [39] A. V. Saetta, B. A. Schrefler, and R. V. Vitaliani, "2-D model for carbonation and moisture/heat flow in porous materials," *Cement Concr. Res.*, vol. 25, no. 8, pp. 1703–1712, 1995, [http://dx.doi.org/10.1016/0008-8846\(95\)00166-2](http://dx.doi.org/10.1016/0008-8846(95)00166-2).
- [40] A. V. Saetta and R. V. Vitaliani, "Experimental investigation and numerical modeling of carbonation process in reinforced concrete structures: Part II. Practical applications," *Cement Concr. Res.*, vol. 35, no. 5, pp. 958–967, 2005, <http://dx.doi.org/10.1016/j.cemconres.2004.06.023>.
- [41] M. Azenha, "Numerical simulation of the structural behaviour of concrete since its early ages," Ph.D. dissertation, Sch. Eng., Univ. Porto, Porto, 2009.
- [42] P. Atkins, *Shriver and Atkins' Inorganic Chemistry*, 5th ed. New York: OUP Oxford, 2010.
- [43] N. R. Buenfeld and N. M. Hassanein, "Life prediction of concrete structures using neural networks," in *Proc. ICE - Struct. Build*, 1998, pp. 38–48.
- [44] F. P. Incropera et al., *Introduction to Heat Transfer*, 5th ed. Hoboken: John Wiley & Sons, 2007.
- [45] M. A. Oliveira, M. Azenha, and P. B. Lourenço, "Simulation of humidity fields in concrete: experimental validation and parameter estimation," *J. Adv. Concr. Technol.*, vol. 13, no. 4, pp. 214–229, 2015., <http://dx.doi.org/10.3151/jact.13.214>.
- [46] J. Stewart, *Calculus*, 6th ed. Boston: Cengage Learn., 2007.
- [47] L. Binda et al., "The collapse of the Civic Tower of Pavia: a survey of the materials and structure," *Mason. Int.*, vol. 6, pp. 11–20, 1992.
- [48] S. Pavia et al., "An assessment of lime mortars for masonry repair," in *Proc. Concr. Res. Irel. Colloq.*, Dublin, 2006, pp. 101–108.
- [49] A. Anzani, E. Garavaglia, and L. Binda, "Long-term damage of historic masonry: a probabilistic model," *Constr. Build. Mater.*, vol. 23, no. 2, pp. 713–724, 2009, <http://dx.doi.org/10.1016/j.conbuildmat.2008.02.010>.
- [50] M. Oliveira, M. Azenha, P. B. Lourenço, A. Meneghini, and E. Guimarães, "Estudo experimental do fluxo de umidade em argamassas de cal aérea," *Rev. Materia*, vol. 24, no. 4, e12520, 2019, <http://dx.doi.org/10.1590/s1517-707620190004.0845>.
- [51] R. Veiga, "Air lime mortars: What else do we need to know to apply them in conservation and rehabilitation interventions? A review," *Constr. Build. Mater.*, vol. 157, pp. 132–140, 2017, <http://dx.doi.org/10.1016/j.conbuildmat.2017.09.080>.

---

**Author contributions:** MA: conceptualization, funding acquisition, supervision, writing; PBL: conceptualization, formal analysis, methodology, writing.

**Editors:** Paulo Cesar Correia Gomes, José Luiz Antunes de Oliveira e Sousa, Guilherme Aris Parsekian.



ORIGINAL ARTICLE

## Strength optimization of reactive powder concrete

### *Otimização da resistência mecânica de concretos de pós reativos*

Abrahão Bernardo Rohden<sup>a</sup> Ana Paula Kirchheim<sup>b</sup> Denise Dal Molin<sup>b</sup> <sup>a</sup>Fundação Universidade Regional de Blumenau – FURB, Departamento de Engenharia Civil, Blumenau, SC, Brasil<sup>b</sup>Universidade Federal do Rio Grande do Sul – UFRGS, Departamento de Engenharia Civil, Porto Alegre, RS, Brasil

Received 11 November 2018

Accepted 17 February 2020

**Abstract:** Recent reports on reactive powder concrete address important aspects regarding its performance. Several techniques are used to improve the design of such concretes. Ultra-high compressive strengths have been reported with the application of pre-setting pressure and autoclave curing. The objective of this work is to evaluate the use of very fine quartz powder to replace fine aggregate, nanosilica, and inorganic pigments to optimize mechanical properties of reactive powder concrete. The experimental work was developed in three distinct phases. In the first phase, mix-proportions of reactive powder concrete have been developed, considering different maximum aggregate sizes (1.2, 0.6, 0.075, and 0.045 mm). In the second phase, the influence of nanosilica on the properties of reactive powder concrete was evaluated. In the third phase, the effect of the addition of yellow, green, orange, and blue inorganic pigments to the reactive powder concrete mix-design was evaluated. Results show that the maximum aggregate size influences the compressive strength of the reactive powder concrete. A decrease from 1.2 mm to 0.045 mm in the maximum aggregate size resulted in 156 MPa increase in the compressive strength. The type of pigment did not significantly influence the compressive strength of the reactive powder concrete. The mix-proportion that resulted in the highest compressive strength (310.7 MPa) was designed using yellow pigment.

**Keywords:** powder-reactive concrete, quartz powder, inorganic pigments, nanosilica.

**Resumo:** Pesquisas acerca do concreto de pós reativo (CPR) têm abordado vários aspectos importantes sobre seu desempenho. São diversas as técnicas de aprimoramento empregadas na elaboração destes concretos. Com isso, resistências à compressão elevadas têm sido relatadas com a aplicação de tensões de pré-adensamento e cura em autoclave. O objetivo deste trabalho foi avaliar a aplicação de pó de quartzo em substituição ao agregado miúdo, de nanosilica e de pigmentos inorgânicos na otimização das propriedades mecânicas do CPR. O trabalho experimental foi desenvolvido em três fases. Na primeira foram dosados traços de CPR com agregados de diferentes dimensões máximas características (1,2; 0,6; 0,075 e 0,045 mm). Na segunda fase avaliou-se a influência da nanosilica nas propriedades do CPR. Na terceira fase avaliou-se o efeito da adição de pigmento amarelo, verde, laranja e azul, todos inorgânicos, na dosagem de CPR. Como principais resultados, observou-se que a resistência à compressão do CPR é influenciada pela dimensão máxima característica do agregado. Ao passar a dimensão máxima do agregado de 1,2 mm para 0,045 mm à resistência a compressão do concreto aumentou 156 MPa. O tipo de pigmento empregado no CPR não influenciou à resistência a compressão de forma significativa. O traço de maior resistência foi dosado com pigmento amarelo e teve uma resistência média de 310,7 MPa.

**Palavras-chave:** concreto de pó-reativo, pó de quartzo, pigmentos inorgânicos, nanosilica.

**How to cite:** A. B. Rohden, A. P. Kirchheim, and D. Dal Molin, “Strength optimization of reactive powder concrete,” *Rev. IBRACON Estrut. Mater.*, vol. 13, no. 5, e13507, 2020, <https://doi.org/10.1590/S1983-41952020000500007>

**Corresponding author:** Abrahão Bernardo Rohden. E-mail: [abrcivil@gmail.com](mailto:abrcivil@gmail.com)

**Financial support:** The participation of APK was sponsored by CNPq (Brazilian National Council for Scientific and Technological Development) through the research fellowships PQ2017 303753/2017-0.

**Conflict of interest:** Nothing to declare.



This is an Open Access article distributed under the terms of the Creative Commons Attribution License, which permits unrestricted use, distribution, and reproduction in any medium, provided the original work is properly cited.

## 1 INTRODUCTION

The development of reactive powder concretes (RPC) can be achieved by applying some principles to the formulation, among which, the elimination of coarse aggregates, granular optimization, pressure application during casting, thermal treatment after hardening and incorporation of metallic microfibers [1], [2].

Techniques for granular optimization can be used to strengthen RCP mechanical performance and consistency. The fine aggregates most used in RCP are quartz aggregates and metallic aggregates, which present high mechanical strength. However, other aggregates of basaltic, granitic, and calcareous origin can also be used. In RCP, the aggregate is not a limiting factor of compressive strength; i.e. concretes with more than 200 MPa can be produced using low strength aggregates such as limestone (83 MPa) [3].

RCP compositions have higher contents of supplementary cementitious materials (SCM) than standard high-performance concretes. Silica fume is the most used SCM in RCP. However, other SCMs such as fly ash, blast furnace slag, pulverized phosphorus slag, glass powder and recycled powder of ceramic bricks are also used to increase granular density [4]–[9]. Also, the improvement of the mixture performance in the fresh state [10] or the reduction in the superplasticizer [11], [12] and in the cement consumption [13] can be achieved using these materials. Other lines of research seek to improve RCP performance by incorporating nanoparticles like those of nanosilica and titanium dioxide [14].

For being composed of fines powders, RPC demands high energy to be mixed. The mixing method also influences the RPC characteristics. Hiremath and Yaragal [15] investigated the effect of the mixing speed (25, 50, 100, 125, and 150 rpm) and time of mixture (10, 15, 20, 25, and 30 min) on fresh RPC characteristics. The authors verified that the mixture speed must be between 50 and 100 rpm, low speeds compromise the performance. On the other hand, high speeds showed high contents of air entrained. The time of mixture of 15 min showed better fluidity and strength characteristics than those of the others studied.

In conventional strength concretes (Class I), the application of thermal cure improves strength in the first ages but tends to reduce strength at 28 days and more. In the RPC, this condition is not observed, and the thermal cure presents far superior results, even at 28 days [16], [12].

RPCs with 200 MPa compressive strength can be mixed with fine quartz sand and quartz powder, and thermal treatment at 90°C. The application of steel microfibers increases material ductility and its tensile strength. On the other hand, to obtain RPC with strength superior to 600 MPa, casting procedure with application of compression loads while fresh of around 50 MPa is necessary, as well as thermal treatment at temperatures from 250°C to 400°C in an autoclave. The incorporation of metallic aggregates to replace quartz aggregates can further improve its mechanical performance [1].

The use of steel fibers increases the RPC ductility as well as its flexural strength and fracture energy [1]. Han et al. [17] pointed out that the use of stainless-steel fibers with diameters of 8  $\mu\text{m}$  and 20  $\mu\text{m}$  and the incorporation of 0.5% in volume significantly increased flexural strength and fracture energy, similar to what happens with steel fibers.

Ji et al. [18] investigated the effect of the content of steel fiber (1%, 2%, 3%, and 4%) on RPC crack resistance. According to the authors, the steel fiber content shows the most significant effect on RPC behavior concerning cracking. Other factors, like water/binder ratio or sand/binder ratio, are not so relevant. Also, according to the authors, 3% content of fiber in volume was the one that provided the best performance regarding cracks.

Pressure application in casting allows a substantial increase in compressive strength. Ipek et al. [19] studied the effect of the use of densification strain assisted by a piston specially developed for this purpose. The concretes studied received densification strains of 25, 50, 75, 100, and 125 MPa. The higher compressive strength reached in the study was 475 MPa, which corresponded to 100 MPa casting strain. In addition to the application of pressure in casting, the concretes received thermal treatment at 300°C for 12 hours. Aydin et al. [3] demonstrated that the strength increase could reach 130 MPa when comparing a concrete cured simply in an autoclave (270 MPa) with a concrete pressed and cured in an autoclave (400 MPa).

In addition to compressive strength, other RPC properties are also improved with the application of the densification strain. Ipek et al. [20] studied the effect of the application of strain in RPC densification with six levels (0, 5, 10, 15, 20, 25 MPa) assessing the flexural tensile strength and the fracture energy. For the lowest level of densification strain, an increase in flexural tensile strength was 34%. Fracture energy, on the other side, increased in up to 3 times for the highest level of densification strain.

The application of autoclave curing has also been studied to improve RPC mechanical performance. Yazıcı et al. [21] determined the influence of pressure-temperature (0MPa-20°C; 1 MPa-180°C; 2 MPa-210°C and 3MPa-235°C) and time of autoclave curing (0h; 4h; 6h; 12h and 24h) in their research. The authors observed that the RPC compressive strength increases significantly after the application of autoclave curing and that it occurs due many reactive components remain unreacted under the cure conditions at room temperature (0MPa-

20°C). The authors also observed that there is a critical time (optimum) for each level of temperature-pressure applied. Mostofinejad et al. [22] reached a considerable increase (174%) in RPC strength by using autoclave curing with temperatures between 125 and 220°C. Zerb [23], on the other hand, investigated not only the time of autoclave curing but also the heating and cooling ramp. The author verified that autoclave curing time is the factor that has the most critical influence in compressive strength. The study also confirmed that autoclave treatment promoted the refining of pores smaller than 100 µm.

Other research is being developed to investigate the use of RPC in structural elements. RPC used in pillars improves the performance of the structural component to impacts as well as its shear strength [24]. Ni et al. [25], on the other hand, used RPC, with fibers, in the development of plates aiming the high ballistic performance.

The low porosity of RPC increases its durability, making it a material potentially appropriate for the storage of nuclear wastes. Matte and Moranville [26] simulated leaching in a recipient containing radioactive wastes during a lifespan of 300 to 500 years. The high contents of active silica avoid the leaching of calcium hydroxide, thus reducing porosity and increasing durability.

Considering all interesting possibilities of this type of concrete, the present work aimed to optimize an RPC composition through the choice of Brazilian aggregates, incorporation of nanosilica, and inorganic pigments, seeking to maximize mechanical performance. Fibers, densification loads, and autoclave curing were not used.

## 2 MATERIALS AND EXPERIMENTAL PROGRAM

Figure 1 presents the research development phases. First, a study was developed to identify the influence of the size of aggregate particles in RPC resistance, and the characterization of the elasticity modulus of the concretes. In Phase 2, the objective was to assess the feasibility of incorporating nanosilica to RPC as a strategy to increase its compressive strength. The test specimens produced in phase 2 were also tested for flexural strength. Finally, in phase 3, the influence of the type of pigment in RPC strength was assessed.

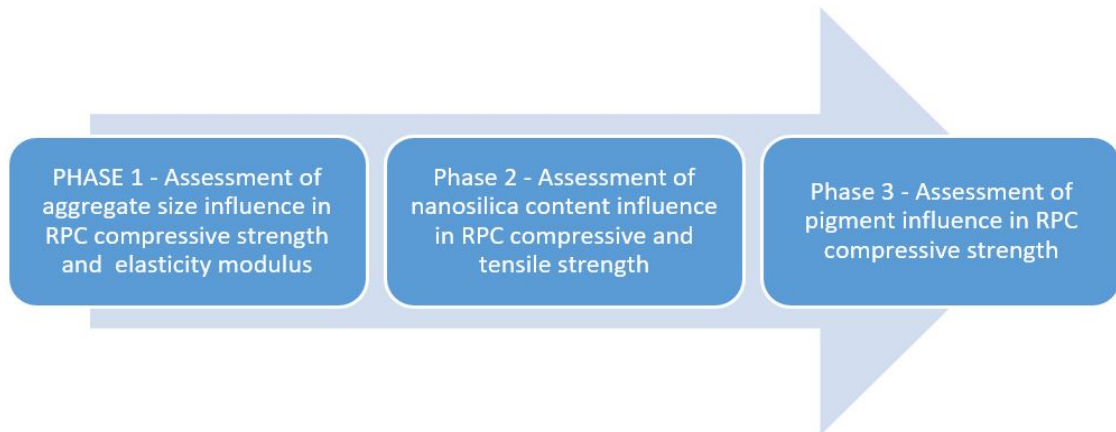


Figure 1. Research phases.

### 2.1 Materials

#### 2.1.1 Portland Cement

Two types of Portland cements were used in the present study. The two first phases of the research were developed using CPV ARI (high early strength Portland cement). In the third phase, CPB 40 Portland cement was used. The pigment utilized to color the concrete in this phase presents a better result when white cement is used.

Table 1 presents the physical and chemical properties of the two cements utilized in this study. Figure 2 shows the particle size distributions of the two cements. The cements surface areas are equal, as well as their strength at 28 days.

**Table 1.** Physical and chemical characteristics of the cements used (Source: the authors, 2020).

Characteristics and properties	Unit	CP V ARI	Limits NBR 5733	CPB 40	Limits NBR12989
Insoluble residues	%	1.0	1.0%	-	-
Loss on ignition	%	3.30	< 4.5	9.81	≤ 12
Magnesium oxide (MgO)	%	1.75	< 6.5	2.22	≤ 6.5
Sulfur trioxide (SO <sub>3</sub> )	%	3.11	< 3.5	4.68	≤ 4
Fineness (residue in the 75 µm sieve)	%	1.5	<6.0	1.88	≤ 12
Setting start time	min.	160	> 60	160	> 60
Setting end time	min.	315	< 600	205	≤ 600
Specific surface area (Blaine Method)	m <sup>2</sup> /kg	446.7	>300	477.2	-
Compressive strength	1 day	MPa	24.2	> 14.0	-
	3 days	MPa	35.5	> 24	33,7
	7 days	MPa	41.0	>34	39,8
	28 days	MPa	50.9	-	48,0
Specific mass (NBR NM 43)	g/cm <sup>3</sup>	3.15	-	2.90	-

### 2.1.2 Silica Fume

The specific mass determined, according to NM 43 [27], was 2.20 kg/dm<sup>3</sup>. The silica fume particle size distribution is shown in Figure 2. The average diameter determined, d<sub>50</sub>, was defined as 5.86 µm.

### 2.1.3 Quartz powder

Two types of quartz powder were used. One presents 50% of grains with a diameter below 11.08 µm and 100% passing through the 45 µm sieve, and 325 mesh. The second presents 50% of grains with a diameter below 22.87 µm and 100% passing through the 75 µ sieve, and this material is traded as 200 mesh. The particle size distribution of both quartz powders is presented in Figure 2. The specific mass determined, according to NM 43 [27], was 2.61 g/cm<sup>3</sup> for the two types of powder.

### 2.1.4 Fine aggregate

Two natural sands were used. The specific mass determined, according to NM 43 [27], was 2.63 g/cm<sup>3</sup> for both sands. Figure 2 presents the particle size distribution for the two natural sands. The two samples show maximum characteristic dimensions of 1.20 mm and 0.60 mm and fineness modules of 2.64 and 1.23, respectively.

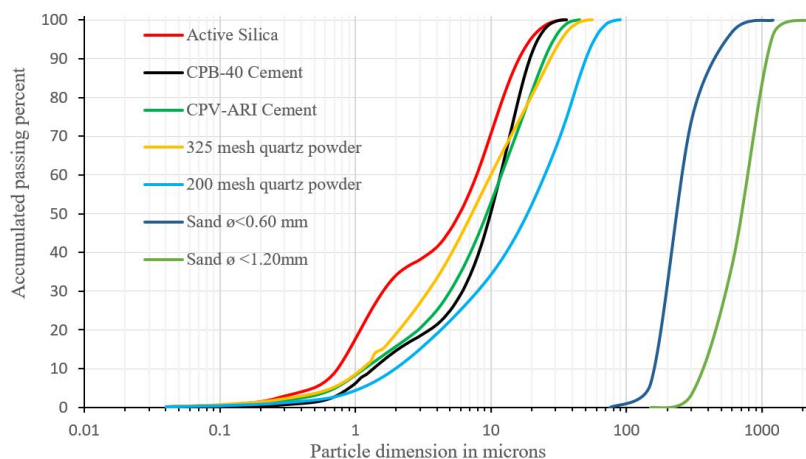


**Figure 2.** Particle size distribution of cement, active silica, quartz powder and fine aggregate particles.

### 2.1.5 Superplasticizer and superplasticizer with nanosilica

Two chemical admixtures were used: a) one polycarboxylate-based superplasticizer (PCE) and, b) one polycarboxylate-based superplasticizer with nanosilica (PCE\_N). The first PCE present, according to the manufacturer, the following technical characteristics: a) density from 1.067 to 1.107 g/cm<sup>3</sup>; b) pH between 5 and 7 and; c) solid content between 38 and 40%.

To assess the superplasticizer efficiency, its saturation point was determined using Part 2 of NBR 7681 [28] which presents the method for the determination of the melt flow index. The procedures for determination of the superplasticizer saturation point followed the recommendation of American standard ASTM C939 [29]. The test to measure the melt flow time and saturation time comprises the paste production; the passage of the mix through the cone; and the determination of its melt flow time.

Differently from conventional and high-performance concretes, in RPC mix proportion, the saturation point is not directly used to define the maxim chemical admixture content used in the mixture. In the mix proportion, superior contents of the chemical admixture saturation point is used due the high amount of powders. The criterion adopted to define the content of the superplasticizer was RPC workability. Formagini [30] described the experimental procedure adopted for the determination of granular packaging by water demand. This procedure starts with a mixture of dry materials, and, with water or superplasticizer increments, three states occur pendular, funicular, and capillary. The chemical admixture content was experimentally defined for the mixture to reach the capillary state. In the present work, the content of the superplasticizer adopted was 4.3% of the binder mass.

The second chemical admixture used in the study is a polycarboxylate based superplasticizer, in a liquid state, where nanosilica is dispersed. The manufacturer of this product does not inform the content of nanosilica present. The PCE\_N specific mass is 1.06 g/cm<sup>3</sup>. The chemical admixture content recommended by the nanosilica manufacturer for high strength concretes is up to 2%. To verify whether the PCE and PCE\_N are compatible with the materials, Marsh funnel test was used. The test followed the same procedures as those used to determine saturation point, however, in addition to cement (2,000 g), silica fume (500 g) was used. The water/cement ratio used was 0.23. Figure 3 presents the results of the flowing times and the saturation point of the PCE. Table 2 shows flowing times measured for the different combinations of PCE\_N and PCE.

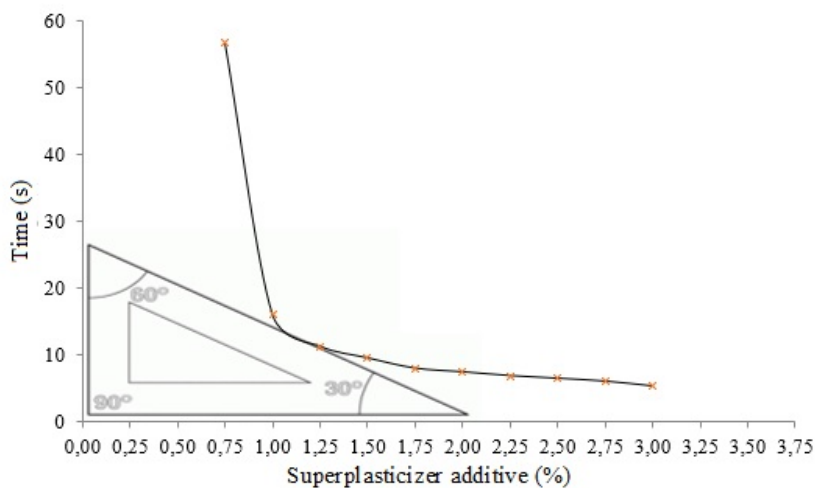


Figure 3. Graphic determination of the PCE saturation point for w/c ratio of 0.23.

Table 2. Flowing time for different proportions of SP and SPN.

Composition	Flowing time (seconds)
0.0% SPN and 4.3% SP	43.7
2.0% SPN and 2.3% SP	71.3
3.0% SPN and 1.3% SP	75.3
4.3% SPN and 0.0% SP	93.85

As can be observed in Table 2, the flowing time increases with an increase in PCE\_N percent. This fact indicates that the PCE is more efficient in the dispersion of fine particles.

### 3.1.6 Inorganic pigments

All pigments used in this work presented high fineness, superior to the 45 μ sieve. The yellow pigment (Color Index 77492) used is composed of iron oxide (Fe<sub>2</sub>O<sub>3</sub>) with a 4.7 g/cm<sup>3</sup> specific mass. The orange pigment (or light Brown – Color Index 77491) used is also composed of iron oxide (Fe<sub>2</sub>O<sub>3</sub>) with a 4.7 g/cm<sup>3</sup> specific mass. The blue pigment (Color Index 74160) was cobalt oxide (Co(Al,Cr)<sub>2</sub>O<sub>4</sub>), while the green pigment (Color Index 77492) was chromium oxide (Cr<sub>2</sub>O<sub>3</sub>).

### 2.2 Mix proportion evaluated

Table 3 presents the mix proportion used in the research. The initial determination of the compositions was made by trial and error, before the development of this work. In the first phase, the influence of the aggregate particle size in RPC was studied. Eight compositions were prepared with two water/binder ratios and four compositions of powders. Water/binder ratios were 0.18 and 0.25. The aggregate compositions, on the other hand, included sand with a maximum dimension of 1.2 mm and quartz powder; only sand with 0.66 mm dimension; only quartz powder with maximum 0.075 mm diameter; and only quartz powder with maximum dimensions characteristic of 0.045 mm. Experimentally, it was not possible to prepare compositions with the two granulometry of the quartz powders with water/binder ration of 0.18 as occurred with the other combinations.

In Phase 2, PCE\_N incorporation occurred instead of the PCE used in Phase 1. Contents of 0%, 2%, 3% and 4% were tested of substitution of PCE for PCE\_N.

In the third Phase, the use of white cement (CPB 40) and different color pigments were assessed in RPC compressive strength. Eight composition from phase 1 were tested in in phase 3. However, as the CPB 40 presents a specific mass smaller than that of cement CPVARI, correction in mass was made for the composition to give the same proportions in absolute volume. Yellow, blue, green, and orange pigments were tested. In all compositions, 2% entrained air volume was considered.

All compositions were mixed in a planetary mixer in 5 L container. The order of placement of materials was as follows: placement of the water, cement, and the superplasticizer. They were homogenized at a rotation speed of 65 rpm. Finally, the aggregate was incorporated into the mix. During the aggregate addition, the mixture speed was 125 rpm.

**Table 3.** Mix proportion of materials studied per phase (kg/m<sup>3</sup>).

Materials	Phase 1								Phase 2				Phase 3			
	1	2	3	4	5	6	7	8	9	10	11	12	13	14	15	16
CPVARI	874	820	874	820	874	820	820	820	820	819	819	819	-	-	-	-
CPB 40	-	-	-	-	-	-	-	-	-	-	-	-	805	805	805	805
Active silica	215	202	215	202	215	202	202	202	205	205	205	205	198	198	198	198
Water	157	205	157	205	157	205	205	205	188	188	188	188	185	185	185	185
PCE	26	24	26	24	26	24	24	24	35	19	11	0	24	24	24	24
PCE_N	-	-	-	-	-	-	-	-	-	16	25	35	-	-	-	-
Quartz powder Ø0.045mm	205	192	-	-	-	-	-	1,095	1,107	1,106	1,106	1,106	1,076	1,076	1,076	1,076
Quartz powder Ø0.075mm	-	-	-	-	-	-	1,095	-	-	-	-	-	-	-	-	-
Sand Ø0.6mm	-	-	-	-	1,167	1,095	-	-	-	-	-	-	-	-	-	-
Sand Ø1.2mm	962	903	1,167	1,095	-	-	-	-	-	-	-	-	-	-	-	-
Yellow pigment	-	-	-	-	-	-	-	-	-	-	-	-	60	-	-	-
Blue pigment	-	-	-	-	-	-	-	-	-	-	-	-	-	60	-	-
Green pigment	-	-	-	-	-	-	-	-	-	-	-	-	-	-	60	-
Orange pigment	-	-	-	-	-	-	-	-	-	-	-	-	-	-	-	60
w/c ratio	0.18	0.25	0.18	0.25	0.18	0.25	0.25	0.25	0.23	0.23	0.23	0.23	0.23	0.23	0.23	0.23
Cement + silica fume consumption	1,089	1,022	1,089	1,022	1,089	1,022	1,022	1,022	1,025	1,024	1,024	1,024	1,003	1,003	1,003	1,003

After the mixture, 3 test specimens (5x10cm) of each composition were molded to determine compressive strength. The test specimens were demolded 24 hours later and were taken to 28 days of thermal cure at 90°C. Special cares were taken while placing the specimens in the thermal bath and in their removal to avoid thermal shocks. Before the test, the specimens were rectified to improve contact with the plates.

Axial compression tests were performed at a loading speed of 0.45 MPa/s. The determination of the elasticity modulus of the molded concretes in phase 1 was made after the application of three pre-loading cycles, and a strain of 30% of the breaking strain was adopted for their calculation. This determination was made in three specimens of each composition. In phase 2, the flexural tensile strength test was performed on three points in prismatic specimens (40mm x 40 mm x 160 mm). The test was performed with three points of support and loading speed of 50 N/s.

### 3 RESULTS AND DISCUSSIONS

#### 3.1 Compressive strength

Table 4 presents the results of compressive strength in the three phases of this work.

**Table 4.** Presents the results of compressive strength in the three phases of this work.

Compositions	Phase 1								Phase 2				Phase 3			
	1	2	3	4	5	6	7	8	9	10	11	12	13	14	15	16
CP1	198.7	159.3	155.3	100.4	193.5	170.5	247.6	265.9	241.3	191.5	239.8	189.5	310.8	296.9	281.9	286.0
CP2	192.0	160.0	122.1	101.6	189.5	165.8	252.4	257.6	244.1	227.5	207.5	237.1	309.4	266.3	302.7	292.5
CP3	175.0	153.3	119.8	91.9	156.3	164.5	233.7	238.1	246.2	231.0	236.3	241.1	311.8	291.1	271.3	280.7
Average (MPa)	188.6	157.5	132.4	97.9	179.7	166.9	244.6	253.9	243.8	216.7	227.9	222.5	310.7	284.8	285.3	286.4
Standard deviation (MPa)	10.0	3.0	16.2	4.3	16.7	2.6	7.9	11.6	2.0	17.9	14.4	23.5	1.0	13.3	13.0	4.8
Variation coefficient (%)	5.3	1.9	12.2	4.4	9.3	1.5	3.2	4.6	0.8	8.2	6.3	10.5	0.3	4.7	4.6	1.7

In phase 1, the influence of the aggregate particle size in RPC strength was assessed. Results show very consistently that the maximum characteristic dimension of the aggregate impacts, significantly, the RPC compressive strength. Table 5 presents the result of phase 1 compressive strength variance analysis. As described in Table 5, the probability of the average strengths to belong to the same population is much inferior to 5% (p = 0.05). That is, the maximum characteristic dimension has significant influence in RCP compressive strength, for 95% reliability.

**Table 5.** ANOVA – Phase 1, only compositions with 0.25 water/cement ratio – the influence of granular skeleton.

Variation source	<i>SQ</i>	<i>gl</i>	<i>MQ</i>	<i>F</i>	<i>value-P</i>	<i>F critical</i>
Between groups	50846.48	4	12711.62	182.17	2.69E-09	3.48
Within groups	697.80	10	69.78			
Total	51544.28	14				

Figure 4 present the average results of compressive strength in phase 1, for w/c ratio of 0.25. There is a representative reduction of 61% to RPC axial compression strength when quartz powder with grains passing through the sieve with a mesh opening of 0.045 mm is replaced by sand with a maximum dimension of 1.2 mm.

De Larrard e Sedran (1994) proposed a model to explain the increase in compressive strength in concretes. According to the authors, the maximum thickness of the pasts (Equation 1) is the second most important factor (the first is the w/c ratio).

$$e_M = D * \left( \sqrt[3]{g^* / g - 1} \right) \tag{Equation 1}$$

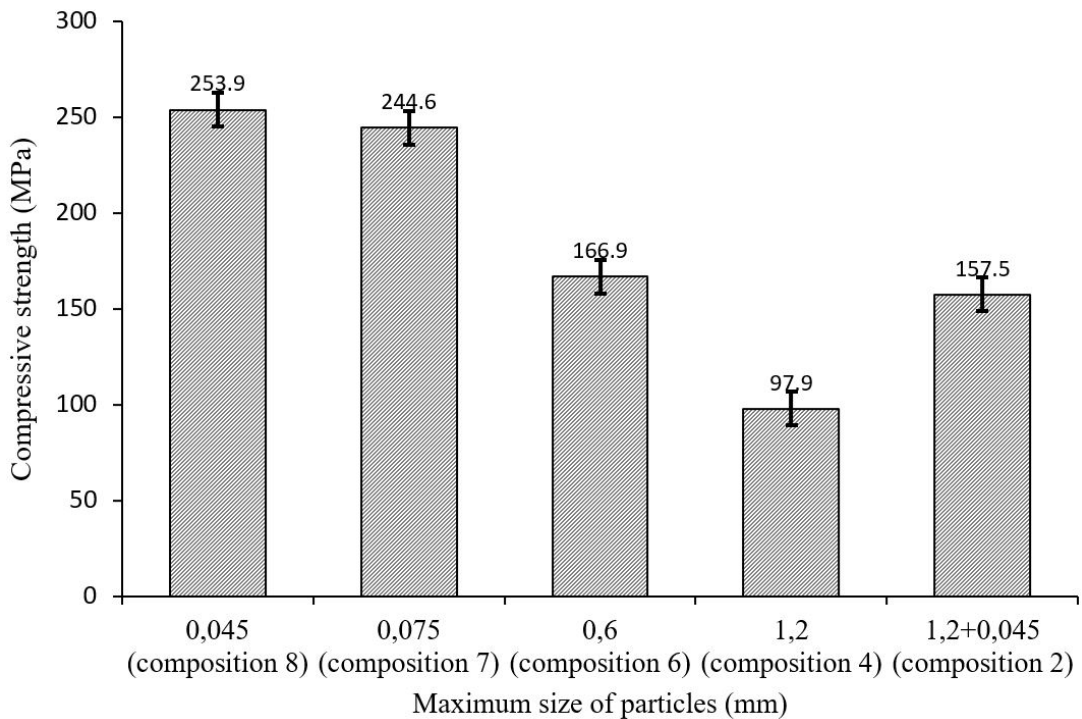


**Figure 4.** Influence of MAS (Maximum aggregate size) of the aggregate in RPC with 0.25 w/c ratio – Phase 1.

Where  $e_M$  is the maximum paste thickness,  $D$  is the maximum size of the aggregate,  $g^*$  is the aggregate packaging density (existing relationships among the volume of solid present in a given unit volume), and  $g$  is the total volume of aggregate used per cubic meter of concrete. In Phase 1, the aggregate packaging density and the total volume was not changed, so the paste thickness of the different compositions was change only by the maximum aggregate size ( $D$ ). The experimental results of this work can be explained by the model proposed by de Larrard and Sedran [16] because the smaller the aggregate grain size, the lower the maximum thickness of the paste. And the more confined is the paste, the higher is the RPC compressive strength. The difference in thickness of the paste of RPC dosed with 0.045 mm aggregate ( $e_M = 0.004416$  mm) is more than 25 times smaller than the paste thickness of RPC dosed with 1.2 mm aggregate ( $e_M = 0.117762$  mm). These 25 times difference resulted in a 156 MPa increase.

Though being known for quite a long time, the maximum thickness reduction of paste has been used to optimize the RPC differently. Several works use quartz sands with a maximum size of 0.5 and 0.6 mm [1], [4], [6], [10], [15], [19], [23], 0.8 and 1.0 mm [17], [22], 3 mm [11], [12], [21] and even 4 mm [3].

After the composition with the higher strength was determined, in phase 2, a study was conducted to assess the effect of nanosilica incorporation in the compressive strength. Differently from the maximum size, nanosilica content did not show significant impact in compressive strength. Table 6 shows a summary of the variance analysis made for phase 2, the probability (value-p) of strengths belonging to one single distribution is superior to 0.05 (5%), that is, the content of chemical admixture with nanosilica did not significantly change the RPC compressive strength. Figure 5 shows the average strengths determined in phase 2. Despite that, other works, like that of Han et al. [14], verified a 10.32% increase in compressive strength while using 5% of titanium dioxide coated with nanosilica particles in one composition of RPC.

**Table 6.** ANOVA Phase 2 – the influence of nanosilica content.

Variation source	<i>SQ</i>	<i>gl</i>	<i>MQ</i>	<i>F</i>	value- <i>P</i>	<i>F critical</i>
Between groups	1225.78	3	408.59	1.01	0.438	4.07
Within groups	3244.44	8	405.56			
Total	4470.22	11				

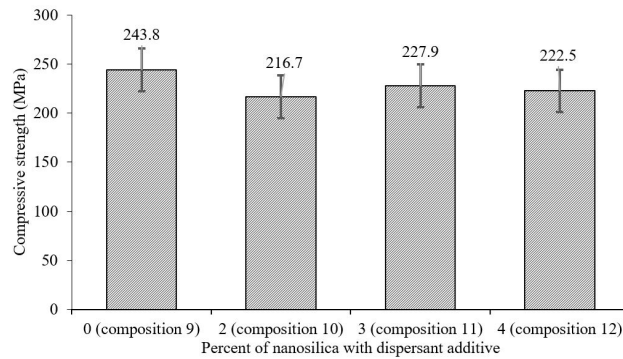


**Figure 5.** Influence of nanosilica content in powder reactive concrete compressive strength – Phase 2.

The objective of phase 3 was to assess the incorporation of inorganic pigments in the RPC. Similar to phase 2, in phase 3, eight composition of phase 1 was used. To improve the concrete aspect, CP V-ARI (HE PC - high early strength Portland cement) was replaced by CP-B-40. The results of phase 3 can lead us to two conclusions. The first is that there is no significant difference across the different pigments studied in the RPC compressive strength. As can be observed in Table 7, the variation across the averages is not significant for 95% confidence (value-p is higher than 0.05). Figure 6 presents the average strengths for compositions of phase 3. The second conclusion is that the pigmented concretes exhibited compressive strength significantly superior to that of the RPC with CPV ARI. The difference in average strength of composition 8 (253.9 MPa) when compared to the composition 13 (310.7 MPa) was 56.8 MPa, which corresponds to a 22% increase in strength. The authors understand that the superior fineness (Table 1) of white cement improved the packaging of particles, as well as the larger surface area of the particle, which provides larger contact surface among particle, favoring the formation of hydration products. Another representative factor that contributed to strength increase was the presence of pigment, composed of highly fine particles. According to Richard and Cheyrezy [1], the increase in granular packaging improves RPC mechanical performance.

Among the different RPC research using natural aggregate, without fibers, those that obtained the highest compressive strengths reached strengths superior or close to 300 MPa [1], [3], [11], [12]. However, to surpass the 300 MPa strength, the authors use pre-densification stress like Yazıcı et al. [11] which get 324 MPa, pre-densification stress with autoclave curing like Aydın et al. [3] which get 325 MPa. Thus, the results presented in phase 3 of this research are relevant due the high strength achieved without any pre-densification or autoclave curing.

**Table 7.** ANOVA Phase 3 – influence of the type of pigment in concrete strength

Variation source	<i>SQ</i>	<i>gl</i>	<i>MQ</i>	<i>F</i>	<i>value-P</i>	<i>F critical</i>
Between groups	1225.78	3	408.59	1.01	0.438	4.07
Within groups	3244.44	8	405.56			
Total	4470.22	11				

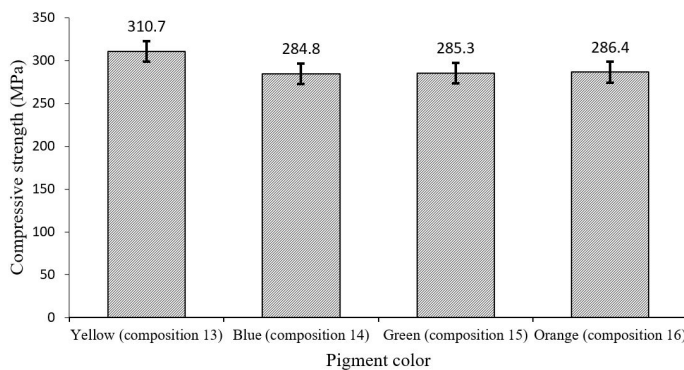


**Figure 6.** Influence of type of pigment in RCP compressive strength – Phase 3.

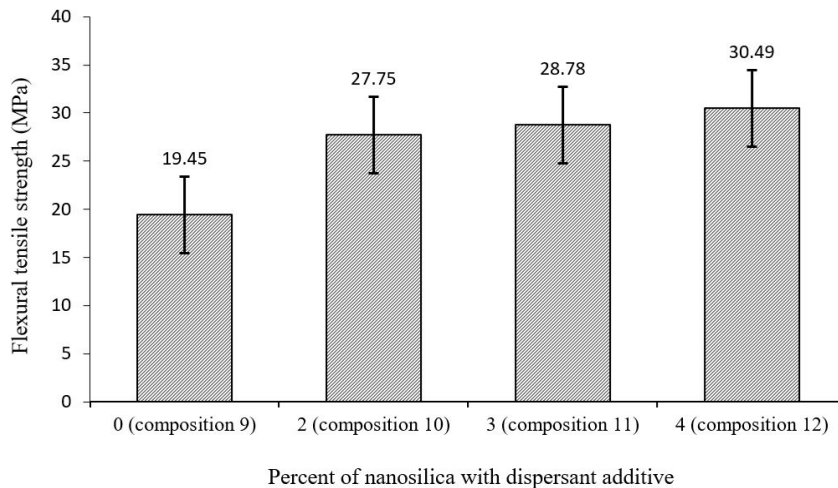
### 3.2 Tensile strength

Figure 7 shows the average values determined for flexural tensile strength. The flexural tensile strength was significantly changed by the incorporation of the superplasticizer containing nanosilica. Table 8 presents a summary of the ANOVA made for phase 2. The probability of having the results determined belonging to one single population is lower than 5% (value-P lower than 0.05).

The difference of composition 9, which does not have nanosilica in its composition, and the other compositions (10; 11; and 12) of phase 2 is outstanding. The presence of nanosilica provided an average increase of 50%. Though there is an increase in flexural tensile strength with an increase in nanosilica content, the difference determined across contents (2%; 3% and 4%) is not significantly different. Han et al. [14] observed an 87% increase in flexural tensile strength at 28 days in RPC with the incorporation of titanium dioxide coated with nanosilica.

**Table 8.** ANOVA Phase 2 – the influence of nanosilica content in concrete tensile strength

<i>Variation source</i>	<i>SQ</i>	<i>gl</i>	<i>MQ</i>	<i>F</i>	<i>value-P</i>	<i>F critical</i>
Between groups	217.09	3	72.36	6.37	0.016272	4.07
Within groups	90.82	8	11.35			
Total	307.91	11				



**Figure 7.** Influence of content of nanosilica in the RPC – Phase 2

### 3.3 Elasticity modulus

For concrete compositions determined in phase 1, the elasticity modulus was also determined. Figure 8 shows the average values for phase 1 compositions' modulus of elasticity. The average elasticity modulus of the different compositions was 44.4 GPa. These results are slightly inferior to those determined by Richard and Cheyrezy [1], who found values from 50 to 60 GPa. However, Vanderlei [2] found similar values (47.3 GPa) analysing RPC without fibers.

The results found in this study demonstrate that the maximum aggregate size did not have a significant influence on the elasticity modulus. Table 9 presents a summary of the variance analysis performed. The probability of having the samples belonging to one single population is superior to 5% (value-p superior to 0.05).

**Table 9.** ANOVA Phase 1 – the influence of the maximum aggregate size in RPC elasticity modulus

<i>Variation source</i>	<i>SQ</i>	<i>gl</i>	<i>MQ</i>	<i>F</i>	<i>value-P</i>	<i>F critical</i>
Between groups	1.77	4	0.44	0.051	0.993	5.19
Within groups	43.37	5	8.67			
Total	45.13	9				

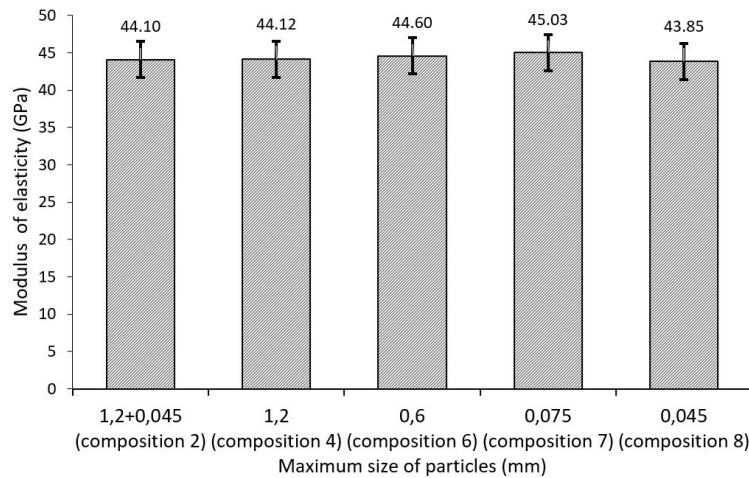


**Figure 8.** Influence of the maximum aggregate size in RPC elasticity modulus– Phase 1.

## 4 CONCLUSIONS

This work aimed at optimizing the mechanical properties of one RPC composition by choosing the aggregate, incorporating nanosilica and inorganic pigments, to maximize the mechanical performance. The main conclusions are described next:

- RCP strength can be significantly increased by reducing the maximum size of the aggregate used. While reducing the maximum size of the aggregate from 1.2 mm to 0.045 mm, the RPC strength increased 156 MPa (61%).
- The maximum size of the aggregate does not significantly change RCP elasticity modulus.
- The addition of nanosilica starting from 2% provided an average increase of 50% in RPC flexural tensile strength. However, a significant change in compressive strength was not observed with the addition of nanosilica.
- The study showed the possibility of producing a colored RPC with compressive strength superior to 300 MPa only with the thermal cure, without the need of pre-densification procedures or even autoclave curing.

As a suggestion for future works, we recommend the study of RPC with different contents of quartz powder to further reduce the maximum thickness of the paste and understand its influence in RPC properties.

## ACKNOWLEDGEMENTS

The authors would like to acknowledge the infrastructure of the Laboratory of Materials and Technology of the Built Environment (LAMTAC/NORIE) of Federal University of Rio Grande do Sul.

## REFERENCES

- P. Richard and M. Cheyrezy, "Composition of reactive power concrete," *Cement Concr. Res.*, vol. 25, no. 7, pp. 1501–1511, 1995, [http://dx.doi.org/10.1016/0008-8846\(95\)00144-2](http://dx.doi.org/10.1016/0008-8846(95)00144-2).
- R. D. Vanderlei, "Análise experimental do concreto de pós reativos: dosagem e propriedades mecânicas," Ph.D. dissertation, Esc. Eng. São Carlos, Univ. São Paulo, São Paulo, 2004.
- S. Aydin, H. Yazici, M. Y. Yardimci, and H. Yigiter, "Effect of aggregate type on mechanical properties of reactive powder concrete," *ACI Mater. J.*, vol. 107, no. 5, pp. 441–449, 2010, <http://dx.doi.org/10.14359/51663963>.
- G. Long, X. Wang, and Y. Xie, "Very-high-performance concrete with ultrafine powders," *Cement Concr. Res.*, vol. 32, no. 1, pp. 601–605, 2001, [http://dx.doi.org/10.1016/S0008-8846\(01\)00732-3](http://dx.doi.org/10.1016/S0008-8846(01)00732-3).
- Z. Yunsheng, S. Wei, L. Sifeng, J. Chujie, and L. Jianzhong, "Preparation of C200 green reactive powder concrete and its static-dynamic behaviors," *Concr. Concr. Compos.*, vol. 30, no. 9, pp. 831–838, 2008, <http://dx.doi.org/10.1016/j.cemconcomp.2008.06.008>.
- M. Jinchuan, O. Zhongwen, Z. Xuxin, L. Jinming, and W. Yahui, "Influence of superabsorbent polymer on shrinkage properties of reactive powder concrete blended with granulated blast furnace slag," *Constr. Build. Mater.*, vol. 146, no. 1, pp. 283–296, 2017, <http://dx.doi.org/10.1016/j.conbuildmat.2017.04.105>.

- [7] W. Kushartomo, I. Bali, and B. Sulaiman, "Mechanical behavior of reactive powder concrete with glass powder substitute," *Procedia Eng.*, vol. 125, no. 1, pp. 617–622, 2015, <http://dx.doi.org/10.1016/j.proeng.2015.11.082>.
- [8] P. Zhu, X. Mao, W. Qu, Z. Li, and Z. J. Ma, "Investigation of using recycled powder waste of clay bricks and cement solids in reactive powder concrete," *Constr. Build. Mater.*, vol. 113, no. 1, pp. 246–254, 2016, <http://dx.doi.org/10.1016/j.conbuildmat.2016.03.040>.
- [9] P. Yanzhou, Z. Jun, L. Jiuyan, K. Jin, and W. Fazhou, "Properties and microstructure of reactive powder concrete having a high content of phosphorous slag powder and silica fume," *Constr. Build. Mater.*, vol. 101, no. 1, pp. 482–487, 2015, <http://dx.doi.org/10.1016/j.conbuildmat.2015.10.046>.
- [10] S. Ahmad, A. Zubair, and M. Maslehuddin, "Effect of key mixture parameters on flow and mechanical properties of reactive powder concrete," *Constr. Build. Mater.*, vol. 99, no. 1, pp. 73–81, 2015., <http://dx.doi.org/10.1016/j.conbuildmat.2015.09.010>.
- [11] H. Yazıcı, H. Yigiter, A. Karabulut, and B. Baradan, "Utilization of fly ash and ground granulated blast furnace slag as an alternative silica source in reactive powder concrete," *Fuel*, vol. 87, no. 1, pp. 2401–2407, 2008., <http://dx.doi.org/10.1016/j.fuel.2008.03.005>.
- [12] H. Yazıcı, M. Y. Yardimci, S. Aydin, and A. S. Karabulut, "Mechanical properties of reactive powder concrete containing mineral admixtures under different curing regimes," *Constr. Build. Mater.*, vol. 23, no. 3, pp. 1223–1231, 2009., <http://dx.doi.org/10.1016/j.conbuildmat.2008.08.003>.
- [13] H. Yiğiter, S. Aydin, H. Yazıcı, and M. Y. Yardimci, "Mechanical performance of low cement reactive powder concrete (LCRPC)," *Compos., Part B Eng.*, vol. 43, no. 8, pp. 2907–2914, 2012., <http://dx.doi.org/10.1016/j.compositesb.2012.07.042>.
- [14] B. Han et al., "Reactive powder concrete reinforced with nano SiO<sub>2</sub>-coated TiO<sub>2</sub>," *Constr. Build. Mater.*, vol. 148, no. 1, pp. 104–112, 2017., <http://dx.doi.org/10.1016/j.conbuildmat.2017.05.065>.
- [15] P. N. Hiremath and S. C. Yaragal, "Influence of mixing method, speed and duration on the fresh and hardened properties of Reactive Powder Concrete," *Constr. Build. Mater.*, vol. 141, no. 1, pp. 271–288, 2017., <http://dx.doi.org/10.1016/j.conbuildmat.2017.03.009>.
- [16] F. de Larrard and T. Sedran, "Optimization of ultra-high-performance concrete by the use of a packing model," *Cement Concr. Res.*, vol. 24, no. 6, pp. 997–1009, 1994., [http://dx.doi.org/10.1016/0008-8846\(94\)90022-1](http://dx.doi.org/10.1016/0008-8846(94)90022-1).
- [17] B. Han et al., "Microstructure related mechanical behaviors of short-cut super-fine stainless wire reinforced reactive powder concrete," *Mater. Des.*, vol. 96, no. 1, pp. 16–26, 2016., <http://dx.doi.org/10.1016/j.matdes.2016.02.004>.
- [18] T. Ji, C. Chen, and Y. Z. Zhuang, "Evaluation method for cracking for cracking resistant behavior of reactive powder concrete," *Constr. Build. Mater.*, vol. 28, no. 1, pp. 45–49, 2012., <http://dx.doi.org/10.1016/j.conbuildmat.2011.08.060>.
- [19] M. Ipek, K. Yilmaz, M. Sümer, and M. Saribiyik, "Effect of pre-setting pressure applied to mechanical behaviors of reactive powder concrete during setting phase," *Constr. Build. Mater.*, vol. 25, no. 1, pp. 61–68, 2011., <http://dx.doi.org/10.1016/j.conbuildmat.2010.06.056>.
- [20] M. Ipek, K. Yilmaz, and M. Uysal, "The effect of pre-setting pressure applied flexural strength and fracture toughness of reactive powder concrete during the setting phase," *Constr. Build. Mater.*, vol. 26, no. 1, pp. 459–465, 2012., <http://dx.doi.org/10.1016/j.conbuildmat.2011.06.045>.
- [21] H. Yazıcı, E. Deniz, and B. Baradan, "The effect of autoclave pressure, temperature and duration time on mechanical properties of reactive powder concrete," *Constr. Build. Mater.*, vol. 42, no. 1, pp. 53–63, 2013., <http://dx.doi.org/10.1016/j.conbuildmat.2013.01.003>.
- [22] D. Mostofinejad, M. R. Nikoo, and S. A. Hosseini, "Determination of optimized mix design and curing conditions of reactive powder concrete (RPC)," *Constr. Build. Mater.*, vol. 123, no. 1, pp. 754–767, 2016., <http://dx.doi.org/10.1016/j.conbuildmat.2016.07.082>.
- [23] T. Zerb, "An analysis of the steam curing and autoclaving process parameters for reactive powder concrete," *Constr. Build. Mater.*, vol. 131, no. 1, pp. 758–766, 2017, <http://dx.doi.org/10.1016/j.conbuildmat.2016.11.026>.
- [24] L. Huynh, S. Foster, H. Valipour, and R. Randall, "High strength and reactive powder concrete columns subjected to impact: Experimental investigation," *Constr. Build. Mater.*, vol. 78, no. 1, pp. 153–171, 2015., <http://dx.doi.org/10.1016/j.conbuildmat.2015.01.026>.
- [25] C. Y. Ni, H. Y. Xia, Q. C. Zhang, W. B. Wang, and Z. H. L. U. Cheng, "Perforation resistance of corrugated metallic sandwich plates filled with reactive powder concrete: experiment and simulation," *Compos. Struct.*, vol. 127, no. 1, pp. 426–435, 2015., <http://dx.doi.org/10.1016/j.compstruct.2015.02.059>.
- [26] V. Matte and M. Moranville, "Durability of reactive powder composites: influence of silica fume on the leaching properties of very low water/binder pastes," *Cement Concr. Compos.*, vol. 21, no. 1, pp. 1–9, 1999., [http://dx.doi.org/10.1016/S0958-9465\(98\)00025-0](http://dx.doi.org/10.1016/S0958-9465(98)00025-0).
- [27] Associação Brasileira de Normas Técnicas, NM 43, 2002.
- [28] Associação Brasileira de Normas Técnicas, NBR 7681, 2013.
- [29] American Society for Testing and Materials, ASTM C939, 2002.

- [30] S. Formagini, “Dosagem científica e caracterização mecânica de concretos de altíssimo desempenho,” Ph.D. dissertation, Rio de Janeiro, Univ. Fed. Rio de Janeiro, 2005.

---

**Author contributions:** Contribution description of each co-author for the study. Denise Dal Molin: conceptualization, funding acquisition, supervision, writing; Abrahão Bernardo Rohden: conceptualization, data curation, formal analysis, methodology, writing; Ana Paula Kirchheim: data curation, formal analysis.

**Editors:** Bernardo Tutikian, José Luiz Antunes de Oliveira e Sousa, Guilherme Aris Parsekian.



## ORIGINAL ARTICLE

# Ultrasonic investigation on the effectiveness of crack repair in concrete

## *Investigação ultrassônica da eficácia do reparo de fissuras no concreto*

Fabio Caon de Souza<sup>a</sup> Roberto Caldas de Andrade Pinto<sup>a</sup> <sup>a</sup>Universidade Federal de Santa Catarina – UFSC, Departamento de Engenharia Civil, Florianópolis, SC, Brasil

Received 20 December 2018

Accepted 17 February 2020

**Abstract:** The crack injection technique using epoxy systems is usually performed in the services of rehabilitation of surface cracks in concrete structures. The evaluation of the injection process can be done by the removal of cores, which is a destructive test not able to evaluate the entire structure. Alternatively, the use of nondestructive testing, specifically those based on the propagation of stress waves can provide information on the effectiveness of injection services. Even though the time-of-flight technique which provides the ultrasonic pulse velocity is the most common parameter used in concrete evaluation, the ultrasound waveform energy-related parameters can be used to indicate if crack was fully filled. The energy of the ultrasound signal depends on the propagated travel path, which differs when the crack is not filled. This paper presents the results of an experimental program with artificial surface cracks filled with epoxy in different depth fractions. Two types of epoxy were used. It was observed that the ultrasound waveform energy-parameters were able to detect repair effectiveness.

**Keywords:** ultrasound, nondestructive methods, energy related parameters, crack repair.

**Resumo:** Os serviços de reabilitação de fissuras superficiais em estruturas de concreto são normalmente realizados com a técnica de injeção utilizando sistemas epóxi. A avaliação do processo de injeção pode ser feita pela retirada de testemunhos, considerado um teste destrutivo, que não é capaz de avaliar a estrutura com completo. Alternativamente, a utilização de ensaios não destrutivos, especificamente os baseados na propagação de ondas de tensão podem fornecer informações sobre a eficácia dos serviços de injeção. Embora a utilização do tempo de propagação de uma onda ultrassônica, que fornece a velocidade do pulso ultrassônico, seja o parâmetro mais comumente utilizado na avaliação de estruturas de concreto, os parâmetros relacionados à energia da onda de ultrassom podem ser usados para indicar se a fissura foi totalmente preenchida. A energia do sinal de ultrassom depende do caminho de percurso propagado, que difere quando a fissura não está completamente preenchida. Este artigo apresenta os resultados de um programa experimental com fissuras superficiais induzidas preenchidas com epóxi em diferentes frações de profundidade. Dois tipos de epóxi foram usados. Observou-se que os parâmetros de energia da onda de ultrassom foram capazes de detectar a eficácia do reparo.

**Palavras-chave:** ultrassom, métodos não destrutivos, parâmetros de energia ultrassônica, reparo de fissuras.

**How to cite:** F. C. Souza and R. C. A. Pinto, "Ultrasonic investigation on the effectiveness of crack repair in concrete," *Rev. IBRACON Estrut. Mater.*, vol. 13, no. 5, e13508, 2020, <https://doi.org/10.1590/S1983-41952020000500008>

## 1 INTRODUCTION

Cracks often occurs in concrete structures because of tensile stresses as well as some degradation mechanisms such as repeated loading, chemical attacks, drying shrinkage, among others. While surface opening cracks affect the aesthetics of the concrete surface, they may also compromise the durability and safety of the structure. In such latter case, there is a need to restore structure integrity.

**Corresponding author:** Fabio Caon de Souza. E-mail: [fabiocaondesouza@gmail.com](mailto:fabiocaondesouza@gmail.com)

**Financial support:** CNPq 133928/2016-0.

**Conflict of interest:** Nothing to declare.



This is an Open Access article distributed under the terms of the Creative Commons Attribution License, which permits unrestricted use, distribution, and reproduction in any medium, provided the original work is properly cited.

A successful crack repair procedure should account for its cause and geometric characteristics [1]. For example, when injection of synthetic resins is used as repair procedure, the correct application and selection of pump pressure depend on the crack width and depth. The main purpose of this repair method is to completely fill the crack, and thus to connect structurally the concrete on both sides of the crack opening [2].

The bond between concrete and the injection material is overly critical. A suitable bond should restore the original stiffness of the material and prevent penetration of water and degrading agents [3].

The effectiveness of the repair can be assessed by taking cores, which is not always able to analyze the complete structure, since it is not used in large scale. Alternatively, the use of a non-destructive test that verifies crack filling ensures efficiency and quality of the rehabilitation technique.

Nondestructive testing (NDTs) can provide support in making decisions for the diagnosis of a structure. According to Hellier [4], NDTs have experienced significant growth in innovation over the last 25 years, playing an important role in minimizing damages in concrete structures.

Quality control, structural evaluation, maintenance and increasing service life have become important issues in the construction industry in recent years. Nondestructive testing has become increasingly essential for the assessment of the integrity of concrete structures [5].

The use of stress wave propagation methods such as ultrasound allows one to indirectly evaluate the cracking process in a convenient and fast approach. The analysis of variations in the ultrasound pulse velocity (UPV) has been successfully applied in the inspection of concrete structures [6]. There are several examples of such technique in the detection and visualization of non-uniformities within the concrete member [7] and in the estimation of depth of surface opening cracks [8] among other applications.

Using the indirect method of transmission, the travel path of an ultrasonic pulse suffers deviation in the presence of surface opening cracks, leading to larger time-of-flight and thus smaller apparent pulse velocities as compared to a travel path in a sound material [6].

The reflection coefficient of a normal incident stress wave on an interface of different materials can be described by the difference of the acoustic impedance of the materials, as expressed by Equation 1 [9].

$$R = \frac{Z_2 - Z_1}{Z_2 + Z_1} \quad (1)$$

Where  $R$  is the reflection coefficient for normal incidence,  $Z_2$  and  $Z_1$  are the acoustic impedances of materials 2 and 1, respectively. According to Krautkrämer and Krautkrämer [10], the acoustic impedance of air is  $413 \text{ kg/m}^2\cdot\text{s}$ , much lower than the value for concrete  $6.9$  to  $10.4 \times 10^6 \text{ kg/m}^2\cdot\text{s}$  [11]. Therefore, there is no transmission through an air-filled crack, with smaller values of UPV recorded.

However, in the study carried out by Carelli [12] for plastic shrinkage cracking, it was found that the ultrasonic pulse velocity sensitivity is significantly lower than those of the other waveform parameters such as amplitude and energy. This finding indicates the importance of signal behavior analysis for a more accurate and efficient evaluation of the cracking condition of the element. It is well recognized that cracking leads to an attenuation of the ultrasonic signal [13]–[15].

When an ultrasonic stress wave collides with an interface formed by materials with different acoustic properties, a portion of the wave energy is dispersed out of the original path while another part undergoes refraction. This results in the reduction of the energy of the scattered waves as they travel through any material [10].

When a surface crack is partially filled due to different acoustic parameters of epoxy and concrete, there is a loss of transmitted energy due to wave reflection in the interface of both materials. However, since there is also refraction in that interface, a portion of the stress wave maintains its travel path, and thus the time-of-flight between transducers positioned on either side of the crack tip would not change significantly. Consequently, this probable reduction on the wave energy would be detected by possible variation on the UPV.

Aggelis et al. [16] found that the increase in epoxy filling percentage in concrete cracks generates an increase in the signal amplitude value. The waveform amplitude showed greater sensitivity to subsurface cracks as compared to UPV, according to Aggelis et al. [17].

This paper presents the results of an experimental program with artificial surface cracks of various depths filled with epoxy in different depth fractions. Two types of epoxy were used. It was observed that the ultrasound waveform energy parameters were able to verify repair effectiveness. There was an observed increase in the waveform amplitude and energy with increasing crack filling.

### 1.1 Ultrasonic waveform parameters

Figure 1 shows a typically ultrasonic waveform in a concrete specimen.

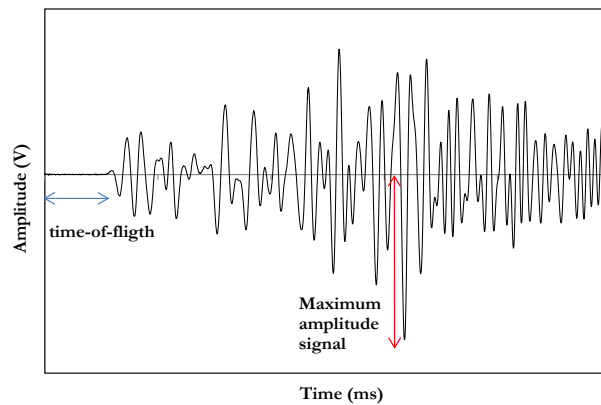


**Figure 1.** Typical waveform

The time-of-flight parameter is the time observed from the initial stress wave propagation until it reaches the receiving transducer, which would yield the UPV; the maximum amplitude and the waveform energy can also be gathered by the waveform.

When ultrasound is being used to evaluate a concrete structure, it is common to use the ultrasound pulse velocity (UPV) to assess the concrete structure. UPV is related to the time-of-flight between two transducers placed at a known distance. Thus, there is no need to obtain information about the whole waveform.

The maximum amplitude is recorded as the maximum value of the amplitude of the waveform, regardless when it occurred, and therefore represents only a discrete point of the whole signal. The energy of the waveform, on the other hand, accounts for the whole amplitude signal. It can be calculated from the rectified amplitude signal (with absolute amplitude values) according to Equation 2 [15], [18].

$$E = \int_0^{t_i} |A(t)| dt \tag{2}$$

where:

$A(t)$  – signal amplitude in time  $t$ ;

$t_i$  – end of time window fixed in the experiments.

The ultrasonic waveform parameters used in this study were the time-of-flight, the maximum amplitude and total energy. The total energy was calculated from Equation 2 considering the acquired signal up to 5000  $\mu$ s. This upper limit value was chosen since there were no observed signal amplitude variations for times greater than 5000  $\mu$ s.

## 2 MATERIALS AND EXPERIMENTAL PROGRAM

Nine concrete prisms with artificially induced surface cracks of different depths and thicknesses were cast. The cracks were repaired in two stages with two types of epoxy. Initially, the crack was partially filled with epoxy, later they were completely filled.

Two series of concrete prisms with artificially induced surface cracks of different depths and thicknesses were cast. Prisms geometry was defined to allow ultrasound estimation of actual crack depth according to a method previously defined [8]. Therefore, prism length was fixed at 800 mm; the width value was fixed at 200 mm and the height was fixed at 150 mm, except in cases of crack depths of 150 and 220 mm, in which prism height was 300 mm. Series 1 consisted of 4 prisms of 200 x 150 x 800 mm with vertical cracks of 25, 50, 75, and 100 mm of depth, and two concrete prisms of 150 x 300 x 800 mm with vertical cracks of 150 mm and 220 mm. All these six prisms had crack widths of 6 mm. The second series comprised of concrete prisms of 200 x 150 x 800 mm with vertical cracks of 50, 75 and 100 mm and crack width of 20 mm. Table 1 presents a summary of the geometric characteristics of all the specimens.

**Table 1.** Specimens geometry

Specimen	Size (width x height x length) in mm	Crack depth (mm)	Crack width (mm)	Epoxy	
Series 1	S1-25-3	250 x 150 x 800	25	3	A
	S1-50-3	250 x 150 x 800	50	3	A
	S1-75-3	250 x 150 x 800	75	3	A
	S1-100-3	250 x 150 x 800	100	3	A
	S1-150-3	150 x 300 x 800	150	3	A
	S1-220-3	150 x 300 x 800	220	3	A
Series 2	S2-50-20	250 x 150 x 800	50	20	B
	S2-75-20	250 x 150 x 800	75	20	B
	S2-100-20	250 x 150 x 800	100	20	B

All cracks were artificially made. During casting, a plate with the specified thickness was placed on the side of the specimen. At approximately six hours after casting, the plate was removed, and the artificial crack formed. Before performing ultrasound measurements, the specimen was rotated 90°. Thus, ultrasound measurements were performed on a flat and smooth surface with any line of testing perpendicular to the crack being at the same level of consolidation.

A Brazilian composite cement with pozzolan addition up to 14% in mass, ASTM C 33 natural fine aggregate and coarse aggregate with maximum aggregate size of 19 mm were used. Concrete compressive strength was evaluated after 28 days. The results indicated a compressive strength of 20 MPa.

The ultrasound measurements were performed with a commercially available equipment using 54 kHz central frequency p-wave transducers with an acquisition frequency of 2 MHz. A coupling agent was previously applied to the concrete surface on which the 50 mm diameter transducers would be placed.

After 28 days of casting, ultrasound time-of-flight was used to estimate the actual crack depth. The procedure presented by Pinto et al. [8], called Method A was used. In this method, as shown in Figure 2, the transducers are placed in at least four equidistant locations from the surface opening crack along a chosen line ( $x_1$  to  $x_4$ ).

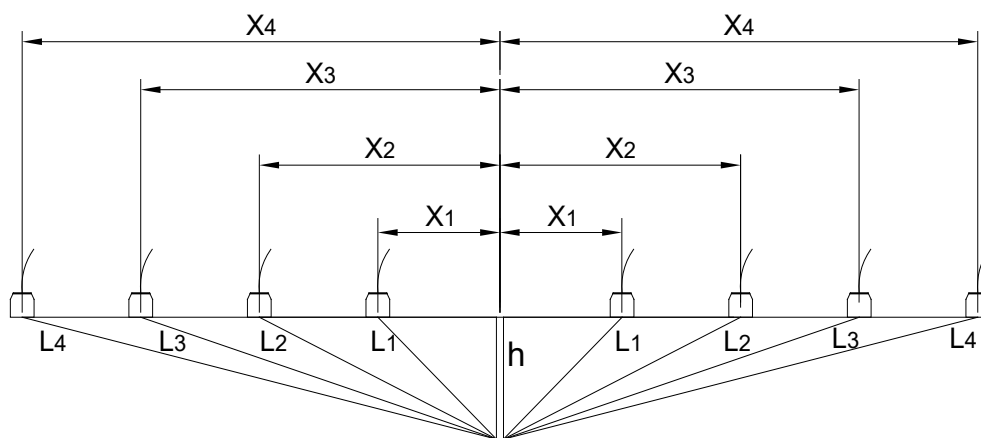


**Figure 2.** Transducer arrangements for graphically-based Method A [8]

Time-of-flight readings are performed at each transducer arrangement. The crack penetration depth,  $h$ , is obtained by plotting the square of the distance between the transducers to the crack with the square of the time recorded. The slope of the best straight line is proportional to the UPV while its intersection is proportional to the crack depth. Table 2 presents crack penetration depth estimates obtained from Method A [8]. The highest error was below 6%, which is below the 15% error reported by Bungey and Grantham [6].

**Table 2.** Estimated crack depths by Method A [8]

Specimen	Crack depth (mm)	Estimated crack depth (mm)	Error (%)
S1-25-3	25	24.4	4.0
S1-50-3	50	49.2	2.0
S1-75-3	75	72.1	4.0
S1-100-3*	100	-	-
S1-150-3	150	144.6	3.7
S1-220-3	220	207.7	5.9
S2-50-20	50	49.0	2.0
S2-75-20	75	74.0	1.3
S2-100-20	100	106.1	5.8

\* specimen broke during test

The resin application was carried out in two stages, as shown in Figures 3 and 4. The first application was performed on the crack surface to simulate partial filling, as can be seen in Figure 3.

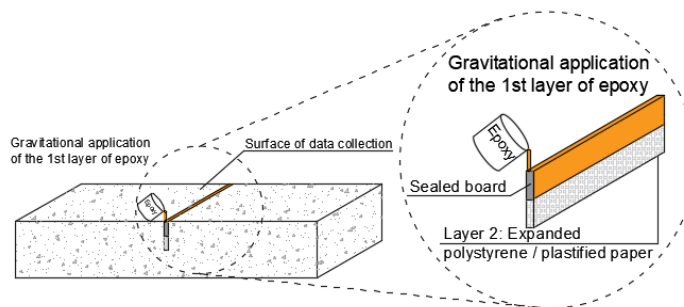


**Figure 3.** 1<sup>st</sup> stage of resin application

The cracks were filled with epoxy by gravity. Expanded polystyrene and plasticized paper were used to prevent epoxy penetration for prisms with crack width of 20 mm and 3 mm, respectively. To prevent leakage, the edges of the prisms were sealed. The procedure for preparing the resins followed the manufacturer's recommendations with curing time between each application of 7 days.

In the first stage, after cleaning the crack with compressive air, expanded polystyrene or plasticized paper layer was applied along with sealing of the edges of the prisms to ensure that the resin would partially fill the crack, as can be seen in Figure 3. After a curing period of 7 days, ultrasound measurements were taken with transducers placed on opposite sides of the crack at 100 mm. A mass of 8.55 kg was placed on the top of the 50 mm diameter transducers, and consequently a constant pressure of 0.047 MPa was applied on the transducers when the waveforms were acquired.

Then, epoxy was applied to complete filling the cracks, as can be seen in Figure 4.

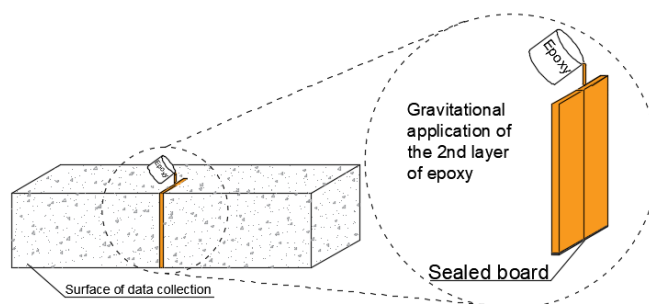


**Figure 4.** 2<sup>nd</sup> stage of resin application

After 7 days, new ultrasound measurements were performed with transducers again placed at 100 mm from the crack tip. Figure 5 shows both stage of resin application.

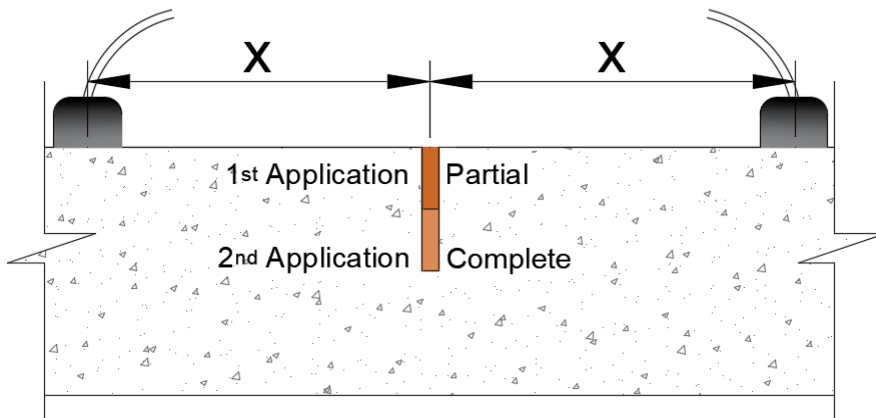


Figure 5. Stages of application of epoxy repair

Two different types of epoxy were chosen. A low-viscosity epoxy, called Epoxi A, was used for prisms of Series 1 with crack width of 3 mm; while a medium-viscosity epoxy, called Epoxi B, was used for prisms of Series 2 with crack width of 20 mm. Concrete and epoxy acoustic characteristics are presented in Table 3.

Table 3. Concrete and epoxy acoustic characteristics.

Material	density (kg/m <sup>3</sup> )	UPV (m/s)	Acoustic impedance (kg/m <sup>2</sup> ·s)
Concrete	2340	4070	9.52 10 <sup>6</sup>
Epoxy A	1100	2513	2.76 10 <sup>6</sup>
Epoxy B	1710	2808	4.80 10 <sup>6</sup>

#### 4 RESULTS AND DISCUSSIONS

Figure 6 presents the waveforms obtained from ultrasound readings for S1-150-3 specimen with unrepaired, partially repaired and fully repaired crack. Figure 6 relates the transmission time with the percentage of the input voltage (500 V).

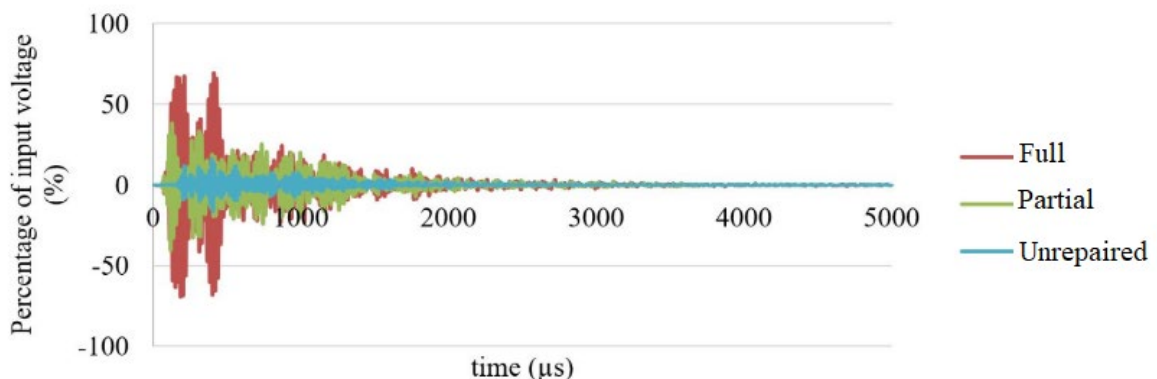


Figure 6. Waveforms from specimen S1-150-3

The signals were superimposed so that each color represents the stage of application of the epoxy. Similar waveforms were obtained from other readings.

There was an observed increase in the amplitudes as the crack was being repaired. From each waveform, time-of-flight, maximum signal amplitude and the total accumulated energy defined as the propagation energy up to 5000  $\mu$ s were recorded. Figures 7 to 9 present the obtained values for all specimens.

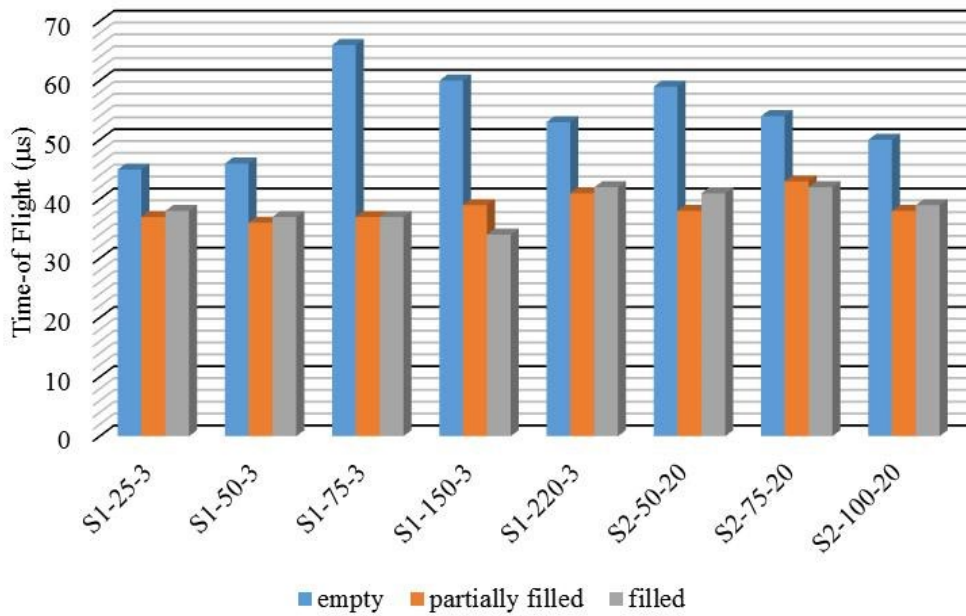


Figure 7. Time-of-flight between transducers 200 mm apart

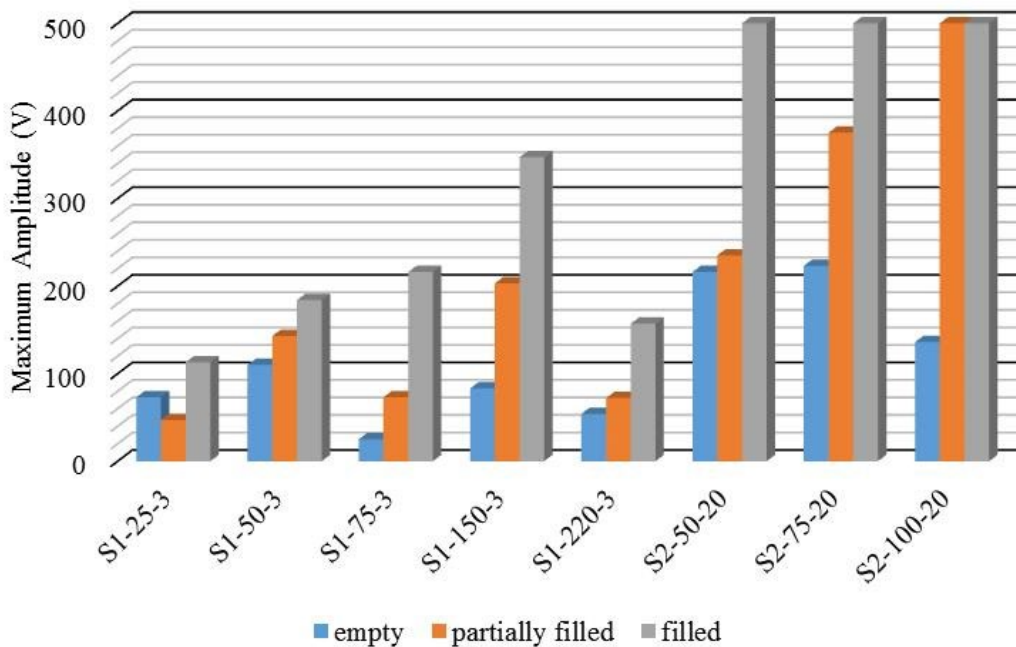


Figure 8. Maximum amplitude values

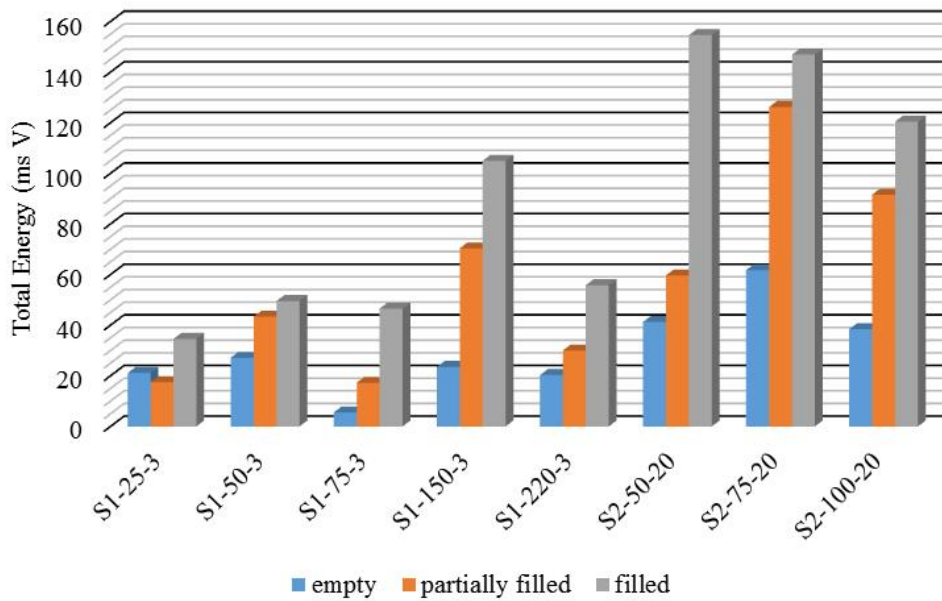


Figure 9. Total energy values

Figure 7 shows that there was not a significant difference between the time of flight when the crack was partially filled or completely filled, and therefore no significant changes on the UPV was recorded. As can be seen in Figure 7, the difference between time-of-flight values for the partially filled and completely filled specimens did not vary more than 3  $\mu$ s, with absolute values ranging from 34  $\mu$ s to 43  $\mu$ s. However, much higher differences were observed among an empty crack specimen and when the crack was partially or fully filled. For instance, the time-of-flight recorded for specimen S1-75-3 was 66  $\mu$ s when the crack was empty and 37  $\mu$ s when it was partially and fully filled. This difference occurred because in the indirect transmission method, even some internal non-homogeneity (such as voids from below the partially filled crack) does not alter the wave propagation path and therefore a decrease in time-of-flight should occur when the crack is partially or fully filled.

On the other hand, as shown in Figures 8 and 9, the waveform parameters, maximum amplitude, and total energy, were sensitive to partial filling. For all specimens, except S1-25-3, there was an increase of energy and amplitude values according to the filling percentage of the crack. A previous research has shown that for small cracks, around 25 mm in depth, the use of ultrasonic pulse velocity was not able to accurately predict crack depth sizes [19].

In few cases, the maximum amplitude values reached the maximum value of 500 V before total filling of the crack (specimen S2-150-20). Therefore, this energy-related parameter may not be suitable to identify effectiveness of crack repair in any situation.

The best waveform parameter seems to be the total energy, as can be seen in Figure 9. The total energy up to 5000  $\mu$ s was able to identify partial filling for all specimens. In all specimens, except S1-25-3 as already discussed, the total energy values for the partially filled specimens were between the values recorded when the crack was empty and when it was completely filled with epoxy. Such an observed increase in total energy as the crack was being filled is due to the higher acoustic impedance of epoxy as compared to air. According to Equation 1, one could conclude that when the crack is being filled with epoxy, less wave reflections at the interface occurs, and therefore higher wave amplitudes arrive at the receiver transducer. Therefore, the total energy should be increase.

From the above discussion, it can be noticed that only relying on the time-of-flight would not guarantee to verify the effectiveness of crack filling. The time-of-flight parameter is an indeed good estimator of crack depth, but to verify if a crack repair service was fully effective, it is recommended that the ultrasonic waveform is acquired.

The ultrasonic waveform indicates changes in the stress wave due reflection and refraction that occurs in any interface of materials with different acoustic properties. For the prisms tested here, an interface of concrete-epoxy would alter the waveform but not the time-of-flight. Wave refraction occurs allowing to maintain a travel path given by the distance between transducers. Thus, by relying solely on time-of-flight, or UPV, one would not be able to detect if a

surface crack was fully filled. However, by analyzing the whole waveform and its energy-related parameters such as amplitude and total energy, changes in crack filling percentages can be detected.

## 5 CONCLUSIONS

The aim of this work was to analyze the sensitivity of the parameters associated to the ultrasonic signal in the evaluation of the integrity of the epoxy system filling in surface crack openings in concrete structures.

After epoxy has been applied to repair the artificially induced cracks, it was verified that the time-of-flight was not a sensitive parameter for different filling percentages, since there was not an observed change when the crack was partially or fully filled.

On the other hand, the total energy and maximum amplitude of the signal were shown to be sensitive parameters for prisms with crack depths greater than 25 mm. As the filling increased, the higher their values were in the signal.

In summary, the parameters of maximum amplitude and total energy of ultrasonic waveform obtained from transducers placed at 100 mm distance of the crack tip were able to detect partial filling of cracks greater than 25 mm.

## ACKNOWLEDGEMENTS

The authors would like to acknowledge CNPq (National Council for Scientific and Technological Development) for financial assistance; to company Pedrita for the supply of aggregates and to GPEND/LEE/UFSC where the research was developed.

## REFERENCES

- [1] American Concrete Institute. ACI Committee 224, *Causes, Evaluation, and Repair of Cracks in Concrete Structures*, ACI 224.1R-07, 2007.
- [2] American Concrete Institute. *Crack Repair by Gravity Feed with Resin*, ACI E706, ACI RAP-2, 2009.
- [3] K. Minoru, K. Toshiro, U. Yuichi, and R. Keitetsu, "Evaluation of bond properties in concrete repair materials," *J. Mater. Civ. Eng.*, vol. 13, no. 2, pp. 98–105, 2001.
- [4] C. Hellier, *Handbook of On-destructive Evaluation*, 2nd ed. New York, NY, USA: McGraw-Hill Education, 2012, , pp. 7.11–7.12.
- [5] G. Karaiskos, A. Deraemaeker, D. G. Aggelis, and D. V. Hemelrijck, "Monitoring of concrete structures using the ultrasonic pulse velocity method," *Smart Mater. Struct.*, vol. 24, no. 11, pp. 113001, 2015.
- [6] J. H. Bungey and M. G. Grantham, *Testing of Concrete in Structures*, 4th ed. London: Blackie Academic & Professional, 2006, 339 p.
- [7] L. P. Perlin and R. C. A. Pinto, "Ultrasonic tomography in concrete," *Ibracon Struct. Mater. J.*, vol. 6, no. 2, pp. 246–269, 2013.
- [8] R. C. A. Pinto, A. Medeiros, I. J. Padaratz, and P. B. Andrade, "Use of ultrasound to estimate depth of surface opening cracks in concrete structures," *E-J. Nondestruct. Test. Ultrason.*, pp. 1–11, 2010.
- [9] L. E. Kinsler, A. R. Frey, A. B. Coppens, and J. V. Sanders, *Fundamentals of Acoustics*, 4th ed. New York: John Wiley & Sons, 2000.
- [10] J. Krautkrämer and H. Krautkrämer, *Ultrasonic Testing of Materials*, 4th ed. Berlin: Springer-Verlog, 1990.
- [11] N. J. Carino, "Stress wave propagation methods," in *Handbook on Nondestructive Testing of Concrete*, 2nd ed., V. M. Malhotra and N. J. Carino, Ed., Boca Raton: CRC Press, 2004.
- [12] J. M. Carelli, "Análise do comportamento de ondas ultrassônicas em elementos fissurados de concreto e argamassa," M.S. thesis, Univ. Fed. Santa Catarina, Florianópolis, 2014.
- [13] W. Suaris and V. Fernando, "Detection of crack growth in concrete from ultrasonic intensity measurements," *Mater. Struct.*, vol. 20, no. 3, pp. 214–220, 1987.
- [14] S. F. Selleck, E. N. Landis, M. L. Peterson, S. P. Shah, and J. D. Achenbach, "J. D., "Ultrasonic investigation of concrete with distributed damage," *ACI Mater. J.*, vol. 95, no. 1, pp. 27–36, 1998.
- [15] T. Shiotani and D. G. Aggelis, "Wave propagation in cementitious material containing artificial distributed damage," *Mater. Struct.*, vol. 42, no. 3, pp. 377–384, 2009.
- [16] D. G. Aggelis, T. Shiotani, and D. Polyzos, "Characterization of surface crack depth and repair evaluation using Rayleigh waves," *Cement Concr. Compos.*, vol. 31, no. 1, pp. 77–83, 2009.
- [17] D. G. Aggelis, E. Leonidou, and T. E. Matikas, "Subsurface crack determination by one-sided ultrasonic measurements," *Cement Concr. Compos.*, vol. 34, no. 2, pp. 140–146, 2012.

- [18] A. V. Hauwert, F. Delannay, and J. F. Thimus, "Cracking behavior of steel fiber reinforced concrete revealed by means of acoustic emission and ultrasonic wave propagation," *ACI Mater. J.*, vol. 96, no. 3, pp. 291–296, 1999.
- [19] P. B. Andrade, "Estimativa da profundidade de fendas no concreto através da utilização do ultrassom e do eco-impacto," M.S. thesis, Univ. Fed. Santa Catarina, Florianópolis, 2010.

---

**Author contributions:** FCS: conceptualization, methodology, data evaluation, writing; RCAP: supervision, writing.

**Editors:** Vladimir Guilherme Haach, José Luiz Antunes de Oliveira e Sousa, Guilherme Aris Parsekian.



ORIGINAL ARTICLE

# Structure and nanomechanical characterization of synthetic calcium-silicate-hydrate with poly-methacrylic acid

*Caracterização nanomecânica e estrutural do silicato de cálcio hidratado sintetizado com poli(ácido metacrílico)*

Fernando Pelisser<sup>a</sup> Philippe Jean Paul Gleize<sup>a</sup> Alexandre Mikowski<sup>b</sup> <sup>a</sup>Universidade Federal de Santa Catarina – UFSC, Departamento de Engenharia Civil, Florianópolis, SC, Brasil<sup>b</sup>Universidade Federal de Santa Catarina – UFSC, Centro de Engenharia da Mobilidade, Joinville, SC, Brasil

Received 29 November 2018

Accepted 20 February 2020

**Abstract:** The principal phase of hardened Portland cement pastes is calcium silicate hydrate (C-S-H), which influences the physical and mechanical properties of construction materials. In this work, calcium silicate hydrate (C-S-H) was synthesized, with the addition of poly-methacrylic acid with sodium (PMA), for the development of C-S-H/ polymer nanocomposites. Among the polymers available, PMA is indicated in the literature as one of those viable for producing C-S-H/polymer complexes. However, no consensus exists regarding the type of interaction this produces. The resulting compounds were characterized by XRD, FT-IR, TGA, carbon content (CHN), TEM, SEM and elastic modulus and hardness were measured by instrumented indentation. A significant change was verified in the nanomechanical properties of C-S-H with PMA, resulting in reduction in the elastic modulus and hardness. The set of results presented do not confirm the intercalation of PMA in the interlayer space of C-S-H, but presented evidence of the potential for intercalation, since changes in the microstructure clearly occurred.

**Keywords:** calcium silicate hydrate, poly-methacrylic acid, nanocomposites, nanoindentation.

**Resumo:** A principal fase do cimento Portland endurecido é o silicato de cálcio hidratado (C-S-H), que influencia as propriedades físicas e mecânicas dos materiais de construção. Nesta pesquisa, silicato de cálcio hidratado (C-S-H) foi sintetizado, com adição de poli(ácido metacrílico) com sódio (PMA), para o desenvolvimento de nanocompósitos C-S-H/polímero. Entre os polímeros disponíveis, o PMA é indicado na literatura como um daqueles viáveis para a produção de nanocompósitos C-S-H/polímero. No entanto, não existe consenso sobre o tipo de interação que pode ocorrer. Os compostos foram caracterizados por DRX, FT-IR, TGA, teor de carbono (CHN), MET, MEV e módulo de elasticidade e a dureza foi medida por nanoindentação instrumentada. Foi verificada uma mudança significativa nas propriedades nanomecânicas do C-S-H com PMA, resultando na redução do módulo de elasticidade e dureza. O conjunto de resultados apresentados não confirma a intercalação do PMA na nanoestrutura do C-S-H, mas mostrou evidências do potencial de intercalação, uma vez que mudanças significativas foram verificadas na microestrutura.

**Palavras-chave:** silicato de cálcio hidratado, poli(ácido metacrílico), nanocompositos, nanoindentação.

**How to cite:** F. Pelisser, P. J. P. Gleize, and A. Mikowski. “Structure and nanomechanical characterization of synthetic calcium-silicate-hydrate with poly-methacrylic acid”, *Rev. IBRACON Estrut. Mater.*, vol. 13, no. 5, e13509, 2020, <https://doi.org/10.1590/S1983-41952020000500009>

## 1. INTRODUCTION

It is well known that calcium silicate hydrate (C-S-H), the main product from Portland cement hydration, has a significant influence on most physical and mechanical properties of cement-based materials. C-S-H is considered a lamellar, crystalline semi-continuum and an inherently complex material, particularly in relation to its “bond” nature forces - ionocovalent forces between individual C-S-H layers or C-S-H layer stacks, separated by strongly localized calcium ions and water molecules.

Corresponding author: Fernando Pelisser. E-mail: [f.pelisser@ufsc.br](mailto:f.pelisser@ufsc.br)

Financial support: This work was financed by CNPq (National Council of Technological and Scientific Development) - 304589/2019-5.

Conflict of interest: Nothing to declare.



This is an Open Access article distributed under the terms of the Creative Commons Attribution License, which permits unrestricted use, distribution, and reproduction in any medium, provided the original work is properly cited.

It consists of order-disorder lamellae stacking of particles, where each lamellae is formed by stacking sheets and each sheet has a central Ca-O sheet that has silicate chains on both sides, which are kinked with a periodicity of three tetrahedral. These chains are called dreierketten [1] and indicate the degree of polymerization of C-S-H. Its structure interferes with the interplanar distance, density [2] and the mechanical behavior of hydrated calcium silicate [3], [4]. C-S-H is similar to the tobermorite-jennite like nanostructure crystal [1], with a complex structure; it is intrinsically fragile with a low flexural strength [5]. The complex nanostructure of C-S-H makes it an excellent candidate for the manipulation and control of its properties, through the intercalation of organic molecules, for the fabrication of C-S-H/polymer nanocomposites [6]. The advancement of nanoscience through the development of C-S-H/nanocomposites is important for the production of materials that are more efficient in relation to the binding forces [7]–[9], thus improving the tensile strength and avoiding the cracking problems inherent to concrete and mortar, which are widely used by the construction industry. Nature has shown that the mixture of organic and inorganic materials is a potential route for the elaboration of more efficient materials; teeth and bones are good examples.

C-S-H/polymer nanocomposites have been successfully synthesized [10]–[19]. Observation of an increase in the interlamellar spacing has been reported, which is explained by the intercalation of polymers between the sheets of C-S-H. Studies have also concluded that polymer intercalation depends on the C-S-H Ca/Si molar ratio, the method of synthesis and the type of organic polymers. Among the polymers tested, anionic polymers were one of the most successful at producing C-S-H/polymer nanocomposites [12], [14], [15], for example poly(acrylic acid) and poly-methacrylic acid. A study [17] has provided evidence for the adsorption and intercalation of polyethylene glycol (PEG) polymers on the surface and within the interlayer spaces of the C-S-H structure (altering the interlayer spacing from 1.5 nm to 4.5 nm). It has also been reported that the presence of PDC in 0.8 Ca/Si C-S-H affects both its nano and mesostructure: the broadening and slight shift in the 002 basal reflections (XRD) and the alteration in C-S-H Si-O-Si bonding (FT-IR) indicate that a part of the PDC is intercalated between the C-S-H lamellae, and; the remaining PDC is probably adsorbed on the surface or in the void space left by the C-S-H particles, affecting its packing density, consequently, significant alterations in the mechanical properties of C-S-H in the presence of PDC were verified [18]. Research evaluating the effect of PVA polymer verified modifications in the interlayer spacing of the C-S-H, such that it increased between 1.53 nm and 1.70 nm, and significant change in the nanomechanical properties of C-S-H occurred in the presence of PVA, resulting in a strong reduction in elastic modulus and hardness [19].

Although numerous studies have observed changes in nanostructures and have associated these changes with the mechanical behavior of the materials, the mechanical tests using instrumented indentation in C-S-H/PMA complexes have never been performed. Thus, this study evaluated the chemical and micro-nanomechanical properties of the synthesis of C-S-H modified with PMA polymer, in order to contribute to the development of C-S-H/polymer nanocomposites.

## 2. MATERIALS AND EXPERIMENTAL PROGRAM

C-S-H and C-S-H/PMA samples were produced by the direct precipitation method [12]. PMA polymer solution was used at 40% in water (4,000-6,000 g/mol -  $[\text{CH}_2\text{C}(\text{CH}_3)(\text{CO}_2\text{Na})]_n$ ). A 1 mol/L calcium nitrate solution was added gradually to a 0.22 mol/L solution of sodium silicate with the polymer (except for pure C-S-H) predissolved in CO<sub>2</sub>-free deionized water to achieve a 2.1 Ca/Si ratio. Chemical analysis by XRF (Table 1) showed that the final Ca/Si ratio (1.62 for C-S-H and 1.73 for C-S-H/PMA) remained proportional to the initial project value. The PMA concentration was 0.5 g/g Ca salt [12]. The total water:solid ratio was 20:1. The pH of the mix was maintained between 13.1 and 13.3 with a NaOH solution (10 mol/L). After maintaining the suspension at 60°C for 35 days under gentle stirring in a CO<sub>2</sub>-free atmosphere, the precipitates were vacuum-filtered and then washed with acetone and CO<sub>2</sub>-free deionized water to eliminate the residual polymers and sodium nitrate ions. Next, the precipitates were dried at 60°C in a vacuum oven for 14 days. One part of the precipitate was ground in an agate mortar and sieved (# 75 µm) for XRD, XRF, FT-IR, TGA and carbon content (CHN), while the other part (small irregular particles) was vacuum-impregnated in 2 cm × 2 cm cylinders with a low viscosity resin and cut with a diamond saw for nanoindentation tests. For TEM observations (JEOL, 100 kV), the ground precipitates (before drying) were dispersed in ethanol and dripped onto a 400-mesh copper grid covered by a carbon film, after which the grid was placed in a vacuum desiccator for 24 h.

**Table 1.** Chemical analyses of the C-S-H and C-S-H/PMA (XRF).

Oxide (mass %)	SiO <sub>2</sub>	CaO	Al <sub>2</sub> O <sub>3</sub>	Fe <sub>2</sub> O <sub>3</sub>	LOI
C-S-H	24.56	37.15	0.04	<0.01	-
C-S-H/PMA	13.66	22.39	<0.01	<0.01	-

The cylinder surface was then ground with silicon carbide papers and polished with diamond pastes (four stages of increasing fineness) to obtain a very flat, smooth surface finish. After each grinding/polishing stage, the samples were placed in an ultrasonic bath to remove the dust and diamond particles left on the surface or in the porous structure.

Nanoindentation was performed using a Nanoindenter XP (MTS System). The unpolished surface of the cylindrical specimens was carefully cut with the diamond saw into sections that were 5-6 mm thick. Twelve indentations were performed in each sample in three different regions (for each region, four individual indentations were performed in 2×2 matrices, with 20 μm spacing) by applying five loading cycles of 2, 4, 8, 16, and 32 mN in each indented location (matrix 1). An additional test was performed using higher loads (matrix 2) to evaluate both the nano- and microstructure of the material over a larger area, verify the homogeneity of the material and make marks that would be visible under SEM, thus achieving a more in-depth interpretation of the results by combining the characteristics of the microstructure, morphology and fractures, with the nanomechanical properties. In this case, a 2×3 points matrix was used up to a load of 512 mN (1, 2, 4, 8, 16, 32, 64, 128, 256, 512 mN). Loading was applied linearly for 10 s. The maximal load ( $P_{max}$ ) was then maintained for 5 s, and unloading occurred over an additional 10 s. Hardness (H) is defined as the mean pressure that a material can support under load, and is determined by [20], [21]:

$$H = \frac{P_{max}}{A(h_c)} \quad (1)$$

Where  $P_{max}$  is the maximum applied load and  $A(h_c)$  is the projected contact area function which corrects for the Berkovich tip rounding effect.

The elastic modulus of the material is determined by [22]:

$$E = \frac{1 - \nu^2}{\left( \frac{1}{E_r} - \frac{1 - \nu_i^2}{E_i} \right)} \quad (2)$$

where,  $E_r$  is the reduced elastic modulus,  $E_i$  and  $\nu_i$  are the indenter elastic modulus and Poisson ratio, and  $E$  and  $\nu$  are the elastic modulus and Poisson ratio of the material respectively. For diamond,  $E_i = 1141$  GPa and  $\nu_i = 0.07$  [20], [21]. Based on relationships developed by Sneddon [23], an expression was derived for the reduced elastic modulus,  $E_r$  [20], [21]:

$$E_r = \frac{\sqrt{\pi}}{2\beta} \frac{S}{\sqrt{A(h_c)}} \quad (3)$$

where  $S = (dP/dh)$  is the stiffness obtained experimentally from the upper part of the unloading curve and  $\beta$  is a constant dependent on the indenter geometry, being equal to 1.034 for a triangular symmetry [20], [22]. After nanoindenter testing, the sample was removed, coated with a gold layer and examined by SEM.

XRD was performed to detect shifts in the C-S-H 002 basal reflections, which are due to polymer intercalation. A Philips X'Pert instrument was used that operates with Cu K $\alpha$  radiation ( $\lambda = 1.5418$  Å) with an output of 40 kV and 30 mA. Scanning was performed from 2° to 10° ( $2\theta$ ) in 0.02° steps, with a collection time of 5 s per step. A Perkin-Elmer 16PC Fourier transform-infrared spectrometer (FT-IR) was used in direct transmission mode ranging from 4000 to 400  $\text{cm}^{-1}$  (4  $\text{cm}^{-1}$  resolution), and the carbon content was determined by CHN (carbon, hydrogen, nitrogen – EA 1100 CE Instruments) elemental analysis. The thermogravimetric analysis (TGA) was performed on samples of approximately 20 mg, using a Shimadzu TGA-50, heating at 10°C/min from 0 to 900°C in a nitrogen atmosphere at a flow rate of 100ml/min.

### 3. RESULTS AND DISCUSSION

#### 3.1. Chemical analysis

C-S-H formation was observed with and without the addition of PMA (Figure 1). C-S-H showed peaks at 15.3Å and 12.2Å, while in the C-S-H/PMA mixture, a small increase in the interplanar distance of 16.4Å was observed, with peaks at 11.4Å and 10Å. The peak at 10Å could refer to the formation of either sodium acetate ( $\text{CH}_3\text{COONa}$ ) or sodium silicate ( $\text{Na}_2\text{O} \cdot \text{SiO}_2$ ).

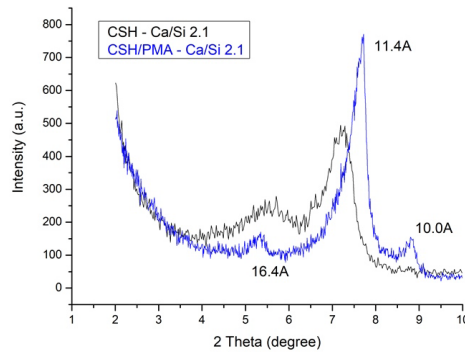


Figure 1. XRD spectra of C-S-H and C-S-H/PMA.

FT-IR spectra analysis verified the presence of the polymer in bonds represented by the bands 2970, 1419, 1458, 1470 and 1250  $\text{cm}^{-1}$  (Figure 2). Hydroxyl ions, nitrate,  $Q^2$  and  $Q^1$  were observed for C-S-H/PMA (Figure 2, Table 2). However, there are two bands for C-S-H/PMA at 957 and 910  $\text{cm}^{-1}$ , and essentially one that refers to the  $Q^2$  bond, at 910  $\text{cm}^{-1}$ , for C-S-H, which indicates an increase in the  $Q^2/Q^1$  ratio and consequently, greater chain lengths and polymerization in the dreierketten region, with the addition of PMA. Very similar behavior was observed by Beaudoin et al. [17], in their research on nanocomposite C-S-H/polymers (polyethylene glycol and hexadecyltrimethylammonium) using the NMR technique.

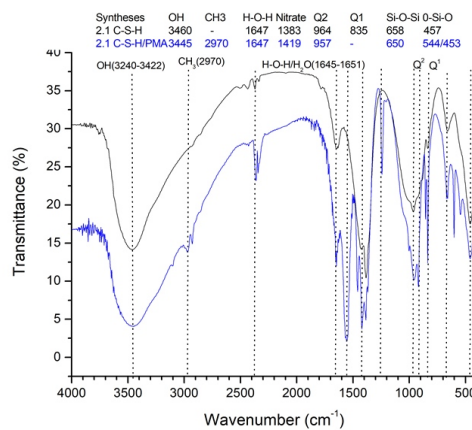


Figure 2. FT-IR spectra of C-S-H and C-S-H/PMA.

Table 2. Selected FT-IR bands of C-S-H and C-S-H/PMA.

Assignment of vibrational spectra	References	Bands ( $\text{cm}^{-1}$ )	
		2.1 C-S-H	2.1 C-S-H /PMA
OH	3268-3375 <sup>(1)</sup>	3508	3445
CH <sub>3</sub>	2925 <sup>(1)</sup>	-	2970
Nitrate	2359 <sup>(2)</sup>	2359	2359
H-O-H	1651 <sup>(1)</sup>	1618	1647
Nitrate/CO <sub>2</sub>	1400/1434 <sup>(2,1)</sup>	1385/1420	1419/1458
C=O-OR	1434 <sup>(1)</sup>	-	1419
Q <sup>2</sup>	969 <sup>(3)</sup>	964	957
Q <sup>2</sup>	903 <sup>(3)</sup>	900	910
Q <sup>1</sup>	814 <sup>(3)</sup>	835	835
$\delta$ (Si-O-Si)	672 <sup>(3)</sup>	651	650
$\delta$ (O-Si-O)	477 <sup>(3)</sup>	457	544/453
-	1647, 1539, 1472, 1416, 1350, 1207, 1101 <sup>(2)</sup>	-	1553, 1460, 1419, 1380, 1350, 1242 <sup>(2)</sup>

<sup>(1)</sup> Mojumdar and Raki [15], <sup>(2)</sup> This research, <sup>(3)</sup> Mostafa et al. [24].

Thermal analyzes (TGA) also showed changes in the structure of C-S-H/PMA in relation to C-S-H. Total mass loss was 15.5% higher for C-S-H/PMA (Figure 3), which is in agreement with the measured carbon content of 16.3% (CHN). Analysis also verified that C-S-H, C-S-H/PMA and PMA lost mass in two major regions: in region 1, from 25 to 250°C, both mixtures showed similar behavior; while in region 2, between 250 and 550°C, PMA polymer was degraded at two temperatures, above 400°C and above 650°C. C-S-H/PMA did not follow this decomposition, however, rather it showed gradual loss of mass from 300°C, different from C-S-H (Figure 3, Table 3). According to Mojumdar and Raki [15], these findings indicate the trapping and intercalation of the polymer within the C-S-H nanostructure.

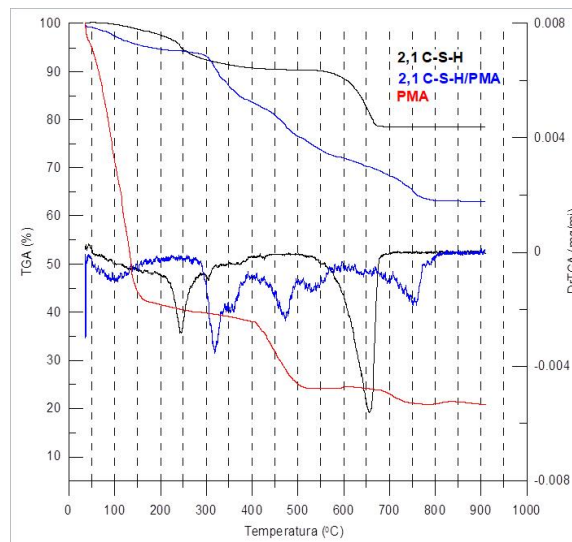


Fig. 3 TG/DTG to C-S-H, C-S-H/PMA and PMA

**Table 3.** Thermogravimetric analysis to C-S-H, PMA and C-S-H/PMA.

Material	DTG/°C
C-S-H	240, 630
PMA	100, 446, 707
C-S-H/PMA	106, 324, 453, 532, 718

### 3.2. Micro-nanomechanical and morphological properties

The nanomechanical properties of elastic modulus and hardness of C-S-H/PMA and C-S-H samples are shown by the following results:

- Results of the three indentation matrices for C-S-H/PMA (Figure 4a - elastic modulus E, Figure 4b – hardness H);
- Mean results for elastic modulus (Figure 5a) and hardness (Figure 5b), comparing C-S-H/PMA and C-S-H for the indentation matrix with loading up to 32 mN;
- Example of load-penetration curves (2 mN) measured by nanoindentation on samples prepared with C-S-H/PMA and C-S-H (Figure 6).
- Load-penetration curves (2-32 mN) obtained by nanoindentation on samples prepared with C-S-H/PMA and C-S-H (Figure 7).
- Mean results for elastic modulus (Figure 8a) and hardness (Figure 8b), comparing C-S-H/PMA and C-S-H for the indentation matrix with loading up to 512 mN, which was then visualized under SEM (Figure 9).

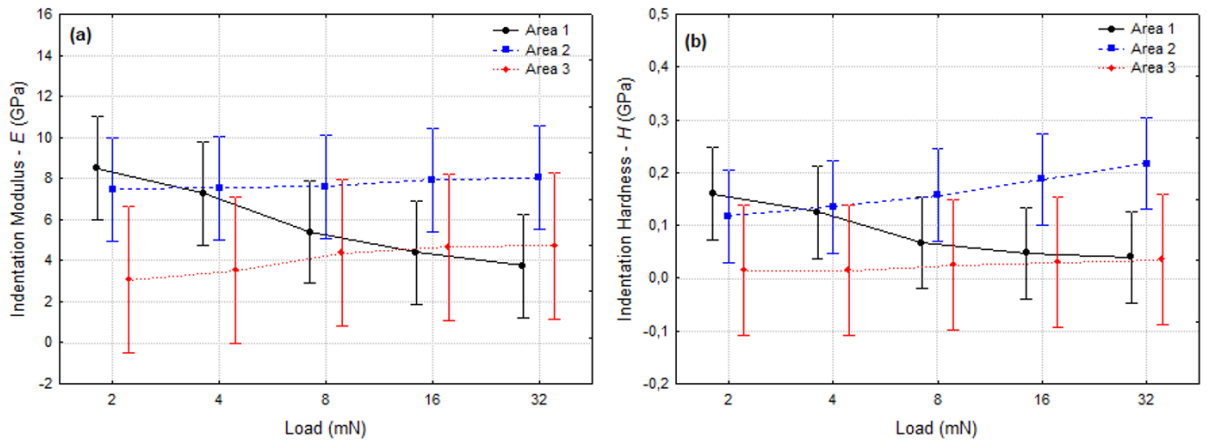


Figure 4. Micro-nanomechanical properties (elastic modulus and hardness) of C-S-H/PMA in specific areas.

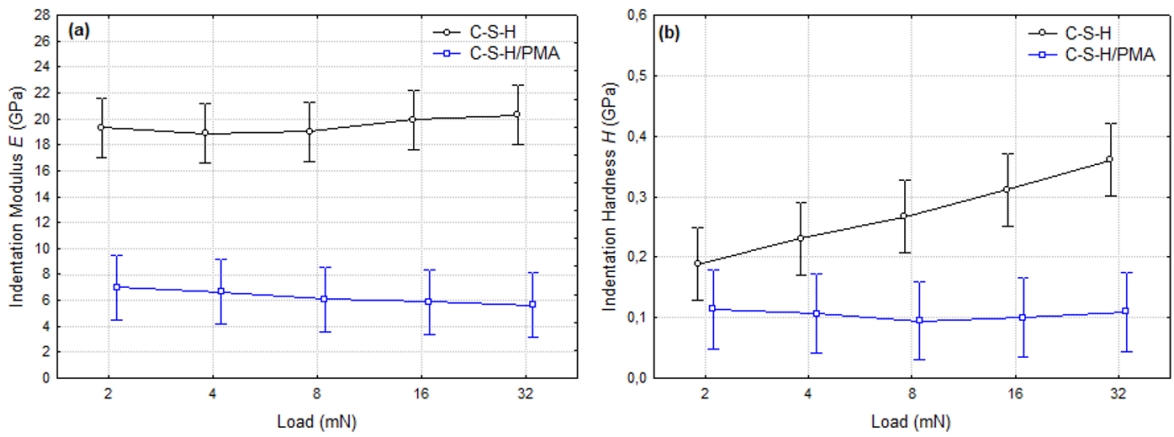


Figure 5. Elastic modulus - E (a) and hardness - H (b) vs applied load - P of C-S-H and C-S-H/PMA until 32 mN (matrix 1).

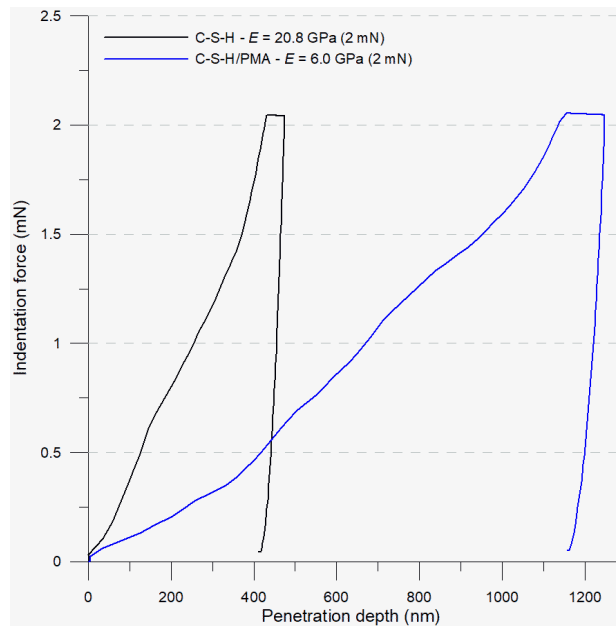


Figure 6. Example of load-penetration curves (2 mN) measured by nanoindentation on samples C-S-H and C-S-H/PMA.

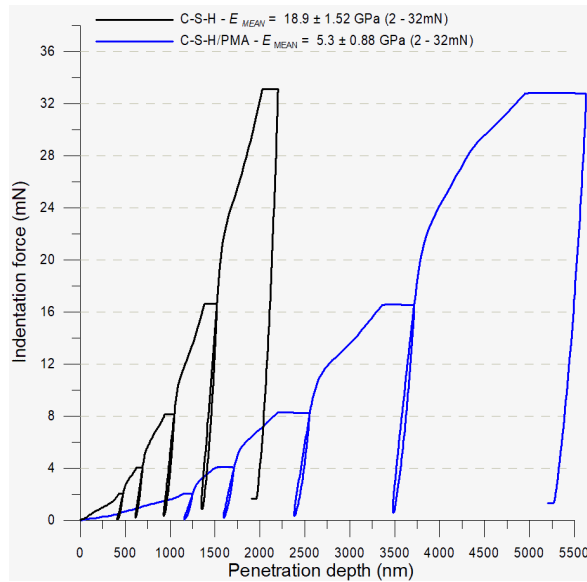


Figure 7. Load-penetration curves (2-32 mN) obtained by nanoindentation on samples C-S-H and C-S-H/PMA.

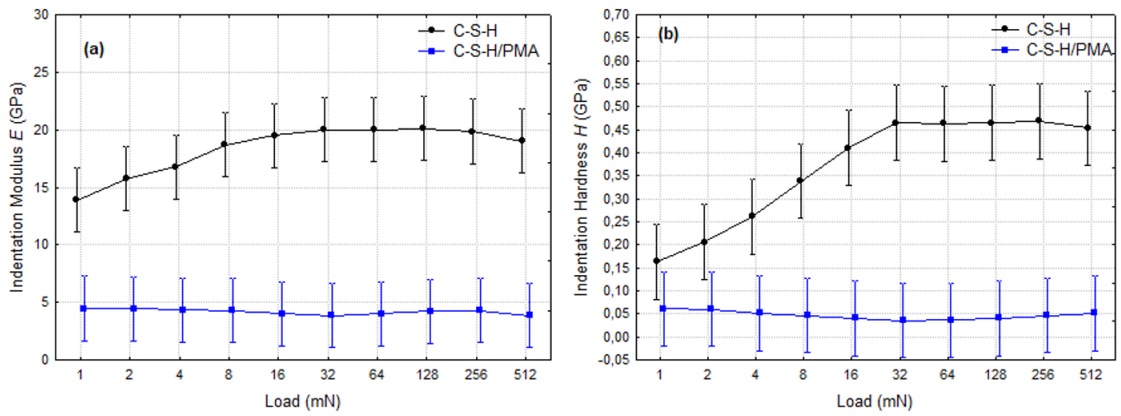


Figure 8. Elastic modulus - E (a) and hardness - H (b) vs applied load - P of C-S-H and C-S-H/PMA until 512 mN (matrix 2).

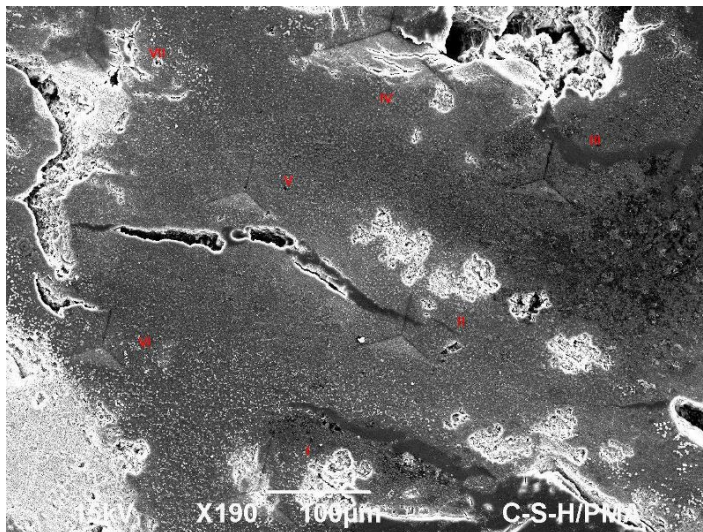


Figure 9. C-S-H/PMA SEM micrograph showing 5 indentations (matrix 2).

A clear difference between C-S-H and C-S-H/PMA mechanical characteristics was determined (Figure 5). The mean elastic modulus and hardness values for the first series of measurements (matrix 1) were  $19.5\pm 4.5$  GPa and  $0.27\pm 0.12$  GPa for C-S-H and  $6.25\pm 2.7$  GPa and  $0.10\pm 0.09$  GPa for C-S-H/PMA (Table 4), indicating the nanostructural alteration. Observation verified that no significant difference occurred between the applied loads in matrix 1 (loaded up to 32 mN), confirming that the effect of surface roughness was not significant (Table 5). Moreover, the SEM micrograph of five C-S-H/PMA indented regions (Figure 9, Table 6), in matrix 2 (load up to 512 mN), exhibited a reasonably regular surface at each point. Visualization of the indented region is an important tool for interpreting and analyzing the results obtained.

**Table 4.** Elastic modulus and hardness of C-S-H and C-S-H/PMA for different loads.

Variables / Results		Matrix 1		Matrix 2	
Material	Load	E(GPa)	H(GPa)	E(GPa)	H(GPa)
C-S-H	2mN	$19.3\pm 1.2$	$0.19\pm 0.05$	$15.8\pm 0.6$	$0.20\pm 0.08$
	32mN	$20.3\pm 3.9$	$0.36\pm 0.11$	$20.0\pm 3.7$	$0.47\pm 0.15$
	512mN	-	-	$19.0\pm 1.6$	$0.45\pm 0.09$
	Average	$19.5\pm 4.5$	$0.27\pm 0.12$	$18.4\pm 4.3$	$0.37\pm 0.16$
C-S-H/ PMA	2mN	$6.34\pm 0.83$	$0.10\pm 0.03$	$4.43\pm 1.47$	$0.06\pm 0.02$
	32mN	$5.65\pm 2.22$	$0.11\pm 0.10$	$3.83\pm 1.33$	$0.04\pm 0.02$
	512mN	-	-	$3.84\pm 0.78$	$0.05\pm 0.01$
	Average	$6.25\pm 2.7$	$0.10\pm 0.09$	$4.17\pm 1.2$	$0.05\pm 0.02$

**Table 5.** Statistical analysis (ANOVA): elastic modulus and hardness.

Variable	Degrees of Freedom	Sum of squares effect	Sum of squares of error	Statistics F	Statistics P	Results	
Modulus	Material	4778.56	1	4778.56	304.70	0.000	Significant.
	Load	4.66	4	1.17	0.074	0.9898	Not-signif.
	Error	1568.28	100	15.68	-	-	-
hardness	Material	0.7558	1	0.7558	69.5601	0.000	Significant.
	Load	0.0946	4	0.0237	2.1777	0.07690	Not-signif.
	Error	1.0865	100	0.0109	-	-	-

**Table 6.** Elastic modulus and hardness values for 32 mN and 512 mN of the indentations showed in Figure 9.

Indented mark in Figure 9	E (GPa)		H (GPa)	
	2mN	512mN	2mN	512mN
I	4.3	5.2	0.07	0.07
III	5.8	3.7	0.08	0.04
V	2.3	3.3	0.03	0.03
VI	5.9	3.5	0.08	0.06
VII	3.9	3.5	0.05	0.06

The results obtained for the five indentations were very similar and approximately 4.4 GPa (Table 4). In indentation V (Figure 9), which presented a surface defect close by, a modulus value of 2.3 GPa was measured. Indentations III and VI (Figure 9) presented values of 5.8 and 5.9 GPa, respectively. Measurements at indentations II and IV (Figure 9), where superficial defects were also observed, could not be performed. Indentations I and VII (Figure 9) achieved values of 4.3 and 3.9 GPa, respectively. These results are presented in Table 6 for loads of 2 mN and 512 mN. Indentations I and V showed increases in the elastic modulus when the load was increased to 512 mN, while the opposite occurred for indentations III, VI and VII. This increase in the elastic modulus occurs due to contributions from lower layers, while decreases are the result of fractures.

The samples were embedded in a carbon-containing resin, which presented a mean elastic modulus of  $3.23\pm 0.07$  GPa and mean hardness of  $0.18\pm 0.002$  GPa. It is important to highlight that the morphology and mechanical

properties of the resin are quite different from the C-S-H and C-S-H/PMA samples (Figure 10) and affirm that the resin did not influence these results. The indentation mark shown in Figure 9 refers to the largest load of 512 mN. The area covered by the minimum load of 1 mN is very small, so the likelihood of two distinct regions occurring is minimal. Figures 5 and 8 show that both the hardness and elastic modulus did not vary according to the load applied and, thus, according to the depth of penetration. As the applied load increases, the probability of the indenter hitting a pore increases, since an increase in the contact area and the projected contact area also occurs. Assuming that the indenter hit a pore of a size that was visible in the microscopy images, the values of hardness and elastic modulus would certainly have decreased. Another factor that encouraged the use of a high load for the indentations (512 mN) was the need to investigate the homogeneity of the C-S-H/PMA nanocomposite, which proved to be homogeneous and showed no significant differences in behavior regarding the load and area of coverage. An additional factor that could have influenced the micro-nanomechanical behavior is excess polymer not incorporated into the matrix, however, it is important to clarify that a small quantity of the polymer was used and that the C-S-H, in gel form, was washed with acetone and filtered to remove free PMA before being dried.

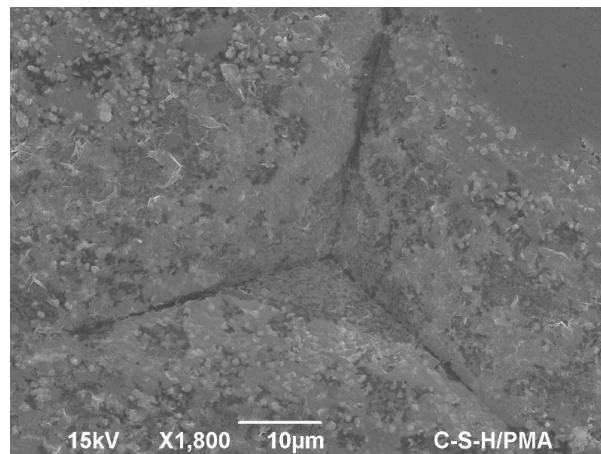


**Figure 10.** C-S-H/PMA SEM micrograph showing one indentation (matrix 2).

Other works have shown changes in the structure of the C-S-H/PDC-cationic polymer that influenced its structure and nanomechanical behavior, such that the presence of PDC in C-S-H affected both its nano (intercalation between the C-S-H lamellae) and mesostructure (C-S-H particles packing density) [18]. When evaluating the effect of the polymer of PVA-neutral [19], a significant change was verified in the nanomechanical properties of C-S-H, resulting in reduced elastic modulus and hardness. However, the set of results presented did not confirm the intercalation of PVA in the interlayer space of C-S-H, rather it confirmed the formation of a C-S-H/PVA mesocomposite, which presented changes in structural packing - in the midst of the PVA polymer film - and in nanomechanical properties.

It is also worth emphasizing that the values obtained for pure C-S-H fall within the same range as the nanoindentation measurements for C-S-H in hydrating Portland cement systems [25]–[27]. The accentuated decrease in elastic modulus of synthesized C-S-H in the presence of PMA could be due to the particle packing density [26] or surface roughness. In order to minimize the effect of surface roughness, higher loads must be applied.

Micrographs (SEM) showed different morphological structures for C-S-H/PMA (Figure 11) and C-S-H (Figure 12). Alterations in the nanostructure formation of C-S-H/PMA were verified by TEM (Figure 13), indicating different structuring for C-S-H (Figure 14). All the images obtained showed this behavior. It is well known that C-S-H is produced by the packing of elementary nanosized particles and that low and high density C-S-H differ according to their aggregation density [25]–[27]. Thus, it can be concluded that any significant alteration in the mechanical properties is due to the packing density of the C-S-H particles in the presence of PMA, as determined qualitatively by TEM.

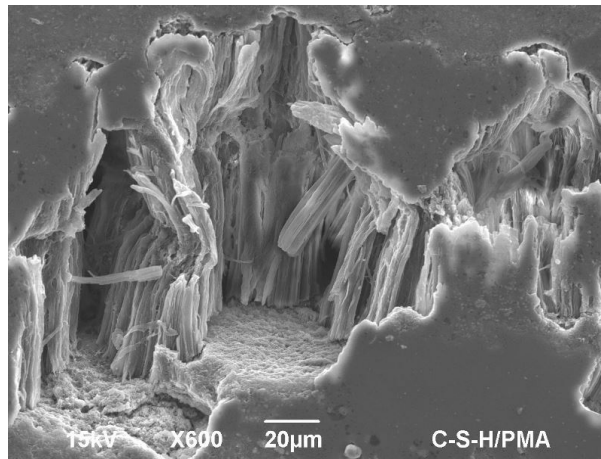


**Figure 11.** C-S-H/PMA SEM micrograph showing morphology of the microstructure.

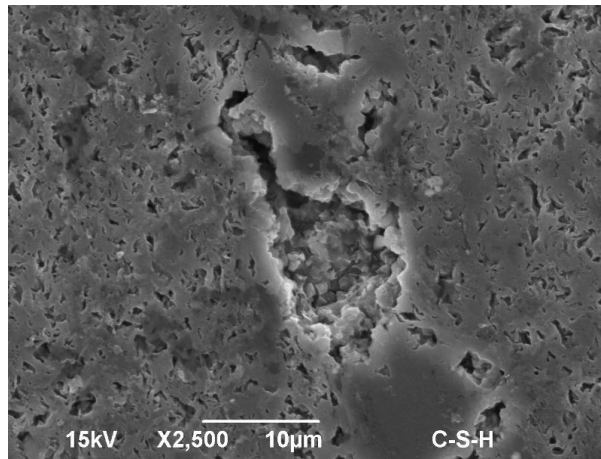


**Figure 12.** C-S-H SEM micrograph showing morphology of the microstructure.

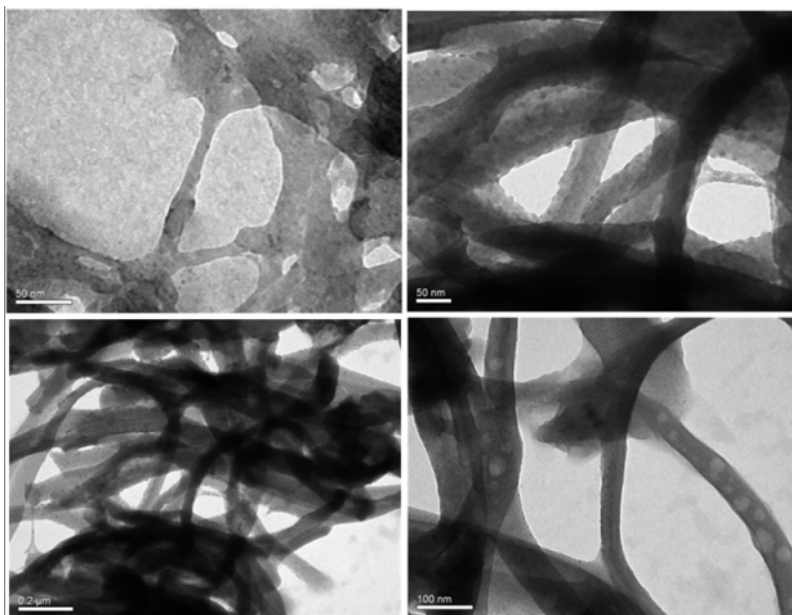


**Figure 13.** C-S-H/PMA (a, b) TEM micrographs.

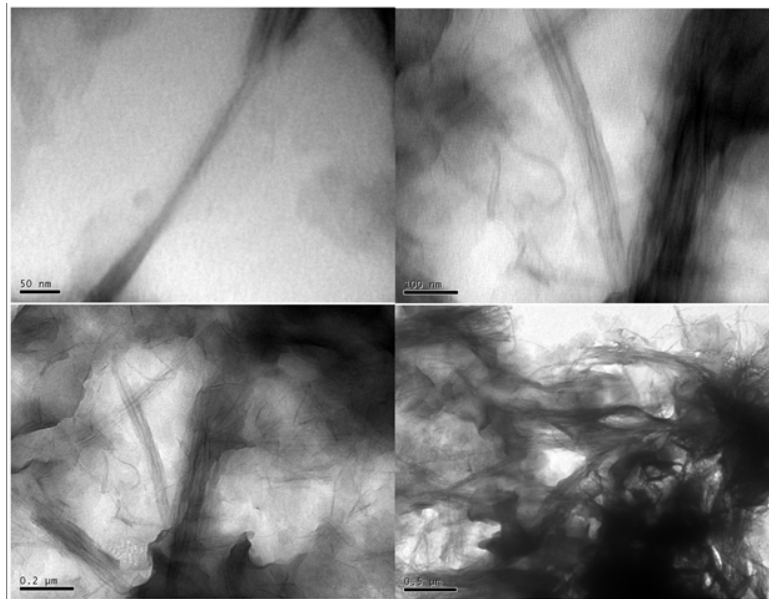


**Figure 14.** C-S-H TEM micrographs.

These results do not exclude the possibility that PMA can increase the cohesion of C-S-H, especially considering its application in the structure of hydrated Portland cement and its effect on a longer drying time. Lee and Rhee [28] used synthesis to verify poly(methyl methacrylate)/SiO<sub>2</sub>-CaO nanocomposites using dimethyldiethoxysilane and tetraethoxysilane, which produced two and four siloxane linkages, respectively, after a sol-gel reaction. This nanocomposite can potentially be applied as a filler material of PMMA bone cement and dental composite resin because of its good apatite-forming ability and improved fracture toughness [28]. On the other hand, the reduction in the mechanical properties of cement obtained in this research, are indicative of lower efficiency and, consequently, higher cost for the same structural performance.

The strong influence of PMA on the mesostructure and nanomechanical properties of C-S-H is evident. These properties and attempts at manipulating the cement nanostructure contribute to the development of nanotechnology applied to more efficient materials [29].

#### 4. CONCLUSIONS

The main results regarding the nanostructural changes in C-S-H modified with PMA are described below:

- The addition of PMA to C-S-H resulted in an increase in interplanar distance, from 1.53 nm to 1.64 nm. These values are lower than those previously described by Matsuyama and Young [12] and similar to those reported by Merlin et al. [6] for other anionic polymers. This small increase in interplanar distance is not considered to be the intercalation of the polymer;
- A significant change was verified in the micro-nanomechanical properties of C-S-H with PMA, resulting in reduction in the elastic modulus and hardness. This reduction of approximately 67% occurred due to the structuring of lower density particles of C-S-H and the presence of the polymer, indicating the formation of a mesocomposite. The formation of a differentiated structure, with increased C-S-H porosity, was observed.

The set of results presented do not confirm the intercalation of PMA in the interlayer space of C-S-H, rather it confirms the formation of a C-S-H/PMA mesocomposite, which presented changes in structural packing and in micro-nanomechanical properties.

## 5. ACKNOWLEDGEMENTS

The authors acknowledge the financial support of the CNPq (National Council of Technological and Scientific Development) and the Central Laboratory of Electronic Microscopy of the Federal University of Santa Catarina (LCME-UFSC) for the SEM and TEM micrographs.

## 6. REFERENCES

- [1] I. Richardson, "The calcium silicate hydrates," *Cement Concr. Res.*, vol. 38, no. 2, pp. 137–158, 2008, <http://dx.doi.org/10.1016/j.cemconres.2007.11.005>.
- [2] J. J. Thomas, H. M. Jennings, and A. J. Allen, "Relationships between composition and density of tobermorite, jennite, and nanoscale CaO–SiO<sub>2</sub>–H<sub>2</sub>O," *J. Phys. Chem. C*, vol. 114, no. 17, pp. 7594–7601, 2010, <http://dx.doi.org/10.1021/jp910733x>.
- [3] H. Manzano, J. Dolado, and A. Ayuela, "Elastic properties of the main species present in Portland cement pastes," *Acta Mater.*, vol. 57, no. 5, pp. 1666–1674, 2009, <http://dx.doi.org/10.1016/j.actamat.2008.12.007>.
- [4] F. Pelisser, P. Gleize, and A. Mikowski, "Effect of the Ca/Si molar ratio on the micro/nanomechanical properties of synthetic C–S–H measured by nanoindentation," *J. Phys. Chem. C*, vol. 116, no. 32, pp. 17219–17227, 2012, <http://dx.doi.org/10.1021/jp302240c>.
- [5] R. Pellenq and H. Van Damme, "Why does concrete set? The nature of cohesion forces in hardened cement-based materials," *Mater. Res. Soc. Bull.*, vol. 29, no. 5, pp. 319–324, 2004, <http://dx.doi.org/10.1557/mrs2004.97>.
- [6] F. Merlin, H. Lombois, S. Joly, N. Lequeux, J. Halary, and H. Van Damme, "Cement-polymer and clay-polymer nano- and meso-composites: spotting the difference," *J. Mater. Chem.*, vol. 12, no. 11, pp. 3308–3315, 2002, <http://dx.doi.org/10.1039/B205279M>.
- [7] C. Glotzbach, D. Stephan, and M. Schmidt, "Measuring interparticle forces: evaluation of superplasticizers for microsilica via colloidal probe technique," *Cement Concr. Compos.*, vol. 36, pp. 42–47, 2013, <http://dx.doi.org/10.1016/j.cemconcomp.2012.11.007>.
- [8] T. Vulic, M. Hadnadjev-Kostic, O. Rudic, M. Radeka, R. Marinkovic-Neducin, and J. Ranogajec, "Improvement of cement-based mortars by application of photocatalytic active Ti–Zn–Al nanocomposites," *Cement Concr. Compos.*, vol. 36, pp. 121–127, 2013, <http://dx.doi.org/10.1016/j.cemconcomp.2012.07.005>.
- [9] A. M. Díez-Pascual, M. A. Gómez-Fatou, F. Ania, and A. Flores, "Nanoindentation in polymer nanocomposites," *Prog. Mater. Sci.*, vol. 67, pp. 1–94, 2015, <http://dx.doi.org/10.1016/j.pmatsci.2014.06.002>.
- [10] H. Matsuyama and J. F. Young, "The formation of C-S-H/Polymer complexes by hydration of reactive β-dicalcium silicate," *Concr. Sc. Eng.*, vol. 1, no. 2, pp. 66–75, 1999.
- [11] H. Matsuyama and J. F. Young, "The formation of C-S-H/polymer complexes with superplasticizing polymers," *Concr. Sc. Eng.*, vol. 1, no. 3, pp. 148–156, 1999.
- [12] H. Matsuyama and J. F. Young, "Synthesis of calcium silicate hydrate/polymer complexes: Part I. Anionic and nonionic polymers," *J. Mater. Res.*, vol. 14, no. 8, pp. 3379–3388, 1999, <http://dx.doi.org/10.1557/JMR.1999.0458>.
- [13] H. Matsuyama and J. F. Young, "Synthesis of calcium silicate hydrate/polymer complexes: Part II. Cationic polymers and complex formation with different polymers," *J. Mater. Res.*, vol. 14, no. 8, pp. 3389–3396, 1999, <http://dx.doi.org/10.1557/JMR.1999.0459>.
- [14] H. Matsuyama and J. F. Young, "Intercalation of polymers in calcium silicate hydrate: a new synthetic approach to biocomposites," *Chem. Mater.*, vol. 11, no. 1, pp. 16–19, 1999, <http://dx.doi.org/10.1021/cm980549l>.
- [15] S. C. Mojumdar and L. Raki, "Preparation and properties of calcium silicate hydrate-poly(vinyl alcohol) nanocomposite materials," *J. Therm. Anal. Calorim.*, vol. 82, no. 1, pp. 89–95, 2005, <http://dx.doi.org/10.1007/s10973-005-0846-8>.
- [16] A. Mansur and H. Mansur, "Interface porcelain tile/PVA modified mortar: a novel nanostructure approach," *J. Nanosci. Nanotechnol.*, vol. 9, no. 2, pp. 1071–1075, 2009, <http://dx.doi.org/10.1166/jnn.2009.C090>.
- [17] J. J. Beaudoin, H. Dramé, L. Raki, and R. Alizadeh, "Formation and properties of C-S-H-PEG nano-structures," *Mater. Struct.*, vol. 42, no. 7, pp. 1003–1014, 2009, <http://dx.doi.org/10.1617/s11527-008-9439-x>.
- [18] F. Pelisser, P. J. P. Gleize, and A. Mikowski, "Effect of poly(diallyldimethylammonium chloride) on nanostructure and mechanical properties of calcium silicate hydrate," *Mater. Sci. Eng. A*, vol. 527, no. 26, pp. 7045–7049, 2010, <http://dx.doi.org/10.1016/j.msea.2010.07.057>.
- [19] F. Pelisser, P. J. P. Gleize, and A. Mikowski, "Structure and micro-nanomechanical characterization of synthetic calcium–silicate–hydrate with Poly(Vinyl Alcohol)," *Cement Concr. Compos.*, vol. 48, pp. 1–8, 2014, <http://dx.doi.org/10.1016/j.cemconcomp.2014.01.004>.
- [20] W. C. Oliver and G. M. Pharr, "An improved technique for determining hardness and elastic modulus using load and displacement sensing indentation experiments," *J. Mater. Res.*, vol. 7, no. 6, pp. 1564–1583, 1992, <http://dx.doi.org/10.1557/JMR.1992.1564>.
- [21] W. C. Oliver and G. M. Pharr, "Measurement of hardness and elastic modulus by instrumented indentation: Advances in understanding and refinements to methodology," *J. Mater. Res.*, vol. 19, no. 1, pp. 3–20, 2004, <http://dx.doi.org/10.1557/jmr.2004.19.1.3>.
- [22] F. R. Brotzen, "Mechanical testing of thin films," *Int. Mater. Rev.*, vol. 39, no. 1, pp. 24–45, 1994, <http://dx.doi.org/10.1179/imr.1994.39.1.24>.

- [23] I. N. Sneddon, "The relation between load and penetration in the axisymmetric boussinesq problem for a punch of arbitrary profile," *Int. J. Eng. Sci.*, vol. 3, no. 1, pp. 47–57, 1965, [http://dx.doi.org/10.1016/0020-7225\(65\)90019-4](http://dx.doi.org/10.1016/0020-7225(65)90019-4).
- [24] N. Y. Mostafa, A. A. Shaltout, H. Omar, and S. A. Abo-El-Enein, "Hydrothermal synthesis and characterization of aluminium and sulfate substituted 1.1nm tobermorites," *J. Alloys Compd.*, vol. 467, no. 1-2, pp. 332–337, 2009, <http://dx.doi.org/10.1016/j.jallcom.2007.11.130>.
- [25] G. Constantinides and F.-J. Ulm, "The nanogranular nature of C–S–H," *J. Mech. Phys. Solids*, vol. 55, no. 1, pp. 64–90, 2007, <http://dx.doi.org/10.1016/j.jmps.2006.06.003>.
- [26] M. Vandamme, F.-J. Ulm, and P. Fonollosa, "Nanogranular packing of C–S–H at substochiometric conditions," *Cement Concr. Res.*, vol. 40, no. 1, pp. 14–26, 2010, <http://dx.doi.org/10.1016/j.cemconres.2009.09.017>.
- [27] H. M. Jennings, "Refinements to colloid model of CSH in cement: CM-II," *Cement Concr. Res.*, vol. 38, no. 3, pp. 275–289, 2008, <http://dx.doi.org/10.1016/j.cemconres.2007.10.006>.
- [28] K.-H. Lee and S.-H. Rhee, "The mechanical properties and bioactivity of poly(methyl methacrylate)/SiO<sub>2</sub>–CaO nanocomposite," *Biomaterials*, vol. 30, no. 20, pp. 3444–3449, 2009, <http://dx.doi.org/10.1016/j.biomaterials.2009.03.002>.
- [29] M. Schmidt, K. Amrhein, T. Braun, C. Glotzbach, S. Kamaruddin, and R. Tänzer, "Nanotechnological improvement of structural materials – impact on material performance and structural design," *Cement Concr. Compos.*, vol. 36, pp. 3–7, 2013, <http://dx.doi.org/10.1016/j.cemconcomp.2012.11.003>.

---

**Author contributions:** Fernando Pelisser: Conceptualization, Investigation, Writing-Original draft preparation, Methodology, Data curation, Writing- Reviewing and Editing. Philippe J. P. Gleize: Supervision, Conceptualization. Alexandre Mikowski: Visualization, Methodology, Data curation.

**Editors:** José Luiz Antunes de Oliveira e Sousa, Guilherme Aris Parsekian.



ORIGINAL ARTICLE

# Numerical simulation of steel-concrete composite beams: updated strategies of finite element modeling

*Simulação numérica de vigas mistas de aço e concreto: estratégias atuais de modelagem por elementos finitos*

Matheus Erpen Benincá<sup>a</sup> Rebeca Jéssica Schmitz<sup>a</sup> Inácio Benvegno Morsch<sup>a</sup>

<sup>a</sup>Universidade Federal do Rio Grande do Sul – UFRGS, Escola de Engenharia, Programa de Pós-graduação em Engenharia Civil, Porto Alegre, RS, Brasil

Received 15 April 2019

Accepted 08 February 2020

**Abstract:** The use of steel-concrete composite beams allows the best properties of these materials to be explored, resulting in more economical solutions. Many researchers have studied the behavior of composite beams from different strategies of numerical modeling, and some of these are presented in this article. In this context, the present work proposes the construction of a tridimensional numerical model using ANSYS software, version 19.2, with current-technology elements and compatible material models. For the simulation of concrete behavior, two models have been used: the first, denominated DP-CONCRETE, is a native ANSYS model, available in the more recent versions of this software; and the second, denominated USERMAT, is a customizable model that was developed based on Ottosen criterion. The results obtained with these models for the analyzed beams presented a good correlation with the experimental results and with numerical results from previous works.

**Keywords:** steel-concrete composite beams, numerical modeling, finite element method.

**Resumo:** O emprego de vigas mistas de aço e concreto permite que sejam exploradas as melhores características mecânicas desses materiais, resultando em soluções estruturais mais econômicas. Vários pesquisadores estudaram o comportamento de vigas mistas a partir de diferentes estratégias de modelagem numérica, algumas das quais são apresentadas neste artigo. Dentro desse contexto, propõe-se a construção de um modelo numérico tridimensional com o software ANSYS, versão 19.2, utilizando elementos finitos atuais e modelos de materiais compatíveis com eles. Para a simulação do comportamento do concreto, foram utilizados dois modelos, o primeiro denominado DP-CONCRETE, disponibilizado nas versões mais recentes do ANSYS; e o segundo customizado com a interface USERMAT, e que tem por base o critério de Ottosen. Os resultados obtidos para as vigas analisadas apresentaram boa correlação com os resultados experimentais e com resultados numéricos de trabalhos anteriores.

**Palavras-chave:** vigas mistas de aço e concreto, modelagem numérica, elementos finitos.

**How to cite:** M. E. Benincá, R. J. Schmitz, and I. B. Morsch, “Numerical simulation of steel-concrete composite beams: updated strategies of finite element modeling”, *Rev. IBRACON Estrut. Mater.*, vol. 13, no. 5, e13510, 2020, <https://doi.org/10.1590/S1983-41952020000500010>

## 1 INTRODUCTION

The use of steel-concrete composite beams has been widespread in the civil construction sector, as it allows the best mechanical properties of the involved materials to be explored. In these beams, a steel profile is connected to a concrete slab through shear connectors, which aim to restrict the longitudinal slip and the vertical separation at the interface [1], ensuring the joint work of the elements. This configuration allows to use these materials more rationally, especially in

Corresponding author: Matheus Erpen Benincá. E-mail: matheuseb@hotmail.com

Financial support: This study was financed in part by the Coordenação de Aperfeiçoamento de Pessoal de Nível Superior - Brasil (CAPES) - Finance Code 001, and by the Conselho Nacional de Desenvolvimento Científico e Tecnológico (CNPq).

Conflict of interest: Nothing to declare.



This is an Open Access article distributed under the terms of the Creative Commons Attribution License, which permits unrestricted use, distribution, and reproduction in any medium, provided the original work is properly cited.

simply supported beams, where the concrete works basically under compression and the steel profile under tension. The result of this rationalization is an increase in the load carrying capacity of the composite beam, when compared to the materials working separately, allowing the design of larger spans and/or the achievement of more economical structural solutions [2], [3].

There are different possible shapes for the shear connectors, and the most common are known as stud bolts. The level of interaction between the steel profile and the concrete slab is a fundamental issue in the design and analysis of composite beams, and can be classified according to two different criteria: strength or stiffness. The Brazilian code NBR 8800 [4] uses the first of them, defining that “complete interaction” occurs between steel and concrete when the connectors present a design strength equal to or greater than the design strength of the steel profile under tension or the concrete slab under compression, whichever is less; and, otherwise, “partial interaction” occurs. Also adopting the strength criterion, but in other words, the Portuguese version of Eurocode NP EN 1994-1-1 [5] and the original Eurocode 4 [6] use the terms “partial shear connection” and “full shear connection”, respectively, to distinguish situations in which an increase in the resistance of the longitudinal shear connection increases, or not, the design bending resistance of the composite beam. However, it is worth mentioning that, in the specialized literature, the term “partial interaction” is often used to characterize a deformable connection between two structural elements [7], i.e., the stiffness criterion is adopted. In fact, according to Queiroz *et al.* [8], a composite beam presents “full interaction” when the connectors can be admitted as infinitely stiff, thus the relative slip between the steel profile and the concrete slab next to the connections is negligible; and that presents “partial interaction” when the deformation of the connectors is significant, resulting in slips that cannot be neglected. It is noteworthy that, in practice, in cases of full connection (or complete interaction, strength criterion), it is common to adopt, for design purposes, the hypothesis of full interaction (stiffness criterion) – reason why the cited codes only use the strength criterion in their classifications. Anyway, the real behavior of a connector can be represented by a slip versus shear force curve ( $\delta x_Q$ ), which can be obtained, along with the ultimate shear force ( $Q_u$ ), from a push-out test, standardized by Eurocode 4 [6]. Therefore, numerical models that incorporate the results of this test to the connectors assume the hypothesis of partial interaction (stiffness criterion) and, therefore, can simulate more realistically the behavior of composite beams, for both partial and full shear connection (strength criterion).

In the first applications, the steel profile of the composite beam was designed to support all the acting loads, assuming that the profile and the slab worked independently. Due to the scarcity of steel in the post II World War period, engineers began to design these beams considering the contribution of the concrete slab, starting the movement for systematic research on the subject [3]. Between the 1960s and the 1970s, several experimental studies were carried out [9]–[11]. More recently, studies using the finite element method for the numerical analysis of these beams have been multiplied, with the construction of models that contemplate the partial interaction [1], [8], [12]–[16].

There are different ways to create a finite element model for the analysis of composite beams. The one-dimensional models are those in which the steel profile and the concrete slab are modeled as bar elements, being connected by spring elements to simulate the shear connectors. An example of this approach is the work of Gattesco [12]. The three-dimensional models are those that use shell elements to model the steel profile, and may present different approaches for modeling the concrete slab and shear connectors.

Tamayo *et al.* [13], Tamayo [14] and Dias [15] developed a computational code at CEMACOM/UFRGS for the analysis of composite beams, considering a three-dimensional finite element model in which the concrete slab was modeled by 8-node degenerated shell elements, the shear connectors by bar elements with penalties and the steel profile by shell elements. ANSYS software was employed by Kotinda [1] and by Marconcin *et al.* [16], with the steel profile being modeled by shell elements (named SHELL43), the concrete slab by hexahedral elements (SOLID65), the shear connectors by bar elements (BEAM189), and using pairs of contact elements (TARGE170 and CONTA173) at the interface between steel and concrete. Queiroz *et al.* [8] also used ANSYS and modeled the steel profile by shell elements (SHELL43), the concrete slab by hexahedral elements (SOLID65) and the connectors by non-linear spring elements (COMBIN39). Figure 1 illustrates the different models mentioned.

The 8-node element SOLID65, employed by the mentioned works, received notoriety for being the only element that can be associated with the constitutive model CONCRETE, made available by ANSYS, and based on the formulation of Willam and Warnke [17]. However, although the software still reads the codes that use this element, it is now classified as a “legacy element” by the ANSYS documentation, version 19.2 [18], being incompatible with several current functionalities, such as the use of embedded elements for reinforcement. In addition, numerical instability problems associated with this model were described by several researchers, who reported the need to disable the crushing option to improve convergence [1], [8].

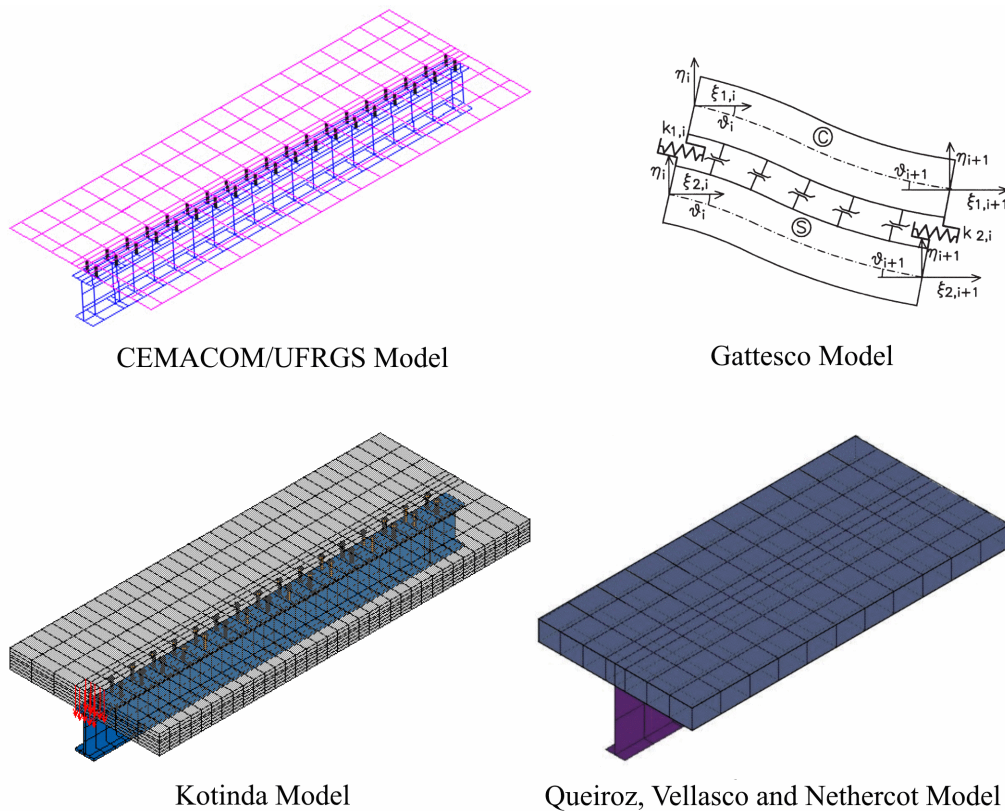


Figure 1. Numerical models developed by previous works [1], [8], [12]–[15].

In this context, the present work proposes the construction of a three-dimensional finite element model for the numerical simulation of composite beams, with ANSYS software, version 19.2, using elements classified as current technology by the software documentation [18]. In this model, the applicability of two different approaches for the simulation of concrete behavior will be evaluated: (i) a customized model by the subroutine USERMAT, based on the Ottosen criterion [19]; and (ii) the DP-CONCRETE model, available in the most recent versions of ANSYS. The validation of the developed model will be carried out from the numerical simulation of two composite beams tested experimentally by Chapman and Balakrishnan [9], which were also numerically simulated by previous works [1], [8], [12], [14], [15].

## 2 NUMERICAL MODEL

The following items present information about the element types, material models and boundary conditions used in the developed finite element model.

### 2.1 Element types

The steel profile was modeled by quadrilateral shell elements, named SHELL181 [18], with four nodes and six degrees of freedom per node (x, y, z translations and rotations), considering both membrane and bending stiffnesses. Its formulation is based on the work of several authors, including Bathe and Dvorkin [20] and MacNeal and Harder [21], and uses Reissner-Mindlin first-order shear-deformation theory. It is applicable to linear and nonlinear problems, including large deformations and rotations. For this reason, the formulation uses logarithmic strain and true stress measures rather than nominal engineering strain and stress. For small deformations, the difference between nominal and true values is negligible. The element can also contain several layers, but in this paper a single and centralized layer was used, with five integration points along the thickness.

The concrete slab was modeled by hexahedral elements with twenty nodes and three degrees of freedom per node (translations in x, y and z), named SOLID186 [18]. In the present work these elements were used in their homogeneous form with full integration. Its formulation is based on Zienkiewicz *et al.* [22]. Because it is a current-technology

element, SOLID186 is compatible with several current ANSYS features, such as the generation of embedded elements and the use of new material models, e.g. DP-CONCRETE.

The connectors were modeled by nonlinear spring elements, named COMBIN39 [18], acting in the longitudinal direction of the beam. Thus, the relative slip between the nodes of the steel profile and the concrete slab in this direction ( $u_x$ ) are governed by points of the force versus slip curve of the element, whose data are obtained from push-out tests. When acting on a single degree of freedom per node, these elements should preferably be applied to coincident nodes [18]. In this work, however, they were applied to nodes spaced by half the thickness of the superior flange ( $t_{fs}/2$ ), because of the model geometry and the centralized positioning of the profile shell elements cross-section, as shown in Figure 2. However, once this distance is very small, it can be assumed that these nodes are practically coincident. At the same time, in the transverse and vertical directions, the couplings of the displacements  $u_y$  and  $u_z$  of these same nodes are performed. Thus, the COMBIN39 element acts only in the longitudinal direction of the beam, and compatibility equations are responsible for simulating the behavior of connectors in the other directions, as in the model proposed by Queiroz *et al.* [8].

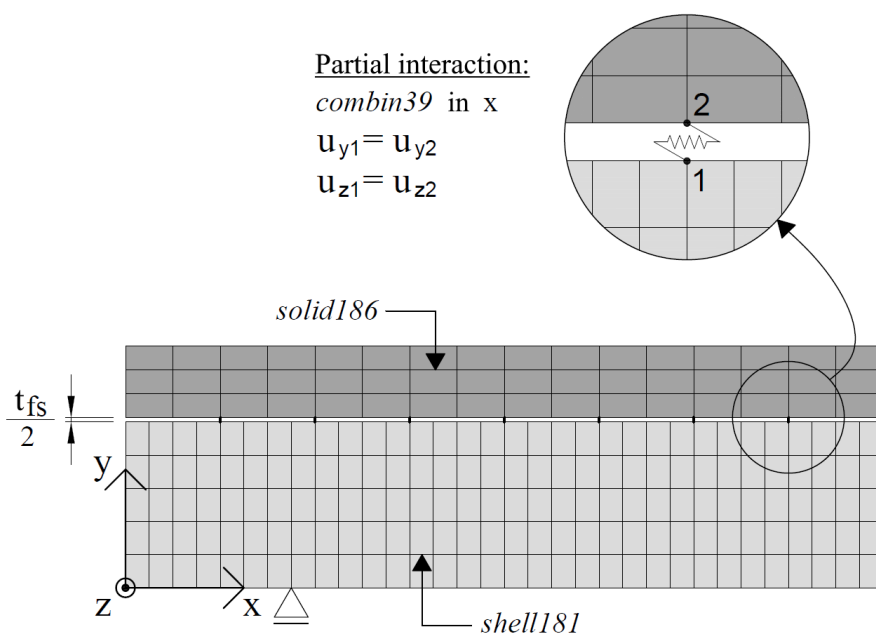
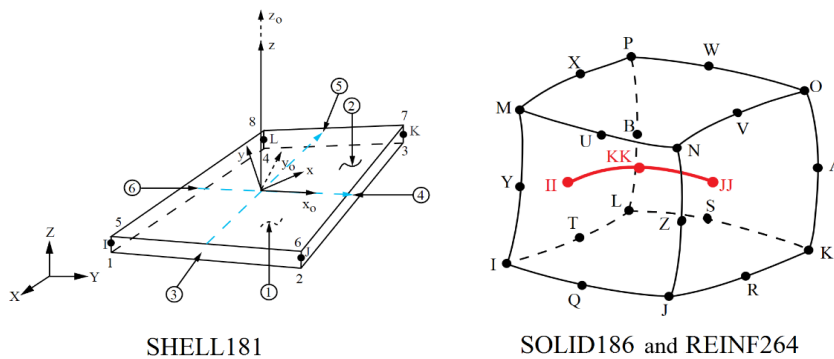


Figure 2. Detail of COMBIN39 nonlinear spring element for connectors modeling.

The reinforcement bars were modeled by discrete embedded elements, named REINF264 [18], which are suitable for simulating steel bars. These elements use the same nodes of the base elements SOLID186, even if their geometric position does not coincide with them. The REINF264 element presents only axial stiffness, thus the stiffnesses to bending, torsion and shear are neglected. A perfect interaction between the reinforcing element and the concrete base element is admitted, so there is no relative movement between them [18].

For the generation of reinforcement embedded elements, a new ANSYS functionality was used, denominated mesh-independent method. This method uses MESH200 elements, which are only guide elements, thus do not directly contribute to the solution, but determine the positions where REINF264 reinforcement elements are created [18]. Therefore, it is possible to insert the positions of the reinforcement bars from the lines drawn in absolute coordinates, unlike the standard method, in which it is necessary to use relative coordinates in respect to the base elements, generating mesh dependence.

The elements SHELL181, SOLID186 and REINF264 are illustrated in Figure 3.



**Figure 3.** Finite elements adopted for modeling the steel profile (SHELL181), the concrete slab (SOLID186) and the embedded reinforcement (REINF264) [18].

### 2.2 Material Models

The profile steel was modeled by von Mises yield criterion with isotropic hardening. As hardening law, the constitutive model proposed by Gattesco [12], shown in Figure 4a, was adopted. This model is divided into three stages of loading: (i) elastic-linear; (ii) yield plateau; (iii) hardening governed by parabolic curve, given by Equation 1.

$$\sigma = f_y + E_h \cdot (\varepsilon - \varepsilon_h) \cdot \left( 1 - \frac{E_h \cdot (\varepsilon - \varepsilon_h)}{4 \cdot (f_u - f_y)} \right) \tag{1}$$

where  $f_y$  and  $f_u$  are the steel yield and ultimate strengths,  $\varepsilon_y = f_y / E$  is the yield strain,  $\varepsilon_h$  is the strain at the initial hardening,  $\varepsilon_u$  is the strain at the ultimate stress,  $E$  is the modulus of elasticity and  $E_h$  is the tangent modulus of elasticity at the start of the hardening stage.

On the other hand, the steel of the reinforcement bars was simplified as perfectly elastoplastic, as shown in Figure 4b.

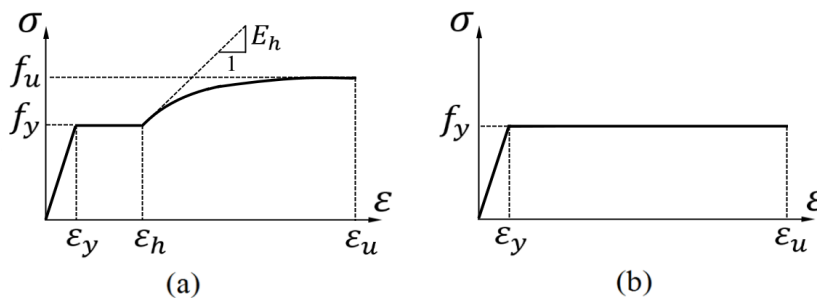


**Figure 4.** Constitutive relations: (a) profile steel; (b) reinforcement steel.

Differently from the other materials, the steel properties of the connectors are not inserted into a material model itself, but rather through real constants of the COMBIN39 spring element. These real constants provide points for the force versus slip curve, obtained experimentally via push-out test. To systematize the model, the theoretical curve given by Equation 2 was adopted, as proposed by Ollgaard et al. [23], adjustable to the push-out test data of stud bolts.

$$Q = Q_u \cdot (1 - e^{-ms})^n \tag{2}$$

where  $Q$  is the shear force acting in the connector, in kN;  $Q_u$  is the ultimate shear force resisted by the connector, in kN;  $s$  is the slip, in mm;  $e = 2.718$  is the Euler number; and  $m, n$  are curve fitting parameters, in  $\text{mm}^{-1}$  and dimensionless, respectively.

For each analyzed example, two numerical models were developed, differing in the way they simulate the concrete's behavior:

- (i) via a customized model with the USERMAT subroutine;
- (ii) via an ANSYS native model, called DP-CONCRETE, recently made available by the software (since 17.0 version).

USERMAT is an ANSYS subroutine that can be programmed to customize a material model [18], [24]. The customized model used in the present work was developed by Lazzari *et al.* [25]. The rupture surface adopted was proposed by Ottosen [19], and is given by Equations 3, 4 and 5.

$$f(I_1, J_2, \cos(3\theta)) = \alpha \cdot \frac{J_2}{f_{cm}^2} + \lambda \cdot \frac{\sqrt{J_2}}{f_{cm}} + \beta \cdot \frac{I_1}{f_{cm}} - 1 = 0 \tag{3}$$

$$\lambda = \begin{cases} c_1 \cdot \cos\left(\frac{1}{3} \arccos(c_2 \cdot \cos(3\theta))\right), & \text{if } \cos(3\theta) \geq 0 \\ c_1 \cdot \cos\left(\frac{\pi}{3} - \frac{1}{3} \arccos(-c_2 \cdot \cos(3\theta))\right), & \text{if } \cos(3\theta) \leq 0 \end{cases} \tag{4}$$

$$\cos(3\theta) = \frac{3\sqrt{3}}{2} \cdot \frac{J_3}{\sqrt{J_2^3}} \tag{5}$$

where  $I_1$  is the first stress invariant;  $J_2$  and  $J_3$  are the second and third deviatoric stress invariants;  $f_{cm}$  is the mean compressive strength of concrete;  $\theta$  is the similarity angle; and  $\alpha, \beta, c_1, c_2$  are material parameters, automatically calculated by USERMAT from equations provided by the *fib2010* model code [26], which uses as input data the values of the mean uniaxial compressive strength of concrete ( $f_{cm}$ ), biaxial compressive strength ( $f_{c2m}$ ), tensile strength ( $f_{ctm}$ ), and triaxial compressive strength, the latter being defined by a point located on the compressive meridian and described by the stresses  $\sigma_{com}$  and  $\tau_{com}$ .

For the compressive behavior, the hardening law adopted is given by Equation 6, illustrated in Figure 5a, as suggested by *fib2010* model code [26].

$$\frac{\sigma_c}{f_{cm}} = \frac{\eta^2 - k \cdot \eta}{1 + (k - 2) \cdot \eta} \tag{6}$$

where  $\sigma_c$  is the compressive stress;  $\varepsilon_c$  is the compressive strain of concrete;  $\varepsilon_{c1}$  is the strain at the maximum compressive stress;  $\varepsilon_{c,lim}$  is the ultimate compressive strain;  $E_{ci}$  is the tangent modulus of elasticity of concrete;  $E_{c1}$  is the secant modulus of elasticity of concrete from the origin to the peak compressive stress;  $k = E_{ci} / E_{c1}$  is the plastic number; and  $\eta = \varepsilon_c / \varepsilon_{c1}$ .

For the tensile behavior, a model of distributed cracks was adopted, considering the tension stiffening effect through the softening law shown in Figure 5b. Initially, the concrete is admitted as linear elastic until the tensile strength ( $f_{ctm}$ ) is reached. After the cracking occurs, the softening is governed by a decreasing line that intersects the vertical axis at the value of  $\alpha \cdot f_{ctm}$  and the horizontal axis at the limit strain value ( $\varepsilon_{ctu}$ ). In the present work, the parameters  $\alpha = 0.6$  and  $\varepsilon_{ctu} = 0.001$  were adopted, as suggested by Martinelli [27]. The customized model also contemplates the reduction of shear stresses transfer in the crack, considering the aggregate interlock mechanism and the reinforcement pin effect, from the reduction of the cracked concrete's transversal elasticity modulus.

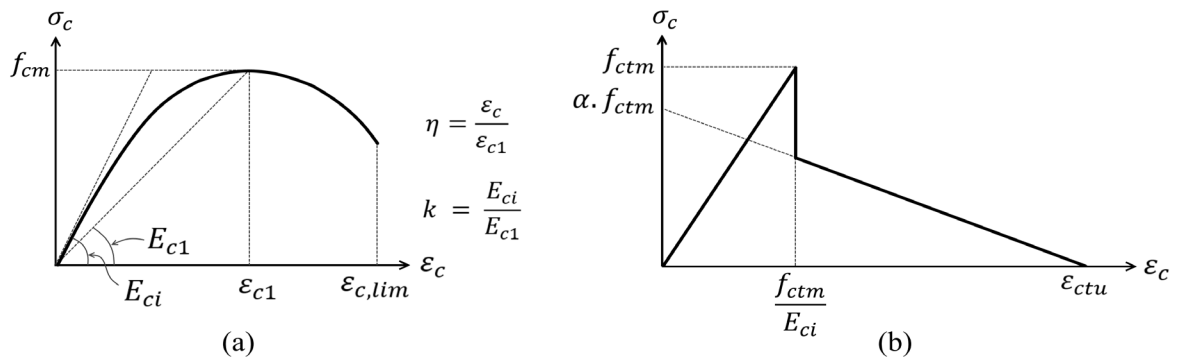


Figure 5. Constitutive relations in the Usermat model: (a) compression; (b) tension.

The second model used to simulate the concrete’s behavior, denominated DP-CONCRETE, is a composition of two distinct surfaces: a Drucker-Prager yield surface for compression, and a second surface, which may be Drucker-Prager or Rankine, for tension and tension-compression. It is necessary to use one of these combinations since a single Drucker-Prager surface does not represent the large differences in tensile and compressive behavior of concrete [18]. Figure 6 illustrates the two possible compositions, in the two-dimensional principal stresses system.

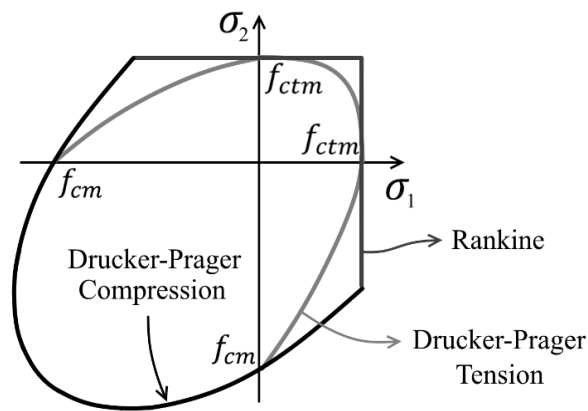


Figure 6. Combinations Drucker-Prager with Rankine or Drucker-Prager with Drucker-Prager (adapted from [18]).

In this paper, the combination of Drucker-Prager (compression) with Rankine (tension) was adopted. These surfaces are defined, respectively, by Equations 7 and 8. The parameters  $\beta_c$  and  $\sigma_{\gamma_c}$  of Equation 7 are calculated with Equations 9 and 10.

$$f_{DPC} = \frac{\beta_c}{3} \cdot I_1 + \sqrt{J_2} - \sigma_{\gamma_c} \cdot \Omega_c = 0 \tag{7}$$

$$f_R = I_1 + 2 \cdot \sqrt{3} \cdot J_2 \cdot \cos(\theta) - 3 \cdot T \cdot \Omega_t = 0 \tag{8}$$

$$\beta_c = \frac{\sqrt{3} \cdot (R_b - R_c)}{2 \cdot R_b - R_c} \tag{9}$$

$$\sigma_{\gamma_c} = \frac{R_b \cdot R_c}{\sqrt{3} \cdot (2 \cdot R_b - R_c)} \tag{10}$$

where  $R_c$  and  $R_b$  are the uniaxial and the biaxial compressive strengths of concrete, respectively;  $T$  is the concrete tensile strength;  $\Omega_c$  and  $\Omega_t$  are hardening and softening functions in compression and in tension. In this work,  $T = f_{ctm}$ ,  $R_c = f_{cm}$  and  $R_b = f_{c2m}$  were adopted.

In function of the HSD (hardening, softening and dilatation) model adopted, the functions  $\Omega_c$  and  $\Omega_t$  assume a certain shape. With these models it is possible to simulate approximately the phenomena of cracking, in tensile behavior, and crushing, in compressive behavior, from increments of plastic strains related to the hardening and softening rules. ANSYS provides four types of HSD models. In this work, the “linear model” was adopted, which is governed by Equations 11 and 12, for compression and tension, respectively. These functions are illustrated in Figure 7.

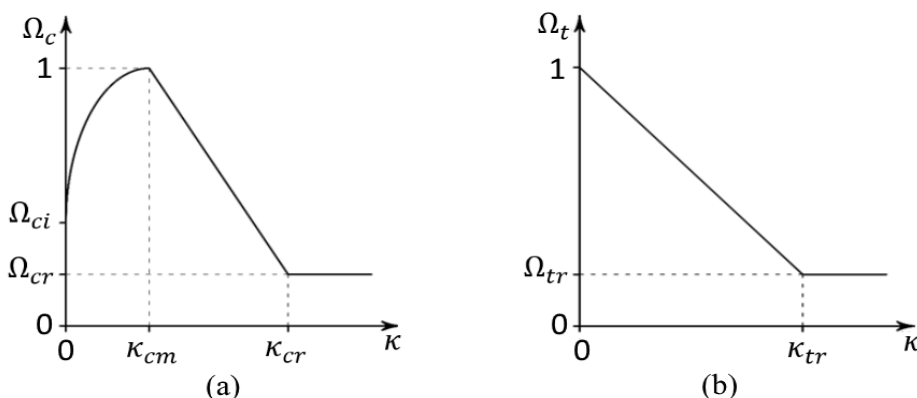


Figure 7. Functions of the linear HSD model: (a) compression; (b) tension [18].

$$\Omega_c = \begin{cases} \Omega_{ci} + (1 - \Omega_{ci}) \cdot \sqrt{2 \cdot \frac{\kappa}{\kappa_{cm}} - \frac{\kappa^2}{\kappa_{cm}^2}}, & \text{if } 0 < \kappa \leq \kappa_{cm} \\ 1 - \frac{1 - \Omega_{cr}}{\kappa_{cr} - \kappa_{cm}} \cdot (\kappa - \kappa_{cm}), & \text{if } \kappa_{cm} < \kappa \leq \kappa_{cr} \\ \Omega_{cr}, & \text{if } \kappa \geq \kappa_{cr} \end{cases} \quad (11)$$

$$\Omega_t = \begin{cases} 1 - (1 - \Omega_{tr}) \cdot \frac{\kappa}{\kappa_{tr}}, & \text{if } 0 < \kappa < \kappa_{tr} \\ \Omega_{tr}, & \text{if } \kappa \geq \kappa_{tr} \end{cases} \quad (12)$$

where  $\kappa$  is the effective plastic strain;  $\kappa_{cm}$  is the plastic strain when the maximum compressive stress is reached;  $\kappa_{cr}$  is the ultimate plastic strain in compression;  $\Omega_{ci}$  is the relative tension at the start of the plastification;  $\Omega_{cr}$  is the residual relative stress in compression;  $\kappa_{tr}$  is the plastic strain when the residual tensile stress is reached;  $\Omega_{tr}$  is the residual relative stress in tension. In order to approximate, as much as possible, the shape of the hardening and softening laws of the two models (USERMAT and DP-CONCRETE), the values of  $\Omega_{ci} = 0.4$ ,  $\Omega_{cr} = 0.65$ ,  $\Omega_{tr} = 0.02$  and  $\kappa_{tr} = 0.001$  were adopted; and the parameters  $\kappa_{cm}$  and  $\kappa_{cr}$  were calculated with Equations 13 and 14, so that the total strains (elastic added to the plastic ones) in compression are equal to  $\epsilon_{c1}$  when the concrete reaches the maximum stress, and to  $\epsilon_{c,lim}$  when the concrete reaches the residual stress.

$$\kappa_{cm} = \epsilon_{c1} - \frac{f_{cm}}{E_c} \quad (13)$$

$$\kappa_{cr} = \varepsilon_{c,lim} - \frac{\Omega_{cr} \cdot f_{cm}}{E_c} \tag{14}$$

Given the fact that in the DP-CONCRETE model the cracking is simulated by increments of plastic strains, it is recommended to use elastic materials at stress concentration points due to external loads, such as at the supports, to avoid an unreal level of strains. In this work, the vertical supports are applied directly to the steel profile, so they do not constitute a problem in this regard. However, the connectors, being represented by discrete spring elements, impose concentrated shear loads on the steel-concrete interface. Thus, to avoid the excessive increase of plastic deformations in this region, it was decided to add a fictitious plate on the lower face of the slab, along the interface, formed by SHELL281 8-node shell elements, with 1 mm thickness, as shown in Figure 8. The plate material is admitted as linear elastic and has the same modulus of elasticity as the concrete.

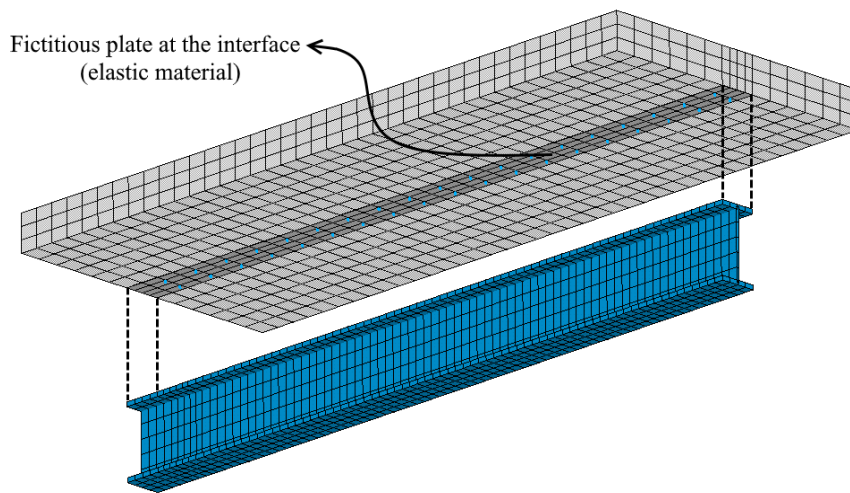


**Figure 8.** Fictitious plate of elastic material added at the interface between steel and concrete in the DP-Concrete model.

### 2.3 Boundary Conditions

The models were developed considering symmetry, thus only half of the beam was modeled. The nodes located near the first support, at the inferior flange of the profile, had the displacements in y and z constrained; and all the nodes located at the midspan had the displacements in x and rotation in y and z constrained. The total applied load on the experiment was divided by two, because of the symmetry, and then it was distributed evenly on the central nodes on the superior face of the concrete slab. These boundary conditions are highlighted in Figure 9. For the solution of the nonlinear system, it was adopted the full Newton-Raphson method.

### 2.4 Comparison to other numerical models

In Table 1 the main characteristics of the developed models are presented, and they are compared to models from previous works [1], [8], [12]–[15]. It can be observed that the employed strategy, in terms of geometry and element types, approaches the strategy used by [8]: the main differences are in the adopted material models for the concrete and in the choice of more current elements. However, it maintains the same constructive logic, using hexahedral solid elements for the slab, spring elements for the connectors and shell elements for the steel profile.

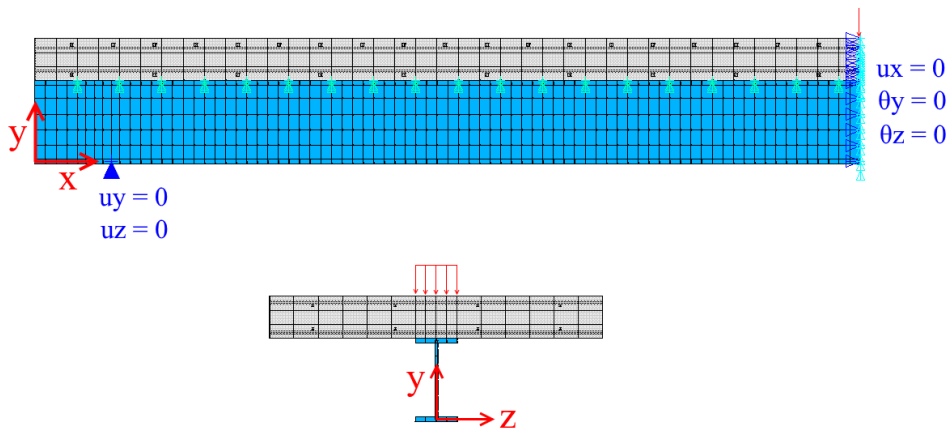


Figure 9. Numerical model of beam A2 with the adopted boundary conditions.

In the present work, discrete embedded elements were used for modeling the reinforcement steel bars of the concrete slab, differently from other works that employed ANSYS [1], [8], in which layers of distributed reinforcement were adopted, once the element SOLID65, used by them, is not compatible with discrete embedded elements. In the CEMACOM model [13]–[15], in which the slab is modeled by degenerated shell elements, the reinforcement is also distributed in layers. For the constitutive relation of the reinforcement steel [1], [8] adopted perfect elastoplastic models, as in the present work, while [13]–[15] considered linear hardening.

Table 1. Comparison between numerical models.

Model	Software	Steel profile	Connectors	Concrete slab
Gattesco [12]	Authorial	Bar elements. Nonlinear hardening.	Spring elements. Curve from push-out test.	Bar elements. Nonlinear constitutive model.
CEMACOM [13]–[15]	Authorial	Shell elements. von Mises criterion with linear hardening.	Bar elements. Curve from push-out test.	Degenerated shell elements. Modified Drucker-Prager model.
Kotinda [1]	ANSYS	Shell elements SHELL43. von Mises criterion with nonlinear hardening [12].	Bar elements BEAM189. von Mises criterion with linear hardening.	Hexahedral elements SOLID65. Model <i>concrete</i> [17].
Queiroz <i>et al.</i> [8]	ANSYS	Shell elements SHELL43. von Mises criterion with nonlinear hardening [12].	Spring elements COMBIN39. Curve from push-out test.	Hexahedral elements SOLID65. Model <i>concrete</i> [17].
Present analysis	ANSYS	Shell elements SHELL181. von Mises criterion with nonlinear hardening [12].	Spring elements COMBIN39. Curve from push-out test.	Hexahedral elements SOLID186. Models: (i) Usermat (ii) DP-Concrete

### 3 ANALYZED EXAMPLES

Two beams that were experimentally tested by Chapman and Balakrishnan [9], denominated A2 and E1, were numerically analyzed in this article. The selection of these beams is justified for comparison of results, once they were also numerically analyzed by previous works [1], [8], [12], [14], [15]. The geometry of the two beams are the same, and the differences between them are in the connectors disposition and in the materials data, as presented in Figure 10 and in Table 2. More details about the tests can be obtained in Chapman and Balakrishnan [9].

The numerical model of beam A2 is illustrated in Figure 9. The concrete's data that were not provided by Chapman and Balakrishnan [9] were calculated according to the model code *fib2010* [26], using the mean compressive strength. For the Usermat model it was used the initial tangent modulus of elasticity ( $E_{ci}$ ), while for the DP-Concrete model it was used the reduced modulus of elasticity ( $E_c = \alpha_i \cdot E_{ci}$ ), once the latter admits an elastic linear stage in compression until reaching the stress of  $0.4 \cdot f_{cm}$ . The parameters  $m$  and  $n$  for the connectors curve, given in equation [2], were adjusted according to the results obtained from push-out tests, which were provided by Chapman and Balakrishnan [9], as shown in Figure 11. All adopted values for connectors, steel and concrete are presented in Table 2.

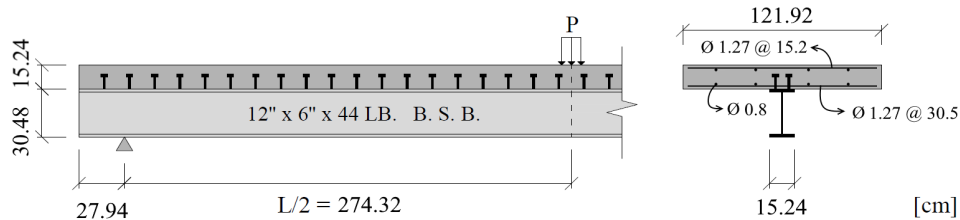


Figure 10. Geometry of the beams tested by Chapman and Balakrishnan [9].

Table 2. Materials data.

Beam		A2	E1	Unit	Source	
Connectors	Total number of connectors	76	100	-	Chapman and Balakrishnan [9]	
	Number of rows	2	2	-	Chapman and Balakrishnan [9]	
	Height	101.6	50.8	mm	Chapman and Balakrishnan [9]	
	Diameter	19	12.7	mm	Chapman and Balakrishnan [9]	
	Ultimate shear force ( $Q_u$ )	120.6	63.76	kN	Chapman and Balakrishnan [9]	
	Parameter $m$	1.2	1.15	1/mm	Ollgaard <i>et al.</i> [23]	
	Parameter $n$	0.55	0.5	-	Ollgaard <i>et al.</i> [23]	
Steel profile	Modulus of elasticity ( $E$ )	Flanges	20216	20520	kN/cm <sup>2</sup>	Chapman and Balakrishnan [9]
		Web	20368	19912	kN/cm <sup>2</sup>	Chapman and Balakrishnan [9]
	Yield strength ( $f_y$ )	Flanges	23	24,5	kN/cm <sup>2</sup>	Chapman and Balakrishnan [9]
		Web	23.9	29.2	kN/cm <sup>2</sup>	Chapman and Balakrishnan [9]
	Ultimate strength ( $f_u$ )	Flanges	41	45.8	kN/cm <sup>2</sup>	Chapman and Balakrishnan [9]
		Web	41.8	45.3	kN/cm <sup>2</sup>	Chapman and Balakrishnan [9]
	Ratio $\epsilon_{th}/\epsilon_y$	Flanges	4.9	2.2	-	Chapman and Balakrishnan [9]
		Web	7.6	1	-	Chapman and Balakrishnan [9]
	Tangent modulus ( $E_h$ )	Flanges	350	350	kN/cm <sup>2</sup>	Kotinda [1]
		Web	350	350	kN/cm <sup>2</sup>	Kotinda [1]
Concrete slab	Uniaxial compressive strength ( $f_{cm}$ )	2.69	3.27	kN/cm <sup>2</sup>	Chapman and Balakrishnan [9]	
	Uniaxial tensile strength ( $f_{ctm}$ )	0.21	0.25	kN/cm <sup>2</sup>	FIB [26]	
	Biaxial compressive strength ( $f_{c2m}$ )	3.16	3.82	kN/cm <sup>2</sup>	FIB [26]	
	Stress $\sigma_{com}$ (on the compressive meridian)	-24	-24	kN/cm <sup>2</sup>	FIB [26]	
	Stress $\tau_{com}$ (on the compressive meridian)	15.3	15.1	kN/cm <sup>2</sup>	FIB [26]	
	Initial tangent modulus of elasticity ( $E_{ci}$ )	2990	3191	kN/cm <sup>2</sup>	FIB [26]	
	Reduced modulus of elasticity ( $E_c$ )	2575	2790	kN/cm <sup>2</sup>	FIB [26]	
	Secant modulus of elasticity ( $E_{c1}$ )	1300	1480	kN/cm <sup>2</sup>	FIB [26]	
	Strain at the max. compressive stress ( $\epsilon_{c1}$ )	2.1	2.2	‰	FIB [26]	
Ultimate compressive strain ( $\epsilon_{c,lim}$ )	3.5	3.5	‰	FIB [26]		
Slab	Modulus of elasticity ( $E$ )	20500	20500	kN/cm <sup>2</sup>	Kotinda [1]	
Reinforcement	Yield strength ( $f_y$ )	32	32	kN/cm <sup>2</sup>	Kotinda [1]	

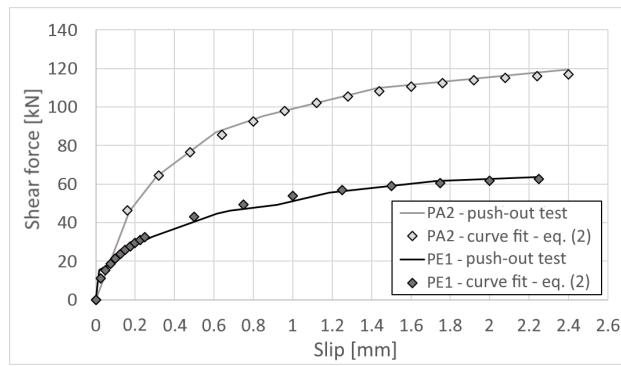


Figure 11. Curve fitting of Equation 2 to the experimental results of the push-out tests.

#### 4 RESULTS AND DISCUSSION

Figures 12 and 13 present the diagram of the applied load versus vertical displacement at midspan for the beams A2 and E1, respectively. Besides the obtained results from the developed model, the results obtained by previous works [1], [8], [12], [14], [15] and the experimental results [9] are also presented.

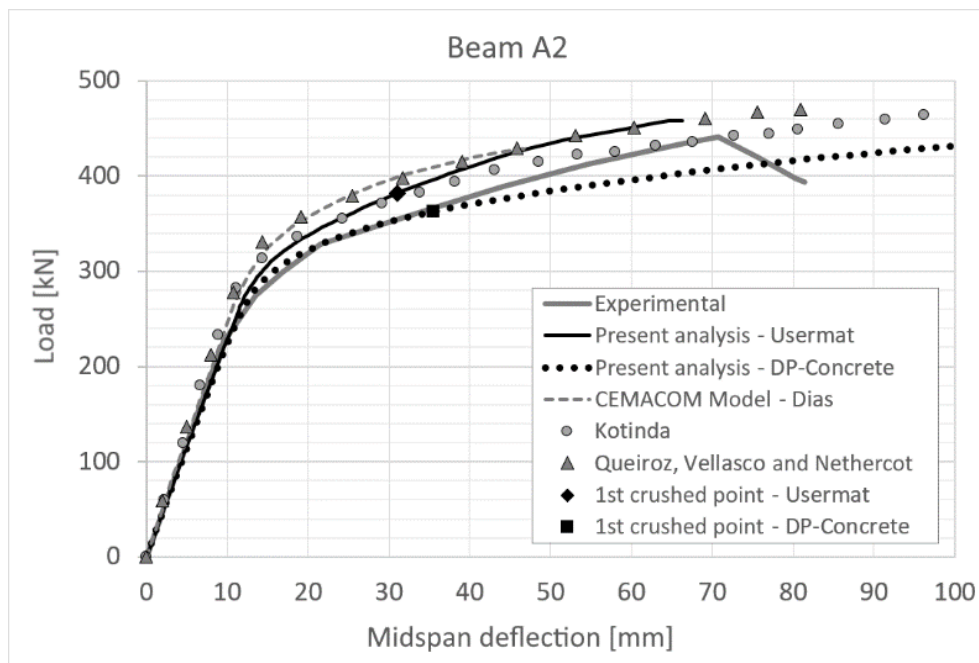


Figure 12. Load-deflection curve – beam A2.

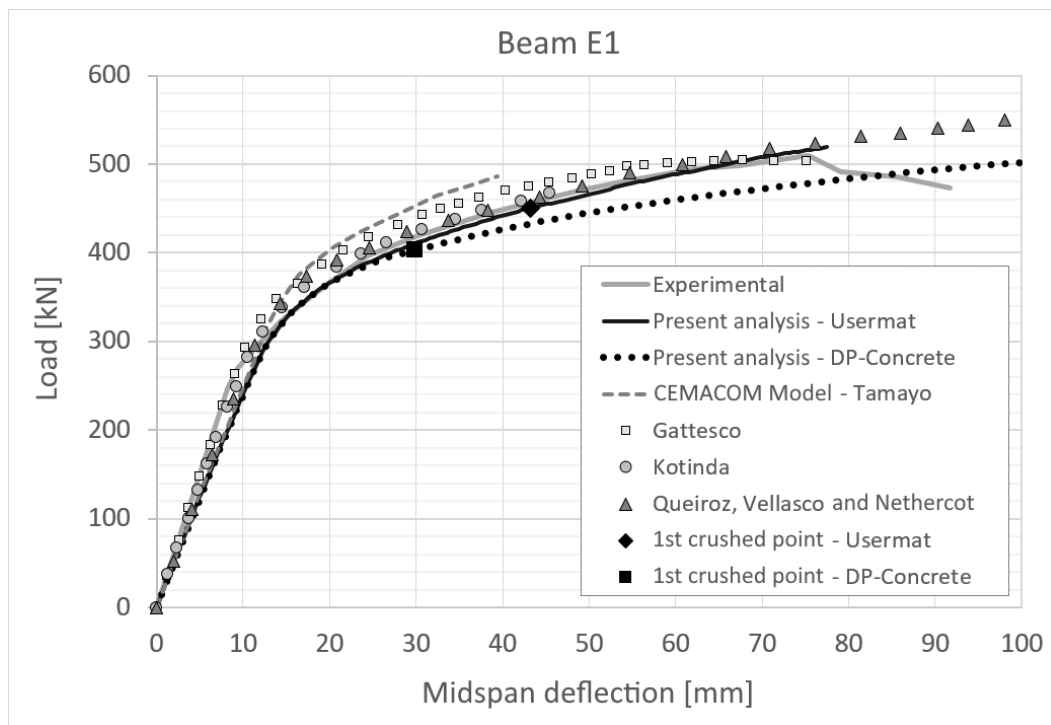


Figure 13. Load-deflection curve – beam E1.

It is observed that both of developed models in this work properly simulated the global behavior of beams A2 and E1, with the DP-Concrete model achieving the best results for beam A2, and the Usermat model for beam E1. In comparison to the models from previous works, it is verified that, in both analyzed beams, the Usermat model presents results relatively near to the obtained by Queiroz *et al.* [8] and by Kotinda [1]. These authors also employed ANSYS, despite the facts that they used different finite elements for profile and slab, a different material model for concrete, and, in the case of Kotinda [1], a different strategy for the connectors modeling. The CEMACOM model [14], [15] presented a greater stiffness in the plastic regime, with smaller displacements for the same load levels, but simulated with good precision the experimental failure loads.

The models with Usermat and with DP-Concrete presented almost identical results in the elastic regime, and differed in the final loading stage, when the concrete reaches high stresses. This difference of behavior in high compression stresses was already expected, once, after the maximum compressive stress is reached, the DP-Concrete model presents linear softening, while the Usermat model presents a curvy softening, as illustrated in Figure 14, that makes a comparison between the constitutive relation in compression used by the two models for the concrete of beam A2. Therefore, the Usermat model is stiffer in the plastic regime. It can be observed, in Figure 12, that the small differences between the obtained results for beam A2 start at the applied load of 300 kN and become more significant from the applied load of 350 kN. When analyzing the equivalent plastic deformation in DP-Concrete model, it was verified that the compressed elements at the midspan started the softening process from the applied load of 343 kN. In Figure 15, the top views of beam A2 for different load levels are presented, and it is indicated the points in which the equivalent plastic strains exceed the value of the plastic strain associated to the maximum stress on the compression constitutive model ( $\kappa_{cm}$ ).

It can be observed that the bigger the number of elements in softening, the more significant becomes the difference between the results of the models. However, it is important to note that other factors may influence the response, for example the shape of the yield surfaces in compression (Drucker-Prager or Ottosen) and the cracking in the regions of the slab under tension. In fact, as shown in Figure 12, differences in the results already exist before the compressive softening, for the applied load between 300 kN and 343 kN. Nevertheless, these initial differences are small, and practically insignificant in comparison to the differences after the softening. Therefore, it is possible to conclude that the smaller stiffness of the DP-Concrete model in the plastic regime can be mainly justified due to the differences between the softening curves in compression.

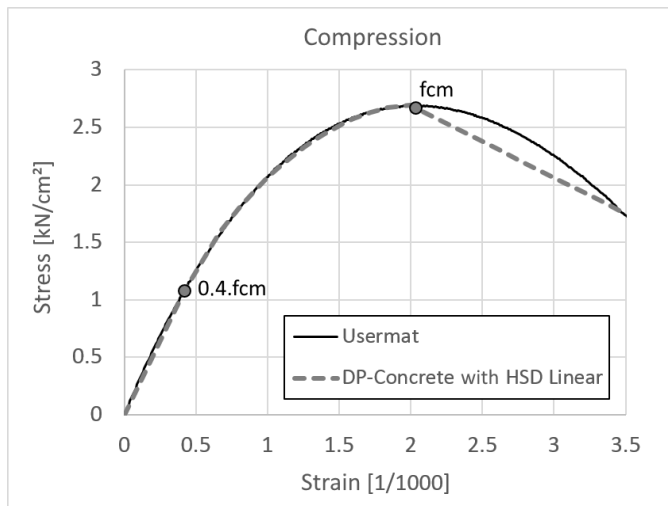


Figure 14. Comparison between the constitutive relations for compression used by the models for beam A2.

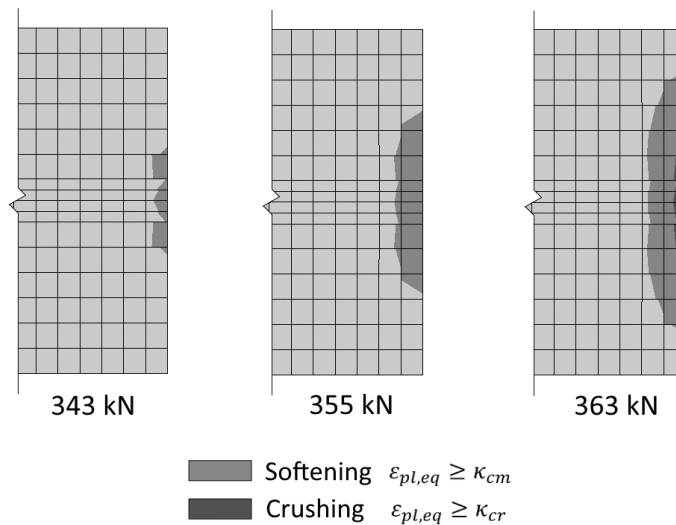


Figure 15. Top views of beam A2 concrete slab midspan: evolution of softening obtained with the DP-Concrete model for different load levels.

#### 4.1 Analysis of crushing

Both of analyzed beams failed by concrete crushing in the experimental tests. The failure loads registered by Chapman and Balakrishnan [9] were 441 kN and 510 kN for beams A2 and E1, respectively.

In Usermat, it was programmed the generation of a text file that lists the elements and their respective crushed integration points at each load substep. In this model, the crushing criterion is presented in relation to deformations. When the equivalent strain exceeds the ultimate strain in compression, adopted as 3.5/1000 in this paper, it admits that the integration point has crushed, and its stresses are zeroed. Analyzing the generated text file, it is verified that the first integration points were crushed at the loads of 382 kN and 450 kN for beams A2 and E1, respectively. These loads are highlighted in Figures 12 and 13. In subsequent substeps, a bigger number of elements and integration points have crushed, and the iterative process continues until ANSYS cannot reach the balance between internal and external forces, so the solution is interrupted. The loads reached at the end of convergence were 458 kN and 518 kN, for beams A2 and E1, respectively, as it is presented in Table 3. It can be observed, for beams A2 and E1, that the crushing failure loads obtained by the experimental tests are between the numerical values of the first crushed integration point and the end of convergence.

In DP-Concrete model, on the other hand, it is not possible to program the generation of a text file to control the number of crushed integration points at each substep, once this model is native from ANSYS, thus it cannot be customized. An alternative to control the crushing is to do a graphical analysis of the equivalent plastic strain evolution on the compressed elements. In this paper, it was adopted a simplified criterion that when the equivalent plastic strain of each point exceeds the ultimate plastic strain in compression ( $\kappa_{cr}$ ), the crushing starts. Top views of beam A2 slab are presented in Figure 16, where the evolution of crushed points is illustrated for different load levels: 363 kN (first points are crushed), 379 kN, 395 kN and 447 kN (end of convergence). As can be observed, despite reaching the load of 447 kN at the last calculated substep, at this stage the crushing is well advanced, with many crushed elements. Therefore, it can be concluded that the numerical model indicates that the failure of beam A2 may occur before, for a load between 363 kN and 447 kN. The experimental failure load, equal to 441 kN, is contained in this interval. The same analysis was performed for beam E1, and it was verified that the first points were crushed at the load of 403 kN and that the end of convergence occurred at 549 kN. Again, the experimental failure load, in this case equal to 510 kN, is contained in this interval. The mentioned results are presented in Table 3. It is worth mentioning that, for both analyzed beams, the load at the end of convergence was bigger than the experimental failure load, which attests the importance to perform a critical analysis of the strain's evolution in the slab. Also, it is worth mentioning that the end of convergence can be considerably influenced by numerical parameters adopted, for example: error tolerance, number of substeps, number of iterations at each substep, among others – one more reason why the failure load obtained by a numerical model must be carefully analyzed.

**Table 3.** Crushing loads.

Model		Beam A2		Beam E1	
		Load P [kN]	(P-P <sub>exp</sub> )/P <sub>exp</sub>	Load P [kN]	(P-P <sub>exp</sub> )/P <sub>exp</sub>
Experimental	P <sub>exp</sub>	441	-	510	-
Numerical (Usermat)	P <sub>1</sub>	382	-13.38%	450	-11.76%
	P <sub>2</sub>	458	3.85%	518	1.57%
Numerical (DP-Concrete)	P <sub>1</sub>	363	-17.69%	403	-20.98%
	P <sub>2</sub>	447	1.36%	549	7.65%

Where: P<sub>1</sub> = load at the first crushed point; P<sub>2</sub> = load at the end of convergence.

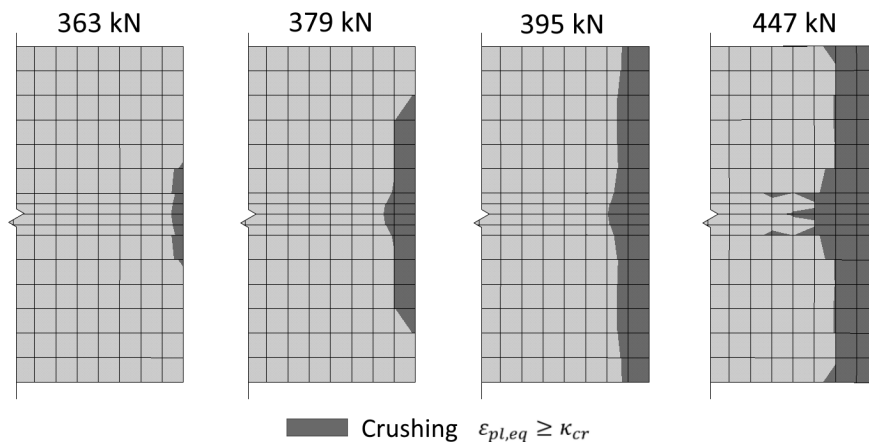


**Figure 16.** Top views of beam A2 concrete slab midspan: evolution of crushing obtained with the DP-Concrete model for different load levels.

The convergence can also stop due to the failure of other component of the structure. Therefore, beyond verifying the strains in the concrete slab, it is recommendable to analyze the evolution of shear forces in the connectors and the stresses in the steel profile, in order to certify that the model really captured the crushing of concrete. Regarding the connectors, it was verified that in all analyses the maximum shear forces did not exceed 55% and 89% of the ultimate

shear forces ( $Q_u$ ) obtained by push-out tests for beams A2 and E1, respectively. Regarding the steel profile, despite the plastification had developed significantly in the region near the midspan at the end of convergence in both beams, it was verified that the von Mises stresses did not exceed, in any analyzed case, the value of 80% of the steel ultimate strength. For illustration, Figure 17 presents the von Mises stresses in the steel profile of beam E1, obtained by the numerical model with Usermat, for the failure load 518 kN: the maximum stress is 34.14 kN/cm<sup>2</sup>, while the ultimate strength of the steel is 45.3 kN/cm<sup>2</sup>. Therefore, it is possible to conclude that the models in fact are capturing the concrete crushing, and not the failure of other components.

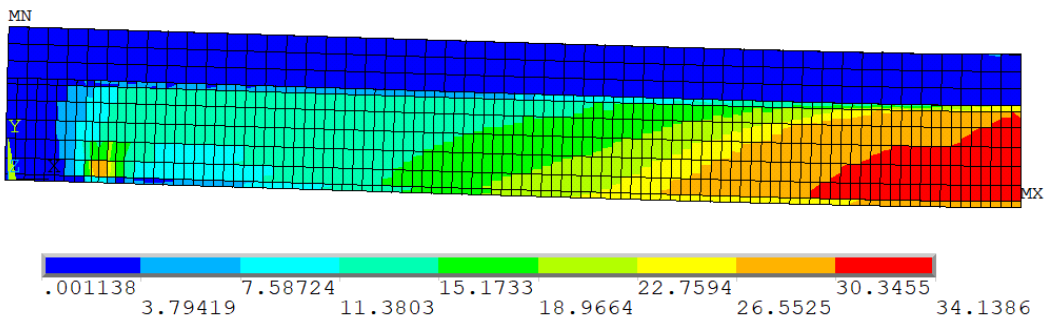


Figure 17. Von Mises stresses in beam E1 at the applied load of 518 kN (Usermat model).

#### 4.2 Importance of adding a fictitious elastic plate in the DP-Concrete model

Figure 18 presents the curves of applied load versus vertical displacement at midspan obtained for beam E1, with and without the fictitious plate, composed by elastic material, added to the inferior face of the slab, at the interface between steel and concrete.

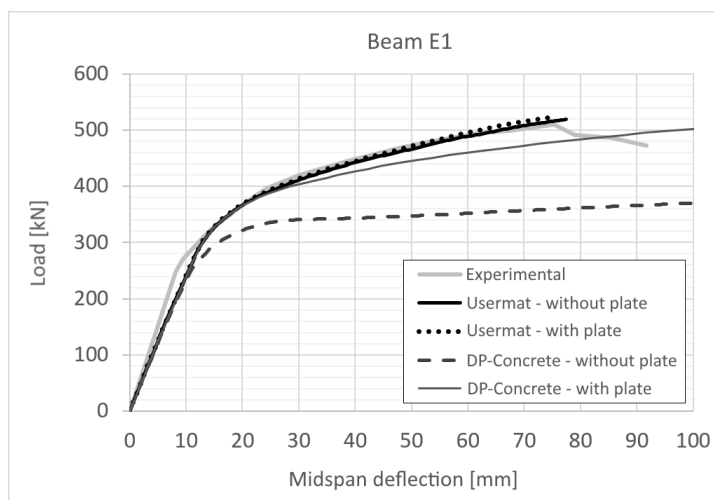


Figure 18. Influence of the fictitious elastic plate at the interface on the beam E1 results.

It can be observed that the plate practically does not change the global behavior of the Usermat model, but it has significant importance in the DP-Concrete model. This fact occurs because, without the plate, the plastic strains in the cracked concrete near the connectors increase in an excessive way, in function of the stress concentrations caused by the concentrated shear forces imposed by the discrete spring elements. In this case, the stresses are not correctly distributed between profile and slab, and the composite beam stiffness decreases considerably when its behavior becomes nonlinear. The same does not occur with the Usermat model, in which the crack is simulated by changing the stiffness matrices of the cracked finite elements.

## 5 CONCLUSIONS

Two numerical models were developed in ANSYS to analyze composite beams, one with a material model recently made available by the software, denominated DP-Concrete, and the other with a customized model programmed in the interface Usermat, developed by Lazzari *et al.* [25], considering the Ottosen criterion [19] for the concrete modeling. Both were developed with finite elements classified as current technology by the ANSYS documentation, version 19.2 [18]. The obtained results for the beams A2 and E1 of Chapman and Balakrishnan [9] were quite satisfactory, presenting a good correlation with the experimental results, as with the results by numerical analysis of previous works [1], [8], [12], [14], [15].

Two alternatives were proposed to carefully analyze the concrete crushing, instead of simply considering the load at the end of convergence as the failure load of the composite beam. In the customized model with Usermat it was programmed the generation of a text file that lists the crushed integration points at each calculated substep. Thus, it is possible to verify when the first point is crushed. Based on a similar idea, the start of crushing in DP-Concrete model was analyzed with a graphical investigation of the equivalent plastic strains at each substep. The delimited intervals between the start of crushing and the end of convergence, obtained with both numerical models, contain the respective experimental failure loads, for both analyzed beams. It was verified that the other components of the composite beams did not reach their respective failure stresses. Therefore, it is possible to conclude that the numerical models were able to capture the concrete crushing phenomenon.

The DP-Concrete model presented good results when a fictitious elastic plate was added at the interface between steel and concrete, aiming to avoid the excessive increase of plastic strains due to the cracking in this region. Without this plate, the quality of results decreased considerably. It was also verified that the same plate, when added to the Usermat model, did not change the results significantly.

At last, it is concluded that the proposed strategies of finite element modeling are proper to the numerical simulation of composite beams. The possibility of using two different material models to simulate the concrete's behavior allows the comparison of results between them, increasing the reliability of the analyses.

## ACKNOWLEDGEMENTS

The authors are grateful to CAPES and CNPq for the financial support for this research, and to CEMACOM/UFRGS for providing the infrastructure for the development of this work.

## REFERENCES

- [1] T. I. Kotinda, "Modelagem numérica de vigas mistas aço-concreto simplesmente apoiadas: ênfase ao estudo interface laje-viga," M.S. thesis, Esc. Eng. São Carlos, Univ. São Paulo, São Carlos, 2006. <http://dx.doi.org/10.11606/D.18.2006.tde-22062006-110301>.
- [2] J. Nie, V. Xiao, and L. Chen, "Experimental studies on shear strength of steel-concrete composite beams," *J. Struct. Eng.*, vol. 130, no. 8, pp. 1206–1213, 2004, [http://dx.doi.org/10.1061/\(ASCE\)0733-9445\(2004\)130:8\(1206\)](http://dx.doi.org/10.1061/(ASCE)0733-9445(2004)130:8(1206)).
- [3] W. Pfeil and M. Pfeil, *Estruturas de Aço – Dimensionamento Prático de Acordo com a NBR 8800:2008*, 8th ed. Rio de Janeiro: LTC, 2013.
- [4] Associação Brasileira de Normas Técnicas, *Projeto de Estruturas de Aço e de Estruturas Mistas de aço e Concreto de Edifícios*, ABNT NBR 8800, 2008.
- [5] Instituto Português da Qualidade, *Projecto de Estruturas Mistas Aço-Betão – Parte 1-1 – Regras Gerais e Regras para Edifícios*, NP EN 1994-1-1, 2011.
- [6] European Committee for Standardization, *Eurocode 4: Design of Composite Steel and Concrete Structures – Part 1-1: General Rules and Rules for Buildings*, CEN EN 1994-1-1, 2004.
- [7] A. R. Silva, "Análise numérica de elementos estruturais com interação parcial," Ph.D. dissertation, Univ. Fed. Ouro Preto., Ouro Preto, 2010. [Online]. Available: <http://www.repositorio.ufop.br/handle/123456789/2254>
- [8] F. D. Queiroz, P. C. G. S. Vellasco, and D. A. Nethercot, "Finite element modelling of composite beams with full and partial shear connection," *J. Construct. Steel Res.*, vol. 63, no. 4, pp. 505–521, 2007, <http://dx.doi.org/10.1016/j.jcsr.2006.06.003>.
- [9] J. C. Chapman and S. Balakrishnan, "Experiments on composite beams," *Struct. Eng.*, vol. 42, no. 11, pp. 369–383, 1964.
- [10] R. G. Slutter and G. C. J. Driscoll, "Flexural strength of steel-concrete composite beams," *J. Struct. Div.*, vol. 91, no. 2, pp. 71–99, 1965.
- [11] J. A. Grant, R. Slutter, and J. W. Fisher, "Composite beams with formed steel deck," *Eng. J.*, vol. 14, pp. 24–43, 1977.
- [12] N. Gattesco, "Analytical modeling of nonlinear behavior of composite beams with deformable connection," *J. Construct. Steel Res.*, vol. 52, no. 2, pp. 195–218, 1999, [http://dx.doi.org/10.1016/S0143-974X\(99\)00026-7](http://dx.doi.org/10.1016/S0143-974X(99)00026-7).

- [13] J. L. P. Tamayo, I. B. Morsch, and A. M. Awruch, "Short-time numerical analysis of steel–concrete composite beams," *J. Braz. Soc. Mech. Sci. Eng.*, vol. 37, no. 4, pp. 1097–1109, 2015, <http://dx.doi.org/10.1007/s40430-014-0237-9>.
- [14] J. L. P. Tamayo, "Análise numérica de vigas mistas pelo método dos elementos finitos," M.S. thesis, Prog. Pós-grad. Eng. Civ., Univ. Fed. Rio Grande do Sul, Porto Alegre, 2011. [Online]. Available: <https://hdl.handle.net/10183/30117>
- [15] M. M. Dias, "Análise numérica de vigas mistas aço-concreto pelo método dos elementos finitos: efeitos de longa duração," M.S. thesis, Prog. Pós-grad. Eng. Civ., Univ. Fed. Rio Grande do Sul, Porto Alegre, 2013. [Online]. Available: <https://hdl.handle.net/10183/77726>
- [16] L. R. Marconcin, R. D. Machado, and M. A. Marino, "Numerical modeling of steel-concrete composite beams," *IBRACON Struct. Mater. J.*, vol. 3, no. 4, pp. 449–476, 2010, <http://dx.doi.org/10.1590/S1983-41952010000400006>.
- [17] K. J. Willam and E. P. Warnke, "Constitutive model for the triaxial behavior of concrete," in *LABSE Seminar on Concrete Structures Subjected to Triaxial Stresses*, Bergamo, Italy, 1974.
- [18] ANSYS Inc., *ANSYS Help System – Version 19.2*, 2018.
- [19] N. S. Ottosen, "A failure criterion for concrete," *J. Eng. Mech. Division*, vol. 103, no. 4, pp. 527–535, 1977.
- [20] K. J. Bathe and E. N. Dvorkin, "A formulation of general shell elements: the use of mixed interpolation of tensorial components," *Int. J. Numer. Methods Eng.*, vol. 22, no. 3, pp. 697–722, 1986, <http://dx.doi.org/10.1002/nme.1620220312>.
- [21] R. H. MacNeal and R. L. Harder, "A refined four-noded membrane element with rotational degrees of freedom," *Comput. Struct.*, vol. 28, no. 1, pp. 75–84, 1988, [http://dx.doi.org/10.1016/0045-7949\(88\)90094-6](http://dx.doi.org/10.1016/0045-7949(88)90094-6).
- [22] O. C. Zienkiewicz, R. L. Taylor, and J. Z. Zhu, *The Finite Element Method: Its Basis and Fundamentals*, 7th ed. Oxford, UK: Elsevier, 2013.
- [23] J. G. Ollgaard, R. G. Slutter, and J. W. Fisher, "Shear strength of stud connectors in lightweight and normalweight concrete," *Eng. J.*, vol. 8, pp. 55–64, 1971. [Online]. Available: <https://preserve.lehigh.edu/engr-civil-environmental-fritz-lab-reports/2010>
- [24] F. P. M. Quevedo, R. J. Schmitz, I. B. Morsch, A. Campos Filho, and D. Bernaud, "Customization of a software of finite elements to analysis of concrete structures: long-term effects," *IBRACON Struct. Mater. J.*, vol. 11, no. 4, pp. 696–718, 2018, <http://dx.doi.org/10.1590/s1983-41952018000400005>.
- [25] P. M. Lazzari, A. Campos Fo., B. M. Lazzari, A. R. Pacheco, and R. R. S. Gomes, "Numerical simulation of the constructive steps of a cable-stayed bridge using ANSYS," *Struct. Eng. Mech.*, vol. 69, no. 3, pp. 269–281, 2019., <http://dx.doi.org/10.12989/sem.2019.69.3.269>.
- [26] Fédération Internationale du Béton, *Fib Model Code for Concrete Structures 2010*, 2013.
- [27] M. Martinelli, "Modelagem de situações de punção em lajes de concreto armado através do método dos elementos finitos," M.S. thesis, Prog. Pós-grad. Eng. Civ., Univ. Fed. Rio Grande do Sul, Porto Alegre, 2003. [Online]. Available: <https://hdl.handle.net/10183/2299>

---

**Author contributions:** Conceptualization, ME Benincá, RJ Schmitz and IB Morsch; Investigation, ME Benincá and RJ Schmitz; Methodology, ME Benincá, RJ Schmitz and IB Morsch; Software, ME Benincá and RJ Schmitz; Supervision, IB Morsch; Validation, ME Benincá, RJ Schmitz and IB Morsch; Visualization, ME Benincá; Writing - original draft, ME Benincá; Writing - review & editing, ME Benincá, RJ Schmitz and IB Morsch.

**Editors:** José Marcio Calixto, José Luiz Antunes de Oliveira e Sousa, Guilherme Aris Parsekian



## ORIGINAL ARTICLE

## Parametric analysis of analytical solutions of the rollover of precast beams on bearing pads

Análise paramétrica da instabilidade por tombamento de vigas pré-moldadas sobre almofadas de apoio

Marina Fernandes Alvarenga Oliveira<sup>a</sup>

Pablo Augusto Krahl<sup>b</sup>

Maria Cristina Vidigal de Lima<sup>a</sup>

<sup>a</sup>Universidade Federal de Uberlândia – UFU, Faculdade de Engenharia Civil, Uberlândia, MG, Brasil

<sup>b</sup>Universidade de Campinas – UNICAMP, Faculdade de Engenharia, Arquitetura e Urbanismo, Campinas, SP, Brasil

Received 04 July 2019

Accepted 26 February 2020

**Abstract:** Due to low stiffness to lateral bending, long prestressed precast concrete beams are subject to lateral instability. For this reason, the safety analysis of these beams during the transitory stages of transport, lifting and assembly is fundamental. This work presents a nonlinear analytical model for the parametrical analysis of beams on bearing pads in their definitive location, without the effective connections being made. Such a solution determines a critical load of instability and considers the geometry of the cross-section, physical characteristics of the materials as well as geometric imperfections. A parametrical simulation is performed for the initial eccentricity, the initial rotation of the beam, concrete resistance, bearing pads dimensions, and the cross-section of the beam. The results show that the parameters of most considerable influence on beam stability are rotation stiffness of the bearing and the geometric characteristics of the cross-section of the beam, which can result in a reduction of about 50% of the critical rollover load. In addition, the cracking load may, in some cases, be close to the critical toppling load.

**Keywords:** stability, precast beams, analytical study, parametric study, Monte Carlo simulation.

**Resumo:** Devido à baixa rigidez à flexão lateral, vigas pré-moldadas protendidas de concreto longas e esbeltas estão sujeitas aos riscos de instabilidade lateral. Nestes termos, é fundamental analisar a segurança dessas vigas durante as fases transitórias de transporte, içamento e montagem. Este trabalho apresenta um modelo analítico não linear para análise paramétrica de vigas já posicionadas em seu local definitivo sobre almofadas de apoio, quando as ligações ainda não foram efetivadas. A força crítica de instabilidade lateral foi calculada considerando a geometria da seção transversal, as características físicas dos materiais, bem como imperfeições geométricas. Uma simulação paramétrica foi feita para a influência da excentricidade lateral inicial da viga, a rotação inicial do apoio, a resistência à compressão do concreto, as dimensões do aparelho de apoio e a seção transversal da viga. Os resultados mostram que os parâmetros de maior influência na estabilidade da viga foi a rigidez a rotação do apoio e as características geométricas da seção transversal da viga, podendo resultar em redução da ordem de 50% da força crítica de tombamento. Além disso, a força de início da fissuração, em alguns casos, pode estar bem próxima a força crítica de tombamento.

**Palavras-chave:** estabilidade, vigas pré-moldadas, estudo analítico, estudo paramétrico, simulação de Monte Carlo.

**How to cite:** M. F. A. Oliveira, P. A. Krahl, and M. C. V. Lima, “Parametric analysis of analytical solutions of the rollover of precast beams on bearing pads,” *Rev. IBRACON Estrut. Mater.*, vol. 13, no. 5, e13511, 2020, <https://doi.org/10.1590/S1983-41952020000500011>

**Corresponding author:** Marina Fernandes Alvarenga Oliveira. E-mail: [marinaalvarenga.engcivil@gmail.com](mailto:marinaalvarenga.engcivil@gmail.com)

**Financial support:** The authors would like to thank FAPEMIG (Public Call 01/2015-APQ00099-15) for the financial support.

**Conflict of interest:** Nothing to declare.



This is an Open Access article distributed under the terms of the Creative Commons Attribution License, which permits unrestricted use, distribution, and reproduction in any medium, provided the original work is properly cited.

## 1 INTRODUCTION

Precast and prestressed concrete beams are elements widely used in the most diverse types of construction systems. Such elements are found with increasing spans, slender cross-sections, and improved mechanical efficiency, due to the advance of technology associated with concretes that are more resistant, along with more precise and efficient manufacturing processes.

During the assembly process of a precast structure, it is common that its elements are maintained in temporary situations until the end of production. In the case of beams for bridges and viaducts, this occurs during the transportation, hoisting, and even after being placed in their permanent position, when there is still no slab or other structural bracing element necessary for guaranteeing the complete stability of such structures. In these stages, the beam is usually bi-supported, without restriction across all movements, and as such subject to actions that can interfere in its stability, which means there exists a high probability of rollover with rigid body rotation, accompanied by deformation and critical stresses.

Rollover of precast beams is a case of collapse due to lateral instability, where support devices produce little restriction to the rotation of the beam to its longitudinal axis. In this type of failure, there typically occurs a combination between lateral flexion, rigid body rotation (around the longitudinal axis) and twisting. The twisted portion usually is much less than the rigid body portion [1] and [2], which can thus be dismissed. There are those factors that directly influence the lateral stability of precast beams, such as the length of the beam, the geometry of the cross-section, in addition to lateral forces, as in the case of wind.

Several accidents caused by lateral instability of precast beams justifies the study on which this paper is based. In June of 2000, the Souvenir Boulevard Bridge, under construction in the city of Laval in Canada, suffered the partial collapse of various precast beams with a span of approximately 33.5 m. The cause of the accident was the inadequate conditions of the supports that produced a state of unstable equilibrium on the beams [3]. In 2007, nine out of the eleven precast beams collapsed that were part of the Red Mountain Freeway in Arizona, United States (Figure 1). Lateral instability caused one beam to collapse, triggering the fall of the eight remaining beams through a domino effect. The rollover of this beam was caused by a critical combination of many factors, such as geometric imperfections of the beam, bad positioning on the support, the presence of wind, and a lack of lateral bracing [4]. The study by Bairán and Cladera [5] analyzed the partial collapse of a structure covering a sports gymnasium, which was caused by the rollover of precast beams. According to these authors, the accident was due, possibly, to the inadequate positioning of the support device, as the position in which it was placed did not present sufficient stiffness to the lateral rotation, so that it guarantees the stability of the beam.



**Figure 1.** Beam collapse in Arizona (EUA). Source: Oesterle et al. [4]

Some analytical studies were performed to present solutions that verify the safety of precast beams on support devices. The study by Mast [1] proposed an equation, through the static equilibrium of moments for determining the safety factor of the beam in a transitory stage, while considering stiffness, rotation and superelevation of the support, the physical properties of the beam and the initial lateral eccentricity. The equation proposed by Mast [1] is considered in a normative sense by the PCI (Precast/Prestressed Concrete Institute), to evaluate the critical rollover load of a beam. Other authors also developed equations to determine the critical self-weight of the beam when supported by support devices, for example in Burgoyne and Stratford [6], Plaut and Moen [7], Lee et al. [8] and Lee [9], in addition to Krahl et al. [10]. Burgoyne and Stratford [6] did not consider the superelevation of the support, neither the initial eccentricity in their equation. Through their research, Plaut and Moen [7] developed an equation that considered a

curved beam under the action of its self-weight and wind. In Lee et al. [8], the proposal was put forward of an equation that also considered the influence of wind, but without initial eccentricity. Lee et al. [8] proposed an equation for a straight beam, under the influence of self-weight, but considered the effect of beam twisting. Krahl et al. [10], through the Rayleigh-Ritz method, proposed an equation for defining the critical load concentrated in the middle of the span, causing lateral instability of the beam, besides the definition of the critical load distributed uniformly, i.e., critical self-weight.

Hurff and Kahn [11] performed experimental analyzes on a beam of a 30.5 m length and cross-section of the BT-54 type, on an elastomeric bearing pad that was reinforced with four steel plates. To perform the test, a concentrated vertical load with a gravitational force simulator was employed, which does not offer resistance to lateral deformations or twisting. The authors concluded that the rigid body rotation to was more significant than rotation due to elastic deformations, and that the initial imperfections of the beam and rotation on the support are substantial when dealing with lateral stability.

This paper has as its objective to study the problem of lateral stability of beams during assembly of the structure onto elastomeric supports, usually in a bi-support arrangement, through an analytical approach. The elastomeric pad support device was chosen as the object of analysis, as it is widely used support in the construction of bridges and viaducts using precast beams. A schematic representation of the beam indicating the initial eccentricity and support rotation parameters are presented in Figure 2.

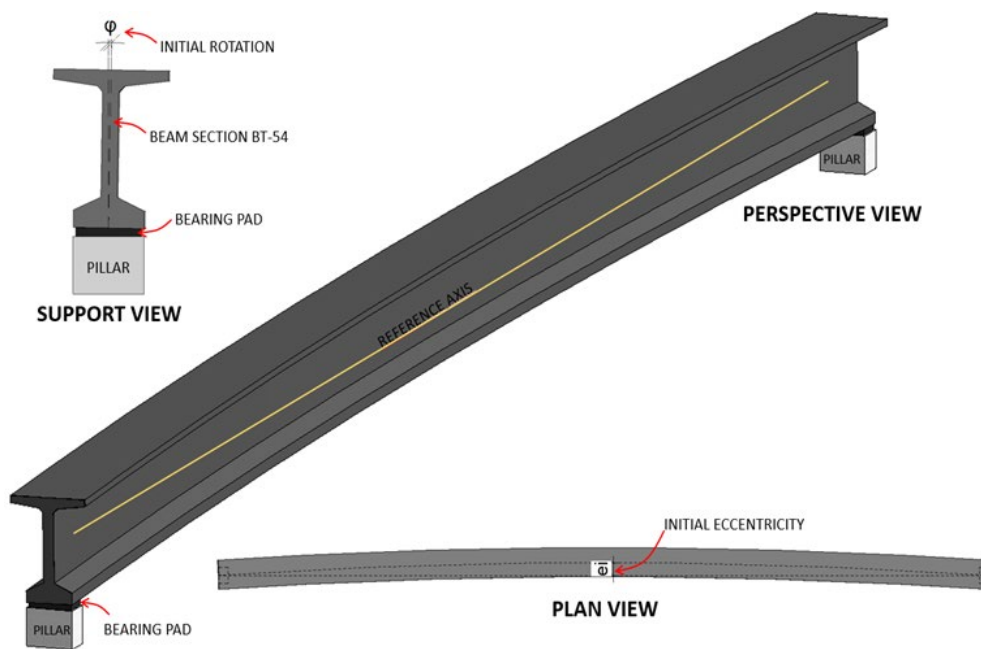


**Figure 2.** Scheme for the analyzed beam. Source: Authors.

The objective of the study was to propose an analytical solution to determine the rollover load with the rigid body rotation of the beam, due to conditions of imperfections of the beam, such as eccentricity and initial rotation, while analyzing the critical stress for initiating cracking of the beam due to additional stress of traction generated during tipping, as well as check for the influence of initial lateral eccentricity, the characteristics of the concrete, the cross-section of the beam and the rigidity of the pad in parametric analytical simulations.

The equations presented in this study for determining the critical rollover load of precast beams were developed with the use of the Rayleigh-Ritz method, which is based on the principle of stationary potential energy.

In order to evaluate the initial cracking of the beam, the calculation was presented for the maximum traction stress of the beam during the rollover, i.e., under the nonlinear geometric regime. Initial cracking was considered in this study, as the moment when traction stress on the beam is higher than the resistance to concrete traction.

Finally, a parametric analysis was developed based on the Monte Carlo simulation to verify the behavior of analytical solutions for the critical loads obtained. As a basis for the analysis, data were used from the beam tested by

Hurff and Kahn [11]. The analysis parameters were: initial lateral eccentricity, initial rotation on the support, the compressive strength of the concrete, dimension of the support device and the cross-section of the beam.

## 2 EQUATION FOR LATERAL INSTABILITY DUE TO ROLLOVER

The problem with the study of balance in nonlinear analysis of precast beams supported on support devices was developed in this paper employing the Rayleigh-Ritz method. This method is based on the principle of stationary potential energy and applies to linear as well as nonlinear structures, which are statistically determined. Therefore, it is possible to obtain the closed-form nonlinear analytic solution to structural problems. For such, one should determine an appropriate function that represents the geometric configuration of the structure concerning instability, through a linear combination of degrees of freedom  $\alpha_i$ . This function was used in the total energy equation  $\Pi$ , which consists of the sum of the internal energy  $U$  and the work carried out by external forces operating in the system  $V$ .

The development of the equations presented in Oliveira [12] and Krahl et al. [13] started with the definition of a trigonometric function due to the degree of freedom ( $\alpha_1$ ), for the lateral displacement of the beam when in a condition of instability.

The general trigonometric function presented in Equation represents lateral rotation due to bending, where  $L$  is the length of the beam and  $\alpha_n$  is a generalized variable that represents the maximum value of  $u_l$ , which is the lateral displacement of the beam. In the case of  $n = 1$ , which represents the first buckling mode of rollover instability, the constant  $\alpha_1$  is the maximum lateral displacement value in mid-span, and the curve is a single sine wave. Other buckling modes can be chosen for values higher than  $n$ . In addition, Equation 1 satisfies the essential boundary conditions of the beam.

$$u_l(x) = \sum_{n=0}^m \alpha_n \sin\left(\frac{n\pi x}{L}\right) \tag{1}$$

The total internal energy of the system is presented Equation 2, including the energy from the rotation of support devices. Highlighted here is that lateral instability of precast beams occurs mainly due to a combination of lateral bending displacements and rigid body rotation.

$$U = \frac{1}{2} \int_0^L (EI_y u_l''^2 + GJ \phi_1'^2 + EI_w \phi_1''^2) dx + k_\theta \phi_1^2 \tag{2}$$

Where  $EI_y$ ,  $GJ$ ,  $EI_w$  are the stiffness to lateral bending, St. Venant torsion and warping, respectively. The last two forms of stiffness were functionally canceled due to twisting,  $\phi_1$  being assumed as constant (rigid body rotation). The parameter  $k_\theta$  represents the rotational stiffness of the support devices and  $u_l$  the lateral displacement of the beam. Approximate solutions for the stiffness of the support, which is nonlinear, were necessary for solving the problem. Rotations were considered constant over the interval with a value of  $\phi_1$ .

In order to obtain the stability equation, the beam was considered as possessing an initial eccentricity ( $e_i$ ) and initial rotation ( $\phi_0$ ), and that is was supported at its extremities by elastomeric pads, subject to its self-weight. Under the condition of instability, the beam presents lateral and vertical displacement due to bending, besides rigid body rotation.

The function that describes the initial eccentricity along the beam axis ( $u_0$ ) is calculated according to Equation 3, where  $e_i$  is the initial mid-span eccentricity.

$$u_0(x) = e_i \sin\left(\frac{\pi x}{L}\right) \tag{3}$$

The tipping action was given by the product of the vertical displacements by the respective loads applied to the structural element. Figure 3 presents the displaced beam configuration due to action resulting from own weight, acting on the center of mass during rollover of the beam with initial imperfections.

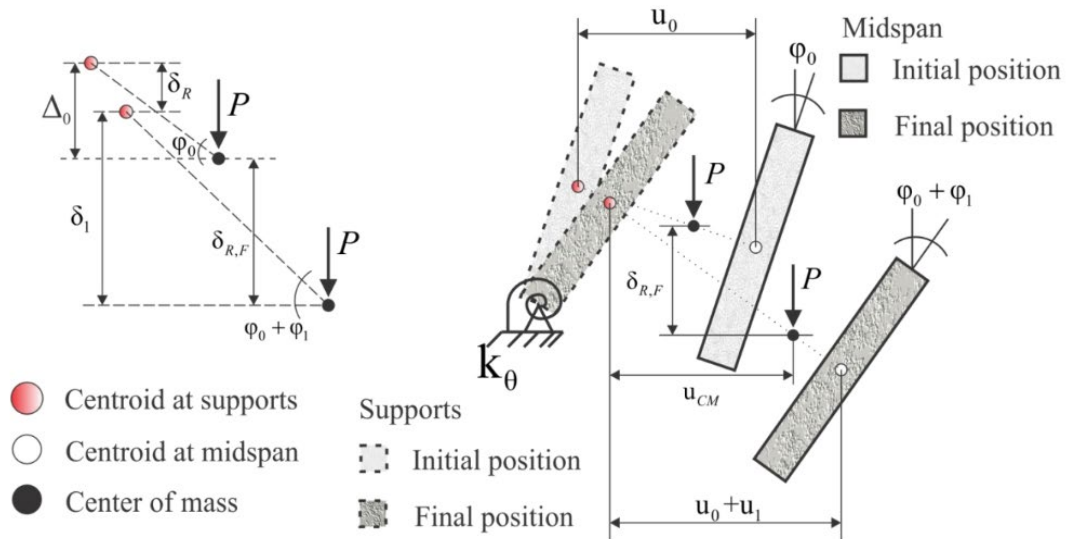


Figure 3. Trajectory of the resulting self-weight during rollover. Source: Adapted from Krahl et al. [13]

In Figure 3, one notes that the total vertical displacement of the mass center during rollover ( $\delta_{R,F}$ ) is a combination of three parts, the sum of  $\delta_R$  with  $\delta_I$ , and subtracted the value of  $\Delta_0$ . As  $\delta_R$  corresponds to the vertical movement of the mass center due to rotation of the rigid body of the beam,  $\delta_I$  is the distance between the centroid on the supports and the mass center in the final position, and  $\Delta_0$  represents the distance between the centroid on the supports and the mass center of the beam in the initial position. The generalized displacement  $u_0$  represents the initial lateral displacement of the beam. The calculation of these displacements and the action performed by the result of self-weight is presented in Equations 4 to 7 in the following.

$$\delta_R = 2 y_b \sin^2\left(\frac{\varphi_I}{2}\right) \tag{4}$$

$$\Delta_0 = \frac{\tan(\varphi_0) L}{L} \int_0^L u_0 \, dx \tag{5}$$

$$\delta_I = \frac{\tan(\varphi_0 + \varphi_1) L}{L} \int_0^L (u_0 + u_1) \, dx \tag{6}$$

$$V = -q L (\delta_I + \delta_R - \Delta_0) \tag{7}$$

Where  $y_b$  is the distance between the centroid of the beam and the axis of rotation located on the support device.

Through the minimization of the energy functional ( $\Pi = U + V$ ), it is possible to determine the solution for the degree of freedom  $\alpha_1$  using Equation 8 and the critical load using Equation 9, thus obtaining the equation for final equilibrium (Equation 10).

$$\alpha_1 \rightarrow \frac{\partial}{\partial \alpha_1} \Pi = 0 \tag{8}$$

$$q \rightarrow \frac{\partial}{\partial \varphi_1} \Pi = 0 \tag{9}$$

$$qL \left\{ 2y_b \sin\left(\frac{\varphi_l}{2}\right) \cos\left(\frac{\varphi_l}{2}\right) + \left[ \frac{8qL^4 \tan(\varphi_0 + \varphi_l)}{\pi^6 E I_y} + \frac{2e_i}{\pi} \right] \left[ 1 + \tan^2(\varphi_0 + \varphi_l) \right] \right\} = 2k_\theta \varphi_l \tag{10}$$

Equation 10 represents the nonlinear relationship between the force distributed along with the beam  $q$  and the beam rotation  $\varphi_l$  dependent on the initial rotation  $\varphi_0$  and initial eccentricity  $e_i$ . When the initial rotation is considered equal to zero, the problem is reduced to the case of initial beam imperfection in the form of lateral displacement. If both initial rotation and displacement are equal to zero, the problem is reduced to the case of lateral instability of the perfect beam with flexible supports. In the latter case, it was possible to determine the critical force for lateral instability, under the hypothesis of rigid body rotation.

Noteworthy is that there exist trials that configure the transitory phase for which the formulation was developed. However, to validate the formula, Krahl et al. [13] linearized Equation 10 and compared it to solutions from Mast [1] and Burgoyne and Stratford [6]. The proposed equation presented results very close to those obtained by equations in the literature. In addition, Oliveira [12] compared the nonlinear solution to a simplified analytic strategy, which consisted of using a linear solution combined with the equation by Southwell [14]. The latter takes into account the linear tipping load and the initial imperfection to obtain the nonlinear response. The results were identified until the peak. However, the equation by Southwell [14] did not predict the unstable behavior of the post-peak, which is characteristic of the problem with high sensitivity to initial imperfection.

### 2.1 Determining initial cracking

According to Mast [1], the cracking of concrete can be admitted as a limit state on the lateral stability of beams. Even though it is understood that prestressing does not influence in the tipping of the beam, the stresses developed due to prestressing should be considered to check for possible cracking. Therefore, the tensile stress critical for cracking  $\sigma_{t,crit}$  was determined in the mid-span section for each rotation angle  $\varphi_l$ , as shown in Figure 4.

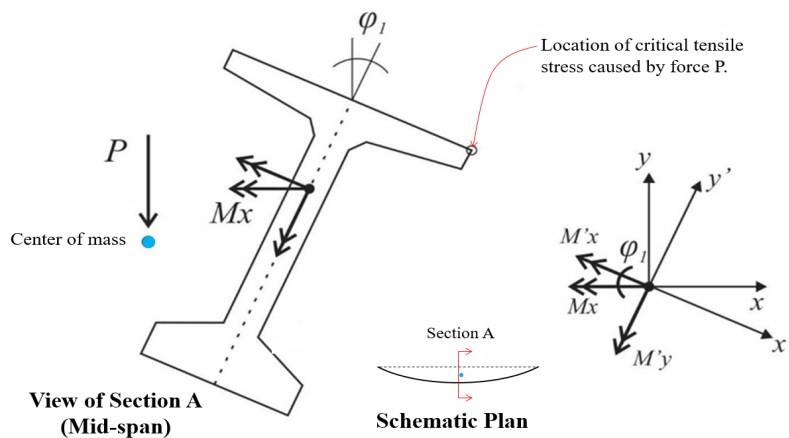


Figure 4. Decomposition for checking the cracking moment. Source: Adapted from Oliveira [12]

The flexibility of the supports during tipping allows one to ignore the effects of twisting. Equation 11 presents the general expression for determining the stress on the cross-section at the mid-span. The compressive stresses were admitted as negative and the bending moments are designated according to the right-hand rule, where  $F$  is the prestressing force,  $A$  the section area,  $e$  the prestress eccentricity,  $M'_x$ , and  $M'_y$  are the components of the moment caused by the distributed vertical force,  $x'$  and  $y'$  are the coordinates of the point of interest on the rotation axis,  $I'_x$  and  $I'_y$  are the inertia moments that also correspond to the rotated axis, and  $M_x$  is the moment due to the own weight of the beam.

$$\sigma = -\frac{F}{A} + \frac{F e y'}{I'_x} - \frac{M'_x y'}{I'_x} + \frac{M'_y y'}{I'_y}$$

$$M'_x = M_x \cos(\varphi_l)$$

$$M'_y = M_x \sin(\varphi_l) \tag{11}$$

The nonlinear equation (Equation 10) allows one to determine the resulting moment  $M_x$  and its components  $M'_x$  and  $M'_y$  acting on the mid-span for each value of  $\varphi_l$  and corresponding force  $q$ . Following this, the stresses can be calculated according to Equation 11, and the critical cracking load  $q_{cr}$  can be obtained when  $\sigma$  reaches the concrete tensile strength  $f_t$ . Such strength can be estimated according to ABNT NBR 6118:2014 [15] as  $f_{ct} = 0.3f_{ck}^{2/3}$ , where  $f_{ck}$  is the characteristic compressive strength of concrete.

### 3 DEVELOPMENT OF THE ALGORITHM AND PARAMETRIC ANALYSIS OF THE ANALYTIC SOLUTIONS

#### 3.1 Development of the algorithm

The parametric study was developed to verify the mechanical component, considering the variation over specific properties of the beam. The method is based on a large number of random samples for evaluating the variation of parameters associated with the model in the mechanical response of the structure. This procedure was developed employing computer programming using the language Python.

To obtain the random sample, for each of the parameters analyzed, 100 thousand simulations are performed. In each simulation, a random value is attributed to the following variables, initial lateral eccentricity, modulus of elasticity of concrete and stiffness to the rotation of the support. These parameters were not variable only when they are the parameter of analysis under focus.

The random values were obtained in the following way, the initial lateral eccentricity and the modulus of elasticity were adopted randomly, according to the normal distribution, for which the average was the value of the default input. The variation coefficient was 0.61 for the initial eccentricity [16] and 0.15 for the modulus of elasticity [17]. In order to take into account the effect from the loss of contact and the possible curve at the bottom flange of the beam in contact with the bearing pad, the variation in stiffness to the rotation of the support device was considered randomly from 25% to 100% of the total stiffness established as the default input value. The default data values of the problem were attributed based on the beam in the trial by Hurff and Kahn [11].

The stiffness to the rotation of the support device was calculated by Equation 12. The axial stiffness of the support device (Equation 13) was calculated according to that proposed by Yazdani et al. [18].

$$k_\theta = \frac{k_v L_a^2}{12} \tag{12}$$

$$k_v = \frac{E_{pad} L_a W_a}{H_a}$$

$$E_{pad} = 6 \cdot G_{pad} \cdot S^2 \tag{13}$$

$$S = \frac{(ni \cdot hi \cdot S1) + (ne \cdot he \cdot S2)}{(ni \cdot hi) + (ne \cdot he)}; S1 = \frac{L_a \cdot W_a}{2 \cdot hi \cdot (L_a + W_a)}; S2 = \frac{L_a \cdot W_a}{2 \cdot he \cdot (L_a + W_a)}$$

With  $k_v$  the stiffness to compression of the pad,  $L_a$ ,  $W_a$  and  $H_a$  the dimensions of the pad,  $E_{pad}$  the modulus of elasticity of the pad,  $G_{pad}$  the shear modulus of the pad,  $ni$  and  $ne$  the number of internal and external layers of the pad respectively,  $hi$  and  $he$  the height of the internal and outer layers of the pad respectively.

The precision of the rigid body rotation angle from the analyses was 0.001 rad. The modulus of elasticity, and  $f_{ct}$  are determined from concrete compressive strength  $f_{ck}$ , according to the formulations from ABNT NBR 6118:2014 [15].

The cross-section stress curve depends on two parameters, the acting force and the rotation angle. The values for the acting force are obtained by Equation 10. With the definition of the stress curve at hand, the value for stress closest to  $f_{ct}$ , was determined, in this way, the load and the angle corresponding to this point are the critical values for the initial cracking of the beam. The structure of the algorithm developed and programmed herein is presented in Figure 5.

### 3.2 Parametric analysis results

The parametric analysis is performed to verify the behavior of the beam for the variation of parameters indicated in Table 1. The properties of the beam used as the basis for the parametric analysis are presented in Table 2. The initial rotation of the beam of  $0.5^\circ$  was considered and an initial eccentricity of  $L/1000$ .

The support device was considered according to the study by Hurff and Kahn[11] with dimensions of  $61 \times 36 \times 7.3 \text{ cm}^3$  composed of 4 steel sheets, three internal elastomeric layers of 15 mm each and two external elastomeric layers of 7.5 mm each, as outlined in Figure 6.

For the stiffness to rotation calculation, the modulus of elasticity to the shear of the support apparatus was used at 670 kPa, which resulted in a rotational stiffness of 33.4 MNm/rad.

**Table 1.** Data for the parametric analysis

ANALYSIS PARAMETER	VALUES ANALYZED
Initial eccentricity	$L/1000$ ; $L/500$ ; $L/250$ ; $L/125$
Initial Rotation	$0.5^\circ$ ; $1.5^\circ$ ; $3.0^\circ$
Concrete strength	50 MPa; 75 MPa; 100 MPa
Support pad dimension	$61 \times 36 \times 7.3 \text{ cm}^3$ ; $61 \times 36 \times 9.8 \text{ cm}^3$ ; $61 \times 36 \times 12.3 \text{ cm}^3$
Beam cross section (*)	BT-54; BT-63; BT-72

\* For each of the three cross-sections of the beam, three cases are analyzed, modifying the dimension of the top flange, with 100% of the standard value; 50% of the standard value; and with length equal to the thickness of the web.

Source: Authors.

**Table 2.** Properties of the base beam parametric analysis

Moment of inertia in relation to the X-axis ( $I_x$ )	0.1116 $\text{m}^4$
Moment of inertia in relation to the Y-axis ( $I_y$ )	0.0155 $\text{m}^4$
Beam height (h)	1.372 m
Height of center of gravity ( $y_b$ )	0.703 m
Width of the top flange (MS)	1.067 m
Area of cross-section (A)	0.425642 $\text{m}^2$
Beam length (L)	30.5 m
Modulus of elasticity of concrete (E)	30820 MPa

Source: Oliveira [12]

Brazilian standards indicate the shear modulus of elasticity or the minimum transverse deformation modulus of 0.80 MPa [19] and 0.85 MPa [20], as such the value of 0.67 MPa was adopted following the studies [10]–[13]. Figure 7 presents the nonlinear curve obtained by Equation 10 for the force values due to the rigid body rotation of the beam. For these data, in absolute values without any variation, the values of 339.87 kN·m for maximum strength and of 0.16041 rad were obtained for the rotation angle that corresponds to this strength.

The strength at initial cracking is of 339.85 kN·m, with an angle of 0.16642 rad. For this particular case, the loads for cracking and rollover were very close, justifying in this way the direct use of Equation 10 in the verification of lateral instability through rollover, while considering the concrete with a linear behavior. This hypothesis has been found in numerical simulations presented in the literature [2], [9], [10], [21]. Also, the emphasis is given to the fact that the formulation can identify the maximum strength value, as it presents unstable post-peak behavior.

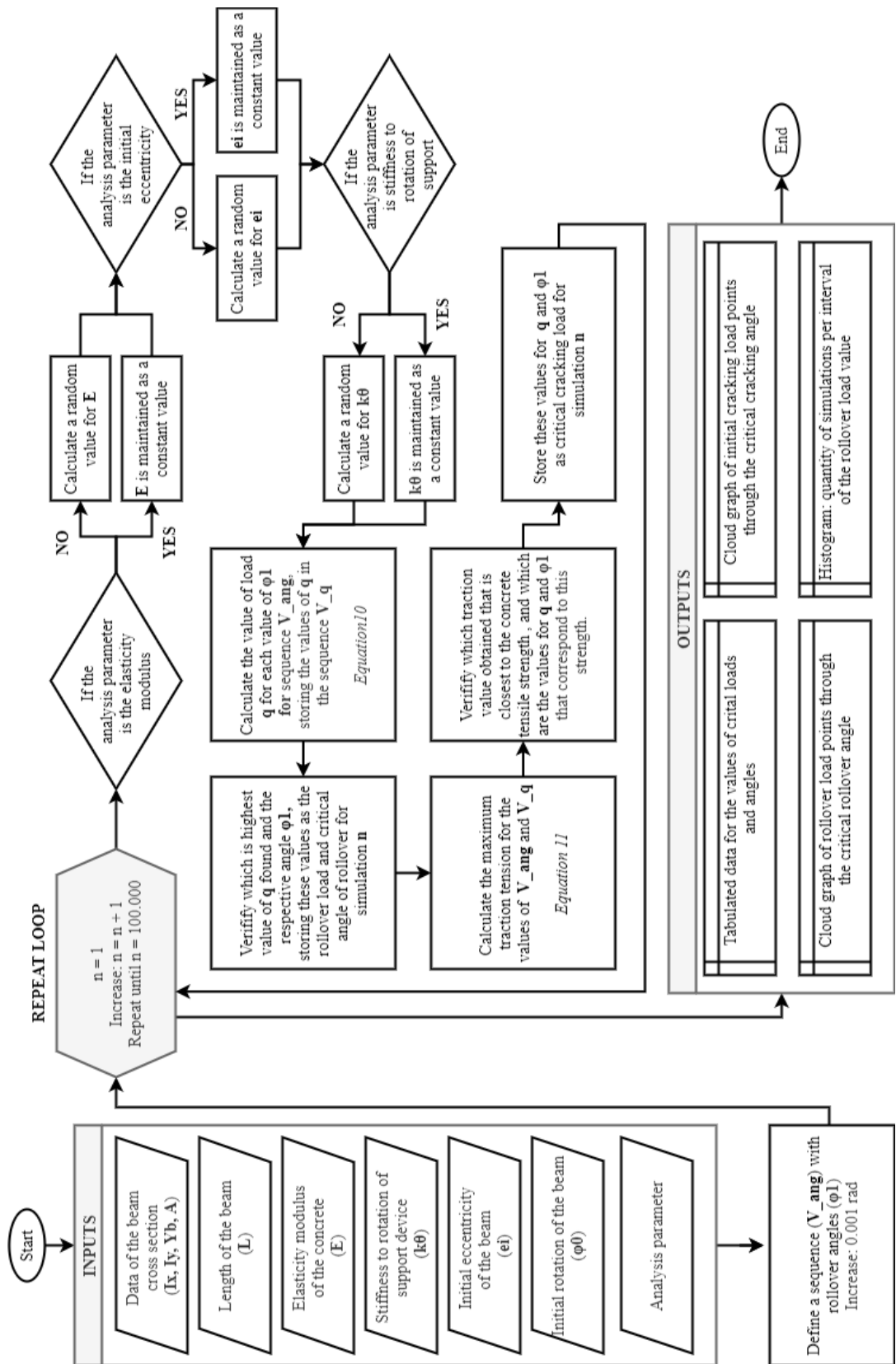
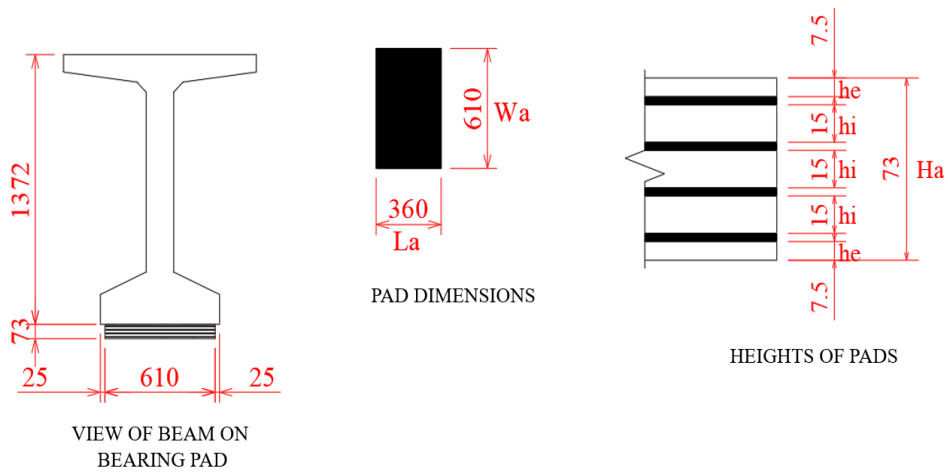
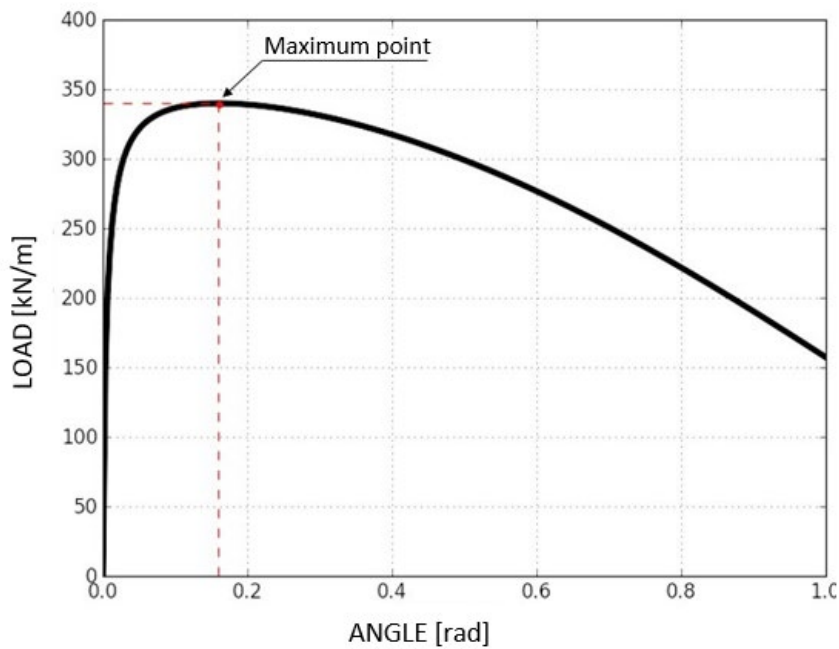


Figure 5. Structure of the parametric analysis algorithm. Source: Authors.



**Figure 6.** Schematic representation of the bearing pad. Units in [mm]. Source: Authors.



**Figure 7.** Load applied by the stiffness to the rotation angle of the beam. Source: Oliveira [12]

Figure 8a represents the value of maximum strength and the respective rollover angle for each of the 100 thousand simulations obtained through Equation 10, considering the randomness of the variables mentioned above, in. Noteworthy here is that the random values for initial lateral eccentricity and the modulus of elasticity were adopted while considering a normal distribution with a coefficient of variation of 0.61 for initial eccentricity and 0.15 for the modulus of elasticity of the concrete. In terms of support stiffness, the random values vary from 25% to 100% of the total rigidity established as the default value. The same was performed while considering the force for the initial cracking of the beam in Figure 8b.

The histogram of Figure 8c refers to the results presented in Figure 8a, where these values were arranged to represent the number of simulations that give the value of maximum strength during a defined interval. Therefore, the x-axis represents the maximum strength intervals considered and the y-axis the number of simulations that result in the maximum strength in this interval.

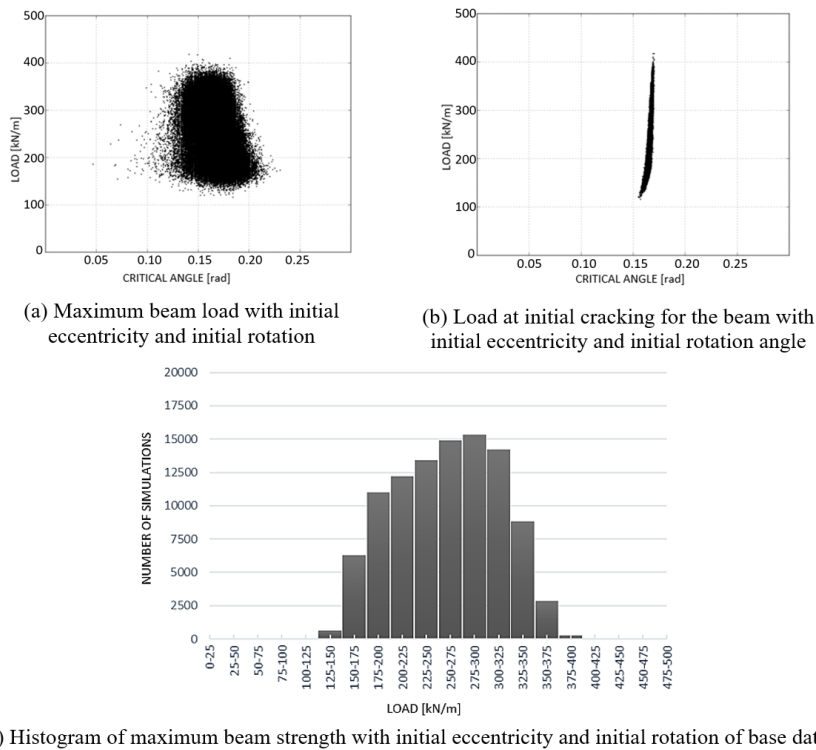


**Figure 8.** Results of base data for beam with initial eccentricity and initial rotation angle. Source: Oliveira [12]

The result from the direct application of the equation is a maximum strength of 339.87 kN/m (Figure 7). For the analysis with statistical variations of the parameters, considering the 100 thousand simulations, one notes that for the strength value obtained in the interval of 325-350 kN/m, which represents a portion around the mark of 9 thousand simulations. However, the majority of the simulations, around 15 thousand simulations, had a result of maximum strength between 275 and 300 kN/m. For these base values, regarding the 100 thousand simulations, the most significant values for maximum strength vary from 175 to 350 kN/m, which corresponds to 90% of the total simulations.

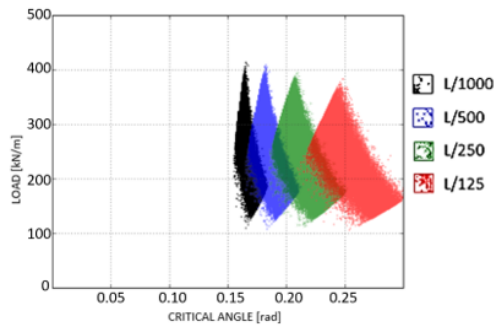
In these simulations, randomness occurs from the combination of random values for the initial lateral eccentricity and the elasticity modulus, while considering a normal distribution with a coefficient of variation of 0.61 for the initial eccentricity and 0.15 for the modulus of elasticity of the concrete; for support stiffness, the random values vary from 25% to 100% of the total stiffness established as a default value.

The average rollover load value obtained from Figure 8a is of 258.49 kN/m. by comparing this result to the value of critical force obtained without considering the variation of the parameters, a reduction of 23.9% was observed, which corresponds to a reduction factor of 1.3. Besides, the fact that one is dealing with the verification of safety in structures, it is common knowledge that statistically, the resistances are considered as holding characteristic values. As such, a normal resistance distribution was considered typically as that presented in Figure 8c, and assumed as a characteristic value is a portion (quantile) of the distribution that represents a degree of confidence, for example, of 95%. This would result in a critical rollover load that is still less than the average. Therefore, the emphasis is placed upon the importance of considering the high degree of uncertainty associated with this transitory phase. Despite the analyzed variability, the beam in question remains stable, since the load due to own weight is of the order of 10 kN/m, and the rollover or cracking loads were above 100 kN/m, which would result in a safety coefficient above 10.

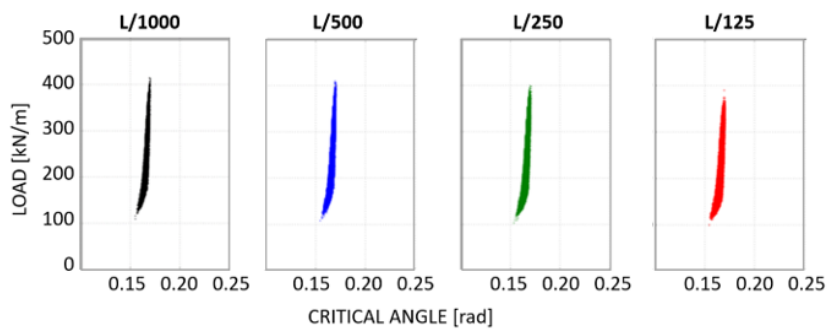
### 3.2.1 Initial Lateral Eccentricity

The first parameter analyzed refers to the influence of the initial lateral eccentricity of the beam, where the following values were considered  $L/1000$ ,  $L/500$ ,  $L/250$  and  $L/125$ , where  $L$  is the length of the beam. For this analysis, eccentricity is maintained constant, equal to the value analyzed, without the attribution of random values to this parameter as in the other analyses. Figure 9 illustrates the results for this analysis.

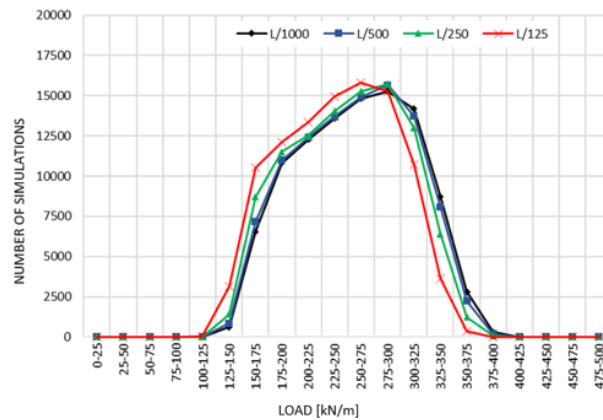
This variable reduces the strength limit with the increase of the critical rotation angle. In the critical cracking strength, the angle obtained was practically the same for the four values observed for eccentricity, a general average of 0.166 radians. The average critical strength suffers a reduction of approximately 1% and the average critical angle increases by almost 11% for the increase in the initial eccentricity from L/1000 to L/500. However, the increase in eccentricity from L/1000 to L/250, the reduction was 3% in critical strength with an increase of 27% in the angle from L/1000 to L/125, and the reduction was of nearly 7% in strength and an increase of 57% in the angle. Under these terms, it became clear that the eccentricity increases the susceptibility significantly for lift-off, which is the loss of contact between the beam and the support device.



(a) Maximum load of the beam with initial eccentricity



(b) Load at cracking of the beam with initial eccentricity



(c) Histogram of the influence from initial eccentricity on maximum strength of the beam

**Figure 9.** Variation of initial lateral eccentricity. Source: Oliveira [12]

Therefore, the increase of initial eccentricity was causing a reduction in critical rollover load, followed by the rise in critical rotation. However, although the critical load at the beginning of cracking is less with the increase in eccentricity, the cracking angle presented values very close to one another, as seen in Figure 9b.

### 3.2.2 Initial rotation

Another parameter of the initial imperfection of the beam that may influence lateral instability was the existence of initial rotation around its longitudinal axis. To observe the influence of this variable (Figure 10), three values of angle are adopted, such as 0.5° (0.008727 rad), 1.5° (0.02618 rad) and 3° (0.05236 rad). Highlighted here is that the study interval was adopted based on the results presented in [12] since these can produce instability on the beam.

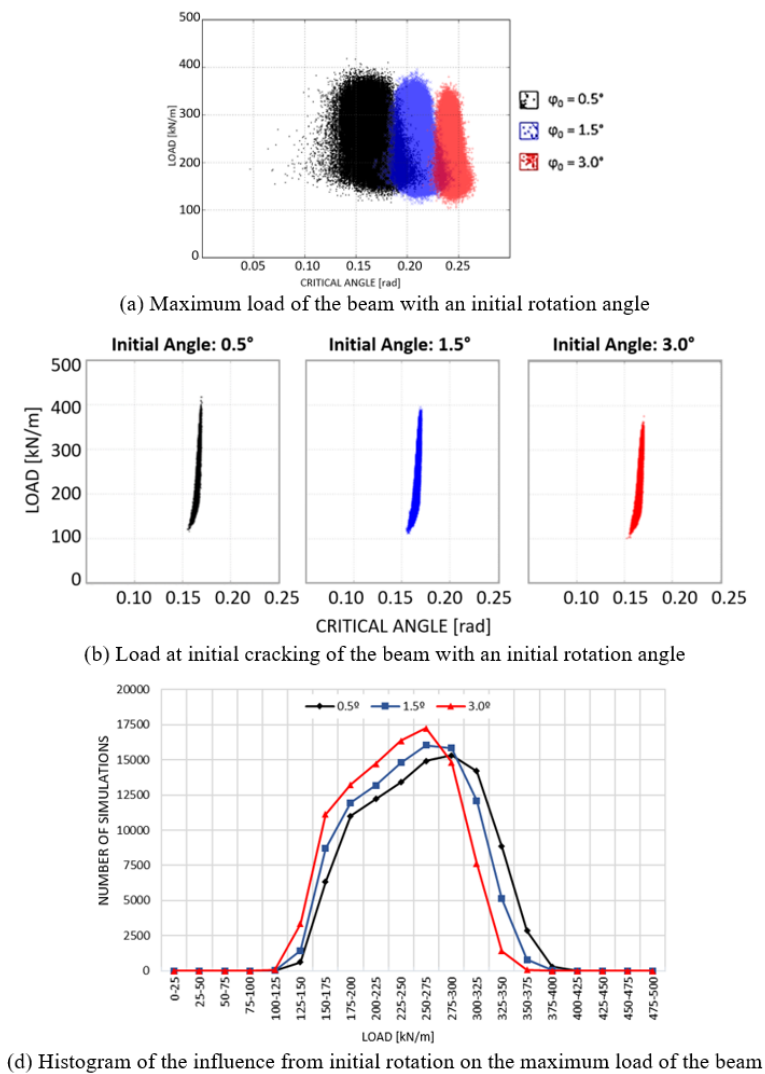


**Figure 10.** Variation of the initial rotation. Source: Oliveira [12]

The increase in the initial rotation of the beam brought about a decrease of the maximum strength value, as the critical rotation angle increased.

Noted in Figure 10a is that for an initial rotation angle less than (0.5°), there was a significant variation in the critical angle, but for the larger angle (3.0°), the results are more concentrated close to the average angle of 0.24 radians. In terms of the critical cracking force (Figure 10b), the critical angle was practically the same for the four values observed, with an overall average of 0.166 radians.

### 3.2.3 Compressive strength of concrete

For the analysis of the influence of the compressive strength of concrete, three concrete compressive strength values were assigned ( $f_{ck}$ ), those being: 50 MPa ( $E = 39597.98$  MPa), 75 MPa ( $E = 48497.42$  MPa) and 100 MPa ( $E = 56000.00$  MPa). The tangent modulus of elasticity was considered in a simplified form, where it was calculated

by  $E = 5600 \sqrt{f_{ck}}$ . For each value of  $f_{ck}$ , its elasticity modulus was maintained constant, without the assigning of random values to this parameter as performed in other analyses. Figure 11 presents the results of this analysis.

In this analysis, the significant influence exerted by the modulus of elasticity of the concrete on the lateral stability of the beam became evident. The elasticity modulus can be related to the compressive strength of the concrete. The higher the compressive strength of the concrete, the greater will be the stability of the system, in such a way that there is a substantial increase in critical stress.

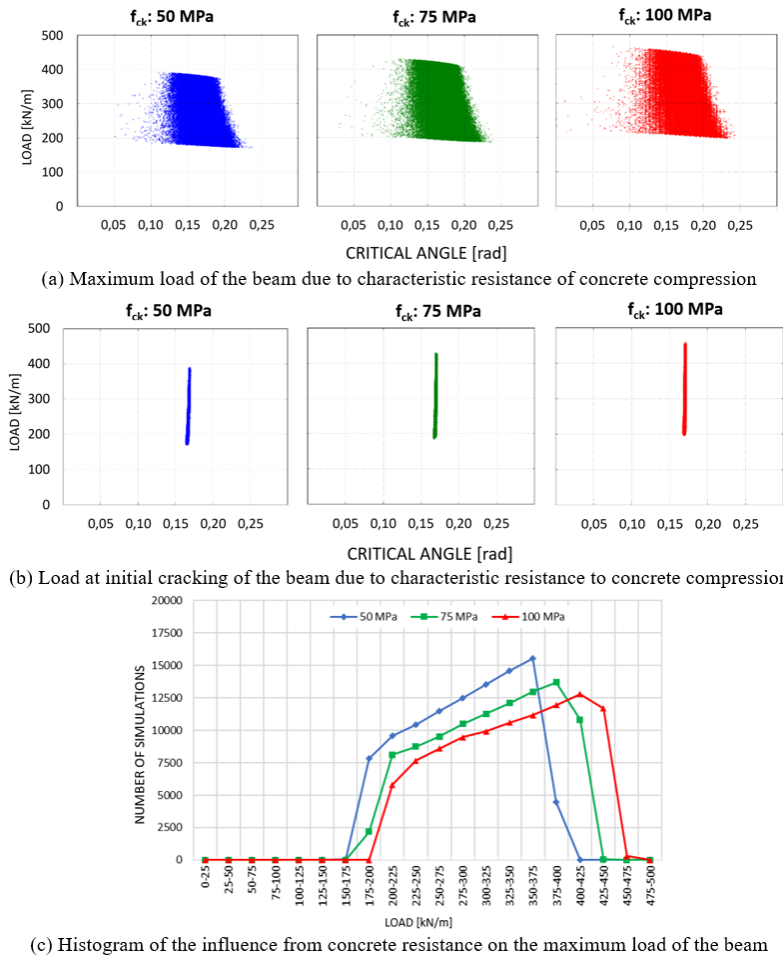


**Figure 11.** Variation of the characteristic resistance to concrete compression. Source: Oliveira [12]

Despite the increase in critical stress, the variation of the corresponding critical angles was minimal. As such, the conclusion was reached that the compressive strength of the concrete of the beam directly influences in the critical stress (Figure 11c), but the rollover angle (Figure 11a), and initial cracking (Figure 11b) was influenced very little.

### 3.2.4 Stiffness of the support device

The stiffness of the support device can have a significant influence over the lateral stability of the beams. To consider the variation and the importance of this parameter in the analyses, a variation of 25% to 100% of the initial value was considered for the pad, where 100% was considered the total stiffness value. Brazilian standards [19] and [20] do not establish limits or calculation methods for the stiffness to the rotation of the support device. In addition, the dimensions of the support device do not possess high flexibility to modification, since these are limited due to the maximum compression admitted by the standards and the dimensions of the bottom flange of the beam. The arrangement of the pad can bring about modifications to the rotation stiffness associated with it. Thus, the influence of this parameter on the lateral stability of the beam will be analyzed in this section.

In the first analysis, the initial dimensions of the support device are considered as  $610 \times 360 \times 73$  mm, with four steel sheets, three internal layers of elastomer of 15 mm each and two external layers of elastomer of 7.5 mm each. According to that presented

in Figure 6, the calculated stiffness to the rotation was equal to 33366.66 kN/m·rad. In the second analysis, an increase of 5 mm was considered for each layer of elastomer, thus resulting in a pad of 610 × 360 × 98 mm and stiffness of 12384.38 kN/m·rad (37.1% of the initial stiffness). In the third analysis, the increase considered was 10 mm for each layer, resulting in dimensions of 610 × 360 × 123 mm and stiffness of 5891.79 kN/m·rad, which corresponds to 17.7% of the initial stiffness analyzed.

The increase in the height of the pads was attributed in a way to significantly modify the stiffness to rotation values of the support device, aiming at a better view of its influence. Such values do not correspond to the tolerance limits accepted by Brazilian standards [19] and [20] since these limits are 5 mm for the width and length of the bearing pad and between 1 mm and 3 mm for the height of the pad. Figure 12 shows the results of this analysis that refer to maximum load, initial load at cracking and the histogram of the number of simulations due to the maximum load for each situation of support device stiffness. With the increase of stiffness, besides the increase in critical load, there was a considerable variation on the critical rollover angle (Figure 12a), which is characteristic of a more unstable system. By taking the stiffness to rotation as a fixed parameter, a lower variation of critical load values occurred, which is noted when one compares the graph from Figure 12a with the first graphs of the previous analyses (Figures 8a, 9a, 10a and 11a). The tendency found was that the critical angle approximate to 0.15 radians, as the pad becomes stiffer. Despite the significant variation in the cracking load values, its initiation maintained the tendency of critical angle with values close to 0.16 radians, for the three observed cases.

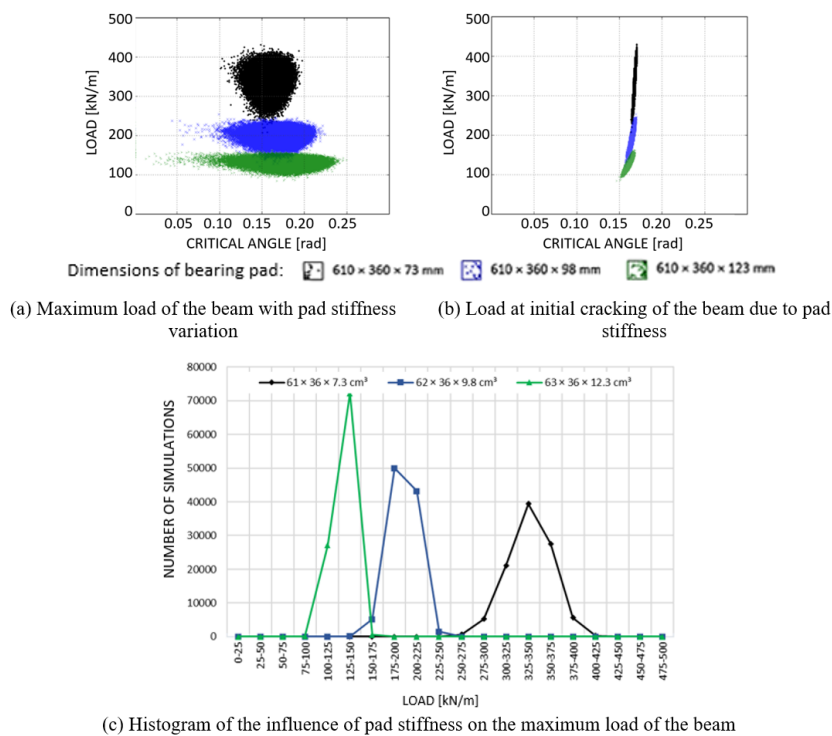


Figure 12. Variation of the stiffness of the bearing pad. Source: Oliveira [12]

### 3.2.5 Cross-section of the beam

The cross-section of the beam in this study was analyzed also considering the possibility of reducing the width of the top flange. In the first analysis, the cross-section and the span of the beam were modified, while maintaining the relationship between the height of the beam and the span proportional. Therefore, the sections BT-54, BT-63 and BT-72 are analyzed with the lengths of 30.5 m, 35 m and 40 m, respectively. The beams classified in the technical literature as BT-54, BT-63 and BT-72 refer to standard cross-sections from PCI (Precast/Prestressed Concrete Institute), widely used in the construction of bridges and viaducts from precast concrete, and the aim of analyses in Lee [9], Krahl et al. [10], Hurff and Kahn [11] and Oliveira [12]. In the second analysis, the influence of slenderness and the lateral moment of inertia were studied about the Y-axis, by modifying the width of the top flange. The top flanges were considered using 100% of the original value, 50% of this value and under a condition where the top flange possesses a width equal to the thickness of the web. Figure 13 and Table 3 present the properties of the beams studied.

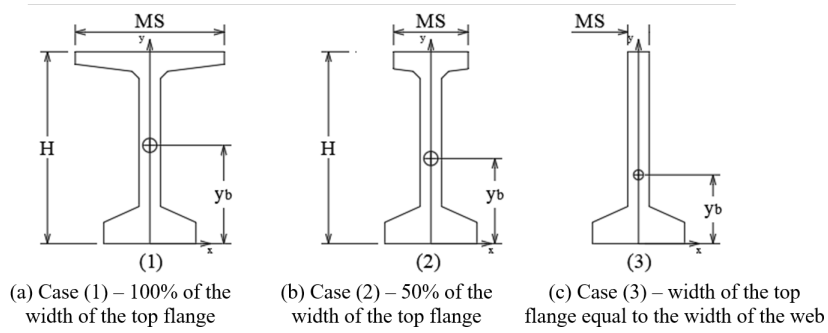


Figure 13. Cross-sections of the beams with modifications to the width of the top flange. Source: Oliveira [12]

Table 3. Properties of the beams of the series PCI-BT

		BT-54			BT-63			BT-72		
		Case (1)	Case (2)	Case (3)	Case (1)	Case (2)	Case (3)	Case (1)	Case (2)	Case (3)
Moment of inertia Y axis	$I_y$ [m <sup>4</sup> ]	0.01550	0.00649	0.00486	0.01560	0.00656	0.00493	0.01570	0.00663	0.00499
Moment of inertia X axis	$I_x$ [m <sup>4</sup> ]	0.11157	0.08687	0.05690	0.16340	0.12907	0.08817	0.22739	0.18188	0.12856
Length of beam	L [m]	30.50	30.50	30.50	35.00	35.00	35.00	40.00	40.00	40.00
Height of center gravity	$y_b$ [m]	0.703	0.609	0.492	0.817	0.715	0.591	0.931	0.822	0.693
Height of beam	H [m]	1.372	1.372	1.372	1.600	1.600	1.600	1.829	1.829	1.829
Width of top flange	MS [m]	1.067	0.5335	0.153	1.067	0.5335	0.153	1.067	0.5335	0.153
Area of cross section	A [m <sup>2</sup> ]	0.42564	0.36922	0.31579	0.46062	0.4042	0.35076	0.49566	0.43924	0.3858
Slenderness		31.08	78.33	414.15	37.55	94.61	500.25	44.87	113.05	597.78

Source: Oliveira [12]

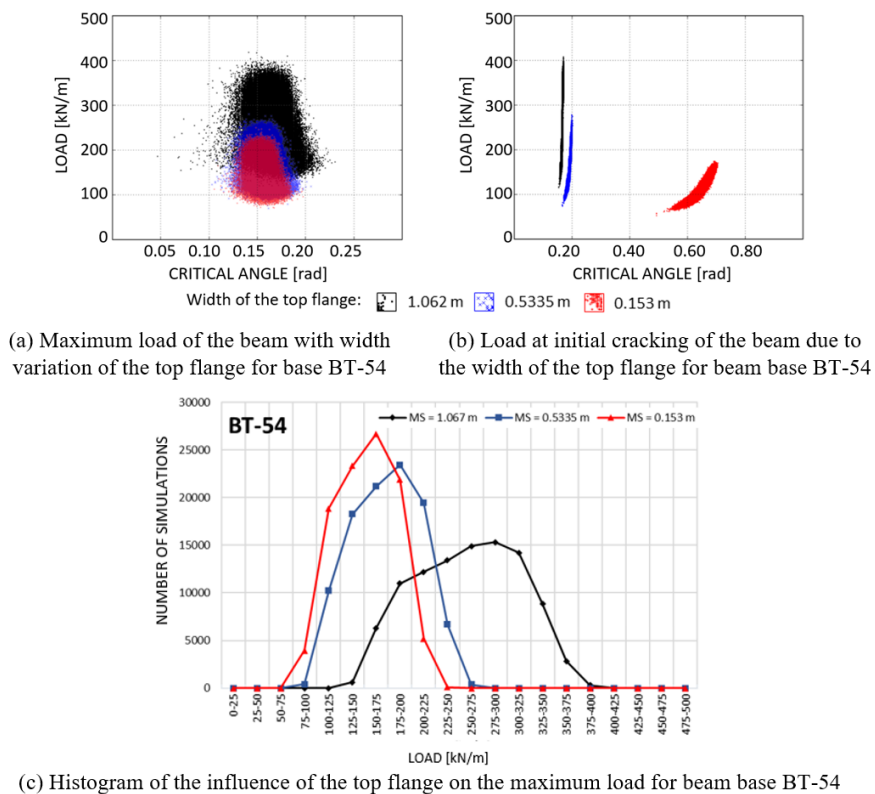
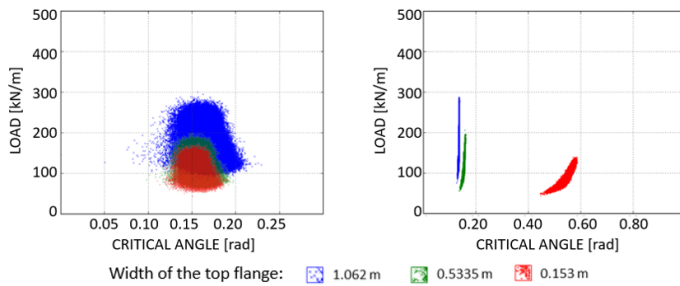
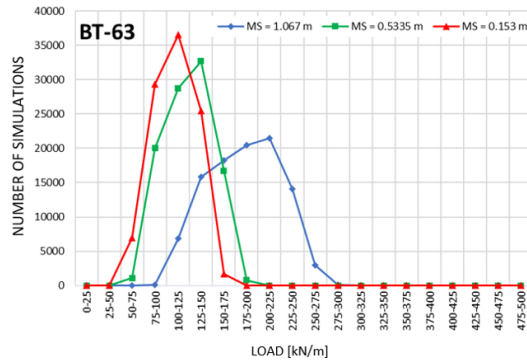


Figure 14. Beam BT-54 with width variation of the top flange. Source: Oliveira [12]



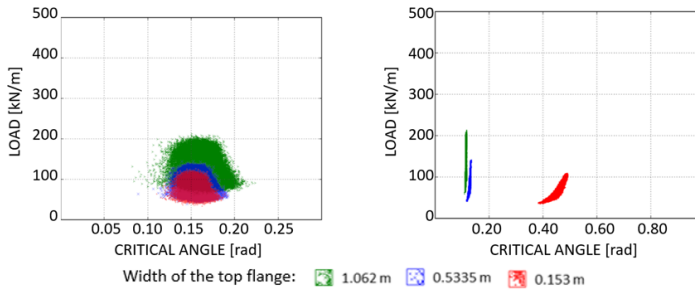
(a) Maximum load of the beam with width variation of the top flange for base BT-63

(b) Load at initial cracking of the beam due to the width of the top flange for beam base BT-63



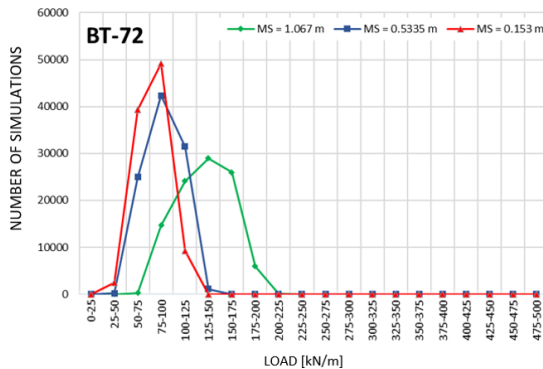
(c) Histogram of the influence of the top flange on the maximum load for beam base BT-63

**Figure 15.** Beam BT-63 with width variation of the top flange. Source: Oliveira [12]



(a) Maximum load of the beam with width variation of the top flange for base BT-72

(b) Load at initial cracking of the beam due to the width of the top flange for beam base BT-72



(c) Histogram of the influence of the top flange on the maximum load for beam base BT-72

**Figure 16.** Beam BT-72 with width variation of the top flange. Source: Oliveira [12]

Figure 14 presents the results obtained in the simulations using beam BT-54 with the three dimensions of the top flange already described, while Figure 15 presents the results for beam BT-63 and Figure 16 for beam BT-72. Figure 17 shows the comparison between the results obtained for the cross-sections of BT-54, BT-63 and BT-72 with values for the complete top flange.

From the obtained results, the properties from the cross-section were seen to possess factors of extreme importance in the lateral stability of precast beams. When the influence of the top flange (MS) of the beam is analyzed (Figure 13), in a way that modifies its slenderness and moment of lateral inertia, besides the significant reduction in the critical load values, one also notes the distinct influence this has on the state of initial cracking. In this situation, besides the modification of critical load, there was an alteration in the critical angle of initial cracking, which is not significant in the other analyses. In this way, the smaller the dimension of the top flange, the greater is the angle of initial cracking and lower the critical rollover load.

The same occurred when the three distinct cross-sections were analyzed (BT-54, BT-63 and BT-72), and which although the three beams present a similar moment of inertia about the Y-axis, the higher the beam, lower will be the critical load. In addition to the decrease in critical load, the taller beams present an angle for initial cracking lower than the beams with lower heights, although the width of the top flange is the same.

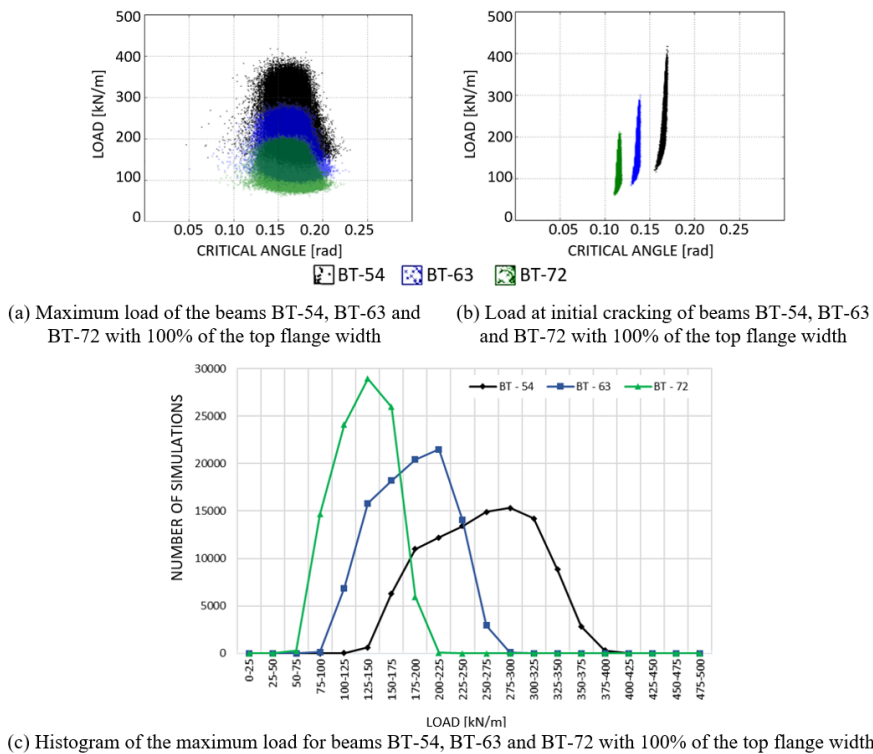


Figure 17. Beams BT-54, BT-63 and BT-72 with 100% of the top flange width. Source: Oliveira [12]

#### 4 CONCLUSIONS

Based on the nonlinear analytical solution presented herein, which describes the behavior of a beam with initial eccentricity and rotation on support devices, it was possible to determine the maximum load supported by the beam before rollover. A solution for defining the initial cracking of the beam during the rollover is also presented.

Based on these solutions, a parametric analysis was developed, where the mechanical behavior of the beam was verified under the influence of specific parameters.

From the results obtained from the parametric analysis, the following conclusions were reached:

The increase in the compressive strength of concrete caused an increase in the rollover load in the order of 9% and 17% for the values of 75 MPa and 100 MPa, respectively, when compared to the values of 50 MPa.

Among the investigated parameters, stiffness to the rotation of the support and the geometry of the cross-section were the factors of foremost influence in the critical rollover load. Therefore, for the situations under analysis, the critical rollover load presents a reduction of:

42% to 62% due to the decrease of the stiffness to the rotation of the support;

33% in length reduction of the top flange of 50% for the reference value, and in 41% length reduction of the top flange equal to the web width ;

29% and 48% due to the increase in the height of the beam for sections BT-63 and BT-72, respectively, when compared to beam section BT-54.

The initial eccentricity and rotation caused significant increases in the critical rollover angle, about 52% for the initial eccentricity values analyzed (of L/1000 to L/125) and 47% for the values of initial rotation (of 0.5° to 3.0°). For the remaining analyzed parameters, the critical rollover angle had a variation of less than 10%.

When there was a decrease in the width of the top flange of the beam (50% of the original), the angle of initial cracking was approximately 15% higher than the angle obtained for the complete cross-section case. The increase of this angle was higher than 300% when the length of the top flange possessed the same thickness as the web of the beam.

In the parametric analysis, it was also possible to verify that the initial load at cracking was very close to the critical rollover load of the beam. Nevertheless, the initial cracking angle was maintained close to 0.16 rad for all the analyses, where the cross-section of beam PCI BT-54 has a top flange equal to 1.067 m in width. However, such angle is sensitive to the variations of the geometric properties of the beam cross-section. As such, it was found that lateral flexural stiffness is the main parameter that governs the cracking of the beam.

However, comparing beams with the same lateral inertia moment, but with differentiated heights, the greater the height, the lower was the angle of initial cracking. This reduction, when compared to beam BT-54, was in the order of 18% for BT-63 and of 31% for BT-72.

The conclusion is that for beam PCI BT-54 with a top flange equal to 1.067 m in width, under the same conditions of support and length, the angle of initial cracking was approximately 0.16 radians, without any direct influence in the analyses from the imperfections of the beam. Noteworthy here is that, in some cases, the critical rollover angle was more significant than the cracking angle. Also, the load for initial cracking is less than the rollover load, highlighting once again that cracking is also unwanted.

In this way, it became evident the importance of safety analyses of precast beams concerning lateral stability during the assembly stage of the structure. The stability of beams is highly dependent on the physical and geometric properties, in what concerns the beam as well as for the support device, where factors of geometric imperfections influence the aspect of safety greatly.

## 5 REFERENCES

- [1] R. F. Mast, "Lateral stability of long prestressed concrete beams - Part 2," *PCI J.*, vol. 38, no. 1, pp. 70-88, Jan-Feb 1993.
- [2] M. C. V. D. Lima, "Contribuição ao estudo da instabilidade lateral de vigas pré-moldadas," Ph.D. dissertation, Esc. Eng. São Carlos, Univ. São Paulo, 2002.
- [3] R. Tremblay and D. Mitchell, "Collapse during construction of a precast girder bridge," *J. Perform. Constr. Facil.*, vol. 20, no. 2, pp. 113-125, 2006.
- [4] R. G. Oesterle et al., *Investigation of Red Mountain Freeway Bridge Girder Collapse* (CTL Group Project 262291). Skokie, IL, USA: Bridge Group, Arizona Dept. Transp., Nov 2007, pp. 67.
- [5] J. M. Bairán and A. Cladera, "Collapse of a precast concrete beam for a light roof. Importance of elastomeric bearing pads in the element's stability," *Eng. Fail. Anal.*, vol. 39, pp. 188-199, Apr 2014.
- [6] C. J. Burgoyne and T. J. Stratford, "Lateral instability of long-span prestressed concrete beams on flexible bearings," *Struct. Eng.*, vol. 79, no. 6, pp. 23-26, Mar 2001.
- [7] R. H. Plaut and C. D. Moen, "Stability of unbraced concrete beams on bearing pads including wind loading," *J. Struct. Eng.*, vol. 69, pp. 246-254, Jun 2014.
- [8] J. H. Lee, I. Kalkan, J.-J. Lee, and J.-H. Cheung, "Rollover instability of precast girders subjected to wind load," *Mag. Concr. Res.*, vol. 69, no. 2, pp. 68-83, 2017.
- [9] J. H. Lee, "Evaluation of the lateral stability of precast beams on an elastic bearing support with a consideration of the initial sweep," *Eng. Struct.*, vol. 143, no. 1, pp. 101-112, 2017.
- [10] P. A. Krahl, R. Carrazedo, and M. K. El Debs, "Analytical solutions for rollover instability of concrete beams on elastomeric bearing pads," *Eng. Struct.*, vol. 174, pp. 154-164, 2018.

- [11] J. B. Hurff and L. F. Kahn, "Rollover stability of precast, prestressed concrete bridge girders with flexible bearings," *PCI J.*, vol. 57, no. 4, pp. 96–107, 2012.
- [12] M. F. A. Oliveira, "Estudo analítico do tombamento de vigas pré-moldadas sobre almofadas de apoio," M.S. thesis, Prog. Pós-grad. Eng. Civ., Univ. Fed. Uberlândia, Uberlândia, 2019.
- [13] P. A. Krahl, M. F. A. Oliveira, G. H. Siqueira, and M. C. V. Lima, "Analytical nonlinear rollover behavior of cambered precast concrete beams on flexible supports," *J. Struct. Eng.*, vol. 146, no. 2, pp. 04019200, 2020.
- [14] R. V. Southwell, "On the analysis of experimental observations in problems of elastic stability," *Proc. R. Soc. Lond.*, vol. 135, pp. 601–616, 1932.
- [15] Associação Brasileira de Normas Técnicas, *Projeto de Estruturas de Concreto – Procedimento*, ABNT NBR 6118:2014, 2014.
- [16] G. R. Consolazio and H. R. Hamilton, *Lateral Bracing of Long-Span Florida Bulb-Tee Girders*. Florida: Univ. Florida, Depart. Civ. Coast. Eng., 2007, pp. 91.
- [17] Joint Committee on Structural Safety, *Probabilistic Model Code Part 3 – Resistance Models, Concrete Properties*, 2000.
- [18] N. Yazdani, S. Eddy, and C. S. Cai, "Effect of bearing pads on precast prestressed concrete bridges," *J. Bridge Eng.*, vol. 5, no. 3, pp. 224–232, 2000.
- [19] Associação Brasileira de Normas Técnicas, *Projeto e Execução de Estruturas de Concreto Pré-moldado*, ABNT NBR 9062:2001, 2001.
- [20] Associação Brasileira de Normas Técnicas, *Aparelhos de Apoio de Elastômero Fretado – Especificação e Métodos de Ensaio*, ABNT NBR 19783:2015, 2015.
- [21] M. T. S. A. Cardoso, "Instabilidade lateral de vigas pré-moldadas sobre apoios elastoméricos considerando o efeito das imperfeições geométricas," M.S. thesis, Prog. Pós-grad. Eng. Civil, Univ. Fed. Uberlândia, Uberlândia, 2017.

---

**Author contributions:** MFAO: data acquisition, methodology, numerical and analytical analysis, writing; PAK: conceptualization, methodology, formal analysis, writing, supervision; MCVL: conceptualization, formal analysis, writing, supervision.

**Editors:** Vladimir Guilherme Haach, José Luiz Antunes de Oliveira e Sousa, Guilherme Aris Parsekian.



## ORIGINAL ARTICLE

# Parametric study of the strength of reinforced concrete polygonal sections submitted to oblique composite flexion

*Estudo paramétrico da resistência de seções poligonais de concreto armado submetidas à flexão composta oblíqua*

Lucas Peres de Souza<sup>a</sup>

Marco André Argenta<sup>a</sup>

<sup>a</sup>Universidade Federal do Paraná – UFPR, Programa de Pós-graduação em Engenharia da Construção Civil – PPGECC, Curitiba, PR, Brasil

Received 21 March 2019

Accepted 28 February 2020

**Abstract:** This work aims to verify the influence of characteristic compressive cylinder strength ( $f_{ck}$ ), section geometry and eccentric axial load on the strength of square, cross, “T” and “L” reinforced concrete sections, under oblique composite flexion. A computational algorithm was created to calculate sections interaction diagram of bending strength, taking into account NBR 6118 idealized parabola-rectangle stress-strain relationships for 20 to 90 MPa  $f_{ck}$  concretes. The results show that  $f_{ck}$  influence is stronger for higher values of axial load and that the failure surface shape in interaction diagrams depends directly on the  $f_{ck}$  and on the rebars distribution in the section. Furthermore, under lower compressive axial loads, higher oblique composite flexion strengths are reached when there is more reinforcement area in tension regions but, as the compression increases, the reinforcement presence and larger concrete areas in compression zones provide higher bending moment strengths.

**Keywords:** reinforced concrete, polygonal sections, oblique composite flexion.

**Resumo:** Este trabalho objetiva verificar a influência da variação da resistência do concreto ( $f_{ck}$ ), da geometria da seção transversal e do esforço axial de compressão excêntrico na resistência à flexão composta oblíqua de seções com formato quadrado, “cruz”, “T” e “L”, com mesmas áreas de concreto e de armaduras. Para isso, cria-se um algoritmo computacional que calcula as envoltórias de resistência, aplicando os diagramas tensão-deformação propostos pela NBR 6118:2014 para concretos com  $f_{ck}$  de 20 a 90 MPa. Os resultados revelam que o  $f_{ck}$  exerce maior influência para esforços de compressão mais elevados e que o  $f_{ck}$  e a distribuição das barras de aço interferem diretamente no formato das envoltórias. Mostra-se também que, sob compressões baixas, a concentração das barras de aço nas zonas de tração leva às maiores resistências mas, à medida que a compressão cresce, a presença da armadura e de maiores áreas de concreto nas zonas de maior compressão é que induzem momentos resistentes maiores.

**Palavras-chave:** concreto armado, seções poligonais, flexão composta oblíqua.

**How to cite:** L. P. Souza and M. A. Argenta, “Parametric study of the strength of reinforced concrete polygonal sections submitted to oblique composite flexion,” *Rev. IBRACON Estrut. Mater.*, vol. 13, no. 5, e13512, 2020, <https://doi.org/10.1590/S1983-41952020000500012>

## 1 INTRODUCTION

Sections subjected to combined bending and axial load are recurrent in reinforced concrete structures. Generally, situations such as columns located in building corners, or even supporting two-way slabs, lead to such types of internal forces [1]. Usually, the representation of reinforced concrete sections strength of combined biaxial bending and axial load is made by axial force ( $N$ ) - bending moment ( $M_x$  and  $M_y$ ) interaction diagrams. These diagrams calculation

Corresponding author: Lucas Peres de Souza. E-mail: [lucasperes.eng@gmail.com](mailto:lucasperes.eng@gmail.com)

Financial support: Financial supports by the Coordination for the Improvement of Higher Education Personnel of Brazil (CAPES) and by the Araucária Foundation are gratefully acknowledged.

Conflict of interest: Nothing to declare.



This is an Open Access article distributed under the terms of the Creative Commons Attribution License, which permits unrestricted use, distribution, and reproduction in any medium, provided the original work is properly cited.

involves an internal section equilibrium iterative process, due to the physical nonlinearity problem because steel and concrete constitutive relationships. There are, in the literature, a variety of methods proposed to reach such strengths. Dall'Asta and Dezi [2] for example, develop an iterative method in which the main unknown of the problem is a minimum required reinforcement steel area, given a section geometry (arbitrary polygon), the number and location of the rebars, and the mechanical behavior materials. Fafitis [3] generates an algorithm based on the Green's theorem analytical integration of concrete compressive stresses, transforming the double integral integrals into integral line along the compressed polygons. Vaz Rodrigues [4], in turn, implements an algorithm based on the section subdivision into trapezoidal elements and uses the Gauss-Legendre stress integration over these elements.

In addition to the ways to reach the sections strengths, there is a need to evaluate the material properties (reinforced concrete) and section geometry effects on the results of these calculation algorithms. In 2014, NBR 6118 [5] began to contemplate concrete characteristic compressive cylinder strength ( $f_{ck}$ ) from 50 to 90 MPa and proposed a parabola-rectangle constitutive relationships to these materials. The equations proposed in this standard idealize the concrete stress-strain behavior as a parabola-rectangle curve and establish the possible deformation domains for reinforced concrete sections under combined bending and axial load by strains  $\epsilon_{c2}$  (concrete compressive strain at the end of parabolic region) and  $\epsilon_{cu}$  (concrete ultimate compressive strain), calculated according to  $f_{ck}$ , combined with steel yield and ultimate strains, according to Figure 1.

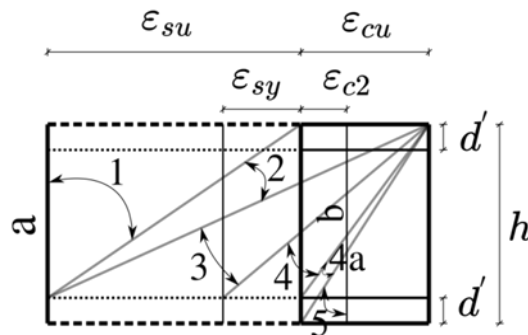


Figure 1. NBR 6118 [5] deformation domains for reinforced concrete sections under combined bending and axial load.

In this context, there are analytical and experimental works that help the understanding of the new formulations. Torrico [6], for example, studies the behavior of high strength concrete slender columns, analyzing, among other factors, the concrete ultimate limit states of rupture both experimentally and numerically.

With the investigation of section geometry effects there are also the possibility of optimizing reinforced concrete structural elements under combined bending and axial load, according to applied forces. Campione et al. [7] perform a study of the parameters such as concrete strength, section shape, confining level, reinforcement ratio and rebars distribution influence. The authors conclude, among other things, that increasing concrete strength does not modify the interaction diagram shape of the section with maximum curvature, although it provides an increase in section deformation capacity by reducing the dimensionless axial force  $\nu$ , calculated according to Equation 1.

$$\nu = \frac{N}{A_c f_{cd}} \tag{1}$$

Based on what already exists in the literature and continuing the study of Souza [8], the present work objectives are: a) the verification of the influence of concrete  $f_{ck}$  variation on the oblique composite flexion of square, cross-format, "T" and "L" reinforced concrete sections, applying the parabola-rectangle of NBR 6118  $f_{ck}$  [5]; b) a comparison of the oblique composite flexion strength among different strength shapes with constant steel and concrete areas, considering the variation of concrete and axial force.

## 2 METHOD

The analysis of the work is based on the results produced by a computational routine developed in *Python 3* language, which reads the input data of the problem, generates the moment-axial force-curvature interaction diagrams and finally calculates the moment-axial force-curvature interaction diagrams for reinforced concrete sections, as shown in Figure 2.

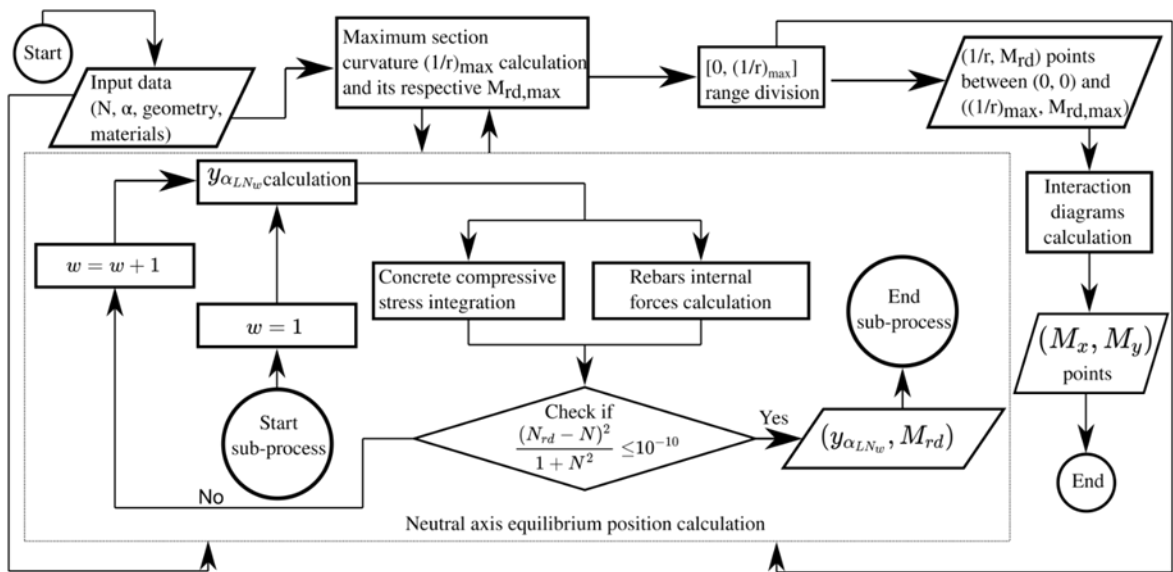


Figure 2. Method sequence.

### 2.1 Input data

The main input data of the problem are the sections geometry, materials constitutive relationships, neutral axis inclination angles and axial forces, for which the moment-axial force-curvature interaction diagrams were calculated.

In view of the definition of the problem geometry, we chose to analyze the square, cross-format, “T” and “L” sections of Figure 3 which have the same reinforcement area equal to 12.57 cm<sup>2</sup> and concrete area equal to 625 cm<sup>2</sup> (convenient values). The definition of  $H_x$ ,  $H_y$ ,  $b_x$  e  $b_y$  dimensions and of all sections departed from the square section of dimensions 25 x 25 cm. Thus, it was arbitrated that, in cross-format, “T” and “L” the section dimensions  $H_x = H_y$  and  $b_x = b_y = H_x / 3 = H_y / 3$ . With such dimension relations and with the concrete area remaining constant, it was possible to calculate the dimensions in Figure 3

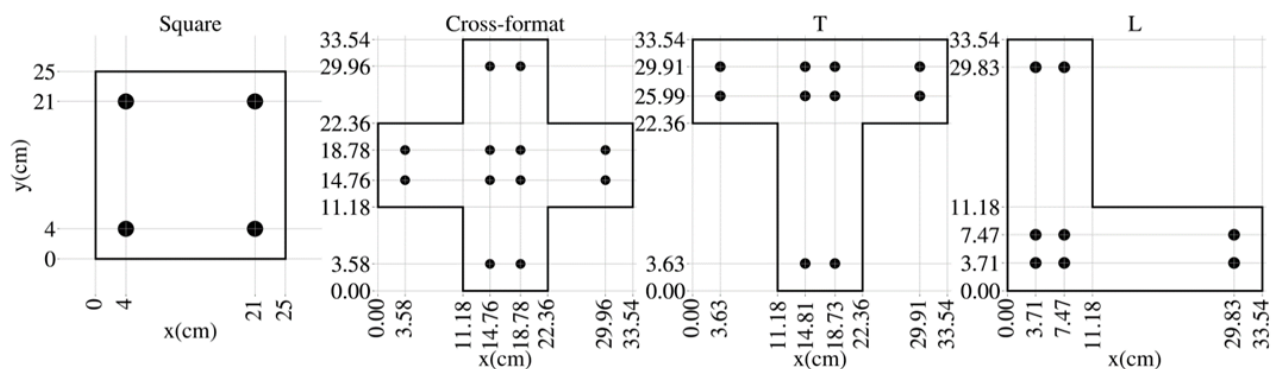


Figure 3. Geometry of analyzed sections.

The definition of the rebars distribution and respective area followed a similar script, in which the first decision is the fixation of the square section reinforcement detailing, with 4 rebars of diameter  $\phi_l$  equal to 2 cm, symmetrically distributed, with  $d'$  distances between section edges and rebars centroid equal to the sum of the concrete nominal cover  $c_{nom}$ , equal to 2.5 cm, with the transverse reinforcement diameter  $\phi_t$ , equal to 0.5 cm, and with longitudinal rebars radius (1 cm), resulting in  $d'$  equal to 4 cm.

By fixing the reinforcement area  $A_s$  at 12.57 cm<sup>2</sup> and using the same value to  $c_{nom}$  and  $\phi_l$  from all sections, a longitudinal rebars area for the sections with other shapes is calculated, and the criterion to define the quantity of rebars was the minimum quantity required to enable transverse fixation reinforcement.

Concrete characteristic compressive cylinder strength ( $f_{ck}$ ) range from 20 to 90 MPa by 10 MPa, i.e. the range of values encompassed by NBR 6118 [5].

The equations for the mathematical representation of the concrete and steel constitutive relationships are also defined from NBR [5]. Concrete tensile strength is neglected and its compressive behavior is represented by the idealized parabola-rectangle diagram, described by Equations 2 to 5 and generalized for application in concretes up to 90 MPa. In turn, the CA-50 longitudinal reinforcement steel has its behavior described by NBR 6118 [5] bilinear elastic perfectly plastic stress-strain relationship, represented by Equation 6, for both tensile and compressive strains.

$$\sigma_c = \begin{cases} 0.85 f_{cd} \left[ 1 - \left( 1 - \frac{\epsilon_c}{\epsilon_{c2}} \right)^n \right], & \text{if } 0 \leq \epsilon_c \leq \epsilon_{c2} \\ 0.85 f_{cd}, & \text{if } \epsilon_{c2} \leq \epsilon_c \leq \epsilon_{cu} \end{cases} \quad (2)$$

$$\epsilon_{c2} = \begin{cases} 0.2\%, & \text{if } f_{ck} \leq 50 \text{ MPa} \\ 0.2\% + 0.0085\% (f_{ck} - 50)^{0.53}, & \text{if } 50 < f_{ck} \leq 90 \text{ MPa} \end{cases} \quad (3)$$

$$\epsilon_{cu} = \begin{cases} 0.35\%, & \text{if } f_{ck} \leq 50 \text{ MPa} \\ 0.26\% + 3.5\% \left( \frac{90 - f_{ck}}{100} \right)^4, & \text{if } 50 < f_{ck} \leq 90 \text{ MPa} \end{cases} \quad (4)$$

$$n = \begin{cases} 2, & \text{if } f_{ck} \leq 50 \text{ MPa} \\ 1.4 + 23.4 \left( \frac{90 - f_{ck}}{100} \right)^4, & \text{if } 50 < f_{ck} \leq 90 \text{ MPa} \end{cases} \quad (5)$$

$$\sigma_s = \begin{cases} \epsilon_s E_s, & \text{if } \epsilon_s \leq \frac{f_{yd}}{E_s} \\ f_{yd}, & \text{if } \frac{f_{yd}}{E_s} < \epsilon_s \leq 1\% \end{cases} \quad (6)$$

where  $\sigma_c$  = concrete compressive stress;  $f_{cd}$  = concrete compressive strength design value;  $\epsilon_c$  = concrete compressive strain;  $\epsilon_{c2}$  = concrete compressive strain at the end of parabolic region;  $n$  = parabolic region exponent;  $\epsilon_{cu}$  = concrete ultimate compressive strain;  $f_{ck}$  = concrete characteristic compressive cylinder strength;  $\sigma_s$  = rebar stress;  $\epsilon_s$  = rebar strain;  $E_s$  = rebar steel elastic modulus design value;  $f_{yd}$  = rebar steel design yield strength.

Axial force values applied to sections,  $N$ , vary depending on the type of analysis desired. In the analysis of the influence of  $f_{ck}$ , values shift from 500 to 1200 kN by 100 kN for square and cross-format sections. For “T” sections,  $N$  values shift from 500 to 1000 kN by 100 kN and, for “L” sections, from 500 to 1100 kN by 100 kN. Different limit superior values (1000, 1100 and 1200 kN) are used because maximum section axial strength is different for each section shape.

Flexural strength comparisons among different section shapes are done for sections subjected to the same dimensionless axial force  $\nu$ , considering that sections compared have the same concrete area and  $f_{ck}$ .

Neutral axial inclination angle,  $\alpha$ , range from 0 to  $2\pi$  rad by  $\frac{\pi}{360}$  rad (720 increments) for moment-axial force-curvature interaction diagrams calculation.

### 2.2 Moment-axial force-curvature interaction diagrams calculation

Moment-axial force-curvature interaction diagrams determine the correspondence between the section curvature and the respective flexural strength, based on the axial force  $N$ , neutral axis inclination angle and section geometry.

Figure 4 iterative process, based on the bisection method, is used to find the section maximum allowed curvature before concrete crushing or reinforcement steel elongation limit. The interval containing the solution is repeatedly bisected until the relative variation between two consecutive iterations is less than 1%.

Rupture verification, inside the section maximum allowed curvature calculation, is done by another iterative algorithm, that aims to calculate neutral axis equilibrium position  $y_{\alpha_{LN}}$ . This procedure is applied to find the section strain field that balances the section curvature  $(1/r)_k$  and the applied axial force  $N$ . As in the algorithm that achieves a section maximum allowed curvature, the bisection method is used until the relative variation between the section axial strength and the applied axial force is less than 1%.

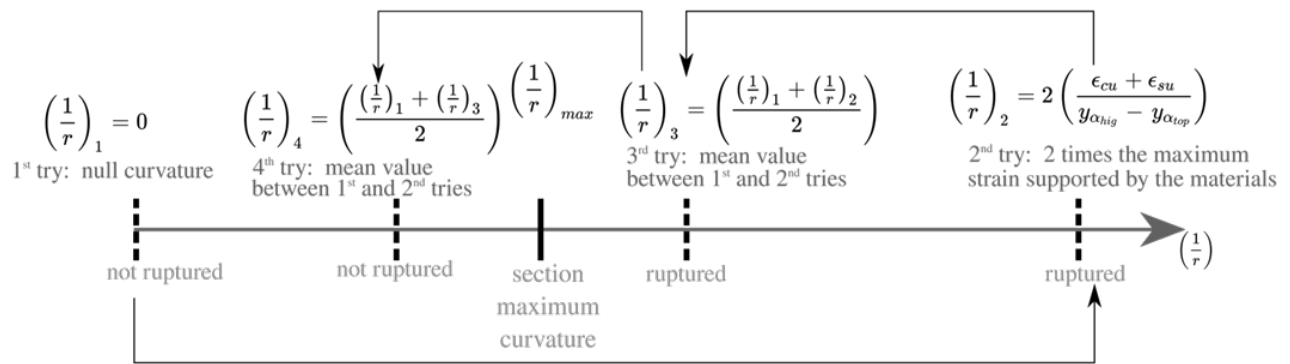


Figure 4. Illustrative scheme of bisection process used to find the section maximum allowed curvature.

Concrete compressive stress integration is solved by using numerical integration to determine the compressed area, the  $y_{\alpha_{e2}}$  coordinate is calculated according to Equation 7.

$$y_{\alpha_{e2}} = y_{\alpha_{LNw}} + \epsilon_{c2} / (1/r)_k \tag{7}$$

where  $y_{\alpha_{e2}} = y_{\alpha}$  coordinate that corresponds to  $\epsilon_{c2}$  strain;  $y_{\alpha_{LNw}}$  = neutral axis  $y_{\alpha}$  coordinate in iteration  $w$ ;  $(1/r)_k$  = section curvature in iteration  $k$ .

The compressed areas vertex coordinates are determined according to Figure 5, using the *Python's Shapely* package (*geometry.polygon.intersection*), from the python shapely package, developed by Gillies [9]. The area  $pol_{intersec}$  results from the intersection between the infinite region  $pol_2$  above neutral axis and section region  $pol_1$ , using  $(x_{\alpha}, y_{\alpha})$  coordinates.

Then,  $pol_{intersec}$  area is meshed with triangles, using *Python's MeshPy* package (*meshpy.triangle*), developed by Klöckner [10]. Mesh generation is controlled by triangles maximum area set as 10 cm<sup>2</sup>. This value represents a balance between computational processing time and results expected precision. The mesh generation output data is a set of  $n_i$  matrices  $[tri]_{i,3x2}$  containing triangle elements vertex coordinates  $(x_{\alpha}, y_{\alpha})$  in compressed area, as in Equation 8.

$$[tri]_{t,3 \times 2} = \begin{bmatrix} x_{\alpha,t,1} & y_{\alpha,t,1} \\ x_{\alpha,t,2} & y_{\alpha,t,2} \\ x_{\alpha,t,3} & y_{\alpha,t,3} \end{bmatrix} \tag{8}$$

where  $[tri]_{t,3 \times 2}$  = vertex coordinates matrix of  $t$ -th triangle.

Concrete axial strength  $R_{cd}$  and its respective position coordinates  $x_{\alpha_{Rcd}}$  and  $y_{\alpha_{Rcd}}$  are calculated according to compressive stress integration Equations 9 and 10 over  $pol_{intersec}$  area  $A_{pol}$ .

$$R_{cd} = \int_{A_{pol}} \sigma_c dA \tag{9}$$

$$y_{\alpha_{Rcd}} = \frac{\int_{A_{pol}} y_{\alpha} \sigma_c dA}{R_{cd}} \text{ and } x_{\alpha_{Rcd}} = \frac{\int_{A_{pol}} x_{\alpha} \sigma_c dA}{R_{cd}} \tag{10}$$

where  $R_{cd}$  = concrete axial strength;  $A_{pol}$  =  $pol_{intersec}$  area;  $y_{\alpha_{Rcd}}$  = concrete axial strength position  $y_{\alpha}$  coordinate;  $x_{\alpha_{Rcd}}$  = concrete axial strength position  $x_{\alpha}$  coordinate.

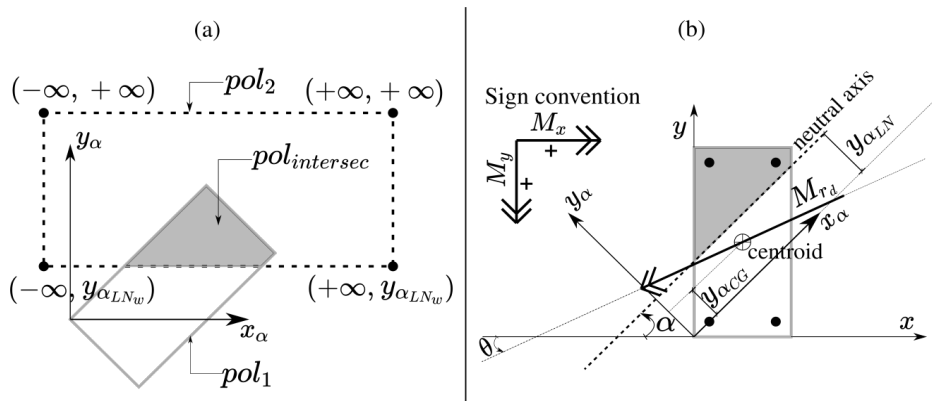


Figure 5. (a) Polygon intersection demonstration; (b) Difference between neutral axis angle  $\alpha$  and flexural strength angle  $\theta$ .

Considering  $A_{pol}$  subdivision in  $n_t$  triangles, Equations 9 and 10 integrals are rewritten as sums of integrals over triangles areas  $A_{tri_t}$  (Equations 11 and 12).

$$\int_{A_{pol}} \sigma_c dA = \sum_{t=1}^{n_t} \int_{A_{tri_t}} \sigma_c dA \tag{11}$$

$$\int_{A_{pol}} y_{\alpha} \sigma_c dA = \sum_{t=1}^{n_t} \int_{A_{tri_t}} y_{\alpha} \sigma_c dA \text{ and } \int_{A_{pol}} x_{\alpha} \sigma_c dA = \sum_{t=1}^{n_t} \int_{A_{tri_t}} x_{\alpha} \sigma_c dA \tag{12}$$

where  $n_t$  = total number of triangles in  $pol_{intersec}$  triangle mesh;  $t$  = number of current analyzed triangle;  $A_{tri_t}$  =  $t$ -th triangle area.

Then, Equations 11 and 12 are solved using Gauss-Legendre quadrature and concrete axial  $R_{cd}$  and flexural strengths  $M_{cd}$  are calculated by Equations 9 and 13.

$$M_{cd} = \left[ \left( y_{\alpha_{Rcd}} - y_{\alpha_{cg}} \right)^2 + \left( x_{\alpha_{Rcd}} - x_{\alpha_{cg}} \right)^2 \right]^{0.5} R_{cd} \quad (13)$$

where  $M_{cd}$  = concrete flexural strength;  $y_{\alpha_{Rcd}}$  = section centroid  $y_{\alpha}$  coordinate;  $x_{\alpha_{Rcd}}$  = section centroid  $x_{\alpha}$  coordinate.

In addition, axial strength rebars  $R_{sb}$  are calculated according to Equation 14 and depends on the stress in  $\sigma_{sb}$  each rebar, obtained by Equation 6 and using Equation 15 to determine rebars  $\varepsilon_{sb}$  strain.

$$R_{sb} = A_{sb} \sigma_{sb} \quad (14)$$

$$\varepsilon_{sb} = \left( y_{\alpha_b} - y_{\alpha_{LNw}} \right) \quad (15)$$

where  $R_{sb}$  = rebar axial strength;  $A_{sb}$  = rebar area;  $\sigma_{sb}$  = rebar stress;  $\varepsilon_{sb}$  = rebar strain;  $y_{\alpha_b}$  = rebar centroid  $y_{\alpha}$  coordinate.

Next, Equation 16 is used to calculate rebars flexural strength  $M_{sb}$  :

$$M_{sb} = \left[ \left( y_{\alpha_b} - y_{\alpha_{cg}} \right)^2 + \left( x_{\alpha_b} - x_{\alpha_{cg}} \right)^2 \right]^{0.5} R_{sb} \quad (16)$$

where  $M_{sb}$  = rebar flexural strength;  $x_{\alpha_b}$  = rebar centroid  $x_{\alpha}$  coordinate.

Thus, reinforcement axial  $R_{sd}$  and flexural  $M_{sd}$  strength is calculated by Equations 17 and 18, by summing over all rebars strengths.

$$R_{sd} = \sum_{b=1}^{n_{rebars}} R_{sb} \quad (17)$$

$$M_{sd} = \sum_{b=1}^{n_{rebars}} M_{sb} \quad (18)$$

where  $R_{sd}$  = reinforcement axial strength;  $n_{rebars}$  = number of rebars in the section;  $M_{sd}$  = reinforcement flexural strength.

Therefore, section axial  $N_{rd}$  and flexural  $M_{rd}$  strength is established in Equations 19 and 20 by summing concrete and reinforcement contributions:

$$N_{rd} = R_{cd} + R_{sd} \quad (19)$$

$$M_{rd} = M_{cd} + M_{sd} \quad (20)$$

where  $N_{rd}$  = section axial strength;  $M_{rd}$  = section flexural strength.

In summary,  $N_{rd}$  and  $M_{rd}$  are the section strengths that balance the equilibrium for a section with a curvature  $(\frac{1}{r})_k$  and a neutral axis inclination angle  $\alpha$ , subjected to an applied axial force  $N$ .

### 2.3 Bending moment-axial force interaction diagrams calculation

Bending moment-axial force interaction diagrams curves are sets of points represented by combined loads (bending and axial) that lead to section failure. These points are determined based on moment-axial force-curvature data processing. Each  $(N, \alpha)$  pair determine a maximum flexural strength  $M_{rd}$ , its respective  $\theta$  inclination angle from the  $x$  axis and its respective neutral axis equilibrium position, as illustrated in Figure 5b. Difference between  $\alpha$  and  $\theta$  angles is due to the asymmetric distribution of concrete compressive stresses and of the rebars stresses in relation to the neutral axis perpendicular line.

The interaction diagrams points coordinates are the applied axial force  $N = N_{rd}$  and the maximum flexural strengths around  $x$ ,  $M_x = -M_{rd} \cos \theta$ , and  $y$  axis,  $M_y = M_{rd} \sin \theta$ .

## 3 RESULTS

### 3.1 Concrete characteristic compressive cylinder strength ( $f_{ck}$ ) influence on section flexural strength

Interaction diagrams of sections with same geometry and subjected to the same applied axial force  $N$ , but with different  $f_{ck}$  values, are compared in order to analyze the  $f_{ck}$  influence on sections flexural strength.

Figure 6 show comparisons for square, cross-format and “T” sections.  $N$  values applied to the square sections are  $N = 500$  kN,  $N = 800$  kN and  $N = 1200$  kN. Regarding to the cross-format sections,  $N$  values also vary from 500 to 1200 kN and the results are presented for  $N = 500$  kN,  $N = 800$  kN and  $N = 1200$  kN. “T” sections, in turn, are subjected to applied axial load values that range from 500 to 1000 kN and Figure 6 exhibits interaction diagrams comparison for  $N = 500$  kN,  $N = 800$  kN and  $N = 1000$  kN. Figure 7 present the results for “L” sections compressed by  $N = 500$  kN (minimum applied axial load),  $N = 800$  kN and  $N = 1100$  kN (maximum applied axial load), respectively. Table 1 summarizes the interaction diagrams results presented in Figures 6 and 7, for  $\theta$  angles varying from 0 to  $\frac{7\pi}{4}$  rad, shifted by  $\frac{\pi}{4}$  rad, in order to facilitate the numeric reading of figures results.

The use of axial force absolute values instead of dimensionless axial force  $\nu$  was chosen because  $f_{ck}$  is variable and, consequently, for the same section subjected to a constant  $\nu$ ,  $N$  absolute value would also vary with the  $f_{ck}$ , something that could distort comparisons.

### 3.2 Shape influence on section flexural strength

Shape influence on section flexural strength is evaluated by comparing side by side the flexural strength interaction diagrams of square, cross-format, “T” and “L” sections of Figure 3, that are composed of concretes of the same  $f_{ck}$ , same reinforcement steel area and subjected to the same dimensionless axial force  $\nu$ . It is noteworthy that, in this case, the analysis by the rates of dimensionless axial force  $\nu$  is possible because the graphs deal with the same  $f_{ck}$  and the same concrete area.

Analyzed sections are composed of 20, 50, 60 and 90 MPa  $f_{ck}$  concretes. These values are selected considering that 20 and 90 MPa are the NBR 6118 [5] stress-strain relationship extreme values and 50 and 60 MPa are values next to the point where Equation 2 change. Figure 8 show interaction for 20 and 50 MPa concrete sections and Figure 9 present comparisons among section shape flexural strengths of 60 and 90 MPa concrete sections.

## 4 DISCUSSION

### 4.1 Concrete characteristic compressive cylinder strength ( $f_{ck}$ ) influence on section flexural strength

The results show three important issues related to  $f_{ck}$  effect on section flexural strength: a) the  $f_{ck}$  variation produced little effect on flexural strength of sections under low axial forces magnitude. However, this effect is enhanced when applied axial force is increased; b) the shape of flexural strength interaction diagrams tends to be modified as the compression is increased, but sections with  $f_{ck} \leq 50$  MPa and with  $f_{ck} > 50$  MPa present opposing trends; c) mainly low axial forces out of sections principal axis of inertia (oblique composite flexion), the 50 MPa sections axial strength is greater than the 60 and 70 MPa one.

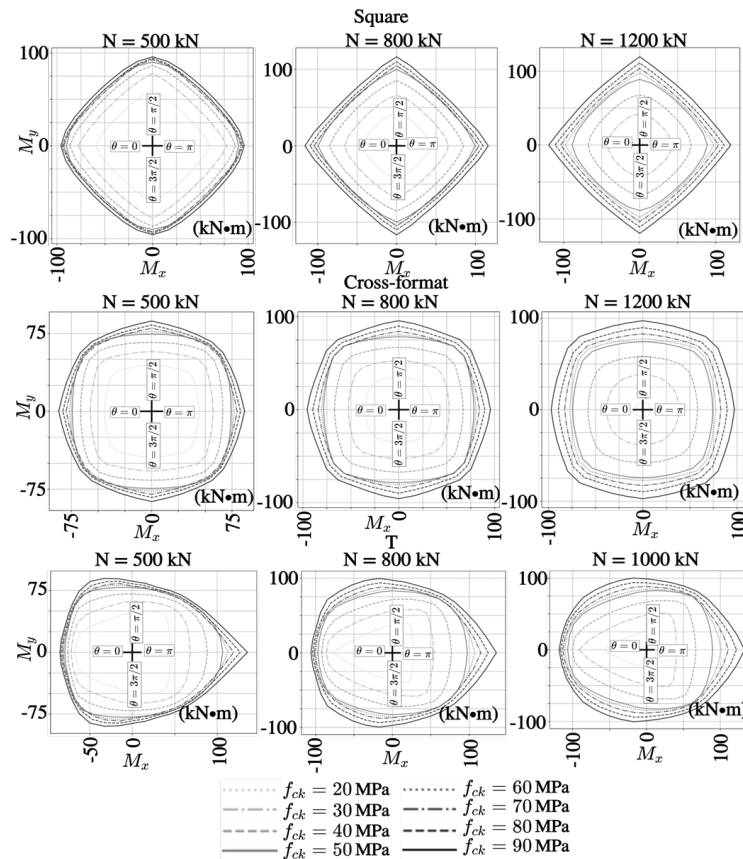


Figure 6. Influence of  $f_{ck}$  on square, cross-format and “T” sections flexural strength.

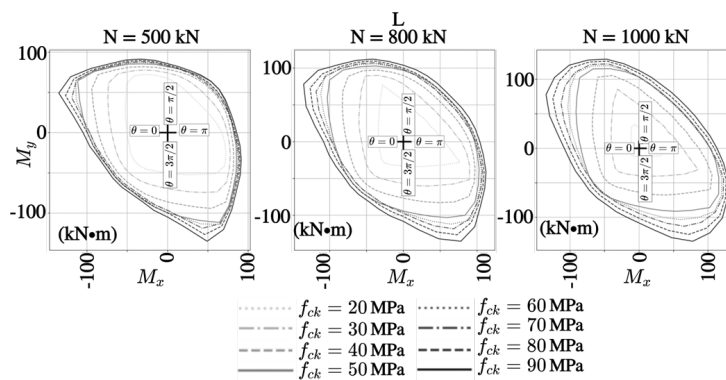


Figure 7. Influence of  $f_{ck}$  on “L” sections flexural strength.

In square sections, flexural strength interaction diagrams of sections with 50, 60, 70 and 80 MPa  $f_{ck}$  are remarkably close, to the point of almost matching under axial force of 500 kN. Even sections composed of concrete with 30 and 40 MPa  $f_{ck}$  did not show significant reductions in their resistance. Evaluating the maximum flexural strength, a section with  $f_{ck} = 40$  MPa could reach 86.80 kN·m, while the section with  $f_{ck} = 90$  MPa has a maximum flexural strength of 95.89 kN·m, indicating a 10.47% increase in flexural strength under a 125% increase in concrete characteristic compressive cylinder strength.

The visualization of the neutral axis equilibrium position at the flexural strength interaction diagrams limits allows to see the stress and strain states in each case. It appears in Figure 10 plot for  $N = 500$  kN that neutral axis intercepts the section in all interaction diagrams for all  $\theta$  angles (NBR 6118 [5] domains 2, 3 and 4) at sections equilibrium limit

states and that high strength concretes require smaller compressed areas. It is also interesting to point out that the concrete flexural strength contribution is higher with the increase of the  $f_{ck}$ . When  $\theta=0^\circ$ , the respective concrete and reinforcement contributions on flexural strength are 47% and 53% for 20 MPa concrete sections and 65% and 35% for 90 MPa concrete sections.

**Table 1.** Sections flexural strength (kN·m).

$\theta$ (rad)	Square									Cross-format								
	N (kN)	$f_{ck}$ (MPa)								N (kN)	$f_{ck}$ (MPa)							
		20	30	40	50	60	70	80	90		20	30	40	50	60	70	80	90
0	500	59.4	78.0	86.8	90.1	92.2	93.2	94.5	95.9	500	44.4	57.4	66.3	74.1	76.9	79.8	83.0	86.8
	800	42.0	65.7	85.3	99.6	104.9	104.6	109.8	116.2	800	35.2	52.6	67.1	78.5	80.7	84.2	89.8	95.6
	1200	9.1	41.3	67.5	88.9	97.7	103.9	111.2	119.6	1200	8.7	38.8	58.2	74.4	77.6	83.0	89.7	97.3
$\pi/4$	500	48.1	62.0	71.9	78.7	78.4	76.7	78.8	81.9	500	51.0	67.1	76.9	83.7	83.4	82.2	84.4	87.2
	800	36.7	55.3	70.4	82.2	81.2	81.4	85.0	89.7	800	38.4	60.0	76.9	90.1	89.3	89.6	93.8	98.7
	1200	9.1	38.4	59.4	76.1	78.0	81.1	85.6	92.6	1200	8.4	39.6	64.5	84.4	88.6	91.7	97.3	105.0
$\pi/2$	500	59.4	78.0	86.8	90.1	92.2	93.2	94.5	95.9	500	44.4	57.4	66.3	74.1	76.9	79.8	83.0	86.8
	800	42.0	65.8	85.3	99.6	104.9	104.6	109.8	116.2	800	35.2	52.6	67.1	78.5	80.7	84.2	89.8	95.6
	1200	9.3	41.5	67.8	88.9	97.7	103.9	111.2	119.6	1200	8.8	38.8	58.2	74.4	77.6	83.0	89.7	97.3
$\theta$ (rad)	T									L								
	N (kN)	$f_{ck}$ (MPa)								N (kN)	$f_{ck}$ (MPa)							
		20	30	40	50	60	70	80	90		20	30	40	50	60	70	80	90
0	500	67.3	72.1	76.0	79.3	80.8	82.0	83.6	85.2	500	49.9	69.4	86.1	99.4	96.7	96.4	99.6	104.8
	800	77.4	86.2	92.2	97.3	100.2	101.9	104.2	106.3	800	33.2	56.5	76.7	94.3	95.6	97.1	101.7	108.2
	1000	57.9	91.5	100.4	106.9	111.2	113.8	116.6	118.6	1100	11.6	39.7	63.5	84.3	90.1	94.4	101.4	108.3
$\pi/4$	500	51.6	68.3	81.8	90.2	91.1	89.3	91.2	94.1	500	72.6	99.2	106.3	112.1	112.9	113.3	115.0	117.4
	800	39.7	60.2	77.8	93.3	95.6	97.4	103.0	109.4	800	47.0	82.4	114.1	132.1	135.7	136.2	138.3	143.1
	1000	27.6	51.8	71.8	89.5	93.8	97.7	104.4	110.9	1100	16.0	56.3	92.4	125.1	137.9	144.0	153.9	159.9
$\pi/2$	500	48.1	62.1	70.9	78.5	79.5	80.6	83.2	86.3	500	67.6	74.3	78.6	81.9	82.5	82.9	84.1	85.7
	800	37.3	55.8	71.4	83.1	86.2	87.2	91.9	97.3	800	55.7	78.7	90.1	96.9	98.3	98.0	100.1	104.0
	1000	27.2	48.7	66.7	82.0	84.5	88.3	93.6	99.0	1100	29.8	63.2	87.0	103.7	102.8	103.5	109.0	113.0
$3\pi/4$	500	57.3	72.9	82.2	89.5	87.6	87.0	89.1	92.1	500	53.4	66.6	76.1	83.2	79.2	77.7	80.3	83.6
	800	36.4	66.1	85.1	96.4	96.2	96.2	99.5	104.0	800	42.2	60.2	74.0	85.3	81.9	81.2	84.5	89.4
	1000	17.6	52.9	80.1	97.5	97.9	99.6	103.9	108.3	1100	21.5	48.2	67.0	82.1	80.8	81.6	86.6	91.6
$\pi$	500	46.2	68.2	88.3	106.4	112.9	119.4	127.1	135.6	500	67.6	74.3	78.6	81.9	82.5	82.9	84.1	85.7
	800	27.1	54.0	76.7	97.5	107.4	115.1	124.8	135.4	800	55.7	78.7	90.1	96.9	98.3	98.0	100.1	104.0
	1000	12.1	40.9	67.0	89.7	101.3	110.9	122.1	133.0	1100	29.8	63.2	87.0	103.7	102.7	103.5	109.0	113.0
$5\pi/4$	500	57.3	72.9	82.2	89.6	87.6	87.0	89.1	92.1	500	72.6	99.3	106.3	112.1	112.9	113.3	115.0	117.4
	800	36.4	65.9	85.1	96.4	96.2	96.2	99.5	104.0	800	47.0	82.4	114.1	132.1	135.7	136.2	138.3	143.1
	1000	17.5	52.9	79.9	97.5	97.9	99.6	103.9	108.3	1100	16.0	56.3	92.4	125.1	137.9	144.0	153.9	159.9
$3\pi/2$	500	48.1	62.1	70.9	78.5	79.5	80.6	83.2	86.3	500	50.0	69.4	86.1	99.4	96.7	96.4	99.6	104.8
	800	37.3	55.8	71.4	83.1	86.2	87.2	91.9	97.3	800	33.2	56.5	76.7	94.3	95.6	97.1	101.7	108.2
	1000	27.2	48.7	66.7	82.0	84.5	88.3	93.6	99.0	1100	11.6	39.7	63.5	84.3	90.1	94.4	101.4	108.3
$7\pi/4$	500	51.6	68.3	81.8	90.2	91.1	89.3	91.2	94.1	500	54.1	69.0	79.2	85.4	84.6	82.9	85.0	88.4
	800	39.7	60.2	77.8	93.3	95.6	97.4	103.0	109.4	800	38.7	60.3	76.7	89.0	85.4	85.1	89.1	93.9
	1000	27.6	51.8	71.8	89.5	93.8	97.8	104.4	110.9	1100	14.9	45.1	66.6	84.1	82.3	83.3	88.6	94.3

The relative proximity of the square sections interaction diagrams with different strength concretes in Figure 6 with  $N = 500$  kN can then be associated with the predominance of bending effects, where low concrete flexural strength

contributions can be offset by the increase in the reinforcement steel contribution, since the applied axial force is relatively low.

On the other hand, the Figure 6 square sections interaction diagrams with  $N = 800$  kN now indicate some differences in relation to  $N = 500$  kN diagrams and greater distance between the interaction diagrams is perceived, being that the order of the flexural strengths agrees the ascending order of the  $f_{ck}$ . The only exception is the comparison of the interaction diagrams of the square sections with 50 and 60 MPa  $f_{ck}$ , which almost coincide outside the principal axis of inertia and move away only when are on them.

It is attested that for square sections with  $N = 800$  kN, there is an increase in concrete flexural strength with  $\theta = 0^\circ$ , which is 56% for a section with  $f_{ck} = 20$  MPa and increases up to 68% for those with  $f_{ck} = 90$  MPa. In addition, Figure 10 plot for  $N = 800$  kN shows that neutral axis equilibrium positions continue to intercept the sections even if the compressed area predominates in the case of concretes with  $f_{ck}$  from 20 to 70 MPa. The increase of concrete contribution on section flexural strength is, in this case, the main factor that interferes in the greatest distance between the Figure 6 square sections interaction diagrams with  $N = 800$  kN.

The differences between the curves are greater in Figure 6 square section diagrams with  $N = 1200$  kN, due to the increase of the compressed areas and, consequently, the concrete contribution on section flexural strength. However, when analyzing square sections equilibrium configuration when the angle  $\alpha$  is zero in Figure 10 plot for  $N = 1200$  kN, it is seen that only the square section with  $f_{ck} = 20$  MPa has neutral axis totally external to the section. All other sections with  $f_{ck}$  values above 20 MPa indicate partial compression, with the neutral axis intercepting the section, even with  $N = 1200$  kN.

The same phenomenon is observed with the variation of the  $N$  for sections with other shapes, showing that  $f_{ck}$  the influence grows as the compressive axial force becomes predominant in relation to the bending moment.

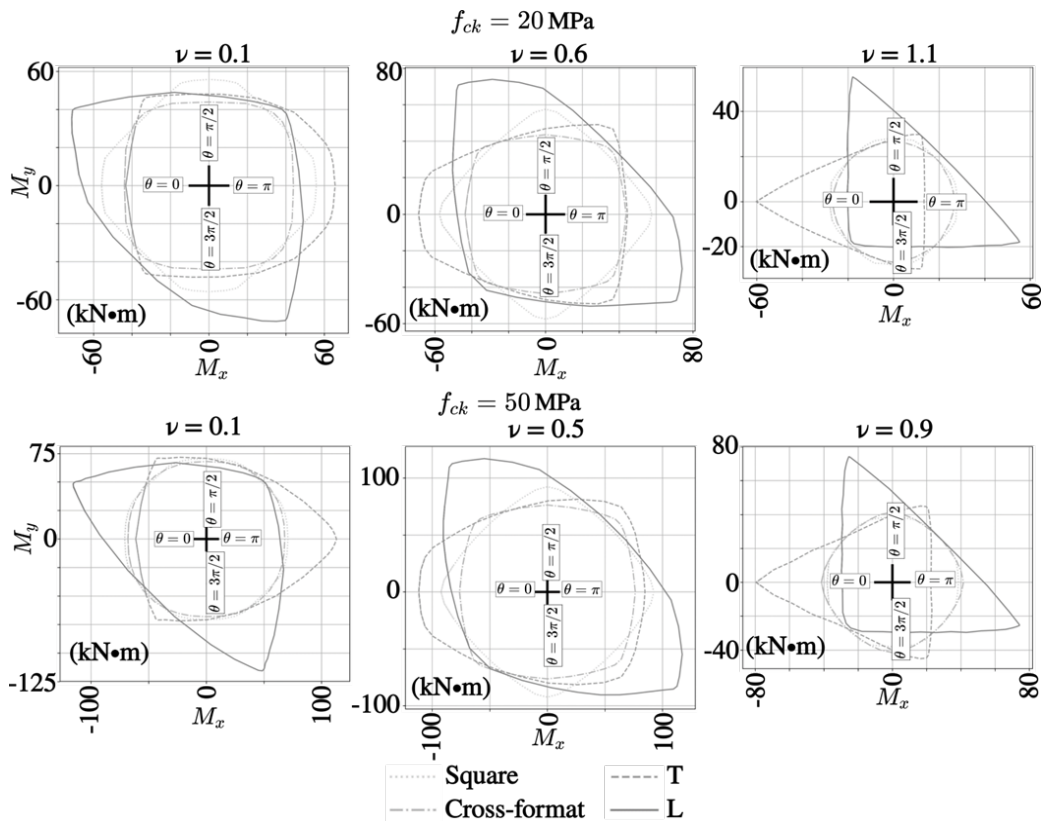


Figure 8. Influence of section shape on sections with  $f_{ck} = 20$  and 50 MPa.

Another interesting perception in Figure 6 refers to the change in the interaction diagrams shape, described in point (b). It is observed that the  $f_{ck} \leq 50$  MPa square sections interaction diagrams come out of a format next to a diamond ( $N=500$  kN) to a more rounded format ( $N=800$  kN). Meanwhile, curves of sections with 60 to 90 MPa  $f_{ck}$  change inversely, having shapes with rounded corners under compression of 500 kN and tending to diamonds when the axial force increases to 800 kN, with sharp corners in the principal axis of inertia. These tendencies become more explicit in Figure 6 diagrams in which the square sections are subjected to  $N = 1200$  kN.

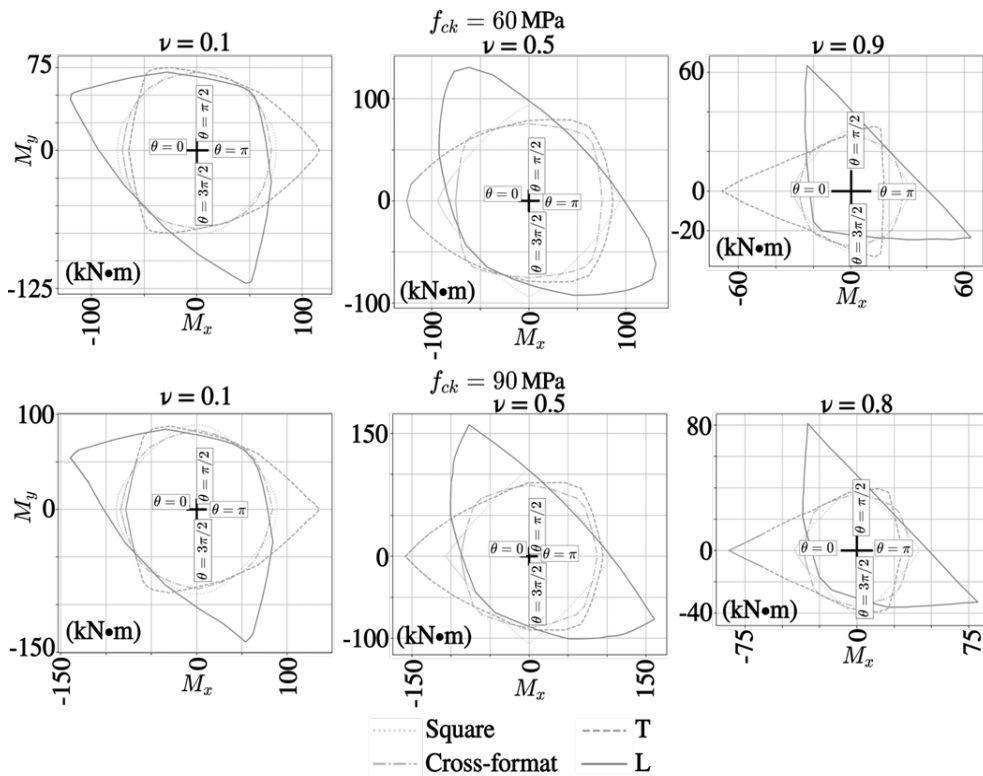


Figure 9. Influence of section shape on sections with  $f_{ck} = 60$  and 90 MPa.

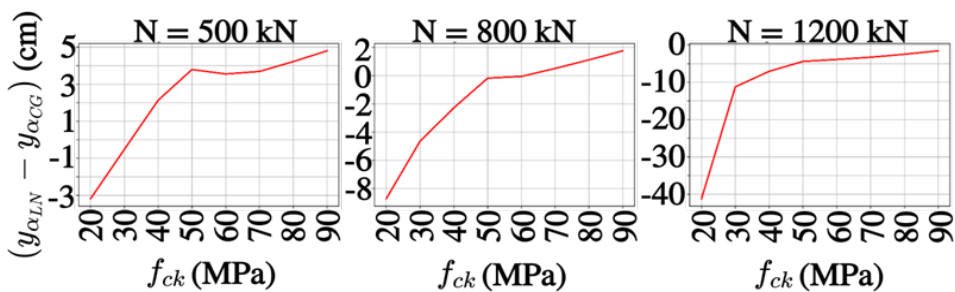


Figure 10. Relative position between neutral axis and centroid of square sections with  $\alpha = 0$  rad.

In the case of square sections, the change of interaction diagram shapes is reversed when changing the formulation used to calculate the concrete compressive strength. As shown in Equations 2 to 5, the stress calculation parameters are different for concretes with  $f_{ck}$  below and above 50 MPa, which is a limit that coincides with the different behaviors identified in the curves.

Interpreting Equations 2 to 5 it is seen that  $\epsilon_{cu} = 0.35\%$  for  $f_{ck} \leq 50$  MPa concretes and this value decreases as  $f_{ck}$  increases, until it reaches 0.26% to  $f_{ck} = 90$  MPa. In parallel to this,  $\epsilon_{c2} = 0.2\%$  to  $f_{ck} \leq 50$  MPa and increases until it

reaches 0.26% to  $f_{ck} = 90$  MPa. This shows that, for high strength concretes ( $f_{ck} \geq 50$  MPa), the plastic stretch (rectangle) of the stress-strain parabola-rectangle idealized diagram is smaller and smaller with the increase of  $f_{ck}$  and does not exist when  $f_{ck} = 90$  MPa.

In addition, the initial (more rigid) stretch of the Equation 2 stress-strain diagrams, which has parabolic shape in concrete of  $f_{ck} \leq 50$  MPa, is closing to a straight line when applied to concretes with greater strength, due to the decay of the  $n$  coefficient value (equal to 1.4 for concretes of 90 MPa).

Observing the square section equilibrium configuration with  $f_{ck} = 20$  MPa under  $N = 500$  kN, with an  $\theta$  angle equal to  $45^\circ$  (outside the principal axis of inertia), it is perceived that flexural strength is about 18% lower than that for  $\theta = 0^\circ$ . Although neutral axis stabilizes in similar positions in relation to the section centroid when  $\theta=0^\circ$  and  $\theta=45^\circ$  and the maximum concrete and reinforcement strains present close values,  $\theta=0^\circ$  strength is higher due to the better reinforcement and compressed concrete areas distribution, making the concrete and the axial reinforcement strengths lever arm greater in relation to the centroid section.

The increase of  $f_{ck}$  tends to reduce the relative differences of flexural strength between  $\theta=0^\circ$  and  $\theta = 45^\circ$  to  $N = 500$  kN, which softens the contours of the interaction diagrams. In the most extreme case, which is that of section with  $f_{ck} = 90$  MPa, the concrete contribution on section flexural strength prevails, representing more than 65% of section flexural strength for  $\theta=0^\circ$  and for  $\theta=45^\circ$ . As the plastic stretch does not exist for  $f_{ck} = 90$  MPa and the respective stress-strain curve is almost linear, the magnitude and the position of section axial strength change little and so the interaction diagrams become more rounded.

For high compression, as in Figure 6 plot for  $N = 1200$  kN, square sections interaction diagrams shapes present change both for  $f_{ck} \leq 50$  MPa and for  $f_{ck} > 50$  MPa concretes. The square section with  $f_{ck}=20$  MPa is fully compressed to all angles and compressed concrete becomes responsible for most of the flexural strength section, being 61% and 55% when  $\theta=0^\circ$  and  $\theta=45^\circ$ , respectively. The section flexural strength, in turn, have a close value for  $\theta$  at both values, reflecting the almost round interaction diagram shape. In sections with  $f_{ck} \leq 50$  MPa, compressive strains tend to increasingly stay with values between  $\varepsilon_{c2}$  and  $\varepsilon_{cu}$ . This indicates that Equation 2 tends to promote uniform compressive strength  $\sigma_c = 0.85 f_{cd}$  throughout the section area. With this,  $R_{cd}$  tends to the value  $0.85 A_c f_{cd}$  in the various  $\theta$  directions, i.e., tend to a constant value and the interaction diagrams look rounded.

In contrast, square sections with  $f_{ck} > 50$  MPa have strains between 0 and  $\varepsilon_{cu}$  when subjected to high compression, in addition to the fact that neutral axis equilibrium position is closer to centroid. Thus,  $\sigma_c$  also tends to vary in a way closer to the linear and  $\theta$  angle variation significantly influences the value and lever arm of  $N_{rd}$ . Therefore, such concretes under  $N = 1200$  kN have interaction diagrams with straight lines and live corners in the principal axis of inertia.

Thus, a direct correlation between concrete constitutive relationship and the reinforced concrete sections behavior under combined bending and axial load is perceived. The sections internal equilibrium is sensitive to  $\sigma_c$  distribution over concrete areas and  $\varepsilon_{cu}$  values of which, in turn, interfere in the reinforcement deformation resulting in different interaction diagrams as the concrete constitutive relationship is modified.

Extending the analyses to the cross-format sections under low compression (Figure 6,  $N = 500$  kN),  $f_{ck} \leq 50$  MPa concretes provide interaction diagrams with format approaching a square with rounded corners, in which  $\theta = (2n + 1) \pi/4$  directions, where  $n = 0, 1, 2, \dots$ , present the maximum flexural strengths. At the same time,  $f_{ck} > 50$  MPa concretes lead to nearly round interaction diagrams shapes.

Shifting  $N$  to 1200 kN, the shapes of  $f_{ck} \leq 50$  MPa diagrams of cross-format sections become almost round, and this becomes sharper the smaller the  $f_{ck}$ . Meanwhile, the shapes of  $f_{ck} > 50$  MPa concretes become almost a smooth square. Comparing such observations with those made for square sections, it is perceived that the same factors guide the process, i.e., the concrete stress-strain relationship and the neutral axis position, associated with compressed areas and reinforcement distribution.

For "T" and "L" sections, the increase of  $N$  also lead to a change in interaction diagrams shape and behaviors continue to be distinct for the two ranges of the Equations 2 to 5. However, both sections have only one axis of symmetry, unlike square and cross-format sections. This implies, among other things, greater reinforcement concentration in some regions (see Figure 3), something that should be taken into account in the analyses. In the case of "T" sections the reinforcement ratio is higher in the meeting of the flange with the web and, in the "L" sections, in the meeting between the two legs.

Interaction diagrams shapes are nearly round for “T” with  $f_{ck} \leq 50$  MPa. For  $f_{ck} = 20$  MPa, the maximum flexural strength happens when  $M_y > 0$  e  $M_x < 0$  (compressed section flange and most of the reinforcement). In this situation a reinforcement maximum tensile strength is the limiting factor for section flexural strength, since the section is inside the 3rd domain of Figure 1 and is the maximum utilization of compressed concrete and stretched reinforcement.

As  $N$  increases to 800 kN on Figure 6 and the neutral axis moves more and more in the direction of the “T” section most compressed point, the maximum flexural strength angle  $\theta$  also changes. In this case, with 50 MPa  $f_{ck}$ , the “T” section still has interaction diagram with almost oval shape, but the maximum flexural strength is achieved when  $M_x > 0$  and  $M_y = 0$  (section web compressed and most of the reinforcement in traction). This is because the increasing of the  $f_{ck}$  moves the neutral axis equilibrium position higher above the centroid section, something that decreases the concrete shortening strain but enhance reinforcement stretching, which becomes a strength limiting factor. The direction of greater flexural strength will then be the one that provides the greatest amount of stretched reinforcement ( $M_x > 0$  and  $M_y = 0$ ).

When  $f_{ck}$  exceeds 50 MPa, interaction diagrams are increasingly tapered in relation to the  $M_x$  axis (positive direction) and the direction of greater flexural strength continues to be when  $M_x > 0$  and  $M_y = 0$ , by the characteristic of stress equilibrium (concrete is compressed and most part of reinforcement is stretched). The bottleneck in question occurs due to the abrupt lowering of the concrete contribution on section flexural strength with small  $\theta$  variations around the  $\pi$  rad value, since the compressed areas vary abruptly, depending on the “T” section geometry.

Increasing compression and reaching up to 1000 kN in Figure 6 “T” sections diagrams, there is a change of flexural strength interaction diagrams shapes of sections with  $f_{ck} \leq 50$  MPa, which begin to taper around the  $M_x$  axis in its negative direction, presenting peak resistance to  $M_y = 0$ . Such a configuration is one in which the maximum shortening strains are in the flange section, region with the highest reinforcement and concrete areas. A different situation is found for  $f_{ck} > 50$  MPa:  $M_x < 0$  and  $M_x > 0$  flexural strengths are closer to each other in module. This means that concrete compressive capacity becomes as significant as reinforcement concentration in some regions, since a section is fully compressed.

In Figure 7 “L” sections diagrams under  $N = 500$  kN,  $f_{ck} \leq 50$  MPa concretes lead to interaction diagrams a little more rounded, tending to present sharp corners as  $f_{ck}$  increases in the directions  $\theta \approx 30^\circ$  and  $\theta \approx 270^\circ$  to 20 MPa  $f_{ck}$ ,  $\theta \approx 40^\circ$  and  $\theta \approx 230^\circ$  to 30 MPa  $f_{ck}$  and  $\theta \approx 50^\circ$  and  $\theta \approx 220^\circ$  to 40 and 50 MPa  $f_{ck}$ . Such sharp corners correspond to flexural maximum strengths. Concretes with  $f_{ck} > 50$  MPa lead to round diagrams when there is a compression at region of section legs meeting and a straight diagram when the section legs free ends are compressed.

Under  $N = 1100$  kN, “L” sections with  $f_{ck} \leq 50$  MPa tend to generate interaction diagrams almost in the shape of a right triangle and this behavior is more pronounced the smaller the  $f_{ck}$  is. Concretes with  $f_{ck} > 50$  MPa, on the other hand, lead to interaction diagrams approaching an ellipse, whose largest dimension is almost parallel to “L” section symmetry axis.

To describe the phenomenon in point (c), we turn to the analysis of square sections. As an example, Figure 6 square sections diagrams with  $N = 500$  kN: it is noticed that for flexural strengths for angles  $\theta$  close to  $\pi/4$ ,  $3\pi/4$ ,  $5\pi/4$  and  $7\pi/4$ , flexural strengths of concretes with  $f_{ck} = 50$  and 60 MPa are greater than flexural strengths of concretes with  $f_{ck} = 70$  MPa. This occurs similarly in all other sections when  $N$  is relatively low.

This fact can be directly correlated to the initial part of the Equation 2 stress-strain curves, in which the curve of  $f_{ck} = 50$  MPa is slightly stiffer than the curves of concretes with  $f_{ck} = 60$  and 70 MPa.

With the increase in compression in the sections, concretes with  $f_{ck} = 60$  and 70 MPa provide greater flexural strength than the concretes with  $f_{ck} = 50$  MPa. However, in some  $\theta$  directions of the “T” and “L” sections, it is still possible to verify the phenomenon of point (c) for  $N$  higher values. In this case, the  $\varepsilon_{cu}$  strain (greater for concretes with  $f_{ck} = 50$  MPa, compared to its corresponding to  $f_{ck} = 60$  and 70 MPa) may be associated with the fact.

#### 4.2 Shape influence on section flexural strength

The comparisons are performed with the section flexural strength interaction diagrams of the four section shapes, grouped in the same graph. The sections are subjected to the same dimensionless axial force  $\nu$  have concretes with same  $f_{ck}$  and same concrete and reinforcement areas.

Regardless evaluated  $f_{ck}$ , it is perceived, by the interpretation of Figure 8 and Figure 9 plots where  $\nu = 0.1$ , that the rebars positioning is predominant. The more reinforcement area close to the most stretched point in the section, the greater the section flexural strength. This is because, under low dimensionless axial forces, the neutral axis tends to intercept the section and when there is a higher amount of tensile resistant material in the stretched areas, greater is the section flexural strength.

Looking at the  $M_x$  value when  $M_y = 0$ , the highest negative values of the interaction diagrams are “L” sections, since the rebars distribution allows a greater reinforcement concentration in the stretched region. On the other hand, when  $M_x > 0$  and  $M_y = 0$ , the “T” section flexural strength prevails, because it presents much of the rebars in the flange (stretched). “L” sections also have the highest flexural strength when  $M_x = 0$  and  $M_y < 0$ , confirming the influence of rebars distribution, concentrated in the meeting of section legs. The square section, in turn, deserves attention when  $M_x = 0$  and  $M_y > 0$  since, in this case, it has the largest reinforcement area close to the section maximum tensile strain point.

Also on Figure 8 and Figure 9  $\nu = 0.1$  plots, it is attested that the cross-format sections interaction diagrams have the smallest coverage area. This fact is due to much of the reinforcement area is concentrating remarkably close to the centroid section, leading to the low utilization of rebars (small lever arm of reinforcement axial strength) and the maximum section allowed curvature. As  $f_{ck}$  increases, however, cross-format sections interaction diagrams become closer to one of square sections. This is likely to occur by changing the position of the neutral axis with the variation of the  $f_{ck}$ , since concretes with higher  $f_{ck}$  tend to require less compressed area. Thus, in the case of cross-format section, more and more rebars tend to get stretched and thus increases the flexural strength.

Under intermediate dimensionless axial forces of Figure 8 and Figure 9, the comparison between the sections changes considerably and the reinforcement distribution remains the predominant factor on flexural strength. However, the influence of rebars occurs differently since the reinforcement concentration in the most compressed regions provides the higher flexural strengths. Contrary to what is perceived for  $\nu = 0.1$ , the  $N$  increase causes the “L” sections interaction diagrams to predominate over the others when  $M_x > 0$  and/or  $M_y > 0$ , that is, when the highest compressive strains occur at the meeting of the section legs where most of the reinforcement steel is. With  $M_y = 0$  and  $M_x < 0$ , there is the predominance of “T” section interaction diagrams, because the largest compressive strains and most of the reinforcement is in the flange section. When  $M_x = 0$  and  $M_y < 0$ , it is perceived that the square section is the one with the highest flexural strength, because 50% of total reinforcement is shortened according to  $\varepsilon_c$  close to  $\varepsilon_{cu}$ , something that does not occur with the other sections.

However, when  $\nu$  increases further and assumes values around 1.0, characterizing high compression rates, it is demonstrated by Figure 8 and Figure 9 that  $f_{ck}$  becomes relevant as reinforcement geometry. When observing the sections whose shape provides concrete and reinforcement areas close to the section point with the maximum compressive strain, they are the same sections that stand out for the highest flexural strength. Thus, the comparison of mechanical behavior of the sections from the point of view of combined bending and compression, it is attested that the concrete and reinforcement geometry optimization will depend on the values of the applied force and the mechanical properties of these materials.

## 5 CONCLUSIONS

This work developed a computational algorithm capable of calculating the moment-axial force-curvature relationship of arbitrary shape polygonal reinforced concrete sections, which uses the NBR 6118 [5] parabola-rectangle diagram as the concrete constitutive relationship. From the elaboration of the calculation routines and the evaluation of the results obtained, it is possible to conclude that:

- the nonlinearity of the calculation process of reinforced concrete sections flexural strengths requires iterative balance calculation, given the number of variables interfering with the problem. Therefore, more efficient convergence methods tend to accelerate the speed at which the problem is solved;
- under low applied axial forces, the  $f_{ck}$  increase has a lower influence, when compared to the interference of this factor in the interaction diagrams for higher applied axial forces;
- the increase of applied axial force tends to change not only the section flexural strength magnitude but also alters the interaction diagrams shape. The changes, however, tend to be different for concretes below and above 50 MPa. It is worth to evaluate whether the behavior change proposed by the Brazilian standard for concrete stress-strain diagrams for  $f_{ck} > 50$  MPa satisfactorily represents the mechanical behavior of structural elements. There is, in the

- vicinity of  $f_{ck} = 50$  MPa, a relevant discontinuity in the function governing limit strains  $\varepsilon_{c2}$  and  $\varepsilon_{cu}$  and the impact of this on the sections calculation is considerable, as shown in the interaction diagrams;
- d) in the initial sections of Equation 2 stress-strain diagrams, concretes with  $f_{ck} = 50$  MPa are more rigid than the concretes of  $f_{ck} = 60$  and 70 MPa, making the flexural strength interaction diagrams of concretes with lower  $f_{ck}$  (50 MPa) more comprehensive than those of concrete with higher  $f_{ck}$  (60 and 70 MPa), especially when the axial force  $N$  is smaller;
- e) as for the evaluation of the performance of sections with different shapes for all  $\nu$  values, the rebars distribution is among the most important factors. If  $\nu$  is low, the reinforcement concentration next to the section most stretched point is what provides the highest flexural strengths. When  $\nu$  increases, the reinforcement concentration in the vicinity of the section most shortened point leads the sections to higher flexural strengths. In the case where  $\nu$  is close to 1.0, the concrete compressive strength assumes a main role and the presence of compressed areas close to the section point with the higher compressive strain interferes with flexural strength sections.

## REFERENCES

- [1] L. Pallarés, P. F. Miguel, and M. A. Fernández-Prada, "A numerical method to design reinforced concrete sections subjected to axial forces and biaxial bending," *Eng. Struct.*, vol. 31, no. 12, pp. 3065–3071, Dec 2009, <http://dx.doi.org/10.1016/j.engstruct.2009.08.006>.
- [2] A. Dall'Asta and L. Dezi, "Design of RC sections with generic shape under biaxial bending," *J. Struct. Eng.*, vol. 118, no. 4, pp. 1138–1143, Apr 1992, [http://dx.doi.org/10.1061/\(ASCE\)0733-9445\(1992\)118:4\(1138\)](http://dx.doi.org/10.1061/(ASCE)0733-9445(1992)118:4(1138)).
- [3] A. Fafitis, "Interaction surfaces of reinforced-concrete sections in biaxial bending," *J. Struct. Eng.*, vol. 127, no. 7, pp. 840–846, Jul 2001, [http://dx.doi.org/10.1061/\(ASCE\)0733-9445\(2001\)127:7\(840\)](http://dx.doi.org/10.1061/(ASCE)0733-9445(2001)127:7(840)).
- [4] R. Vaz Rodrigues, "A new technique for ultimate limit state design of arbitrary shape RC sections under biaxial bending," *Eng. Struct.*, vol. 104, no. 1, pp. 1–17, Dec 2015., <http://dx.doi.org/10.1016/j.engstruct.2015.09.016>.
- [5] Associação Brasileira de Normas Técnicas, *Projeto de Estruturas de Concreto – Procedimento*, NBR 6118, 2014.
- [6] F. A. Torrico, "Análise teórica e experimental do comportamento de pilares esbeltos de concreto de alta resistência, considerando a ductilidade," Ph.D. dissertation, Esc. Eng. São Carlos. Univ. São Paulo, São Carlos, 2010.
- [7] G. Campione, L. Cavaleri, F. Di Trapani, G. Macaluso, and G. Scaduto, "Biaxial deformation and ductility domains for engineered rectangular RC cross-sections: A parametric study highlighting the positive roles of axial load, geometry and materials," *Eng. Struct.*, vol. 107, no. 15, pp. 116–134, Jan 2016, <http://dx.doi.org/10.1016/j.engstruct.2015.10.030>.
- [8] L. P. Souza, "Instabilidade e dimensionamento de pilares de concreto armado de seção poligonal submetidos à flexão composta oblíqua," M.S. thesis, Prog. Pós-grad. Eng. Constr. Civ., Univ. Fed. Paraná, Curitiba, 2017. [Online]. Available: <https://hdl.handle.net/1884/59886>
- [9] S. Gillies. "Shapely 1.6.2.post1". GitHub, 2017. Available: <https://github.com/Toblerity/Shapely> (accessed June 14, 2017).
- [10] A. Klöckner. "Meshpy 2016.1.2". Python Software Foundation, 2016. Available: <https://pypi.python.org/pypi/MeshPy> (accessed Aug 3, 2017).

---

**Author contributions:** LPS: algorithm computational implementation, data analysis, writing; MAA: supervision, revision, translation.

**Editors:** Mauro de Vasconcellos Real, José Luiz Antunes de Oliveira e Sousa, Guilherme Aris Parsekian.



ORIGINAL ARTICLE

# Numerical analysis of composite steel and concrete beams subjected to fire under different support conditions

*Análise numérica de vigas mistas de aço e concreto em situação de incêndio sob diferentes condições de apoios*

Lucas Coscia Romagnoli<sup>a</sup> Valdir Pignatta e Silva<sup>a</sup> <sup>a</sup>Universidade de São Paulo – USP, Escola Politécnica, Departamento de Engenharia de Estruturas e Geotécnica, São Paulo, SP, Brasil

Received 16 October 2019

Accepted 26 February 2020

**Abstract:** To evaluate the behavior of semi-continuous composite beams in fire, six finite elements numerical models with several steel profiles and slab dimensions were developed in ABAQUS software. The models took into account several behaviors usually suppressed in simplified analyzes such as: geometric and materials non-linearity properties and thermal expansion effects, including indirect stresses. Three support conditions were analyzed: simply supported (axial released), axial restrained and semi-continuous, totaling 18 analyzes. The different support conditions results were compared to each other and to the fire resistance time designed by simplified methods, which followed design code recommendations.

**Keywords:** fire, composite steel concrete beam, semi-continuous, numerical analysis.

**Resumo:** Com o objetivo de avaliar o comportamento de vigas mistas semicontínuas em situação de incêndio considerando diversos fenômenos desprezados em análises simplificadas como não linearidade geométrica, não linearidade das propriedades térmicas e mecânicas dos materiais e efeitos da dilatação térmica, incluindo esforços solicitantes indiretos, foram desenvolvidos seis modelos numéricos em elementos finitos no programa de computador ABAQUS com geometrias distintas, alterando as dimensões do perfil de aço e laje que compõe a viga mista. Para cada um dos seis modelos foram analisadas três condições de contorno, sendo elas: simplesmente apoiada (livre axialmente), biapoiada (restringida axialmente) e semicontínua, totalizando 18 análises. Os resultados das diferentes condições de contorno foram comparados entre si, além do TRF do caso semicontínuo encontrado por método simplificado, que seguiu recomendações normatizadas.

**Palavras-chave:** incêndio, viga mista de aço e concreto, semicontínua, análise numérica.

**How to cite:** L. C. Romagnoli and V. P. Silva, “Numerical analysis of composite steel and concrete beams subjected to fire under different support conditions,” *Rev. IBRACON Estrut. Mater.*, vol. 13, no. 5, e13513, 2020, <https://doi.org/10.1590/S1983-41952020000500013>

## 1 INTRODUCTION

### 1.1 Objective

A composite steel and concrete beam designed at room temperature usually does not offer adequate structural safety when checked for fire according to design codes, unless fireproof is provided. Such solution leads to higher costs that, at a national level, often make the choice for structural steel systems impracticable.

This study goal is to assess the behavior of composite steel and concrete beams in fire taking in consideration the rotational stiffness of the supports provided by the slab’s mesh reinforcement and the restriction of the profile’s lower flange, creating a composite connection, as shown in Figure 1, and ensuring a semi-continuous behavior to the beam.

Corresponding author: Lucas Coscia Romagnoli. E-mail: lucas.romagnoli@usp.br

Financial support: Grant 2018/14735-6, São Paulo Research Foundation (FAPESP) and Conselho Nacional de Pesquisa e Desenvolvimento Científico (CNPq).

Conflict of interest: Nothing to declare.



This is an Open Access article distributed under the terms of the Creative Commons Attribution License, which permits unrestricted use, distribution, and reproduction in any medium, provided the original work is properly cited.

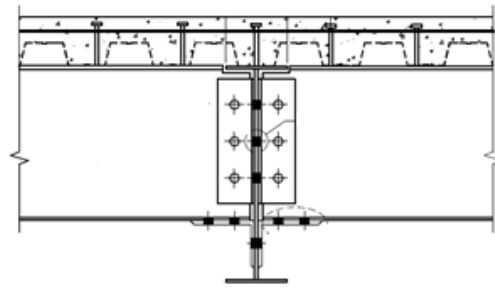


**Figure 1.** Composite connection (Source: adapted from ABNT NBR 8800 [1]).

The semi-continuous solution is able to increase significantly the beam's bending load strength at room temperature. The studies aim to quantify the fire resistance time increase provided by this solution, evaluating the hypothesis of not relying on fireproof coating for cases in which such increase is shown to be sufficient.

However, when a steel beam is under and in contact with a concrete slab, one of its faces is not exposed to fire, since the slab provides protection to the profile's upper flange, leading to a non-uniform internal temperature distribution. This thermal gradient along the cross-section causes additional deformations and indirect stresses due to supports rotational restraints. If the structure is already subject to negative bending moments at the supports, as in the case of a semi-continuous beam, these may be amplified during fire exposure.

This harmful effect was evaluated with aid of nonlinear thermo-structural numerical analysis, exposed in this paper. The numerical models considered effects such as catenary stresses on the slab, resulted from large deformations, and material nonlinear behavior. Both those effects reduces the thermal expansion indirect stresses.

Previous results [2] showed that for semi-continuous composite beams the bending moment capacity increase, compared to the simply supported case, is enough to dispense fireproof coating for standard-fire resistance requirements of less than 30 min. These calculations followed design code procedures that consider the formation of plastic hinges on the supports and mid-span as the ultimate limit state.

These previous studies accounted for simplifying hypotheses, which neglected indirect stresses caused by thermal expansion and thermal gradient. An attempt to propose a method of increasing stresses without considering other complex behaviors such as materials nonlinearity and large deformations would excessively penalize the simplified model, leading to very conservative results (as already evidenced by Silva [3] in case of indirect stresses in axial restrained steel beams and simple frames subjected to temperatures close to critical).

It is important to note that although IT 8 [4] tabular method indicates a minimum standard-fire resistance time of 30 min, it is possible to adopt lower times for small buildings with low fire load by utilizing the equivalent time method. This method is detailed in ABNT NBR 15200 [5], ABNT NBR 14323 [6] and IT 8 [4], and commented by Silva et al. [7].

This present paper analyzed the simplifying hypotheses adopted in Romagnoli and Silva [2]. Additional information is described in detail in Romagnoli [8].

## 1.2 Background

Usually the choice for steel structures is associated with the essential need of adopting fireproof coating. Studies in the field of fire design aim to break this paradigm and better understand the phenomena associated with the fire itself or the behavior of structures at high temperatures, thus allowing safer and more economical buildings.

In 1986 Robinson and Latham (1986 apud Wang [9]) point out that the use of fireproof coatings represented 30% of the total cost of a steel structure, which created a huge disadvantage in relation, mainly, to concrete structures. With this problem in mind, both the steel industry and the scientific community sought to study the effect of fire on structural elements.

The benefits of composite steel and concrete construction in fire resistance, when compared to an isolated steel structural element, have been the subject of studies by several authors. By comparing a composite steel and concrete beam numerical model to Cardington's tests results, Usmani et al. [10] highlight the importance of taking into account the thermal expansion coefficient of the materials so that the results are closer to reality. They also conclude that large deformations in the concrete slab induce a membrane behavior, which is responsible for preventing its collapse, thus

highlighting the importance of slab's mesh reinforcement to resist these stresses and significantly increasing the strength of composite elements.

Bailey et al. [11] investigated the effects of membrane stresses on the behavior of composite slabs in fire through laboratory tests. Subsequently Bailey [12] proposed a theoretical formulation capable of incorporating this effect in the evaluation of the structural collapse of the slab in fire. By numerical models, Lim et al. [13] conclude that for one-direction slabs, if the supports are able to restrain horizontal movements, large deformations allow the structure to behave similarly to a cable, resisting vertical actions by means of tensile stresses, featuring a catenary effect. Advanced numerical models benefit from this, as they incorporate geometric non-linearity. When considering the slab's semi-continuity, the mesh reinforcement at the supports is fundamental to resist these horizontal stresses, indicating that providing composite connections for floor beams can result in an increase in its strength in fire.

Through a series of laboratory tests, Anderson and Najafi [14] confirm that the mesh reinforcements in composite connections have a great influence on support's resilience and rotation capacity. They note that the composite connection capacity can be about 3 times greater than a simple steel connection and the mesh reinforcement ratio have a great influence in this behavior. These results indicate that investigating the influence of the mesh reinforcement in the behavior of composite beams in fire can considerably increase its strength.

Lin et al. [15] highlight the role of concrete slab mesh reinforcement to resist catenary stresses. By finite elements analysis they studied three different reinforcement meshes, noting that the effect of the reinforcement ratio becomes relevant after the unprotected beams reach a temperature of 500 °C, when the catenary effect is introduced by great deformations. The author concludes that the collapse behavior of the concrete slab in a fire is directly dependent on the configuration and strength of the reinforcement mesh.

Ioannides and Mehta [16], who adopted as design criteria the formation of plastic hinges in the mid-span and in the supports, have already proposed considering the semi-continuity of composite beams in a fire and stated, for protected beams, that there is a relevant increase in its bending moment strength. The authors also state that most of composite beams are designed at room temperature to meet deformation limits, thus having a reserve in their bending capacity for fire design, where service limit states are not considered.

Fakury et al. [17] compared simply supported and semi-continuous composite protected beams, using the design method proposed by Eurocode EN 1994-1-2 [18]. As a conclusion, they found out a strength increase of 116% to 123% for the semi-continuous protected composite beams when compared to the simply supported case.

Fischer and Varma [19] analyzed composite beam frames with typical hinged connections (shear plates, single angles and double angles) by three-dimensional finite elements numerical models. They compared simple frame models with multiple frames, taking into account the continuity of the slab through the floor, thus having a negative bending moment in the supports. As a conclusion, they state that the slab's continuity and the reinforcement mesh have a great influence on beam's and connection's structural behavior during fire, also stating that there was no premature failure of the connections during fire exposure.

Romagnoli and Silva [20] studied the behavior of unprotected composite beams in fire by taking into account the rotational stiffness in the supports provided by the slab's reinforcement mesh and restriction of the steel's profile lower flange, forming a composite connection. The calculations followed ABNT NBR 14323 [6] design procedures for standard-fire resistance requirements of 30 min. The authors evaluated that, although there is a significant increase of the semi-continuous beam bending strength compared to the simply supported case (about 90% increase), this procedure is not enough to dispense fireproof coatings. Subsequent studies [2] have shown that, in specific cases, it is possible to dispense fireproof coatings by following design codes procedures for standard-fire resistance requirements lower than 30 min.

### 1.3 Problem analysis

The numerical models were developed in ABAQUS software version 6.12-1 and represents a composite steel and concrete beam made of Gerdau brand steel profile and a 2 meters width solid concrete slab, that is, without steel sheeting, with shear connectors welded directly to the steel profile's upper flange. The slab has a steel reinforcement mesh made of steel bars located 3 cm away from the slab's upper face. The rebar longitudinal spacing varies from case to case for each model according to the calculated reinforcement ratio while the transversal spacing is 20 cm for all models.

Thermal loading is applied on the bottom face of the concrete slab and on all faces of the steel profile, excluding the steel's profile upper flange upper face, which is in direct contact with the concrete slab. The room's temperature starts at 20 °C and changes over time according to ISO 834 curve. The  $\alpha_c$  convection heat transfer coefficient was

defined constant and equal to 25 W/(m<sup>2</sup>.°C) and the emissivity equal to 0.7, as recommended by ABNT NBR 14323 [6] in order to follow the hypotheses adopted in the simplified method. Shading effects were not take into account.

To associate the composite connection bending strength only with the steel profile characteristics, bolts strength and sitting angle thickness were admitted compatible with the steel profile, thus, eliminating the need to evaluate various conditions. In other words the conditions presented in Equation 1, according to ABNT NBR 8800 [1], must be satisfied during the evaluation of the semi-continuous composite beam bending strength in fire.

$$n_b F_{b,Rd} \geq 1,25 f_{yd} A_{f,inf} \tag{1a}$$

$$F_{L,yd} A_L \geq 1,25 f_{yd} A_{f,inf} \tag{1b}$$

where:  $n_b$  is the number of bolts;  $F_{b,Rd}$  is the bolt shear design strength;  $F_{L,yd}$  is the lower angle yield design strength;  $A_{f,inf}$  is the steel profile lower flange cross-sectional area; and  $A_L$  is the lower angle cross-sectional area.

## 2 NUMERICAL MODEL VALIDATION

For validation of finite elements techniques used, numerical models were developed prior to the study. The validation models' results were compared to the experimental results collected by Wainman and Kirby [21], who performed several tests in Swinden's laboratories in Rotterdam, England. They evaluated the behavior of composite beams subjected to high temperatures, registering the furnace, lower flange, web and upper flange temperatures and the vertical mid-span displacement of the beam over time. The tests chosen as a reference for validation will be the so-called test 15 and test 16. The choice for these tests is due to the fact they represent unprotected steel profiles, thus, being the closest to the subsequent models evaluated in the paper.

Both tests follow the configuration as seen by the longitudinal section in Figure 2. It represents a composite beam with a British steel profile UB 254x146x43 and a concrete slab 642 mm wide and 130 mm thick, two lines of 19 mm diameter shear connectors spaced 95 mm across and 280 mm longitudinally, providing composite interaction between the parts. The beam covers a 4530 mm span and the steel profile is supported on rollers that allow its ends to rotate and move. The concrete slab has a reinforcement mesh of 8 mm diameter steel bars spaced 200 mm apart and arranged 35 mm from the slab's bottom face. Four concentrated forces spaced 1133 mm and symmetrical in relation to the middle span are applied throughout the test. The steel profile is class BS 43A and the concrete has a compressive strength of 30 MPa.

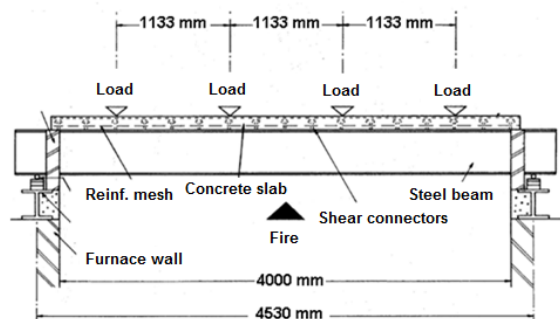


**Figure 2.** Test arrangement longitudinal section (Source: adapted from Wainman [21]).

The profile steel yield strength at room temperature was measured in laboratory, resulting in 280 MPa for test 15 and 273 MPa for test 16. Steel's ultimate strength resulted in 469 MPa for test 15 and 481 MPa for test 16 at an elongation of 25%.

Each of the four applied forces is equivalent to 32.47 kN for test 15 and 62.36 kN for test 16.

The furnace used in tests is gas powered and horizontal, 4 m long, 3 m wide and 1.8 m high. The furnace temperatures sought to follow the curve defined in BS 476: 1972 - part 8, which is similar to the ISO 834 curve.

The thermal analysis used three-dimensional prismatic elements with 20 node each, these located at the vertices and midpoint of the prism edges, called DC3D20 by Abaqus. Figure 3 illustrates the finite element mesh, its density was defined after analyzing several results of previous models.

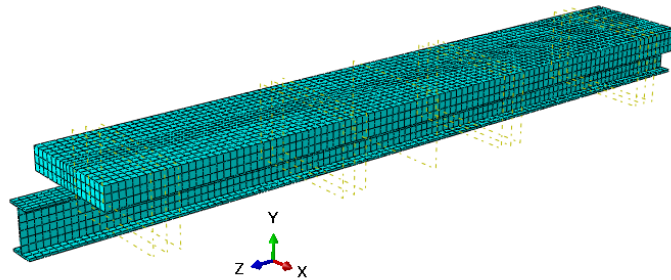


**Figure 3.** Finite element mesh.

The material’s thermal properties followed ABNT NBR 14323 [6] and ABNT NBR 15200 [5] recommendations. Stefan Boltzmann's constant was defined as  $5.669 \times 10^{-8} \text{ W}/(\text{m}^2 \cdot ^\circ\text{C})$  and absolute zero temperature as  $-273.15 \text{ }^\circ\text{C}$ . Unlike ABNT NBR 14323 [6] recommendation of a constant emissivity of 0.7, the model followed the recommendations of Wong [22] and Cedeno et al. [23] that determine the furnace equivalent emissivity as dependent on the gases and structural element temperatures, according to Equation 2, simulating a more realistic condition.

$$\epsilon_{eq} = \frac{\epsilon_g T_g^4 - \alpha_g T_s^4}{T_g^4 - T_s^4} \tag{2}$$

where:  $\alpha_g$  and  $\epsilon_g$  are given by Equations 3 and 4.

$$\alpha_g = X_1 T_s^{X_2} + T_g^{X_3} \tag{3}$$

$$\epsilon_g = X_4 + X_5 T_g \tag{4}$$

where:  $X_1$  a  $X_5$  coefficients (Table 1) were defined empirically by Wong [22] as a function of  $L_m$  length, given by Equation 5, and are related to the furnace length  $L$ , width  $w$  and height  $h$ .

$$L_m = \frac{1.8 h w}{h + w + \frac{h w}{L}} \tag{5}$$

**Table 1.**  $X_1$  to  $X_5$  coefficients.

$L_m$	$X_1$	$X_2$	$X_3$	$X_4$	$X_5$
0.5	6.432499	-1.02349	0.499770	0.302	-0.000118
1	4.249018	-0.91824	0.493256	0.373	-0.000135
2	2.578352	-0.77310	0.457589	0.443	-0.000140
3	1.845211	-0.68851	0.441610	0.479	-0.000133
4	1.448499	-0.63266	0.434033	0.501	-0.000124
5	1.202279	-0.59368	0.431480	0.517	-0.000115
6	1.036789	-0.56531	0.431575	0.527	-0.000106

Source: Wong [22].

Using the temperature field resulted by the thermal analysis, a structural analysis of the same finite element mesh was performed, but now with first order and reduced integration prismatic finite elements, called C3D8R by Abaqus. The steel's and concrete's mechanical properties reduction due to high temperatures followed ABNT NBR 14323 [6] and ABNT NBR 15200 [5] recommendations. Shear connectors and mesh rebars were modeled as Timoshenko beam elements, called B31 by Abaqus and embedded in the concrete slab as shown in Figure 4.

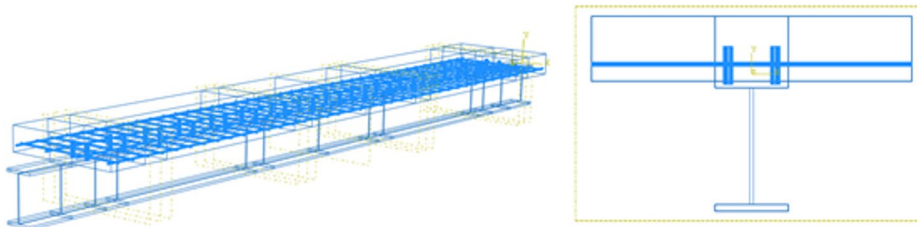


Figure 4. Slab embedded beam elements.

Steel's constitutive model was represented by the Classical Metal Plasticity model being applied to the steel profile, shear connectors and mesh reinforcement elements, with their stress values as function of deformation and temperature as seen in Figure 5. The concrete behavior was represented by the Concrete Damaged Plasticity, with input parameters according to Kmiecik and Kaminski [24] recommendations and temperature dependent mechanical properties as seen in Figure 6 and Figure 7.

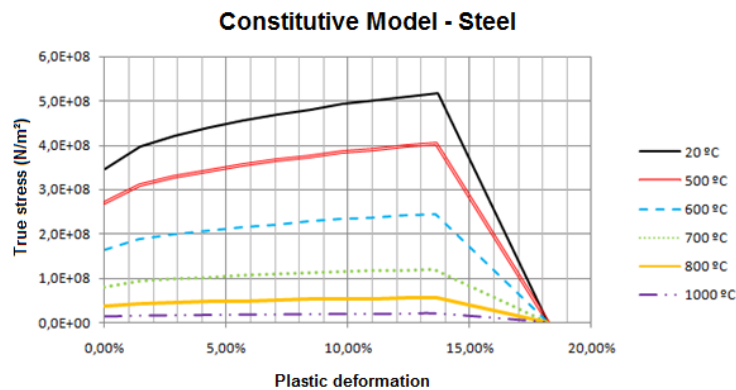


Figure 5. Steel mechanical properties.

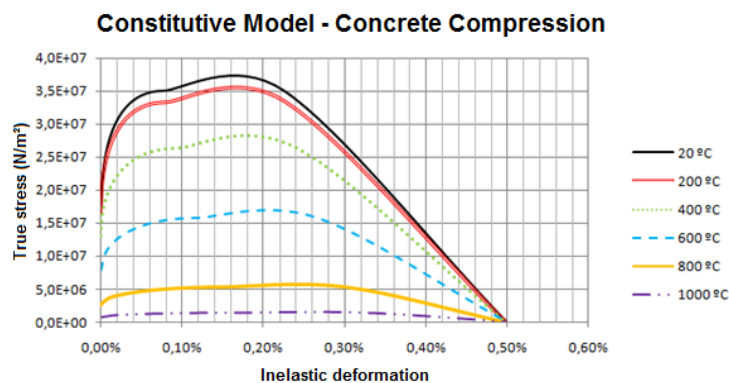


Figure 6. Concrete mechanical properties under compression.

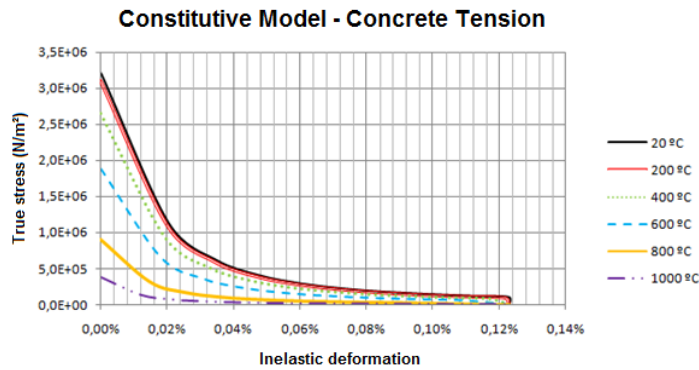


Figure 7. Concrete mechanical properties under tension.

The boundary conditions are such that they prevent the vertical and transverse displacement of the beam’s ends, while allowing its rotation and longitudinal movement. Figure 8 illustrates the web region in which all the nodes were prevented from moving along the Y axis. In addition to self-weight, applied as a gravitational field, each of the four concentrated forces reported in the tests was applied as a distributed load in the slab’s upper face in a rectangle area with one side equals to the steel profile flange width (also seen in Figure 8), in order to avoid stress concentration in a single mesh node.

The graphs in Figure 9, shows the lower flange, web and upper flange temperature resulted in the numerical thermal analysis and compared to Wainman and Kirby [21] records of test 15 and the mid-span vertical displacement over time.

Figure 10 graphs record lower flange, web and upper flange temperatures found in the numerical thermal analysis and compared to Wainman and Kirby [21] for test 16 and the vertical displacement in the middle of the span over time.

The results of both thermal and structural analysis showed good relations with laboratory tests, indicating that the materials properties, mesh density and finite element type, numerical precision, boundary conditions and other adopted parameters are acceptable to represent a real case scenario.

### 3 NUMERICAL MODELS

#### 3.1 Geometry

Table 2 shows each numerical model geometric characteristics, being:

$d$  the steel profile height;  $t_w$  the steel profile web thickness;  $b_f$  the steel profile flange width;  $t_f$  the steel profile flange thickness;  $t_c$  the concrete slab thickness;  $b$  the concrete slab effective width;  $\rho$  the maximum reinforcement ratio for the fire resistance time determined by the simplified method;  $\varnothing$  the rebar diameter;  $s$  the rebar spacing;  $L$  the beam span;  $n_{cs}$  the number of shear connectors required for full composite interaction at room temperature;  $M_{Rd}^+$  the positive bending moment strength designed for room temperature;  $q$  the uniformly distributed load which results in a positive bending moment same as  $M_{Rd}^+$  for the simply supported case;  $0.7q$  70% of  $q$ , representing a load reducing factor for fire design; “FRT simpl.” the Fire Resistance Time determined from the simplified method adopting a load factor of 0.7 for the same geometrical parameters.

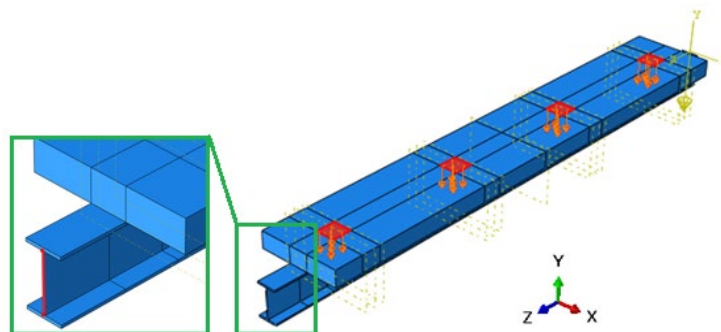


Figure 8. Load applied regions and Y axis restrained region.

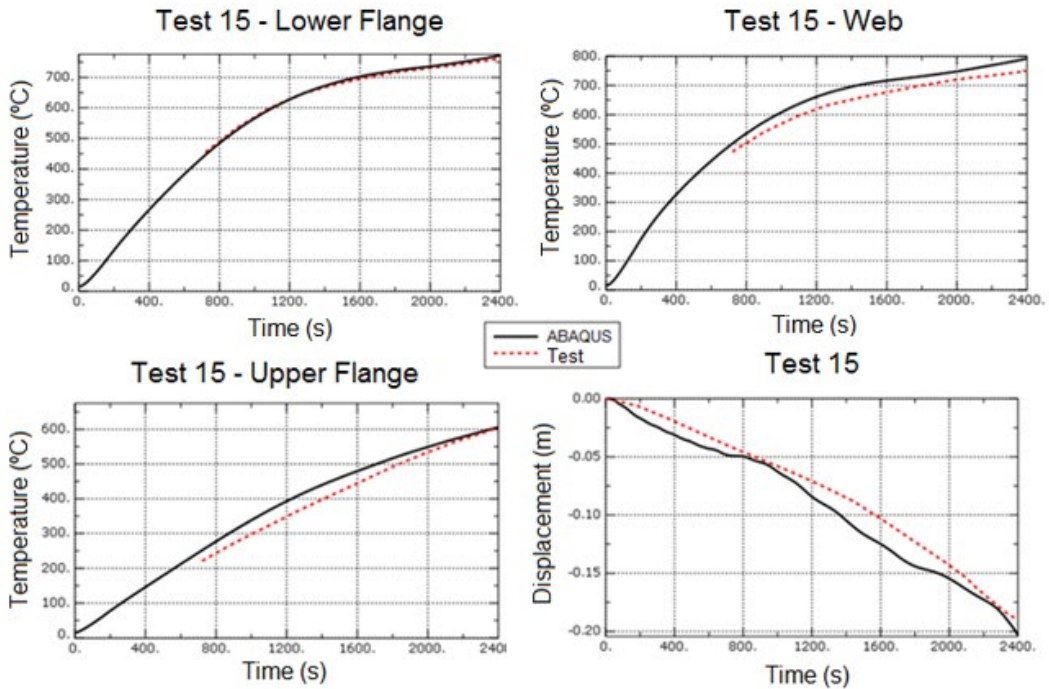


Figure 9. Numerical model compared to Test 15 results.

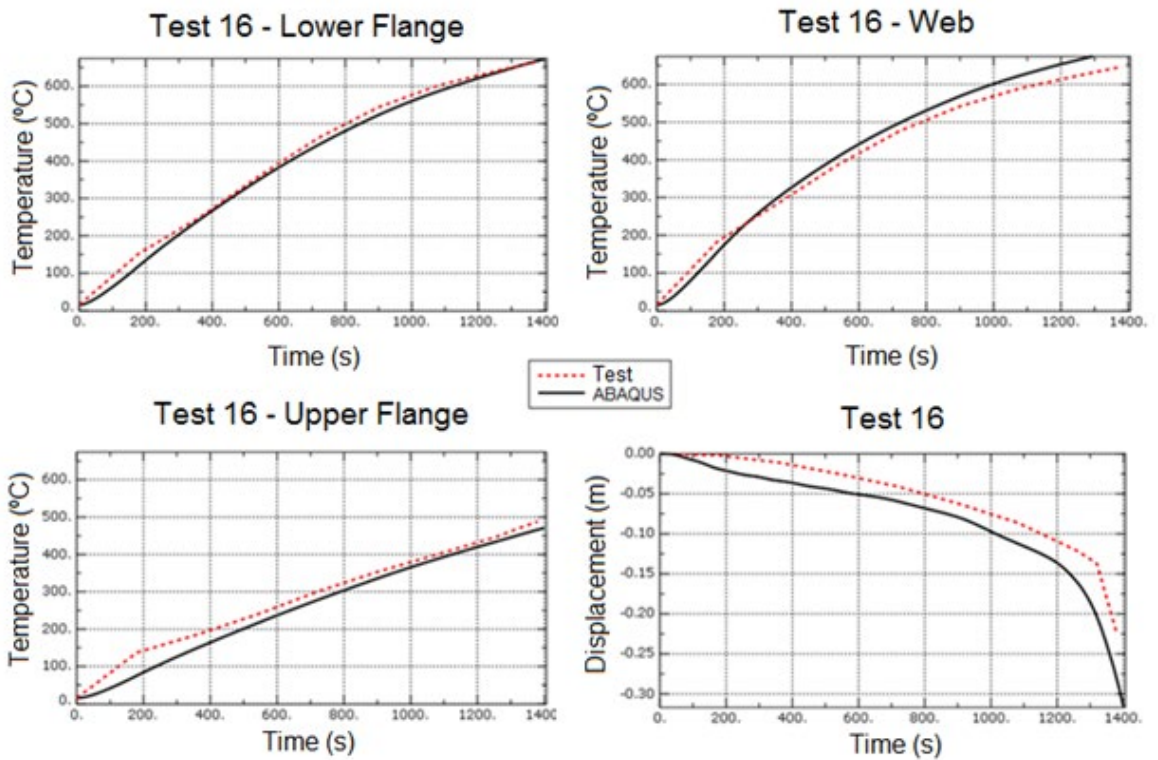


Figure 10. Numerical model compared to Test 16 results.

**Table 2.** Model parameters.

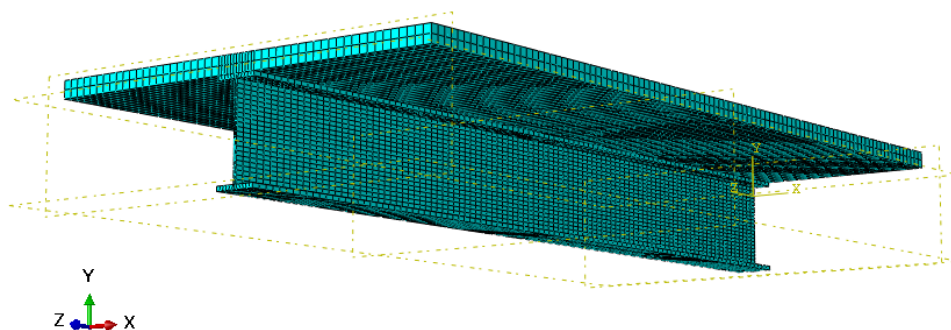
Profile	Model 1	Model 2	Model 3	Model 4	Model 5	Model 6	
	W250x25.3	W460x106.0	W530x85.0	W250x89.0	W360x51.0	W610x174.0	
$d$	257	469	535	260	355	616	mm
$t_w$	6.1	12.6	10.3	10.7	7.2	14.0	mm
$b_f$	102	194	166	256	171	325	mm
$t_f$	8.4	20.6	16.5	17.3	11.6	21.6	mm
Slab characteristics							
$t_c$	8	8	12	12	18	18	cm
$b$	200	200	200	200	200	200	cm
$\rho$	0.48	2.41	1.32	1.36	0.52	1.68	%
$\emptyset$	10	20	20	20	16	25	mm
$s$	10	8	10	9	10	8	cm
General parameters							
$L$	5.0	8.0	8.0	5.0	8.0	12.0	m
$n_{cs}$	20	60	68	72	40	132	un.
$M_{Rd}^+$	194.2	1094.1	1141.1	712.2	658.1	2720.7	kN.m
$q$	62.1	136.8	142.6	227.9	82.3	151.1	kN/m
$0.7q$	43.5	95.7	99.8	159.5	57.6	105.8	kN/m
FRT simpl.	<15	22	18	25	17	25	min.

Material's thermal and mechanical properties followed all ABNT NBR 14323 [6] and ABNT NBR 15200 [5] recommendations.

The steel class adopted is ASTM A572 Gr. 50 with 345 MPa yield strength and 450 MPa ultimate strength. The start elongation at yield was defined as 0.2% and at break as 15%. The reinforcement mesh was defined as steel class CA50 with 500 MPa yield strength. Shear connectors were modeled with a 450 MPa ultimate strength steel.

Concrete has a compressive strength of 30 MPa, tensile strength was defined following ABNT NBR 6118 [25] recommendations.

Finite element mesh has an average size of 5 cm, resulting in meshes with density similar to that used in the validation model, as shown in Figure 11. For the thermal analysis, DC3D20 elements were used, while for the structural analysis, steel profile and the concrete slab were modeled with C3D8R solid elements and shear connectors and mesh rebars with B31 beam elements.

**Figure 11.** Finite elements mesh density representation.

### 3.2 Boundary conditions

For each numerical model, three different boundary conditions were studied: axial released, axial restrained and semi-continuous. Table 3 summarizes the restrain conditions for each region of each element that form the composite beam (Figure 12), characterizing the boundary conditions mentioned.

**Table 3.** Boundary conditions.

Support Element	Condition		
	Axial Released	Axial Restrained	Semi-continuous
Slab + Reinf. Mesh	Free	Fully restrained (X,Y and Z)	Fully restrained (X,Y and Z)
Upper flange	Free	Free	Free
Web	Y Restrained	Fully restrained (X,Y and Z)	Fully restrained (X,Y and Z)
Lower flange	Free	Free	Fully restrained (X,Y and Z)

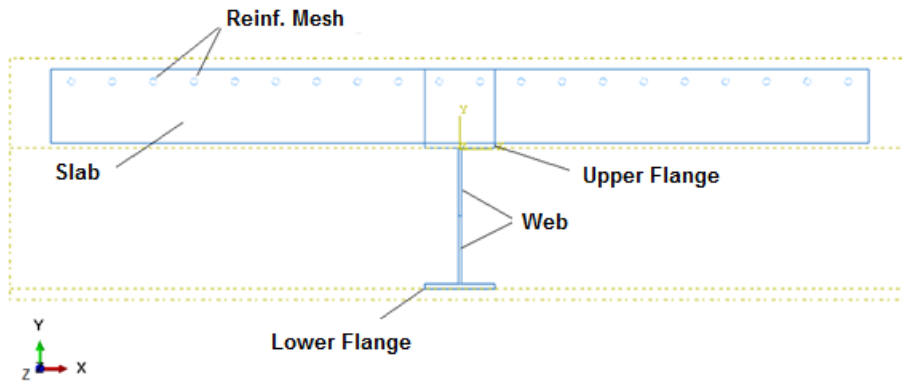


**Figure 12.** Support region sub-elements.

The axial released condition aims to assess the behavior of the beam in the hypothetical situation of a simplified analysis, where indirect axial forces resulting from thermal expansion or catenary effects due to large deformations do not contribute for the beam’s bending strength. Such a condition is hardly found in practice, especially in building floors, due to the complexity of the connection elements for releasing such movements.

The axial restrained condition evaluates a composite beam with its web restrained in the vertical and axial direction. The concrete slab is also restricted, simulating its continuity but with a minimum reinforcement ratio, made of 5 mm diameter rebars, commonly found in anti-cracking meshes. The idea here is to consider the most common conditions found in a floor beam, where there is only a connection between the profile’s web and the primary beam or column and minimum anti-cracking mesh. By comparing the results with the axial released condition, it is possible to assess whether the behavior of common constructive dispositions is close to the hypotheses considered in the simplified method.

The semi-continuous condition considers the restriction of the steel’s profile lower flange and increase of the concrete slab reinforcement mesh according to the simplified calculation as specified in Table 2, in addition to the restrictions of the axial restrained condition. By comparing the results to the axial restrained condition, it is possible to verify the effect of the lower flange restriction and increase of the slab’s reinforcement ratio on the composite beam behavior in fire.

The composite beams were loaded vertically on the slab’s upper face by a uniformly distributed load over the area equivalent to the beam’s entire length and width equal to the steel profile’s upper flange width  $b_f$ , as shown in Figure 13.

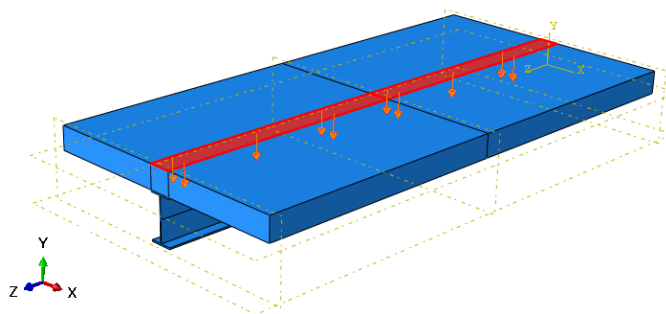


**Figure 13.** Distributed load application region.

The restraints represent perfect elastoplastic conditions, simulating a protected large beam or column as support for the composite beam. Besides the end supports, there are no transverse restrictions over the beam’s length.

A uniformly distributed horizontal load equivalent to 0.1% of the vertical load was applied to the steel profile’s lower flange to create an initial geometric imperfection and prevent numerical convergence for an unstable equilibrium. This load magnitude is sufficiently small to not interfere with the beam’s initial stress during the analysis.

#### 4 RESULTS AND DISCUSSIONS

For the thermal analysis, Figure 14 graphs show the normalized temperature values, that is, for each coordinate the temperature value was divided by the square root of the sum of the squares of all values, standardizing the results and illustrating the temperature distribution along the height of the steel profile for each of the six models. The horizontal axis represents the distance from the lower flange to the upper flange, with zero being the steel profile’s lowest point.

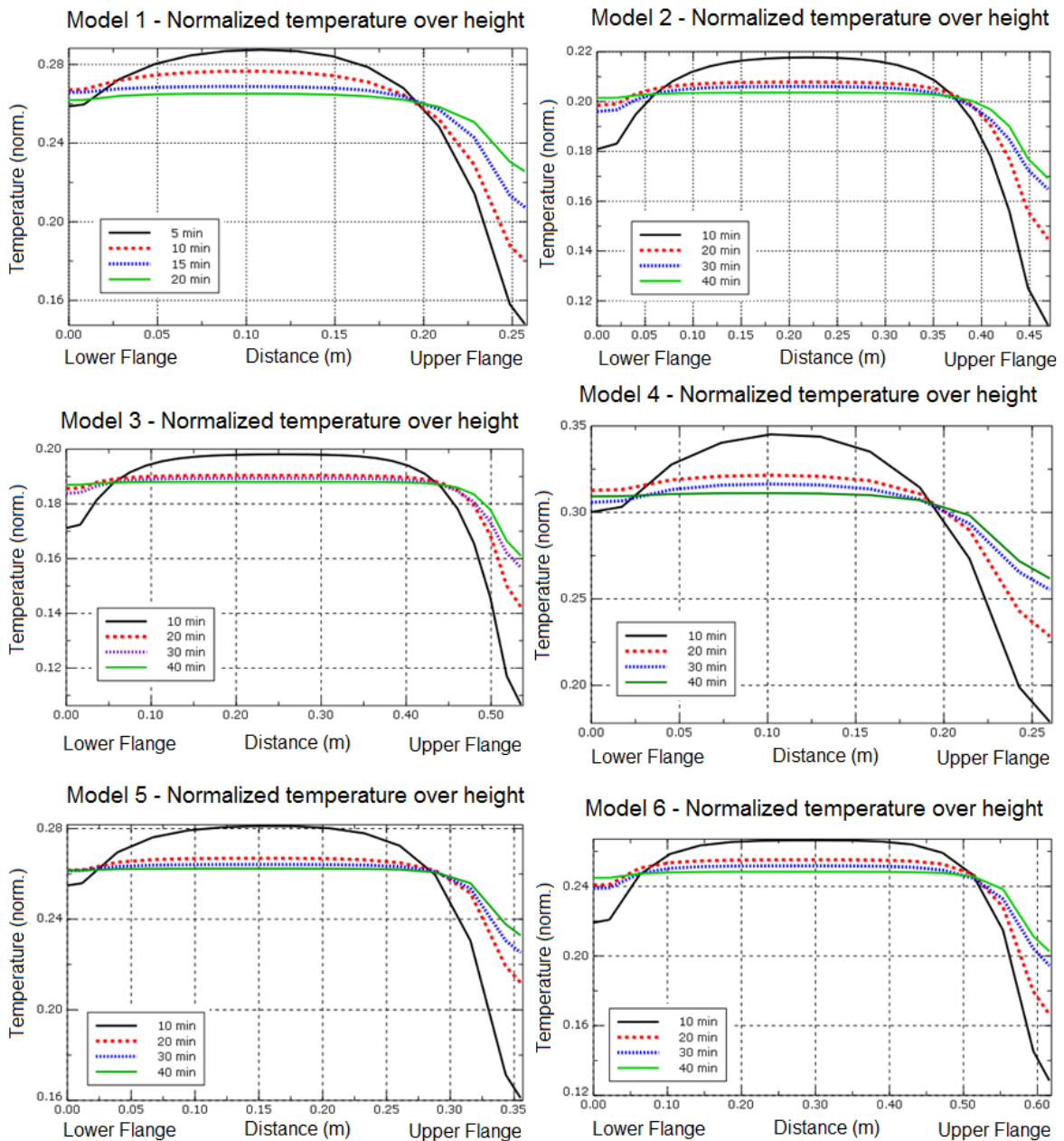


Figure 14. Normalized temperature over height.

It is noted in all models that the temperature distribution becomes uniform with the evolution of the standard fire, so that effects related to the thermal gradient are not evident for times greater than 15 min. The steel profile's lower flange and web have almost uniform temperatures, with a noticeable decrease only in the upper portion, equivalent to approximately 1/5 of the steel profile's total height, where it changes in a linear way up to the upper face.

For the structural analysis, graphs in Figure 15 show the mid-span vertical displacement, comparing the different boundary conditions proposed according to Table 3. Figure 16 illustrates the deformed model for the semi-continuous case at the exact moment when failure criteria was observed.

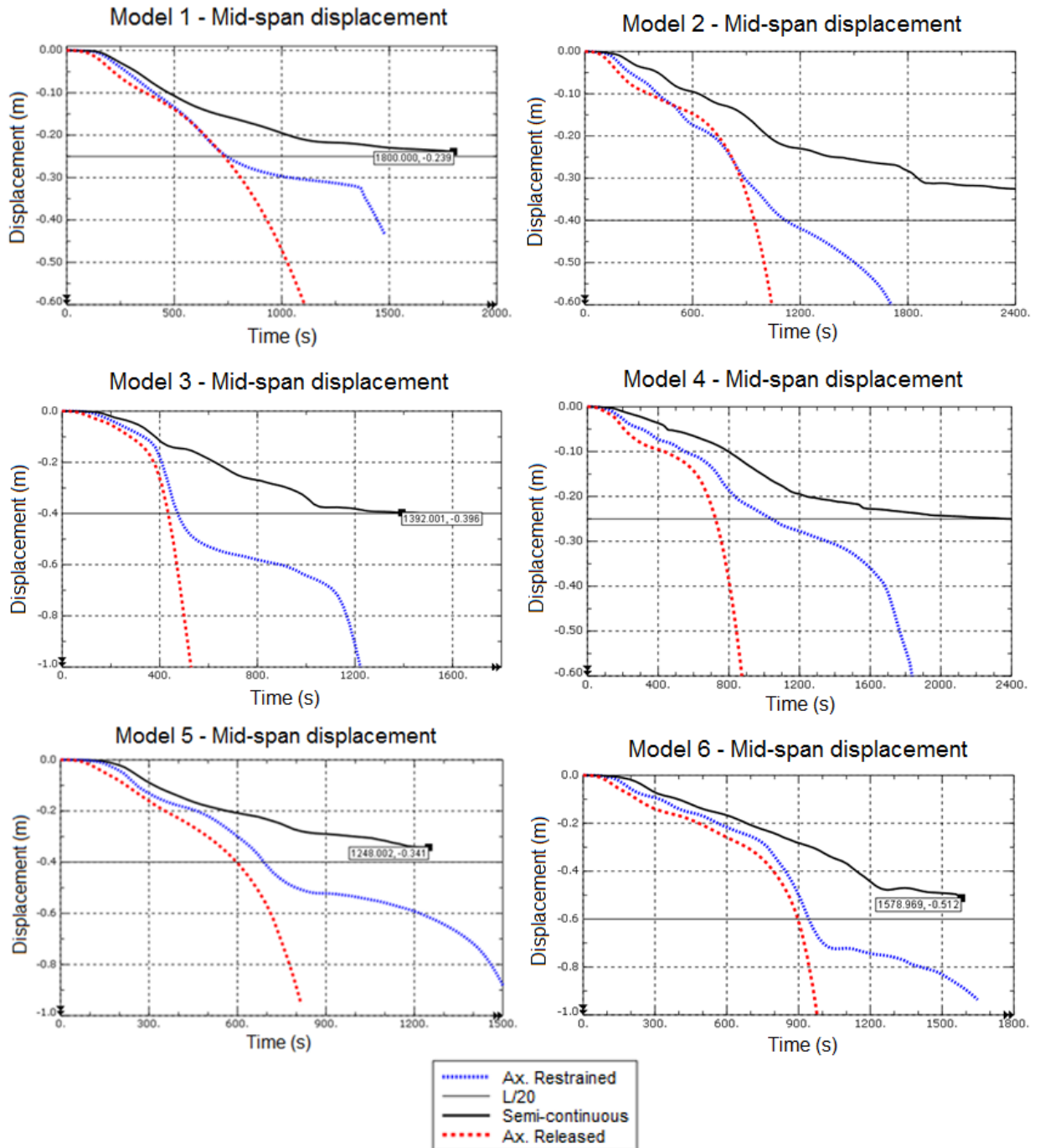
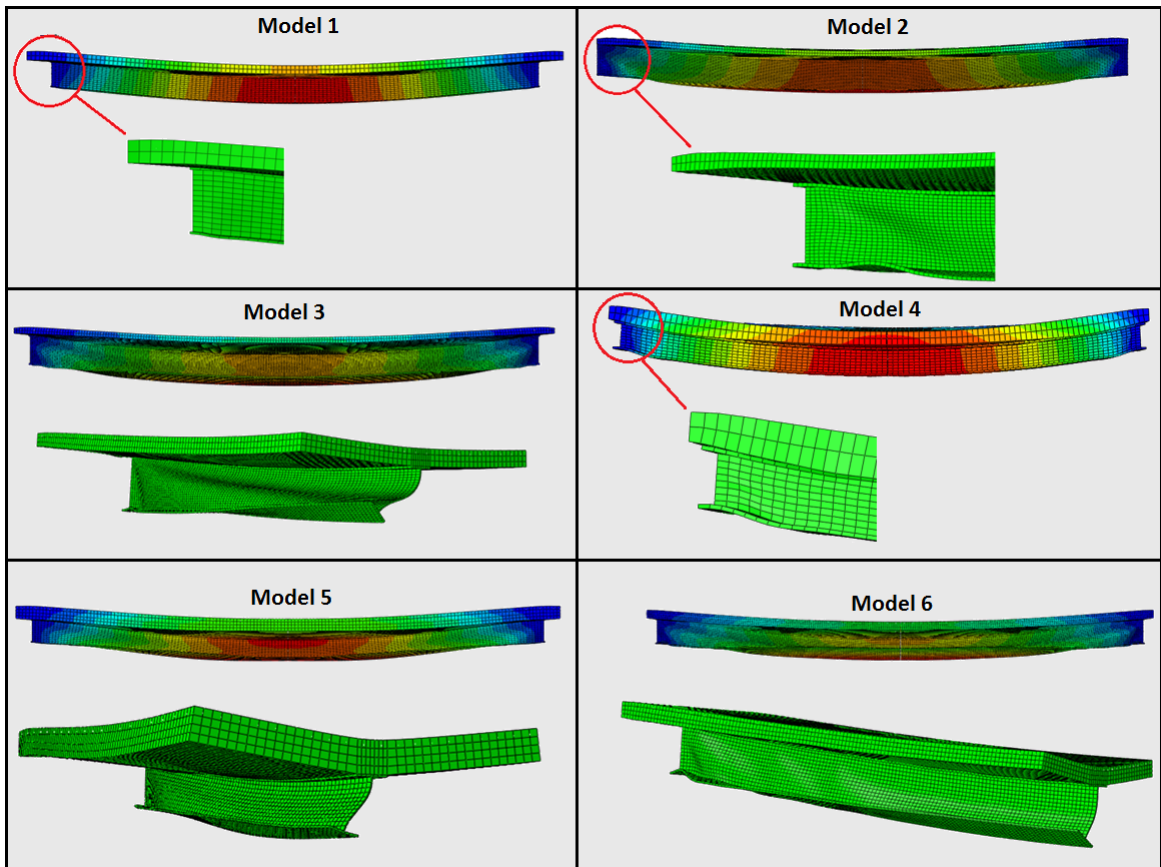


Figure 15. Mid-span displacement over time.



**Figure 16.** Deformation results for the semi-continuous case at collapse.

As a numerical nonlinear analysis is able to find equilibrium mechanisms usually overlooked in simplified analyzes, there is an intrinsic difficulty in characterizing structural collapse. Thus, following the same criteria as Wainman and Kirby [21] and Cedeno et al. [23], the collapse was defined according to BS 476 recommendations [26]. It is assumed that collapse is characterized as the first occurrence between (I) mid-span displacement greater than  $L/20$  and (II) a displacement rate greater than  $L^2/9000d$  after a displacement greater than  $L/30$ .

In addition, numerical non-convergence of the model, normally associated with excessively distorted elements, was considered a failure criterion, assuming that the beam no longer has the capacity to resist stresses properly.

For displacements below  $L/20$  it can be noted that there is little difference between the axial released and axial restrained condition in all models, so that the hypothesis adopted in simplified methods, that is, neglecting axial indirect stress and the slab's continuity, are acceptable. For displacements greater than  $L/20$ , however, the displacement rate for the axial restrained case is notably lower when compared to the axial released case, so that collapse does not occur abruptly. For very high deformations, it is likely that large cracks will form on the slab, losing its fire sealing property, so it is important to follow the  $L/20$  limit even if catastrophic failure does not occur.

In the semi-continuous condition, where the steel profile's lower flange was restrained and the slab's reinforcement ratio was considerably increased, the behavior of the composite beam changed dramatically, with an increase in its strength. The mid-span displacement rate was much lesser and catastrophic failure did not occur in any model, even after complete yield of the exposed steel profile.

Table 4 compares the fire resistance times (FRT) obtained in the numerical analysis for the semi-continuous case with values provided by the simplified method, in addition to indicating the failure criterion observed. Collapse condition (II) was not observed for the semi-continuous case, with numerical convergence and displacements greater than  $L/20$  being the critical criteria for characterizing the composite beam collapse.

The numerical analysis predicted higher FRTs than the simplified method in all cases. The consideration of geometric and material nonlinearity allowed the concrete slab, provided with a reinforcement mesh, to resist vertical loads due to catenary effects. The large deformations, limited to  $L/20$  as recommended by BS 476 [26], and being the

reinforced mesh protected from the temperature increase ensure that stresses are resisted in a behavior similar to a cable, a hypothesis already proven by several authors and ignored by the simplified method.

**Table 4.** Simplified method and numerical analysis FRTs comparison.

	FRT Simpl. Method	FRT Num. Analysis	Num. Analysis Fail Criteria
Model 1	< 15 min	30 min	$\delta = L/20$
Model 2	22 min	> 40 min	Not observed
Model 3	18 min	~23 min	$\delta = L/20$
Model 4	25 min	40 min	$\delta = L/20$
Model 5	17 min	~21 min	Numerical instability
Model 6	25 min	~26 min	Numerical instability

It is important to note that in order to take advantage of this phenomenon, it is necessary that the mesh reinforcement ratio is present in the entire length of the beam, and not only in negative bending moment region.

Another important aspect is the fact that the semi-continuous condition resulted in a large tensile area on the slab, especially in the region close to the supports. Such a region is highly subject to cracking. The proposed numerical models, however, are not able to assess the size of these cracks, so there is a possibility of loss of slab’s fire sealing property, allowing the heated gases to permeate the upper floor.

Models 3, 5 and 6 steel profiles suffered web distortion in the mid-span and local buckling in the support region, drastically reducing its strength in the first minutes (less than 15 min).

Such phenomenon, however, did not cause abrupt deformation of the composite beam. The mid-span displacement remained within the  $L/20$  limit during fire, with the slab’s catenary effect being enough to resist the stresses and allowing equilibrium. Thus, even with the occurrence of web buckling, the numerical model FRT were superior to those found by the simplified method, where such effect was not considered. The occurrence of local instabilities caused greater deformations, which would be relevant for room temperature design where elastic behavior is sought through the building’s life span. For fire design, however, the local buckling was not enough to cause collapse or loss of fire sealing property within the time limits listed in Table 4.

It is important to note that the web distortion was not an exclusive phenomenon of the semi-continuous case, occurring for all boundary conditions in models 3, 5 and 6, including the axial released one, as illustrated by Figure 17.

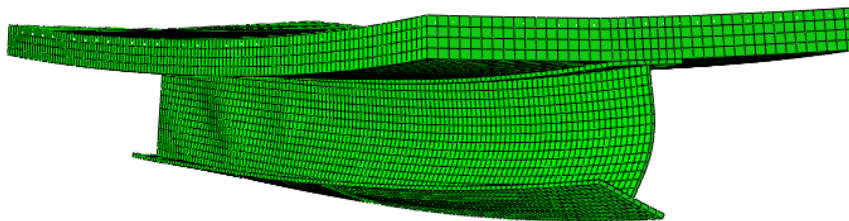


**Figure 17.** Web distortion detail for model 6, axial released case.

Despite being classified as a compact cross-section, large deformations induced web buckling as soon as the steel’s modulus of elasticity was reduced (temperatures above 300°C), since there is no presence of any intermediate stiffener or transverse bracing. Web stiffeners in mid-span allowing a connection between the lower and upper flanges could prevent this phenomenon.

Web distortion occurred for models with web slenderness greater than 40. It is suggested additional studies of this phenomenon for composite beams in fire.

## 5 CONCLUSIONS

Six unprotected composite steel and concrete beams numerical models were developed and submitted to a non-linear thermal and structural analyzes subjected to the standard fire while considering indirect stresses generated by

thermal expansion. For each model, three different boundary conditions were studied, namely: axial released, axial restrained and semi-continuous. The semi-continuous condition considers restriction of the steel profile lower flange and the continuity of the concrete slab over the end supports, with sufficient reinforcement mesh to develop the composite cross section maximum negative bending moment strength.

Structural analyses were performed for all conditions, and the results compared to FRT (Fire Resistance Time) values found by simplified analysis following design code procedures, where thermal expansion and geometric and material non-linearity effects are neglected.

By analyzing the results, it can be concluded that:

The temperature distribution along the steel profile's height becomes close to uniform with the standard fire evolution, so that effects associated with thermal gradient are reduced over time.

For a standard fire exposure greater than 15 min, the steel profile's temperature distribution along its height is close to uniform up to 1/5 of the upper portion, where it varies linearly to the upper face that is in direct contact with the slab.

For displacements below  $L/20$  there is little difference between the axial released and axial restrained cases in all models, so that the hypotheses of neglecting the axial thermal expansion indirect stresses and the slab's continuity adopted in the simplified methods are acceptable. For displacements greater than  $L/20$ , however, the mid-span displacement rate of the axial restrained case is notably less pronounced compared to the axial released case, so that collapse does not occur abruptly.

If only the slab continuity over the supports are considered, by not increasing the reinforcement mesh and without restricting the profile's lower flange, there is no significant change in the composite beam FRTs compared to the axial released case, despite avoiding a catastrophic collapse. Since the axial restrained condition has resulted in higher FRTs than the axial released case, there is no need to consider the stress increase by thermal expansion and thermal gradient in simplified analysis.

The steel profile's lower flange restriction and an increase in the slab's reinforcement ratio, allowing the semi-continuous behavior of the composite beam, considerably increased FRTs for all analyzed models. Even after total yield of the steel profile, the beam maintained its equilibrium due to catenary forces presented on the slab caused by large deformations and horizontal restriction of the slab supports.

The results confirm the hypothesis of the simplified method adopted in [2] and [20]. All FRTs found in the numerical analysis for the semi-continuous cases were higher than those estimated by the simplified method. The hypothesis of neglecting indirect stresses caused by thermal expansion and thermal gradient are valid, since considering geometric and material non-linearity was sufficient to significantly reduce those effects. It is worth mentioning that the slab's reinforcement mesh must extend over the beam's entire length, and not only in the negative bending moments region to take advantage of such beneficial effects. Thus, slab's catenary effect is guaranteed, and it is possible to achieve an equilibrium mechanism even after complete yield of the steel profile.

The semi-continuous case resulted in a large tensile region on the slab, especially close to the end supports. It is expected that such region will be subject to cracking, however the model is not able to assess the size of these cracks, so that there is a possibility of loss of slab's fire sealing property, allowing the heated gases to permeate the upper floor. The conclusions presented in this paper are valid only if vertical fire compartmentation is not a design requirement, a usual practice for small buildings that allow for standard fire resistance requirement times less than 30 minutes. It is recommended that future studies evaluate the size of these cracks and the potential loss of the slab's fire sealing property.

Web distortion in the mid-span occurred for steel profiles with web slenderness greater than 40, even in the axial released case (indicating that it was not caused due to restriction of the profile's lower flange), which resulted in much lower FRTs compared to models where it did not occur. Further studies are suggested to investigate this phenomenon for unprotected composite beams in fire with long unbraced lengths. Even with the occurrence of web buckling, fire resistance times for the semi-continuous case were higher than those estimated by the simplified method, where no buckling was considered.

## ACKNOWLEDGMENTS

Grant 2018/14735-6, São Paulo Research Foundation (FAPESP) and Conselho Nacional de Pesquisa e Desenvolvimento Científico (CNPq).

## REFERENCES

- [1] Associação Brasileira de Normas Técnicas, *Projeto de Estruturas de Aço e de Estruturas Mistas de Aço e Concreto de Edifícios*, NBR 8800, 2008.
- [2] L. C. Romagnoli and V. P. Silva, "About the consideration of semi-continuity in simply supported composite steel and concrete beams, to remove fireproof coatings for less than 30 minutes standard-fire resistance time," *Rev. IBRACON Estrut. Mater.*, vol. 12, pp. 1183–1204, 2019, <http://dx.doi.org/10.1590/s1983-41952019000500011>.
- [3] V. P. Silva, *Estruturas de Aço em Situação de Incêndio*, São Paulo: Zigurate, 2001.
- [4] São Paulo. Polícia Militar. Corpo de Bombeiros, "Instrução técnica nº 08: resistência ao fogo dos elementos de construção," DO, 2011.
- [5] Associação Brasileira de Normas Técnicas, *Projeto de Estruturas de Concreto em Situação de Incêndio*, NBR 15200, 2012.
- [6] Associação Brasileira de Normas Técnicas, *Projeto de Estruturas de Aço e de Estruturas Mistas de Aço e Concreto de Edifícios em Situação de Incêndio*, NBR 14323, 2013.
- [7] V. P. Silva, C. N. Costa, and A. Melão, "Procedure for decreasing the required time for fire resistance of the multistory buildings," *Rev. IBRACON Estrut. Mater.*, vol. 10, no. 5, pp. 1141–1162, 2017., <http://dx.doi.org/10.1590/s1983-41952017000500011>.
- [8] L. C. Romagnoli "Análise de vigas mistas de aço e concreto semicontínuas em situação de incêndio," M.S. thesis, Dep. Eng. Estr. Geotéc., Esc. Politéc., Univ. São Paulo, São Paulo, 2018.
- [9] Y. C. Wang, *Steel and Composite Structures – Behavior and Design for Fire Safety*. London: Spon Press, 2002.
- [10] A. S. Usmani, J. M. Rotter, S. Lamont, A. M. Sanad, and M. Gillie, "Fundamental principles of structural behavior under thermal effects," *Fire Saf. J.*, vol. 36, no. 8, pp. 721–744, 2001, [http://dx.doi.org/10.1016/S0379-7112\(01\)00037-6](http://dx.doi.org/10.1016/S0379-7112(01)00037-6).
- [11] C. G. Bailey, D. S. White, and D. B. Moore, "The tensile membrane action of unrestrained composite slabs simulated under fire conditions," *Eng. Struct.*, vol. 22, no. 12, pp. 1583–1595, 2001, [http://dx.doi.org/10.1016/S0141-0296\(99\)00110-8](http://dx.doi.org/10.1016/S0141-0296(99)00110-8).
- [12] C. G. Bailey, "Membrane action of unrestrained lightly reinforced concrete slabs at large displacements," *Eng. Struct.*, vol. 23, no. 5, pp. 470–483, 2000., [http://dx.doi.org/10.1016/S0141-0296\(00\)00064-X](http://dx.doi.org/10.1016/S0141-0296(00)00064-X).
- [13] L. Lim, A. H. Buchanan, and P. J. Moss, "Restraint of fire-exposed concrete floor systems," *Fire Mater.*, vol. 28, no. 24, pp. 95–125, 2004., <http://dx.doi.org/10.1002/fam.854>.
- [14] D. Anderson and A. A. Najafi, "Performance of composite connections: major axis end plate joints," *J. Construct. Steel Res.*, vol. 31, no. 1, pp. 31–57, 1994, [http://dx.doi.org/10.1016/0143-974X\(94\)90022-1](http://dx.doi.org/10.1016/0143-974X(94)90022-1).
- [15] S. Lin, Z. Huang, and M. Fan, "The effects of protected beams and their connections on the fire resistance of composite buildings," *Fire Saf. J.*, vol. 78, pp. 31–43, 2015, <http://dx.doi.org/10.1016/j.firesaf.2015.08.003>.
- [16] S. A. Ioannides and S. Mehta, *Restrained Versus Unrestrained Fire Ratings for Steel Structures – a Practical Approach*. Chicago, USA: Modern Steel Construction, 1997.
- [17] R. H. Fakury, E. B. Casas, F. F. Pacifico, and L. M. P. Abreu, "Design of semi-continuous composite steel-concrete beams at the fire limit state," *J. Construct. Steel Res.*, vol. 61, no. 8, pp. 1094–1107, 2005., <http://dx.doi.org/10.1016/j.jcsr.2005.02.003>.
- [18] European Committee for Standardization, *Design of Composite Steel and Concrete Structures – Part 1-2 – General Rules – Structural Fire Design*, EN 1994-1-2: Eurocode 4, 2005.
- [19] E. C. Fischer and A. H. Varma, "Fire resilience of composite beams with simple connections: parametric studies and design," *J. Construct. Steel Res.*, vol. 128, pp. 119–135, 2017., <http://dx.doi.org/10.1016/j.jcsr.2016.08.004>.
- [20] L. C. Romagnoli and V. P. Silva, "About the use of semi-continuity to remove fireproof coatings in simply supported composite steel and concrete beams," *Rev. IBRACON Estrut. Mater.*, vol. 11, no. 2, pp. 296–306, 2018., <http://dx.doi.org/10.1590/s1983-41952018000200005>.
- [21] D. E. Wainman and B. R. Kirby, *Compendium of UK Standard Fire Test Data – Unprotected Structural Steel – 1*. Rotherham: BSC, 1987.
- [22] M. B. Wong, "Effect on temperatures of structural steel in fire," *J. Struct. Eng.*, vol. 131, no. 1, pp. 16–20, 2005., [http://dx.doi.org/10.1061/\(ASCE\)0733-9445\(2005\)131:1\(16\)](http://dx.doi.org/10.1061/(ASCE)0733-9445(2005)131:1(16)).
- [23] G. A. Cedeno, A. H. Varma, and J. Gore, "Predicting the standard fire behavior of composite steel beams," *Compos. Constr. Steel Concr.*, vol. 6, pp. 642–656, 2011., [http://dx.doi.org/10.1061/41142\(396\)53](http://dx.doi.org/10.1061/41142(396)53).
- [24] P. Kmiecik and M. Kaminski, "Modelling of reinforced concrete structures and composite structures with concrete strength degradation taken into consideration," *Arch. Civ. Mech. Eng.*, vol. 11, no. 3, pp. 623–636, 2011., [http://dx.doi.org/10.1016/S1644-9665\(12\)60105-8](http://dx.doi.org/10.1016/S1644-9665(12)60105-8).
- [25] Associação Brasileira de Normas Técnicas, *Projeto de Estruturas de Concreto – Procedimento*, NBR 6118, 2014.
- [26] Comité Européen de Normalisation, *Fire Tests on Building Materials and Structures – Part 20: Method for Determination of the Fire Resistance of Elements of Construction (General Principles)*, BS 476, 1987.

---

**Author contributions:** VPS: conceptualization, methodology, supervision; LCR: data curation, methodology, writing, formal analysis.

**Editors:** José Marcio Calixto, José Luiz Antunes de Oliveira e Sousa, Guilherme Aris Parsekian.



## ORIGINAL ARTICLE

# Study of the physical and mechanical properties of permeable concrete with the addition of TiO<sub>2</sub> for the treatment of sewage

## *Estudo das propriedades físicas e mecânicas do concreto permeável com adição de TiO<sub>2</sub> para o tratamento de esgoto sanitário*

Wendel Melo Prudêncio de Araújo<sup>a</sup> Flávio Pessoa Avelino<sup>b</sup> Marcelo de Souza Picanço<sup>a</sup> Alcebíades Negrão Macêdo<sup>a</sup> <sup>a</sup>Universidade Federal do Pará – UFPA, Departamento de Engenharia Civil, Belém, PA, Brasil<sup>b</sup>Instituto Federal do Piauí – IFPI, Departamento de Engenharia Civil, Teresina, PI, Brasil

Received 02 November 2019

Accepted 17 March 2020

**Abstract:** The sewage treatment stations (STSs), located in Teresina-PI, were designed to receive domestic sewage, however, in 2011 they began to receive unknown sewer from clean pit vehicles. This sewage is compromising the effluent treatment efficiency. The permeable concrete with the addition of titanium dioxide (TiO<sub>2</sub>) presents itself as an alternative process to assist in the treatment of sanitary sewage due to its photocatalytic properties. Therefore, the objective of this work was to evaluate the mechanical, hydraulic, and microstructural properties of permeable concrete with the addition of 3, 6 and 10% of TiO<sub>2</sub>. The results determined that the variation in the concentration of TiO<sub>2</sub> significantly influenced the properties analyzed in this research. The addition of TiO<sub>2</sub> to the permeable concrete to a concentration of 6% impairs its physical and hydraulic properties and improves its mechanical properties.

**Keywords:** mechanical properties, physical properties, permeability, microstructure, TiO<sub>2</sub>.

**Resumo:** As estações de tratamento de esgoto (ETEs), situadas em Teresina-PI, foram projetadas para o recebimento de esgoto doméstico, porém, em 2011 começaram a receber esgoto desconhecido proveniente dos veículos Limpa Fossas. Este esgoto está comprometendo a eficiência do tratamento dos efluentes. O concreto permeável com adição de dióxido de titânio (TiO<sub>2</sub>) apresenta-se como um processo alternativo para auxiliar no tratamento de esgoto sanitário devido suas propriedades fotocatalíticas. Com isso, o objetivo deste trabalho foi avaliar as propriedades mecânicas, hidráulicas e microestruturas do concreto permeável com a adição de 3, 6 e 10% de TiO<sub>2</sub>. Os resultados determinaram que a variação na concentração de TiO<sub>2</sub> influenciou significativamente as propriedades analisadas nesta pesquisa. A adição de TiO<sub>2</sub> no concreto permeável até uma concentração de 6% prejudica suas propriedades físicas e hidráulicas e melhora suas propriedades mecânicas.

**Palavras-chave:** propriedades mecânicas, propriedades físicas, permeabilidade, microestrutura, TiO<sub>2</sub>.

**How to cite:** W. M. P. Araújo, F. P. Avelino, M. S. Picanço, and A. N. Macêdo, “Study of the physical and mechanical properties of permeable concrete with the addition of TiO<sub>2</sub> for the treatment of sewage,” *Rev. IBRACON Estrut. Mater.*, vol. 13, no. 5, e13514, 2020, <https://doi.org/10.1590/S1983-41952020000500014>

## 1 INTRODUCTION

The disorderly growth of society, associated with the processes of degradation of water quality, has been creating serious problems of quantitative and qualitative water scarcity, in addition to conflicts of use, even in natural regions with excess water. Industrial and domestic activities release many aggressive agents in the air, water, and soil, generating consequences that society needs to resolve. The residues produced in generally contain toxic pollutants and

**Corresponding author:** Wendel Melo Prudêncio de Araújo. E-mail: [wendelprudencio@hotmail.com](mailto:wendelprudencio@hotmail.com)

**Financial support:** None.

**Conflict of interest:** Nothing to declare.



This is an Open Access article distributed under the terms of the Creative Commons Attribution License, which permits unrestricted use, distribution, and reproduction in any medium, provided the original work is properly cited.

are resistant to conventional treatment systems (coagulation/flocculation; adsorption with activated carbon; precipitation; biological degradation, among others) [1].

The sewage treatment stations in Teresina-PI were planned to receive domestic sewage, however, as of 2011, by the decision of the Government of the State of Piauí, they began to receive sewage transported by clean pit vehicles, which collect sewage from pits installed in regions that do not receive coverage from basic sanitation. The effluents, coming from the pit cleaners, possibly contain a complex mixture of agents that cause the mutagenic effect, which can compromise the efficiency of the treatment in the effluent treatment plants. Physical-chemical analyzes revealed that the collected waters and effluents have high concentrations of electrical conductivity, detergents and phosphorus, in addition to high levels of thermotolerant coliforms, requiring alternative processes to ensure greater efficiency of the treatment sewage station [2].

Currently, in the treatment of contaminated effluents, mainly with toxic organic compounds, Advanced Oxidative Processes (AOPs) have been highlighted. These processes can degrade organic compounds and can even break them down into mineral compounds. This capacity is due to the high oxidizing power of hydroxyl radicals ( $\bullet$ OH), which are produced during the entire treatment process. These AOPs can also destroy toxic organic loads or convert them into more biodegradable forms [3].

Photocatalysis is a chemical reaction induced by photo-absorption of solid material, or photocatalyst, which remains chemically unchanged during and after the reaction. Its performance is affected by environmental factors such as light wavelength, humidity, temperature, and concentration of the photocatalyst. Titanium dioxide ( $\text{TiO}_2$ ) is one of the most efficient photocatalysts due to its high catalytic activity, being highly stable, economical, non-toxic (for environments and humans), containing strong oxidizing power and chemical resistance. Photocatalysis with  $\text{TiO}_2$  is a popular research area and finds its application in several fields such as air purification, hydrophilic coating, self-cleaning devices, water disinfection, wastewater treatment [4].

$\text{TiO}_2$  concrete is already used in pavements, paints, concrete panels and tiles, when added to concrete,  $\text{TiO}_2$  keeps the surface self-cleaning, eliminates biological organisms such as algae, bacteria, fungi and degrades airborne pollutants, such as nitrogen oxides ( $\text{NO}_x$ ) [5].

Other factors that can affect the efficiency of  $\text{TiO}_2$  photocatalysis, when applied to concrete, include porosity, type of aggregate, size of aggregate and method of application. The higher rate of voids and surface roughness, coupled with a larger surface area, can increase the bond, performance, and durability of  $\text{TiO}_2$  applied to permeable concrete [6].

$\text{TiO}_2$ -permeable concrete can be used for the decomposition of natural and inorganic mixtures, removal of heavy metals and eliminating infectious microscopic organisms. It can be used in the same way to assist the decay in the concentration of humid substances [7].

The incorporation of nanomaterials, such as  $\text{TiO}_2$ , in the concrete matrix or in the coating formulations, even in small quantities, results in greater resistance to biodeterioration and greater durability of the concrete structures used in sewage systems [8].

The addition of  $\text{TiO}_2$  to the permeable concrete causes important changes at the macrostructural and microstructural level and its understanding is fundamental for the effectiveness in its application in the treatment of sanitary sewage [9]. The objective of this research was to study the influence of the addition of  $\text{TiO}_2$  on the mechanical, physical and hydraulic properties of the permeable concrete and also to evaluate the microstructural modification on the surface of the permeable concrete with addition of  $\text{TiO}_2$ .

## 2 MATERIALS AND EXPERIMENTAL PROGRAM

### 2.1 Materials

#### 2.1.1 Cement

For the formulation of permeable concrete traces, PC-V ARI RS cement was used, following NBR 16697 [10]. This cement was chosen due to its property of resisting aggressive sulfated media, such as those found in sewage, wastewater or industrial networks, in seawater and some types of soils.

#### 2.1.2 Coarse Aggregate

As a coarse aggregate, crushed stone of basaltic origin was used, sold commercially as gravel 0, with five different gradations: 2.36, 4.75, 6.30, 9.50 and 12.50 mm, with specific mass and unit mass. of  $2810 \text{ kg/m}^3$  and  $1400 \text{ kg/m}^3$ , respectively, verified, based on NBR NM-53 [11].

The granulometric analysis (Table 1) and the granulometry curve (Figure 1) were performed according to NBR NM-248 [12], where it was observed that the coarse aggregate has a maximum characteristic dimension of 9.50 mm.

The coarse aggregate used in this study fits after the upper limit of the 9.5/25 sieves and has a uniformity coefficient (Cu) equal to 1.5. According to Lima and Silva [13], the Cu of the aggregate must be between 1.4 and 1.6, to provide better filtering of particles suspended in the water, avoiding greater risks of loss of efficiency due to clogging. Therefore, the aggregates used in this research meet the specifications found in the literature for use in the treatment of sanitary sewage.

**Table 1** - Granulometric analysis of crushed stone

Sieve Opening (mm)	Material retained in the sieve (g)	Material retained in the sieve (%)
25	0.00	0.00
12.5	10.00	1.00
9.5	415.40	42.54
6.3	499.80	92.52
4.75	25.90	95.11
2.36	47.20	99.82
Bottom	1.70	100.00
Maximum Characteristic Dimension	9.50 mm	

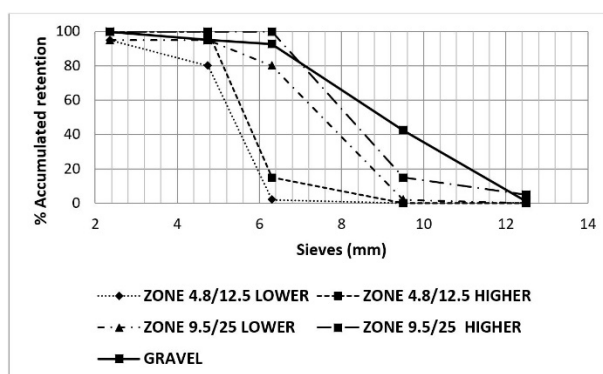


**Figure 1** Granulometric curve of coarse aggregate.

### 2.1.3 Titanium Dioxide

To produce photocatalytic permeable concrete, titanium dioxide P25 was used as a catalyst. Its chemical composition was determined by X-ray fluorescence by dispersive energy (FRX), where 99.95% purity was observed. Mineralogical characterization to identify the crystalline phases present was performed using the X-ray diffraction technique (XRD), Figure 2.

According to the micrographs obtained by scanning electron microscopy (SEM), at point A, the TiO<sub>2</sub> samples (Figure 3a), present particles with uniform distribution, spherical morphology, and slight agglomeration. There were no significant variations in grain morphology. According to Casagrande et al. [14], TiO<sub>2</sub> powder tends to agglomerate, has a spherical shape, however, due to agglomeration, does not have a well-defined shape.

The graph of TiO<sub>2</sub> powder obtained by the dispersive energy spectroscopy (EDS) technique (Figure 3b), at point A, shows high titanium (Ti) and oxygen peak (O) peaks, which are the constituent elements of the TiO<sub>2</sub> nanoparticles [15]. The presence of these peaks in the sample confirming the purity found in the X-ray fluorescence analysis, observing a carbon peak (C) in the EDS, which corresponds to the metallization tape used.

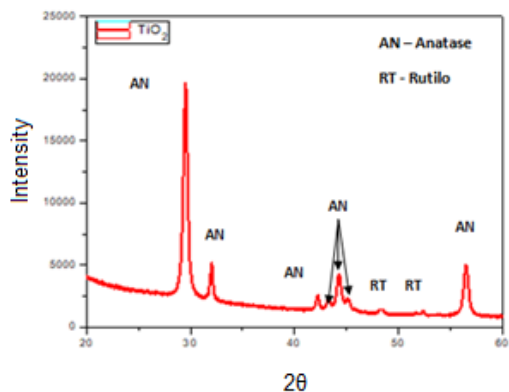


Figure 2 Titanium dioxide (TiO<sub>2</sub>) diffractogram.

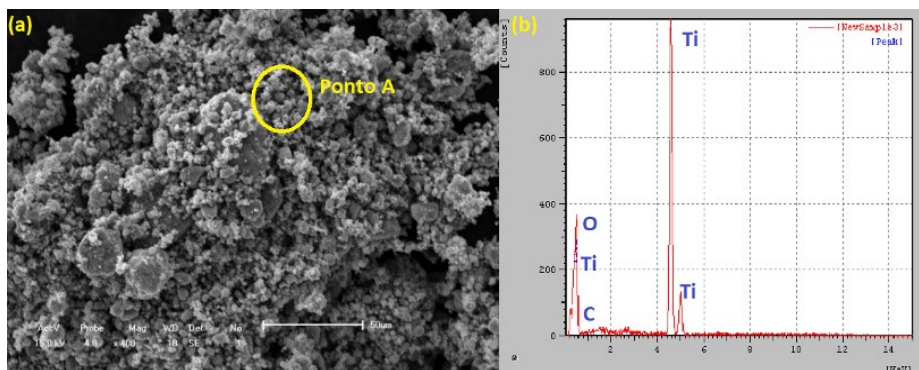


Figure 3 (a) Image obtained by SEM of the TiO<sub>2</sub> powder; (b) EDS image of TiO<sub>2</sub> powder.

## 2.2 Experimental Program

### 2.2.1 Permeable concrete characterization tests

The specific mass of the permeable concrete in the fresh state was determined according to NBR 9833 [16]. The porosity of the permeable concrete was determined according to Joshaghani et al. [17]. In the test to measure the permeability coefficient, the method described by the American Concrete Institute - ACI 522 R-10 [18] was used, which uses a variable load permeameter.

Permeable concrete samples were collected with and without TiO<sub>2</sub> to characterize its surface using the Scanning Electron Microscopy (SEM) method with Dispersive Energy Spectroscopy (DES).

### 2.2.2 Molding of specimens

Two types of specimens were prepared: cylindrical and prismatic. The molding of cylindrical specimens was performed according to NBR 5738 [19] with dimensions of 10 cm in diameter and 20 cm in height, being used in permeability and compression resistance tests, whereas the prismatic specimens were made from the recommendations of NBR 16416 [20], with dimensions of 10 cm × 10 cm × 40 cm, being used in the flexural strength test.

### 2.2.3 Permeable concrete dosage

Eighteen types of samples were produced, where they are identified as reference concrete (RC), using gravel 0 and permeable concrete (PC) in their composition, using aggregate with single granulometry (12.5; 9.5; 6.3; 4.75; 2.36 mm), water/cement ratio (0.25, 0.30 and 0.35) (Table 2).

**Table 2** Proportion of materials in the samples.

Samples	Ratio water/cement	Cement (kg/m <sup>3</sup> )	Aggregate (kg/m <sup>3</sup> )	Water (kg/m <sup>3</sup> )
RC.0.25.B0	0.25	487.45	1462.35	121.86
RC.0.30.B0	0.30	390.41	1561.66	117.12
RC.0.35.B0	0.35	325.59	1627.99	113.96
PC.0.25.12.5	0.25	481.82	1445.47	120.45
PC.0.30.12.5	0.30	385.60	1542.42	115.68
PC.0.35.12.5	0.35	321.42	1607.10	112.49
PC.0.25.9.5	0.25	399.66	1598.66	99.91
PC.0.30.9.5	0.30	331.92	1659.60	99.57
PC.0.35.9.5	0.35	458.94	1376.84	160.63
PC.0.25.6.3	0.25	337.12	1685.64	84.28
PC.0.30.6.3	0.30	470.37	1411.12	141.11
PC.0.35.6.3	0.35	378.80	1515.23	132.58
PC.0.25.4.75	0.25	398.65	1594.60	99.66
PC.0.30.4.75	0.30	331.04	1655.21	99.31
PC.0.35.4.75	0.35	457.94	1373.82	160.27
PC.0.25.2.36	0.25	338.33	1691.67	84.58
PC.0.30.2.36	0.30	471.78	1415.34	141.53
PC.0.35.2.36	0.35	380.02	1520.11	133.00

This procedure resulted in 108 specimens for the determination of compressive strength (18 samples x 6 repetitions), tested at 28 days; 108 specimens for flexural tensile testing (18 samples × 6 specimens), tested at 28 days and 108 specimens for calculating porosity, density and permeability (18 samples × 6 specimens). The RC.0.25.B0 to RC.0.35.B0 samples have particle sizes ranging from 2.36 to 12.50 mm and PC.0.25.12.5 to PC.0.35.2.36 single particle size, as shown in Table 3.

**Table 3** Sample granulometry, in percentage.

Sample Identification	Granulometry (mm)				
	12.50	9.50	6.30	4.75	2.36
RC.0.25.B0	5.26	28.86	48.4	12.59	4.89
RC.0.30.B0	5.26	28.86	48.4	12.59	4.89
RC.0.35.B0	5.26	28.86	48.4	12.59	4.89
PC.0.25.12.5	100	0	0	0	0
PC.0.30.12.5	100	0	0	0	0
PC.0.35.12.5	100	0	0	0	0
PC.0.25.9.5	0	100	0	0	0
PC.0.30.9.5	0	100	0	0	0
PC.0.35.9.5	0	100	0	0	0
PC.0.25.6.3	0	0	100	0	0
PC.0.30.6.3	0	0	100	0	0
PC.0.35.6.3	0	0	100	0	0
PC.0.25.4.75	0	0	0	100	0
PC.0.30.4.75	0	0	0	100	0
PC.0.35.4.75	0	0	0	100	0
PC.0.25.2.36	0	0	0	0	100
PC.0.30.2.36	0	0	0	0	100
PC.0.35.2.36	0	0	0	0	100

### 2.2.4 Mechanical tests

The compressive strength test was performed according to the NBR 5739 standard [21] and the flexural strength test was performed by the standard NBR 12142 [22].

### 2.2.5 TiO<sub>2</sub>- permeable concrete

After the tests with the permeable concrete, one of the eighteen compositions was chosen and TiO<sub>2</sub> was added to the cement, before the concrete production, for a determined time of two hours in the ball mill, to guarantee a greater homogeneity between the two materials. With the obtaining of the previous mixture, gravel and water were added to the 150-liter concrete mixer to obtain the concrete.

This choice was made considering the feature that best suits the conditions of durability and performance for use in sewage systems. According to Noeiaghahi [8], the concrete used in sewage systems must have a water-cement ratio lower than 0.45 and have high resistance, because concretes with low resistance reduce the durability of the sewage system, increasing the repair cost and maintenance throughout the life of the system.

Four samples were used to analyze the addition of TiO<sub>2</sub> in the permeable concrete, a control sample, without TiO<sub>2</sub> and three samples containing 3, 6, and 10% of TiO<sub>2</sub>, in substitution of the cement, by mass. The concentrations of TiO<sub>2</sub> in the permeable concrete were adopted based on the work of Melo et al. [23], where the efficiency of the incorporation of TiO<sub>2</sub> in paving blocks was evaluated. The samples of concrete permeable with TiO<sub>2</sub> were subjected to the same tests, physical and mechanical, carried out on permeable concrete without TiO<sub>2</sub>.

The tests resulted in 24 specimens for compression (4 samples × 6 repetitions), tested at 28 days; 24 specimens for traction in flexing (4 samples × 6 repetitions), tested at 28 days and 24 specimens for calculating porosity, density, and permeability (4 samples × 6 specimens).

Samples of TiO<sub>2</sub>-permeable concrete were collected from the broken specimens from the compressive strength test to characterize its surface using the Scanning Electron Microscopy (SEM) method with Dispersive Energy Spectroscopy (EDS).

### 2.2.6. Statistical analysis

The data obtained in the tests were treated statistically, through the analysis of variance (ANOVA) to check the significant effects at a 95% confidence level, in addition to the test of multiple comparisons of means (Tukey's test), to check which averages showed statistical differences at the level of 5% probability.

## 3 RESULTS AND DISCUSSIONS

### 3.1 Porosity and specific mass

The average values of specific mass and porosity obtained in this study vary from 1565.53 kg/m<sup>3</sup> to 2082.29 kg/m<sup>3</sup> and 15.25% to 31, which can be verified in Figures 4 and 5. By the Tukey Test, admitting if a p-value ≤ 0.05 it can be seen that there was a difference between the eighteen samples.

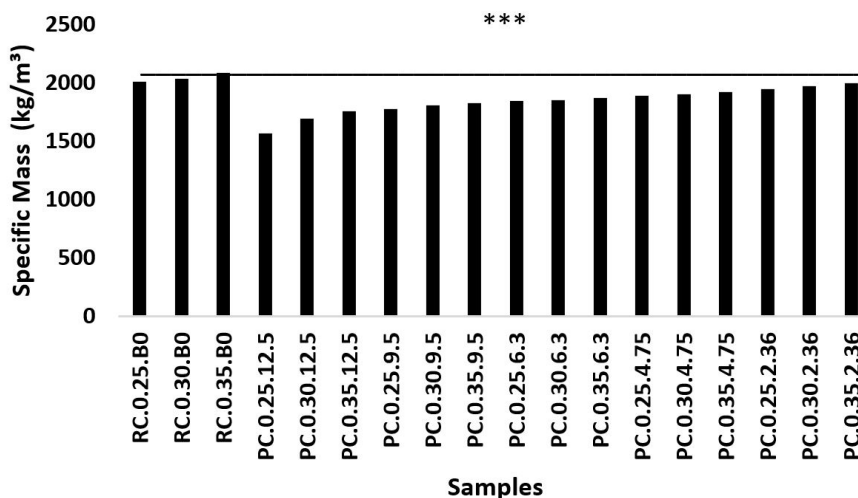


Figure 4 Average samples results of specific mass tests. \*\*\* Significant statistical difference by the Tukey test p <0.001.

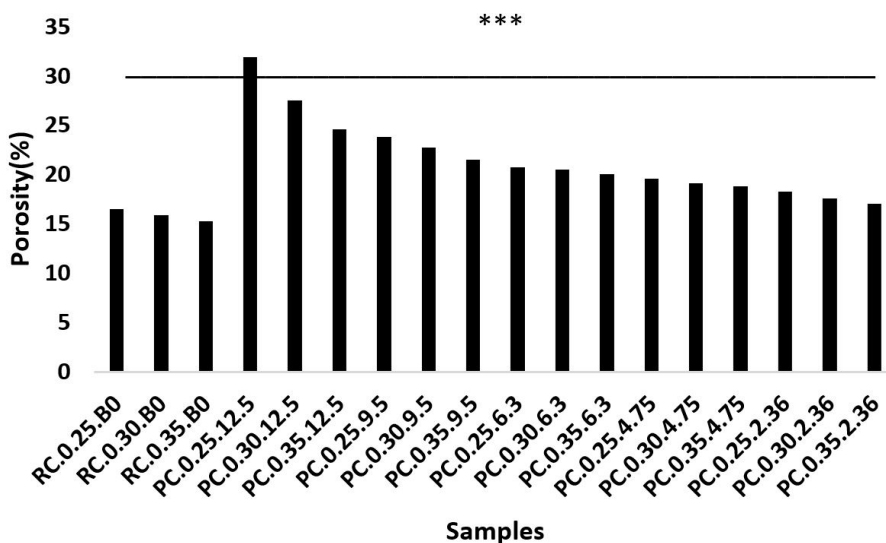


Figure 5 Average samples results of porosity tests. \*\*\* Significant statistical difference by the Tukey test  $p < 0.001$ .

The samples PC.0.35.B0 and PC.0.25.12.5 obtained the highest and lowest specific mass, respectively, concerning the eighteen samples analyzed in this study. This indicated that the increase in the granulometry of coarse aggregates, with a lower water-cement ratio, offered more resistance to compaction, which decreased the specific mass and increased the porosity, which according to Ibrahim et al. [24], as the ratio cement-aggregate increases, the volume of intergranular void decreases due to the decrease in the resistance to compaction offered by the reduced amount of aggregates, which was evidenced by the tests performed.

The mixtures that had in their composition varied granulometry (PC.0.25.B0, PC.0.30.B0 and PC.0.35.B0), presented the highest specific masses because the voids generated by the aggregates with larger particle sizes (12.5 mm), it may have been sufficient to accommodate the smaller aggregates (4.75 and 2.36 mm), resulting in a greater compaction factor, which had already been verified by Ibrahim et al. [24] where the values of specific mass, obtained in different water-cement ratios, are functions of the compaction method and the degree of lubrication of the sample.

### 3.2 Permeability

It is observed that the average permeability values obtained in this study vary from 0.74 to 18.68 mm/s (Figure 6). By the Tukey test, assuming a value of  $p \leq 0.05$ , it can be observed that there was a difference between the eighteen samples.

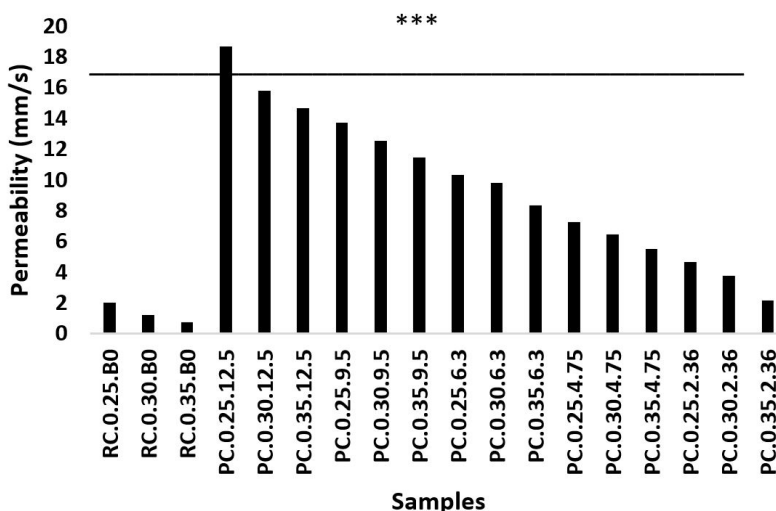


Figure 6 Average samples results of permeability tests. \*\*\* Statistically significant difference by the Tukey test  $p < 0.001$ .

The permeability of the mixtures that present in their composition coarse aggregates with a single size (PC.0.25.12.5 to PC.0.35.2.36) reached a rate above that recommended by the ACI 522R-10 standards [18], which establishes a minimum value of 1mm/s for permeable concretes. Neptune and Putman [25] verified in his study about the effect of the size of the coarse aggregate in permeable concrete mixtures that, the highest permeability values were obtained in the dosages that had coarse aggregates of one size.

The permeable concrete mixtures that used coarse aggregates with dimensions of 12.5, 9.5, and 6.3 mm (PC.0.25.12.5 to PC.0.35.6.3), obtained a higher permeability due to the smallest surface area of the aggregates. The samples with coarse aggregates with dimensions of 4.75 and 2.36 mm (PC.0.25.4.75 to PC.0.35.2.36) had a larger surface area of aggregates, decreasing porosity and permeability, but it was observed enough cement paste just to coat them.

The samples PC.0.25.B0, PC.0.30.B0, and PC.0.35.B0, composed of aggregates of size ranging from 2.36 to 12.5 mm, obtained greater compaction, requiring more cement paste to coat the aggregates. Chandrappa and Biligiri [26] found that permeable concretes that contain coarse aggregate in their composition with continuous graduation, require greater amounts of cement paste to coat the aggregates, with this, they present a lower permeability, because a part of this cement paste fills the voids intergranular, reducing porosity. This was evidenced in the sample PC.0.35.B0, where the permeability was below the specification of the ACI 522R-10 standard [18].

According to Kia et al. [27], the permeability of permeable concretes is related to the porosity of the material, since the greater the porosity, the greater the permeability. Still in this context, the compaction procedure must be selected and applied with care, since, even the material having high porosity, the use of an inadequate compaction procedure can cause the reduction of interconnectivity between the pores, impairing the permeable capacity of the material.

### 3.3 Compressive strength

The average values of compressive strength obtained in this study ranged from 9.55 to 22.17 MPa (Figure 7). By the Tukey test, assuming a value of  $p \leq 0.05$ , it can be observed that there was a difference between the eighteen samples.

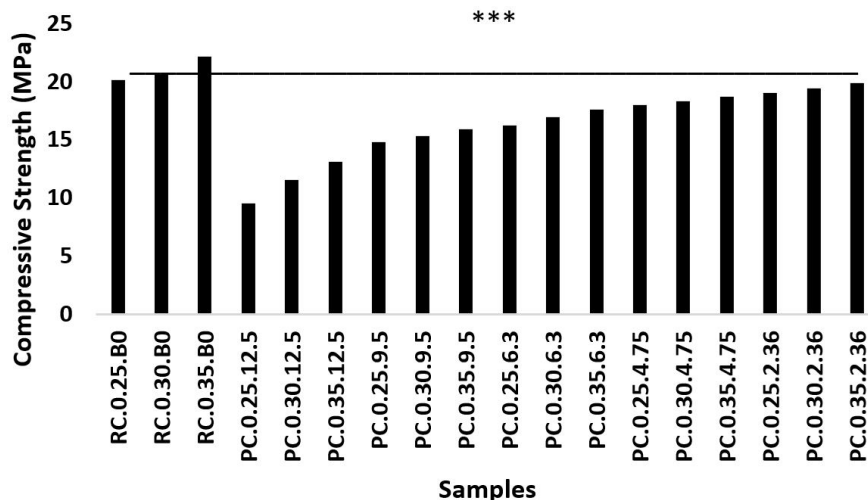


Figure 7 Average samples results of compressive strength tests. \*\*\* Statistically significant difference by the Tukey test  $p < 0.001$ .

average compressive strength after 28 days of curing (22.17 MPa). When the water-cement ratio was less than 0.35, for the same size of coarse aggregate, the compressive strength decreased in all samples analyzed. The PC.0.25.12.5 mixture with a water-cement ratio of 0.25 and a single coarse aggregate of 12.5 mm produced the lowest average compressive strength of 9.55 MPa, at 28 days.

Yeih et al. [28] studied the use of slag from the electric arc furnace as aggregate for permeable concrete and found that the lowest compressive strength was recorded for the mixture produced from a single type of aggregate, with a dimension of 12.5 mm, and the water-cement ratio that guaranteed greater resistance in the samples was 0.35, corroborating with the current study.

Figure 8 shows the relationships between porosity, compressive strength, and permeability for permeable concrete. This figure can be used to estimate the porosity required for mixtures that have specifications for use in terms of permeability and strength of permeable concrete. As an example, with 30% porosity, the permeable concrete will have a permeability of 20.00 mm/s and compressive strength of 10.0 MPa.

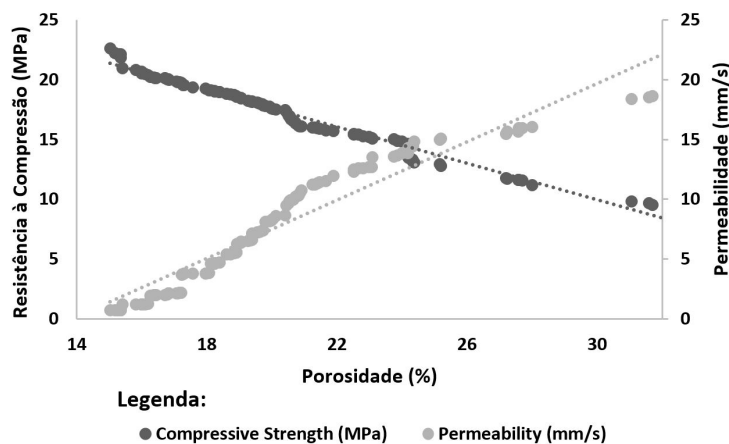


Figure 8 Relationship between Porosity, Compression Resistance and Permeability.

### 3.4 Flexural tensile strength

It is observed that the mean values of flexural tensile strength obtained in this study vary from 1.22 to 4.82 MPa (Figure 9). By the Tukey test, assuming a value of  $p \leq 0.05$ , it can be observed that there was a difference between the eighteen samples.

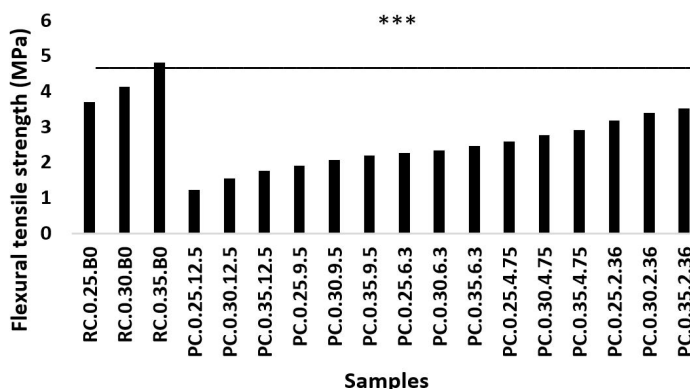


Figure 9 Average samples results of flexural tensile strength tests. \*\*\* Statistically significant difference by the Tukey test  $p < 0.001$ .

It was observed that the ratio between the flexural strength and the compressive strength ranges from 0.12 (PC.0.25.12.5) to 0.21 (RC.0.35.B0), this relationship increases as the porosity decreases. Yeih and Chang [29] assessed the influences of the type of cement and curing conditions on the properties of permeable concrete and found that the ratio between flexural strength and compressive strength ranges from 0.16 to 0.26. As the sample porosity increases, a greater reduction in compressive strength compared to flexural strength has occurred.

The size of the aggregate affects the tensile strength in flexion in all types of samples analyzed. The mixture PC.0.35.B0, using in its composition coarse aggregates ranging from 2.36 to 12.5 mm, reaches the maximum average tensile strength in flexion of 4.82 MPa corresponding to the lowest porosity and a water factor cement of 0.35. However, the PC.0.25.12.5 mixture, which has a single aggregate size of 12.5 mm, has the lowest average tensile strength in flexion of 1.22 MPa due to the greater porosity and a water-cement factor of 0.25.

According to Brake et al. [30], the coarse aggregate grain size and the water-cement ratio significantly affect its flexural strength. The larger size of the aggregates and a lower water-cement ratio results in decreasing the specific mass of permeable concrete. Therefore, the contact forces between the aggregates become weaker, which leads to a reduction in the permeable concrete strength. Joshaghani et al. [17] found that the permeable concrete that contains coarse aggregates with unique sizes in its composition, showed a reduction in tensile strength in flexion as the coarse aggregate size increased.

### 3.5 Addition of TiO<sub>2</sub> to permeable concrete

Following the recommendations of Noeiaghahi [8], the PC.0.35.2.36 mixture was chosen to add TiO<sub>2</sub>, since the concrete used in sewage systems must have a water-cement ratio lower than 0.45 and have high resistance, therefore, concrete with low resistance reduces the durability of the sewage system, increasing the cost of repair and maintenance throughout the system's useful life.

Four permeable concrete samples were produced, the detailed experimental proportions are provided in Table 4. The water-cement ratio remained constant with a value of 0.35. Yeih et al. [28] found that water-cement ratios equal to 0.35, in permeable concrete, improve their mechanical properties.

**Table 4** Proportion of materials in the samples.

Sample Type	Water/cement ratio	Cement (kg/m <sup>3</sup> )	Aggregate (kg/m <sup>3</sup> )	TiO <sub>2</sub> (kg/m <sup>3</sup> )	Water (kg/m <sup>3</sup> )
PC	0.35	380.00	1520.11	0.00	133.00
PC.3.TiO <sub>2</sub>	0.35	368.60	1520.11	11.40	130.00
PC.6.TiO <sub>2</sub>	0.35	357.20	1520.11	22.80	126.00
PC.10.TiO <sub>2</sub>	0.35	342.00	1520.11	38.00	121.00

#### 3.5.1 Porosity and specific mass

Figures 10 and 11 show the average porosity and specific mass of the samples. The higher the concentration of TiO<sub>2</sub> in the permeable concrete, the lower the porosity and the higher the specific mass, up to a concentration of 6%. For a 10% concentration of TiO<sub>2</sub>, the porosity of the permeable concrete increases and the specific mass decreases. By the Tukey test (Figures 10 and 11), assuming a p-value  $\leq 0.05$ , it can be observed that there was a difference between the four samples. The addition of 3, 6 and 10% of TiO<sub>2</sub> decreased the porosity by 10.86, 15.79, and 11.80% respectively and the specific mass increased by 5.17, 8.81 and 2.00%, respectively, in relation to the PC sample. Chen et al. [31] studied the porosity in cement mortars with the addition of TiO<sub>2</sub> and found that the addition of TiO<sub>2</sub> in the cement paste can decrease the porosity and increase the specific mass, since the TiO<sub>2</sub> particles fill the voids, mainly the capillary pores. Besides, it was found that TiO<sub>2</sub> does not have pozzolanic activity, being inert in the mortar and can be used as fine aggregate.

According to Magesvari and Narasimha [32], the voids between coarse aggregates cannot be filled by a cement paste, the use of fine aggregate can increase the bonding area between cement paste and coarse aggregates, resulting in less porosity and greater specific mass, but it is necessary to control the addition of the fine material so as not to compromise the permeability considerably.

The PC.10.TiO<sub>2</sub> sample showed an increase in porosity and a decrease in specific gravity in relation to the PC.6.TiO<sub>2</sub> sample, the TiO<sub>2</sub> content made the mixture less workable, providing greater resistance to compaction, resulting in greater porosity and less mass-specific.

#### 3.5.2 Permeability

Figure 12 shows that, with the increase in the percentage of TiO<sub>2</sub> in the permeable concrete mixture, there is a gradual decrease in the permeability value. The greatest reduction in permeability was in the PC.10.TiO<sub>2</sub> sample, with a decrease of 12.5% about the PC sample. However, all samples were above that required by ACI 522R-10 [18], which establishes a minimum permeability value of 1mm/s for permeable concretes. Using the Tukey test (Figure 12), assuming a p value  $\leq 0.05$ , it can be observed that there was a difference between the four samples.

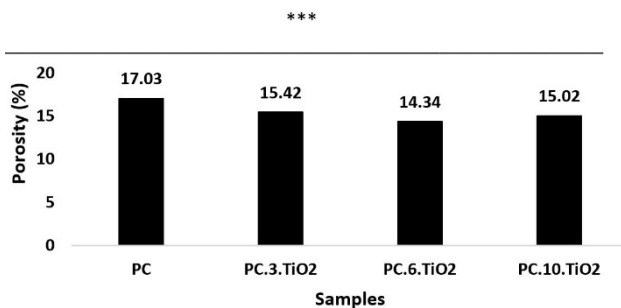


Figure 10 Average samples results of porosity tests. \*\*\* Statistically significant difference by the Tukey test  $p < 0.001$ .

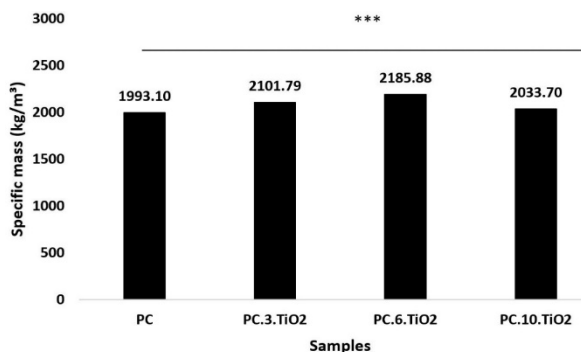


Figure 11 Average samples results of specific mass tests. \*\*\* Statistically significant difference by the Tukey test  $p < 0.001$ .

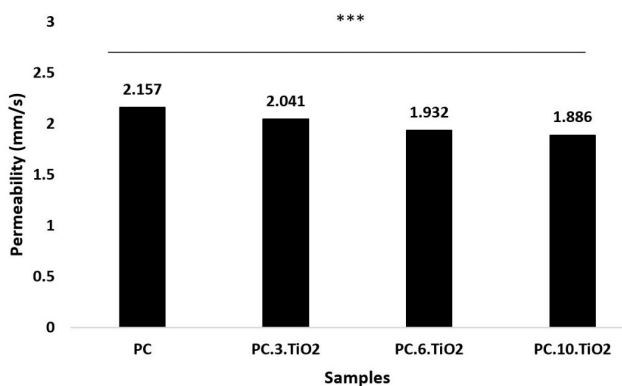


Figure 12 Average of samples obtained in the Permeability test. \*\*\* Statistically significant difference by the Tukey test  $p < 0.001$ .

In his study, Bolt et al. [33], adding 10% of  $\text{TiO}_2$  to a permeable concrete mixture that had 45% of the aggregates passing through the 4.75 mm number sieve, reduced its permeability by 11.29% and the addition of 15% of  $\text{TiO}_2$ , permeability of permeable concrete decreases by approximately 47%, compromising its permeability.

In his research, Lian et al. [34] found that permeability depends on the size of coarse aggregates, the thickness of cement paste, water/cement ratio, as well as the addition of fine aggregates. Permeability increases with the use of aggregates of greater particle sizes. However, it decreases with the increase of fine aggregate content. Thus, the addition of  $\text{TiO}_2$  to the permeable concrete must be carried out in such a way that it does not compromise its permeability.

### 3.5.3 Compressive strength

According to Figure 13, the PC.3. $\text{TiO}_2$  and PC.6. $\text{TiO}_2$  samples increased their compressive strength, compared to the PC sample, the increase in the concentration of  $\text{TiO}_2$  in the mixture, resulted in an increase in compressive strength by 9, 56 and 22.8%, respectively. With the addition of  $\text{TiO}_2$ , the contact area between the

cement paste and the coarse aggregate increases, making the permeable concrete more resistant. By the Tukey test (Figure 13), assuming a p-value  $\leq 0.05$ , it can be observed that there was a difference between the four samples.

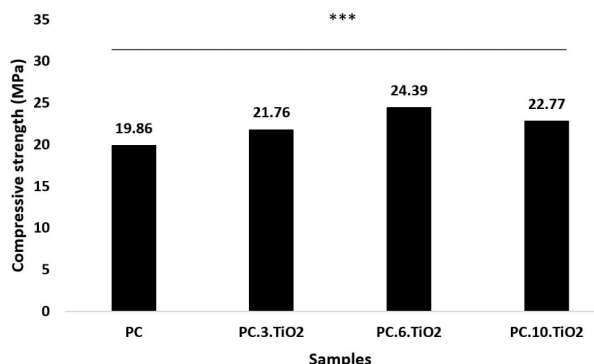


Figure 13 Average samples results of Compression Resistance tests. \*\*\* Statistically significant difference by the Tukey test  $p < 0.001$ .

Manoj Kumaar et al. [35] studied the influence of the addition of 2%  $\text{TiO}_2$  on the compressive strength of permeable concrete, using a single aggregate with a size of 10 mm. A 7.64% increase in compressive strength was observed. Andrade et al. [36] found that the addition of  $\text{TiO}_2$  to autoclaved cellular concrete reduces the porosity of the cement paste, improving its mechanical properties.

The PC.10. $\text{TiO}_2$  sample showed a decrease in compressive strength of 6.92% compared to the PC.6. $\text{TiO}_2$  sample, this may have occurred due to the less workability of the mixture. Senff et al. [37] reported that the increase in the concentration of  $\text{TiO}_2$  in cement mortars decreases its workability, impairing the mechanical properties of the mortar. Meng et al. [38] studied the influence of the addition of  $\text{TiO}_2$  in cement pastes and observed that the addition of 10% of  $\text{TiO}_2$  decreases the workability by 40%, thus the compressive strength decreased by 9% concerning the sample with 5% of  $\text{TiO}_2$ .

### 3.5.4 Tensile strength in flexion

Figure 14 shows the average tensile strength in the flexion of the samples. The higher the concentration of  $\text{TiO}_2$  in permeable concrete, the greater the increase in tensile strength in flexion, up to a concentration of 6%. For a concentration of 10% of  $\text{TiO}_2$  the tensile strength in the permeable concrete flexion decreases. Using the Tukey test (Figure 14), assuming a p value  $\leq 0.05$ , it can be observed that there was a difference between the four samples.

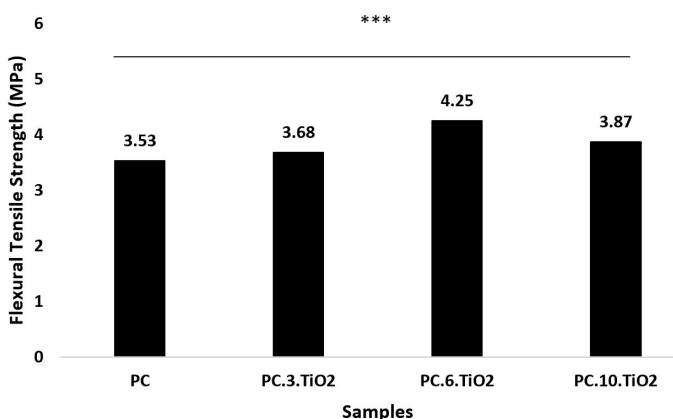


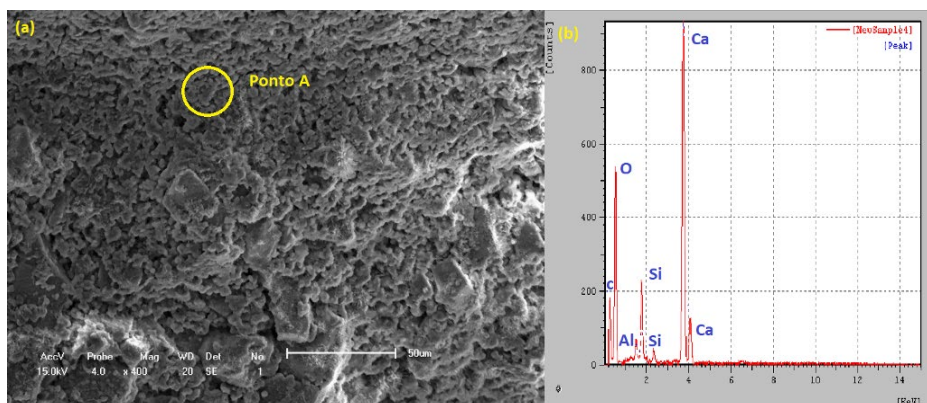
Figure 14 Average of the samples obtained in the Flexural Tensile Strength test. \*\*\* Statistically significant difference by the Tukey test  $p < 0.001$ .

The permeable concrete samples PC.3.TiO<sub>2</sub> and PC.6.TiO<sub>2</sub> increased the tensile strength in flexion by 4.25 and 20.39%, respectively, in relation to the sample PC. Zade et al. [39] used a concentration of 5% of TiO<sub>2</sub> in the permeable concrete with coarse aggregate ranging from 6, 10 and 20 mm and obtained an increase in the tensile strength in flexion of 18.86%. This relationship can be compared to the addition of fine aggregate to the permeable concrete. According to Lian and Zhuge [40], the fine aggregate is generally excluded from permeable concrete, but adding a small fraction, up to 7%, increases the tensile strength in flexion, compression, and specific gravity.

The flexural tensile strength decreases by 8.70% in the PC.10.TiO<sub>2</sub> sample, compared to the PC.6.TiO<sub>2</sub> sample. According to Jalal et al. [41], the increase in the concentration of TiO<sub>2</sub> in the cement paste decreases the content of calcium hydroxide Ca(OH)<sub>2</sub> responsible for the formation of hydrated calcium silicate (CSH), which is responsible for the strength gain of the concrete.

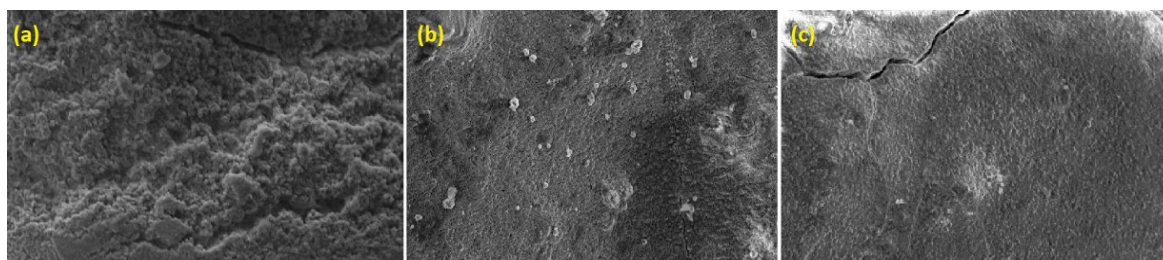
### 3.6 Characterization of permeable concrete

Figure 15a shows the SEM of the permeable concrete surface of the PC sample, where there is a rough and irregular region with the presence of many pores. Figure 15b, at point A, verified the DES of the PC sample, where the peaks of the elements, aluminum (Al), silicon (Si), oxygen (O) and calcium (Ca), characteristic for the formation of oxides in the cement paste, which give rise to hydrated silicates (CSH) and calcium hydroxide (Ca(OH)<sub>2</sub>), for example (MEHTA, 2014). Observing a carbon peak (C) in the DES, which corresponds to the metallization tape used.



**Figure 15** (a) SEM images of the permeable concrete surface increased 400 times; (b) DES analysis of the permeable concrete surface.

Figures 16a, 16b and 16c correspond to samples PC.3.TiO<sub>2</sub>, PC.6.TiO<sub>2</sub> and PC.10.TiO<sub>2</sub>, respectively. The change in the concentration of TiO<sub>2</sub> changed the surface of the permeable concrete, influencing the decrease in the porosity of the cement paste that surrounds the coarse aggregates in the permeable concrete, when the higher the concentration of TiO<sub>2</sub>, a less porous surface is observed. It was not possible to identify the TiO<sub>2</sub> particles by SEM images because the particles in the concrete were similar to the TiO<sub>2</sub> particles. According to Shen et al. [6], the permeable concrete particles have a shape similar to the TiO<sub>2</sub> particles and their rough texture helps to camouflage the TiO<sub>2</sub> particles, in addition, the porosity and roughness of the permeable concrete surface allow more TiO<sub>2</sub> particles to have contact with UV lights and thus improve its photocatalytic properties.



**Figure 16** SEM images of the permeable concrete surface: (a) 3% TiO<sub>2</sub>; (b) 6% TiO<sub>2</sub>; 10% TiO<sub>2</sub>.

DES (Figure 17) confirmed the presence of TiO<sub>2</sub> on the permeable concrete surface, showing peaks of titanium (Ti), calcium (Ca), oxygen (O), aluminum (Al), silicon (Si), carbon (C) and niobium (Nb). In this analysis, the metallized tape used had the chemical element Niobium in its composition, hence the presence of peaks in the DES.

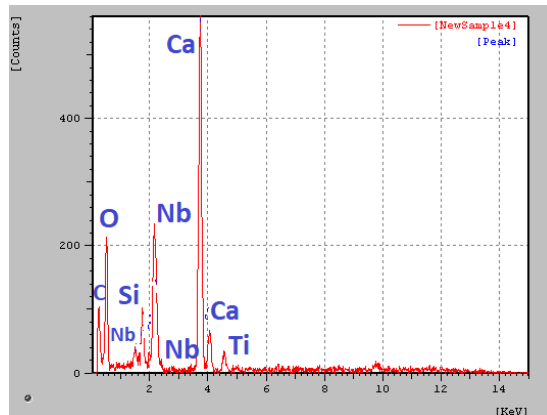


Figure 17- DES analysis of the permeable concrete surface with 10% TiO<sub>2</sub>.

#### 4 CONCLUSIONS

This research studied the addition, in different concentrations, of TiO<sub>2</sub> in the permeable concrete to evaluate its mechanical, hydraulic, and microstructural properties to use it in the sanitary sewer system. Based on the results presented, it is concluded that:

- (a) With the increase in coarse aggregate granulometry, in mixtures containing single aggregate size, there is an increase in the value of porosity, permeability and a reduction in specific gravity, resistance to compression and flexural tensile strength;
- (b) Samples with varying granulometry, due to greater compaction, an increase in specific gravity, compressive strength, tensile strength in flexion and a decrease in permeability and porosity;
- (c) As the concentration of TiO<sub>2</sub> increases, up to a concentration of 6%, in the permeable concrete dosage, there is an increase in the compressive strength, flexural tension and specific mass, and a reduction in porosity. This fact occurs due to the expansion of the connection area between the cement paste and the coarse aggregate, with the addition of TiO<sub>2</sub>;
- (d) The permeable concrete samples, which had 10% TiO<sub>2</sub> in their mixture, showed a lack of workability, with this, there was a reduction in compressive strength, flexural traction, specific mass, and an increase in porosity;
- (e) For all TiO<sub>2</sub> concentrations studied in this research, in permeable concrete, there was a reduction in permeability in relation to the sample containing 0% TiO<sub>2</sub>. However, all samples were above that required by ACI 522R-10, which establishes a minimum permeability value of 1mm/s for permeable concretes;
- (f) The increase in the concentration of TiO<sub>2</sub>, changes the surface of the permeable concrete, leaving the cement paste, which involves the coarse aggregate, less porous.

The permeable concrete with the addition of TiO<sub>2</sub> presents itself as an alternative process to assist in the treatment of sanitary sewage, but it is necessary to control its addition in order not to considerably compromise the permeability and the mechanical properties of the permeable concrete.

#### 5 REFERENCES

- [1] N. Serpone, S. Horikoshi, and A. V. Emeline, "Microwaves in advanced oxidation processes for environmental applications – a brief review," *J. Photochem. Photobiol. Photochem. Rev.*, vol. 11, no. 2, pp. 114–131, 2010.
- [2] V. M. Costa, "Avaliação da genotoxicidade e mutagenicidade em amostras de esgotos tratados por lagoas de estabilização em Teresina-Piauí," *Rev. DAE*, vol. 66, pp. 59–72, 2018.
- [3] H. Ren, P. Koshy, W. F. Chen, S. Qi, and C. C. Sorrell, "Photocatalytic materials and technologies for air purification," *J. Hazard. Mater.*, vol. 325, pp. 340–366, 2017.

- [4] S. Singh, H. Mahalingam, and P. K. Singh, "Fot polymer-supported titanium dioxide photocatalysts for environmental remediation: a review," *Appl. Catal. A Gen.*, vol. 462, pp. 178–195, 2013.
- [5] V. Augugliaro, V. Loddo, M. Pagliaro, G. Palmisano, and L. Palmisano, *Clean by Light Irradiation: Practical Applications of Supported TiO<sub>2</sub>*. Cambridge: Royal Society of Chemistry, 2010.
- [6] S. Shen, M. Burton, B. Jobson, and L. Haselbach, "Pervious concrete with titanium dioxide as a photocatalyst compound for a greener urban road environment," *Constr. Build. Mater.*, vol. 35, pp. 874–883, 2012.
- [7] M. R. Hasan, M. F. M. Zain, R. Hamid, A. B. M. A. Kaish, and S. Nahar, "A comprehensive study on sustainable photocatalytic pervious concrete for storm water pollution mitigation: a review," *Mater. Today Proc.*, vol. 4, no. 9, pp. 9773–9776, 2017.
- [8] T. Noeiaghaci, A. Mukherjee, N. Dhami, and S.-R. Chae, "Biogenic deterioration of concrete and its mitigation technologies," *Constr. Build. Mater.*, vol. 149, pp. 575–586, 2017.
- [9] S. Asadi, M. M. Hassan, J. T. Kevern, and T. D. Rupnow, "Development of photocatalytic pervious concrete pavement for air and storm water improvements," *Transp. Res. Rec.*, vol. 2290, no. 1, pp. 161–167, 2012.
- [10] Associação Brasileira de Normas Técnicas, *Cimento Portland – Requisitos*, NBR 16697, 2018.
- [11] Associação Brasileira de Normas Técnicas, *Agregado Graúdo – Determinação da Massa Específica, Massa Específica Aparente e Absorção de Água*, NBR NM-53, 2009.
- [12] Associação Brasileira de Normas Técnicas, *Agregados – Determinação da Composição Granulométrica*, NBR NM-248, 2003.
- [13] J. A. Lima Jr. and A. L. P. Silva, "Diâmetro efetivo e coeficiente de uniformidade de areia utilizada em filtros empregados no sistema de irrigação," *Enciclopédia Biosfera*, vol. 6, no. 11, pp. 1–8, 2010.
- [14] C. A. Casagrande, D. Hotza, W. L. Repette and L. F. Jochem, "Utilização de dióxido de titânio (TiO<sub>2</sub>) em matriz de cimento como fotocatalisador de óxidos de nitrogênio (NO<sub>x</sub>)," in *An. 56º Cong. Bras. Cer.*, 2012.
- [15] P. Anandgaonker et al., "Synthesis of TiO<sub>2</sub> nanoparticles by electrochemical method and their antibacterial application," *Arab. J. Chem.*, vol. 12, no. 8, pp. 1815–1822, 2019.
- [16] Associação Brasileira de Normas Técnicas, *Concreto Fresco – Determinação da Massa Específica e do Teor de Ar pelo Método Gravimétrico*, NBR 9833, 2009.
- [17] A. Joshaghani, A. A. Ramezaniapour, O. Ataei, and A. Golroo, "Optimizing pervious concrete pavement mixture design by using the Taguchi method," *Constr. Build. Mater.*, vol. 101, pp. 317–325, 2015.
- [18] Instituto Americano de Concreto. Organização Internacional para Padronização. *Pervious Concrete (ACI 522-10) and Commentary*, 2010.
- [19] Associação Brasileira de Normas Técnicas, *Concreto – Procedimento para Moldagem e Cura de Corpos-de-Prova*, NBR 5738, 2015.
- [20] Associação Brasileira de Normas Técnicas, *Pavimentos Permeáveis de Concreto – Requisitos e Procedimentos*, NBR 16416, 2016.
- [21] Associação Brasileira de Normas Técnicas, *Concreto – Ensaio de Compressão de Corpos-de-Prova Cilíndricos*, NBR 5739, 2007.
- [22] Associação Brasileira de Normas Técnicas, *Concreto – Determinação da Resistência à Tração na Flexão de Corpos de Prova Prismáticos*, NBR 12142, 2010.
- [23] J. V. S. Melo, G. Trichês, P. J. P. Gleize, and J. Villena, "Development and evaluation of the efficiency of photocatalytic pavement blocks in the laboratory and after one year in the field," *Constr. Build. Mater.*, vol. 37, pp. 310–319, 2012.
- [24] A. Ibrahim, E. Mahmoud, M. Yamin, and V. C. Patibandla, "Experimental study on Portland cement pervious concrete mechanical and hydrological properties," *Constr. Build. Mater.*, vol. 50, pp. 524–529, 2014.
- [25] A. I. Neptune and B. J. Putman, "Effect of aggregate size and gradation on pervious concrete mixtures," *ACI Mater. J.*, vol. 107, no. 6, pp. 625, 2010.
- [26] A. K. Chandrappa and K. P. Biligiri, "Comprehensive investigation of permeability characteristics of pervious concrete: a hydrodynamic approach," *Constr. Build. Mater.*, vol. 123, pp. 627–637, 2016.
- [27] A. Kia, H. Wong, and C. R. Cheeseman, "Clogging in permeable concrete: a review," *J. Environ. Manage.*, vol. 193, pp. 221–233, 2017.
- [28] W. Yeih, T. C. Fu, J. J. Chang, and R. Huang, "Properties of pervious concrete made with air-cooling electric arc furnace slag as aggregates," *Constr. Build. Mater.*, vol. 93, pp. 737–745, 2015.
- [29] W. Yeih and J. J. Chang, "The influences of cement type and curing condition on properties of pervious concrete made with electric arc furnace slag as aggregates," *Constr. Build. Mater.*, vol. 197, pp. 813–820, 2019.
- [30] N. A. Brake, H. Allahdadi, and F. Adam, "Flexural strength and fracture size effects of pervious concrete," *Constr. Build. Mater.*, vol. 113, pp. 536–543, 2016.
- [31] J. Chen, S. Kou, and C. Poon, "Hydration and properties of nano-TiO<sub>2</sub> blended cement composites," *Cement Concr. Compos.*, vol. 34, no. 5, pp. 642–649, 2012.
- [32] M. Magesvari and V. L. Narasimha, "Studies on characterization of pervious concrete for pavement applications," *Procedia Soc. Behav. Sci.*, vol. 104, pp. 198–207, 2013.

- [33] J.R. Bolt, Y. Zhuge, F. Bullen, "The impact of photocatalytic on degradation of poly aromatic hydrocarbons through permeable concrete," in *Proc. 23rd Australas. Conf. Mech. Struct. Mater. (ACMSM 23)*, 2014.
- [34] C. Q. Lian, Z. G. Yan, and S. Beecham, *Evaluation of Permeability of Porous Concrete*. Trans Tech Publications, 2011.
- [35] C. Manoj Kumar, U.K. Mark Vivin Raj and D. Mahadevan, "Effect of titanium di-oxide in pervious concrete," *Int. J. Chemtech Res.*, vol. 8, no. 8, pp. 183–187, 2015.
- [36] F. V. Andrade et al., "A novel TiO<sub>2</sub>/autoclaved cellular concrete composite: from a precast building material to a new floating photocatalyst for degradation of organic water contaminants," *J. Water Process Eng.*, vol. 7, pp. 27–35, 2015.
- [37] L. Senff, D. Hotza, S. Lucas, V. M. Ferreira, and J. A. Labrincha, "Effect of nano-SiO<sub>2</sub> and nano-TiO<sub>2</sub> addition on the rheological behavior and the hardened properties of cement mortars," *Mater. Sci. Eng. A*, vol. 532, pp. 354–361, 2012.
- [38] T. Meng, Y. Yu, X. Qian, S. Zhan, and K. Qian, "Effect of nano-TiO<sub>2</sub> on the mechanical properties of cement mortar," *Constr. Build. Mater.*, vol. 29, pp. 241–245, 2012.
- [39] C. Zade et al., "Effects of use of titanium dioxide in pervious concrete," *Imp. J. Interdiscip. Res.*, vol. 2, no. 7, pp. 425–429, 2016.
- [40] C. Lian and Y. Zhuge, "Projeto ideal de mistura de concreto permeável aprimorado – uma investigação experimental," *Constr. Build. Mater.*, vol. 24, no. 12, pp. 2664–2671, 2010.
- [41] M. Jalal, M. Fathi, and M. Farzad, "Effects of fly ash and TiO<sub>2</sub> nanoparticles on rheological, mechanical, microstructural and thermal properties of high strength self compacting concrete," *Mech. Mater.*, vol. 61, pp. 11–27, 2013.

---

**Author contributions:** Flávio Pessoa Avelino: Statistical analysis; Marcelo de Souza Picanço: Conceptualization, formal analysis, data curation, writing, methodology.; Alcebíades Negrão Macêdo: Conceptualization, formal analysis, data curation, writing, methodology.

**Editors:** Bernardo Tutikian, José Luiz Antunes de Oliveira e Sousa, Guilherme Aris Parsekian.



ORIGINAL ARTICLE

# Nonlinear analysis of monolithic beam-column connections for reinforced concrete frames

*Análise não linear de ligações viga-pilar monolíticas em pórticos de concreto armado*

Gerson Alva<sup>a</sup>

Alexandre Tsutake<sup>a</sup>

<sup>a</sup>Universidade Federal de Uberlândia – UFU, Faculdade de Engenharia Civil, Uberlândia, MG, Brasil

Received 10 March 2019  
Accepted 12 February 2020

**Abstract:** This paper deals with nonlinear analysis of deformability of monolithic beam-column connections for bending moments in framed reinforced concrete structures. Due to the simplicity, the connections deformability is considered by using an analytical model of moment-rotation curve. Material nonlinearity of the structural elements is considered by using the flexural stiffness obtained in moment-curvature relationship of the sections. The formulation of the analytical model to obtain the relative rotations between beam and column and the formulation to construct moment-curvature curves is deduced and presented to allow the computational implementation in structural analysis software. The numerical simulations carried out in this study indicated that even in the case of monolithic connections, taking into account the bending moment deformability of the connections leads to significantly better results than the hypothesis of fully rigid connections.

**Keywords:** bending deformability, beam-column connections, nonlinear analysis, reinforced concrete structures, structural analysis.

**Resumo:** Este trabalho trata da análise não linear da deformabilidade de ligações monolíticas viga-pilar de concreto armado devido ao momento fletor em estruturas reticuladas de concreto armado. Em função da simplicidade, a deformabilidade das ligações é considerada por meio de modelo analítico de curva momento-rotação e a não-linearidade física dos elementos estruturais, por meio da rigidez à flexão obtida em relações momento-curvatura das seções. A formulação do modelo analítico para a obtenção das rotações relativas entre viga e pilar e a formulação relacionada com a geração das curvas momento-curvatura foram deduzidas e apresentadas, com o intuito de permitir a implementação desses modelos em rotinas computacionais. As simulações numéricas realizadas neste trabalho comprovaram que, mesmo em se tratando de ligações monolíticas, levar em conta a deformabilidade das ligações ao momento fletor conduz a resultados significativamente melhores que a hipótese de ligações perfeitamente rígidas.

**Palavras-chave:** deformabilidade ao momento fletor, ligações viga-pilar, análise não linear, estruturas de concreto armado, análise estrutural.

**How to cite:** G. Alva and A. Tsutake, "Nonlinear analysis of monolithic beam-column connections for reinforced concrete frames," *Rev. IBRACON Estrut. Mater.*, vol. 13, no. 5, e13515, 2020, <https://doi.org/10.1590/S1983-41952020000500015>

## 1 INTRODUCTION

In reinforced concrete structures, cracking of concrete, plastification of materials and bond-slip behavior between steel and concrete are responsible for the material nonlinear behavior of these structures.

For Ultimate Limit State procedures in the design of frames structures for buildings, the material nonlinearity of structural elements in global analysis can be considered simply by flexural stiffness reductions of these elements for use in linear analysis, as recommended by NBR 6118 [1] and others international codes. Alternatively, in the need for

Corresponding author: Gerson Alva. E-mail: [alva\\_gerson@yahoo.com.br](mailto:alva_gerson@yahoo.com.br)

**Financial support:** CNPq (Process: 308720/2018-0), CAPES (Process: 1769743).

**Conflict of interest:** Nothing to declare.



This is an Open Access article distributed under the terms of the Creative Commons Attribution License, which permits unrestricted use, distribution, and reproduction in any medium, provided the original work is properly cited.

checking the design based on simplified linear analysis, nonlinear analysis can be employed with the use of moment-curvature relationships of the sections. In this case, the framed structure is discretized, and the flexural stiffness of each section is calculated as a function of its moment-curvature relationship.

The nonlinear effects that occur in beam-column connections of monolithic reinforced concrete structures - such as the slippage of flexural reinforcement of the beams in the joint region and the formation of flexural cracks at the beam extremity - induce the generation of relative rotations between the beam and the column. Thus, monolithic connections, strictly speaking, are not perfectly rigid under bending moment. Evidently, there is greater concern with the bending deformability in precast concrete structures. However, the consideration of bending deformability in monolithic connections brings benefits to the structural analysis justified by the greater precision in obtaining stresses and displacements - as shown in this paper.

Due to the simplicity and the good results they can provide, analytical models are the most attractive way in design procedures to consider the effects of the slippage of the beam reinforcement inside the column and the effects induced by the flexural cracks at the beam extremity on the bending deformability. Examples of these models can be found in Paultre et al. [2], Sezen and Moehle [3], Sezen and Setzler [4], Kwak and Kim [5], Ferreira et al. [6], Alva et al. [7] and Alva and El Debs [8], the latter being emphasized in this study.

The Alva and El Debs [8] model was proposed for exterior beam-column connections. Due to the formatting of the formulation, this model can be easily implemented in software programs for nonlinear analysis of frames that use moment-curvature relationships for the consideration of the material nonlinearity of structural elements.

There are three central objectives of this paper, namely:

- Complement the investigations on the efficiency of the model proposed by Alva and El Debs [8] to consider the bending deformability caused by the slippage of flexural reinforcement of the beams in the joint region;
- Present an analytical formulation to obtain moment-curvature relationships of reinforced concrete rectangular sections, aiming to consider the material nonlinearity of beams and columns and the application of the analytical model proposed by Alva and El Debs [8] in nonlinear analysis of reinforced concrete frames;
- Show the efficiency of the constitutive models employed for considering material nonlinearity of the structural elements (by moment-curvature relationships) and bending deformability in nonlinear analysis of framed reinforced concrete structures.

## 2 PREVIOUS STUDIES

Although there are numerous researches in the literature (especially international) on the behavior of monolithic beam-column connections, few studies that focus on analytical models for considering the deformability of connections subjected to bending moment are found.

There are analytical models that exclusively consider the portion of rotation resulting from the slippage of the flexural reinforcement in the anchorage region, such as those found in Paultre et al. [2], Sezen and Moehle [3] and Sezen and Setzler [4]. Paultre et al. [2] used a tri-linear moment-rotation curve with points defined by the cracking of the concrete, yielding of the reinforcement and failure of the beam section. For the calculation of the rotations, the authors used a simplified distribution of bond stresses in the elastic and inelastic ranges (after reinforcement yielding). Sezen and Moehle [3] and Sezen and Setzler [4] proposed an analytical model applicable to the case of slippage of longitudinal tension reinforcement of columns (anchored in foundations) or beams (anchored in beam-column joints). As in Paultre et al. [2], Sezen and Moehle [3] and Sezen and Setzler [4] used a simplified distribution of bond stresses but proposed an additional simplification regarding the distribution of the axial strains of the reinforcement in the anchorage regions.

Among the analytical models that consider both portions of relative rotations - those resulting from slippage of the flexural reinforcement inside the joint and those resulting from cracking at the beam extremity - the following models can be cited: Kwak and Kim [5], Ferreira et al. [6], Alva et al. [7] and Alva and El Debs [8]. Kwak and Kim [5] proposed an analytical model which accounts for the effects of relative rotations by reducing the flexural stiffness along the equivalent plastic length of the beams (extremities). The total rotation calculated by the model is associated with the slippage of flexural reinforcement of the beam inside the column added the rotation induced by the crack at the beam-column interface. These rotations are obtained by solving the differential equations which represent the bond-slip behavior. The analytical models presented in Ferreira et al. [6], Alva et al. [7] and Alva and El Debs [8] take into account the two rotation portions, but consider that the slippage induced by flexural cracking occurs in a certain length of the beam extremity, associated with its effective depth. Ferreira, El Debs and Elliott [6] model was proposed for

connections between precast elements, being later extended to monolithic connections, as presented in Alva et al. [7]. Subsequently, Alva and El Debs [8] presented a specific analytical model for exterior beam-column monolithic connections. This model has the advantage of including in the formulation parameters not considered in Alva et al. [7], such as bond strength in the joint region and the diameter of the beam reinforcement bars, a parameter that influences the flexural crack widths in this member (beam).

### 3 MODEL PROPOSED BY ALVA AND EL DEBS [8]

Based on the conceptual model proposed by Ferreira et al. [6], Alva and El Debs [8] proposed a theoretical model which is capable of representing the bond-slip behavior of the reinforcement without the need for parameters from experimental tests. In addition, it can be easily implemented in software programs for structural analysis. In this model, it is assumed that the bending deformability is the result of two mechanisms, which produce relative rotations between the beam and the column (Figure 1):

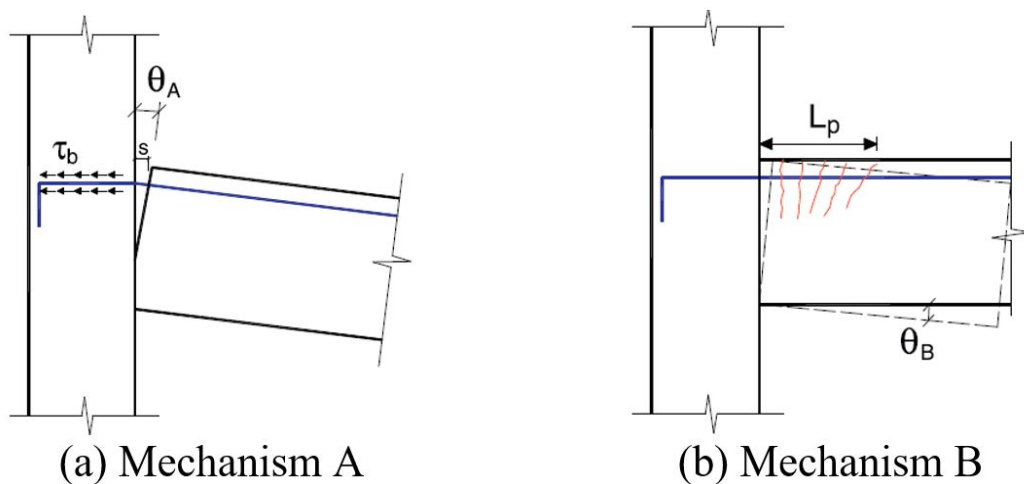


Figure 1. Deformation mechanisms: Alva and El Debs model [8]

- Mechanism A: Relative rotations produced by the slippage of tensile reinforcement of the beam inside the column (joint region);
- Mechanism B: Relative rotations produced by the cumulative effect of the slippage caused by flexural cracks formed along the plastic hinge length  $L_p$  (region where there is a greater concentration of cracks)

The total beam-column rotation related to the bending deformability consists of the sum of the rotations caused by the two mechanisms (Equation 1):

$$\theta = \theta_A + \theta_B \tag{1}$$

where  $\theta_A$  is the rotation due to Mechanism A and  $\theta_B$  is the rotation due to Mechanism B.

#### 3.1 Mechanism A

The contribution of Mechanism A is calculated through the model proposed by Sezen and Moehle [3], which assumes the distribution of bond and axial stresses of the steel bar as shown in Figure 2. Bond stresses are divided into two uniformly distributed portions:  $\tau_{by}$  for the elastic range ( $\epsilon_s \leq \epsilon_y$ ) and  $\tau_{bu}$  for the inelastic range ( $\epsilon_s > \epsilon_y$ ).

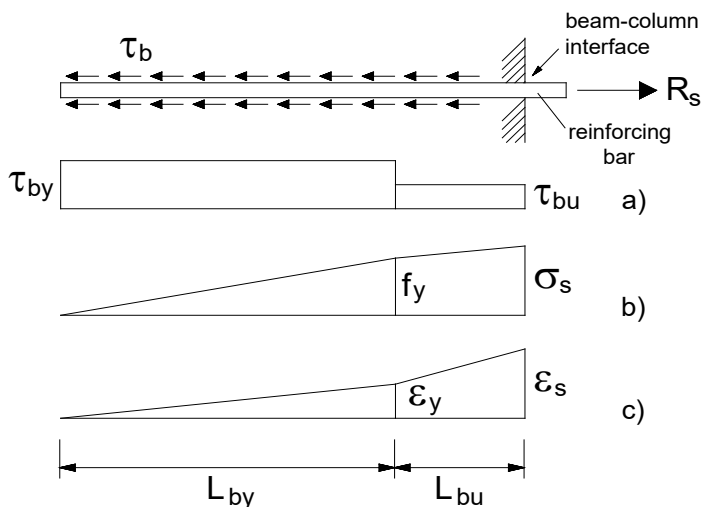


**Figure 2.** Bond-slip model proposed by Sezen and Moehle [3]: (a) bond stress distribution; (b) axial stress distribution; (c) axial strain distribution.

The values proposed by the authors are  $\tau_{by} = 1,0\sqrt{f_c}$  and  $\tau_{bu} = 0,5\sqrt{f_c}$ , where  $f_c$  is the concrete compressive strength in MPa. Thus, the slip ( $s$ ) of the steel bar is obtained from the difference between the steel bar strain ( $\varepsilon_s$ ) and the concrete strain ( $\varepsilon_c$ ):

$$s = \int_0^x (\varepsilon_s - \varepsilon_c) dx \tag{2}$$

Disregarding the concrete strain (very small when compared with steel bar), solving the Equation 2 and applying the equilibrium equations, Sezen and Moehle [3] deduced Equations 3 and 4 for calculating the slip.

Elastic range ( $\varepsilon_s \leq \varepsilon_y$ ):

$$s = \frac{\varepsilon_s \cdot \sigma_s \cdot \varnothing}{8 \cdot \tau_{by}} \tag{3}$$

Inelastic range ( $\varepsilon_s > \varepsilon_y$ ):

$$s = \frac{\varepsilon_y \cdot f_y \cdot \varnothing}{8 \cdot \tau_{by}} + \frac{(\varepsilon_s - \varepsilon_y) \cdot \varnothing \cdot (\sigma_s - f_y)}{8 \cdot \tau_{bu}} \tag{4}$$

where

- $\varepsilon_s$  is the steel bar axial strain;
- $\sigma_s$  is the steel bar axial stress;
- $\varnothing$  is the steel bar diameter;
- $\varepsilon_y$  is the steel strain at yield strength;
- $f_y$  is the steel yield strength of steel.

Knowing the slip resulting from Mechanism A, it is possible to calculate the respective relative rotation between the beam and column elements:

$$\theta_A = \frac{s}{d-x} \tag{5}$$

where  $d$  is the effective depth of the beam and  $x$  is the neutral axis depth of the beam.

As a simplification, Alva and El Debs [8] suggest that constant values of neutral axis depth  $x$  be used in each range. In the elastic range, the authors suggest the value  $x = x_{II}$  corresponding to Stage II (cracked section), since this value becomes practically constant after crack stabilization. In the inelastic range, the authors suggest the value  $x = x_u$  corresponding to the ultimate moment, since in Stage III there is a rapid stabilization of the  $x$  values between the yielding moment and the ultimate moment.

### 3.2 Mechanism B

The relative rotation related to Mechanism B is caused by the sum of the slips induced by the flexural cracks at the extremity of the beam next to the column along the length  $L_p$ . As shown in Figure 3, cracks are supposed equally spaced ( $s_R$ ) in Alva and El Debs [8] model. The corresponding slips  $s_i$  are assumed equal to half the value of the crack width  $w_i$ .

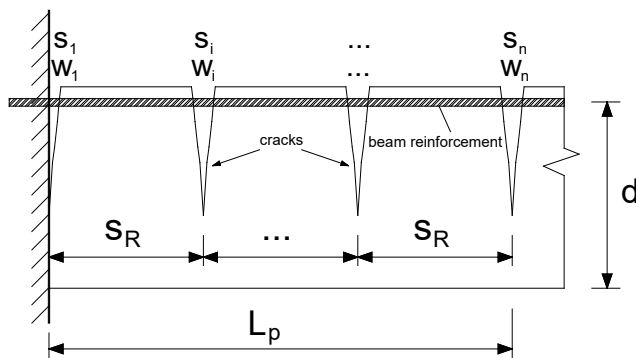


Figure 3. Mechanism B: slips caused by flexural cracks - Alva and El Debs model [8]

Therefore, the total rotation along the length  $L_p$  induced by a number of cracks  $n$  is given by Equation 6.

$$\theta_B = \sum_{i=1}^n \frac{s_i}{d-x_i} = \sum_{i=1}^n \frac{0,5 \cdot w_i}{d-x_i} \tag{6}$$

where

$x_i$  is the neutral axis depth at the section where the crack occurs (crack width:  $w_i$ ). In this case, the simplification suggested by the authors can be used ( $x_i = x_{II}$  or  $x_i = x_u$ ).

Assuming small differences between the values of  $w_i$  along the length  $L_p$ , it is possible to obtain a single crack opening value in that length by the Equation 7:

$$w = s_R \cdot (\varepsilon_{sm} - \varepsilon_{cm}) \tag{7}$$

where

$s_r$  is the crack spacing;

$\varepsilon_{sm} - \varepsilon_{cm}$  is the difference between the average reinforcement strain and the average concrete strain.

Again ignoring the strain of the concrete in tension and knowing that the spacing between cracks  $s_r$  allows the evaluation of the probable number of cracks along the length  $L_p$ , Alva and El Debs [8] deduced the following expression for relative rotation resulting from Mechanism B:

$$\theta_B = 0,5 \cdot (L_p + s_R) \cdot \left( \frac{\varepsilon_{sm}}{d-x} \right) = 0,5 \cdot (L_p + s_R) \cdot \frac{1}{r} \tag{8}$$

where

$x$  is the neutral axis depth, which can be simplified as suggestion of the authors ( $x = x_{II}$  or  $x = x_u$ );

$\varepsilon_{sm}$  is the average deformation in the reinforcement, considering the contribution of tensioned concrete (tension stiffening);

$1/r$  is the curvature of the beam section, considering the contribution of tensioned concrete (tension stiffening).

Knowing the bending moment  $M$  at the end of the beam, it is possible to find the axial stresses and strains in the reinforcement (Equations 3 and 4) and also the curvature  $1/r$  of Equation 8. Hence, the model proposed by Alva and El Debs [8] can be deduced, according to Equations 9 and 10.

In the elastic range:  $M \leq M_y$

$$\theta = C_1 \cdot M^2 + C_2 \cdot \left( \frac{1}{r} \right) \tag{9}$$

In the inelastic range:  $M_y < M \leq M_u$

$$\theta = C_1 \cdot M_y^2 + C_2 \cdot \left( \frac{1}{r} \right) \tag{10}$$

where

$M_y$  is the beam yielding moment;

$M_u$  is the beam ultimate moment;

$C_1$  is the constant related to Mechanism A, given by Equation 11.

$$C_1 = \frac{\theta}{\delta \cdot E_s \cdot \tau_{by} \cdot (d-x) \cdot A_s^2 z^2} \tag{11}$$

$E_s$  is the steel modulus of elasticity;

$A_s$  is the beam area of flexural reinforcement;

$z$  is the lever arm between the tensile and compressive forces in the beam section;

$C_2$  is the constant related to Mechanism B, given by Equation 12.

$$C_2 = 0,5 \cdot (L_p + s_R) \tag{12}$$

The spacing between cracks  $s_R$  can be evaluated from codes expressions or from formulations found in literature. In this paper, the expression presented in Eurocode 2 [9] was used:

$$s_R = k_3 \cdot c + \frac{k_1 \cdot k_2 \cdot k_4 \cdot \varnothing}{\rho_{eff}} \tag{13}$$

where

$\varnothing$  is the diameter of the beam steel reinforcement bars;

$k_1$  is a coefficient which considers for the bond properties of the reinforcement steel bars (equal to 0.8 for high-bond bars and equal to 1.6 for plain surface bars);

$k_2 = 0,5$ ;  $k_3 = 3,4$ ;  $k_4 = 0,425$ ;

$c$  is the concrete cover;

$$\rho_{eff} = \frac{A_s}{A_{c,eff}}$$

$A_{c,eff}$  is the effective tension area of concrete protected by the steel reinforcement bars along the height  $h_{c,eff}$ , which assumes the lowest value between  $2,5(h-d)$ ,  $(h-x)/3$  or  $h/2$  (see Figure 4).

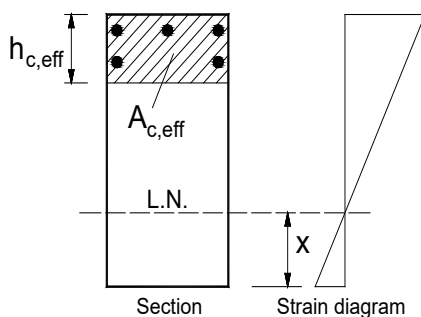


Figure 4. Definition of effective area  $A_{c,eff}$  - Eurocode 2 [9]

#### 4 MOMENT-CURVATURE RELATIONS

This item presents the analytical formulation for obtaining the moment-curvature relationships necessary to consider the material nonlinearity of the structural members (beam and column). It should be noted that the model proposed by Alva and El Debs [8] uses the curvature value at the beam end (next to the joint region) to calculate the relative rotation component resulting from flexural cracks (Mechanism B). Item 4.1 presents the analytical formulation for the construction of moment-curvature curves of rectangular sections from the integration of the material stresses and the equilibrium and strain compatibility equations, applicable for concrete up to C50. For concretes between C55 and C90, the analytical formulation can be found in Alva [10]. The analytical formulation of item 4.1 was implemented in a computational procedure in FORTRAN language and the results were validated by free and commercial software for structural analysis found in Brazil, as presented in Alva [10]. The computational procedure was used in the examples presented in item 5.

##### 4.1 Integration of stresses and equilibrium equations in reinforced concrete section (columns and beams)

To understand the problem of rectangular sections subjected to axial load and bending moment, as well the analytical formulation, it is shown in Figure 5 a generic rectangular section with known (or pre-defined) longitudinal reinforcement. Figure 5 also contains diagrams representing the section strains, the internal resultant forces, the stresses in the concrete and the internal resultant forces in the longitudinal reinforcement.

For the equilibrium of the horizontal forces, the applied axial force  $N_{Sd}$  must be equal to the sum of the resultant internal forces of concrete and reinforcement:

$$N_{Sd} = R_{cc} + \sum A_{si} \cdot \sigma_{si} - R_{ct} \tag{14}$$

where

$R_{cc}$  is the resultant of the concrete compressive stresses;

$R_{ct}$  is the resultant of concrete tensile stresses;

$A_{si}$  is the area of the longitudinal reinforcement steel bar  $i$  (or layer  $i$ );

$\sigma_{si}$  is the stress in the longitudinal reinforcement steel bar  $i$  (or layer  $i$ ) (positive sign for compression).

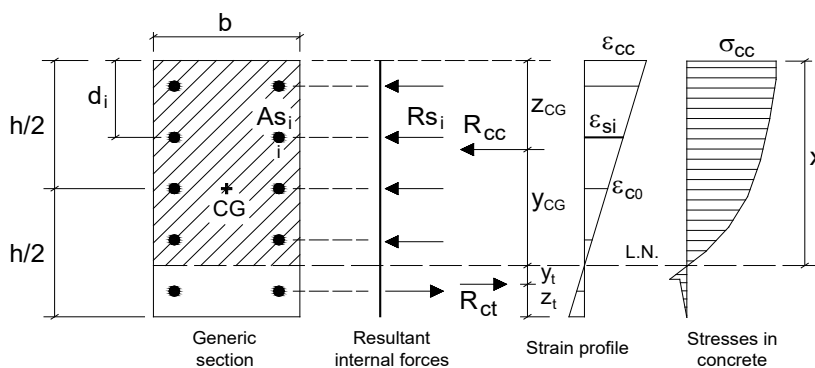


**Figure 5.** Generic rectangular section - strains, stresses in concrete and internal resultant forces

The moment resulting by the internal forces of the section in relation to the center of gravity of the concrete gross section can be calculated by Equation 15:

$$M = R_{cc} \cdot \left(\frac{h}{2} - z_{CG}\right) + \sum A_{s_i} \cdot \sigma_{s_i} \cdot \left(\frac{h}{2} - d_i\right) + R_{ct} \cdot \left(\frac{h}{2} - z_t\right) \tag{15}$$

where

$h$  is the section height;

$d_i$  is the distance between extreme compression fiber of the section and the steel bar  $i$  (or layer  $i$ ) of the longitudinal reinforcement;

$z_{CG}$  is the distance between extreme compression fiber of the section and resultant of the compressive stresses in the concrete  $R_{cc}$ . According to Figure 5, this distance is obtained by:

$$z_{CG} = x - y_{CG} \tag{16}$$

where:

$x$  is the neutral axis depth;

$y_{CG}$  is the distance from the neutral axis to the centroid of the compressive stress in concrete along the section height.

This distance defines the point of application of the resultant  $R_{cc}$ . Likewise, the distances  $y_t$  and  $z_t$  define the position of the tensile resultant  $R_{ct}$ .

The formulation for sections subjected to axial load and bending moment follows the cases of strains presented in items 4.1.1 to 4.1.4. To verify the case in which the section is found, obtain the stresses in the longitudinal reinforcements, and generate the points of the moment-curvature curve, strain compatibility equations are used, according to Equation 17.

$$\frac{1}{r} = \frac{\epsilon_{cc}}{x} = \frac{\epsilon_{c0}}{x - h/2} = \frac{\epsilon_{s_i}}{x - d_i} \text{ (positive sign for compression)} \tag{17}$$

where

$1/r$  is the section curvature;

$\epsilon_{cc}$  is the strain of the concrete extreme compression fiber;

$\epsilon_{c0}$  is the strain at the gross section centroid;

$\epsilon_{s_i}$  is the strain of the longitudinal reinforcement steel bar  $i$  (or layer  $i$ ).

The constitutive models for concrete in compression and non-prestressed steel reinforcement according to NBR 6118 [1] are illustrated in Figure 6.

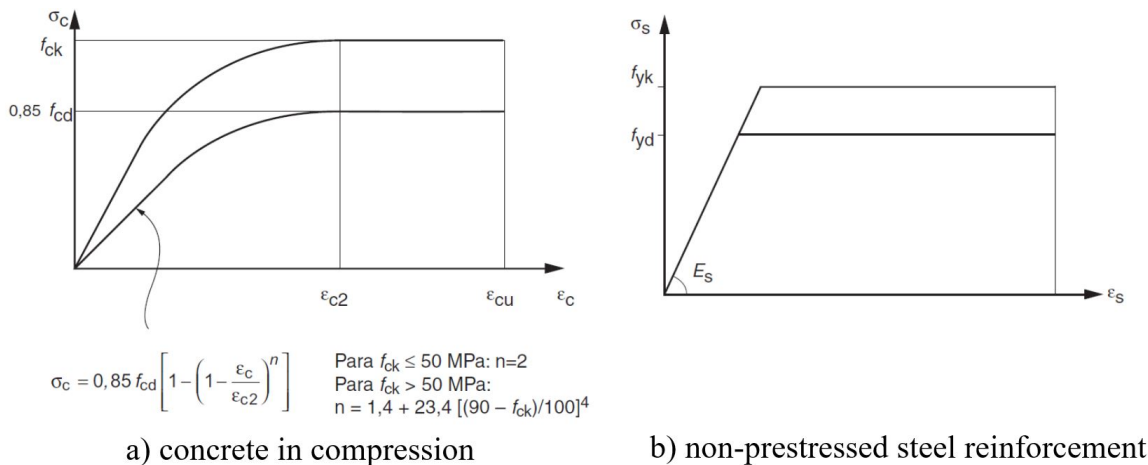


Figure 6. Idealized stress-strain curves for materials – NBR 6118 [1]

In Figure 6:

- $f_{ck}$  and  $f_{cd}$  are the concrete compressive strength (the characteristic and the design values, respectively);
- $\epsilon_{c2}$  is the strain of beginning of plastification of the concrete (equal to 2 ‰ for concrete up to C50);
- $\epsilon_{cu}$  is the ultimate strain of the concrete (assumed equal to 3,5 ‰ for concrete up to C50).

The curvature value is chosen and a value  $\epsilon_{c0}$  is estimated (which can be done from the applied axial force at the first point of the curve) for the generation of a point of the moment-curvature diagram. An iterative process begins until the equilibrium of forces occurs in the section. The detailed solution algorithm is presented in item 4.1.6.

To deduce the analytical expressions for the compressive resultant in the concrete  $R_{cc}$  and its position in relation to the neutral axis  $y_{CG}$ , Equation 18 is used, which expresses the proportionality between the strain and the ordinate  $y$ , (Figure 7) - consequence of the assumption that plane sections remain plane.

$$\epsilon_c = k \cdot y \tag{18}$$

where  $k$  is the constant that relates the concrete strain and the ordinate  $y$ . This constant represents the curvature of the section.

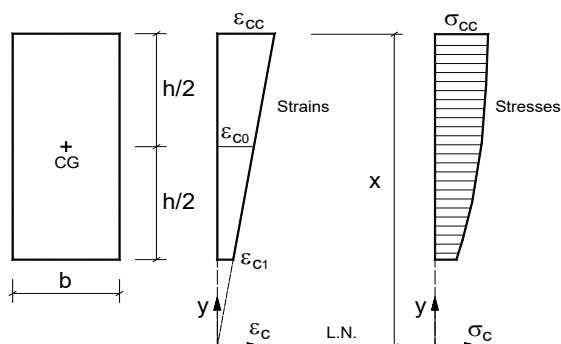


Figure 7: General scheme of strains and stresses in concrete along the section height

The analytical expressions for the compressive resultant in the concrete  $R_{cc}$  and its position in relation to the neutral axis  $y_{CG}$  for concretes C20 to C50 are presented in items 4.1.1 to 4.1.4. Depending on the strain of the extreme compression fiber of concrete  $\epsilon_{cc}$  and the value of the neutral axis depth  $x$ , 4 possible cases are defined for sections subjected to axial load and bending moment, as shown in Figure 8.

In this paper, the values of strains in the concrete are expressed in units per thousand, due to the values assumed by  $\epsilon_{c2}$  and by the exponent  $n$  of the parabolic function of the stress-strain curve for concretes up to C50. Thus, the values of  $y_{c2}$  (ordinate corresponding to the strain  $\epsilon_{c2}$  according to Figure 8) are calculated by:

$$y_{c2} = \frac{\epsilon_{c2}}{k} = \frac{2}{k} (\epsilon_{c2} \text{ in units per thousand}) \tag{19}$$

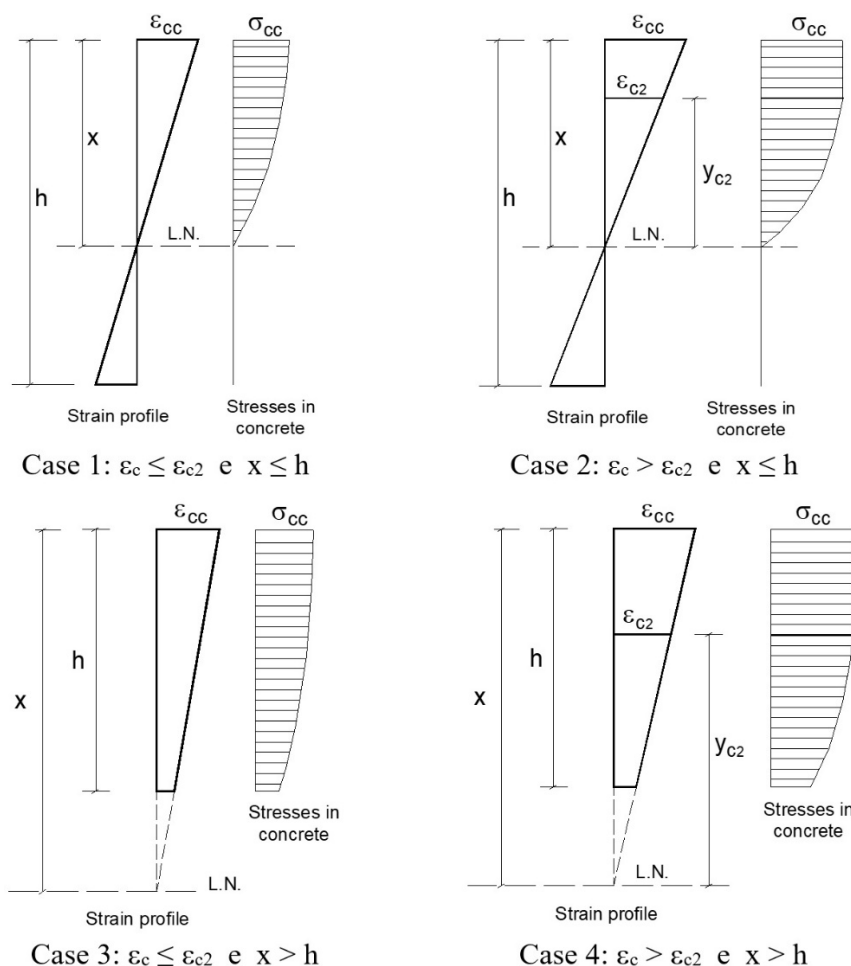


Figure 8. Possible cases - RC sections subjected to axial compressive load and bending moment

#### 4.1.1 Case 1: $\epsilon_{cc} \leq \epsilon_{c2}$ e $x \leq h$

In this case, the neutral axis passes through the section and the concrete has not yet reached its maximum stress (strength). The resultant  $R_{cc}$  is calculated from the integration of the stresses over the compressed area of concrete:

$$R_{cc} = \int_0^x \sigma_c \cdot b \cdot dy = b \cdot \int_0^x \sigma_c \cdot dy \tag{20}$$

where

$b$  is the section width (constant for rectangular section);

$\sigma_c$  is the compressive stress of concrete as a function of the neutral axis depth  $x$ . In this case, the stress diagram takes on a parabolic format as shown in Figure 6.

The position of the resultant  $R_{cc}$  in the section is defined with the calculation of  $y_{CG}$ , expressed by:

$$y_{CG} = \frac{\int_0^x \sigma_c \cdot b \cdot y \cdot dy}{\int_0^x \sigma_c \cdot b \cdot dy} = \frac{b \cdot \int_0^x \sigma_c \cdot y \cdot dy}{R_{cc}} \tag{21}$$

Equation 22 can be deduced from substituting the analytical expression of the parabola that describes the compressive stress of the concrete in the integral of Equation 20:

$$R_{cc} = b \cdot \int_0^x 0,85 \cdot f_{cd} \cdot \left[ 1 - \left( 1 - \frac{\varepsilon_c}{2} \right)^2 \right] \cdot dy \tag{22}$$

From Equation 18, it is possible to rewrite  $R_{cc}$  according to the ordinate  $y$  :

$$R_{cc} = 0,85 \cdot f_{cd} \cdot b \cdot \int_0^x \left[ 1 - \left( 1 - \frac{k \cdot y}{2} \right)^2 \right] \cdot dy \tag{23}$$

Solving the integral expressed in Equation 23, results in:

$$R_{cc} = 0,85 \cdot f_{cd} \cdot b \cdot k \cdot \left( \frac{x^2}{2} + \frac{k \cdot x^3}{12} \right) \tag{24}$$

In the numerator of Equation 21, the analytical expression of the parabolic curve of the concrete compressive stress is used to calculate the integral:

$$y_{CG} = \frac{b \cdot \int_0^x 0,85 \cdot f_{cd} \cdot \left[ 1 - \left( 1 - \frac{\varepsilon_c}{2} \right)^2 \right] \cdot y \cdot dy}{R_{cc}} \tag{25}$$

From Equation 18, it is possible to rewrite  $y_{CG}$  as a function of the ordinate  $y$  :

$$y_{CG} = \frac{0,85 \cdot f_{cd} \cdot b \cdot \int_0^x \left[ 1 - \left( 1 - \frac{k \cdot y}{2} \right)^2 \right] \cdot y \cdot dy}{R_{cc}} \tag{26}$$

Solving the integral of the numerator of Equation 26 results in:

$$y_{CG} = \frac{16 \cdot x^3 - 3 \cdot k \cdot x^4}{24 \cdot x^2 - 4 \cdot k \cdot x^3} \tag{27}$$

**4.1.2 Case 2:**  $\varepsilon_{cc} > \varepsilon_{c2}$  e  $x \leq h$

The resultant  $R_{cc}$  and its position in the section represented by  $y_{CG}$  are calculated from the integration of the concrete compressive stresses over two regions: where the stresses assume parabolic distribution and in where the stresses assume a constant value equal to  $0,85 \cdot f_{cd}$  (Figure 8).

$$R_{cc} = \int_0^{y_{c2}} \sigma_c \cdot b \cdot dy + \int_{y_{c2}}^x 0,85 \cdot f_{cd} \cdot b \cdot dy \tag{28}$$

$$y_{CG} = \frac{\int_0^{y_{c2}} \sigma_c \cdot b \cdot y \cdot dy + \int_{y_{c2}}^x 0,85 \cdot f_{cd} \cdot b \cdot y \cdot dy}{\int_0^{y_{c2}} \sigma_c \cdot b \cdot dy + \int_{y_{c2}}^x \sigma_c \cdot b \cdot dy} = \frac{b \cdot \int_0^{y_{c2}} \sigma_c \cdot y \cdot dy + 0,85 \cdot f_{cd} \cdot b \cdot \int_{y_{c2}}^x y \cdot dy}{R_{cc}} \tag{29}$$

Solving the integrals of Equations 28 and 29 provides the expressions for  $R_{cc}$  and  $y_{CG}$ :

$$R_{cc} = 0,85 \cdot f_{cd} \cdot b \cdot \left( k \cdot \frac{y_{c2}^2}{2} - k^2 \cdot \frac{y_{c2}^3}{12} + x \cdot y_{c2} \right) \tag{30}$$

In Equation 29, substituting the parabolic function that describes the compressive stress in concrete  $\sigma_c$  and using Equation 18 that relates  $\varepsilon_c$  and  $y$  result in:

$$y_{CG} = \frac{0,85 \cdot f_{cd} \cdot b}{R_{cc}} \left( \frac{k \cdot y_{c2}^3}{3} - \frac{k^2 \cdot y_{c2}^4}{16} + \frac{k \cdot x^2}{2} - \frac{k \cdot y_{c2}^2}{2} \right) \tag{31}$$

**4.1.3 Case 3:**  $\varepsilon_{cc} \leq \varepsilon_{c2}$  e  $x > h$

In this case, the section is completely compressed, and the concrete has not yet reached its maximum stress (strength). The integrals used for the calculation of  $R_{cc}$  and  $y_{CG}$  must be calculated within the range of ordinates  $y$  that cover the section, according to Equations 32 and 33.

$$R_{cc} = \int_{x-h}^x \sigma_c \cdot b \cdot dy = b \cdot \int_{x-h}^x \sigma_c \cdot dy \tag{32}$$

$$y_{CG} = \frac{\int_{x-h}^x \sigma_c \cdot b \cdot y \cdot dy}{\int_{x-h}^x \sigma_c \cdot b \cdot dy} = \frac{b \cdot \int_{x-h}^x \sigma_c \cdot y \cdot dy}{R_{cc}} \tag{33}$$

Solving the integrals of Equations 32 and 33 provides the expressions for  $R_{cc}$  and  $y_{CG}$ :

$$R_{cc} = 0,85 \cdot f_{cd} \cdot b \cdot k \cdot \left[ \frac{x^2}{2} - \frac{(x-h)^2}{2} - \frac{k \cdot x^3}{12} + \frac{k \cdot (x-h)^3}{12} \right] \tag{34}$$

$$y_{CG} = \frac{0,85 \cdot f_{cd} \cdot b \cdot k \cdot \left[ \frac{x^3}{3} - \frac{(x-h)^3}{3} - \frac{k \cdot x^4}{16} + \frac{k \cdot (x-h)^4}{16} \right]}{R_{cc}} \tag{35}$$

**4.1.4 Case 4:**  $\varepsilon_{cc} > \varepsilon_{c2}$  e  $x > h$

In the same way as case 2,  $R_{cc}$  and  $y_{CG}$  are calculated from the integration of the concrete compressive stresses over two regions: for the parabolic segment and for the constant stress segment. The complete integration interval comprises the entire height of the section.

$$R_{cc} = \int_{x-h}^{y_{c2}} \sigma_c \cdot b \cdot dy + \int_{y_{c2}}^x b \cdot \sigma_c \cdot dy = b \cdot \left( \int_{x-h}^{y_{c2}} \sigma_c \cdot dy + 0,85 \cdot f_{cd} \cdot \int_{y_{c2}}^x \sigma_c \cdot dy \right) \tag{36}$$

$$y_{CG} = \frac{\int_{x-h}^{y_{c2}} \sigma_c \cdot b \cdot y \cdot dy + \int_{y_{c2}}^x b \cdot \sigma_c \cdot y \cdot dy}{\int_{x-h}^{y_{c2}} \sigma_c \cdot b \cdot dy + \int_{y_{c2}}^x b \cdot \sigma_c \cdot dy} = \frac{b \cdot \left( \int_{x-h}^{y_{c2}} \sigma_c \cdot y \cdot dy + \int_{y_{c2}}^x \sigma_c \cdot y \cdot dy \right)}{R_{cc}} \tag{37}$$

Solving the integrals of Equations 36 and 37 provides the expressions for  $R_{cc}$  and  $y_{CG}$ :

$$R_{cc} = 0,85 \cdot f_{cd} \cdot b \cdot \left[ \frac{k \cdot y_{c2}^2}{2} - \frac{k \cdot (x-h)^2}{2} - \frac{k^2 \cdot y_{c2}^3}{12} + \frac{k^2 \cdot (x-h)^3}{12} + x - y_{c2} \right] \tag{38}$$

$$y_{CG} = \frac{0,85 \cdot f_{cd} \cdot b}{R_{cc}} \left[ \frac{k \cdot y_{c2}^3}{3} - \frac{k \cdot (x-h)^3}{3} - \frac{k^2 \cdot y_{c2}^4}{16} + \frac{k^2 \cdot (x-h)^4}{16} + \frac{x^2}{2} - \frac{y_{c2}^2}{2} \right] \tag{39}$$

**4.1.5 Tension Stiffening**

For considering the contribution of tensioned concrete between cracks (tension stiffening), Torres et al. [11] model was used, which assumes a stress-strain curve for concrete in tension as shown in Figure 9.

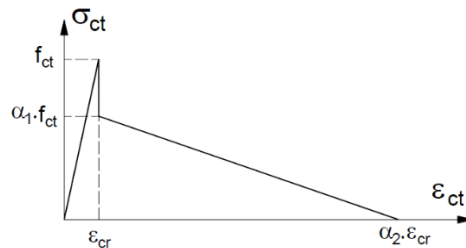


**Figure 9.** Equivalent stress-strain curve for concrete in tension (tension stiffening) – Torres et al. [11]

In Figure 9:

$f_{ct}$  is the tensile concrete strength (peak value);

$\varepsilon_{cr}$  is the strain corresponding to the maximum tensile stress (peak value);

$\alpha_1$  and  $\alpha_2$  are the coefficients which define the tension stiffening model and are obtained with Equations 40 and 41:

$$\alpha_1 = 0,4 \cdot \left( 1 - \frac{N}{A \cdot f_{ct}} \right) \geq 0 \tag{40}$$

$$\alpha_2 = 20,3 - 15,1 \cdot \frac{d}{h} + \frac{1,31}{\alpha_e \cdot \rho} - \frac{1,06}{\alpha_e \cdot \rho} \cdot \frac{d}{h} \tag{41}$$

where

$N$  is the axial compressive force (positive sign for compression);

$A$  is the cross-section area;

$d$  is the cross-section effective depth;

$h$  is the cross section total height;

$\alpha_e$  is the ratio between the modulus of elasticity of steel to the concrete modulus of elasticity;

$\rho$  is the tensile reinforcement ratio (related to the section effective depth).

The values  $\alpha_1$  and  $\alpha_2$  are calculated in case of tensile stresses in the section. The value of the tensile resultant in concrete  $R_{ct}$  and its position (with the distances  $y_t$  and  $z_t$ , as shown in Figure 5) are calculated using the equations of equilibrium and compatibility of the section.

#### 4.1.6 Algorithm for generating the points of the moment-curvature diagrams

In a simplified way, the solution algorithm used in this paper for the generation of each point of the moment-curvature diagram is presented:

(1) Set the curvature value  $1/r$

(2) Estimate the initial value  $\varepsilon_{c0} = \frac{N_{Sd}}{E_{ci} \cdot (bh)}$

(3) Iterative Process: While ErrorN > Tolerance

$$\varepsilon_{cc} = \varepsilon_{c0} + 1/r \cdot \left(\frac{h}{2}\right)$$

$$x = \frac{\varepsilon_{cc}}{1/r}$$

$$k = \frac{\varepsilon_{cc}}{x}$$

(4) Identify the case applicable to members under bending and axial loads from  $\varepsilon_{cc}$  and  $x$

(5) Calculate  $R_{cc}$ ,  $y_{CG}$ ,  $z_{CG}$

(6) Calculate  $R_{ct}$ ,  $y_t$ ,  $z_t$

(7) Calculate the strains (Equation 17) and the stresses in the reinforcements

(8) Calculate  $M = R_{cc} \cdot \left(\frac{h}{2} - Z_{CG}\right) + \sum A_{si} \cdot \sigma_{si} \cdot \left(\frac{h}{2} - d_i\right) + R_{ct} \cdot \left(\frac{h}{2} - Z_t\right)$

(9) Calculate  $N = R_{cc} + \sum A_{si} \cdot \sigma_{si} - R_{ct}$

(10) Calculate  $\Delta\varepsilon_{c0} = \frac{N_{Sd} - N}{E_{ci} \cdot (bh)}$

(11) Recalculate  $\varepsilon_{c0} = \varepsilon_{c0} + \Delta\varepsilon_{c0}$

(12) Calculate  $ErrorN = \frac{|N_{Sd} - N|}{b \cdot h \cdot f_{cd}}$

(13) Return to step (3) and check the end of the iterative process

In the presented algorithm, ErrorN is associated with the relative error in terms of axial force. Tolerance must be defined: values around 0.001 (0.1%) are sufficient to achieve good accuracy.

#### 4.2 Equivalent Branson stiffness (beams only)

A simpler alternative than that presented in item 4.1 in beams is the use of the expression suggested by Branson [12] to calculate the equivalent flexural stiffness in Stage II (cracked). Thus, the moment-curvature curve is defined by the

cracking moment, by the ultimate moment (strength) - both calculated by usual design of reinforced concrete sections - and by the segment obtained by relations indicated in Equations 42 and 43 corresponding to Stage II:

$$\frac{I}{r} = \frac{M}{(EI)_{eq}} \tag{42}$$

$$(EI)_{eq} = E_c \cdot \left\{ \left( \frac{M_r}{M} \right)^3 \cdot I_I + \left[ I - \left( \frac{M_r}{M} \right)^3 \right] \cdot I_{II} \right\} \tag{43}$$

where

$E_c$  is the concrete modulus of elasticity;

$M_r$  it is the cracking moment;

$M$  it is the section applied moment;

$I_I$  is the uncracked section second moment of area (inertia, Stage I);

$I_{II}$  it is the cracked section second moment of area (inertia, Stage II).

The moment-curvature diagrams of the reinforced concrete beam for one of the connections analyzed by numerical simulations of item 5 (LVP1) is shown in Figure 10 for the purpose of comparison between the differences found when using the equilibrium equations of the section (item 4.1) and when using Branson expression in the Stage II.

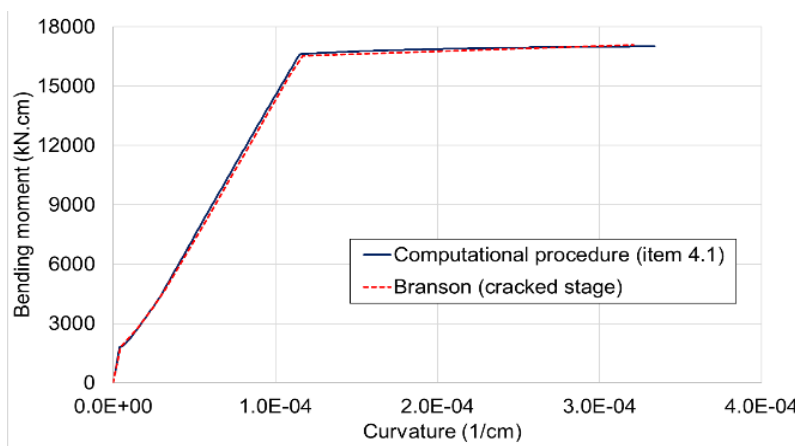


**Figure 10.** Moment-curvature curves generated using computational procedure (item 4.1) and using Branson’s expression (cracked stage) for LVP1: Alva [13]

## 5 NUMERICAL SIMULATIONS

In this item, numerical simulations of beam-column connections of reinforced concrete frames are presented for the comparison between theoretical and experimental results. To obtain the theoretical results, the analytical model proposed by Alva and El Debs [8] was applied to account for the deformability under bending moment (item 3). Moment-curvature relationships (as per item 4) were used in the consideration of the material nonlinearity.

Figure 11 illustrates the geometry of the beam-column connections analyzed by the numerical simulations, as well as the loading scheme applied and the longitudinal reinforcement of beams and columns of these connections.

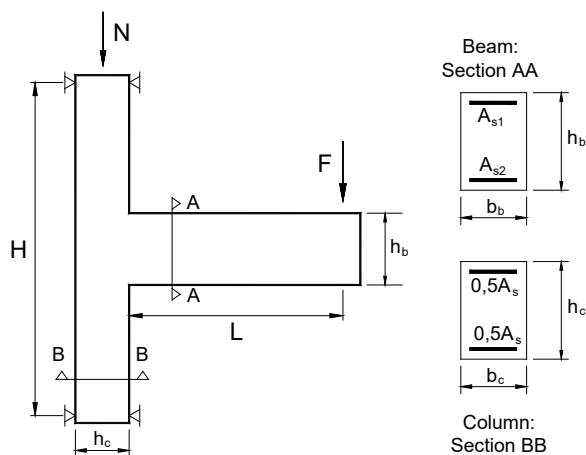


**Figure 11.** Detail of the beam-column connections of the numerical simulations

The mechanical characteristics are summarized in Table 1 (concrete and longitudinal reinforcements). The dimensions of the connections and the area of longitudinal reinforcements of beams and columns are shown in Table 2. Table 3 contains the constants values of the model presented in Alva and El Debs [8] for the connections analyzed by the numerical simulations. It should be noted that all parameters of the analytical model were calculated based on the mechanical properties of the materials (characterization tests).

**Table 1.** Mechanical properties of concrete and longitudinal steel reinforcement of the beam-column connections

Connection	$f_c$ (MPa)	$f_{ct}$ (MPa)	$E_c$ (GPa)	$f_y$ (MPa)	$E_s$ (GPa)
Alva [13]	LVP1	44,18	3,30	33,60	630
	LVP2	23,89	1,95	28,32	594
	LVP3	24,62	2,08	28,47	594
	LVP4	25,91	2,20	28,74	594
Lee et al. [14]	Specimen 2	28,94	2,89	25,91	335
	Specimen 5	24,80	2,48	23,70	351

$f_c$  – concrete compressive strength  $f_{ct}$  – concrete tensile strength.  $E_c$  – modulus of elasticity of concrete.  $f_y$  – yield stress of steel reinforcement.  $E_s$  – modulus of elasticity of steel reinforcement

**Table 2.** Dimensions and area of the longitudinal reinforcement of the beam-column connections

Connections	L (cm)	H (cm)	$h_b$ (cm)	$b_b$ (cm)	$h_c$ (cm)	$b_c$ (cm)	$A_{s1}$ (cm <sup>2</sup> )	$A_{s2}$ (cm <sup>2</sup> )	$A_s$ (cm <sup>2</sup> )
Alva [13] LVP1-LVP4	155,0	250,0	40,0	20,0	30,0	20,0	8,04	8,04	20,10
Lee et al. [14] Specimen 2	118,1	152,4	25,4	20,3	27,9	20,3	5,70	4,00	11,35
Lee et al. [14] Specimen 5	104,8	152,4	25,4	20,3	27,9	20,3	5,70	4,00	11,35

**Table 3.** Constants of Alva and El Debs [8] analytical model

Connections	$M_y$ (kN.cm)	$\phi$ (mm)	$L_p$ (cm)	$s_R$ (cm)	$C_1$ (kN.cm) <sup>-2</sup>	$C_2$ (cm)
Alva [13]	LVP1	16577	16	30	12,9	9,526E-12
	LVP2	15645	16	30	12,9	7,861E-12
	LVP3	15369	16	30	12,9	1,132E-11
	LVP4	15380	16	30	12,9	1,114E-11
Lee et al. [14]	Specimen 2	3298	19	20,3	17,2	1,609E-10
	Specimen 5	3458	19	20,3	17,2	1,774E-10

### 5.1 Beam-column connections: Alva [13]

Alva [13] performed tests on exterior beam-column connections subjected to alternating cyclic loads. The first stage of loading was the same to all connections: application of cyclic loads with amplitude increments of 10 kN up to the value of 60 kN. This loading in the first cycle generated a maximum bending moment corresponding to 60% of the yielding moment. Higher loads were applied at the end of the beam in the second stage of loading until the failure of the connection, as shown in Figure 12.

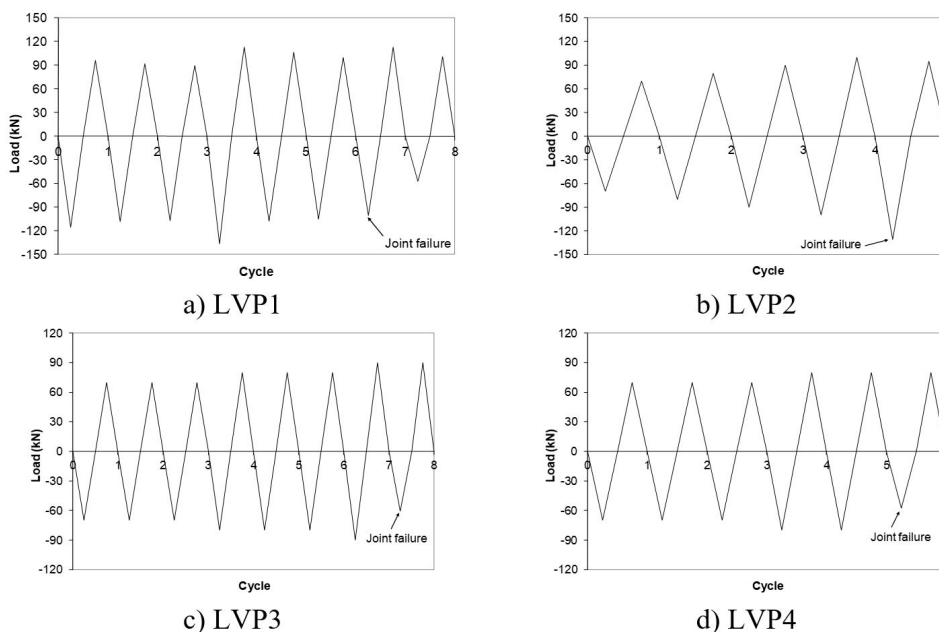


Figure 12. Loading history at the last stage of loading - Alva [13]

In all connections, the failure occurred by crushing the diagonal strut due to beam-column joint shear forces. In the connections LVP1 and LVP2, the connection failure occurred with yielding of the beam flexural reinforcement. In the connections LVP3 and LVP4, the failure of the connection occurred without the yielding of the beam flexural reinforcement. Further information about the experimental investigation is found in Alva [13] and Alva and El Debs [8].

To obtain the relative rotations between beam and column, horizontal displacement transducers were used, as shown in Figure 13.

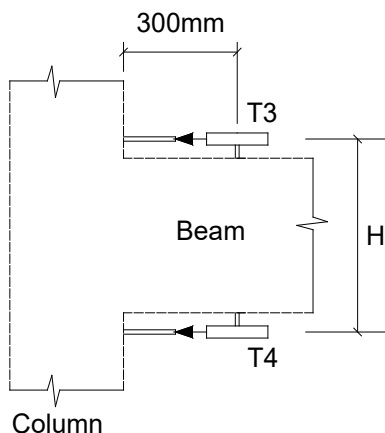


Figure 13. Displacement transducers used to evaluate relative rotations - Alva [13]

In this case the relative rotation is calculated by:

$$\theta = \frac{\delta_3 - \delta_4}{H} \tag{44}$$

where  $\delta_3$  and  $\delta_4$  are the displacements measured by the transducers T3 and T4 and  $H$  is the distance between the transducers.

According to Figure 13, the length  $L_p$  to be used in Alva and El Debs [8] model is equal to 300 mm (see transducers position in relation to the column face).

The moment-rotation curves of the connections tested by Alva [13] are shown in Figures 14 to 17 for the two stages of loading mentioned.

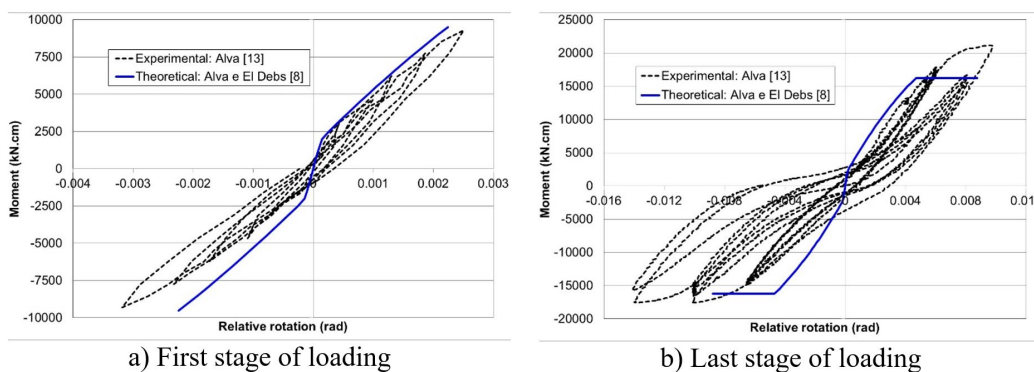


**Figure 14.** Experimental and theoretical moment-rotation curves for LVP1 - Alva [13]

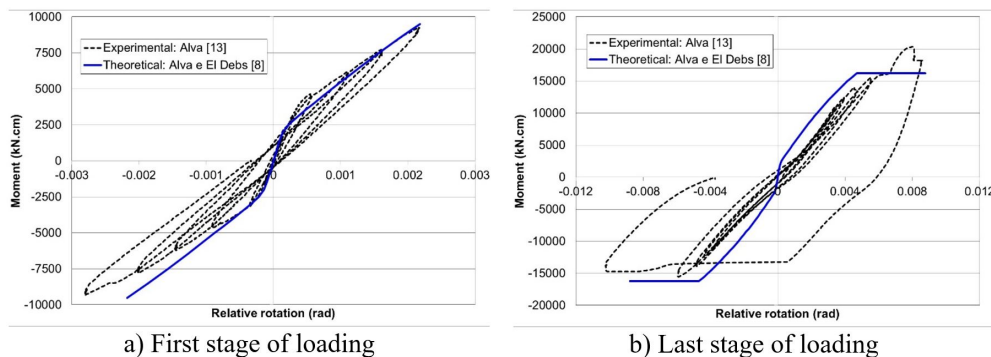


**Figure 15.** Experimental and theoretical moment-rotation curves for LVP2 - Alva [13]

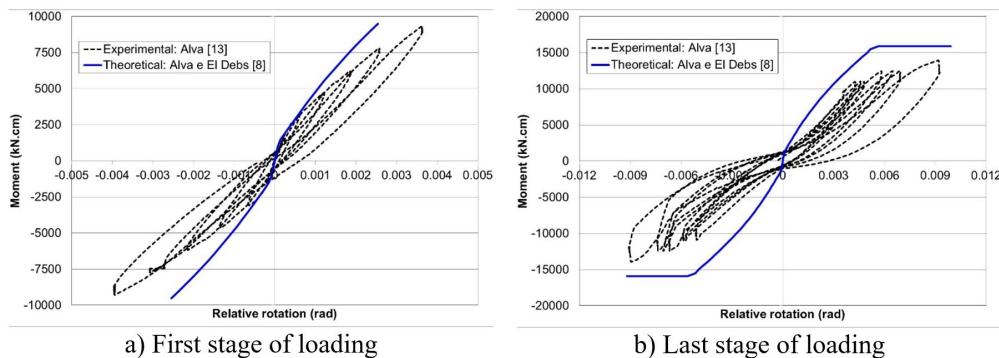


**Figure 16.** Experimental and theoretical moment-rotation curves for LVP3 - Alva [13]

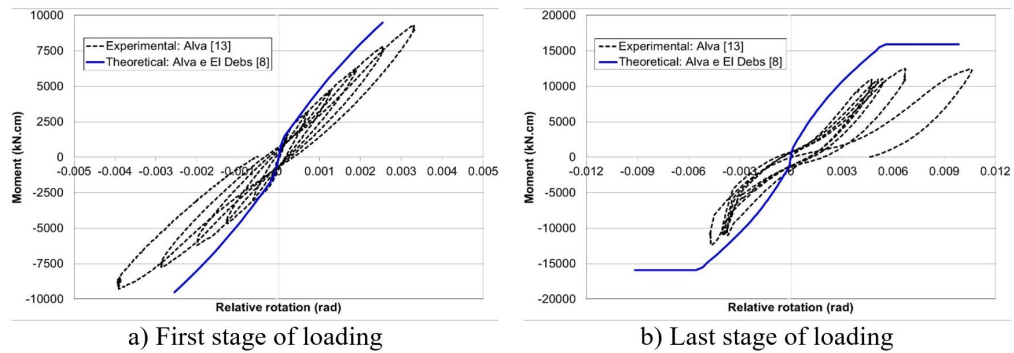


**Figure 17.** Experimental and theoretical moment-rotation curves for LVP4 - Alva [13]

In a general way, it can be concluded that Alva and El Debs [8] analytical model simulates satisfactorily the bending deformability of the connections. For the second loading stage of the connections LVP3 and LVP4, the results provided by the analytical model were less satisfactory, since the shear joint failure did not allow the connection to reach the yielding moment of the beams.

**5.2 Beam-column connections: Lee et al. [14]**

Lee et al. [14] presented experimental results of beam-column connections subjected to seismic loads. Specimen 2 and Specimen 5 were chosen for comparison with the theoretical results. Figure 18 illustrates the structural model used to obtain the theoretical force-displacement curves using the finite element software ANSYS. The moment-rotation behavior of the beam-column connections was simulated by nonlinear springs, using the COMBIN39 element. The joint region was simulated with rigid offsets. Beams and columns were discretized and represented by frame elements, using the finite element BEAM188, which allows the consideration of material nonlinearity by moment-curvature relationships. The points of the moment-curvature curves were obtained by the formulation presented in item 4. The iterative incremental Newton-Raphson method was used for the numerical solution of the nonlinear problem, with convergence criteria based on the residual forces and moments.

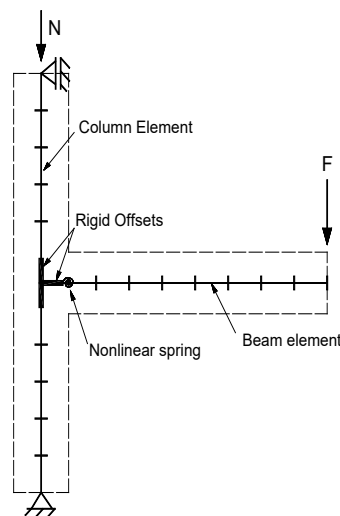


**Figure 18.** Structural model for obtaining the theoretical curves - Lee et al. [14]

Figure 19 contains the theoretical force-displacement curves (fully rigid and deformable connections) and the experimental curve for the first loading cycle. It can be seen from the referred curves that the consideration of the bending deformability led to significantly better results than those obtained by the hypothesis of a fully rigid connection.

There are no experimental results from moment-rotation curves in Lee et al. [14]. Thus, the experimental relative rotations between beam and column were obtained indirectly from the experimental displacements, according to Equation 45:

$$\theta = \frac{\delta_{exp} - \delta_{teor}}{L} \tag{45}$$

where

$\delta_{exp}$  is the experimental displacement at the beam end at the loading point;

$\delta_{teor}$  is the theoretical displacement at the beam end obtained by the hypothesis of fully rigid connection;

$L$  is the distance from the load application point at the beam end to the face of the column.

Figure 20 contains the experimental moment-rotation curves (obtained indirectly by Equation 45) and the curves obtained using Alva and El Debs [8] analytical model. The comparison of results reveals that the analytical model simulates in a very satisfactory way the bending deformability of the beam-column connections.

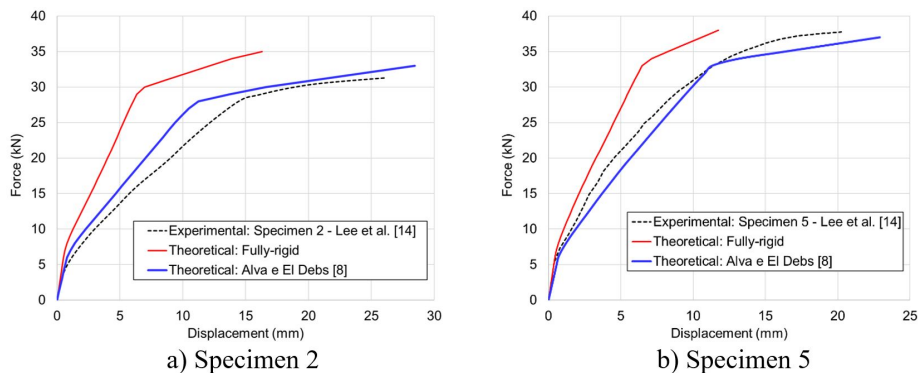


Figure 19. Experimental and theoretical force-displacement curves - Lee et al. [14]

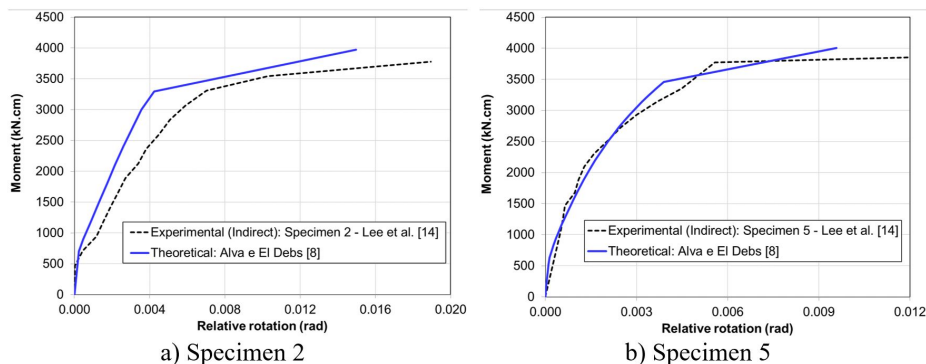


Figure 20. Experimental and theoretical moment-rotation curves - Lee et al. [14]

## 6 FINAL CONSIDERATIONS AND CONCLUSIONS

This paper dealt with the question of the deformability of reinforced concrete monolithic beam-column connections in the nonlinear analysis of framed reinforced concrete structures. To consider the deformability under bending moment, Alva and El Debs [8] analytical model was used. To consider the material nonlinearity of structural elements, moment-curvature relationships were used. The entire formulation of the constitutive models was deduced and presented, to allow the implementation of these models in computational procedures.

The numerical simulations carried out in this paper prove that taking into account the bending deformability of the connections leads to significantly better results than the hypothesis of fully rigid connections, even in the case of monolithic connections. In addition, Alva and El Debs [8] model proved to be suitable for use in structural models that employ moment-curvature relationships in nonlinear analysis of reinforced concrete frames.

## ACKNOWLEDGEMENTS

To CNPq for the financial support to the first author (Process: 308720/2018-0). To CAPES for the financial support to the second author (Process: 1769743).

## REFERENCES

- [1] Associação Brasileira de Normas Técnicas, *Projeto de Estruturas de Concreto – Procedimento*, NBR 6118, 2014.
- [2] P. Paultre, D. Castele, S. Rattray, and D. Mitchell, "Seismic response of reinforced concrete frame subassemblages – a Canadian code perspective," *Can. J. Civ. Eng.*, vol. 16, no. 5, pp. 627–649, 1989, <http://dx.doi.org/10.1139/189-097>.
- [3] H. Sezen and J. Moehle, "Bond-slip behavior of reinforced concrete members," in *Proc. Fib Symp. (CEB-FIP) – Concr. Struct. Seismic Reg.*, 2003, pp. 1-10.
- [4] H. Sezen and E. Setzler, "Reinforcement slip in reinforced concrete columns," *ACI Struct. J.*, vol. 105, no. 3, pp. 280–289, 2008.
- [5] H. Kwak and S. Kim, "Simplified monotonic moment-curvature relation considering fixed-end rotation and axial force effect," *Eng. Struct.*, vol. 32, no. 1, pp. 69–79, 2010, <http://dx.doi.org/10.1016/j.engstruct.2009.08.017>.
- [6] M. Ferreira, M. El Debs, and K. Elliott, "Determinação analítica da relação momento-rotação em ligações viga-pilar de estruturas pré-moldadas de concreto," in *An. Simp. EPUSP Estrut. Concr.*, 2003, pp. 1-20.
- [7] G. Alva, M. Ferreira, and A. El Debs, "Partially restrained beam-column connections in reinforced concrete structures," *Ibracon Struct. Mater. J.*, vol. 2, no. 4, pp. 356–379, 2009., <http://dx.doi.org/10.1590/S1983-41952009000400004>.
- [8] G. Alva and A. El Debs, "Moment–rotation relationship of RC beam-column connections – experimental tests and analytical model," *Eng. Struct.*, vol. 56, pp. 1427–1438, 2013, <http://dx.doi.org/10.1016/j.engstruct.2013.07.016>.
- [9] European Committee for Standardization, *Design of Concrete Structures – Part 1: General Rules and Rules for Building*, Eurocode 2, 2004.
- [10] G. Alva, "Formulação analítica para a determinação de diagramas momento-curvatura em seções de concreto armado retangulares submetidas à flexão normal composta," in *An. 59° Congr. Bras. Concr.*, 2017, pp. 1-16.
- [11] L. I. Torres, F. López-Almansa, and L. Bozzo, "Tension-stiffening model for cracked flexural concrete members," *J. Struct. Eng.*, vol. 130, no. 8, pp. 1242–1251, 2004, [http://dx.doi.org/10.1061/\(ASCE\)0733-9445\(2004\)130:8\(1242\)](http://dx.doi.org/10.1061/(ASCE)0733-9445(2004)130:8(1242)).
- [12] D. Branson, *Instantaneous and Time-dependent Deflections of Simple and Continuous Reinforced Concrete Beams* (HPR Publication 7 part 1). Alabama: Alabama High. Depart., U. S. Bur. Publ. Roads, 1965, pp. 1-78.
- [13] G. Alva, "Estudo teórico-experimental do comportamento de nós de pórtico de concreto armado submetidos a ações cíclicas," Ph.D. dissertation, Esc. Eng. São Carlos, Univ. São Paulo, São Carlos, 2004. [Online]. Available: <http://www.teses.usp.br>
- [14] L. Lee, J. Wight, and R. Hanson, "RC beam-column joints under large load reversals," *J. Struct. Div.*, vol. 103, no. 12, pp. 2337–2350, 1977.

---

**Author contributions:** Gerson Alva (G.A.): conceptualization, data curation, formal analysis, investigation, methodology, validation, writing. Alexandre Tsutake (A.T.): investigation, methodology, validation, writing.

**Editors:** Osvaldo Luís Manzoli, José Luiz Antunes de Oliveira e Sousa, Guilherme Aris Parsekian.